https://doi.org/10.15388/vu.thesis.112
https://orcid.org/0000-0003-3625-198X

VILNIUS UNIVERSITY
CENTER FOR PHYSICAL SCIENCES AND TECHNOLOGY

Augustas
VAITKEVIČIUS

Oxide materials as efficient, radiation tolerant and fast scintillators

DOCTORAL DISSERTATION

Natural Sciences,
Physics (N 002)

VILNIUS 2020

This dissertation was written between 2015 and 2019 at the Institute of Photonics and Nanotechnology, Vilnius University.
The research was supported by the Research Council of Lithuania: scholarships for academical accomplishments (DOK- 17470 and P-DAP-18-327).

Academic supervisor:

Prof. Habil. dr. Gintautas Tamulaitis (Vilnius University, Natural Sciences, Physics – N 002).

Dissertation Defense Panel:
Chairman – Prof. dr. Vincas Tamošiūnas (Vilnius University, Natural Sciences, Physics – N 002).

Members:
Dr. Tomas Čeponis (Vilnius University, Technological Sciences, Materials Engineering – T 008);
Dr. Andrius Devižis (Center for Physical Sciences and Technology, Natural sciences, Physics – N 002);
Dr. Vitali Nagirnyi (University of Tartu, Natural sciences, Physics – N 002);
Doc. dr. Artūras Plukis (Center for Physical Sciences and Technology, Natural sciences, Physics – N 002).

The dissertation will be defended at a public meeting of the Dissertation Defense Panel at 2 p.m. on the 11th of December 2020, in the A101 auditorium of the National Center for Physical Sciences and Technology.

Address: Saulėtekio av. 3, LT-10257, Vilnius, Lithuania, tel. +37052648884; e-mail: office@ftmc.lt.

The text of this dissertation can be accessed at the libraries of Vilnius University and the Center for Physical Sciences and Technology, as well as on the website of Vilnius University:
www.vu.lt/lt/naujienos/ivykiu-kalendorius

https://doi.org/10.15388/vu.thesis.112
https://orcid.org/0000-0003-3625-198X

VILNIAUS UNIVERSITETAS
FIZINIŲ IR TECHNOLOGIJOS MOKSLŲ CENTRAS

Augustas
VAITKEVIČIUS

Efektyvūs, radiacijai atsparūs ir spartūs oksidiniai scintiliatoriai

DAKTARO DISERTACIJA

Gamtos mokslai,
Fizika (N 002)

VILNIUS 2020

Disertacija rengta 2015 – 2019 metais Vilniaus universiteto Fotonikos ir nanotechnologijų institute.
Mokslinius tyrimus rėmė Lietuvos mokslo taryba: stipendijos už akademinius pasiekimus (DOK- 17470 ir P-DAP-18-327).

Mokslinis vadovas:
Prof. habil. dr. Gintautas Tamulaitis (Vilniaus universitetas, gamtos mokslai, fizika – N 002).

Gynimo taryba:
Pirmininkas – prof. dr. Vincas Tamošiūnas (Vilniaus universitetas, gamtos mokslai, fizika – N 002).
Nariai:
Dr. Tomas Čeponis (Vilniaus universitetas, technologiniai mokslai, medžiagų inžinerija – T 008);
Dr. Andrius Devižis (Fizinių ir technologinių mokslų centras, gamtos mokslai, fizika – N 002);
Dr. Vitali Nagirnyi (Tartu universitetas, gamtos mokslai, fizika – N 002);
Doc. dr. Artūras Plukis (Fizinių ir technologinių mokslų centras, gamtos mokslai, fizika – N 002),

Disertacija ginama viešame Gynimo tarybos posėdyje 14h, gruodžio 12 d. 2020 m. Nacionalinio fizinių ir technologijos mokslų centro A101 auditorijoje. Adresas: Saulėtekio al. 3, LT-10257, Vilnius, Lietuva, tel. +37052648884; el. paštas office@ftmc.lt.

Disertaciją galima peržiūrėti Vilniaus universiteto ir Fizinių ir technologijos mokslų centro bibliotekose ir Vilniaus universiteto interneto svetainėje adresu: *https://www.vu.lt/naujienos/ivykiu-kalendorius*

Acknowledgements

I would like to thank my family, friends and colleagues without whose support this dissertation would not have happened. First of all, I was fortunate to have prof. Gintautas Tamulaitis as my supervisor, who despite my meandering performance during my undergraduate years still encouraged me to pursue a career in science. Only thanks to his supervision and mentoring I have managed to reach this far.

I also can not thank enough all the people at the Institute of Photonics and Nanotechnology at Vilnius University: Dr. Saulius Nargelas for all the hard work he put in that made this PhD project possible, Dr. Jūras Mickevičius and Dr. Darius Dobrovolskas for continous mentoring from my first days at the Semiconductor Physics Department and even now, Dr. Jonas Jurkevičius and Dr. Ramūnas Aleksiejūnas for all the fruitful discussions about physics and other important sides of life.

I am also grateful to Dr. Mikhail Korjik and Dr. Etienette Auffray for allowing me to reach out to the wider world of international science and participate in projects at CERN.

I would like to thank my parents, my girlfriend and the wonderful community of Tolkien Lietuva for supporting me through these years.

Contents

LIST OF ABBREVIATIONS

BGO	Bismuth germanate
CCD	Charge-coupled device
CT	Charge transfer
CTR	Coincidence time resolution
DA	Differential absorption
DOS	Density of states
FCA	Free carrier absorption
FTD	Frenkel type defect
FWHM	Full width at half maximum
GAGG	Gadolinium Aluminum Gallium Garnet
LED	Light emitting diode
LSO	Lutetium orthosilicate
LYSO	Lutetium Yttrium orthosilicate
PET	Positron emission tomography
PDE	Photon detection efficiency
PL	Photoluminescence
PWO	Lead Tungstate
REI	Rare earth ions
RT	Room temperature
SiPM	Silicon photo-multiplier
TA	Transient absorption
TOF-PET	Time of flight positron emission tomography
TSL	Thermally stimulated luminescence
XRD	X-ray diffraction
V_c	Cation vacancy
V_o	Oxygen vacancy
V_{Pb}	Lead vacancy
$I(\lambda)$	Intensity of probe beam
E_{TA}	Thermal activation energy
E_g	Band gap energy
E_{TA}	Thermal activation energy
E_{irr}	Irradiation energy

INTRODUCTION

In view of the goal for substantially better timing properties of radiation detectors with the ambitious target of 10 ps time resolution put forward by Crystal Clear Collaboration at CERN, the excitation transfer in scintillating materials has become a hot topic. Up to now, the luminescence decay time was considered to be the key parameter limiting the response time of scintillating material. However, the rise time of the luminescence response becomes increasingly important as the time resolution has recently improved: the coincidence time resolution below 100 ps FWHM has already been reached in laboratory conditions by several research groups.

The luminescence rise edge can be studied with a subpicosecond time resolution after short-pulse optical excitation. However, the energy of photons used in optical excitation (below 6 eV in conventional instrumentation) is too small to imitate the excitation by X-rays or gamma quanta and is useful for characterization of only the final stages of excitation transfer and carrier recombination. Time-resolved cathodoluminescence ensures generation of high-energy electron-hole pairs, however, the time resolution in such experiments is limited at least by the electron beam pulse width, typically 200 ps. The time resolution in the luminescence spectroscopy of scintillators by exploitation of high-energy quanta of pulsed synchrotron radiation is also basically limited by the pulse width, which is typically above 10 ps, e.g., 50 ps in SUPERLUMI station at HASYLAB, DESY. The experimental schemes exploiting a gamma source and two scintillation detectors operated in start-stop configuration enable a good time resolution evidenced by resolution of the fast response spike due to Cherenkov radiation but suffer from difficulties due to a very long measuring time of approximately a day for each measurement to collect the acceptable signal statistics.

We suggest characterizing the processes limiting the luminescence rise time by exploiting the differential optical absorption in pump and probe configuration. The time resolution of this technique is limited just by the pulse width of the laser used in the experiment, thus, could be in the subpicosecond domain. Due to the limited capability of upconversion of the laser output photon energy deep into UV (maximal photon energy for pump photon in our experiments was 5.9 eV) this technique enables studying only the final stages of excitation transfer and carrier relaxation and recombination. However, selective excitation into specific energy levels enabled by tuneable pump photon energy and capability to follow the time evolution of the spectrum of differential absorption offer high flexibility in studying the dynamics of nonequilibrium population of free and localized states in the crystal.

From the point of view of the fast excitation transfer to the activator ions, it is important that scintillating materials usually contain considerable concentration of trapping centers with the thermal activation energy comparable to the thermal energy at room temperature. The traps are formed due to certain impurities and structural defects. In multicomponent crystals, the carriers might also be localized in the minima of the potential fluctuations due to the band gap modulation caused by fluctuations in composition. This kind of carrier trapping is an increasingly important research topic, since multicomponent scintillators are prospective for different reasons. For example, Ce-doped Lu_2SiO_5 (LSO:Ce) has a prospective combination of scintillation properties but is quite expensive due to the high price of lutetium. Substitution of a part of Lu atoms by substantially less expensive yttrium deteriorates the scintillation properties of the crystal not substantially. Therefore, exploitation of $Lu_{2(1-x)}Y_{2x}SiO_5$:Ce (LYSO:Ce) instead of LSO:Ce is acceptable, especially, in the applications requiring large volumes of scintillating materials like in large-scale high-energy physics experiments. Cerium-doped garnet-type scintillators is another example of multicomponent scintillators with promising prospective for applications in high-energy physics and medical imaging. The selection of garnets with multicomponent composition is attractive due to possibility to apply band gap engineering and engineering of the position of activator level within the band gap. In particular, introduction of gallium decreases the band gap of gadolinium aluminum gallium garnet $Gd_3A_{l2}Ga_3O_{12}$ (GAGG), so that shallow traps for electrons are buried in the conduction band. Meanwhile, gadolinium in Ce-doped GAGG changes the crystal field in the sites occupied by Ce^{3+} ions and lowers the position of the first excited level $5d^1$ Ce^{3+} ion, so that the level separation from the bottom of the conduction band is sufficiently large to efficiently prevent the thermal ionization of the excited state at room temperature. The multicomponent scintillators might compile the best features of the constituent compounds like in $Y(Nb_xTa_{1-x})O_4$ crystals by combining an efficient emission in NbO_4 with a high density of TaO_4 and exhibiting the intensity of exciton emission (under interband excitation for composition at $x = 0.4$), which is superior to that of the constituents $YTaO_4$ and $YNbO_4$. Thus, at least several multicomponent scintillators are currently prospective in applications. Consequently, studying the carrier trapping in these materials is scientifically interesting and practically important. In the current study, the carrier relaxation and trapping in Ce-doped GAGG and LYSO were investigated.

Main Goal

Revealing processes of excitation transfer in scintillating materials, which are important for developing efficient, radiation tolerant detectors of ionizing radiation with targeted time resolution of 10 ps.

Objectives of the study were to:

1. analyze the key properties of scintillating materials prospective for fast radiation detectors with time resolution of the order of a few tens of picoseconds;
2. adapt the capabilities of nonlinear optical absorption technique in pump and probe configuration for studying carrier dynamics in self-activated and Ce-doped scintillators;
3. reveal correlation between characteristics of carrier dynamics obtained by nonlinear optics techniques with the parameters determining the time resolution in coincidence time resolution technique using gamma-quanta;
4. compare Ce-doped LSO, LYSO, GAGG and other high-light-yield scintillators in view of their application in fast radiation detectors;
5. search for novel prospective scintillators and phosphors based on ceramic materials.

Novelty and importance

The upcoming experiments in high-energy physics require the time resolution of scintillation detectors of the order of 10 ps. This is not feasible using the conventional scintillation detectors with the time response limited by the time of carrier recombination at the radiative recombination centers in the scintillator material. Several novel ways to substantially improve the response time of the scintillation detectors are investigated in this thesis.

Using the phenomena occurring in parallel with the carrier relaxation within the very first picoseconds after the ionization starts is the most novel approach in study of timing properties of scintillators. One of the phenomena is the elastic polarization due to the local lattice distortion caused by the displacements of electrons and holes generated by the ionization. This local distortion in the lattice results in redistribution of the density of electron states of in the conduction band in close vicinity of the hole. The key feature of the elastic polarization is its short response time, which makes it prospective for using as an optically detectable time mark. Nonlinear optical absorption of femtosecond light pulses at appropriate wavelength is considered to be a tool to form the mark.

Searching for inorganic crystalline media exhibiting a fast scintillation response as well as strong non-linear absorption of ultra-short laser pulses were targeted as the second research direction. Accordingly, we selected several scintillation crystals: self-activated lead tungstate $PbWO_4$, mixed gadolinium garnet ($Gd_3(Ga_{0.5}Al_{0.5})_5O_{12}$:Ce, GAGG) and lutetium oxyorthosilicates (Lu_2SiO_5:Ce, LSO) as well as scintillating glass ceramics. The latter is a novel class of materials, favored for its low price and easy production techniques, however it in the early stages of development and a lot of attention has to be focused on structural properties and choice of production technique. Meanwhile, lead tungstate is currently the most extensively used scintillation material in high energy physics experiments, while the recently developed mixed garnet crystals showed fast response and high light yield up to 56000 ph/MeV. Due to a high light yield of up to 50000 phot/MeV, a short luminescence decay time (< 100 ns), and good matching of the emission band with the sensitivity spectrum of conventional SiPMs, Ce doped $Gd_3Al_2Ga_3O_{12}$ crystalline material (GAGG) is a promising scintillation material for medical imaging and might compete with Ce-doped Lu_2SiO_5 crystal for PET application. Moreover, GAGG:Ce, co-doped with Mg, shows spectacular time resolution at different excitation. GAGG is dense high light yield scintillator, hence, it can be applied for a high resolution radiation spectrometry similar to recently developed halide scintillators.

Thesis statements

I. A fast luminescence decay component with characteristic decay time of ~5 ps has been discovered in lead tungstate scintillator.

II. Aliovalent codoping of cerium-activated garnet or oxyorthosilicate scintillators reduces the effect of electron trapping and accelerates the luminescence rise time down to the subpicosecond domain even at doping levels as low as 5 ppm.

III. Intracenter relaxation time in trivalent cerium ion acting as activator in garnet-type scintillators has been determined to be 500 fs, substantially shorter than the time of excitation transfer limiting the luminescence response time of these scintillating materials.

Thesis layout

The main goal, objectives as well as novelty and importance are laid out in the introduction of the thesis.

A brief overview of experimental techniques and samples under study is provided in the beginning of the thesis, in Chapter I.

A review of literature regarding typical self-activated emitters, such as PWO, and cerium-activated materials, specifically garnets and orthosilicates, their crystal structure, excitation transfer processes and luminescence dynamics is given in Chapter II.

Chapter III is dedicated to presenting and discussing the results obtained. It is divided in to four parts.

The first part is dedicated to discussing the results on self-activated scintillators, namely PWO.

The second part describes the properties of novel orthosilicate scintillators doped with cerium. Mechanisms of charge transfer through the crystal lattice to cerium ions are discussed as well as other factors influencing the emission of cerium ions.

The third part presents the results on cerium doped garnet scintillators. Special attention is given to gadolinium aluminum gallium garnets. Analyses of nonequilibrium carrier dynamics and a comparison between experimental and numerical modeling results are presented.

The last part of chapter III reports on the results on amorphous and glass ceramic scintillators. Due to a wide range of application of this type of materials, properties relevant to scintillation and white light LEDs are investigated.

Results of the thesis are summarized with concluding statements in Chapter IV.

LIST OF PUBLICATIONS

On the dissertation topic

P1. E. Auffray, O. Buganov, M. Korjik, A. Fedorov, S. Nargelas, G. Tamulaitis, S. Tikhomirov, **A. Vaitkevičius**, Application of two-photon absorption in PWO scintillator for fast timing of interaction with ionizing radiation, Nucl. Instruments Methods Phys. Res. Sect. A Accel. Spectrometers, Detect. Assoc. Equip. 804 (2015) 194–200. doi:10.1016/j.nima.2015.09.017.

P2. M.V. Korjik, **A. Vaitkevičius**, D. Dobrovolskas, E.V. Tret'yak, E. Trusova, G. Tamulaitis, Distribution of luminescent centers in Ce3+-ion doped amorphous stoichiometric glass BaO–2SiO$_2$ and dedicated glass ceramics, Opt. Mater. (Amst). 47 (2015) 129–134. doi:10.1016/j.optmat.2015.07.014.

P3. E. Auffray, M. Korjik, M.T. Lucchini, S. Nargelas, O. Sidletskiy, G. Tamulaitis, Y. Tratsiak, **A. Vaitkevičius**, Free carrier absorption in self-activated PbWO$_4$ and Ce-doped Y$_3$(Al$_{0.25}$Ga$_{0.75}$)$_3$O$_{12}$ and Gd$_3$Al$_2$Ga$_3$O$_{12}$ garnet scintillators, Opt. Mater. (Amst). 58 (2016) 461–465. doi:10.1016/j.optmat.2016.06.040.

P4. E. Auffray, R. Augulis, A. Borisevich, V. Gulbinas, A. Fedorov, M. Korjik, M.T. Lucchini, V. Mechinsky, S. Nargelas, E. Songaila, G. Tamulaitis, **A. Vaitkevičius**, S. Zazubovich, Luminescence rise time in self-activated PbWO$_4$ and Ce-doped Gd$_3$Al$_2$Ga$_3$O$_{12}$ scintillation crystals, J. Lumin. 178 (2016) 54–60. doi:10.1016/j.jlumin.2016.05.015.

P5. Y. Tratsiak, Y. Bokshits, A. Borisevich, M. Korjik, **A. Vaitkevičius**, G. Tamulaitis, Y$_2$CaAlGe(AlO$_4$)$_3$:Ce and Y$_2$MgAlGe(AlO$_4$)$_3$:Ce garnet phosphors for white LEDs, Opt. Mater. (Amst). 67 (2017) 108-112. doi: 10.1016/j.optmat.2017.03.047

P6. M. V Korjik, E. Auffray, O. Buganov, A.A. Fedorov, I. Emelianchik, E. Griesmayer, V. Mechinsky, S. Nargelas, O. Sidletskiy, G. Tamulaitis, S.N. Tikhomirov, **A. Vaitkevičius**, Non-Linear Optical Phenomena in Detecting Materials as a Possibility for Fast Timing in Detectors of Ionizing Radiation, IEEE Trans. Nucl. Sci. 63 (2016) 2979–2984. doi:10.1109/TNS.2016.2617461.

P7. G. Tamulaitis, **A. Vaitkevičius**, S. Nargelas, R. Augulis, V. Gulbinas, P. Bohacek, M. Nikl, A. Borisevich, A. Fedorov, M. Korjik, E. Auffray, Subpicosecond luminescence rise time in magnesium codoped GAGG:Ce scintillator, Nucl. Instruments Methods Phys. Res. Sect. A

Accel. Spectrometers, Detect. Assoc. Equip. 870 (2017) 25–29. doi:10.1016/j.nima.2017.07.015.

P8. M. Korjik, V. Alenkov, A. Borisevich, O. Buzanov, V. Dormenev, G. Dosovitskiy, A. Dosovitskiy, A. Fedorov, D. Kozlov, V. Mechinsky, R.W. Novotny, G. Tamulaitis, V. Vasiliev, H.-G. Zaunick, **A. Vaitkevičius**, Significant improvement of GAGG:Ce based scintillation detector performance with temperature decrease, Nucl. Instruments Methods Phys. Res. Sect. A Accel. Spectrometers, Detect. Assoc. Equip. 871 (2017) 42–46. doi:10.1016/j.nima.2017.07.045.

P9. E. Auffray, R. Augulis, A. Fedorov, G. Dosovitskiy, L. Grigorjeva, V. Gulbinas, M. Koschan, M. Lucchini, C. Melcher, S. Nargelas, G. Tamulaitis, **A. Vaitkevičius**, A. Zolotarjovs, M. Korzhik, Excitation Transfer Engineering in Ce-Doped Oxide Crystalline Scintillators by Codoping with Alkali-Earth Ions, Phys. Status Solidi Appl. Mater. Sci. 215 (2018) 1–10. doi:10.1002/pssa.201700798.

P10. E. Trusova, **A. Vaitkevičius**, Y. Tratsiak, M. Korjik, P. Mengucci, D. Rinaldi, L. Montalto, V. Marciulionyte, G. Tamulaitis, Barium and lithium silicate glass ceramics doped with rare earth ions for white LEDs, Opt. Mater. (Amst). 84 (2018) 459–465. doi:10.1016/j.optmat.2018.07.030.

P11. G. Tamulatis, G. Dosovitskiy, A. Gola, M. Korjik, A. Mazzi, S. Nargelas, P. Sokolov, **A. Vaitkevičius**, Improvement of response time in GAGG: Ce scintillation crystals by magnesium codoping, J. Appl. Phys. 124 (2018) 215907. doi:10.1063/1.5064434.

P12. M.T. Lucchini, O. Buganov, E. Auffray, P. Bohacek, M. Korjik, D. Kozlov, S. Nargelas, M. Nikl, S. Tikhomirov, G. Tamulaitis, A. **Vaitkevičius**, K. Kamada, A. Yoshikawa, Measurement of non-equilibrium carriers dynamics in Ce-doped YAG, LuAG and GAGG crystals with and without Mg-codoping, J. Lumin. 194 (2018) 1–7. doi:10.1016/j.jlumin.2017.10.005.

P13. Y. Tratsiak, E. Trusova, Y. Bokshits, M. Korjik, **A. Vaitkevičius**, G. Tamulaitis, Garnet-type crystallites, their isomorphism and luminescence properties in glass ceramics, CrystEngComm. 21 (2019) 687–693. doi:10.1039/C8CE01547C.

P14. M. Korzhik, A. Gola, J. Houžvička, A. Mazzi, S. Nargelas, S. Sýkorová, G. Tamulaitis, A. Vaitkevičius, S. Sykorová, G. Tamulaitis, **A. Vaitkevičius**, Timing properties of Ce-doped YAP and LuYAP scintillation crystals, Nucl. Instruments Methods Phys. Res. Sect. A Accel. Spectrometers, Detect. Assoc. Equip. 927 (2019) 169–173. doi:10.1016/j.nima.2019.02.036.

P15. G. Tamulaitis, A.N. Vasil’ev, M. Korzhik, A. Mazzi, A. Gola, S. Nargelas, **A. Vaitkevicius**, A. Fedorov, D. Kozlov, Improvement of the time resolution of radiation detectors based on $Gd_3Al_2Ga_3O_{12}$ scintillators with SiPM readout, IEEE Trans. Nucl. Sci. 66 (2019) 1879–1888. doi:10.1109/TNS.2019.2919898.

P16. E. Auffray, G. Dosovitskiy, A. Fedorov, I. Guz, M. Korjik, N. Kratochwill, M. Lucchini, S. Nargelas, D. Kozlov, V. Mechinsky, P. Orsich, O. Sidletskiy, G. Tamulaitis, **A. Vaitkevičius**, Irradiation Effects on $Gd_3Al_2Ga_3O_{12}$ Scintillators Prospective for Application in Harsh Irradiation Environments, Radiat. Phys. Chem. 164 (2019) 108365. doi:10.1016/j.radphyschem.2019.108365.

P17. G. Tamulaitis, E. Auffray, A. Gola, M. Korzhik, A. Mazzi, V. Mechinski, S. Nargelas, Y. Talochka, **A. Vaitkevičius**, A. Vasil'ev, Improvement of the timing properties of Ce-doped oxyorthosilicate LYSO scintillating crystals, J. Phys. Chem. Solids. 139 (2020) 109356. doi:10.1016/j.jpcs.2020.109356.

P18. M. Korzhik, V. Alenkov, O. Buzanov, G. Dosovitskiy, A. Fedorov, D. Kozlov, V. Mechinsky, S. Nargelas, G. Tamulaitis, **A. Vaitkevičius**, Engineering of a new single-crystal multi-ionic fast and high-light-yield scintillation material $(Gd_{0.5}\text{-}Y_{0.5})_3Al_2Ga_3O_{12}$:Ce,Mg, CrystEngComm. 22 (2020) 2502–2506. doi:10.1039/D0CE00105H.

Other

P19. V. Kononets, O. Benamara, G. Patton, C. Dujardin, S. Gridin, a. Belsky, D. Dobrovolskas, **A. Vaitkevičius**, G. Tamulaitis, V. Baumer, K. Belikov, O. Sidletskiy, K. Lebbou, Growth of Ce-doped LGSO fiber-shaped crystals by the micro pulling down technique, J. Cryst. Growth. 412 (2015) 95–102. doi:10.1016/j.jcrysgro.2014.11.036.

P20. D. Dobrovolskas, J. Mickevičius, S. Nargelas, **A. Vaitkevičius**, Y. Nanishi, T. Araki, G. Tamulaitis, Influence of defects and indium distribution on emission properties of thick In-rich InGaN layers grown by the DERI technique, Semicond. Sci. Technol. 32 (2017) 25012. doi:doi:10.1088/1361-6641/32/2/025012.

Conference presentations

1. G. Tamulaitis, E. Auffray, R. Augulis, O. Buganov, A. Fedorov, V. Gulbinas, M. Korjik, M.T. Lucchini, V. Mechinsky, S. Nargelas, E. Songaila, S. Tikhomirov, **A. Vaitkevičius**, Fast optical phenomena in self-activated and Ce-doped materials prospective for fast timing in radiation detectors, Book of Abstracts of the Fifth International Conference "Engineering of Scintillation Materials and Radiation

Technologies", ISMART 2016, September 26-30, 2016, Minsk, Belarus, p.121. (Invited)

2. G. Tamulaitis, E. Auffray, R. Augulis, A. Fedorov, V. Gulbinas, M. Korjik, M.T. Lucchini, V. Mechinsky, S. Nargelas, E. Songaila, **A. Vaitkevičius**, Fast luminescence response in self-activated and Ce-doped scintillation materials, 2016 IEEE Nuclear Science Symposium, Strasbourg, France, 29 October – 5 November, 2016 (oral).
3. **A.Vaitkevičius**, J.Mickevičius, D.Dobrovolskas, H.Svidras, G.Tamulaitis, B.Foltynski, C.Giesen, and M.Heuken, "Photoluminescence inhomogeneity in InGaN/GaN core-shell multiple quantum wells on self-organized GaN rods grown on silicon", Program of the E-MRS 2016 Fall Meeting, September 19-22, 2016, Warsaw, Poland, p. E-P2.4
4. **A. Vaitkevičius**, M. Korjik, E. Tretyak, E. Trusova, G. Tamulaitis, Photoluminescence of Barium and Lithium Silicate Glasses and Glass Ceramics Doped with Rare Earth Ions, ICGST, October 10-11, 2016, New York, USA.
5. E. Auffray, M. Korjik, M. Lucchini, V. Mechinsky, S. Nargelas, G. Tamulaitis, **A. Vaitkevičius**, Free carrier dynamics in GAGG:Ce scintillation crystal with aliovalent cooping, IEEE 2017 Nuclear Science Symposium, 21-28 October, 2017, Atlanta, Georgia, USA.
6. G. Tamulaitis, S. Nargelas, **A. Vaitkevicius**, M. Korjik, M. Lucchini, E. Auffray, Free carrier absorption for study of fast excitation transfer in scintillation crystals, 14th International Conference on Scintillating Materials and their Applications (SCINT 2017), 18-22 September, 2017, Chamonix, France (oral)
7. **A. Vaitkevičius**, S. Nargelas, E. Tratsiak, E. Trusova, M. Korjik, G. Tamulaitis, Luminescence properties of rare earth ions in novel garnets and glasses, 14 th International Conference on Scintillating Materials and their Applications (SCINT 2017), 18-22 September, 2017, Chamonix, France.
8. **A. Vaitkevičius**, V. Marčiulionytė, E. Trusova, Y. Tratsiak, M. Korjik, G. Tamulaitis, Investigation of novel glasses and garnets doped with rare earth ions, 42nd Lithuanian National Physics Conference (LNFK-42): Program and Abstracts, 4-6 October, 2017, Vilnius, Lithuania, p. 211.
9. V. Marčiulionytė, **A. Vaitkevičius**, E. Trusova, Y. Tratsiak, M. Korjik, G. Tamulaitis, Luminescence in two-component silicate glass doped with Ce, Dy, Eu, and Tb ions for high-power white light sources, 42nd Lithuanian National Physics Conference (LNFK-42): Program and Abstracts, 4-6 October, 2017, Vilnius, Lithuania, p. 198.

10. .G. Tamulaitis, E. Auffray, M. Korjik, S. Nargelas, **A. Vaitkevicius**, Exploitation of free carrier absorption in quest for ten picosecond target for time resolution of radiation detectors, 6th International Conference on Radiation and applications in various fields of Research, June 8-22, 2018, Ohrid, Macedonia. p. 239 (oral).
11. G. Tamulaitis, S. Nargelas, **A. Vaitkevičius**, E. Auffray, M. T. Lucchini, A. Gola, A. Mazzi, C. Piemonte, M. Korjik, A. Fedorov, V. Mechinsky, O. Sidletsky, Timing properties of GAGG:Ce and LSO:Ce scintillators with and without codoping, 10th International Conference on Luminescent Detectors and Transformers of Ionizing Radiation (LUMDETR), 9-14 September 2018, Prague, Czech Republic, p. 23. (oral)
12. **A. Vaitkevičius**, S. Nargelas, G. Tamulaitis, E. Auffray, M. T. Lucchini, M. Korjik, A. Fedorov, V. Mechinsky, O. Sidletsky, Timing properties of GAGG:Ce and LSO:Ce scintillators with and without codoping, 10th International Conference on Luminescent Detectors and Transformers of Ionizing Radiation (LUMDETR), 9-14 September 2018, Prague, Czech Republic, p. 76.
13. S. Nargelas, **A. Vaitkevičius**, G. Tamulaitis, E. Auffray , M. Korjik, A. Fedorov, V. Mechinsky, O. Sidletsky, Influence of Mg codoping on excitation dynamics in GAGG:Ce scintillators, 10th International Conference on Luminescent Detectors and Transformers of Ionizing Radiation (LUMDETR), 9-14 September 2018, Prague, Czech Republic, p. 63.
14. G. Tamulaitis, S. Nargelas, **A. Vaitkevičius**, M. Lucchini, E. Auffray, A. Fedorov, V. Mechinsky, M. Korjik, “Transient phenomena in scintillation materials”, Sixth International Conference “Engineering of Scintillation Materials and Radiation Technologies” (ISMART 2018), October 9–12 2018, Minsk, Belarus. (oral)
15. S. Nargelas, **A. Vaitkevičius**, M. Lucchini, E. Auffray, A. Fedorov, V. Mechinsky, M. Korjik, G. Tamulaitis, “Transient absorption technique as a tool for characterization of scintillator timing properties”, Sixth International Conference “Engineering of Scintillation Materials and Radiation Technologies” (ISMART 2018), October 9–12 2018, Minsk, Belarus. (oral)
16. G. Tamulaitis, S. Nargelas, **A. Vaitkevicius**, V. Gulbinas, M. Korjik, D. Kozlov, V. Mechinsky, A. Gola, A. Mazzi, E. Auffray Hillemanns, M. Lucchini, C. G. Tully, Engineering of Ce-doped scintillation materials for high-energy physics experiments, IEEE Nuclear Science Symposium, 10-17 Nevember 2018, Sydney, Australia. (oral)
17. E. Auffray Hillemanns, G. Dosovitskiy, M. Korzhik, M. Lucchini, S. Nargela, A. Fedorov, D. Kozlov, V. Mechinsky, G. Tamulaitis, **A.**

Vaitkevicius, Study of mixed garnet scintillators for future particle physics experiments, IEEE Nuclear Science Symposium, 10-17 Nevember 2018, Sydney, Australia. (oral)

18. G.Tamulatis, S.Nargelas, **A.Vaitkevičius**, A.Gola, A.Mazzi, M.Korjik, Influence of Mg codoping on carrier dynamics in GAGG:Ce scintillation crystals, Seventh International Conference on Radiation in Various Fields of Research DAG7, June 10-14, 2019, Herceg Novi, Montenegro (oral)
19. **A. Vaitkevičius**, S. Nargelas, V. Marčiulionytė, V. Mechinsky, D. Petrudec, V. Slegel, V. Gulbinas, M. Korjik, G. Tamulaitis, Investigation of Self-activated PWO and BGO Scintillators in Subpicosend Domain, SCINT 2019 Conference on Scintillating Materials and their Aplications, 29 September - 4 October 2019, Sendai, Japan.

Author's contribution

The author performed all measurements of spatially resolved luminescence spectroscopy and steady-state absorption. With the support offered by the COST Action FAST, the author performed coincidence timing resolution measurements in Trento, Italy, and scintillator efficiency measurements in Giessen, Germany. The author used experimental data obtained by his colleagues to perform analysis of differential absorption and time resolved photoluminescence results and participated in all stages of manuscript preparation.

The differential absorbtion measurements were performed by dr. Saulius Nargelas (Vilnius University), the time resolved luminescence measurements were performed by the research group lead by Prof. Vidmantas Gulbinas (FTMC). The coincidence time resolution measurements were performed with the help of dr. Alberto Gola and dr. Alberto Mazzi (Fondazione Bruno Kessler, Italy).

Synthesis and structural analysis of non-crystalline scintillators and measurements involving ionizing radiation were performed by the research group led by Dr. Mikhail Korjik (Belarusian State University). Other crystalline samples were obtained in collaboration with colleagues from the Crystal Clear Collaboration at CERN.

1 LITERATURE REVIEW

1.1 Lead tungstate scintillators

Lead tungstate ($PbWO_4$, PWO) has been know at least since 1948 [1] but has not been extensively investigated until the last decade of the 20th century when it was noticed for being a good compromise between performance and cost. A strong R&D program led by the Crystal Clear Collaboration at CERN was started. The aim of that program was to improve material properties of PWO for use in a new generation of high energy physics experiments [2] [3]. PWO is a birefringent scheelite type crystal with a tetragonal unit cell [4] and belongs to the space group 88, $I4_1/a$ [5]. These crystals are typically grown by the Czochralski technique [6]. They are also non-hydroscopic and mechanically strong [2]. Additionally, PWO is noted for its radiation tolerance [7]. One downside of this material is its rather low light yield, but despite this shortcoming it has been adapted for multiple large scale high energy physics experiments, such as PANDA at GSI as well as CMS and ATLAS [8–10] at CERN. Other physical and chemical properties of PWO are given in table 1.1.1. The band gap of PWO at room temperature is 4.3-4.5 eV [11]. Thus, a defect-free PWO crystal has no optical absorption in the visible region.

Table 1.1.1. Physical and chemical properties of lead tungstate.

Density (g/cm^3)	8.3
Radiation length (cm)	0.89
Melting point (°C)	1123
Hardness (Moh)	4
Refractive index along Z axis ($\lambda = 632$ nm)	2.16

During crystal growth there are unavoidable losses of lead ions, due to a higher rate of evaporation of lead oxide in comparison to tungsten oxides, leading to formation of cation vacancies V_c on the lead site of the host. The charge balance in the crystal imposes the creation of oxygen vacancies. Intrinsic defects based on electron or hole capture by anion or cation vacancies such as F^+ (V_o+ e) and O^- (O^{2-} +h) have no energy levels in the band gap. Therefore, the only candidates for creation of color centers in irradiated PWO crystals are cation vacancies capturing two holes of the type $O^-V_cO^-$ or oxygen vacancies capturing even amounts of electrons. Such centers are deep and they are filled mostly by tunneling mechanisms. Through intense study it has been determined that scintillator mechanisms in PWO are not damaged by irradiation, when the crystals are grown in optimal conditions. This is due to the following unique features of PWO. Firstly, the regular anionic tungstate group is stable under ionizing radiation. Additionally, deep color centers do not release electrons in the conduction band when they spontaneously decay. This leads to scintillator kinetics not being affected by the accumulated dose. However, afterglow intensity can be dependent on irradiation if the concentration of V_o based defects or Mo impurities is sufficiently large. [12]

PWO is an intrinsic, self-activated scintillator. The photoluminescence spectra of PWO is complex and composed of multiple overlapping bands [11]. However, the spectrum overlaps well with the sensitivity spectra of conventional photodetectors [13]. High-energy luminescence band, referred to as the blue band, is located in the range 445-455 nm (2.72-2.78 eV), has a FWHM of 0.59-0.69 eV and is usually attributed to an overlapping set of narrow bands due to recombination of the self-trapped exciton at the host oxy-anionic complex WO_4^{2-}. These bands are also characterized by a quenching temperature, i.e. the temperature where emission intensity decreases to half of its maximum value. The quenching temperatures can be between 147 K to 197 K or even below 80K, depending on the crystal [14,15]. Similar emission has also been observed in other tungstate compounds [16].

Two types of green emission have been identified. Green emission of the first type peaks around 520-540 nm (2.3-2.37 eV), depending on the crystal. It is qualitatively similar to the blue band and is thermally quenched at 180-210 K. It has been proven that this emission also arises from the WO^{2-}_4 group [14]. Green emission of the second type is located at 495 nm (2.5 eV). It is responsible for the slow (μs-ms) decay component of PWO emission. This emission appears at temperatures above 150 K and reaches maximum intensity at 220 K. This type of emission is observed only in crystals containing isolated lead and oxygen vacancies (V_{Pb}, V_O). Additional doping of PWO with trivalent rare-earth ions has been shown to significantly decrease the intensity of this type of emission. This is due to the trivalent ion decreasing the number of both oxygen (due to the extra positive charge) or lead (due to formation of associate structures between the trivalent ion and V_{Pb}) vacancies [17–19].

There is also the third type of emission, referred to as red emission. Red emission is separated in to two types as well. At 4.2 K, the red emission of the first type is centered around 1.57 eV. When temperature is increased to RT, peak position shifts to 1.63 eV. At 4.2 K, the second type of red emission is centered around 1.48 eV. At RT, the red emission of the second type is actually absent. Red emission of the first type is very sensitive to excitation energy. At

4.2 K, the ratio of blue to red emission can vary between 0.2 to 29 when excitation energy is varied between 4.02 and 4.4 eV. However, removal of this type of emission has been shown after annealing in a nitrogen atmosphere for crystals grown by the Czochralski method. Alternatively, for crystals grown by the Bridgman method, annealing in air at 1000 °C has been shown to be effective. In Cd-doped PWO crystals, the red emission is not observed [20].

As usual for a self-activated scintillator [21], photoluminescence rise time is very short, in the subpicosecond domain. However, regarding photoluminescence decay time, PWO with decay time of 2-20 ns is atypically fast for a tungstate compound [2,22]. This is due to PWO exhibiting thermally quenched luminescence. The luminescence decay time in this material is determined not by the rate of radiative recombination, but rather by nonradiative recombination of thermally activated carriers. In practice, it is important that major emission components decay at the same rate. The decay rate has also been shown not to be influenced by the density of free charge carriers. This leads to good proportionality of scintillator detectors based on PWO.

Decay of the blue and green light emission has originally been described using a three level excited state model [23]. However, a more complicated model has since been adopted. Very slow, non-exponential components have been observed, even on the 10^{-4} s time scale. It was determined that this component was even contributing to “background enhancement” due to the slow decay and repetitive nature of measurements. Later, more advanced measurements revealed that thermally-induced exciton disintegration above 150 K leads to creation of free electrons and holes. Their localization and eventual radiative recombination gives rise to this slow component. [24] Because of the large role of free carriers, shallow traps in PWO become important, because they can strongly modify the carrier diffusion by re-trapping the free carriers.

The presence of shallow trap levels is sensitive to the growth conditions, annealing and doping of PWO. For example, doping with antimony has been shown to improve PWO luminescence by increasing its light yield and suppressing red luminescence, similarly to the effect of annealing in air [25]. Doping with La has been shown to significantly improve radiation hardness, likely due to the reduction of temporary color centers [26]. A systemic review of doping with various trivalent ions (La^{3+}, Lu^{3+}, Gd^{3+}, Y^{3+}, Sc^{3+}) has shown that doping with trivalent ions gives significant improvement in transmittance and even removes the slowest component of luminescence decay, in the case of Lu^{3+}, Gd^{3+} and Y^{3+} [27]. This effect is likely due to removal of deep traps, as evident by the absence of TSL peaks above 120 K. Ions like Sc^{3+} are likely too small to substitute for lead in the crystal lattice [28]. However, large dopant doses can lead to decrease in light yield. In the case of gadolinium, the concentration of about 100 ppm has been shown to be optimal [29]. PWO emission properties can also be affected by mechanical processing of the crystal surface, due to many of the emission properties being affected by surface defects [30].

As a result of the extensive research program led by the Crystal-Clear Collaboration, a new generation of PWO crystals was developed. Referred to as PWO-II, this new version is distinguished by the luminescence yield enhancement of 80 %, compared to that of previously produced PWO [31].

From the point of view of timing, PWO is interesting because it is a likely candidate for a qualitatively novel approach for employing optically detectable time mark, based on elastic polarization. When the scintillator interacts with ionizing radiation, there is an instantaneous elastic effect due to the displacement of lattice atoms because of the charge redistribution when the electrons are displaced and holes generated by the interaction [32]. The formation of a hole in the shell of an atom in the crystal lattice naturally results in the transformation of the atom environment due to charge compensation. Since these atom displacements are produced via interaction with phonons, the lattice distortion occurs on the time scale comparable with the period of lattice vibrations, i.e., within 10^{-14} to 10^{-12} s. This local distortion in the lattice results in the redistribution of the electron density in the conduction band in the close vicinity of the hole. The relaxation of the elastic polarization might proceed via different radiative and non-radiative channels. The key feature of the elastic polarization is its short response, which makes it promising to use as an optically detectable time mark.

1.2 Cerium-doped garnet-type scintillators

$R_3Al_5O_{12}$ (where R = Lu, Y, Gd) garnets have been under study for use as optical materials for over 50 years [33,34]. Application of garnets as scintillators has only been proposed over 20 years ago [35], however a lower light yield than other compounds stifled any development in this direction. Only recently, when the studies showing dramatic improvement of light yield came out, interest in garnets as scintillators was resurrected [36–42]. One way for optimization of garnet compounds is manipulation of the garnet structure through mixing of component oxides in the process creating so called multicomponent garnets [43].

Typically inferior scintillator performance in garnets is attributed to cation antisite defects [44]. They create traps for electrons and this results in a slower scintillation response [45]. Usual defect engineering approach is not effective here, because these defects are charge neutral and their formation energy is low. However, it was suggested that adding Ga to Al-based garnets decreases the influence of antisite defects [46]. Nonetheless, Ga is closer in size to the R ion, than Al [47], leading to a higher concentration of antisite defects in Ga-doped garnets than that in pure aluminate garnets [48,49]. Later on, it was shown that the positive effect of Ga admixing comes from the shift in conduction band in a way that it covers the trap state associated with the antisite defect [43,48]. This is an excellent example of “band gap engineering” applied to defect management. It is also known that adding Ga to $Lu_3Al_5O_{12}$ makes energy transfer to luminescent centers more efficient and faster, leading to an enhanced scintillation response [46].

Gadolinium-based garnet scintillator would be an excellent scintillator, due to its high density and absence of intrinsic radioactivity [37]. However, it is not possible to grow $Gd_2Al_5O_{12}$ from the melt [50]. Moreover, the emitting 5d-4f transition of the Ce^{3+} ion is quenched in this material due to the position of 5d states in the host conduction band [51]. It is known that mixing large amounts of Gd into a garnet host can shift the $5d_1$ level of Ce^{3+} to diminish the unwanted ionization.

Band gap of GAGG varies from sample to sample in the 6-7 eV range [52,53]. The GAGG crystal has a refractive index of 1.92 [54], lattice constant of 12.29-12.24 Å (depending on Ga concentration) [55] and the melting temperature of 1850°C. Photoluminescence of cerium-doped GAGG is centered around 510-530 nm, depending on the sample [55,56]. Photoluminescence decay curves for Ce:GAGG are generally multicomponent, complex and vary greatly between crystals of different producers. For example, depending on Ga concentration it can range from 97 ns to 353 ns for the faster component and from 353 to 1932 ns for the slower component [55]. However, it has been demonstrated that codoping the crystal with magnesium can lower these values to 60 ns and 188 ns [57].

Cerium-doped gallium gadolinium garnets ($Gd_3Al_2Ga_3O_{12}$, GAGG) attracted considerable attention due to high stopping power to gamma radiation and neutrons, a high light yield, luminescence decay time shorter than 80 ns, and excellent matching of the emission peak at ~520 nm with the sensitivity spectrum of the conventional silicon photo-multipliers (SiPMs) [58,59].

In comparison with binary garnets, the multicomponent garnets have an inherent feature: disordering of the matrix due to local variation in the content of isovalent ions. The random distribution of matrix-building ions causes spatial fluctuations of the band gap, reduces the carrier diffusion lengths, facilitates recombination of geminate pairs [60] and, as a consequence, leads to an increase of the light yield due to the improved conversion efficiency [60–62]. The disorder also results in inhomogeneous broadening of the 4f-related emission lines of activator ions, caused by various positions of the ion in the lattice distorted by the fluctuations of crystal composition [63–65], which is absent in binary garnets. Moreover, the random distribution of cations in the multicomponent garnets leads to the shrinkage of the band gap [38,66,67] observed in $(Lu_{1-x}Y_x)AlO_3$:Ce and many other multicomponent oxides [68]. The down-shifted conduction band might cover shallow traps located below the bottom of this band [69] and, as a consequence, diminish the scintillation efficiency losses due to carrier trapping.

Contrary to self-activated materials, the luminescence of Ce-doped scintillation materials is caused by inter-configurational d-f luminescence, having a high quantum yield and low temperature quenching effect in the vicinity of room temperature. Thus, only a minor gain of the light yield of the Ce activated scintillation material is expected with decrease of the crystal temperature. Moreover, some of oxide scintillators doped with Ce, particularity perovskites $YAlO_3$-$LuAlO_3$ demonstrate 10-20% decrease of the light yield when temperature is lowered from room to -20 °C.

Aliovalent codoping has been recently demonstrated to be a productive approach to improve the scintillation properties of bulk Ce-doped scintillators with different host structures. Codoping of GAGG:Ce single crystals with the divalent cation Mg^{2+} is highly promising for applications of this scintillator in the new generation of positron emission tomography (PET) scanners. This scintillator is a product of purposeful engineering of the band gap and the energy position of the activator levels in the gap. The crystal exhibits a high light yield of up to ~70000 phot/MeV [70], has luminescence decay time shorter than 100 ns, and its emission band peaks at ~520 nm which perfectly matches the sensitivity spectrum of conventional SiPMs. Thus, the crystal might compete with LSO:Ce and LYSO:Ce in time-of-flight PET (TOF-PET) applications. Moreover, GAGG:Ce might become the scintillator of choice in high-resolution radiation spectrometry and compete with the halide scintillators recently developed for this purpose [71–73]. However, the outstanding characteristics of GAGG:Ce detectors are accompanied by certain shortcomings hindering extensive application of the material in radiation detection. Particularly, the material exhibits strong phosphorescence, both under photoexcitation and excitation by ionizing radiation. It has been demonstrated that the phosphorescence might be diminished by codoping of the GGAG:Ce crystals with Mg [74]. Unfortunately, the codoping results in a lower scintillation light yield, contrary to the divalent calcium or magnesium codoping of LSO:Ce and LYSO:Ce [75].

This aliovalent doping, in which a trivalent ion is substituted by a divalent second group cation in the host matrix, results in the formation of anionic vacancies that compensate for the resulting charge. The formation of a hole-type defect including Mg^{2+} and O^- in close proximity is also quite probable [76]. Moreover, the co-doping of Ce-activated crystals by divalent ions (even at the level of less than 1 atomic%) causes oxidation of part of the Ce^{3+} ions to Ce^{4+}. Both cerium ions are involved in the scintillation process as follows from general consideration in [54,75,77]. Codoping Ca^{2+} or Mg^{2+} in high temperature crystallized oxide material seems to introduce similar defects in the matrix due to similarity of the cation properties at the localization in the same host, though different dependence of the light yield on their concentration was observed in GAGG:Ce [74].

1.3 Cerium-doped orthosilicates

Scintillators of the family of lutetium oxyorthosilicate Lu_2SiO_5:Ce (LSO) are currently studied as very prospective for fast timing applications. Originally, it was designed for well-logging applications [78] to substitute BGO. Though LSO is by a factor of 7 faster and by a factor of 3 brighter than BGO [13], the application of LSO in oil field services was limited by performance deterioration at high temperatures. Success was waiting in another area: medical imaging, particularly, in PETs [79]. LSO scintillators are especially prospective to develop for PET devices operating in time-of-flight mode enabling improved spatial resolution of PET images [80], to introduce multi-modal systems and to move progressively to an ambitious target: full-body PET scanner. The last generations of PET scanners are equipped with silicon photomultipliers enabling substantially improved read-out properties, whereas the speed of electronics for data acquisition and signal processing has currently been effectively boosted [81,82]. As a result, the material properties of scintillators become the limiting factor in improving the timing properties of PET devices.

Standard LSO scintillators emit light at 420 nm [83]. Their luminescence decay curve is typically described by bi-exponential functions; fast component is typically between 8 and 12 ns, whereas the slow component is between 33 and 40 ns [83,P12]. They have a density of 7.4 g/cm3 [84] and band gap of 6.5 eV [85]. The melting point of LSO is 2150 °C [84].

A substantial impact on improvement of LSO properties was achieved by introduction of mixed oxyorthosilicate $(Lu_xY_{1-x})_2SiO_5$:Ce (LYSO) with a part of lutetium ions substituted by yttrium [86], in a similar way as in another Lu-based system – perovskites [87]. Substitution of a part of lutetium by yttrium in the crystal matrix to fabricate multicomponent oxyorthosilicate $(Lu_xY_{1-x})_2SiO_5$ (LYSO) not only reduced the cost of the material and the crystallization temperature but also diminished the scintillation afterglow and improved the light yield of the material. In addition, it was shown that annealing of oxyorthosilicate in oxidizing atmosphere diminish the amount of oxygen vacancies in the material and improves the time response of these scintillators [88].

Another approach to improve the LYSO:Ce properties is the codoping of the crystals with aliovalent ions. When oxyorthosilicate crystal is co-doped with divalent calcium, its scintillation properties are significantly improved: the light yield increases, the luminescence decay becomes faster, and the afterglow is diminished [75,76,89,90]. The positive effect of aliovalent codoping is also observed in other oxide and halide scintillation crystals, such as Y_2SiO_5:Ce, $LaBr_3$:Ce, and $CeBr_3$ [76,91,92].

1.4 Non-crystalline scintillators

Amorphous materials attract attention as host for activator ions to obtain scintillators at substantially lower price than those based on single crystals. Development of such scintillators is enhanced by applicability of these materials as phosphors in white light-emitting diodes (LEDs), which have a large market.

Currently, the commercial white LEDs are composed of a blue InGaN LED covered by epoxy containing phosphor (usually YAG:Ce^{3+}) converting the blue emission to a broad band in yellow spectral region [93,94]. However, the epoxy materials in use suffer from poor stability when exposed to short-wavelength light and high temperatures [95]. This hampers the progress in the development of specific light sources powered by near UV LEDs, in production of LEDs operating in harsh environment, and in laser-diode-pumped high-luminosity light sources [96], which are currently on increasing demand.

Due to substantially higher operational performance, glass ceramics might be a relatively inexpensive alternative to the epoxy materials. The glass ceramics not only exhibit high stability at elevated temperatures and under exposition to UV radiation but also have high thermal conductivity [97]. These properties enable the development of high-power white LEDs and laser diodes with increased lifetime and higher light output. Moreover, the glass ceramic materials can be obtained via thermal annealing of glasses without affecting their external geometry [13]. It is well known that crystalline silicates doped with rare earth ions (REI), e.g., Gd_2SiO_5 (GSO), Y_2SiO_5 (YSO); SiO_2, are prospective emitting materials and are extensively used as phosphors or scintillation materials . Silicates in a glass form are efficiently emitting materials too (e.g., GS20 from Scintacor or lithium or barium disilicate glasses) [98–100]. Two types of crystallization, avalanche and homogenous, might occur in glasses. The latter allows for controlling the formation of crystalline phase and, as a result, the transparency of the glass ceramics, which is important for their use in combination with LEDs.

When using UV LEDs as an excitation source to generate white light, the UV LED emission should be converted into blue, red and green light [101]. Several REI are considered to be promising activators for phosphors suitable to be exploited in combination with LEDs. The simultaneous LED excitation of three phosphors enables selection of the color temperature of the white light by changing the contribution of blue, green, and red components and, on the other hand, to achieve good uniformity of the light field. Ions Ce^{3+} , Tb^{3+}, Dy^{3+}, Eu^{3+}, and Eu^{2+} are promising REI for generation of blue, green [100], and red [102,103] light. To use the emission efficiently, appropriate glass hosts have to be selected and fabricated. The glasses allowing simultaneous doping with these REI are of especial interest. Furthermore, glass ceramics might be fabricated to improve the thermal conductivity and stability of the phosphor, which, in combination with mechanical hardiness and good color rendering, improve the performance of LED-based lighting [104,105].

It is well known that the emission spectra of Ce^{3+} and Eu^{2+} due to d-f transitions strongly depend on the crystal field [106,107]. At excitation in UV region, weakening of the crystal field results in a blue shift of the Ce^{3+} emission band (e.g., from 550 nm in YAG:Ce to 450 nm in DSB:Ce [108]). The emission of Eu^{2+} in glasses and crystalline materials are predominantly located in the blue spectral region. Thus, Eu^{2+} is a suitable dopant in glasses or glass ceramics for generating blue emission. Meanwhile, Tb^{3+}, Dy^{3+}, and Eu^{3+} emission due to f-f transitions are weakly affected by the crystal field. As a result, they are suitable to generate green (intense ${}_5D^4 - {}_7F^5$ transition of Tb^{3+}

ions at 545 nm) [109], yellow ($_4F^{9/2}$ – $_6H^{13/2}$ transition of Dy^{3+} ions at 575 nm) [110], and red ($_5D^0$ – $_7F^2$ transition of Eu^{3+} at 612 nm) [111] emission at UV LED excitation.

However, the lack of emission in the red part of the spectra is the cause of the drawback of the YAG:Ce phosphor: the resulting light is characterized by a low color rendering index and the light temperature being far from optimal, which limits the use of the YAG:Ce light sources in illumination [112]. Nevertheless, a number of methods allowing one to increase the luminescence intensity in the red region of spectra are described in the literature [113–116]. There are two approaches: introduction into the host matrix of other rare earth (RE) ions (Eu^{3+}, Pr^{3+}, Sm^{3+}) along with the Ce^{3+} ones or partial isovalent replacement of Y^{3+} and Al^{3+} ions with other suitable cations.

Partial isovalent replacement of the host matrix cations allows one to control the parameters of Ce^{3+} d-f interconfiguration luminescence by changing the crystalline field in the position of the doping ion localization. So, in the frame of the crystal engineering, new combinations of the cations which differ from a simple $Y_3Al_5O_{12}$ crystal while allowing to maintain the garnet structure will be useful. Mixing trivalent cations, partially rare earth ones, and partial replacement of Al^{3+} ions with Ga^{3+} in garnets showed a spectacular improvement of the scintillation light yield by a factor of two as compared to YAG:Ce in ceramics [117]. Impressive results were also obtained with the single crystals of the mixed garnets [118]. In addition to the change of the local crystal field, solid solutions also allow control of the compound band gap. It should be noted that a blue shift of the resulting luminescence band is achieved by introduction of In^{3+} or Ga^{3+} ions [119–121], whereas a red shift is achieved by introduction of Gd^{3+}, Tb^{3+} or La^{3+} ions [119–123] into the YAG:Ce structure.

Another approach is exploiting the isomorphism in garnets to obtain new compounds of this class. The compounds with garnet structure belong to the Ia_3d space group, and their general formula can be presented in the form $\{C\}_3[B]_2(A)_3O_{12}$, where {}, [] and () correspond to the cations in different crystalline positions: in distorted dodecahedral, octahedral, and tetrahedral, respectively [124–127]. RE ions are located in dodecahedral positions. High tolerance of garnet crystal lattice allows one to relatively easy replace cations. This feature leads to the corresponding change of "metal-oxygen" bond length and, as a consequence, affects the luminescence properties of RE ions through the distortion of their crystalline surroundings. It should be noted that heterovalent replacement of Y^{3+} and Al^{3+} ions in garnets is feasible too, but with strict control over charge compensation [128,129].

2 EXPERIMENTAL METHODS

2.1 Optical Pump and Probe Technique

The dynamics of nonequilibrium carriers can be studied by measuring the time evolution of the spectrum of the optical absorption induced by a pump pulse. In optical pump and probe configuration, the pump pulse is used to generate nonequilibrium carriers, whereas the changes in optical absorption are probed by a probe pulse delivered to the sample with a variable delay. The measured signal of the differential absorption (DA) is recorded as

$$DA(\lambda) = ln\left(\frac{I(\lambda)_{unexc}}{I(\lambda)_{exc}}\right) \tag{2.1.1}$$

Here, $I(\lambda)_{\mathrm{unexc}}$ and $I(\lambda)_{\mathrm{exc}}$ are the intensities of probe beam, recorded when the sample is unexcited and excited, respectively. By probing the sample with a broad-spectrum pulse, DA in a wide spectral range might be recorded for each probe pulse.

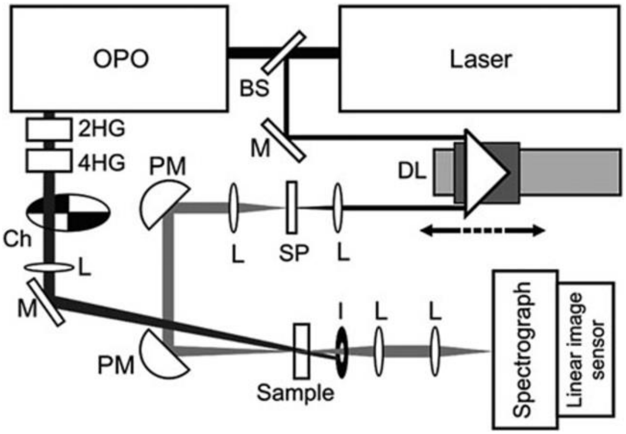

Fig. 2.1.1. Layout of time-resolved differential absorption setup: OPA – optical parametric amplifier, BS – beam splitter, M – mirror, L – lens, DL – delay line, SW – sapphire plate, PM – parabolic mirror, I – iris, 2HG and 4HG – β-BBO crystals for frequency doubling and quadrupling, Ch – chopper. [P13]

The variable delay of the probe pulse enables step by step measurements of the time evolution of the DA spectrum. A typical layout of a setup for studying the time-resolved DA in pump and probe configuration is presented in Fig. 2.1.1. The setup is based on a pulsed laser. The time resolution of the measurement depends on the pulse duration of the laser used. Lasers emitting femtosecond or picosecond pulses are usually exploited. The output of the laser is split into two beams by a beam splitter. The major part of the initial pulse energy is directed to the pump beam. Harmonics generators based on nonlinear crystals are used to increase the photon energy of the pump beam. To continuously tune the photon energy, optical parametric oscillators are exploited. The probe beam passes an optomechanical delay line, where the length of the pulse path is variably changed by moving a retroreflector on a motorized translation stage. The maximal delay between the pump and probe pulses is limited by the length of the delay line and is typically of the order of 10 ns. After the delay line, the probe pulse is focused on a plate of transparent material to generate a quasi-white light continuum. Sapphire was used to generate the probe pulse with a quite flat spectrum in a wide spectral range.

The probe light is focused by parabolic mirrors on the sample surface into a spot overlapping with the pump beam spot. To ensure a good overlap, the pump spot is usually larger (typically ~300 μm) than the probe spot (~100 μm). The probe light transmitted through the sample is dispersed by a spectrograph and recorded using a CCD camera. The pump beam is equipped with a chopper to periodically open and block the pump pulses. Thus, the probe light transmitted when the sample is excited and unexcited is recorded, and the DA is calculated according to Eq. 2.1.1. The final measurement result is a matrix of DA values recorded at different spectral positions and time delays. Cross-sections of the matrix provide either the DA spectrum at a fixed delay or the DA kinetics at a fixed spectral position.

The DA occurs due to the light absorption by any kind of nonequilibrium electrons and holes, whether they are free, trapped or in the excited states of activator ions. The DA efficiency depends on the absorption cross-section and the density of final states and, most importantly, is directly proportional to the density of the absorbing carriers. Thus, the DA intensity reflects the density of certain kind of nonequilibrium carriers, provided that the type of the carriers responsible for the DA is known. In DA experiments, the simultaneous measurement of spectral and kinetic features facilitates identification of the origin of the feature. Another degree of freedom in the DA experiments is the capability to tune the photon energy of the pump beam and perform selective excitation. Finally, the time resolution in these measurements is limited only by the duration of the laser used. Thus, by using a femtosecond laser, the time resolution in femtosecond domain is achieved.

The experimental setup for time-resolved differential absorption measurements is based on a commercial Yb:KGW (Yb:KGd(WO$_4$)$_2$) femtosecond laser (Pharos, Light Conversion). The output of the laser was split into two beams. The main part was used to pump the optical parametric amplifier (OPA, Orpheus, Light Conversion) producing tunable-wavelength light for excitation. The output of OPA was frequency doubled/quadrupled using β-BBO crystals to extend the pumping light wavelength to UV. The remaining part of the fundamental laser radiation was sent through a delay line (a moving retroreflector on a motorized translation stage) and then focused into a sapphire plate, where a white-light supercontinuum is generated. The generated probe light was focused by parabolic mirrors on the sample into a spot overlapping with the excitation beam spot. Typical diameters of pump and probe beams used in our experiments are 100 μm and 250–300 μm on the sample surface, respectively. The probe light transmitted through the sample was dispersed by a spectrograph and recorded using a linear image sensor.

2.2 Time-Resolved Luminescence Spectroscopy

Streak camera was used for time-resolved luminescence spectroscopy. A sketch of the device is presented in Fig. 2.2.1. The light to be studied is transformed into photoelectrons, which are accelerated to fluorescent screen and deflected by applying a linearly increasing transversal electric field. The intensity of the fluorescence excited by the electrons reflects the intensity of initial light, whereas the variation of the light intensity in time is transformed into spatial profile of the fluorescence intensity. The profile is recorded by an array of photodetectors. A CCD camera is exploited for the read-out. The system forming the spatial imaging of time profile is coupled in the streak camera with a spectrometer deflecting the incident light in perpendicular direction proportionally to its wavelength. As a result, the photoelectrons form a 2D image on the fluorescence screen. The image is red out by a 2D CCD matrix. The intensity distribution of the image provides the distribution of the luminescence signal studied both in time and in wavelength.

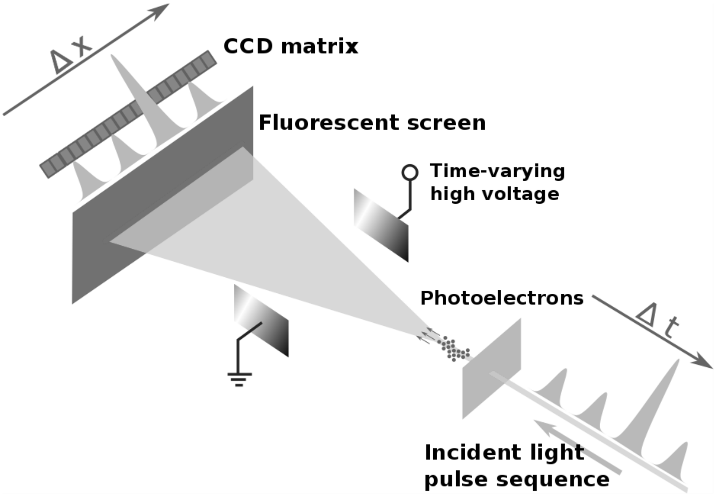

Fig. 2.2.1. The configuration of a streak camera.

The time resolution of the streak camera is limited by the instrumental function, which depends on the design and operation mode of the camera. In time-resolved photoluminescence measurements, the net time resolution might be also limited by the pulse duration of the laser used for photoexcitation. Usually, a laser emitting pulses shorter than the instrumental function of the camera is exploited. The best time resolution in our experiments was 2 ps.

In these studies the time-resolved photoluminescence was performed by using a femtosecond Yb:KGW oscillator (Light Conversion Ltd.) emitting at 1030 nm. The oscillator produced 80 fs pulses at 76 MHz repetition rate. A harmonics generator (HIRO, Light Conversion Ltd.) was used to produce the third 343 nm (3.64 eV) and fourth 254 nm (4.9 eV) harmonics of the oscillator emission. The excitation beam was focused on the sample surface into a spot ~100 μm in diameter, resulting in excitation pulse energy density of about 15m J/cm^2. The PL signal was detected using a Hamamatsu streak camera. Synchoscan detection mode with the 2.95 ps full-width at half maximum (FWHM) of instrumental response function was used for the measurements in subnanosecond time domain. The deconvolution of the instrumental response function and the PL signal enabled a subpicosecond resolution. Meanwhile, in the study of samples with significant long decay components, the camera could be operated only in single sweep mode with considerably poorer time resolution.

Photoluminescence measurements were performed at room temperature, which is a typical operation temperature of ionizing radiation detectors in laboratory conditions.

2.3 Coincidence time resolution

To measure coincidence time resolution (CTR), scintillator pixels were combined into detecting modules with SiPMs developed at Fondazione Bruno Kessler (FBK SiPMs). The detectors employed in this study were 4x4 mm^2 RGB-HD SiPMs with 25 µm cell pitch. RGB-HD technology is based on an n-on-p junction and features a peak PDE of more than 40% at 550 nm, considering 25 µm cells 15. The pixels were wrapped in Teflon and optically coupled to SiPMs by using Cargille Meltmount optical glue (refractive index n = 1.539).

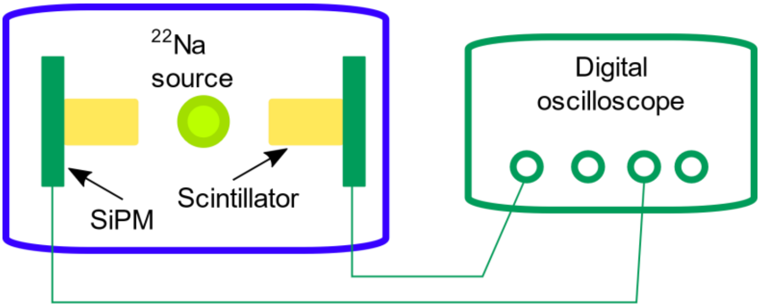

Fig. 2.3.1. Configuration of CTR measurement setup.

The CTR setup, pictured in fig. 2.3.1 consisted of two identical detecting modules placed on the same axis, at the same distance from a ^{22}Na source providing 511 keV coincidence events. The SiPMs were loaded on two double-stage amplifiers with two outputs. The first stage was used to measure the energy of the detected gamma quanta in order to select only the events in the 511 keV photopeak. The second stage, based on the pole-zero filtering, was used for high-resolution timing measurements. The energy discrimination was performed through charge integration within a time window of 500 ns. CTR was measured on couples of identical detecting modules as a function of voltage threshold and of SiPM excess bias under controlled temperature (+20°C).

2.4 X-ray diffraction

X-ray diffraction (XRD) was used for identification of crystalline materials and obtaining information on the crystal structure. X-ray diffraction is based on constructive interference of monochromatic X-rays passing through crystalline structure. Filtered, to produce a monochromatic beam, X-rays are collimated and directed towards the sample. When conditions satisfy Bragg's law ($n\lambda=2d\sin\theta$, where λ is the wavelength of the radiation, d is the lattice spacing and θ is the diffraction angle), constructive interference is produced and, after scanning over a range of angles, information about all possible diffraction directions is collected and compared to reference data.

XRD measurements were performed using diffractometer DRON 3 with CoKα radiation source. The software DICVOL06 from FULLPROF package was used to calculate the lattice constants.

2.5 Confocal microscopy

Confocal microscopy is advantageous when compared to conventional optical microscopy. Advantages of confocal microscopy include a shallow depth of field and elimination of out-of-focus emission [130].

The method of image formation in a confocal microscope is fundamentally different when compared to a conventional wide field microscope. In this case illumination is focused into a spot as small as possible, in contrast to the large field illuminated in conventional microscopy. This illumination acts as excitation for luminescence. The luminescence is then collected from that single excited spot the area of interest is examined point by point. By moving the sample or the imaging system it is then possible to draw a spatial distribution of photoluminescence parameters.

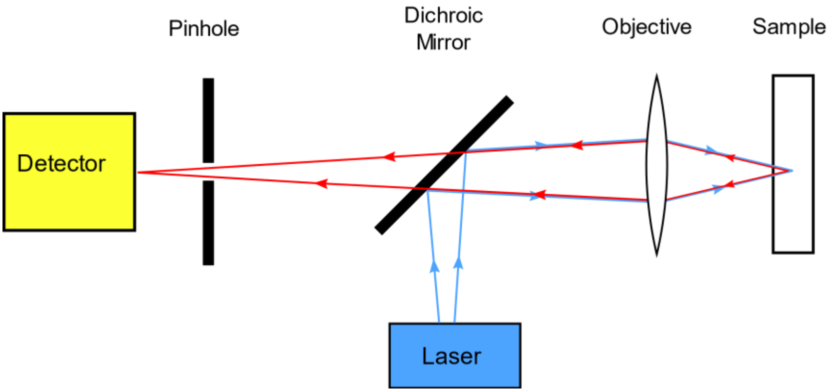

Fig. 2.5.1. The configuration of confocal microscope.

One typical configuration of the confocal microscope is shown in Fig. 2.5.1. The same objective is used for excitation and collection of luminescence. The luminescence is reflected by a beam splitter and is focused into the detector. Before detection, a pinhole spatially filters out the light originating from the parts of the sample which are above or below the focal plane of the objective. Both the resolution and the image contrast are improved.

In these studies PL measurements were performed by using microscopic system WITec Alpha 300S operated in confocal mode. An objective with the numerical aperture NA = 0.6 was used for excitation and collection of the PL signal and ensured the spatial in-plane resolution of ~ 250 nm and the axial resolution of ~ 1.6 μm. A CW laser diode (ALPHALAS) emitting at 405 nm was exploited for excitation. The microscope system was connected by an optical fiber to a spectrometer equipped with a thermoelectrically cooled CCD camera.

3 RESULTS AND DISCUSSION

3.1 Carrier dynamics in self-activated lead tungstate scintillators

Kinetics of photoluminescence in PWO

The sample under study was grown by Czochralski technique described in detail in [7]. The 2×2×0.1 cm^3 sample was prepared from the ingot of PWO-II quality [131]. The polished 2×2 cm^2 planes were perpendicular to the crystallographic axis **a**.

Figure 3.1.1 shows a typical image of the photoluminescence intensity dependence on time and wavelength, which has been obtained with the streak camera for the PWO sample under study.

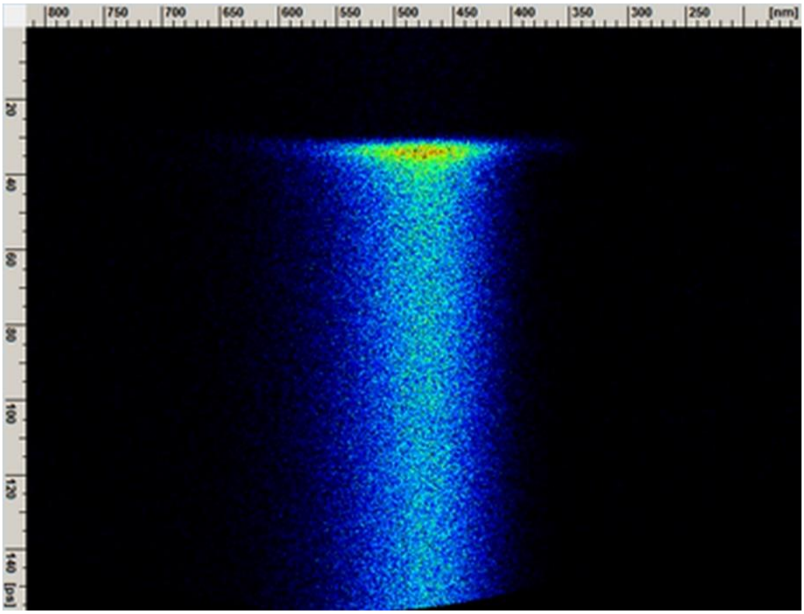

Fig. 3.1.1. Typical streak camera image of PL intensity versus wavelength (horizontal) and time (vertical) in PbWO$_4$. [P4]

Figure 3.1.2 shows the time-integrated PWO fluorescence spectra, measured at different excitation wavelengths. At the excitation into conduction band at 254 nm, the typical PWO blue luminescence is observed. For the excitation wavelength shifted to 343 nm, the green luminescence band due to recombination at oxygen deficient oxy-anionic complexes WO_3 [7] is also observed.

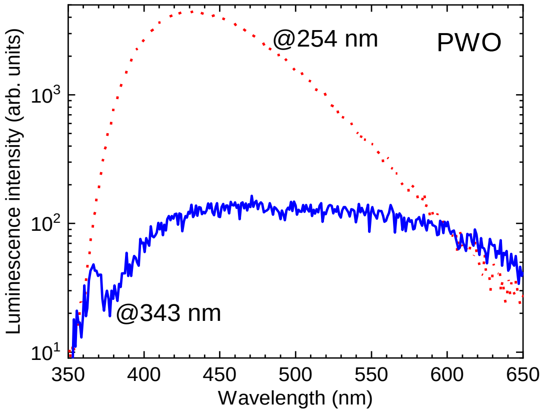

Fig. 3.1.2. Time-integrated $PbWO_4$ luminescence spectra after excitation at 254 nm (red dotted line) and 343 nm (blue solid line). [P4]

The PL intensity decay proceeds approximately at the same rate for all wavelengths within the PL spectrum. The initial part in the kinetics of the PL intensity spectrally integrated within the entire band (400-600 nm) is presented in Fig. 3.1.3 together with the instrumental response function and the fit with a bi-exponential decay function. The full width at half maximum (FWHM) of the instrumental function was 2.95 ps. The measured PL rise is completely defined by the rise of the instrumental response function. This evidences that the PL rise time in PWO scintillation crystals is in subpicosecond domain.

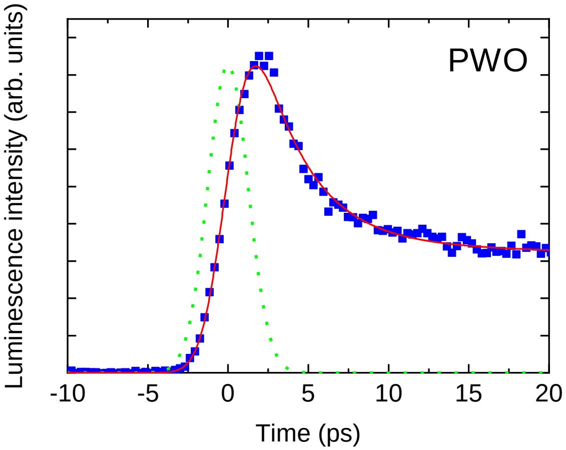

Fig. 3.1.3. Initial stage of spectrally integrated photoluminescence kinetics in $PbWO_4$ at 253 nm excitation (dots), the instrumental response function (green dotted line), and the best fit obtained using a bi-exponential decay function (red solid line). [P4]

It is interesting to note that both regular and defect-related WO_3 luminescence centers show the same leading edge of the luminescence transient. This is an indication that no intermediate recapturing processes are involved in the energy transfer processes. Figure 3.1.4 shows the initial stage of PL decay. The decay has two decay components. Fitting the experimental PL transients with a bi-exponential decay function renders two effective decay times:τ_1 = 3.8 ps and τ_2 = 683 ps at 343 nm excitation and τ_1 = 5.9 and τ_2 = 824 ps at 254 nm excitation. At the tail part of the measured kinetics curve, certain contribution of the slower component with the time constant of 8-10 ns, which is observed in routine start–stop measurements of PWO luminescence kinetics, might be traced. The intermediate component with decay times of approximately 700-800 ps is consistent with that reported in [132], while the fast component has not been observed before. The comparison of the PL transients measured at different excitation intensities (see Fig. 4) shows that the ratio between the two components does not depend on the density of the nonequilibrium carriers. The kinetics at 343 nm excitation was also measured in two spectral ranges: 400-500 and 500-600 nm. We found no significant difference in the response shape when the intensities of blue and green luminescence bands became roughly the same. This is an indication that the fastest decay component is due to green luminescence emitting centers.

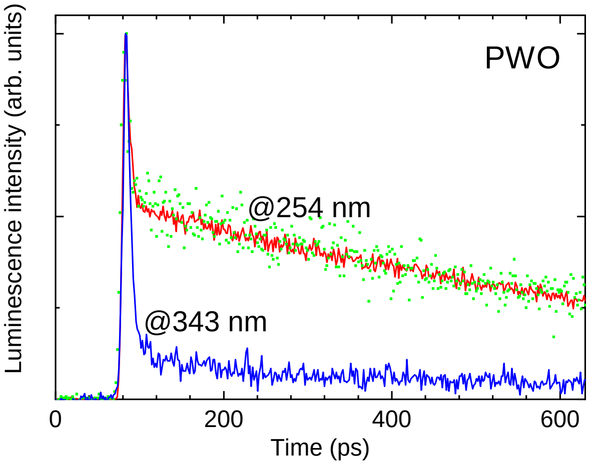

Fig. 3.1.3. Initial part of $PbWO_4$ photoluminescence kinetics at 343 nm excitation (blue line) and 254 nm excitation with pulse energy of 15 mJ/cm^2 (red solid line) and 1.5 mJ/cm^2 (green dotted line). [P4]

The subpicosecond rise time of luminescence in lead tungstate is a clear indication that the relaxation of nonequilibrium carriers to recombination centers is an intrinsic process and is not significantly affected by any defects in a standard PWO II crystal. The short rise time at the excitation with photon energy of 4.9 eV (254 nm), which is larger than E_g by 0.6 eV [7], is consistent with the model of relaxation of germinal carrier pairs to the radiating states at oxy-complexes WO_4^{2-}. However, the fast rise time is observed also at excitation with energy 3.64 eV (343 nm), which is 0.6 eV smaller than E_g. This indicates that the process of release of electrons into conduction band from shallow traps is a weak process in this crystal. This is consistent with the assumption that the color centers with a captured electron (F^+ type centers) are completely unstable in $PbWO_4$ structure at room temperature [7]. The F^+ centers are based on WO_3 defect oxy-complexes and most probably have the ground state inside the conduction band, so they appear simultaneously with excited regular oxy-anionic groups.

The fast PL decay component with the decay time τ = 4-6 ps is more pronounced at the excitation bellow E_g. Therefore, we assume that the fastest component in the luminescence kinetics is caused by the radiative decay of F^+ centers. The second, intermediate decay component with the decay time τ = 600-800 ps, which was explicitly revealed in our experiments using a high-time-resolution streak camera, might be interpreted by WO_4^{2-} luminescence originating from quenched luminescence of complexes WO_4^{2-}+RE^{3+} (RE = La^{3+} and Y^{3+}) [7]. Therefore, the intermediate decay component (600-800 ps) and the component with the decay time of 8-10 ns, originating from regular WO_4^{2-} complexes [132], provide simultaneous contributions to luminescence, which is strongly quenched at room temperature. The PWO crystals fabricated on a large scale for high energy physics applications are doped with trivalent La and Y ions at the total level of 100 ppm [7]. As a result, radiative recombination centers WO_4^{2-}+La^{3+} and WO_4^{2-}+Y^{3+} are formed with the ground states approximately 0.1 eV below the bottom of the conduction band. Therefore, in addition to the thermal quenching, they have additional nonradiative losses due to the thermal ionization to the conduction band, so their kinetics becomes shorter.

Our results are obtained under photoexcitation near the bottom of the conduction band. Under ionizing radiation, the geminal pairs might be separated during the thermalization process. Nevertheless, a dramatic increase in the rise time of the scintillation pulse is not expected, since the thermalization of the nonequilibrium carriers via the emission of phonons occurs on the time scale of picoseconds or even shorter. Moreover, the energy deposit in the high energy physics experiments, when PWO crystals interact with high-energy particles with energies of hundreds of GeV, like in LHC experiments at CERN, exceeds several GeV within a time of less than 1 ns. Therefore, the density of free carriers becomes high enough to provide prompt coupling of electrons and holes for recombination. Due to this reason, we do not expect substantial increase of the scintillation rise time compared to photoluminescence rise time and estimate it at the level of less than 10 ps. Thus, the rise time of the intrinsic scintillation of PWO crystals might probably be used for fast timing with PWO crystals in high energy particle detectors with optical readout.

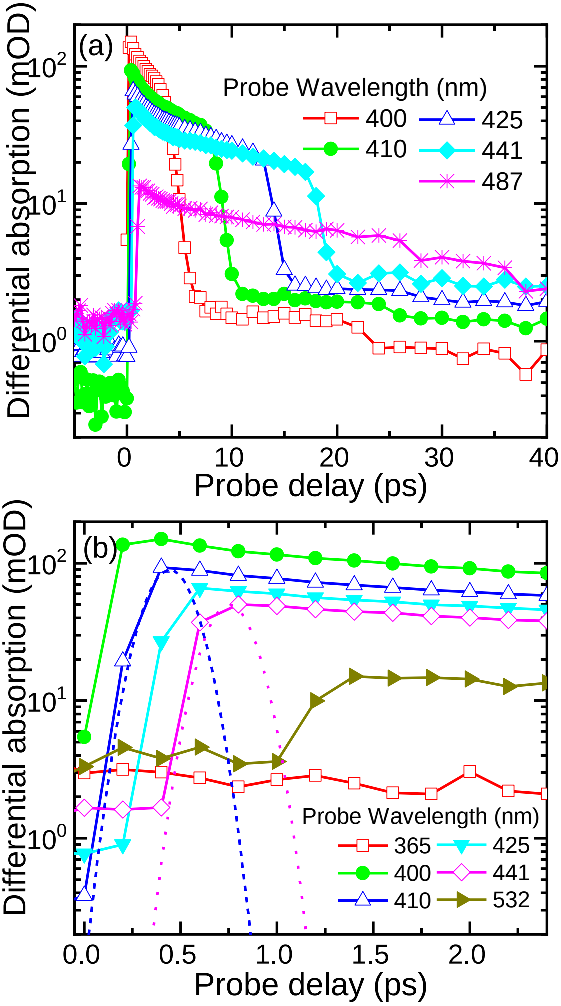

Fig. 3.1.4. Differential absorption (a) and the initial part of it (b) in PWO scintillation crystal at 394 nm pump and different probe wavelengths (indicated). The pump pulse shapes are depicted by dashed curves. [P1]

The change in the optical density for the probe beam induced by the pump at the wavelength of 394 nm is presented in Fig. 3.1.4. The shape of the response is similar to that reported in [133]. It has a short rise time, a decay with characteristic time constant of few picoseconds, and a faster decay afterwards. The fast decrease of the absorption at the rear part of the response could be explained by the separation in space of the pump and probe beams, which are impinging the sample surface at slightly different angles. The overlap volume in a thick sample depends on the wavelengths of the two beams due to the light velocity dispersion. Thus, the delay between the leading front and the rear part of the nonlinear absorption depends on the pump and probe wavelengths because of the light group velocity dispersion.

The leading edge of the differential transmittance is displayed in Fig. 3.1.4b for several wavelengths of the probe beam. The figure proves that the time response on the leading edge is limited by the laser pulse shape rather than by the material properties. Thus, the processes responsible for the nonlinear absorption happen on a femtosecond time scale.

Figure 3.1.5 presents the differential optical absorption versus the energy density of the pump pulse at 394 nm for different wavelengths of the probe pulse delayed by 1 ps. The data for Fig. 3.1.5 were obtained in the experiment configuration with the electric field of the probing light parallel to the **c** axis (***E*** II **c**). Quite similar dependences have been observed in the ***E*** II **b** configuration (not shown in this paper). The observed dependences of the differential absorption of the probe signal with the pump pulse energy density are approximately linear. This is the experimental evidence that the absorption is caused by a two-photon absorption process involving one pump and one probe photon [134].

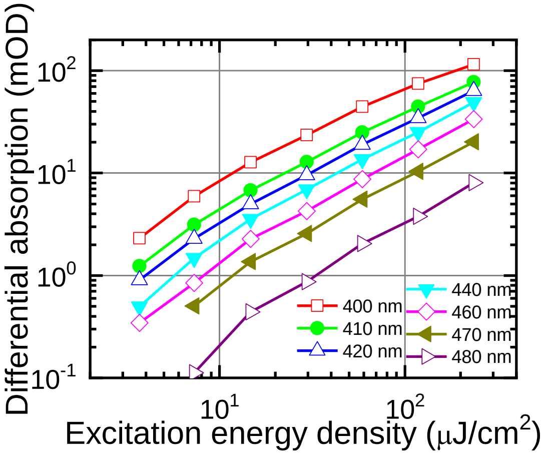

Figure 3.1.5. Differential absorption versus energy density of pump pulse at 393 nm for different wavelengths (indicated) of the probe pulse delayed by 1 ps. [P1]

Nonlinear absorption as a function of pump photon energy

Depending on the combination of the wavelengths of the pump and the probe pulses, the absorption is caused by either two-photon or two-step absorption in the sample. In the latter case, the formation of a color center at the first absorption step might be expected. The major difference between these two absorption modes is that the two-photon absorption is an instantaneous process and takes place only if pump and probe pulses overlap in time inside the sample, while the time response in the two-step absorption depends on the population of real electronic states. The absorption from the state occupied after the absorption of the pump photon depends on the intra-state relaxation and the rate of the color center recombination. It is well known [7] that point defects, particularly the oxygen vacancies (V_O), form a variety of shallow electron traps in $PbWO_4$ crystal with the thermal activation energy E_{TA} in the range from 0.029 to 0.7 eV. Two centers, WO_4^{3-} polaronic center (E_{TA} = 0.05 eV) and WO_4^{3-}+RE (RE = Y, La), were detected using electron paramagnetic resonance (EPR) at the temperatures of liquid nitrogen or lower. Thus, they should relax very fast at room temperature. Some other centers were detected only by means of the thermo-stimulated luminescence (TSL). They have no paramagnetic states, so it was supposed that they are stable after capturing two electrons and forming centers $F(V_O + 2e^-)$. Consequently, the centers $F^+(V_O+e^-)$ in the host matrix do not become stable after capturing an electron [7].

As discussed above, the differential absorption induced by pump at 394 nm (3.15 eV) is caused by two-photon absorption. Meanwhile, the excitation involving electron transition to a real state close to the band gap was observed when the pump wavelength was shifted to 346 nm.

Figure 6 presents the spectra at different delays and the decay kinetics at different wavelengths of the differential absorption induced by pump at 360 nm (3.44 eV). The experiments were performed in ***E*****IIc** configuration for the light polarization. Figure 4a depicts only the region of the high energy band, since the spectral range in the second setup used in these experiments was limited.

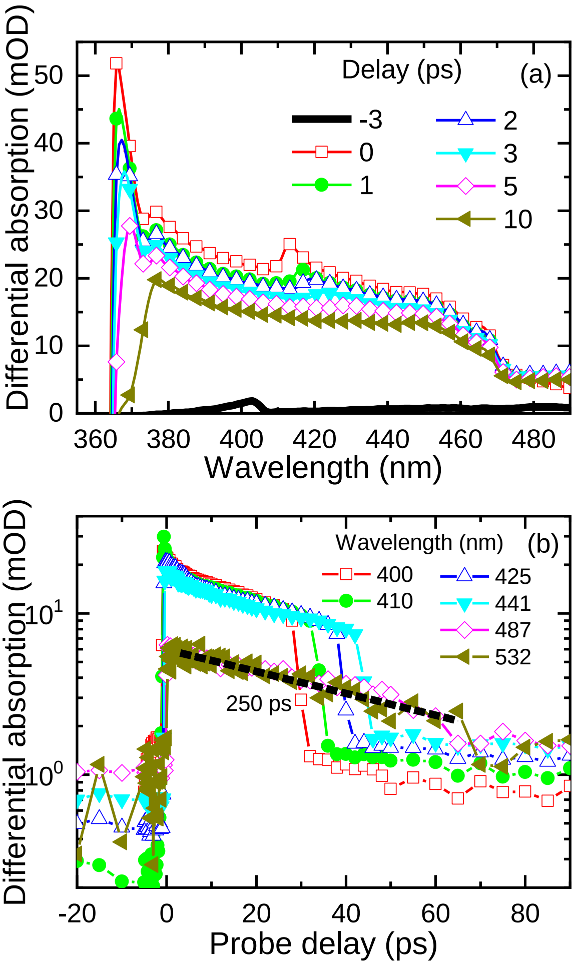

Figure 3.1.6. Spectra (a) at different delays (indicated) and decay kinetics (b) at different wavelengths (indicated) of the differential absorption induced by pump at 360 nm (3.44 eV). [P1]

The decay kinetics of the induced absorption (Fig. 3.1.6b) is characterized by a fast increase, then a nearly exponential decay with the same rate for all probe wavelengths, a fast decrease due to separation of pump and probe in real space, and, finally, a slow decay with the time constant considerably exceeding the time scale in our experiments. The excitation of PWO at 360 nm deliver electrons to the deepest electron-type center in PWO, a Frenkel type defect (FTD), which is an oxygen vacancy V_O with a neighboring oxygen ion in the interstitial position. Capturing only one electron at this center does not form a stable color center [13]. Thus, the observed fast kinetics with 250 ps time constant for the induced probe absorption decay (see Fig. 4) is probably determined by subsidence of FTDs charged with one electron.

Moreover, the induced absorption is still observed even after the long delays (exceeding tens of picoseconds), when the pump and probe beams do not overlap in space and the probe absorption is influenced just by the carriers excited by probe photons. This behavior is in agreement with the transient absorption observed in PWO under excitation with nanosecond electron pulses [135].

As shown in Fig. 3.1.7a, the differential absorption is considerably weaker and its spectrum changes substantially when the pump wavelength is shifted to 346 nm (3.58 eV). In contrast to the spectra induced by the photons of smaller energy, no band corresponding to two-photon absorption is observed. Instead, two broad, strongly overlapping bands peaking at 380 and 410 nm appear at zero delay. At delays above 1 ps, a short wavelength wing of a new broad band (with the peak obviously beyond the spectral range of our experiment) is observed. The new band probably evidences that, in addition to FTD, V_O-based centers are populated with electrons generated by pump. Similarly, as for FTDs, capturing of one electron does not ensure the stability of these centers. As a result, the induced absorption decreases with time delay. The kinetics presented in Fig. 3.1.7b show that the decay is exponential with a time constant of 60 ps. The decay is caused by the electron relaxation to the bottom of the state or by trapping of the electrons to deeper defect-related states.

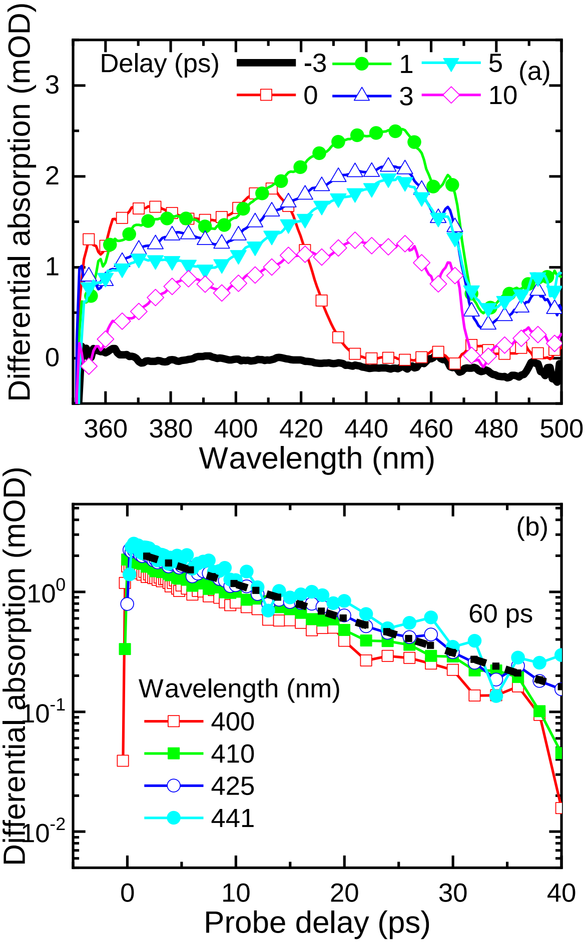

Figure 3.1.7. Spectra (a) at different delays (indicated) and decay kinetics (b) at different wavelengths (indicated) of the differential absorption induced by pump at 346 nm (3.58 eV) in in ***E*** II**c** configuration. [P1]

It is worth noting that the light polarization in respect to the crystallographic axes is practically unimportant when color centers are involved in the process. Figure 3.1.8 presents the spectra and kinetics of the differential absorption induced by pump in ***E*** II**b** configuration. Comparison with the corresponding results obtained in ***E*** II**c** configuration (see Fig. 3.1.5) shows that the spectra are quite similar and the decay kinetic is characterized by time constants of the same order of magnitude (60 and 25 ps) in both configurations.

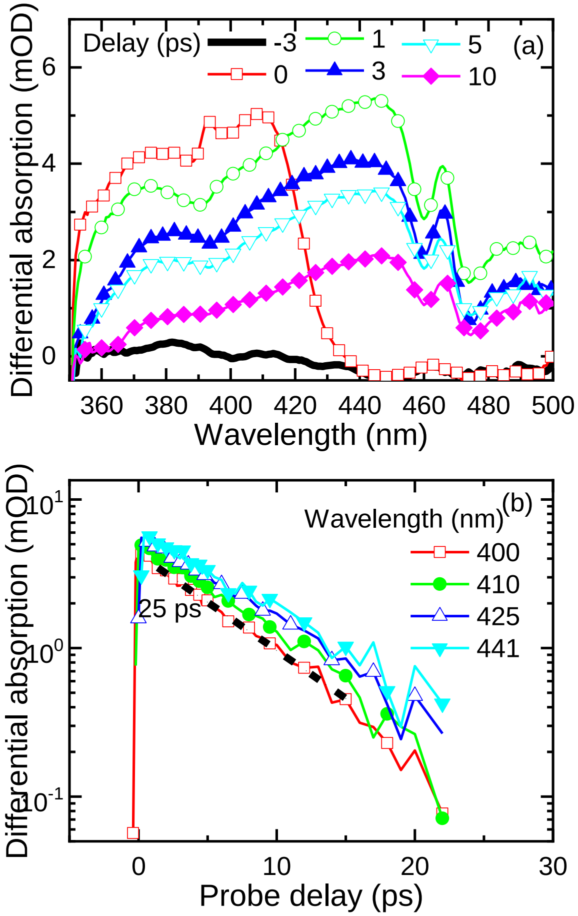

Figure 3.1.8. Spectra (a) at different delays (indicated) and decay kinetics (b) at different wavelengths (indicated) of the differential absorption induced by pump at 346 nm (3.58 eV) in E IIb configuration. [P1]

The spectrum of the differential absorption at pump photon energy of 1.9 eV (654 nm) is presented in Fig. 3.1.9. The spectrum has two overlapping bands peaking at 380 and 410 nm and is similar to that obtained for UV pump at 3.58 eV (346 nm). Probably, the same centers are populated by absorption of a single 3.58 eV photon and by two-photon absorption of 1.9 eV photons.

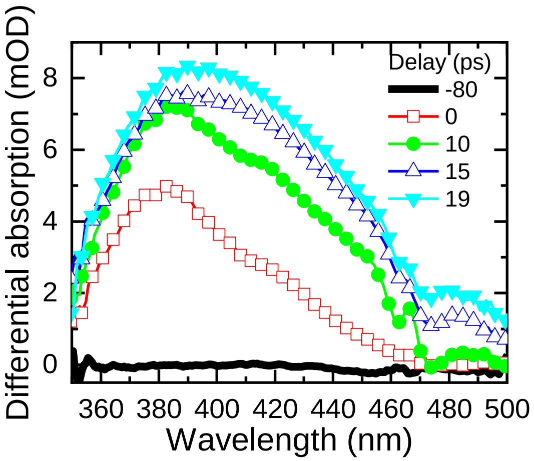

Figure 3.1.9. Spectra at different delays (indicated) of the differential absorption induced by pump at 654 nm (1.9 eV). [P1]

The dependence of the spectral and time properties of the differential absorption on pump wavelength discussed above demonstrates that the selection of the proper wavelength to observe the nonlinear response from PWO crystals without population of defect-related states is of importance for implementation of this material in fast radiation detection systems.

The excitation at 254 nm corresponds to interband transitions in lead tungstate crystal. Figure 3.1.10 shows the decay of the excitation-induced free carrier absorption (FCA) in PWO crystal at different pulse energy densities of the excitation. The initial part of this decay is presented in Fig. 3.1.11. The increase in excitation intensity results in increased contribution of the fast decay component. The dependence of the peak induced absorption on excitation intensity is presented in Fig. 3.1.12 as the dependence of the induced absorption at the probe wavelength (1030 nm) on pump pulse energy density.

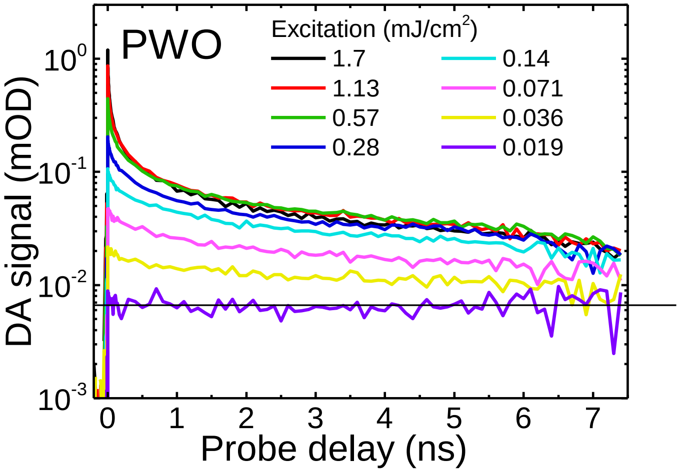

Fig. 3.1.10. Kinetics of optical density induced by short pulse excitation of PWO crystal at 254 nm, probed at 1030 nm, for different excitation pulse energy densities (indicated). [P3]

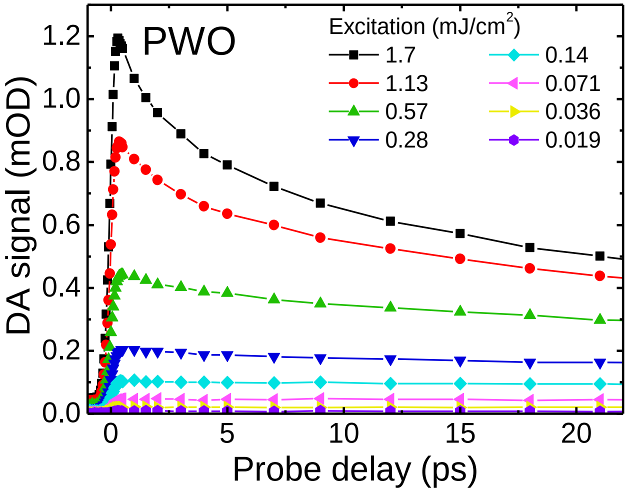

Fig. 3.1.11. Initial part of the kinetics presented in Fig. 3.1.10. [P3]

The optical density of the induced absorption in PWO and in other two samples under study (not shown) was found to be proportional to the energy density in a wide dynamic range, as expected for free carrier absorption. This evidence confirms the assumption that the probe absorption originates exclusively from the carriers created via pumping.

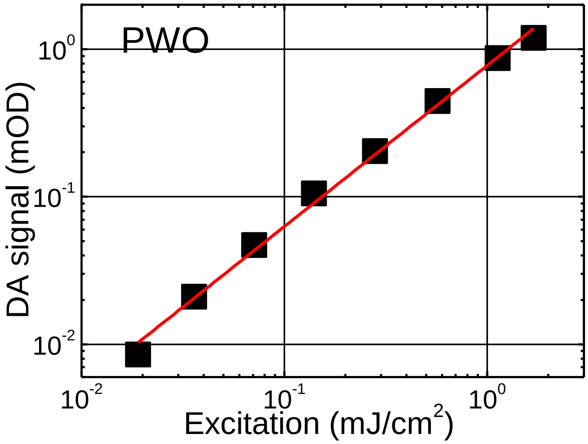

Fig. 3.1.12. Induced optical density at 1030 nm probe wavelength at 0.3 ps delay after short pump pulse at 254 nm versus pump pulse energy density. [P3]

The subpicosecond rise time of FCA at interband excitation in the self-activated luminescent lead tungstate is a clear indication that the nonequilibrium free electrons appear in the conduction band within subpicosecond time scale. This is in consistence with interpretation that the luminescent matrix-forming oxy-anionic complexes WO_4^{2-} provide conditions for formation of self-localized excitons. Furthermore, the FCA exhibits a response kinetics, which correlates with the photoluminescence kinetics observed by us before [P4].

The excitation at 254 nm generates free carriers in the PWO crystal in the subpicosecond domain. As the excitation density is increased, the probability of the non-germinal carrier recombination shows an increase resulting in acceleration of the initial part of the FCA decay.

Influence of gamma irradiation on the nonlinear absorption

Figure 3.1.13 presents the spectra of the differential absorption for different delays between pump and probe within the first 400 fs. Standard deviations of the data on the plots were estimated from spectra recorded at minus 1 ps probe pulse delay and found to be 1.9 mOD at 500 nm and 3 mOD at 700 nm wavelengths.

For the pump light polarization along the crystal axis **b**, the spectrum has a band peaking at ~3.13 eV (400 nm). Taking into account the pump photon energy of 3.15 eV (395 nm), the energy of the optical transition in this two-photon absorption is equal to 6.28 eV. This value is in agreement with our previous result observed in a crystallographically unoriented PWO crystal [136] and matches well with the energy of the second peak in the spectrum of the density of states calculated in [137]. When the pump light polarization is rotated away from the axis **b**, an additional band peaking at 2 eV (620 nm) appears simultaneously with the first band in the differential absorption spectrum. The peak position corresponds to the total transition energy of 5.15 eV and matches well with the low-energy band in the spectrum of the density of states [137].

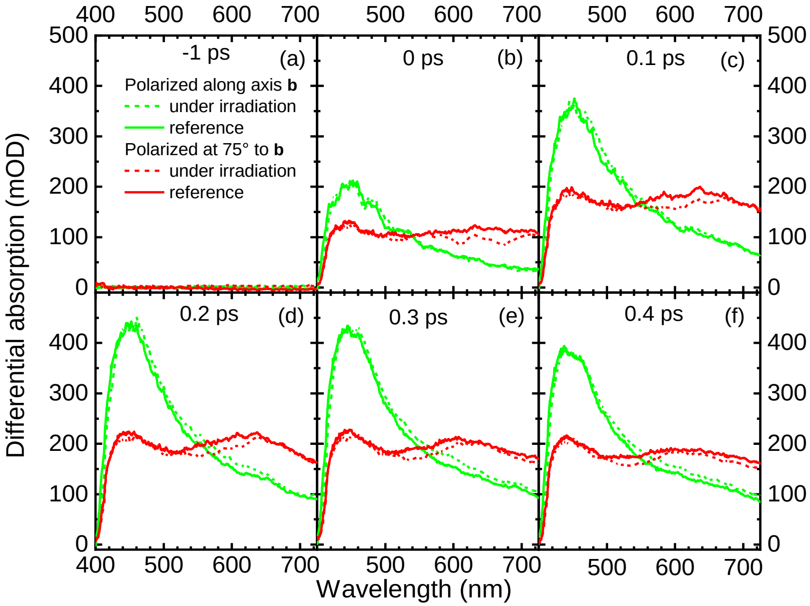

Figure 3.1.13. Spectra of differential optical absorption induced by 500 mJ/cm^2 pump at 395 nm polarized along the crystal axis **b** and polarized at 75° to the crystal axis **b** (indicated) under (dashed lines) and without (solid lines) gamma irradiation. Delays of probe pulse are indicated. [P1]

The spectra in figure 13 were measured under and without gamma irradiation. No significant influence of the gamma irradiation was observed in the polarization configuration ***E*****IIb**, when only one band peaking around 450 nm in the differential absorption spectrum was observed. Meanwhile, certain damping of the low energy band peaking in the vicinity of 620 nm was observed under the influence of the irradiation in the second polarization configuration (see Fig. 3.1.13c, d). This change in the optical absorption could be used for the fast timing in radiation detectors.

We also observed a small change in the front shape of the response under irradiation, however, the change in the pulse shape is too weak to be exploited in a real detector.

Since the amplitudes of the electric field in the light wave of the probe and even pump (10^3 V/cm) are considerably lower than the typical crystal field (10^7-10^8 V/cm), the pump and probe experiments do not induce significant distortion to the crystal symmetry including the structural polyhedrons. However, the situation considerably changes under ionizing radiation. The electrons generated from the inner atom shells, move to a distance of up to several tens of microns during their thermalization. Meanwhile, the holes relax within distances comparable to the interatomic distance. As a result, an excessive positive charge is created along the track of the gamma or the particle in ionizing radiation. The electric dipoles form a low-symmetry component of the electric field, which acts in addition to the usual crystal field. As discussed above, this results in a redistribution of the electronic density. For example, the electric field of the dipole created by the hole and electron near the first coordination sphere of hole is proportional to the distance r as r^{-3} and reaches 10^5-10^7 V/cm at the distance of ~5 nm. A more accurate estimation of the electric field in the tracks requires application of the Ewald mathematical apparatus and is beyond the scope of this work.

Since the bottom of the conduction band in PWO is formed by polyhedrons WO_4^{2-}, we can estimate the fraction of distorted polyhedrons in the crystal under irradiation used in our experiments. In our experimental conditions, not fewer than $3x10^{10}$ electron-hole pairs per second are generated by the gamma irradiation. The average track of the hot electron in PWO occupies a volume with approximately 0.2 μm in diameter and 40 μm in length, thus, $\sim 0.4\times10^{-12}$ cm^3 in volume. Accordingly, the total rate of the track volume formation is 1.2×10^{-2} cm^3 per second. Since the density of WO_4^{2-} polyhedrons in the PWO single crystal is $\sim 10^{22}$ cm^{-3}, the density of the polyhedrons within the volume of the irradiation-formed tracks equals approximately 10^{20} cm^{-3}. We should take into account that the lifetime of the elastic deformation is limited by the relaxation of free carriers. In PWO, the relaxation occurs via radiative recombination with a time constant of ~10 ns. Therefore, the non-equilibrium density of the polyhedrons distorted by irradiation is below 10^{12} cm^{-3}. This density seems to be too low for reliable detection. Thus, the crystal volume with polyhedrons distorted by elastic polarization supposedly extends outside the track volume. The dependence of the experimentally observed effect on the light polarization in respect to the crystallographic axes is an indication that the distortion of the low-symmetry structural polyhedrons is more effective along certain directions in the crystal matrix.

Applications in detection of ionizing radiation

The effects observed in our study might be exploited for detection of ionizing radiation in parallel with the detection of scintillation signal in the same material. The two-photon absorption can be used as a time tag to detect the initial moment of the interaction of ionizing radiation with the detector material, while the scintillation signal provides information on the absorbed energy. In the case of PWO, the wavelength of 500 nm corresponding to the total energy of two photons of 5 eV would be optimal.

The light propagating along the scintillation crystal and reflecting from the front face of the crystal could be used to observe the two-photon absorption. This configuration would also reduce the problems of the spatial overlap of the beams. Particularly, we consider this approach to be suitable for application in inorganic scintillation fibers in the detecting modules of SPOCAL or dual readout types [138,139]. The detection could be technically achieved by using a set of sub-picosecond pulses, e.g. 100 pulses with the total set duration of 0.1-1 ns. The set is injected into the crystal or fiber slightly before the time when the interaction products of the collision are expected to reach the detector modules. The laser pulses should be injected not in all fibers of the detecting modules but just to the specialized fibers in the module which are used for timing. The initial moment of the interaction between the collision products and the detector module is detected by comparing the set of pulses reflected back out of the crystal and a reference set. Thus, introducing the set of laser pulses with short spacing in the detecting module establishes a short-period time scale. The time resolution would be equal to the time span between the pulses in the set.

The radiation-induced changes either in spectral or time properties of the optical response could be exploited in the detectors. Further study is necessary to make the right choice ensuring a higher detection accuracy. The results obtained in our work are in favor of the exploitation of the change in the amplitude of the response at certain wavelengths.

The influence of ionizing radiation on the parameters of the two-photon absorption, which we observe in PWO crystal, should be observed also in other crystals and, probably, amorphous materials. The figures of merit for selection of the prospective materials should be a high point symmetry of the polyhedrons of metal ions forming the bottom of the conduction band, a high optical transparency at the wavelength used in the detection, and a high density of d-type electronic states in the lower part of the conduction band. The materials suitable for fabrication in a fiber shape have some additional advantages. Moreover, the experience accumulated on the propagation of ultrashort laser pulses in waveguides could be exploited in the development of such ultrafast detectors.

3.2 Cerium-doped orthosilicates

Currently, time resolution becomes the property of scintillation detectors needing substantial improvement for applications of the detectors in the coming high-luminosity high-energy physics experiments and in medical imaging to develop devices with a better spatial resolution and full-body positron emission tomography (PET) scanners containing thousands of scintillator pixels. As the requirements for the time resolution move to the ambitious target of 10 ps and the readout electronics exhibits spectacular progress, timing properties of scintillator material become a bottle-neck in the development of fast radiation detectors. Scintillators of the family of lutetium oxyorthosilicate Lu_2SiO_5:Ce (LSO) are currently studied as very prospective for fast timing applications. Originally, it was designed for well-logging applications [78] to substitute BGO. Though LSO is by a factor of 7 faster and by a factor of 3 brighter than BGO [13], the application of LSO in oil field services was limited by performance deterioration at high temperatures. Success was waiting in another area: medical imaging, particularly, in PETs [79]. LSO scintillators are especially prospective to develop for PET devices operating in time-of-flight (TOF) mode enabling improved spatial resolution of PET images [80], to introduce multi-modal systems and to move progressively to an ambitious target: full-body PET scanner. The last generations of PET scanners are equipped with silicon photomultipliers (SiPM) enabling substantially improved read-out properties, whereas the speed of electronics for data acquisition and signal processing has recently been effectively boosted [81,82]. As a result, the material properties of scintillators become the limiting factor in improving the timing properties of PET devices.

Samples

Ce-doped lutetium yttrium oxyorthosilicates $Lu_{1.6}Y_{0.4}SiO_5$ with different level of codoping by calcium for this study were fabricated by CPI (USA), Shanghai Project Crystal Co, Ltd (China), and Saint Gobain (France). A typical sample of LSO:Ce has also been used for comparison. The oxyorthosilicate ingots were grown by Czochralski method in inductively heated iridium crucibles in atmosphere containing nitrogen with a small fraction of oxygen (less than 1%). The samples in the shape of blocks with the dimensions of $3\times3\times5$ mm^3 for the coincidence time resolution (CTR) measurements and 10×10×(1-3) mm^3 for the measurements by optical pump and probe technique have been prepared from the same crystal ingots. All surfaces of the blocks have been polished.

Results

The typical optical absorption spectra of LYSO and LSO samples studied are presented in Fig. 3.2.1. The absorption spectrum of LSO:Ce in the spectral range studied exhibits three bands due to optical transitions from the ground state 4f to three lowest excited states of the activator ion Ce^{3+} $5d^{1,2,3}$ split by a low-symmetry crystal field. The intensity of the absorption bands slightly depends on the light polarization to the crystallographic orientation of the sample, since LSO has a monoclinic lattice and Ce ions occupy two sites in the lattice with different surrounding [78]. The spectral overlap of two absorption bands due to two different positions of Ce^{3+} in LSO lattice, Ce(1) and Ce(2), is too strong to be resolved at room temperature. The ground state of Ce^{3+} is split into two sublevels $^4F_{5/2}$ and $^4F_{7/2}$ [140], however, only the lower spin-orbital sublevel causes absorption, since the upper sublevel is by 0.24 eV above and is not populated at room temperature. Introduction of yttrium into the lattice of LSO does not significantly affect the spectral position of the Ce-ion-related absorption bands (compare the spectra of LSO and LYSO1 samples in Fig. 3.2.1). Meanwhile, the introduction of calcium (5 ppm in sample LYSO2 and 30 ppm in LYSO3) results in the formation of a broad (full width at half maximum, FWHM, of 1.66 eV) absorption band peaked at 4.9 eV, as observed before [89]. The formation of this band has been linked with the increasing part of Ce ions in Ce^{4+} charge state observed in Ca-codoped LSO:Ce by X-ray Absorption Near Edge Spectroscopy (XANES) and attributed to the absorption via charge transfer transitions from oxygen to Ce^{4+} ions [76]. The photon energies for pump beam in our DA experiments (3.47 eV and 4.75 eV) were selected in accordance with the spectra presented in Fig. 3.2.1 and are indicated by arrows there.

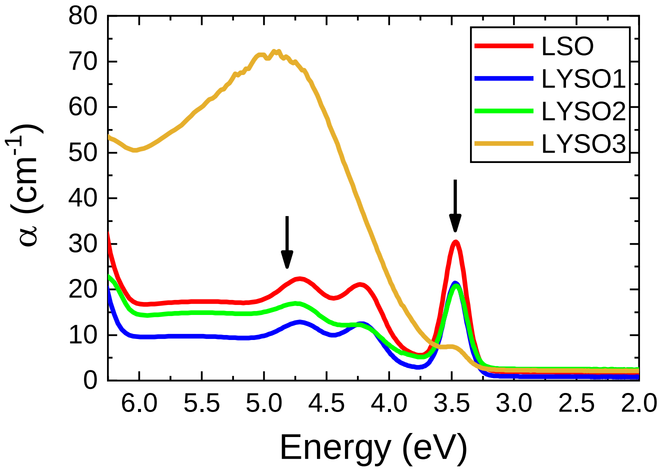

Fig. 3.2.1. Absorption spectra of LSO and LYSO crystals doped with Ce (LYSO1) and codoped with increasing content of Ca (samples LYSO2 and LYSO3, respectively). Excitation photon energies used in pump and probe experiments are indicated by arrows. [P16]

At excitation by 3.47 eV photons, Ce^{3+} transitions to the first excited level are expected. CT transitions from oxygen orbitals building the top of the valence band to the unoccupied electron state in Ce^{4+} ion are also feasible. According to Ref. [141], a negligible part of Ce ions in LSO:Ce are in a Ce^{4+} state, but the part increases with Ca-codoping. The same behavior of Ce charge state is expected also for LYSO:Ce. Accordingly, two DA components are evident in the data carpets presenting the DA intensity as a function of time and spectral position of probe photon (see Fig. 3.2.2) and in cross-sections of such carpets presented in Fig. 3.2.3 to show the kinetics of DA signal at two typical probe photon energies. The spectrum of the first feature is approximately flat in the range studied (1.3-2.4 eV). The decay of this DA component is in nanosecond domain and coincides with the luminescence decay reflecting the decay of the population of the first excited state of Ce^{3+}. Consequently, this component should be attributed to the absorption from the first excited level of Ce^{3+}. The fast DA decay component is spectrally centered at ~2.3 eV and has a characteristic decay time of ~5 ps. This DA component might be attributed to the absorption by free holes generated due to pump-induced CT transitions from the valence band to Ce^{4+}. The component is more pronounced in samples with a high Ca content (see the carpet for LYSO3) in Fig. 3.2.2. The time-integrated contribution of this fast component is small compared with the contribution of the component decaying at the rate of luminescence decay.

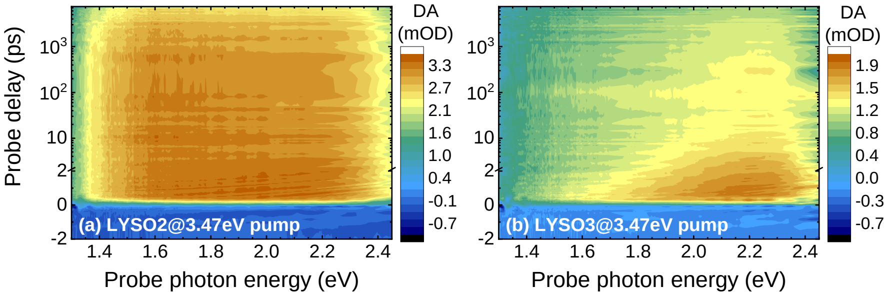

Fig. 3.2.2. Dependence of the intensity of differential absorption (color-coded as indicated by sidebar) as a function of probe photon energy and delay between pump and probe beams in LYSO:Ce with (a) low (sample LYSO2) and (b) high (sample LYSO3) level of Ca-codoping. [P16]

The fast component is not evident in the uncodoped crystal and becomes pronounced in the Ca-codoped crystals (see Fig. 3.2.3). This enhancement can be explained by increasing density of Ce ions in Ce^{4+} state in the codoped crystal, as it is expected in view of the results presented in [76]. The differential absorption presented in Fig. 3.2.3 is normalized for each sample according to its thickness and absorption coefficient for the pump pulse to compare the DA response to the same number of photogenerated carriers. Note that the slow DA component has the same absolute value and kinetics in all samples studied. This feature supports the assumption that the slow component is caused exclusively by the absorption of the probe photons by electrons occupying the lowest excited state of Ce^{3+} ion. Meanwhile, the fast component appears on the top of the slow one, as might be expected, provided that a part of Ce^{3+} is converted to Ce^{4+} due to Ca-codoping. Note, however, that a time-integrated contribution of the fast component is rather small compared to that of the slow component.

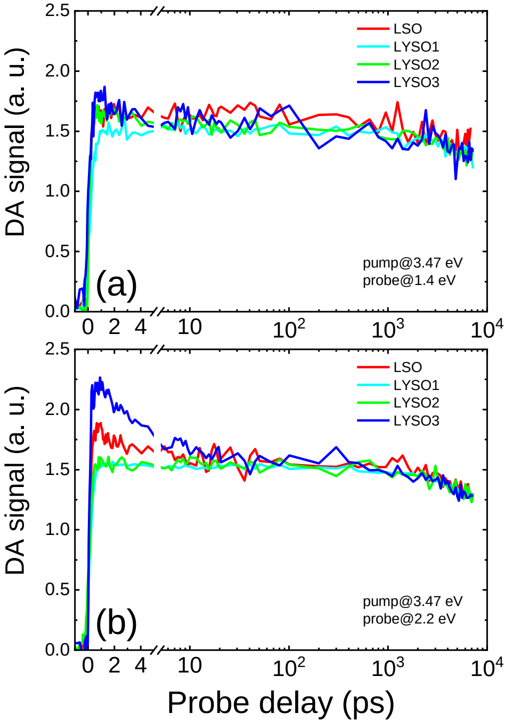

Fig. 3.2.3. Kinetics of differential absorption of LSO and three LYSO:Ce samples (indicated) at two probe energies, 1.4 eV (a) and 2.2 eV (b), after pumping with 3.47 eV photons. The arbitrary units are normalized for all the samples by taking into account their thicknesses and absorption coefficients. [P16]

The pump photon energy of 4.82 eV corresponds to the optical transition in Ce ion from the ground state to the third excited state, which is in the conduction band. The photoexcited electron can intracentrally relax down to the lowest excited state of Ce^{3+} and recombine radiatively afterwards, as in the resonant excitation to the lowest excited state, or leave the Ce^{3+} to become a free electron in the conduction band. The conditions of CT excitation from the oxygen orbitals in the valence band to the ground state of Ce^{4+} are similar to those at the excitation with 3.47 eV photons. In addition, the photon energy of 4.82 eV corresponds to the peak of the broad absorption band appearing in the absorption spectrum of Ca-codoped crystal (see Fig. 3.2.1). The assumption that this absorption band is at least partially caused by the optical transitions from valence band to defect centers induced by Ca-codoping leads to a conclusion that additional holes are generated via this mechanism at 4.82 eV pump. This conclusion is in line with the observation that free hole absorption peaked at 2.2 eV is enhanced by changing the pump photon energy from 3.47 eV to 4.82 eV.

The DA kinetics at two typical probe photon energies are presented Fig. 3.2.4. A new fast component appears in the response, especially well pronounced in sample LYSO3 for the probe photon energy at 1.4 eV (see Fig. 3.2.4a). This component is probably related with the generation of free electrons, which were not generated at pump photon energy of 3.84 eV. This contribution of electrons overlaps with the contribution of free holes in the vicinity of 2.2 eV, where the free hole absorption is most pronounced. Thus, the DA kinetics in this spectral region are less informative (see the DA kinetics at 2.2 eV in Fig. 3.2.4b).

The generation of free electrons results also in a slower front edge of the DA response observed for uncodoped samples. The calcium codoping eliminates the slow rise of DA response.

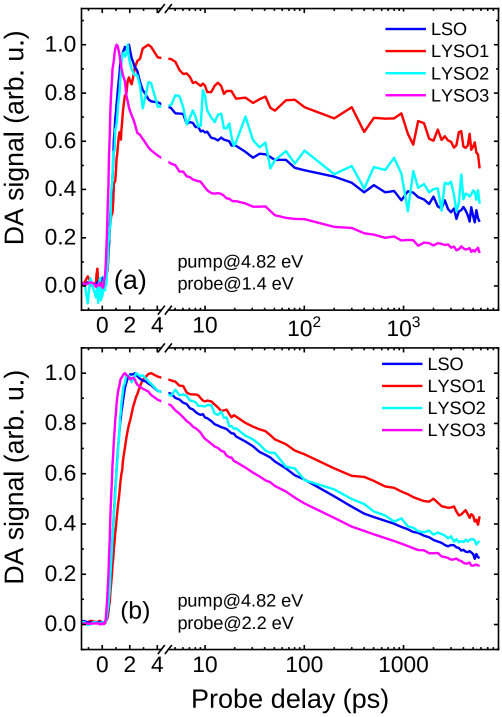

Fig. 3.2.4. Kinetics of differential absorption (normalized to peak value) in LSO sample and three LYSO:Ce samples (indicated) with different content of Ca at two different probe photon energies (indicated) after pumping with 4.82 eV photons. [P15]

The fast decay component and delayed rise in DA kinetics are well pronounced in uncodoped LYSO:Ce at pumping with 5.91 eV photons. This photon energy is still below the band gap of LYSO but sufficient for optical transitions from the valence band to defect-related states below the bottom of the conduction band. The excitation of Ce^{3+} to higher excited states or via CT transitions to the Lu 5d states [142] forming the conduction band is still expected like the Ce^{3+} excitation for smaller pump photon energies, as discussed above.

The data carpets comparing the differential absorption in LSO:Ce and LYSO:Ce are presented in Fig. 3.2.5.

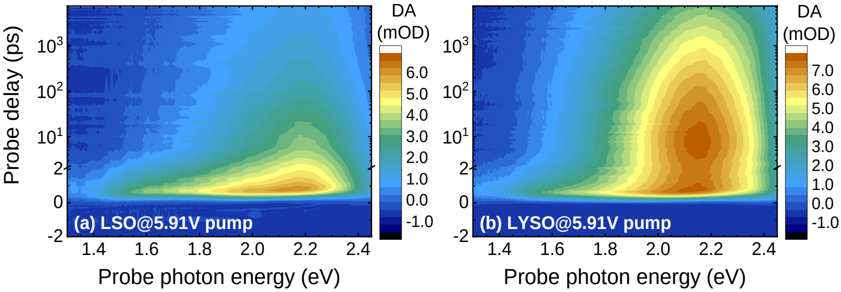

Fig. 3.2.5. Dependence of the intensity of differential absorption (color-coded as indicated by sidebar) as a function of probe photon energy and delay between pump and probe beams in LSO:Ce and LYSO:Ce. [P16]

Typical DA kinetics of LYSO:Ce are presented in Fig. 3.2.6b. Within the first 10 ps after pump, the kinetics in the low-energy part of the probing spectrum is dominated by the fastest decay component. The slow rising component is better pronounced for probe photons of larger energy. In the DA kinetics of LSO:Ce (see Fig. 3.2.6a), the same features might be qualitatively traced as in LYSO:Ce. Just the rising component is substantially less pronounced.

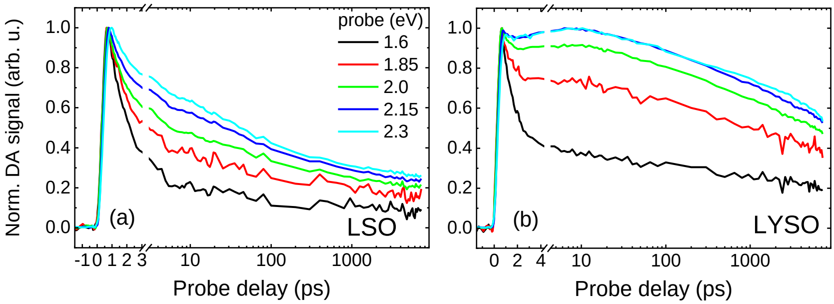

Fig. 3.2.6. Kinetics of normalized DA signal at different probe photon energies (indicated) in LSO:Ce (a) and LYSO:Ce (b) after pumping by 5.91 eV photons. [P16]

To link the properties in carrier dynamics observed by DA technique with the response time after excitation with gamma-quanta, we performed the CTR measurements on the same crystals (at 511 keV). The measurements were performed at three temperatures: 200 °C, 0 °C, and -20 °C, and the results are provided in Table 3.2.1.

Table 3.2.1. FWHM (in ps) in coincidence time resolution (CTR) measurements at different temperatures.

Sample	LSO	LYSO1	LYSO2	LYSO3
20^{o}C	115+/-1	105+/-1	93+/-1	93+/-1
0^{o}C	117+/-2	106+/-1	95+/-2	93+/-1
-20^{o}C	121+/-1	109+/-1	104+/-2	101+/-2

The CTR FWHM of LSO:Ce and LYSO:Ce crystals presented in Table 3.2.1 are similar to those reported in recent publications for similar size: 85 ps [143], 77-117 ps [58] or 197 ps [144], and, recently, 58 ± 3 ps and 98 ± 3 ps for 2×2×3 mm3 and 2×2 ×20 mm3, respectively [145]. The absolute values of the FWHM observed in CTR measurements strongly depend on sample shape and size, experiment geometry, coupling of the samples to SiPMs, types of the SiPMs, etc., and might be influenced by the readout system used. Since there are no standards for performing the CTR experiments and reporting the experiment conditions, the comparison of the absolute values obtained and reported by different research groups are not obvious. Meanwhile, all the samples in our CTR experiments had the same size and were measured at nominally the same conditions. The largest CTR FWHM is observed in LSO:Ce (sample LSO). It is shorter in LYSO:Ce (sample LYSO1) and is further reduced by Ca-codoping (samples LYSO2 and LYSO3). Note that even such a small amount of Ca as 5 ppm in LYSO2 is sufficient to substantially decrease the CTR FWHM, while the further increase in Ca content up to 30 ppm does not further improve the time response. The comparison of the samples studied shows that the temperature decrease results in degradation of the CTR for all samples. This temperature dependence is more pronounced in LYSO samples, especially in those codoped with Ca (samples LYSO2 and LYSO3).

The CTR results correlate with the results obtained by DA technique. The DA results show that the free electrons disappear with the characteristic decay time of ~1.2 ps (the fastest decay component in the DA response to short-pulse excitation). Meanwhile, the population of the lowest excited state of Ce^{3+} by electrons from the conduction band occurs in uncodoped LSO:Ce with certain delay of the order of ~5 ps, which is longer than the decay time of free electron contribution. This delay might be attributed to the contribution of electrons trapped on shallow traps, as suggested to explain the electron dynamics in GAGG:Ce and GAGG:Ce, Mg [P11]. The trapped electrons have certain probabilities to relax down to deeper defect centres acting as the centres of nonradiative recombination or to be thermally detrapped and to reach the radiative Ce^{3+} centres; probably after multiple trapping and detrapping. Oxygen vacancies are shown to be the main electronic defects in LYSO [146]. The density of oxygen vacancies is decreased by adding oxygen in the atmospheres of growth [147] and annealing [87]. Recently, it is claimed that introduction of Li codopants reduce the density of oxygen vacancies [148]. As observed in many samples and demonstrated in Fig. 6, the delay in population of Ce^{3+} level $5d^1$ by nonequilibrium electrons in LYSO:Ce is more pronounced than that in LSO:Ce. This feature might be explained by additional trapping centres formed in the mixed LYSO crystal due to composition fluctuations, as discussed above.

Our experiments show that the slow rise component of Ce^{3+} level 5d1 population is the feature most sensitively reflecting carrier trapping. Note that codoping of LYSO:Ce with Ca eliminates the slow rise component even at the codoping level as small as 5 ppm. Such a small amount of calcium ions can hardly affect the ratio of the number of Ce ions in trivalent and tetravalent state. The change of valency is feasible for crystal growth in conditions favourable for coherent doping, i. e., for the incorporation of Ca in close vicinity of Ce. Thus, the stabilization of Ce^{4+} by Ca might probably be expected only at high codoping levels. X-ray absorption (XANES) measurements show that Ce^{4+} content in uncodoped LSO:Ce is negligible [141], while 35% of Ce ions are in the state Ce^{4+} in LYSO:Ce,Ca containing 30-40 ppm of Ca [76]. Therefore, other effects than the influence of Ce^{4+}, which is currently being extensively exploited in discussions of aliovalent codoping (see, e.g., the review [53]), should be employed to interpret the elimination of the delay in population of the lowest excited state of Ce ion. Suppression of carrier trapping might be pointed out as such effect. Trapping centres due to oxygen vacancies in the crystal are expected to be the dominant electron traps in LSO/LYSO. It is assumed that Ca^{2+} ion compensates the oxygen vacancy [75], though the compensation mechanism is still not clarified. The decrease of trap concentration was observed in thermoluminescence measurements of YSO:Ce [90] and LSO:Ce [89] with increasing content of Ca. This decrease is a result of the competition between two effects of aliovalent codoping. In fact, co-dopants are introduced in the initial charge in excess to its stoichiometric composition, thus, during the crystal growth, the co-dopants decrease the concentrations of cation vacancies and, simultaneously, of anion vacancies [149]. On the other hand, the aliovalent substitution of a trivalent ion by a divalent ion in the host matrix leads to an increase of the anion vacancy concentration. Furthermore, we observe that the faster population of Ce^{3+} radiative level after optical excitation of Ce ions is linked with faster response in CTR experiments, where the material is excited with 511 keV γ-quanta. Moreover, the CTR FWHM increases with decreasing temperature (see Table 3.2.1), while this temperature dependence becomes less pronounced in Ca-doped material. This behaviour is consistent with the interpretation that the transfer of electron back to Ce^{4+} ion created after ionization of Ce^{3+} by pump photons occurs by thermally-activated transfer via localized states. The correlation of the electron dynamics observed in optical pump and probe experiments with the response time of the material after excitation by ionizing particles should be considered in view of five qualitatively different processes occurring between the moment of generation of an electron-hole pair with high energy compared to the band gap and photon emission at the activator ion Ce^{3+}: i) relaxation of the electron and hole down to the edges of the band gap, ii) migration of electrons and holes to Ce ions, iii) transfer of the energy of electron-hole pair to excite the Ce ion, iv) relaxation of electron at the excited Ce^{3+} ion to the lowest excited state $5d^1$, and v) optical transition of the electron between $5d^1$ and ground state by emitting a photon. A part of the generated electron hole pairs recombines nonradiatively and do not contribute to scintillation signal.

To conclude, the population kinetics of selectively excited Ce^{3+} ion in LSO:Ce and LYSO:Ce scintillators was studied by using optical pump and probe technique in subpicosecond domain. A delay in the population of the emitting level $5d^1$ of Ce^{3+} was observed. The delay increases with increasing excitation photon energy and is more pronounced in LYSO:Ce than in LSO:Ce. The delay is eliminated by aliovalent codoping by calcium even at Ca concentrations as low as 5 ppm. The delay is interpreted to be caused by electron trapping, which is probably enhanced in LYSO due to additional trapping states due to composition fluctuations in this mixed crystal. Timing properties after γ-excitation were studied by performing CTR measurements. It is shown that Ca-codoping results in improvement of the LYSO:Ce CTR FWHM to 93 ps.

3.3 Cerium-doped garnet scintillators

The material under study in this chapter is a cerium-doped scintillator GAGG:Ce. The crystal exhibits a high light yield of up to 50000 ph/MeV, has a short luminescence decay time (less than 100 ns) [150,151], and its emission band is peaked at ~540 nm perfectly matching the sensitivity spectrum of conventional SiPMs. Thus, this crystal might compete with LYSO:Ce and LSO:Ce in TOF-PETs and other applications. However, due to the considerably different ionic radii of Ga^{3+} and Al^{3+} in both octahedral and tetrahedral oxygen coordinations, the compound of gadolinium garnets of gallium and aluminum should contain a higher density of structural defects with respect to that of single-component garnets. Introduction of a gallium ion in close proximity of aluminum ion or vice versa results in considerable lattice strain and, as a consequence, leads to distortion of the polyhedra, which serve as trapping centers for nonequilibrium carriers. This feature has been confirmed by observation of the broadening of XRD lines in mixed gallium-gadolinium garnets [152]. Moreover, the distribution of gallium and aluminum in these garnets is basically random, however, local inhomogeneities in compound composition might significantly affect the processes of energy transfer and relaxation of electronic excitations. Moreover, GAGG crystal has several different lattice positions for the trivalent dopant ions and exhibits significant inhomogeneous broadening in the absorption and emission spectra. These inhomogeneities are being exploited for the generation of ultra-short laser pulses enabled by inhomogeneous broadening of 4f and 3d spectral lines of the activator ion, which is peculiar of the mixed garnets and is absent in single-component garnets [153]. Therefore, substantial influence of structural defects on the spectra and other properties of luminescence in $Gd_3Al_2Ga_3O_{12}$:Ce is expected.

Time-resolved luminescence spectroscopy was exploited in the current study of the rise time of luminescence after short-pulse photoexcitation. To get a better understanding of the dynamics of nonequilibrium carriers generated by irradiation, the luminescence decay in these materials was also investigated, whereas the thermally stimulated luminescence characteristics were studied to get information on defect centers in GAGG:Ce.

Samples

$Y_3(Al_{0.25}Ga_{0.75})_3O_{12}$ and $Gd_3Al_2Ga_3O_{12}$ crystals doped with Ce were grown by Czochralski method from the melt containing 1 at.% of Ce in a slightly oxidized neutral atmosphere. The samples under study with dimensions 0.7x0.7x0.5 cm^3 were cut from the seed part of the ingots exhibiting higher optical quality. The light yield of YAGG:Ce was found to be by smaller a factor of 7 than that of GAGG:Ce.

Photoluminescence kinetics of in Ce-doped GAGG

Figure 3.3.1 shows the transmission and absorption spectra of GAGG:Ce crystal at room temperature. In UV-visible range, they are formed by $4f^15d^0 \rightarrow 4f^05d^1$ interconfiguration transitions of Ce^{3+} ions and $^8S \rightarrow {}^6P$, ^6I, ^6D interconfiguration transition of Gd^{3+} ions. Gd^{3+} is a matrix-building ion, so P, I and D states form narrow subbands. The photons of 254 nm wavelength excite both Ce^{3+} and Gd^{3+} subsystems in the crystal, whereas 343 nm photons excite predominantly Ce^{3+} ions.

The photoluminescence spectra of GAGG:Ce are presented in Fig. 3.3.2. The shape of the spectra is similar for both excitation wavelengths. In consistency with the published data [151], the spectra consist of two strongly overlapping bands caused by spin-orbit splitting of ground **f** level. Meanwhile, the emission intensity under matrix excitation (at 254 nm) is by two orders of magnitude lower than that under direct excitation of Ce ions (at 343 nm). Since the absorption coefficient is similar for the two wavelengths (see Fig. 3.3.1), it seems that the difference in PL intensity is caused by the losses of the nonequilibrium carriers due to nonradiative recombination in the process of carrier transfer from the matrix to the Ce^{3+} ions.

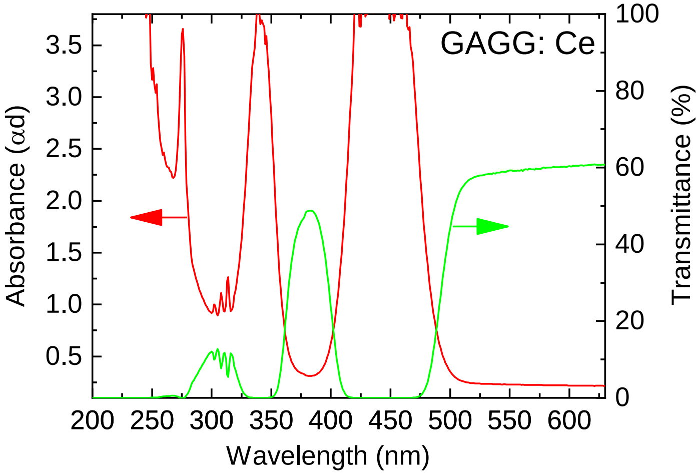

Fig. 3.3.1. Room temperature transmittance (green) and absorption (red) spectra of GAGG:Ce sample. [P4]

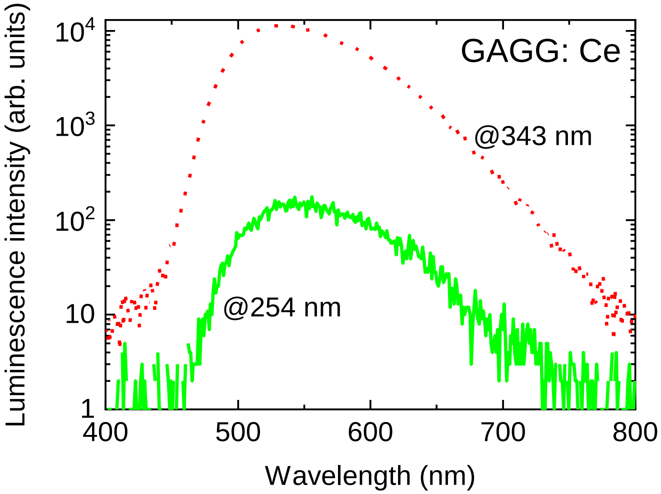

Fig. 3.3.2. Photoluminescence spectra of GAGG:Ce after short-pulse excitation at 254 nm (red solid line) and 343 nm (green dotted line). [P4]

The photoluminescence responses after a short-pulse excitation at 254 nm and 343 nm are presented in Fig. 3.3.3. Due to the presence of long PL decay components, the initial part of the response is measured at the instrumental function with the FWHM of 100 ps. The response was deconvoluted by taking into account the instrumental response function, an exponential rise with time constant τ_r and an exponential decay with time constant τ_d. The major part of the luminescence follows the leading edge of the instrumental function. However, at the excitation of Ce^{3+} luminescence through the matrix (at 254 nm), a slow rise with time constant $\tau_r = 8$ ns is observed. For the 343 nm excitation corresponding to the absorption band of Ce^{3+} ions, the slow rise component has a shorter time constant $\tau_r = 2.5$ ns, but is still substantially longer than the instrumental response function. This is in consistence with the 2 ns rise time observed in GAGG:Ce under gamma irradiation [77].

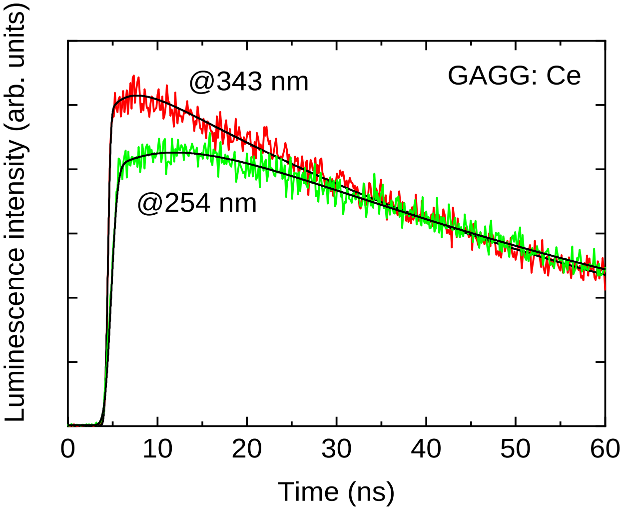

Fig. 3.3.3. The initial part of PL response to a short excitation pulse after resonant excitation of Ce^{3+} ions at 343 nm and via the matrix of GAGG single crystal at 254 nm (indicated). Smooth lines represent the fitting functions. [P4]

Figure 3.3.4 presents the PL kinetics on a longer scale obtained at two excitation wavelengths. The decay is mono-exponential with the decay times of 70 and 60 ns at 254 nm and 343 nm excitation wavelengths, respectively. The slightly longer decay time at excitation through the matrix might be explained by the process of Ce^{3+} luminescence sensitization [154].

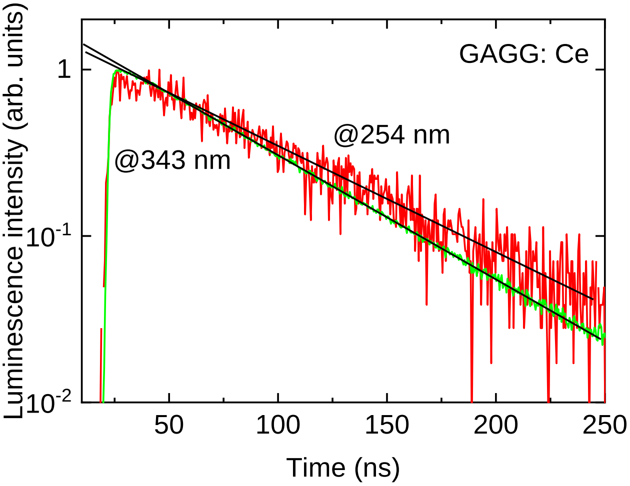

Fig. 3.3.4. Luminescence kinetics of Ce^{3+} at excitation directly to cerium ion at 343 nm and via the matrix of GAGG at 254 nm (indicated). Straight lines represent single exponential fits. [P4]

Thermally stimulated luminesce in GAGG:Ce

Excitation of the GAGG:Ce crystal in the Ce^{3+}-related absorption bands results not only in the fast (ns) photoluminescence of Ce^{3+} but also in strong phosphorescence due to effective formation of stable electron and hole centers. These centers can be detected by TSL. As seen from Fig. 3.3.5, the TSL glow curves measured after irradiation of the GAGG:Ce crystal with different energies E_{irr} are similar.

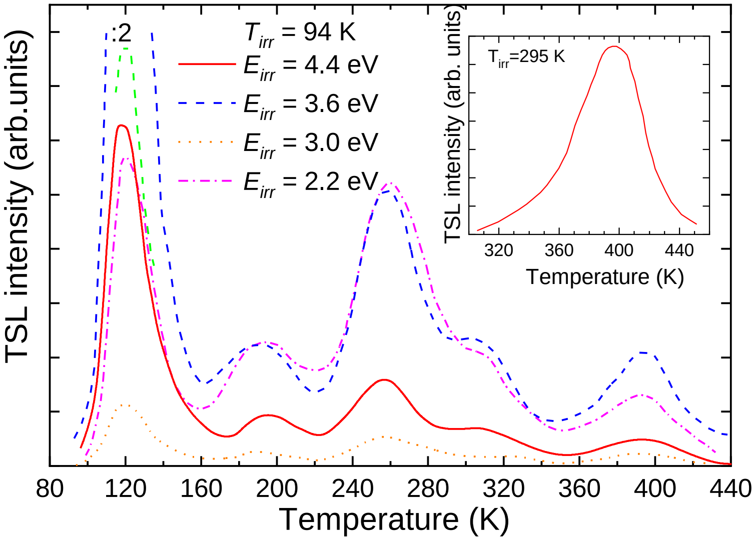

Fig. 3.3.5. Glow curves of thermally stimulated luminescence measured after irradiation of GAGG:Ce crystal at 94 K with photons of different energies E_{irr} (indicated). In the inset, the TSL glow curve measured after irradiation with E_{irr} = 3.6 eV at 295 K. [P4]

After irradiation at 94 K, the TSL glow curve peaks located at 110, 190, 260, 310, and 395 K are observed. Most of the low temperature bands were described in detail elsewhere [155–157]. After irradiation at 295 K, we observe a peak at 395 K (see the inset in Fig. 3.3.5). The resolved TSL peak above room temperature is detected for the first time. All the TSL peaks are observed for the Ce^{3+}-related emission peaked at 2.25 eV. This is an indication that all the TSL glow peaks are caused by thermally stimulated release of electrons from different electron traps and their subsequent recombination with the hole Ce^{4+} centers.

The dependences of the maximum TSL intensity at 395 K on the irradiation energy E_{irr} measured at T_{irr} = 94 K and T_{irr} = 295 K are presented in Figs. 3.3.6a and 3.3.6b, respectively (points). For comparison, excitation spectra of the Ce^{3+} emission, measured at exactly the same conditions, are also shown (solid lines). We observed that the excitation band consist of two overlapping bands. Only one of them, peaked at 460 nm (2.7 eV), coincides with the absorption band related to Ce^{3+}, as seen in Fig. 3.3.1.

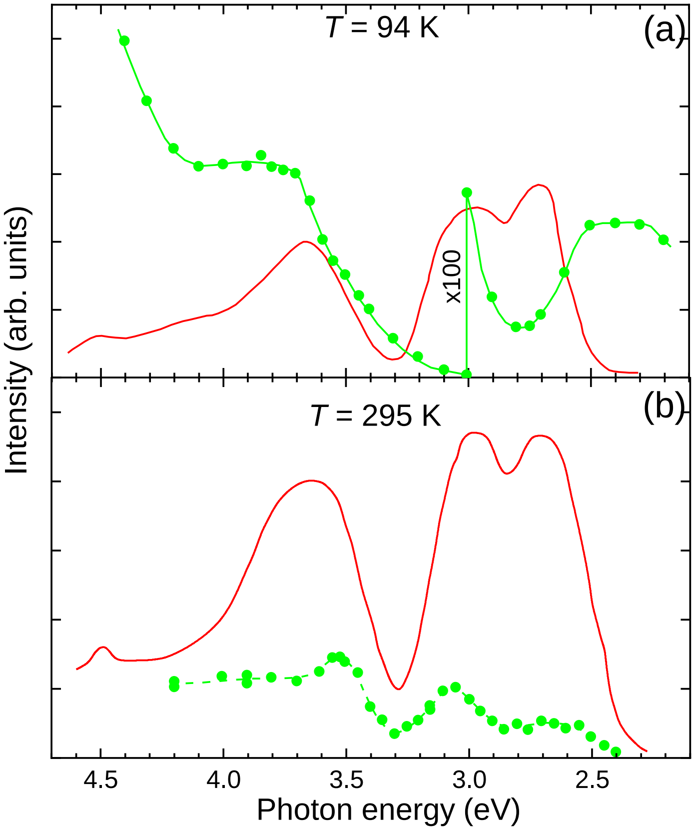

Fig. 3.3.6. Dependences of the maximum TSL intensity at 395 K on irradiation energy (points) and PL excitation spectra of the Ce^{3+} luminescence (lines) measured at irradiation temperatures of 94 K (a) and 295 K (b). [P4]

For GAGG:Ce scintillating crystals, the excitation with 4.9 eV (254 nm) photons corresponds to $^8S \rightarrow ^6D_{7/2,9/2}$ transition of Gd^{3+} ions. The edge of the conduction band has energy near 6.2 eV (200 nm) [67], so the wavelength of 254 nm predominantly corresponds to excitation of Gd^{3+} ions. The excitation with 3.64 eV (343 nm) photons corresponds to a direct excitation of cerium ions in the second Stark component of $5d^1f^0$ configuration of Ce^{3+} ions. It is worth noting that the kinetics at both excitations have a rise component on a nanosecond scale. The rise time at the sub-bandgap excitation (4.9 eV) is only by a factor of three longer than that at the direct Ce^{3+} excitation. This is an indication of a considerable exchange of electrons between the radiative Ce^{3+} centers, the sub-bands created by Gd^{3+} ions, traps, and the conduction band, where they might become trapped and reach the Ce^{3+} radiative centers with certain delay. This exchange results in slowing of the PL rise time even at the excitation wavelength corresponding to intracenter excitation.

To clarify the excitation transfer process in the crystal, we analyzed the dependences of the maximum TSL intensity at 395 K on irradiation energy. We observed that the creation spectrum of recombining electron and hole centers is located in the Ce^{3+}-related absorption bands located at $E_{irr} > 3.3$ eV and originating from the second Stark component of $5d^1f^0$ configuration (the band at 3.65 eV) and the upper electron transitions of Ce^{3+}. The population efficiency of these centers in the region of the lowest-energy absorption band of Ce^{3+} (around 2.8 eV) is substantially smaller (at least by two orders of magnitude). At 295 K, the radiative centers are optically populated under irradiation in all the absorption bands of Ce^{3+} (Fig. 6b). These data indicate that the second Stark component of $5d^1f^0$ configuration of Ce^{3+} is located inside the conduction band, so that the excitation into Ce^{3+} results in the ionization of Ce^{3+} even at 94 K. As a result, the hole centers Ce^{4+} and the electrons trapped at different electron traps are optically created. Their thermally stimulated recombination results in the TSL glow curve peaks shown in Fig. 3.3.5.

The fast rise time in the Ce^{3+} luminescence kinetics at both 4.9 eV and 3.64 eV excitations indicates that Gd^{3+} ions play a significant role in the excitation transport even at Ce^{3+} intracenter excitation. After Ce^{3+} excitation into the second Stark component and subsequent electron relaxation into conduction band, a considerable part of the electrons are captured by matrix-building Gd^{3+} ions. An important role of Gd^{3+} ions was revealed in the study of Gd_2SiO_5:Ce crystals [158]. The migration of the electrons along Gd^{3+} subsystem in the crystal slows down the rate of the electron transfer back to the Ce^{3+} ions, where they recombine radiatively.

Another, less effective energy transfer process is also possible. This effect takes place at low temperatures under irradiation of the GAGG:Ce crystal in the energy range $E_{irr} < 3.0$ eV. Indeed, TSL peaks at the same positions but of considerably lower intensity appear even after irradiation with $E_{irr} = 2.2$ eV at 94 K (see Fig. 3.3.5), however, the TSL intensity under this irradiation is even larger than that under irradiation into the absorption band ($E_{irr} = 2.8$ eV) (Fig. 3.3.6a). Probably, optically initiated population of defects in this case can be explained by charge transfer processes, analogous to those considered in [159] for Ce^{3+}-doped oxyorthosilicates, e.g., by the optically stimulated electron transfer from the valence band to various electron traps existing in the crystal.

The TSL peak corresponding to the activation temperature near 395 K is also of interest. At room temperature, this color center undergoes slow spontaneous thermal ionization and can be a source of carriers for the subsequent capture by ions Ce^{3+}. Our results lead to certain considerations on the position of the energy level of this color center in the conduction band. Since the center is partially populated at room temperature, the position should not be above ^6P level of Gd^{3+}. The activation energy for the 395 K TSL peak under irradiation in the lowest absorption band (determined from the $\ln I_{\mathrm{TSL}}$ dependence on $1/T_{\mathrm{irr}}$) is about 0.33 eV. The activation energy for quenching the Ce^{3+} luminescence is reported to be equal to 0.25 eV in a sintered sample [157] and 0.36 eV in a crystal [160]. Thus, we concluded that the ground states of both the Ce^{3+} radiating level and the color center are ~0.3 eV below the bottom of the conduction band. The nature of the color center needs further study. The available investigation results point out that the spontaneous electron release from this color center at room temperature does not substantially affect the luminescence kinetics. As seen in Fig. 3.3.4, the decay is slightly slower at the excitation through Gd^{3+} ions but the difference in the decay times is less than 20%.

When the scintillation occurs in GAGG:Ce crystal under ionizing radiation, the major part of the carriers will be captured by matrix-building Gd^{3+} ions. Thus, the rise time of the scintillation is expected in the range of a few nanoseconds. The relatively long rise time of the scintillation might be the limiting factor to achieve acceptably fast timing by using the radiation detectors based on GAGG:Ce, especially in PET scanners, where the energy deposit is considerably lower than that in high-energy physics applications.

Transient absorption in Ce-doped $Y_3(Al_{0.25}Ga_{0.75})_3O_{12}$ and $Gd_3Al_2Ga_3O_{12}$ garnet scintillators

A more detailed study of the role of Gd^{3+} subsystem in the energy transfer processes in garnet crystals plays important role in future optimization of these crystals for exploiting as scintillation material. In particular, scintillation crystals and phosphors based on mixed garnets doped with cerium attract considerable interest due to capability of manipulation with their luminescent and scintillation properties by changing the Al/Ga ratio in the compound [55]. This capability is enabled by the change in the strength of the crystal field acting on the activator ions and, consequently, by shifting the energy levels of Ce^{3+} relative to the bottom of the conduction band. Moreover, optimization of garnet composition serves also for the enhancement of the light yield of these scintillators [61]. The most impressive results have recently been achieved in GAGG:Ce, where the scintillation yield of up to 58000 ph/MeV was demonstrated both in single crystals and transparent ceramics [55,161].

After demonstration of the formation of $Y_3Al_2Ga_3O_{12}$ (YAGG) via sol-gel synthesis [162] and the micro-pulling down method [37], this mixed garnet attracts considerable interest as host material for Ce-based phosphors and scintillators. YAGG:Ce might be used as a green phosphor in light-emitting diodes with high color rendering [163]. Strong persistent green [164] and yellow [165] luminescence was also observed in $Y_3Al_2Ga_3O_{12}$:Ce ceramics co-activated with chromium ions [164,165]. In both garnets, GAGG and YAGG, the second and third Stark components of $4f^05d^1$ configuration of Ce^{3+} ion are located in the conduction band [165]. However, the host matrix of YAGG does not contain Gd^{3+} sublattice. Therefore, the comparison of Ce-doped GAGG and YAGG offers an informative insight into the influence of gadolinium on the dynamics of nonequilibrium carriers.

The measured absorption spectrum of Ce^{3+} in YAGG:Ce crystal is similar to that reported before [166]: it contains three bands peaked at 448, 350, and 250 nm. Thus, pumping at 254 nm coincides quite well with the upper, third, absorption band due to interconfiguration electronic transition $4f^15d^0 \rightarrow 4f^05d^1$ of Ce^{3+} ions. Figure 3.3.7 shows transient absorption kinetics in YAGG:Ce crystal for different excitation energy densities at 254 nm. The initial part of the decay kinetics is depicted in Fig. 3.3.8. The kinetics consists of three components. The fast and intermediate components have characteristic decay times of 2 ps and ~100 ps, respectively, with no significant dependence on excitation intensity. The decay time of the slow decay component is in nanosecond domain and decreases down to a few nanoseconds as the excitation intensity increases.

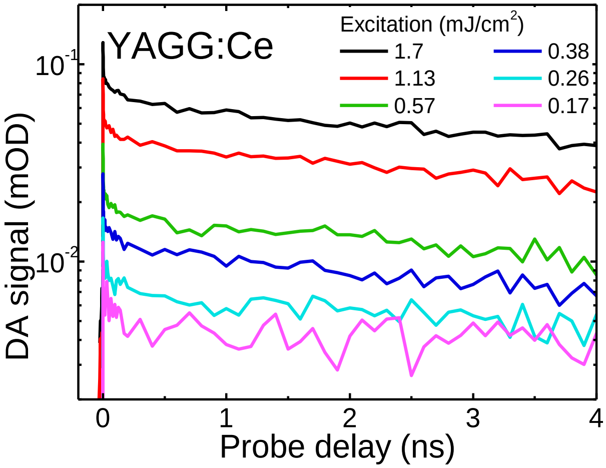

Fig. 3.3.7. Kinetics of optical density induced by short-pulse excitation of YAGG:Ce crystal at 254 nm for different excitation pulse energy densities (indicated). [P3]

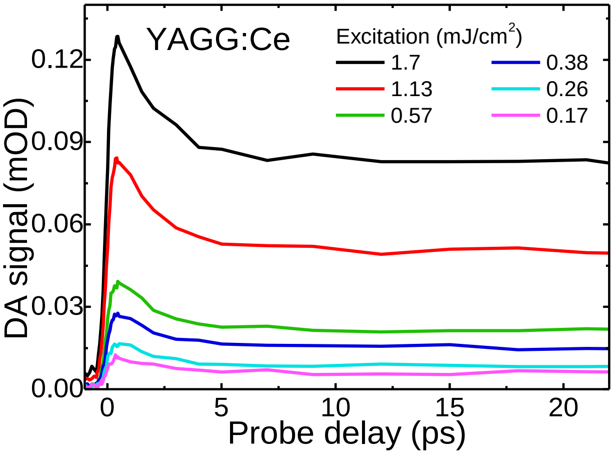

Fig. 3.3.8. Initial part of the kinetics presented in Fig. 3.3.7 [P3]

Since the excitation YAGG:Ce crystal with 4.9 eV (254 nm) photons corresponds to transition to the third Stark component of $4f^05d^1$ configuration of Ce^{3+} ions, and the edge of the conduction band in Al/Ga mixed garnets has energy near 6.2 eV (200 nm) [67], the wavelength of 254 nm corresponds to the predominant excitation of Ce^{3+} ions. However, a fast delocalization of the electrons from Ce^{3+} is highly probable, since the excited state is within the conduction band. Thus, the initial transient absorption decay is, most probably, caused by fast delocalization within ~2 ps, the further kinetics of transient absorption with the decay time in the 100 ps range proceeds after the equilibrium between the processes of depopulation and repopulation of Ce^{3+} and recombination is established. The decay in the nanosecond time domain is influenced by capturing of electrons from the conduction band by traps due to shallow defect states, which are present in abundance in mixed garnets.

Influence of gadolinium on carrier dynamics in GAGG:Ce

Figure 3.3.9 shows the absorbance spectrum of GAGG:Ce crystal at room temperature. The spectrum consists of absorption bands due to $4f^15d^0 \rightarrow 4f^05d^1$ interconfiguration transitions of Ce^{3+} ions and $^8S \rightarrow {}^6P$, ^6I, ^6D interconfiguration transitions of matrix-building gadolinium ions forming narrow subbands due to P, I, and D states. The absorption band corresponding to the transition to the third Stark component of $4f^05d^1$ configuration is shifted to short wavelength range in GAGG in comparison with that in YAGG. Therefore, the photons of 254 nm wavelength excite Ce^{3+} ion only into the long-wavelength shoulder of the absorption band due to the third interconfiguration electronic transition $4f^15d^0 \rightarrow 4f^05d^1$ and Gd^{3+} subsystem directly via $^8S \rightarrow {}^6D$ transitions.

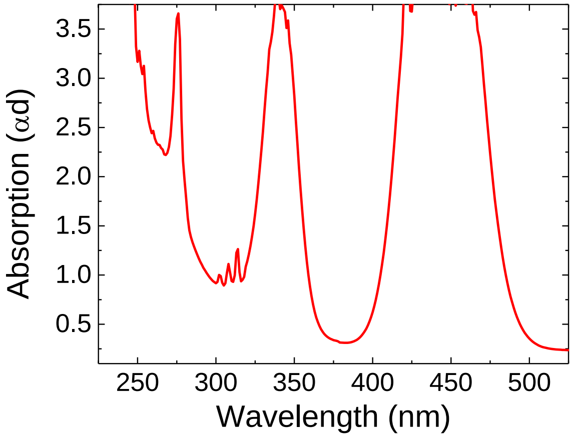

Fig. 3.3.9. Room temperature absorbance spectrum of GAGG:Ce. [P3]

Figures 3.3.10 and 3.3.11 show transient absorption kinetics in GAGG:Ce crystal at different excitation pulse energy densities at the wavelength of 254 nm in the range of nanoseconds and within the first 20 picoseconds after short-pulse excitation, respectively.

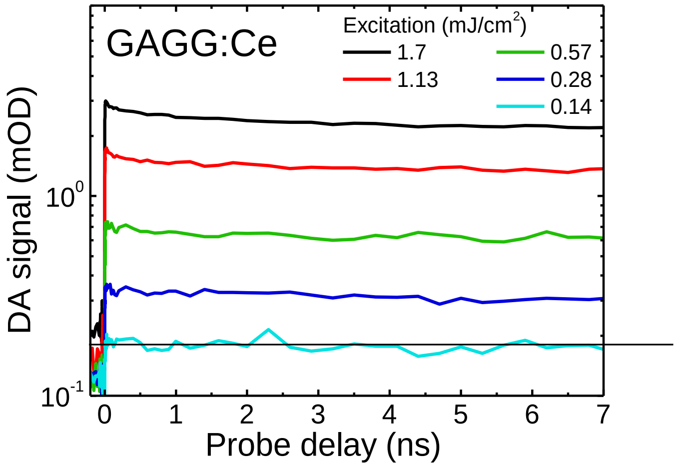

Fig. 3.3.10. Kinetics of optical density induced by short pulse excitation of GAGG:Ce crystal at 254 nm for different excitation pulse energy densities (indicated). [P3]

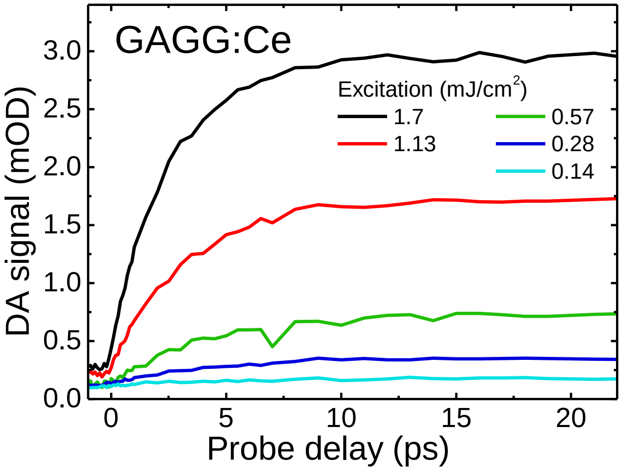

Fig. 3.3.11. Initial part of the kinetics presented in Fig. 3.3.10. [P3]

The TA decay at low excitation intensities is monoexponential with the characteristic decay time substantially exceeding the time range under study (8 ns). The decay becomes increasingly nonexponential at elevated excitation intensities. The most interesting feature in the TA response to a short pulse excitation is the rising part of the response. In contrast to PWO and YAGG:Ce, where the rise time is below the time resolution in our experiments (200 fs), the rise of the TA response in GAGG:Ce is considerably slower. The rise time is approximately 10 ps at low excitation of 0.14 mJ/cm^2 and decreases to 5 ps as the excitation is increased by an order of magnitude.

For GAGG:Ce scintillating crystals, the excitation with 4.9eV (254 nm) photons corresponds to $^8S \rightarrow ^6D_{7/2,9/2}$ transition of Gd $^{3+}$ ions and a weak excitation into the long wavelength wing of the band corresponding to transition to the third Stark component of $4f^05d^1$ Ce^{3+} electronic configuration. Similarly to YAGG crystal, the band gap due to p→d interband transitions has energy near 6.2 eV (200 nm) [67], thus, the wavelength of 254 nm corresponds to the predominant excitation of Gd^{3+} ions. Consequently, electrons do not appear in the conduction band due to this transition. Thus, the TA signal we observed here is due to absorption by free holes, which are released from Gd^{3+} ^8S ground state into the valence band. This assumption is in good agreement with the analysis performed by P. Dorenbos [167], showing that the ground state of Gd^{3+} in $4f^7$ shell is localized in the valence band. The rise of TA, which takes a few picoseconds, is caused by delocalization of holes from Gd^{3+} to valence band. When the hole is localized at the Gd^{3+} f-level, its direct transfer by absorption of photons to p orbitals, forming the top of valence band is forbidden. However, the transition might occur via mixed p-d orbitals in the valence band. This relaxation takes 5-10 ps, depending on the density of nonequilibrium holes, which is observed as the rise time in TA experiments. The decay of TA kinetics proceeds rather slow in comparison with that in PWO and YAGG:Ce, with the characteristic decay time of 1 ns even at the first decay stages and even more slowly afterwards. This time is required for the hole to be captured from the valence band by Ce^{3+} ion. This interpretation is consistent with the published observation that the luminescence rise time in GAGG:Ce equals several nanoseconds [P4].

Influence of doping on free carrier absorption response time in GAGG

This subchapter is focused on the investigation of the origin of slow component in the luminescence response of GAGG:Ce and the influence of magnesium co-doping on the response time at different Mg contents in the crystal by studying the kinetics of electron population at cerium ions. We exploited the optical pump and probe technique and used the capabilities of this technique: i) high time resolution limited by the laser pulse duration (200 fs in our experiments), ii) selective excitation of different structural units of the crystal, and iii) simultaneous monitoring of time and spectral characteristics of the response enabling to spot specific features due to the contributions of different structural units and response mechanisms. A set of

GAGG:Ce samples with different level of codoping was prepared for the study, a sample cut from a crystal without any intentional doping was also added to the set for comparison. The response time of the samples under study in our optical pump and probe experiments was tested and compared under gamma-ray excitation using coincidence time resolution technique, which is a conventional measurement configuration in medical imaging applications and in many high-energy physics experiments.

Four samples were prepared for the study: nominally undoped GAGG (labeled hereafter as S0), GAGG:Ce with 550 ppm of Ce (S1), GAGG:Ce,Mg with 530 ppm of Ce and 10 ppm of Mg (S2), and GAGG:Ce,Mg,Ti codoped with 800, 20, and 20 ppm of Ce, Mg, and Ti, respectively (S3). The samples used in this study were doped by Ce at a similar level, which has been measured by means of the Glow Discharge Mass Spectroscopy (GDMS) for sample S2 or estimated by comparing the optical absorption at the peak of the first allowed f-d transition of Ce3+ ions in other samples. The codoping of the GAGG:Ce crystals by magnesium was applied at different levels and estimated by comparing the optical absorption due to Mg-related defects, as described in [P9]. The small amount of titanium was introduced with expectation to inhibit stabilization of Ce^{4+} ions. The crystal samples in the shape of blocks with the dimensions of 3x3x5 mm^3 for CTR measurements and 10x10x1-3 mm^3 for study by nonlinear optics technique have been prepared from single-crystal ingots having the diameter not less than 45 mm and the length exceeding 80 mm. All surfaces of the blocks have been polished.

The absorption spectra of GAGG with different doping are provided in Fig. 3.3.12. The nominally undoped GAGG exhibits narrow lines attributed to the f-f absorption bands of matrix-building gadolinium ions [P7 and a broad absorption tail towards the band gap energy. The spectra of Ce-containing samples have, as usual, two distinct absorption lines due to optical transition from the ground state to two components of d level split by crystal field. Magnesium introduces a broad absorption band in the near UV region, most probably caused by a charge transfer transition to a defect state, stabilized by Mg^{2+}, from the valance band [P12].

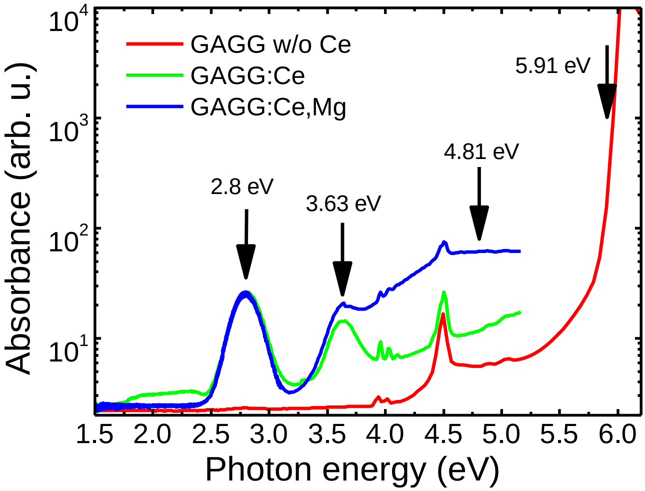

Fig. 3.3.12. Absorption spectra of nominally undoped GAGG, GAGG:Ce, and GAGG:Ce,Mg. Pump energies used in our transient absorption experiments are indicated by arrows. [P11]

Photons at the energy of 2.8 eV (443 nm) were used for resonant intracenter excitation of Ce^{3+} ions from the ground state into the first excited level $5d^1$. In Fig. 3.3.13, the color-coded intensity of differential absorption, i.e., the difference in the absorption of probe with and without pump, is presented as a function of the probe photon energy and the delay between subpicosecond pump and probe pulses for samples S1 (a) and S2 (b). The nonlinear absorption is spectrally centered at ~1.35 eV and extends to the high-energy side for a few hundreds of meV. No detectable influence of Mg-doping on the nonlinear absorption at this pump photon energy was observed either in the sample S2, as depicted in Fig. 13b, or in the samples with higher Mg content. The nonlinear absorption in the nominally undoped GAGG was by orders of magnitude lower and indicated a low content of unintentionally introduced Ce. Therefore, this feature in the nonlinear absorption might be attributed to the electrons populating the first excited state of Ce^{3+} ion. As expected, the population of the state instantaneously follows the excitation pulse (in subpicosecond domain in our experiments) and decays in nanosecond domain, in consistence with many luminescence measurements in nanosecond domain (see, e.g., [P4]).

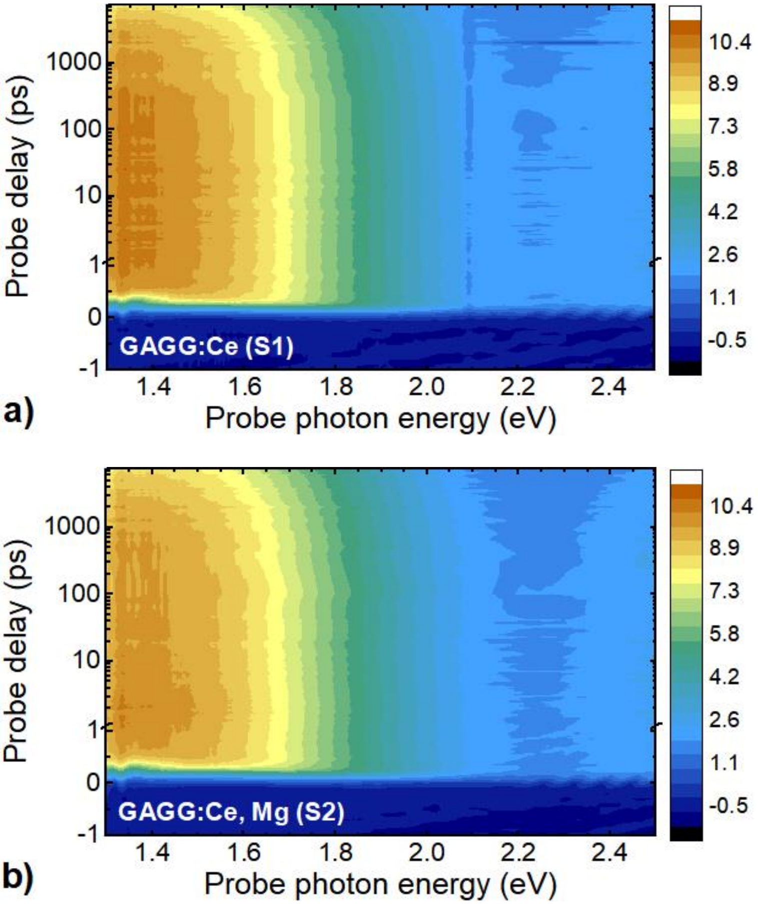

Fig. 3.3.13. Differential absorption of GAGG:Ce without, sample S1, (a) and with Mg codoping, S2, (b) as a function of probe photon energy and delay between pump and probe pulses at pump photon energy of 2.8 eV. Note the scale change from linear to logarithmic at 1 ps. [P11]

The photon energy of 3.63 eV (342 nm) was selected to excite the Ce^{3+} ion into the second excited level $5d^2$, which is above the bottom of the conduction band [160,168].

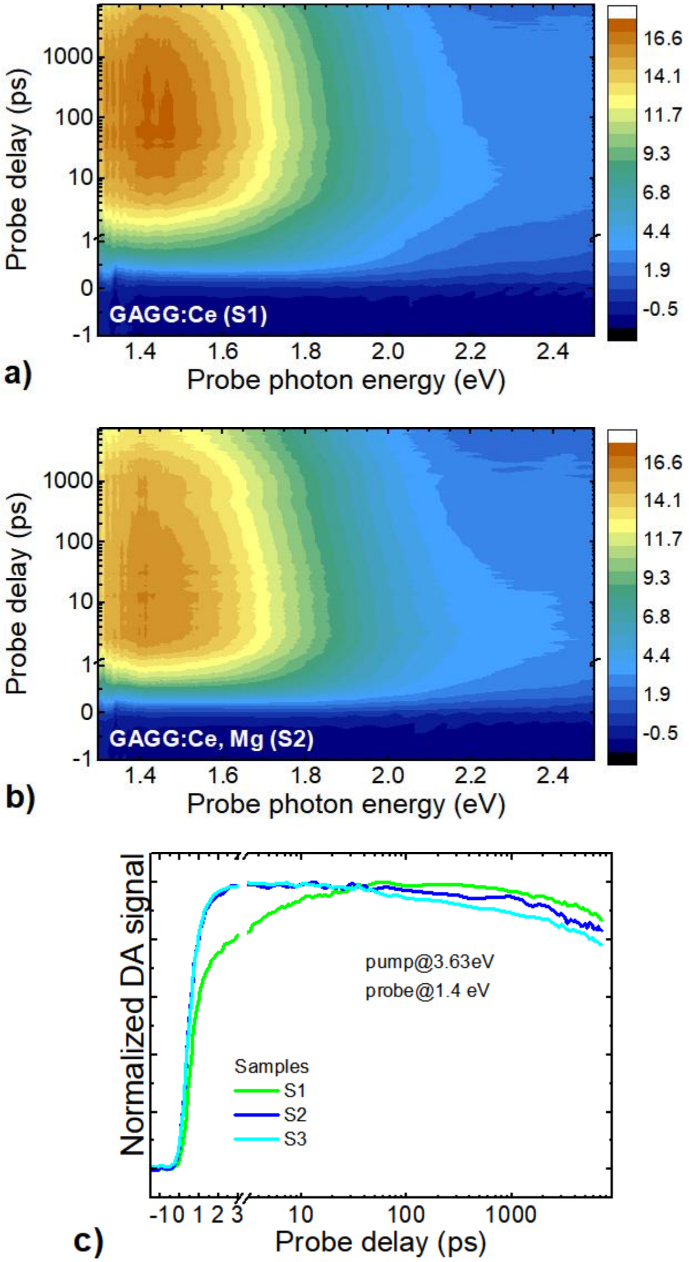

Fig. 3.3.14. Differential absorption of GAGG:Ce without, sample S1, (a) and with Mg codoping, S2, (b) as a function of probe photon energy and delay between pump and probe pulses at pump photon energy of 3.63 eV and kinetics of differential absorption at 1.4 eV in the samples with different doping (c). Note the scale change from linear to logarithmic at 1 ps in (c). [P11]

The spectrum of nonlinear absorption at this pump photon energy (see Fig. 3.3.14a,b) is also dominated by the component attributed, see above, to the absorption from the lowest Ce^{3+} excited state. All codoped samples exhibit actually the same spectral features and time evolution of their nonlinear absorption. Meanwhile, a slow component in the rising part of the nonlinear response is observed in the S1 sample without codoping. The kinetics of the differential absorption (i.e., the vertical cross-sections of the data carpets like those in Fig. 3.3.14 a,b) at the probe photon energy of 1.4 eV are provided in Fig. 3.3.14c. Note that the magnesium-doping is sufficient to eliminate this slow rise component even at the Mg content as low as 10 ppm (sample S2).

The pump photons with energy of 4.81 eV (258 nm) excite the Gd^{3+} ions via $^8S_{7/2}$-^6I_j electronic transition, whereas this photon energy is also sufficient for charge-transfer optical transitions from Ce^{3+} ions to the conduction band. A typical differential absorption data carpet for this pump photon energy is presented in Fig. 3.3.15a. A new feature appears both in spectral and time domains: strong induced absorption with broad spectrum ranging to ~2.5 eV and decaying within a few picoseconds is observed. We attribute this component to nonlinear absorption due to the excitation of gadolinium ions. The kinetics of this component at its peak photon energy of 2.2 eV is presented in Fig. 3.3.15b. Both components, the fast one due to Gd and the Ce-related component, though much weaker, have their contributions to the kinetics.

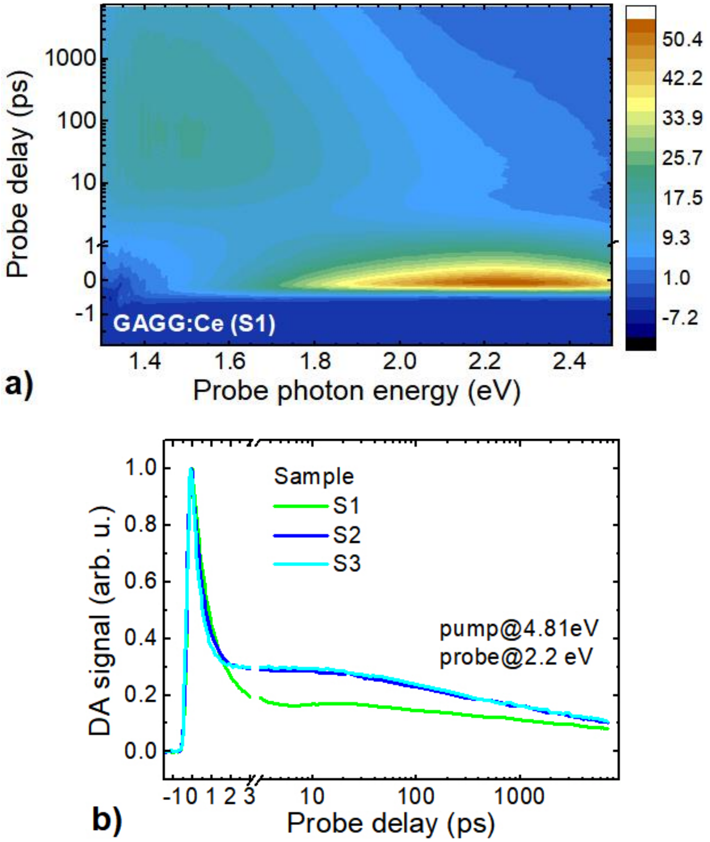

Fig. 3.3.15. Differential absorption of GAGG:Ce, sample S1, (a) as a function of probe photon energy and delay between pump and probe pulses at pump photon energy of 4.81 eV (a) and kinetics of differential absorption at 2.2 eV after short-pulse excitation of GAGG with different doping at 4.81 eV (b). [P11]

In Fig. 3.3.16, the data carpets displaying the dynamics of the differential absorption after excitation with the photon energy of 5.91 eV (210 nm) are presented for samples S0, S1, and S2. All the structural units discussed above as well as the trapping centers below the band gap might be excited at this pump photon energy. Both components previously attributed to the absorption by electrons populating the lowest excited Ce^{3+} state and by absorption at Gd^{3+} ion are observed at the 5.91 eV pump. As predicted theoretically [160] and evidenced experimentally [P7], the ground state of gadolinium is in the valence band. Thus, the excited electrons as well as the holes at the ground state of Gd or relaxed to the valence band might contribute to the differential absorption. However, the differential absorption extends to the probe photon energies well below 0.8 eV [P9], i.e., to the energies substantially smaller than the energy gap between the excited state of Gd^{3+} and the bottom of the conduction band. Consequently, the absorption is dominated by nonequilibrium holes. A short decay time of the corresponding component is an indication that the intracenter recombination of photoexcited electron and hole at Gd ion occurs without relaxation of the holes to the valence band.

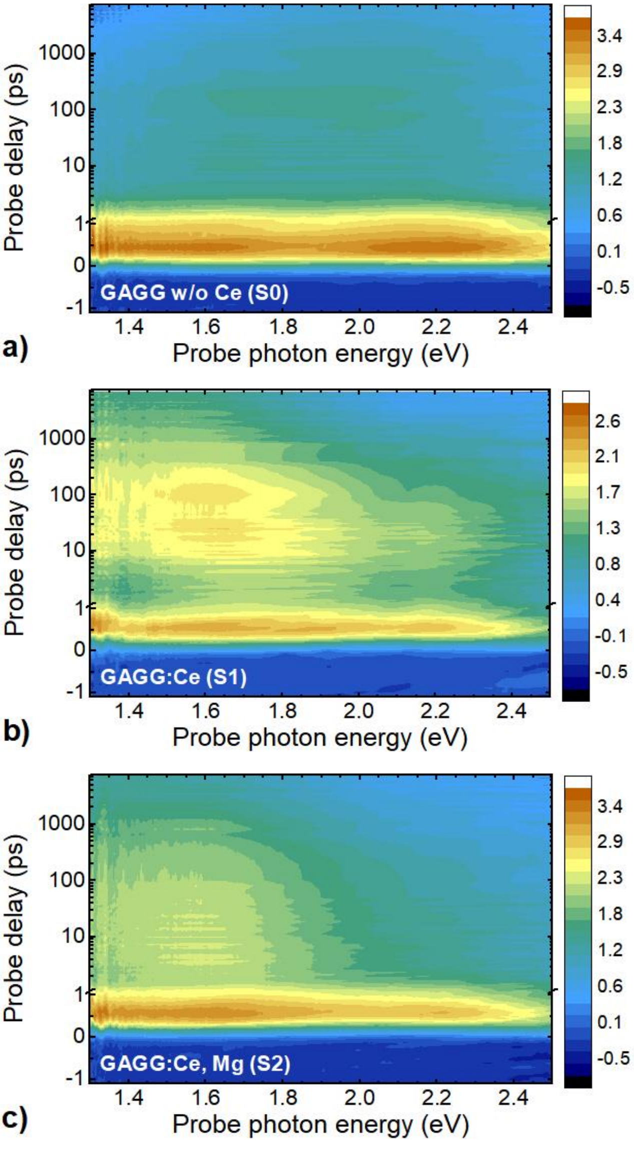

Fig. 3.3.16. Differential absorption of GAGG as a function of probe photon energy and delay between pump at photon energy of 5.91 eV and probe pulses in samples S0 (a), S1 (b) and S2 (c). Note the scale change from linear to logarithmic at 1 ps. [P11]

The kinetics of differential absorption probed at 1.4 eV in all the samples studied after their excitation at 5.9 eV are compared in Fig. 3.3.17. The fast component due to the absorption by nonequilibrium holes at Gd ions and the component caused by electrons populating the first excited state of Ce^{3+} are evident in all the samples (as discussed above, the weak Ce-related component in sample S0 is caused by trace amount of Ce). The population of Ce^{3+} has two components. The characteristic population rise time is below 1 ps for the fast component and of the order of a few picoseconds for the slow one. Codoping by magnesium results in the elimination of the slow component.

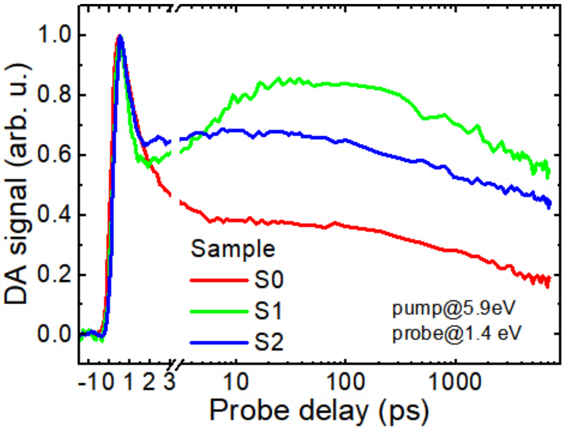

Fig. 3.3.17. Kinetics of differential absorption at 1.4 eV after short-pulse excitation of GAGG with different doping at 5.91 eV. [P11]

The correlation of the features in carrier dynamics observed by optical pump and probe technique with the time response in detecting gamma quanta was tested by performing CTR measurements. The full width at half maximum (FWHM) of the timing histogram is presented in Fig. 18 as a function of overvoltage. These data were obtained by using GAGG:Ce crystals without and with codoping. The measurements were performed at +20°C and the data reported in Fig. 3.3.18 are taken at the voltage threshold optimal for each overvoltage. Sample S1 (GAGG:Ce) provided an optimal CTR of 193±4 ps, which, to the best of our knowledge, is the best result currently observed for GAGG:Ce [58,169]. A further improved time resolution was obtained in the measurements with codoped crystals: samples S2 and S3 reached an optimal CTR of 169±3 ps and 165±3 ps, respectively. The data presented here show that the codoping by Mg even at the level as low as 10 ppm is sufficient to substantially improve the timing performance. These results confirm the previous indications that GAGG:Ce codoped with Mg is capable of better time resolution [58] but now at a significantly improved level.

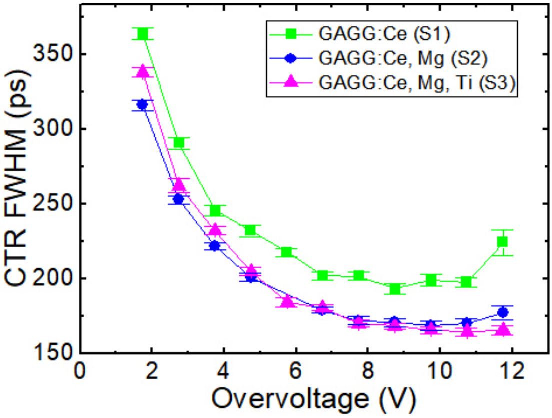

Fig. 3.3.18. CTR FWHM as a function of the overvoltage applied to RGB-HD SiPMs. The silicon detectors were coupled to 3x3x5 mm3 GAGG:Ce (S1), GAGG:Ce, Mg (S2) and GAGG:Ce, Mg, Ti (S3). [P11]

The improvement of the time resolution by introduction of Mg even at the level of 10 ppm observed here should be pointed out as one of the key results of this work. The best value of FWHM demonstrated in coincidence time resolution experiment was 165 ps. This is a remarkable result in view of prospective applications. The time resolution might be improved by dedicated matching of the scintillator and purposefully designed and fabricated SiPMs.

As presented above, the codoping by Mg eliminates the slow component of population of Ce^{3+} excited state, when the nonequilibrium electrons are generated into the conduction band. The entire set of the results on the differential absorption finds an explanation by trapping of the nonequilibrium electrons moving through the crystal matrix. There are several processes influencing the population dynamics. To describe temporal characteristics of the processes, we used a set of rate equations (3.3.1-3) describing populations of the first (N_{5d1}) and second (N_{5d2}) excited states of Ce^{3+} and the population of electron traps N_T. Besides unintentional impurities and structural defects, the band gap modulation due to composition fluctuations in multicomponent garnet crystal GAGG might serve to form trapping centers for electrons in this crystal. All these traps are generalized in the model for rate equations by a single trapping level or band. The energy scheme is presented in Fig. 3.3.19, where the relaxation and recombination routes are marked by arrows with the corresponding time constants indicated. The time constants τ_{21}, τ_{2T}, τ_{T1}, and τ_{1G} are for relaxation transitions from state $5d^2$ to $5d^1$, state $5d^2$ to trapping level, trapping level to state $5d^1$, and $5d^1$ to ground state, respectively. $G(t)$ denotes the Gaussian distribution function representing initial laser pulse.

$$\frac{dN_{5d2}}{dt} = G(t) - \frac{N_{5d2}}{\tau_{21}} - \frac{N_{5d2}}{\tau_{2T}} \tag{3.3.1}$$

$$\frac{dN_T}{dt} = \frac{N_{5d2}}{\tau_{2T}} - \frac{N_T}{\tau_{T1}} \tag{3.3.2}$$

$$\frac{dN_{5d1}}{dt} = \frac{N_{5d2}}{\tau_{21}} + \frac{N_T}{\tau_{T1}} - \frac{N_{5d1}}{\tau_{1G}} \tag{3.3.3}$$

Fittings of the kinetics of differential absorption at 1.4 eV obtained experimentally in uncodoped and codoped GAGG:Ce after excitation at pump photon energy of 3.63 eV are presented in Fig. 3.3.20. The characteristic time of relaxation from the second to the lowest excited state was maintained constant in all fittings. All the time constants for three samples with Ce and different Mg content are presented in Table 3.3.1. The fitting enabled us to estimate the time of intracenter electron relaxation time to be ~500 fs. The fitting results provide certain estimates of characteristic times for the main processes governing the nonequilibrium electron dynamics in uncodoped and codoped GAGG:Ce and evidences a clear feature that the constants experience significant change in the Mg-codoped crystals.

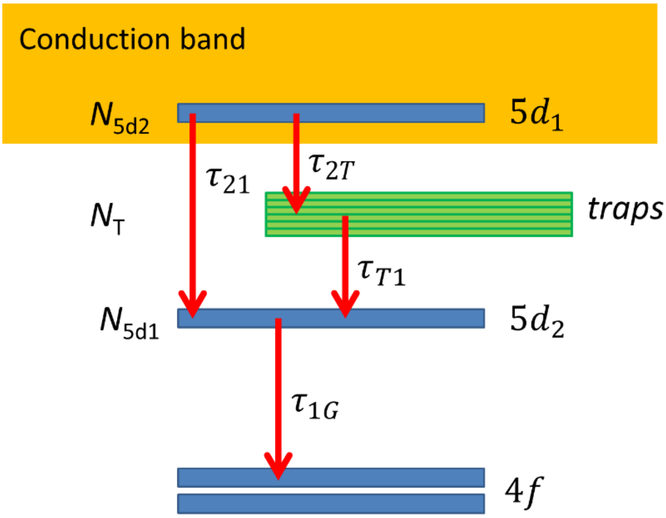

Fig. 3.3.19. Energy scheme of Ce^{3+} in GAGG (not to scale) with relaxation and recombination transitions described by eqs. 3.3.1-3 indicated by arrows and labeled by the corresponding time constants for these transitions. [P11]

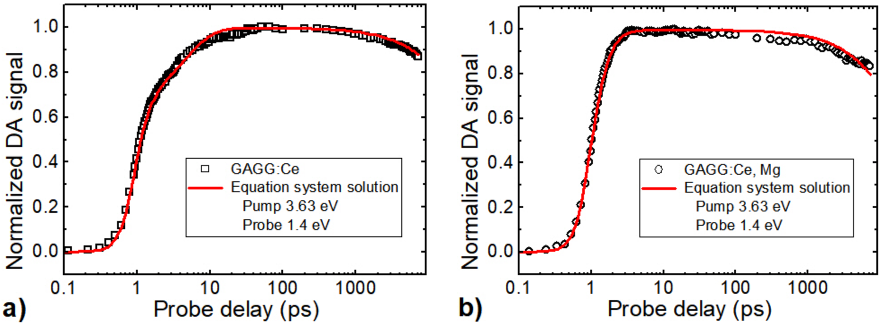

Fig. 3.3.20. Fittings of experimental (black points) and simulated (red lines) kinetics of differential absorption at 1.4 eV in uncodoped (a) and codoped (b) GAGG:Ce (samples S1 and S2, respectively). [P11]

Table 3.3.1. Time constants used in fitting the differential absorption kinetics obtained experimentally and simulated using eqs. 3.3.1-3.

Sample	**Mg content, ppm**	τ_{2T}, **,ps**	τ_{T1}, **ps**	τ_{21}, **ps**	τ_{1G}, **ns**
S1	**-**	1.1	4.1	0.52	**56**
S2	**10**	11.8	1.4	0.52	**32**
S3	**20**	89	1	0.52	**24**

The improvement of the time response by Mg-codoping at excitation of GAGG:Ce by gamma quanta is observed and interpreted by shifting of the valence state of Ce ions in favor of Ce^{4+} (see, e.g. [170]). Our results on nonlinear optical absorption are not in line with this interpretation. First of all, we showed that the fast and slow rise components in population of the emitting level of Ce ion occur even at direct excitation of cerium ions, when the availability of hole at the ground state in Ce^{4+} provides no advantage in view of response time over directly excited Ce^{3+} ion. The second important point is that we observe the improvement of time response even at Mg-codoping as low as 10 ppm. It might hardly be expected that the doping at such level could significantly change the ratio between the concentrations of Ce^{3+} and Ce^{4+}, which is close to 1:1 even in uncodoped GAGG:Ce.

Provided that magnesium distribution in the crystal is homogeneous, Mg concentration at 10 ppm corresponds to one Mg^{2+} ion per 2700 nm^3 (~1400-unit cells) of the GAGG matrix. At the Ce concentration of ~500 ppm and homogeneous distribution, one Ce ion correspond to the volume of ~60 nm^3 (or less than 40 unit cells). Thus, the probability of Mg-Ce pairing to create a charge-balanced link Ce^{4+}-Mg^{2+} is low. To estimate the probability, the localization of Ce and Mg ions in specific sites of the garnet structure has to be taken into account. Let us assume that the pairing occurs when Ce and Mg ions appear at least in the second cation coordination sphere of each other. Garnet-type crystal structure belongs to the cubic space group Ia3d (#230) with cations at special positions (on 16a, 24c and 24d sites) and oxygen anions at general positions (on 96h sites). Three cations have tetrahedral coordination (24d sites) and two cations have octahedral (16a sites) coordination formed by oxygen ions [171]. The 8th coordinate sites (dodecahedral, 24c sites) accommodate Gd ions. There are eight formula units in a unit cell. In the first coordination sphere of cation in position 24d, there are four atoms in position 16a, while in the first coordination sphere of cation in position 16a, there are six atoms in position 24d. In two cation coordination spheres, Mg ion has in total 34 positions suitable for Ce stabilization. Thus, only nearly 1% of Ce^{3+} ion have a chance to appear in the first and second coordination spheres around Mg ion. Consequently, the creation of Ce^{4+} due to pairing with Mg^{2+}, which is reported to be considerable at high codoping concentration in the crystals [172], are not significant in codoping of GAGG:Ce with 10 ppm of Mg.

Taking into account the results obtained in the current study and the results on luminescence rise time [P7], carrier trapping should be considered as the key mechanism causing the luminescence response delay in GAGG:Ce. The observation that Mg-doping eliminates the slow component in population of Ce^{3+} is in line with the published results evidencing that the doping inhibits formation of shallow traps [173]. The origin of these traps is still a subject for further studies. Considerable influence of certain dopants in low concentrations on trap formation is known in other scintillators. For example, there are experimental evidences of strong rearranging of traps in $PbWO_4$ crystal doped by La and Y at the level of 20-40 ppm [7]. It was demonstrated that such doping effectively inhibits the formation of di-vacancy centers, because the formation probability is proportional to the vacancy density squared. The suppression of di-vacancy related defects might be important also in GAGG. Certain results on thermo-stimulated luminescence in codoped GAGG crystals [P9,176,177] are consistent with this assumption.

The results of this study, which investigates predominantly geminate carrier pairs, can be extrapolated to the case of excitation by ionizing radiation. In this case, population of shallow traps caused by disordering in the crystal and di-vacancy centers becomes a more efficient competitor for cerium ions to capture electrons. Therefore, the build-up of the population of Ce^{3+} radiating level would be longer than that observed in our study, since the average path of the migration of the nonequilibrium carriers through the matrix to the radiative Ce center would be longer. Consequently, even a partial elimination of trapping would result in a significant enhancement for the population of the radiative Ce centers. This assumption is supported by the correlation of acceleration of the luminescence build up by Mg codoping with the improvement of response time in CTR measurements, shown in Fig. 3.3.18.

The introduction of Mg results not only in improvement of luminescence response time but also in a decreased light yield [P7], since the Mg-doping facilitates also the formation of nonradiative recombination centers. Our current observation of a significant improvement of the luminescence response time at low Mg content implies that such improvement might be achieved at a small loss in scintillation efficiency.

Optical probing of the decay of population of different structural units in GAGG:Ce evidenced that carrier trapping has the main influence on the rise time of the luminescence response of this scintillation crystal. It was also shown that codoping of GAGG:Ce by divalent ions of magnesium diminishes the influence of traps. The disappearance of the slow component in the luminescence rise time is correlated with the decrease in the FWHM in CRT measurements.

The best fits of the experimental data on kinetics of population of excited Ce^{3+} levels with the populations calculated by using the rate equations are obtained at the time of intracenter relaxation time for $5d^2$ to$5d^1$ transition of ~500 fs.

The time resolution in CRT measurements depends also on the type of SiPM used. Thus, the best FWHM value of 165 ps achieved in these measurements could be further improved by optimization of matching of GAGG:Ce,Mg scintillator and dedicated SiPM and might be attractive for medical imaging devices and applications in high-energy physics experiments.

Irradiation effects on cerium doped $Gd_3Al_2Ga_3O_{12}$

This subchapter is focused on the study of GAGG scintillator capabilities to operate in harsh irradiation environment typical for collider experiments. The results obtained under irradiation with high-energy protons can be adopted to estimate the influence of neutrons and exploited for designing detectors for reactor research, industrial facilities, and spallators. Comparison of the properties of GAGG:Ce with LSO:Ce and LYSO:Ce is provided. Particular attention is paid to the damage in the materials imposed by irradiation by 24 GeV proton beam at CERN PS at different fluences of up to $3.1\cdot10^{15}$ p/cm^2 and to the study of nonequilibrium carrier dynamics in the crystals after γ-irradiation.

The induced optical absorption of GAGG:Ce,Mg,Ti in the range of Ce emission at the level of a few m^{-1} after irradiation with protons at a fluence of $3.1\cdot10^{15}$ p/cm^2 is reported [175]. The change in optical absorption coefficient of GAGG:Ce,Mg,Ti induced by proton irradiation at a fluence of $5\cdot10^{14}$ p/cm^2 is presented in Fig. 3.3.21. No significant induced absorption in the vicinity of luminescence peak of this scintillator (520 nm) was observed. A negligible influence of proton-induced defects on the light yield of the scintillation element was observed, a shift of the photo-peak after irradiation was estimated to be less than 1% of the total light emitted by Ce^{3+}. However, the scintillator performance might be affected by the long- and short-living isotopes introduced in GAGG by proton irradiation.

The content and activity of the long-living proton-induced isotopes in codoped GAGG was simulated using FLUKA code and measured elsewhere [175]. We used these results to verify the correctness of the simulation of isotope set in irradiated crystal and to estimate the influence of the short- and long-living isotopes to the emission noise background of the scintillator.

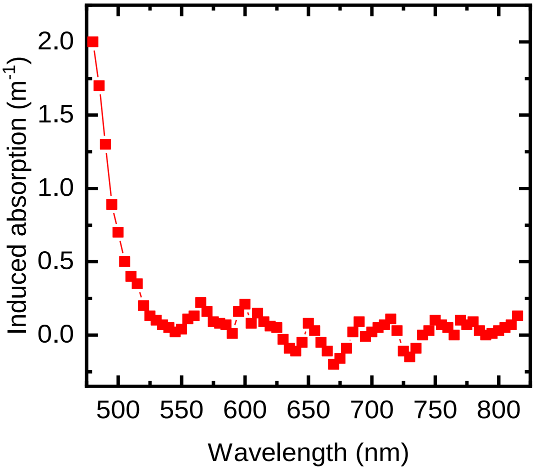

Fig. 3.3.21. Change in optical absorption coefficient of GAGG:Ce,Mg,Ti induced by proton irradiation at a fluence of $5x10^{14}p/cm^2$. [P15]

The proton-induced radioisotopes excite the scintillator and produce a harmful luminescence. This effect is stronger in high-light-yield scintillation materials. The harmful luminescence might be excited by all products of radioactive decay: γ-quanta, alpha and $\beta^{+,-}$ particles. Taking both short- and long-living isotopes into account in our simulation, we estimated the energy distribution of the number of γ-quanta and $\beta^{+,-}$ particles emitted by the radio-isotopes formed after irradiation (see Fig. 3.3.22). Alpha particles are also emitted by radio-nuclides, however, their quantity was estimated to be negligible. The similar simulations performed for LSO at the same fluence showed approximately similar distribution. This is an indication that the dose absorbed in small-volume GAGG and LSO scintillation crystals is practically the same.

Figure 3.3.23 shows the simulated change of the dose rate due to γ and $\beta^{+,-}$ radio-isotopes in a GAGG plate with the dimensions of 2x2x0.2 cm^3 (typical dimensions of a scintillation element in the "shaslik"-type cell with tungsten absorber). The irradiation profile used in the simulations corresponded to 6 months of operation of HL LHC. The proton flux of $9.7 \cdot 10^7$ p/cm^2/s and the total fluence of $1.5 \cdot 10^{15}$ p/cm^2 were used in the calculations. A similar dependence obtained for LSO (LYSO) detecting elements with the same dimensions did not show a significant difference in the behavior of the residual nuclei dose rate.

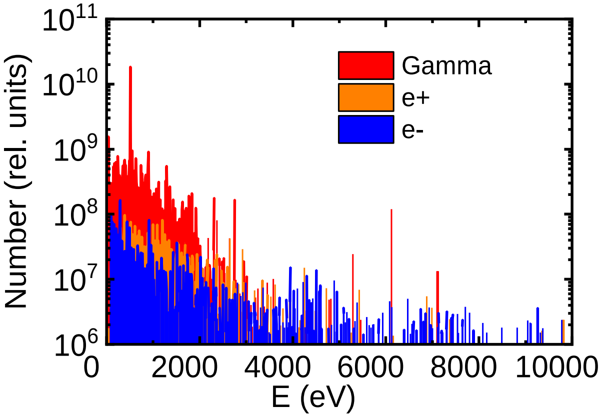

Fig. 3.3.22. Energy distribution of the number of gamma-quanta, electrons and positrons emitted by radio-isotopes after irradiation of GAGG at a fluence of $1.5 \cdot 10^{15}$ p/cm^2. [P15]

The dose rate increases at the beam front and decreases after the beam termination with a time constant of ~10^4 s, which is a typical decay time of the most short-lived isotopes. At the beam termination, the dose rate decreases by a factor of ~100, what means that the dominant fraction of the dose rate is caused by the short-lived isotopes.

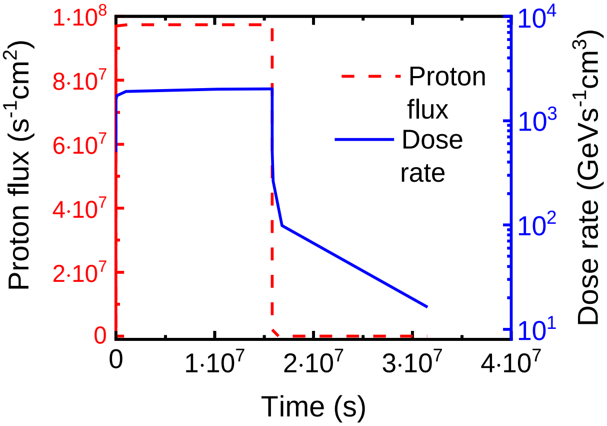

Fig. 3.3.23. Time evolution of proton flux (dashed red line) and residual nuclei dose rate (solid blue line) in a single GAGG detecting element with dimensions of $2x2x0.2\ cm^3$. [P15]

The radionuclides in the scintillator excite the harmful luminescence, which contributes, similarly to phosphorescence, to the optical noise. The intensity of the harmful luminescence I_{noise} in the entire sample can be estimated by using the following formula:

$$I_{noise}[\text{ph/s}] = G \cdot V \cdot LY \tag{3.3.4}$$

where G is the absorbed dose rate [in MeV/(s·cm^3)], V is the sample volume (cm^3), and LY is the light yield of the material (ph/MeV).

The scintillation signal is formed within a limited time interval determined by the scintillation kinetics. Meanwhile, the optical noise is emitted permanently. Consequently, for a correct comparison of the scintillation signal and the noise, it is necessary to reduce the value of the harmful luminescence intensity in accordance with the specific time window, the time interval of 25 ns between the collisions of the beams, in our case. The contribution of harmful luminescence photons in the noise pedestal can be estimated as in [176]. The harmful luminescence also leads to broadening of the energy resolution by adding the noise energy equivalent ΔE_{noise}. For the time window Δt, the value of ΔE_{noise} can be estimated as:

$$\Delta E_{\text{noise}} = \frac{2.35\sqrt{G \cdot V \cdot \text{LY} \cdot \Delta t}}{\text{LY} \cdot \eta} \tag{3.3.5}$$

Here, η is the fraction of the scintillation photons emitted during the time window Δt = 25 ns.

The results of the simulation of the harmful luminescence intensity within the time window of 25 ns, its contribution into the noise pedestal and the noise energy equivalent of GAGG and LSO samples with the same dimensions (2x2x0.2 cm^3) at the moment of termination of the irradiation with the dose rate profile shown in Fig. 3.3.23 are summarized in Table 3.3.2. As evident in Table 3.3.2, the effect of activation by hadrons in LSO and GAGG is practically similar.

Table 3.3.2. Contribution of harmful luminescence in optical noise, noise pedestal, and noise energy equivalent within 25 ns gate in GAGG and LSO crystals with dimensions of 2x2x0.2 cm^3.

Scintillator	GAGG	LSO
Additional noise intensity, ph	1600	1350
Additional pedestal, keV	156	108
Additional noise energy equivalent, keV	9.2	6.9

The high radiation tolerance of GAGG might be explained by the influence of the sublattice of lattice-building gadolinium. Gadolinium ions have numerous energy levels of electronic configuration f7 located within a large energy range in the upper part of the band gap. A high concentration of Gd^{3+} ions in the crystal inhibits the long-term stabilization of electronic-type color centers with the ground energy states more than 2 eV below the bottom of the conduction band. Therefore, no energy transfer from the color centers to Gd^{3+} sublattice and further to Ce^{3+} ions occurs.

As discussed above, the irradiation-induced color centers do not have substantial influence on reabsorption in GAGG:Ce. The spectrum of irradiation-induced optical absorption can be easier revealed in undoped crystals, where it is not masked by a strong influence of activators [177,178]. As in other garnets [179,180], the irradiation of undoped GAGG crystals does introduce certain amount of color centers having absorption over visible spectral range, however, the induced absorption is not strong enough to cause significant reabsorption of the Ce^{3+} emission peaked at 520 nm. Moreover, Ce-doping substantially reduces the density of color centers in oxide crystals [178,181] and, consequently, increases the radiation hardness of GAGG:Ce.

As reported before [P9,P11], the time resolution of GAGG:Ce is influenced by carrier trapping and can be controlled by appropriate co-doping. To study the influence of irradiation on trapping, we performed the measurements of dynamics of nonequilibrium carriers using optical pump and probe technique in undoped GAGG crystal, in which a large concentration of color centers can be created even under gamma-irradiation. As mentioned above, the formation of color centers is suppressed in Ce-doped crystals. Thus, the study of undoped crystals can provide information on the interaction of the Gd sub-lattice and defects in the crystal, since Gd^{3+} ions play a major role in excitation transfer to emitting Ce^{3+} ions. It is most important to understand the influence of color centers and traps in the irradiated crystals on slowing the excitation transfer. This effect is hardly observable in proton-irradiated crystals, mainly because the samples are available for studying only in two months after irradiation (due to radiation safety reasons). Pump photon energy of 5.9 eV selected for generation of nonequilibrium carriers corresponded to the edge of band-to-band absorption of GAGG and excited electrons to shallow traps. To avoid the contribution to the differential absorption by the carriers populating the states of Ce^{3+}, the undoped GAGG was studied.

The differential absorption, i.e. the difference between the optical absorption with and without short-pulse (200 fs) excitation, as a function of probe photon energy and time after the excitation, is presented for GAGG crystal at room temperature in Fig. 3.3.24.

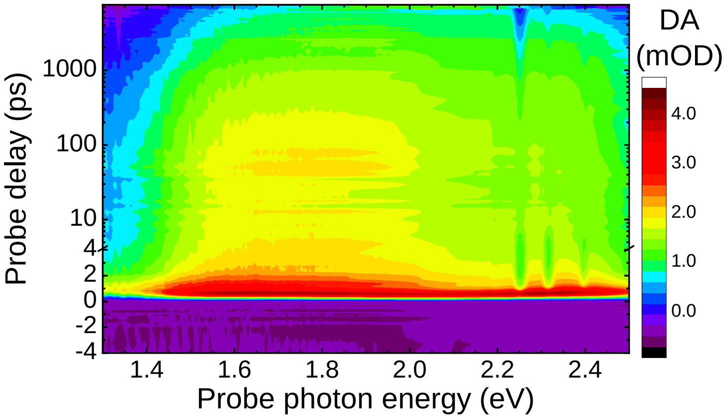

Fig. 3.3.24. Time evolution of the spectrum of differential absorption induced by a short pulse in undoped GAGG crystal at room temperature. [P15]

The differential absorption has two components. They strongly overlap spectrally but have substantially different decay time (see Fig. 3.3.25). The first component with a characteristic decay time of 2 ps reflects the density of free carriers, while the second, slow component decaying with the time constant of ~50 ns is caused by the absorption of trapped carriers.

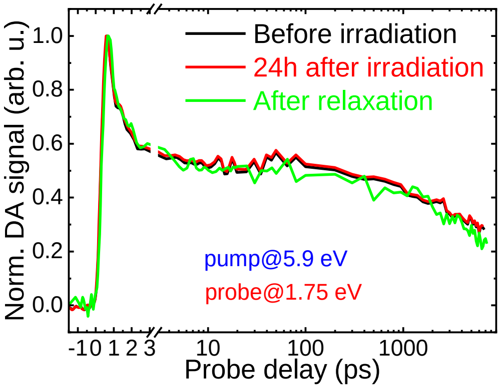

Fig. 3.3.25. Kinetics of differential optical absorption at 1.75 eV induced by a 200-fs pulse at 5.9 eV in undoped GAGG crystal before irradiation, 24 hours after irradiation, and after spontaneous relaxation. [P15]

No changes in the kinetics of both components have been observed after irradiation. This observation leads to the conclusion that the irradiation damage effects do not affect the carrier trapping and, consequently, the timing properties of GAGG scintillator.

To conclude, the proton irradiation at a fluence of $5 \cdot 10^{14}$ p/cm^2 imposes no significant change in the optical transmittance of GAGG:Ce scintillators without and with Mg codoping. Thus, the proton-induced defects have no influence on the output of the light emitted by Ce^{3+} in the conditions typical of the future detectors at LHC operating at high luminosity. The contribution of harmful luminescence to optical noise, noise pedestal, and noise energy equivalent in GAGG is similar to that in LSO scintillators and is acceptable for application. The irradiation does not affect the kinetics of free carrier relaxation and the trapping rate; thus, the irradiation damage does not affect the carrier trapping and, consequently, the timing properties of GAGG scintillator. The obtained results show that the multicomponent garnet-type GAGG:Ce crystals could be prospective candidates for new detectors for reactor research facilities, spallators, and high-energy hadron colliders with harsh radiation environment.

3.4 Non-crystalline scintillators

Glass ceramics are potentially inexpensive substitute of single crystals as host matrix for activated scintillators. The technology of fabrication of ceramics-based scintillators is still in the early stage of development, whereas the physical properties determining the performance of such scintillators are poorly investigated. In the current study, glass ceramics developed based on complex substituted garnets with two compositions: $Y_2CaAlGe(AlO_4)_3$:Ce and $Y_2MgAlGe(AlO_4)_3$:Ce were investigated. Two possible methods of producing glass ceramic garnets were tested: thermal annealing of glasses [P5] and direct precipitation from a solution [P11].

To transform the glasses into ceramic material, the glass cubes were annealed in air at 1300–1500°C for 105–180 min. The annealed blocks of glass ceramics were cut and polished into 1-mm-thick plates. The glasses containing Ca^{2+} and Mg^{2+} ions were labeled as Glass 1 and Glass 2, respectively, whereas the corresponding glass ceramics obtained by annealing Glass 1 and Glass 2 at 1500°C were labeled GC1 and GC2, respectively.

The differential scanning calorimetry (DSC) curves obtained during heat treatment are presented in Fig. 3.4.1. For both glasses, they look basically similar, indicating that the processes at heat treatment proceeds identically in both glasses. The small discrepancy of the DSC curves might be caused by differences in chemical nature (composition) of the glasses and, as a result, in different temperatures for the same modification to occur. For both glasses, endothermic effects in a wide temperature range from 810 to 1050°C, strong exothermic effect between 1050°C and 1150°C, and a few endothermic effects within the temperature ranges 1217-1230°C and 1337-1361°C are observed.

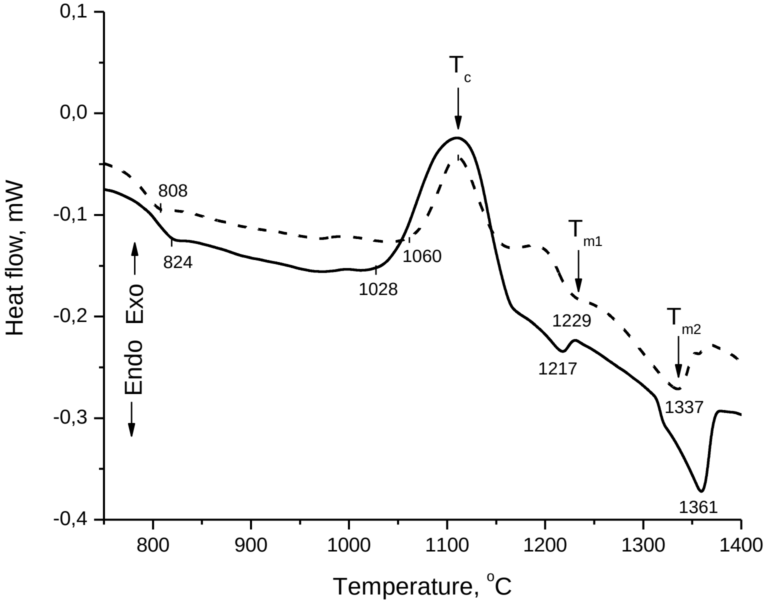

Figure 3.4.1. DSC curves for Glass 1 (solid line) and Glass 2 (dashed line)

The wide endothermic effect within the temperature range 810-1050°C for both glasses might be caused by simultaneous softening and microliquation processes in close temperature ranges [182,183]. The glass microliquation proceeds as formation of nuclei and their subsequent growth. Several microliquation processes might proceed in parallel at the same or close temperatures. As a result, the nuclei of different composition are formed and grow simultaneously. The DSC feature due to the exothermic effect at 1030-1150°C corresponds to the complete glass crystallization (the crystallization temperature is indicated as T_c), whereas the wide range of the feature evidences the formation of nuclei of different phases in the glass matrix. The endothermic effects at temperatures above 1200°C (marked as T_{m1} and T_{m2}) are observed for both glasses and are caused by gradual melting of the crystalline phases. Their low intensities indicate a low content of such crystalline phases in the glass matrix. Thus, the temperatures above 1300 °C were used for the heat treatment of the glasses.

The XRD patterns of the glass ceramics obtained by heat treatment of Glass 1 and Glass 2 at 1300–1500 °C are presented on Fig. 3.4.2.

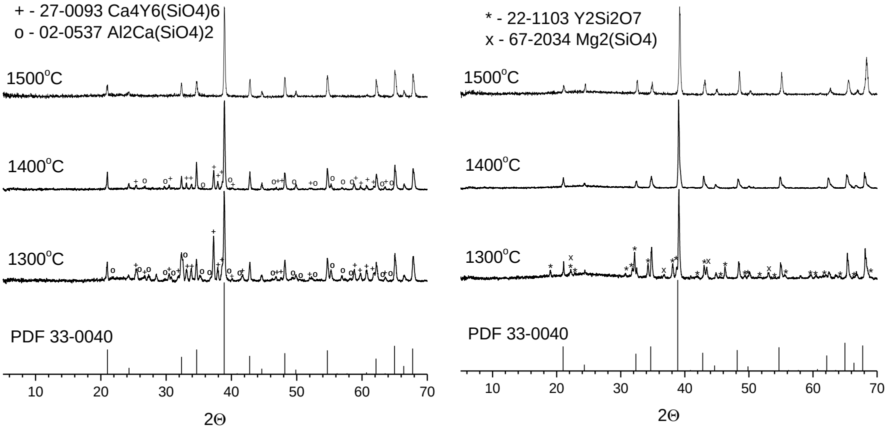

a b

Figure 3.4.2. XRD patterns for glass ceramics obtained by heat treatment of Glass 1 (a) and Glass 2 (b) at different temperatures (indicated). Vertical line corresponds to the reference reflection [33-0040] of YAG single crystal. Impurity phases are indicated as (+) for $Ca_4Y_6(SiO_4)_6$ (PDF 27-0093), (○) for $Al_2Ca(SiO_4)_2$ (PDF 02-0537), (*) for $Y_2Si_2O_7$ (PDF 22-1103), and (×) for Mg_2SiO_4 (PDF 67-2034).

As seen in Fig. 3.4.2 a and c, an increase in the heat treatment temperature leads to a decrease in the contribution of impurity phases. This feature might be explained as a result of their dissolution in the glass matrix. The glass ceramics containing no other phases except of a garnet phase are formed at 1500°C for Glass 1 and at 1400°C for Glass 2. The heat treatment of initial glasses at temperatures higher than 1500°C leads to formation of transparent yellowish glasses due to complete dissolution of crystallites and oxidation of Ce^{3+} ions to state Ce^{4+}. No luminescence under excitation at 450 nm is observed in these glasses.

The fine structure of XRD reflections for GC1 and GC2 is presented in Fig. 3.4.2 a and b. A shift of the reflection in respect of its position in YAG indicates formation of substituted garnets, whereas the reflection asymmetry is related with the formation of garnets with different degrees of substitution. The formation of garnets with different degree of substitution may be related with fluctuations in the composition of glass in the vicinity of garnet nuclei at their formation. The composition fluctuations might be caused by a small discrepancy between the ratios of elements in the garnet structure and in the glass matrix. Thus, incorporation of the excessive elements into new nuclei or during their subsequent growth is quite probable. This effect should lead to an increase in the substitution degree of the garnet. In general, the proposed mechanism is similar to epitaxial growth of films, when each subsequent layer inherits the structure of previous one but might have slightly different composition. The garnet nucleus plays here the role of a substrate.

The dependence of the photoluminescence properties on the garnet composition in the vicinity of the emitting Ce ions was studied by using confocal microscopy. Typical mapping images of PL intensity, band peak position and its FWHM are presented for GC1 and GC2 in Fig. 3.4.3.

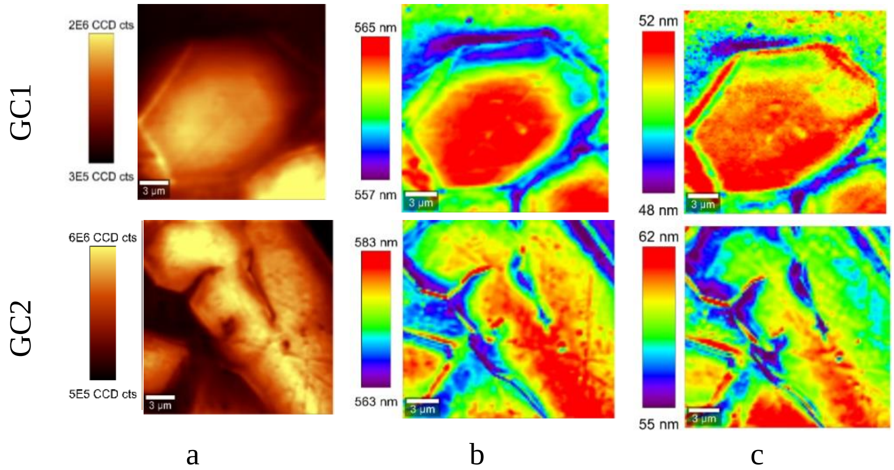

Figure 3.4.3. Mapping images of PL intensity (column a), band peak position (column b) and FWHM (column c) under excitation at 442 nm recorded for typical areas of 20×20 μm in size for ceramics GC1 and GC2

The morphology of GC1 and GC2 is slightly different. In GC1, most of crystallites have hexagonal habitus, which is typical of garnet structure. The crystallites in GC2 are in average bigger and have predominantly elongated shape. This difference in shape and habitus of crystallites in ceramics GC2 might be caused by their partial dissolution. Ceramics GC2 exhibits stronger PL than that of GC1.

Strong correlation between photoluminescence characteristics and position in and outside the grains are evident for both ceramics (see in Fig. 3.4.3). A blue shift of the PL peak position in the direction from crystallite center to its border is observed. This feature might be explained by different crystal field acting on the emitting Ce^{3+} ions as a result of different garnet composition in the vicinity of the ions. The variable composition is probably caused by the layer-by-layer growth of the crystallite, as discussed above. The FWHM increasing from the middle to the edge of crystallites evidences increasing fluctuations of the crystallite composition in the vicinity of Ce ion as the crystallite grows from nucleus to the size of a few micrometers and more.

Morphology of the $Y_2CaAlGe(AlO_4)_3$:Ce and $Y_2MgAlGe(AlO_4)_3$:Ce garnets prepared by direct precipitation is presented in Figure 3.4.4. $Y_2CaAlGe(AlO_4)_3$:Ce and $Y_2MgAlGe(AlO_4)_3$:Ce powders look similar.

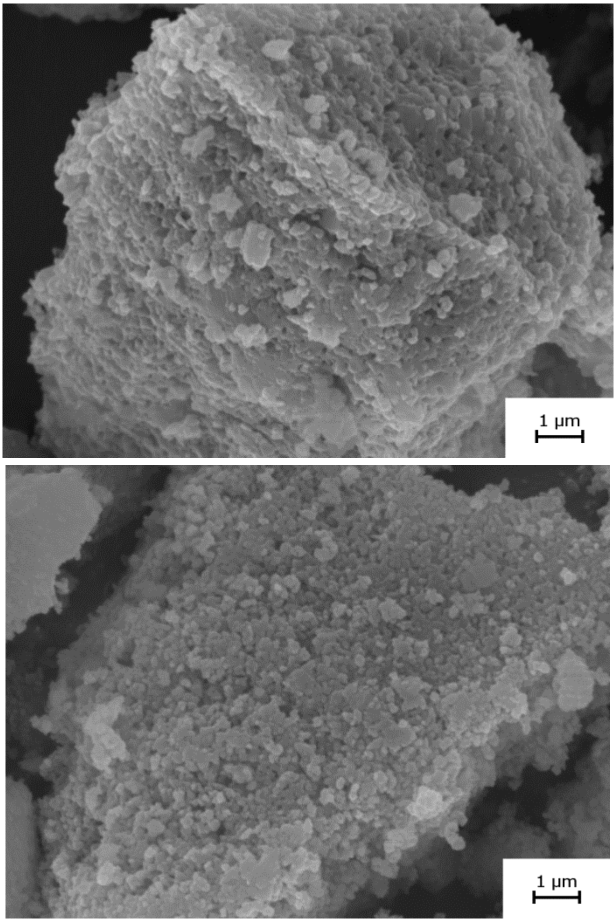

Figure 3.4.4. SEM images of $Y_2CaAlGe(AlO_4)_3$:Ce (top) and $Y_2MgAlGe(AlO_4)_3$:Ce (bottom) samples

The particles are highly porous aggregates sizing from 0.5 to 100 μm. The dimensions of crystallites forming the aggregates are ~200 nm and ~130 nm for $Y_2CaAlGe(AlO_4)_3$:Ce and $Y_2MgAlGe(AlO_4)_3$:Ce, respectively. Appearance of pores at the surface of the aggregates may be caused by the gases evolving under heat treatment of precursors or by sintering of small particles under the heat treatment followed by the exposure of intergranular voids at the surface of aggregates as pores.

Luminescence excitation and luminescence spectra for Ce^{3+} ions in the garnet structure are described in detail in the literature [115,128,184–191]. Emission spectra for $Y_2MgAlGe(AlO_4)_3$:Ce are characterized by a high reproducibility from aggregate to aggregate as can be seen in Figure 3.4.5. This indicates that the aggregates consist of crystallites emitting similar luminescence.

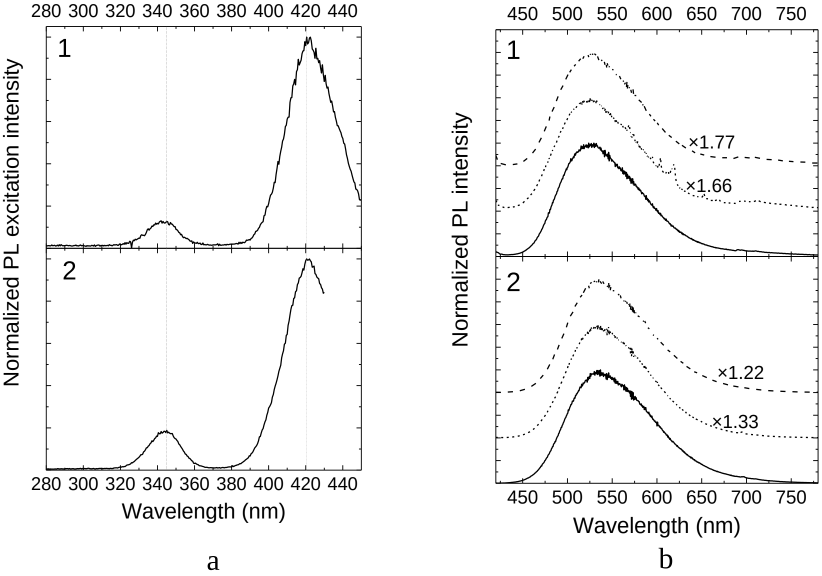

Figure 3.4.5. Normalized luminescence excitation spectra (a) on registration at 550 nm. Luminescence signal (b) from three different powder grains on 405 nm excitation. Normalization factors are indicated. Data for $Y_2CaAlGe(AlO_4)_3$:Ce and $Y_2MgAlGe(AlO_4)_3$:Ce samples are denoted respectively 1 and 2.

However, as can be seen from Figure 3.4.5(b), the luminescence intensity was found to vary in both compounds, most probably due to inhomogeneity of the aggregates. We assume that the presence of aggregates differing in their density and ability to scatter light in the material leads to the detection of luminescence signal of varying intensity.

In conclusion, garnet-structure glass ceramic materials based on the complex substituted garnets $Y_2CaAlGe(AlO_4)_3$:Ce and $Y_2MgAlGe(AlO_4)_3$:Ce are fabricated by controlled crystallization of glasses or direct precipitation from a solution. The average cell parameters obtained for these ceramics by

XRD correlates well with those expected after substitution of Y^{3+} ion by Ca^{2+} and Mg^{2+} and Al^{3+} ion by Si^{4+} and Ge^{4+} in garnet structure, whereas the thin structure of XRD lines confirm the contribution from areas with a different degree of substitution in the garnet composition. Study of photoluminescence with the spatial resolution high enough to obtain the spectra from individual aggregates showed that these spectra coincide. This is an additional evidence of high quality of the crystalline garnet structure of the particles in aggregates. The aggregate-to-aggregate variation of luminescence intensity (of the order of 25%) might be attributed to different excitation and light extraction conditions for each aggregate.

4 CONCLUDING STATEMENTS

1. The rise and initial decay components of luminescence in lead tungstate (PWO) scintillators are short enough to be exploited for a sub-10-picosecond readout.
2. Under band-to-band excitation of PWO single crystals, free electrons are generated into the conduction band within subpicosecond time and their density is proportional to the pump energy density over a wide dynamic range. This feature can be exploited in the development of ultrafast radiation detectors.
3. The radiation influence on two-photon absorption can be used to form a time mark to detect the initial moment of the interaction of the ionizing radiation with the detector material, while the luminescence signal provides the information on absorbed energy.
4. The population of the emitting level $5d^1$ of Ce^{3+} after a short-pulse excitation of the cerium ions in LSO occurs with certain delay of the order of a few picoseconds, which is caused by electron trapping.
5. The delay in the population of the emitting level $5d^1$ of Ce^{3+} after a short-pulse excitation is more pronounced in LSO:Ce than that in LYSO:Ce., because the nonequilibrium electron trapping in LYSO:Ce occurs at the traps of two different origins: at the traps due to impurities and structural defects and at the minima of potential fluctuations of the bottom of the conduction band due to the fluctuations in composition of the mixed crystal.
6. The delay in the population of the emitting cerium state in LSO and LYSO is eliminated by codoping the scintillators with aliovalent impurity of calcium even at concentrations as low as 5 ppm.
7. The time of intracenter relaxation in Ce^{3+} from level $5d^2$ to emitting level $5d^1$ is 500 fs.
8. Hole trapping at Gd sublattice is an important factor deteriorating luminescence response in scintillators based on mixed garnets containing gadolinium.
9. Gadolinium ground state in GAGG is located by ~1 eV below the top of the valence band.
10. Codoping with magnesium diminishes the influence of electron trapping in GAGG:Ce leading to better timing properties of this scintillator.
11. Irradiation conditions typical of the future conditions at LHC will have no influence on the light yield of GAGG:Ce scintillators, as well as on their timing properties.

12. High-quality crystalline garnet crystallites can be obtained by controlled crystallization of glasses or direct precipitation from a solution.
13. $Y_2CaAlGe(AlO_4)_3$:Ce and $Y_2MgAlGe(AlO_4)_3$:Ce crystallites produced by controlled crystallization of glass exhibit a gradient in their emission properties: a blue shift and broadening of the photoluminescence band occurs in the direction from the crystallite center to its border.
14. In crystallites formed by precipitation from a solution, the emission center of mass in $Y_2MgAlGe(AlO_4)_3$:Ce is red-shifted by 7 nm in respect to that in $Y_2CaAlGe(AlO_4)_3$:Ce due to the substitution of Mg^{2+} and Ge^{4+} for Y^{3+} and Al^{3+} ions in the garnet structure, which results in increasing of the crystal field in the vicinity of Ce^{3+} ions.

SANTRAUKA

Įvadas

Krūvininkų pernaša scintiliatoriuose yra pasauliniu mąstu aktuali tema, ypač CERN kolaboracijai *Crystal Clear Collaboration*, išsikėlusiai tikslą matavimuose panaudojant scintiliacinius spinduliuotės detektorius pasiekti 10 ps laikinę skyrą. Iki šiol liuminescencijos gesimo trukmė buvo laikoma svarbiausiu parametru, ribojančiu scintiliacinės medžiagos atsako spartą. Tačiau didėjant laikinės skyros svarbai, ir laboratorinėmis sąlygomis pasiekiant vis trumpesnes laikinės skyros vertes ribojančiu veiksniu tampa liuminescencijos įsižiebimo trukmė.

Liuminescencijos dinamiką galima tyrinėti su subpikosekundine skyra naudojant žadinimą trumpais impulsais. Tačiau tokiam sužadinimui dažniausiai naudojamų optinių šviesos šaltinių emituojamų fotonų energija (dažniausiai iki 6 eV) yra per maža, kad imituotų sužadinimą rentgeno ar gama spinduliuote. Tokie metodai vertingiausi charakterizuojant paskutines krūvininkų persisktymo ir rekombinacijos procesų stadijas. Katodoliuminescencija, bandinį žadinant trumpais elektronų impulsais, leidžia kurti aukštos energijos elektronų-skylių poras, tačiau tokiuose eksperimentuose laikinę skyrą riboja elektronų impulso trukmė, paprastai apie 200 ps. Scintiliatorių liuminescencijos tyrimai su laikine skyra naudojant aukštos energijos spinduliuotę impulsiniuose sinchrotronuose irgi yra ribojama impulso trukmės, dažniausiai apie 50 ps, kaip SUPERLUMI eksperimentiname komplekse, HASYLAB laboratorijoje, DESY sinchrotrone. Laikinės skyros matavimo eksperimentai, kai naudojamas gama spinduliuotės šaltinis ir spinduliuotė detektuojama dviem identiškais scintiliatoriais, leidžia tiksliai išmatuoti laikinę skyrą, tačiau matavimai trunka labai ilgai.

Šiame darbe liuminescencijos įsižiebimo spartą ribojantys procesai tirti naudojant skirtuminę optinę sugertį žadinimo ir zondavimo konfigūracijoje. Šio metodo laikinė skyra yra ribojama tik lazerio impulso trukmės, tad gali būti net subpikosekundinėje laiko skalėje. Šis metodas leidžia tirti nepusiausvirųjų krūvininkų dinamiką selektyviai sužadinus struktūrinius vienetus scintiliaciniame kristale. Rezultatai, gauti žadinimo ir zondavimo metodu, buvo analizuojami kartu su rezultatais, gautais sutapimo laiko skyros ir kitais metodais, krūvininkų dinamika buvo modeliuota pasitelkiant kinetines spartos lygtis.

Vertinant scintiliacines medžiagas greito sužadinimo pernešimo link aktyvatorių jonų požiūriu svarbų vaidmenį vaidina krūvininkųgaudyklės, kurių aktyvavimo energija yra palyginama su termine energija kambario temperatūroje. Krūvio gaudyklės susiformuoja dėl priemaišų ir struktūrinių defektų. Daugiakomponenčiuose kristaluose krūvininkai gali būti lokalizuoti ir dėl potencialo fluktuacijų, susidarančių dėl draustinio tarpo moduliacijos nulemtos kristalo sudėties fliuktuacijų. Tokios rūšies krūvininkų pagava daugiakomponenčiuose scintiliatoriuose darosi vis svarbesnė tyrimų sritis, kadangi šie scintiliatoriai yra perspektyvūs dėl įvairių priežasčių. Pavyzdžiui, ceriu legiruotas lutecio oksiortosilikatas pasižymi labai perspektyvia scintiliacinių savybių kombinacija, tačiau yra gan brangus dėl aukštos lutecio kainos. Galima dalį lutecio atomų pakeisti ženkliai pigesniu itriu, tačiau tai paveikia medžiagos savybes. Naudoti lutecio itrio oksiortosilikatą $Lu_{2(1-x)}Y_{2x}SiO_5$:Ce (LYSO:Ce) vietoje LSO:Ce priimtina, ypač kai reikia ypatingai didelio scintiliacinės medžiagos kiekio, pavyzdžiui, didelio mastelio aukštų energijų fizikos eksperimentuose. Ceriu legiruoti granatiniai scintiliatoriai yra dar vienas perspektyvaus daugiakomponenčio scintiliatoriaus pavyzdys. Daugiakomponenčiai granatai yra patrauktūs dėl galimybės naudoti draustinio tarpo inžinerijos metodus ir aktyvuojančių priemaišų energijos lygmenų inžineriją keičiant kristalo sudėtį. Pridėjus gadolinio, gadolinio aliuminio galio granato $Gd_3Al_2Ga_3O_{12}$ (GAGG) draustinis tarpas sumažėja tiek, kad seklios elektronų gaudyklės, esančios netoli draustinio tarpo viršaus, paskandinamos laidumo juostoje. Tuo tarpu, ceriu legiruotame GAGG kristale gadolinio pridėjimas pakeičia kristalinį lauką taip, kad Ce^{3+} jono žemiausia sužadinta būsena tampa pakankamai atskirta nuo laidumo juostos, kad sužadinti Ce jonai nebūtų termiškai jonizuojami kambario temperatūroje. Naudojant daugiakomponentes medžiagas galima pasiekti geriausių jas sudarančių medžiagų savybių kombinacijas. Pavyzdžiui, $Y(Nb_xTa_{1-x})O_4$ kristaluose, sujungiant našią NbO_4 komplekso emisiją ir didelį TaO_4 tankį gauname, kad $YTaO_4$ ir $YNbO_4$ mišraus kristalo (kai $x = 0,4$), eksitoninės emisijos intensyvumas yra didesnis nei jo sudėtinių dalių. Daugelis multikomponenčių medžiagų klasės scintiliatorių yra perspektyvūs įvairiems taikymams. Krūvininkų dinamikos tyrimai šiose medžiagose yra įdomūs tiek moksliniu, tiek praktiniu požiūriu. Šiame darbe buvo tirta krūvininkų relaksacija ir pagava ceriu legiruotuose GAGG ir LYSO kristaluose.

Pagrindinis tikslas

Atskleisti krūvio pernašos procesus, kurie yra svarbūs kuriant sparčius, našius ir radiacijai atsparius scintiliatorius, skirtus jonizuojančiosios spinduliuotės detektavimui su artima 10 ps laikine skyra.

Disertacijos siekiniai

1. Ištirti poreikį scintiliacinėms medžiagoms, perspektyvioms greitam spinduliuotės detektavimui su dešimčių pikosekundžių laikine skyra.
2. Pritaikyti skirtuminės optinės sugerties metodą žadinimo ir zondavimo konfiguracijoje tirti krūvininkų dinamiką savuosiuose ir ceriu legiruotuose scintiliatoriuose.
3. Atskleisti koreliaciją tarp krūvininkų dinamikos charakteristikų, gautų netiesinės optikos metodais ir matuojant įvykių sutapimo laikinę skyrą žadinant gama kvantais.
4. Palyginti ceriu legiruotus LSO, LYSO, GAGG ir kitus didelio šviesinio našumo scintiliatorius jų pritaikomumo sparčiuose jonizuojančiosios spinduliuotės detektoriuose požiūriu.
5. Ieškoti naujų perspektyvių keramikinių scintiliatorių ir fosforų.

Naujumas ir svarba

Planuojamiems aukštų energijų fizikos eksperimentams CERN ir kitur reikia scintiliacinių detektorių su aukšta, 10 ps eilės laikine skyra. Tai nėra įmanoma naudojant dabartinius scintiliacinius detektorius, kurių atsako trukmę riboja krūvininkų rekombinacija spindulinės rekombinacijos centruose. Šiame darbe pristatomi keli nauji būdai pagerinti scintiliacinių detektorių laikinę skyrą.

Parodyta, kad laikinę skyrą galima pagerinti išnaudojant procesus, vykstančius lygiagrečiai krūvininkų relaksacijai. Vienas iš šių procesų yra elastinė poliarizacija. Ją sukelia lokalus krūvininkų persiskirstymas po sąveikos su jonizuojančiąja spinduliuote, dėl ko deformuojama kristalo gardelė. Tai pakeičia būsenų tankio pasiskirstymą ir skirtuminės sugerties spektrą. Pagrindinis šio proceso privalumas, sąlygojantis jo patrauklumą – ypatingai didelė atsako sparta. Teisingai parinkus zondavimo bangos ilgį galima būtų išnaudoti šį procesą laikinės žymos suformavimui.

Antras šio darbo prioritetas buvo neorganinių kristalinių medžiagų, pasižyminčiu greitu scintiliaciniu atsaku ir stipria netiesine trumpų impulsų sugertimi, paieška. Siekdami šio tikslo pasirinkome kelias perspektyvias medžiagas: savajį scintiliatorių švino volframatą (PWO), įvairios sudėties ceriu legiruotus gadolinio aliuminio galio granatus ($Gd_3(Ga_{0.5}Al_{0.5})_5O_{12}$:Ce GAGG), ceriu legiruotus lutecio oksiortosilikatus (LSO) ir keramikinius granatinius scintiliatorius. Pastarieji yra visiškai nauja medžiagų klasė, tad jų tyrimai buvo nukreipti į struktūrinių savybių, bei gamybos sąlygų parinkimo klausimus. Savo ruoštu, PWO yra šiuo metu populiariausia aukštų energijų fizikos eksperimentuose naudojama scintiliacinė medžiaga. Švino volframato liuminescencijoje išskyrėme tris gęsimo komponentes, nustatėme, kad sparčiausios komponentės charakteringa gęsimo trukmė lygi ~ 5 ps. Tuo tarpu nesenai sukurti mišrūs granatai demonstruoja greitą atsako trukmę ir aukštą emisijos našumą, iki 56000 fotonų / MeV. Dėl aukšto našumo, spartaus liuminescencijos gesimo (charakteringa trukmė < 100 ns) ir gero emisijos spektro sutapimo su detektorių jautrumo spektru ceriu legiruoti mišrūs granatai yra daug žadanti scintilaicinė medžiaga medicininio vaizdinimo prietaisuose. Šioje srityje mišrūs granatai gali varžytis su lutecio ortosilikatais, šiuo metu pozitronų emisijos tomografų (PET) rinkoje dominuojančia kristaline medžiaga. Šiame darbe parodyta, kad ceriu legiruotų granatinių ir oksiortosilikatinių scintiliatorių liuminescencijos atsakas gali būti paspartintas juos legiruojant aliovalentinėmis priemaišomis netgi esant labai mažai (~5 ppm) jų koncentracijai. Atskleista prilipimo lygmenų įtaka elektronų pernašai į cerio jonus, nustatytos relaksacijos iš sužadintų jono Ce^{3+} lygmenų trukmės.

Ginamieji teiginiai

I. Švino volframate aptikta sparti liuminescencijos gesimo komponentė, kurios charakteringa gesimo trukmė lygi ~ 5 ps.

II. Ceriu legiruotų granatinių ar oksiortosilikatinių scintiliatorių aliovalentinis kolegiravimas sumažina elektronų pagavimo į prilipimo lygmenis poveikį ir pagreitina scintiliatorių įsižiebimo trukmę iki subpikosekundinių verčių, net ir esant tokiam mažam kolegiravimo lygiui kaip 5 ppm.

III. Nustatyta, kad cerio jono, veikiančio kaip aktivatorius granatiniuose scintiliatoriuose, vidinė relaksacijos trukmė yra 500 fs, trumpesnė nei sužadinimo pernašios trukmė, kuri ir riboja luminescencijos atsako spartą.

Disertacijos sandara

Pagrindinis tikslas, siekiniai, naujumas, svarba ir publikacijų bei pranešimų konferencijose sąrašai yra pateikti disertacijos pradžioje.

Pirmajame skyriuje „Eksperimentiniai metodai“ trumpai apžvelgti disertacijoje naudojami metodai.

Antrajame skyriuje apžvelgiama literatūra apie saviaktyvuotus scintiliatorius, ypatingai didelį dėmesį skiriant PWO, ceriu aktyvuotas scintiliacines medžiagas, ypač granato ir oksiortosilikato struktūros scintiliacinius kristalus, sužadinimo pernašos procesus ir liuminescencijos dinamiką.

Trečiasis skyrius „Rezultatai ir jų aptarimas“ yra skirtas eksperimentinių rezultatų pristatymui ir yra padalintas į keturias dalis. Pirmoje dalyje aptariami PWO tyrimų rezultatai. Antroje dalyje aptariami naujausi rezultatai, susiję su ceriu legiruotais ortosilikatiniais scintiliatoriais; aptariami krūvio pernašos šiame scintiliatoriuje mechanizmų tyrimų rezultatai bei kiti cerio jonų emisiją įtakojantys veiksniai. Trečiojoje dalyje pristatomi ceriu legiruotų granato struktūros scintiliatorių tyrimų rezultatai, gauti gilinantis į galio gadolinio aliuminio granate generuotų nepusiausvyrųjų krūvininkų dinamiką, pateikiamas eksperimentinių rezultatų ir skaitinio modeliavimo palyginimas. Paskutinė rezultatų skyriaus dalis skiriama iki šiol mažai ištirtiems scintiliatoriams stiklo keramikų pagrindu ir miltelių pavidalo scintiliatoriams.

Ketvirtajame skyriuje pagrindiniai disertacijos rezultatai yra apibendrinti išvadų pavidalu.

Darbe naudotos literatūros sąrašas (198 vnt.) pateiktas disertacijos gale.

Publikacijų sąrašas

Disertacijos tema:

P1. E. Auffray, O. Buganov, M. Korjik, A. Fedorov, S. Nargelas, G. Tamulaitis, S. Tikhomirov, A. Vaitkevičius, Application of two-photon absorption in PWO scintillator for fast timing of interaction with ionizing radiation, Nucl. Instruments Methods Phys. Res. Sect. A Accel. Spectrometers, Detect. Assoc. Equip. 804 (2015) 194–200. doi:10.1016/j.nima.2015.09.017.

P2. M.V. Korjik, A. Vaitkevičius, D. Dobrovolskas, E.V. Tret’yak, E. Trusova, G. Tamulaitis, Distribution of luminescent centers in Ce3+-ion doped amorphous stoichiometric glass BaO–2SiO2 and dedicated glass ceramics, Opt. Mater. (Amst). 47 (2015) 129–134. doi:10.1016/j.optmat.2015.07.014.

P3. E. Auffray, M. Korjik, M.T. Lucchini, S. Nargelas, O. Sidletskiy, G. Tamulaitis, Y. Tratsiak, A. Vaitkevičius, Free carrier absorption in self-activated PbWO4 and Ce-doped Y3(Al0.25Ga0.75)3O12 and Gd3Al2Ga3O12 garnet scintillators, Opt. Mater. (Amst). 58 (2016) 461–465. doi:10.1016/j.optmat.2016.06.040.

P4. E. Auffray, R. Augulis, A. Borisevich, V. Gulbinas, A. Fedorov, M. Korjik, M.T. Lucchini, V. Mechinsky, S. Nargelas, E. Songaila, G. Tamulaitis, A. Vaitkevičius, S. Zazubovich, Luminescence rise time in self-activated PbWO4 and Ce-doped Gd3Al2Ga3O12 scintillation crystals, J. Lumin. 178 (2016) 54–60. doi:10.1016/j.jlumin.2016.05.015.

P5. Y. Tratsiak, Y. Bokshits, A. Borisevich, M. Korjik, A. Vaitkevičius, G. Tamulaitis, Y2CaAlGe(AlO4)3:Ce and Y2MgAlGe(AlO4)3:Ce garnet phosphors for white LEDs, Opt. Mater. (Amst). 67 (2017) 108-112. doi: 10.1016/j.optmat.2017.03.047

P6. M. V Korjik, E. Auffray, O. Buganov, A.A. Fedorov, I. Emelianchik, E. Griesmayer, V. Mechinsky, S. Nargelas, O. Sidletskiy, G. Tamulaitis, S.N. Tikhomirov, A. Vaitkevičius, Non-Linear Optical Phenomena in Detecting Materials as a Possibility for Fast Timing in Detectors of Ionizing Radiation, IEEE Trans. Nucl. Sci. 63 (2016) 2979–2984. doi:10.1109/TNS.2016.2617461.

P7. G. Tamulaitis, A. Vaitkevičius, S. Nargelas, R. Augulis, V. Gulbinas, P. Bohacek, M. Nikl, A. Borisevich, A. Fedorov, M. Korjik, E. Auffray, Subpicosecond luminescence rise time in magnesium codoped GAGG:Ce scintillator, Nucl. Instruments Methods Phys. Res. Sect. A Accel. Spectrometers, Detect. Assoc. Equip. 870 (2017) 25–29. doi:10.1016/j.nima.2017.07.015.

P8. M. Korjik, V. Alenkov, A. Borisevich, O. Buzanov, V. Dormenev, G. Dosovitskiy, A. Dosovitskiy, A. Fedorov, D. Kozlov, V. Mechinsky, R.W. Novotny, G. Tamulaitis, V. Vasiliev, H.-G. Zaunick, A. Vaitkevičius, Significant improvement of GAGG:Ce based scintillation detector performance with temperature decrease, Nucl. Instruments Methods Phys. Res. Sect. A Accel. Spectrometers, Detect. Assoc. Equip. 871 (2017) 42–46. doi:10.1016/j.nima.2017.07.045.

P9. E. Auffray, R. Augulis, A. Fedorov, G. Dosovitskiy, L. Grigorjeva, V. Gulbinas, M. Koschan, M. Lucchini, C. Melcher, S. Nargelas, G. Tamulaitis, A. Vaitkevičius, A. Zolotarjovs, M. Korzhik, Excitation Transfer Engineering in Ce-Doped Oxide Crystalline Scintillators by

Codoping with Alkali-Earth Ions, Phys. Status Solidi Appl. Mater. Sci. 215 (2018) 1–10. doi:10.1002/pssa.201700798.

P10. E. Trusova, A. Vaitkevičius, Y. Tratsiak, M. Korjik, P. Mengucci, D. Rinaldi, L. Montalto, V. Marciulionyte, G. Tamulaitis, Barium and lithium silicate glass ceramics doped with rare earth ions for white LEDs, Opt. Mater. (Amst). 84 (2018) 459–465. doi:10.1016/j.optmat.2018.07.030.

P11. G. Tamulatis, G. Dosovitskiy, A. Gola, M. Korjik, A. Mazzi, S. Nargelas, P. Sokolov, A. Vaitkevičius, Improvement of response time in GAGG: Ce scintillation crystals by magnesium codoping, J. Appl. Phys. 124 (2018) 215907. doi:10.1063/1.5064434.

P12. M.T. Lucchini, O. Buganov, E. Auffray, P. Bohacek, M. Korjik, D. Kozlov, S. Nargelas, M. Nikl, S. Tikhomirov, G. Tamulaitis, A. Vaitkevičius, K. Kamada, A. Yoshikawa, Measurement of non-equilibrium carriers dynamics in Ce-doped YAG, LuAG and GAGG crystals with and without Mg-codoping, J. Lumin. 194 (2018) 1–7. doi:10.1016/j.jlumin.2017.10.005.

P13. Y. Tratsiak, E. Trusova, Y. Bokshits, M. Korjik, A. Vaitkevičius, G. Tamulaitis, Garnet-type crystallites, their isomorphism and luminescence properties in glass ceramics, CrystEngComm. 21 (2019) 687–693. doi:10.1039/C8CE01547C.

P14. M. Korzhik, A. Gola, J. Houžvička, A. Mazzi, S. Nargelas, S. Sýkorová, G. Tamulaitis, A. Vaitkevičius, S. Sykorová, G. Tamulaitis, A. Vaitkevičius, Timing properties of Ce-doped YAP and LuYAP scintillation crystals, Nucl. Instruments Methods Phys. Res. Sect. A Accel. Spectrometers, Detect. Assoc. Equip. 927 (2019) 169–173. doi:10.1016/j.nima.2019.02.036.

P15. G. Tamulaitis, A.N. Vasil’ev, M. Korzhik, A. Mazzi, A. Gola, S. Nargelas, A. Vaitkevicius, A. Fedorov, D. Kozlov, Improvement of the time resolution of radiation detectors based on Gd3Al2Ga3O12 scintillators with SiPM readout, IEEE Trans. Nucl. Sci. 66 (2019) 1879–1888. doi:10.1109/TNS.2019.2919898.

P16. E. Auffray, G. Dosovitskiy, A. Fedorov, I. Guz, M. Korjik, N. Kratochwill, M. Lucchini, S. Nargelas, D. Kozlov, V. Mechinsky, P. Orsich, O. Sidletskiy, G. Tamulaitis, A. Vaitkevičius, Effects on Gd3Al2Ga3O12 Scintillators Prospective for Application in Harsh Irradiation Environments, 2019.

P17. G. Tamulaitis, E. Auffray, A. Gola, M. Korzhik, A. Mazzi, V. Mechinski, S. Nargelas, Y. Talochka, A. Vaitkevičius, A. Vasil’ev, Improvement of the timing properties of Ce-doped oxyorthosilicate LYSO scintillating crystals, J. Phys. Chem. Solids. 139 (2020) 109356. doi:10.1016/j.jpcs.2020.109356.

P18. M. Korzhik, V. Alenkov, O. Buzanov, G. Dosovitskiy, A. Fedorov, D. Kozlov, V. Mechinsky, S. Nargelas, G. Tamulaitis, A. Vaitkevičius, Engineering of a new single-crystal multi-ionic fast and high-light-yield scintillation material (Gd0.5-Y0.5)3Al2Ga3O12:Ce,Mg, CrystEngComm. 22 (2020) 2502–2506. doi:10.1039/D0CE00105H.

Kitos

P19. V. Kononets, O. Benamara, G. Patton, C. Dujardin, S. Gridin, a. Belsky, D. Dobrovolskas, A. Vaitkevičius, G. Tamulaitis, V. Baumer, K. Belikov, O. Sidletskiy, K. Lebbou, Growth of Ce-doped LGSO fiber-shaped crystals by the micro pulling down technique, J. Cryst. Growth. 412 (2015) 95–102. doi:10.1016/j.jcrysgro.2014.11.036.

P20. D. Dobrovolskas, J. Mickevičius, S. Nargelas, A. Vaitkevičius, Y. Nanishi, T. Araki, G. Tamulaitis, Influence of defects and indium distribution on emission properties of thick In-rich InGaN layers grown by the DERI technique, Semicond. Sci. Technol. 32 (2017) 25012. doi:doi:10.1088/1361-6641/32/2/025012.

Autoriaus indėlis

Autorius atliko visus liuminescencijos su erdvine skyra bei nuostoviosios sugerties matavimus, pasinaudojęs COST veiklos FAST teikta finansine parama atliko scintiliatorių našumo matavimus Gysene, Vokietijoje, bei įvykių sutapimo laikinės skyros matavimus Trente, Italijoje. Naudodamasis kolegų išmatuotais eksperimentiniais duomenimis autorius atliko skirtuminės sugerties bei fotoliuminescencijos su laikine skyra matavimo rezultatų analizę ir dalyvavo visuose mokslinių publikacijų ruošimo etapuose.

Skirtuminės sugerties matavimus Vilniaus universiteto Fotonikos ir nanotechnologijų institute atliko dr. Sauliaus Nargelas, liuminescencijos su laikine skyra matavimai buvo atliki prof. habil. dr. Vidmanto Gulbino vadovaujamoje tyrimų gupėje Fizinių ir technologinių mokslų centre. Įvykių sutapimo laikinės skyros matavimai buvo atlikti su dr. *Alberto Gola* ir dr. *Alberto Mazzi* pagalba institute *Fundazione Bruno Kessler*, Trente, Italijoje.

Inovatyvių keramikinių medžiagų sintezė ir struktūriniai matavimai buvo atlikti Dr. *Mikhail Korjik* vadovaujamoje grupėje Baltarusijos valstybiniame universitete. Tyrimuose naudoti monokristaliniai scintiliatoriai buvo gaminti įvairių tiekėjų ir gauti bendradarbiaujant su CERN *Crystal Clear Collaboration* partneriais.

Eksperimentiniai metodai

Šiame darbe scintiliatorių charakteristikos, nepusiausvyrųjų krūvininkų dinamika ir struktūrinės savybės buvo tirtos naudojant šias pagrindines metodikas: optinio žadinimo ir zondavimo, liuminescencinės spektroskopijos su laikine skyra ir įvykių sutapimo laikinė skyra. Struktūrinėms medžiagų savybėms tirti taip pat buvo naudojamos konfokalinė mikroskopija ir rentgeno spindulių difraktometrija.

Optinio žadinimo ir zondavimo metodika

Naudojant šią metodiką tiriami pokyčiai bandinyje atsiradęę po žadinimo trumpu lazerio impulsu. Keičiant zondavimo impulso kvanto energiją ir vėlinimo trukmę galima charakterizuoti medžiagoje vykstančių reiškinių dinamiką. Tipinė šio eksperimento schema pavaizduota pav. 1.

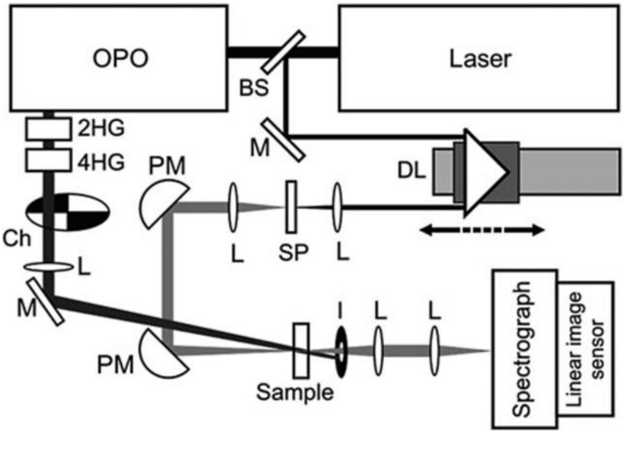

1 pav. Skirtuminės sugerties registravimo schema: OPA – optinis parametrinis stiprintuvas, BS – spindulio daliklis, M – veidrodis, L – lęšis, DL – vėlinimo linija, SW – safyro plokštelė, PM – parabolinis laikrodis, I – rainelė, 2HG ir 4HG – β-BBO kristalai, naudojami antros ir ketvirtos harmonikos generavimui, Ch – spindulio pertraukiklis. [P13]

Skirtuminė sugertis yra sąlygojama bet kokių nepusiausvirųjų krūvininkų sugerties, nesvarbu ar tie krūvininkai yra laisvi, pagauti pagauti į lokalizuotus centrus ar yra sužadintose aktyvatorių jonų būsenose. Skirtuminės sugerties intensyvumas priklauso nuo sugerties skerspjūvio, būsenų, į kurias vyksta optinis šuolis, tankio ir nuo sugeriančių krūvininkų tankio. Mūsų eksperimentai buvo atliekami tokiomis sąlygomis, kad pirmieji du parametrai būtų pastovūs. Todėl registruojamo signalo intensyvumas buvo proporcingas krūvininkų tankiui.

Skirtuminės sugerties matavimai leidžia vienu metu tirti sugerties procesų spektrines ir laikines savybes, o tai yra didelis privalumas siekiant nustatyti tą sugertį lemiančių procesų prigimtį. Dar vienas šios metodikos privalumas yra galimybė keisti sužadinimo kvanto energiją ir taip atlikti selektyvų įvairių kristalo struktūrinių elementų žadinimą. Metodikos laikinę skyrą riboja tik naudojamo lazerio impulso trukmė, tad pasitelkus femtosekundinį lazerį galima pasiekti subpikosekundinę laikinę skyrą.

Šiame darbe naudota skirtuminės sugerties su laikine skyra matavimo įranga yra paremta komerciniu Yb:KGW (Yb:KGd(WO_4)$_2$) femtosekundiniu lazeriu (Pharos, Šviesos Konversija). Lazerio spinduliuotė buvo padalinama į dvi šakas. Pagrindinė dalis buvo naudojama optiniam parametriniam stiprintuvui sužadinti (Orpheus, Šviesos Konversija) ir jame generuoti keičiamo dažnio šviesą, naudojamą bandinio žadinimui. Bandinį žadinanti šviesa buvo nukreipiama į dažnį dvigubinančius/keturgubinančius β-BBO kristalus taip padidinant žadinančio kvanto energiją iki UV srities. Antroji spinduliuotės dalis buvo nukreipiama į vėlimo liniją ir po jos sufokusuojama į safyro plokštelę, kurioje buvo generuojamas baltos šviesos superkontiniumas. Praėję pro bandinį zonduojančios šviesos impulsai buvo registruojami spektrografu.

Liuminescencinė spektroskopija su laikine skyra

Šiame darbe liuminescencijos su spektrine skyra matavimai buvo atlikti naudojant skleidžiančiąją kamerą (*streak camera*), kurios principinė schema pateikta pav. 2. Tiriama šviesa yra verčiama į fotoelektronus, kurie pagreitinami link fluorescencinio ekrano ir atlenkiami statmena sklidimui kryptimi naudojant tiesiškai augančius įtampos impulsus. Taip išskleidus šviesos impulsą, jo laikines savybes galima tirti kaip signalo ant fluorescencinio ekrano erdvinį pasiskirstymą. Šią sistemą kombinuojant su spektrometru galima vienu metu tirti tiek spektrines, tiek laikines fotoliuminescencijos savybes.

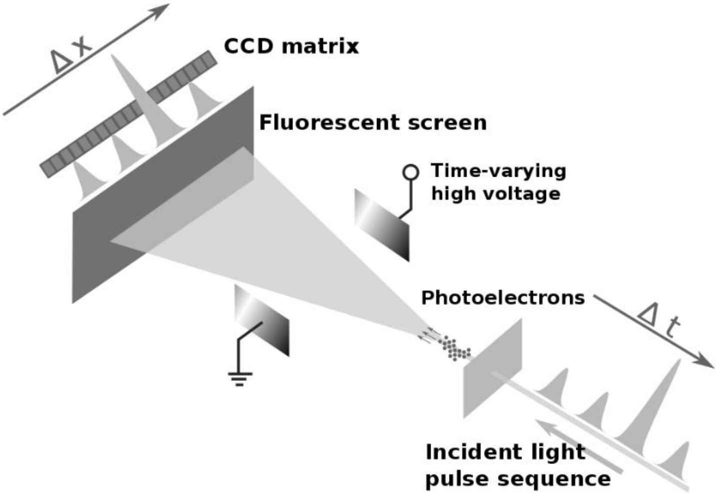

2 pav. Skleidžiančiosios kameros principinė schema.

Šiame darbe matavimai buvo atlikti naudojant femtosekundinį Yb:KGW lazerį (Šviesos Konversija), spinduliuojantį 1030 nm bangos ilgio 80 fs trukmės impulsus, pasikartojančius 76 MHz dažniu. Harmonikų generatorius (HIRO, Šviesos Konversija) buvo naudojamas generuoti 343 nm ir 254 nm bangos ilgių šviesą. Fotoliuminescencijos signalas buvo registruotas naudojant *Hamamatsu* skleidžiančiąją kamerą. Matavimus atliekant sinchroniniame (*synchroscan*) režime instrumentinės atsako funkcijos pusplotis 2.95 ps. Atlikus instrumentinės atsako funkcijos ir fotoliuminescencijos signalo dekonvoliuciją buvo pasiekta subpikosekundinė laikinė skyra. Matavimai buvo atlikti kambario temperatūroje, kaip yra įprasta charakterizuojant medžiagas scintiliatoriniams detektoriams.

Įvykių sutapimo laikinės skyros metodas

Siekiant išmatuoti įvykių sutapimo laikinę skyrą buvo tiriami iš scintiliatorių pagaminti pikseliai, sujungti su silicio fotodaugintuvais, pagamintais *Fundazione Brune Kessler* institute Italijoje. Pikseliai buvo apvynioti teflonu ir priklijuoti prie detektorių *Cargille Meltmount* optiniais klijais.

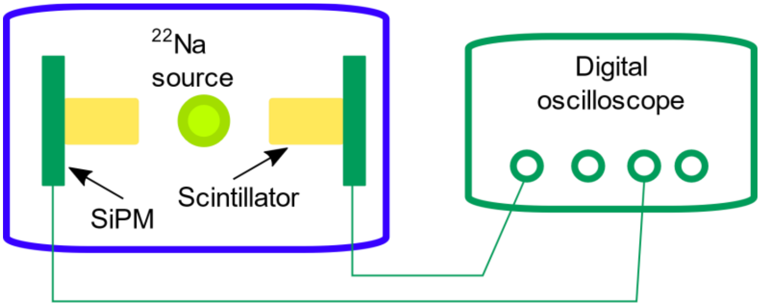

3 pav. Įvykių sutapimo laiko skyros matavimų schema.

Matavimų schema pateikta pav. 3. Ją sudaro dvi identiškos scintiliatorių ir fotodaugintuvų poros patalpintos vienodu atstumu nuo ^{22}Na gama kvantų šaltinio. Vienam iš natrio izotopo skilimo produktų, pozitronui, anihiliuojantis susiformuoja du vienodos energijos gama kvantai, sklindantys priešingomis kryptimis. Detektoriams registruojant gama kvantus, fiksuojamas jų detektavimo laikų skirtumas. Užregistravus statistiškai reikšmingą įvykių skaičių, apskaičiuojamas registravimo skirtumo pasiskirstymo pusplotis, kuris parodo medžiagos ir detektoriaus laikinę skyrą.

Rezultatai ir jų aptarimas

Švino volframatas

Švino volframas šiuo metu yra viena iš plačiausiai naudojamų scintiliacinių medžiagų aukštų energijų fizikos eksperimentuose. Naudojant inovatyvias liuminescencijos su laikine skyra bei žadinimo ir zondavimo metodikas švino volframato kristalai buvo ištirti siekiant atskleisti tolesnes šio kristalo taikymo galimybes.

Tipiniai laike integruoti švino volframato liuminescencijos spektrai yra pateitkti 4 pav. Kai žadinimui naudojama 254 nm bangos ilgio šviesa, vyksta žadinimas į laidumo juostą. Taip žadinant, liuminescencijos spektras yra sudarytas iš vienos plačios juostos, susijusions su optiniais šuoliais atomų grupėje WO_4^{2-}. Naudojant žemesnės energijos žadinimą (343 nm), liuminescencijos intensyvumas sumažėja, ir spektre atsiranda žalia komponentė dėl optinių šuolių, kylančių iš struktūrinio defekto susidariusioje atomų grupėje WO_3.

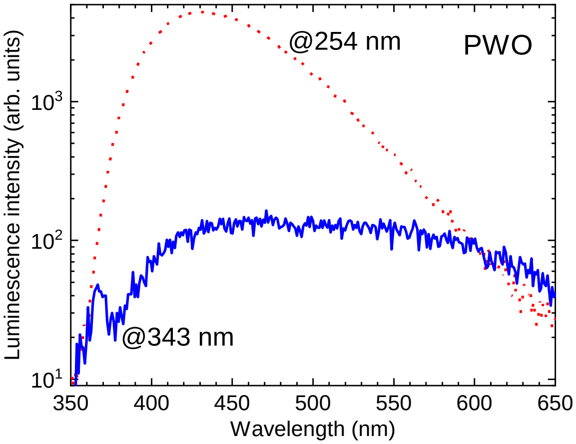

4 pav. Tipiniai švino volframato fotoliuminescencijos spektrai naudojant skirtingus žadinimo bangos ilgius (nurodyta)

Paveikle 5 yra pateikta spektriškai integruotos fotoliuminescencijos kinetikos pradžia. Kartu paveizduota ir matavimo sistemos instrumentinė atsako funkcija. Atsako funkcijos plotis ties puse maksimumo – 2.95 ps. Užregistruotas signalo kilimas yra ribotas atsako funkcijos. Tai rodo, kad fotoliuminescencijos įsižiebimo trukmė švino volframate yra subpikosekundinė.

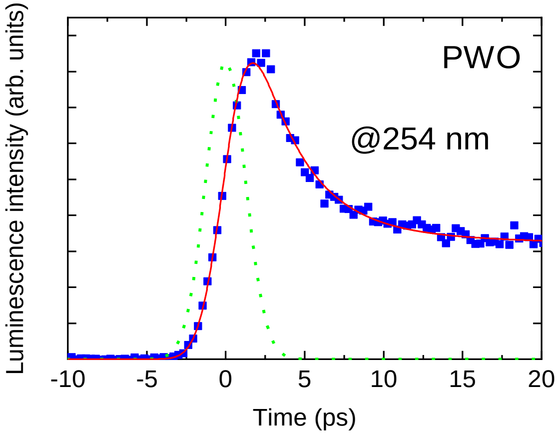

5 pav. Charakteringa švino volframato fotoliuminescencijos kinetikos pradžia (mėlyni taškai), matavimo sistemos istrumentinė atsako funkcija (žali taškai) ir geriausias matematinis kinetikos aprašymas naudojant bieksponentinę įsižiebimo ir gesimo funkciją (raudona linija)

Įdomu pastebėti, kad tiek reguliarių, tiek defektinių grupių emisija įsižiebia ta pačia sparta. Tai rodo, kad procese nedalyvauja jokie tarpiniai krūvio pagavos centrai. Paveiksle 6 pateikta fotoliuminescncijos dinamika per pirmasias 600 ps. Fotoliuminescencijos gesimas gali būti aprašytas daugiaeksponentine funkcija. Ilgiausia ir vidutinė gesimo komponentės jau buvo aprašytos literatūroje, tuo tarpu greičiausia komponentė iki šiol nebuvo stebėta. Greičiausios komponentės charakteringa gesimo trukmė yra 3,8-5,9 ps.

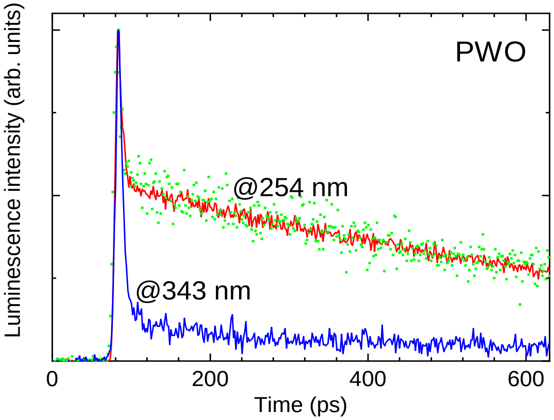

6 pav. Pradinė švino volframato kinetikos dalis išmatuota naudojant 343 nm žadinimą (mėlyna linija) ir 254 nm žadinimą, kai impulso energija lygi 15 mJ/cm^2 (raudona linija) ir 1.5 mJ/cm^2 (žali taškai).

Šie rezultatai yra gauti žadinant medžiagą fotonais kurių energija yra artima švino volframato draustiniam tarpui. Žadnant jonizuojančiąją spinduliuotę, dalis sugeneruotų elektronų ir skylių porų termalizacijos metu gali išsiskirti erdvėje. Nepaisant to, nenumatome ženklaus signalo kilimo trukmės padidėjimo žadinant bandinius jonizuojančiaja spinduliuote, kadangi termalizacija tetrunka pikosekundes arba trumpiau. Be to, vykdant aukštų energijų fizikos eksperimentus švino volframato kristalai per mažiau nei 1 ns apšviečiami kelių GeV energijos doze, tad sparčiai rekombinacijai reikalingas elektronų ir skylių porų tankis bus pakankamas.

Skirtuminės sugerties spektrai, atliekant matavimus su skirtingu uždelsimu tarp žadinimo ir zondavimo impulsų, pateikti 7 pav. Matavimai buvo atlikti per pirmas 400 fs po žadinimo.

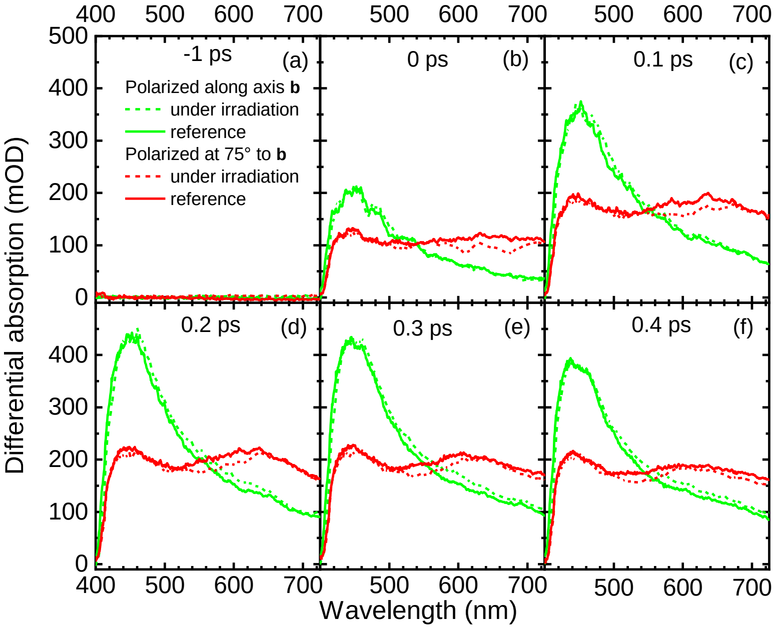

7 pav. Skirtuminės sugerties spektrai, išmatuoti žadinimui naudojant poliarizuotą 395 nm šviesą. Bandiniai orientuoti skirtingomis kryptimis (nurodyta). Matavimai atlikti su (brūkšninė linija) ir be (tolydi linija) gama spinduliuotės. Laikas tarp žadinimo ir zondavimo laiko nurodytas greta grafikų.

Išmatavus skirtuminės sugerties spektrus su ir be gama spinduliuotės poveikio, buvo pastebėtas jonizuojančios spinduliuotės poveikis. Nors atliekant matavimus lazerio spindulį orientavus lygiagrečiai švino volframato **b** ašiai ir nebuvo pastebėta jokio skirtumo, tačiau pastebimas skirtuminės sugerties juostos susilpnėjimas kai bandinio **b** ašis orientuota kampu į lazerio poliarizacijos vektorių. Šis pokytis gali būti išnaudotas jonizuojančios spinduliuotės detektavimui.

Ceriu legiruoti liutecio oksiortosilikatai

Viena iš medžiagų, kurios yra perspektyvios naudoti sparčiuose jonizuojančios spinduliuotės detektoriuose, naudojamuose naujuose didelės erdvinės skyros vaizdinimo prietaisuose medicinoje ir aukštų energijų fizikos eksperimentuose, Yra ceriu legiruoti Lu_2SiO_5 (LSO) bei liutecio ir itrio oksiortosilikato $Lu_{2-x}Y_xSiO_5$ (LYSO) monokristalai. Kristalai buvo tirti panaudojant selektyvaus optinio žadinimo ir zondavimo metodiką su subpikosekundine laikine skyra. Selektyvus žadinimas leido sužadinti trivalenčio cerio jonus į pasirinktas sužadintas būsenas ir taip tirti nepusiausvirųjų elektronų dinamiką šiose medžiagose. Tyrimas buvo vykdomas rezultatus lyginant su tų pačių bandinių tyrimo rezultatais, gautais pasitelkiant įvykių sutapimo laikinės skyros metodą detektuojant sinchroniškai išspinduliuotus 511 keV γ kvantus. Pastarieji matavimai buvo atlikti CERN *Crystal Clear Collaboration* partnerių laboratorijoje ir *Fondazione Bruno Kessler* institute Italijoje.

Ypatingas dėmesys buvo skirtas netiesinės sugerties atsako augimą lemiančių mechanizmų tyrimui. Tipiškos skirtuminės sugerties kinetikos iliustruojamos 8 pav. Mūsų gautų eksperimentinių rezultatų palyginimas su Maskvos Lomonosovo universiteto profesoriaus A. Vasil‘ev teoriniais skaičiavimais parodė, kad netiesinės sugerties atsako kilimą žadinant didelės energijos fotonais lemia elektronų pagavimas į prilipimo lygmenis.

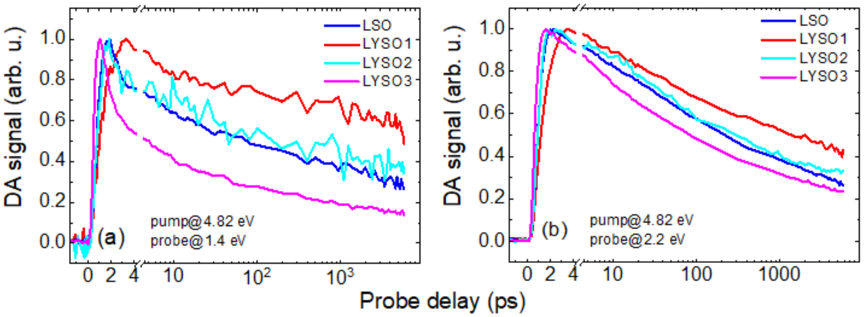

8 pav. Skituminės sugerties signalo kinetika skirtingos sudėties LSO:Ce ir LYSO:Ce bandiniuose žadinant juos 4.82 eV fotonais ir zonduojant 1.4 eV (a) ir 2.2 eV (b) fotonais. Bandinys LYSO1 buvo nekolegiruotas, LYSO2 – kolegiruotas 5 ppm, o LYSO3 – 30 ppm kalcio.

Stebėjimo rezultatai rodo, kad emituojantis cerio jono lygmuo $5d^1$ yra užpildomas su kelių pikosekundžių uždelsimu. Tai gali būti paaiškinta elektronų pagavimu į prilipimo lygmenis. Nustatėme, kad ši elektronų pagava yra stipresnė mišriuose LYSO kristaluose, kuriuose dalis liutecio jonų pakeista itrio jonais, nes šiuose kristaluose dėl sudėties fliuktuacijų atsiranda laidumo juostos dugno potancialo fliuktuacijos, kuriose gali būti pagaunami elektronai. Parodėme, kad uždelsimas, kuris tiesiogiai veikia liuminescencijos atsako spartą, gali būti eliminuotas LYSO kristalą kolegiruojant kalciu. Šis efektas stebimas net esant tokiems mažiems legiravimo kiekiams kaip 5ppm (3 pav, mėlyna ir žydra kreivės). Spartesnė elektronų pernašos kinetika koreliuoja su geresne įvykių sutapimo laikine skyra. Tai rodo, kad skirtuminės sugerties metodiką galima bus panaudoti skirtingomis sąlygomis pagamintų LYSO kristalų atrinkimui CERN CMS eksperimento atnaujinime planuojamam naujam scintiliacinių detektorių sluoksniui (BTL).

Ceriu legiruoti gadolinio aliuminio galio granatai

Buvo atlikti detalūs GAGG:Ce skirtuminės sugerties tyrimai, suteikiantys daugiau informacijos apie nepusiausvyruosius krūvininkus pikosekundinėje laikų skalėje. Sugerties pokyčiai kristale buvo zonduojami pasitelkus rezonansinį skirtingų granato kristalo struktūrinių vienetų žadinimą femtosekundiniais impulsais. Nustatyti procesai, vykstantys po cerio jonų sužadinimo: greita laisvų skylių sugertis gadolinio jonuose ir elektronų, užimančių sužadintą cerio jonų būseną, relaksacija iki žemiausios sužadintos būsenos. Skylių pagavimas vyksta per kelias pikosekundes, tuo tarpu cerio jono viduje vykstanti relaksacija vyksta apie 500 femtosekundžių. Parodyta, kad pagrindinis efektas, dėl kurio sužadintų cerio jonų būsenos užsipildo su kelių pikosekundžių vėlavimu yra nepusiausvyrųjų elektronų pagavimas į prilipimo lygmenis. Eksperimentų rezultatai rodo, kad GAGG:Ce kristalo kolegiravimas magniu net tokia maža koncentracija kaip 10 ppm pašalina šią lėtąją signalo komponentę. Skirtuminės sugerties signalo augimo pagreitėjimas koreliuoja su įvykių laiko sutapimo skyros matavimų rezultatais. Šis eksperimentas rodo, kad kolegiravus GAGG:Ce kristalą magniu pagreitėja kristalo įsišvietimo trukmė jį veikiant gama spinduliuote, ir padidėja scintiliatoriaus sąveikos su spinduliuote momento nustatymo tikslumas. Šis rezultatas, rodo, kad GAGG:Ce,Mg kristalai yra ypatingai perspektyvūs medicininių vaizdinimo prietaisų gamybai ir taikymams aukštos energijos dalelių fizikos eksperimentuose.

9 paveiksle pavaizduota skirtuminės sugerties dinamika skirtingai kolegiruotuose GAGG:Ce kristaluose. Kristalai buvo zonduojami 3.63 eV (342 nm) energijos fotonais rezonansiškai žadinanačiais Ce^{3+} jonus į antrąjį sužadintą lygmenį $5d_2$, kuris šioje medžiagoje yra virš kristalo laidumo juostos dugno. Skirtuminės sugerties spektruose (9 pav., a, b) dominuoja komponentė, priskiriama žemiausioje sužadintoje trivalenčio cerio jono būsenoje esančių elektronų sugerčiai. Visų magniu kolegiruotų kristalų sugerties spektrai ir kinetikos vystosi panašiai. Tuo tarpu nekolegiruotame GAGG:Ce stebima lėtesnė kilimo komponentė (9 pav., c, S1 kreivė).

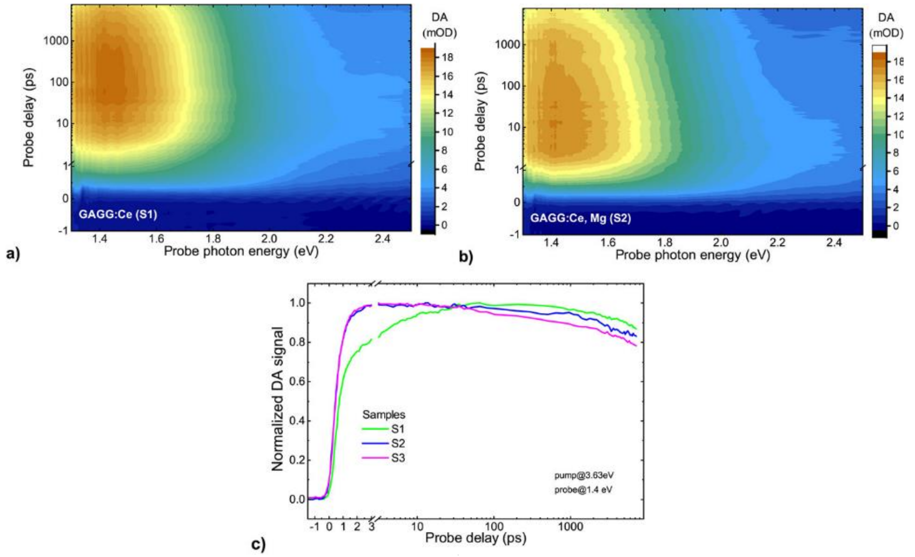

9 pav. Skirtuminės sugerties GAGG:Ce be (bandinys S1, a) ir su (S2, b) kolegiravimu magniu priklausomybės nuo zondo energijos ir laiko tarp zonduojančio ir žadinančio impulsų bei skirtuminės sugerties kinetika zonduojant ties 1.4 eV (c).

Eksperimentų rezultatai parodė, kad lėtąją GAGG:Ce kinetikos komponentę, susietą su kristale esančių Ce^{3+} jonų žemiausios sužadintos būsenos užpildymu, galima eliminuoti šį kristalą kolegiruojant magnio jonais. Ši būsena yra emituojanti, tad jos užpildymo spartėjimas veda link spartesnio liuminescencijos atsakos. Parodėme, kad šis rezultatas gali būti pasiekiamas ir tokiu mažu kolegiravimu kaip 10 ppm. Įvertinta, kad toks kolergiravimo laipsnis nėra pakankamas, jog reikšmingą dalį Ce^{3+} jonų paverstų į Ce^{4+} jonus. Pastaruoju procesu buvo aiškinama kolegiravimo įtaka GAGG:Ce greitaveiksmiškumui. Mūsų rezultatai rodo, kad svarbiausias efektas, lemiantis liuminescencijos atsako į sužadinimą pagreitėjimą, yra prilipimo lygmenyse pagautų elektronų relaksacija į gilesnius lygmenis dėl defektų, susijusių su kolegiranto jonais.

Taigi, naudojantis optiniais nepusiausvyrųjų krūvininkų zondavimo metodais parodyta, kad nepusiausvyrųjų krūvininkų prilipimas yra pagrindinis veiksnys, lemiantis GAGG kristalų liuminescencijos atsako kilimo spartą. Įvairių kristalo struktūrinių vienetų optinis zondavimas parodo, kad legiravimas dvivalenčiais magnio jonais sumažina prilipimo centrų poveikį. Šis efektas taip pat veikia sužadinimo pernašą scitiliatorių žadinant didelės energijos fotonais ir pasireiškia įvykių sutapimo laikinės skyros matavimuose, kurie yra plačiausiai naudojamas, bet specialaus bandinių paruošimo reikalaujantis ir atsikartojamumo problemų turintis metodas scintiliatoių greitaveiksmiškumui vertinti. Papildoma informacija yra gauta eksperimentines diferencinės sugerties kinetikas aprašant kinetinėmis lygtimis, aprašančiomis būsenų užpildas. Šiuo būdu pirmą kartą nustatyta, kad trivalenčio cerio jono vidujcentrinė relaksacija iš $5d_2$ į $5d_1$ lygmenį trunka 500 fs. Be to parodėme, kad GAGG:Ce kolegiruojant magniu galima pasiekti trumpesnę nei anksčiau GAGG:Ce stebėtą atsako puspločio įvykių laiko sutapimo eksperimente vertę: 165 ps.

Taip pat buvo tiriamas GAGG scintiliatorių tinkamumas veikti didelės apšvitos sąlygomis, kurios yra būdingos dalelių greitintuvų eksperimentuose. Kristalai buvo švitinami aukštos energijos (24 GeV) protonais ir gama spinduliais (^{60}Co šaltinis). Apšvitinti bandiniai buvo tiriami skirtuminės sugerties spektroskopijos metodu, leidžiančiu įvertinti pokyčius nepusiausvyrųjų krūvininkų dinamikoje prieš apšvitinimą, iš karto po apšvitinimo (matuota po 24 h) ir įsisotinus krūvininkų spontaninei relaksacijai (matuota praėjus 2 mėn.). Skirtuminės sugerties spektro evoliucija ir skirtuminės sugerties kinetikos nelegiruotame GAGG kristale pavaizduotos 10 pav., atitinkamai A ir B dalyse.

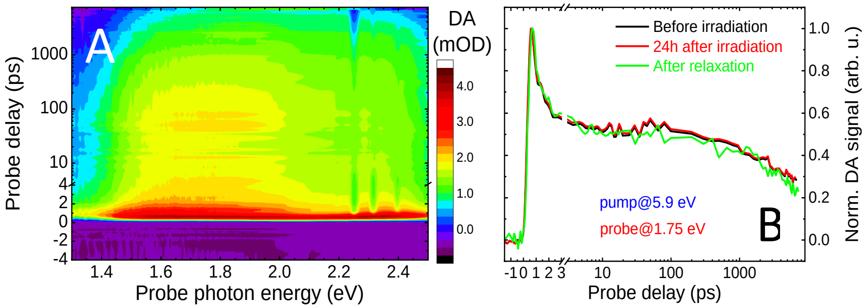

10 pav. Laikinė skirtuminės sugerties spektro evoliucija (A) ir skirtuminės sugerties ties 1.75 eV kinetikos (B) nominaliai nelegiruotame GAGG kristale, jį 5,9 eV energijos fotonais rezonansiškai žadinant į Ce^{3+} lygmenį 5d1 200 fs trukmės impulsu kambario temperatūroje.

Nustatyta, kad $5\cdot10^{14}$ p/cm^2 protonų įtėkis nekeičia optinio GAGG:Ce kristalų pralaidumo tiek nekolegiruotuose GAGG:Ce kristaluose, tiek ir magniu kolegiruotuose kristaluose. Tai leidžia teigti, kad tipinėse detektorių veiklos sąlygose planuojamuose hadronų kolaideriuose protonų kuriami defektai neturės apčiuopiamos įtakos ceriu legiruotų GAGG scintiliatorių savybėms. GAGG:Ce atsakas į sužadinimą palygintas su LSO:Ce ir LYSO:Ce ir nustatyta, kad liuminescencijos dėl apšvitinant atsirandančių radioaktyvių jonų įtaka optiniam triukšmui GAGG kristale yra panašaus dydžio kaip ir LSO scintiliatoriuose. Taigi GAGG:Ce ir šiuo požiūriu yra tinkamas panaudoti tokiuose kolaideriuose. Apšvitinimas juntamai nekeičia GAGG laikinių charakteristikų: ženklios įtakos laisvų krūvininkų relaksacijai bei pagavimo spartai nestebėta. Taigi, daugiakomponenčiai granato tipo GAGG:Ce kristalai yra perspektyvūs kandidatai kuriant naujus, didelės apšvitos sąlygomis veikiančius optiškai nuskaitomus spinduliuotės detektorius.

Keramikiniai scintiliatoriai

Ieškant naujų scintiliacinių medžiagų, tinkančių spartiems scintiliatoriams, vertos dėmesio keraminės medžiagos. Jų gamyba daug pigesnė nei monokristalų, o tai itin svarbu aukštų energijų fizikos eksperimentuose naudojamose didelėse spinduliuotės detektavimo sistemose, kurių kainoje kaštai scintiliacinėms medžiagoms sudaro didelę dalį. Pastaruoju metu pavyksta pagaminti skaidrias keramikas, ir tai labai padidina jų taikymą kaip scintiliacinę terpę. Detaliems tyrimams pasirinkome ceriu legiruotas granato struktūros stiklo keramikas. Bandiniai šiems tyrimams buvo pagaminti partnerių Baltarusijos valstybiniame universitete valdomos stiklo $CaO(MgO)$-Y_2O_3-Al_2O_3-GeO_2-SiO_2-CeO_2 kristalizacijos būdu. Smulkioji XRD vaizdų struktūra rodo, kad susiformuoja granato struktūros kristalitai su skirtingu granato komponenčių santykiu. Konfokalinės spektroskopijos metodu atlikę fotoliuminescencijos parametrų erdvinio pasiskirstymo tyrimus su submikrometrine erdvine skyra (žr. 11 pav.) nustatėme, kad kristalitai turi sluoksninę struktūrą. Pasiūlėme sluoksniuotos struktūros formavimosi mechanizmą: tai procesas, kurio metu kiekvienas susiformavęs sluoksnis veikia kaip katalizatorius sekančio, skirtingos sudėties sluoksnio formavimuisi.

Cerio jonų emisijos priklausomybė nuo granato sudėties matomi 11 paveiksle, kuriame pateikti tipiniai fotoliuminescencijos parametrų pasiskirstymai dviejose granato tipo keramikose – $Y_2CaAlGe(AlO_4)_3$:Ce ir $Y_2MgAlGe(AlO_4)_3$:Ce. Matavimai su erdvine skyra rodo, kad kristalitų morfologija skiriasi: vienu atveju jie yra heksagoniški, kaip įprasta granato struktūrai, kitu atveju kristalitų forma netaisyklinga, jie didesni ir ištempti. Šių kristalitų liuminescencijos signalas yra stipresnis. Nustatyta, kad tolstant nuo kristalito centro fotoliuminescencijos juosta slenka į aukštesnių energijų pusę. Šis reiškinys paaiškintas tuo, kad kinta kristalio sudėtis ir kristalinis laukas, veikiantis cerio joną. Kintanti sudėtis gali būti susijusi su sluoksniuoto kristalito formavimosi procesu. Spektro plotis auga tolstant nuo kristalito centro. Tai rodo, kad didėjant kristalitui auga ir granato sudėties fluktuacijos.

Iš tirpalo išgautų scintiliacinių kristalitų fotoliuminescencijos spektrai bei skenuojančiu elektronų mikroskopu gauti paviršiaus vaizdai pateikti 12 paveiksle. Rezultatai rodo, kad skirtingų kristalitų emisijos spektrai pasižymi aukštu atsikartojamumu. Skiriasi fotoliuminescencijos intensyvumas, tačiau tai galima paaiškinti skirtinga šviesos ištrūka iš skirtingų kristalitų.

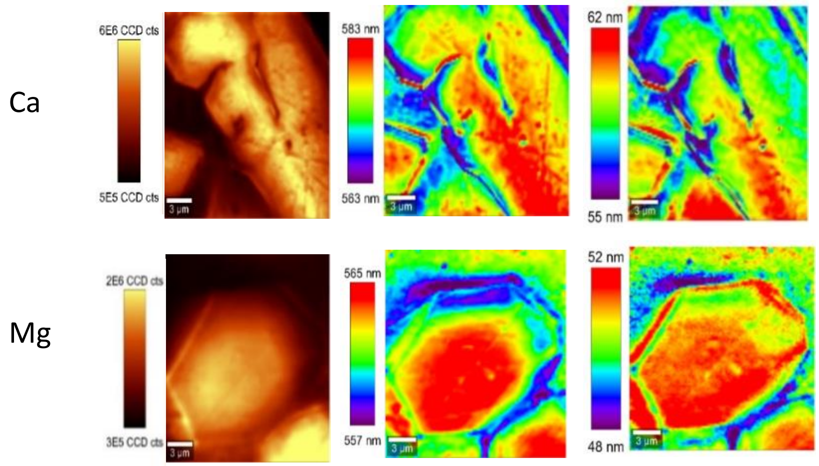

11 pav. Erdviniai fotoliumiescencijos parametrų pasiskirstymai: spektriškai integruotas intensyvumas (kairėje), juosto smailės padėtis (centre) ir juostos plotis (dešinėje) skirtingos sudėties stiklo keramikos bandiniuose žadinant 442 nm lazeriu ir tiriant 20×20 μm^2 plotą skirtingos sudėties keramikose $Y_2CaAlGe(AlO_4)_3$:Ce ir $Y_2MgAlGe(AlO_4)_3$:Ce.

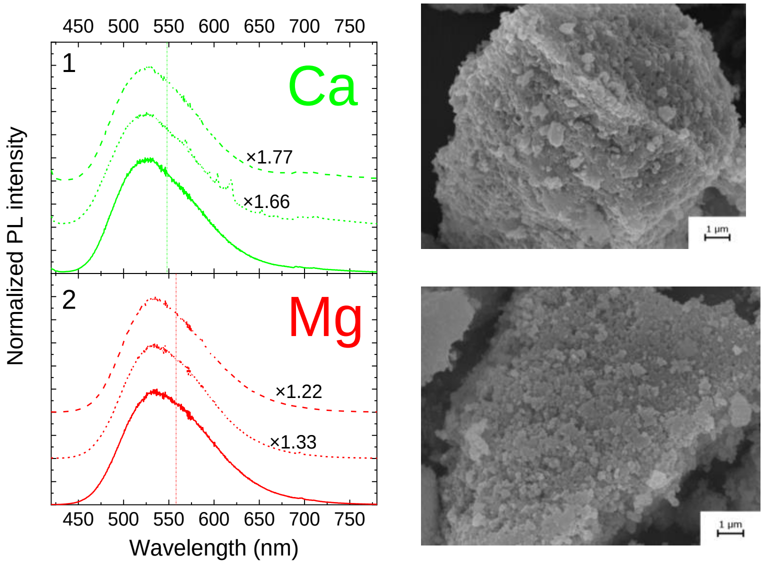

12 pav. $Y_2CaAlGe(AlO_4)_3$:Ce ir $Y_2MgAlGe(AlO_4)_3$:Ce fotoliumescencijos spektrai (kairėje) ir skenuojančios elektronų mikroskopijos vaizdai.

Išvados

1. Liuminescencijos kilimo ir pirmoji gęsimo komponentės švino voframate yra pakankamai sparčios, kad tiktų išnaudoti detektoriuje su mažesne nei dešimt pikosekundžių laikine skyra.
2. Vykstant tarpjuostiniam sužadinimui PWO kristaluose, laisvi elektronai yra generuojami laidumo juostoje subpikosendune sparta ir jų tankis plačiame dinaminiame diapazone yra tiesiogiai proporcingas žadinimo impulso energijos tankiui. Tai gali būti pritaikoma sparčių jonizuojančiosios spinduliuotės detektorių kūrimui.
3. Jonizuojančios spinduliuotės poveikis dvifotonei sugerčiai gali būti panaudotas detektuoti medžiagos sąveikos su jonizuojančia spinduliuote pradžią. Tuo tarpu liuminescencija gali duoti informacijos apie sugertą spinduliuotės dozę.
4. LSO:Ce kristale Ce^{3+} jonų emituojančio lygmens $5d^1$ užpildymas po sužadinimo lazerio impulsu vyksta su kelių pikosekundžių užlaikymu dėl elektronų pagavimo į prilipimo lygmenis.
5. LYSO:Ce kristaluose Ce^{3+} jonų lygmens $5d^1$ užpildos delsa yra ilgesnė nei LSO:Ce kristaluose, nes elektronų prilipimas LYSO:Ce vyksta tiek dėl struktūrinių defektų, tiek dėl laidumo juostos dugno moduliacijų, susijusių su mišraus kristalo sudėties fluktuacijomis.
6. Spindulinio lygmens cerio jonuose užpildos užlaikymą LSO:Ce ir LYSO:Ce kristaluose galima panaikinti kolegiruojant aliovalentine kalcio priemaiša net iki tokių mažų koncentracijų kaip 5 ppm.
7. Vidujcentrinės elektronų relaksacijos iš aktyvatoriaus jono Ce^{3+} lygmens $5d^2$ į lygmenį $5d^1$ trukmė GAGG:Ce kristaluose yra lygi 500 fs.
8. Skylių pagavimas Gd subgardelėje yra svarbus veiksnys, gadinantis liuminescencijos atsaką mišriuose granato tipo scintiliatoriuose, kurių sudėtyje yra gadolinio.
9. Gadolinio pagrindinė būsena GAGG kristale yra ~1 eV žemiau nei valentinės juostos viršus.
10. GAGG:Ce kolegiravimas magniu sumažina elektronų prilipimo poveikį ir spartina liuminescencijos atsaką.
11. Apšvitinimas tokiose sąlygose, kurių tikimasi būsimuose LHC eksperimentuose, neturės poveikio GAGG:Ce šviesos išeigai ar laikinėms savybėms.
12. Aukštos kokybės keramikiniai scintiliatoriai gali būti pagaminti naudojant kontroliuojamą kristalizaciją arba tiesioginį nusodinimą iš tirpalo.

13. Kontroliuojamos kristalizacijos būdu pagamintuose $Y_2CaAlGe(AlO_4)_3$:Ce ir $Y_2MgAlGe(AlO_4)_3$:Ce kristalituose yra jų spinduliuotės parametrų gradientas: kryptimi nuo kristalito centro link jo krašto fotoliuminescencijos juosta slenkasi į trumpabangę pusę ir platėja.
14. Nusodinimo iš tirpalo būdu pagamintuose $Y_2MgAlGe(AlO_4)_3$:Ce kristalituose liuminescencijos masės centras yra 7 nm pasislinkęs į ilgabangę pusę lyginant su analogiškais $Y_2CaAlGe(AlO_4)_3$:Ce kristalitais dėl Mg^{2+} ir Ge^{4+} jonų pakeitimo Y^{3+} ir Al^{3+} jonais, kas didina kristalinį lauką Ce^{3+} jonų aplinkoje.

BIBLIOGRAPHY

[1] F. A. Kröger, *Some Aspects of the Luminescence of Solids* (Elsevier Publishing Company, 1948).

[2] P. Lecoq, I. Dafinei, E. Auffray, M. Schneegans, M. V. Korzhik, O. V. Missevitch, V. B. Pavlenko, A. A. Fedorov, A. N. Annenkov, V. L. Kostylev, and V. D. Ligun, Nucl. Inst. Methods Phys. Res. A **365**, 291 (1995).

[3] P. Lecoq, Nucl. Instruments Methods Phys. Res. Sect. A Accel. Spectrometers, Detect. Assoc. Equip. **537**, 15 (2005).

[4] N. H. Winchell and A. N. Winchell, *Elements of Optical Mineralogy: An Introduction to Microscopic Petrography. 2. Descriptions of Minerals: With Special Reference to Their Optical and Microscopical Characters* (Wiley, 1951).

[5] Q. Lin, X. Feng, and J. Chen, J. Alloys Compd. **307**, 245 (2000).

[6] C. H. Yang, G. Chen, B. Wang, and P. F. Shi, Cryst. Res. Technol. **36**, 543 (2001).

[7] A. A. Annenkov, M. V. Korzhik, and P. Lecoq, Nucl. Instruments Methods Phys. Res. Sect. A Accel. Spectrometers, Detect. Assoc. Equip. **490**, 30 (2002).

[8] A. Breskin and R. Voss, editors , *The CERN Large Hadron Collider: Accelerator and Experiments* (CERN, Geneva, 2009).

[9] C. M. S. Collaboration, C. TDR **4**, 2002 (1997).

[10] R. Novotny, AIP Conf. Proc. **867**, 106 (2006).

[11] I. N. Shpinkov, I. A. Kamenskikh, M. Kirm, V. N. Kolobanov, V. V. Mikhailin, A. N. Vasilev, and G. Zimmerer, Phys. Status Solidi Appl. Res. **170**, 167 (1998).

[12] P. Lecoq, A. Annenkov, A. Gektin, M. Korzhik, and C. Pedrini, 1 (2012).

[13] P. Lecoq, A. Gektin, and M. Korzhik, *Inorganic Scintillators for Detector Systems* (Springer International Publishing, 2017).

[14] V. V. Laguta, M. Nikl, and S. Zazubovich, Radiat. Meas. **42**, 515 (2007).

[15] A. Krasnikov, M. Nikl, and S. Zazubovich, Phys. Status Solidi Basic Res. **243**, 1727 (2006).

[16] M. Nikl, P. Bohacek, E. Mihokova, M. Kobayashi, M. Ishii, Y. Usuki, V. Babin, A. Stolovich, S. Zazubovich, and M. Bacci, J. Lumin. **87**, 1136 (2000).

[17] V. V. Laguta, M. Martin, F. Meinardi, A. Vedda, A. Hofstaetter, B. K. Meyer, M. Nikl, E. Mihóková, J. Rosa, and Y. Usuki, Phys. Rev. B **62**, 109 (2000).

[18] V. V. Laguta, M. Martini, A. Vedda, M. Nikl, E. Mihóková, P. Boháček, J. Rosa, A. Hofstätter, B. K. Meyer, and Y. Usuki, Phys. Rev. B - Condens. Matter Mater. Phys. **64**, 1 (2001).

[19] B. Han, X. Feng, G. Hu, P. Wang, and Z. Yin, J. Appl. Phys. **84**, 2831

(1998).
[20] P. Bohacek, N. Senguttuvan, V. Kiisk, A. Krasnikov, M. Nikl, I. Sildos, Y. Usuki, and S. Zazubovich, Radiat. Meas. **38**, 623 (2004).
[21] M. J. Weber, S. E. Derenzo, and W. W. Moses, J. Lumin. **87**, 830 (2000).
[22] G. P. Pazzi, P. Fabeni, M. Nikl, P. Bohacek, E. Mihokova, A. Vedda, M. Martini, M. Kobayashi, and Y. Usuki, J. Lumin. **102–103**, 791 (2003).
[23] W. van Loo, Phys. Status Solidi **28**, 227 (1975).
[24] M. Nikl, Phys. Status Solidi a-Applied Res. **178**, 595 (2000).
[25] Y. Chen, C. Shi, and G. Hu, J. Appl. Phys. **87**, 1503 (2000).
[26] M. Kobayashi, Y. Usuki, M. Ishii, T. Yazawa, K. Hara, M. Tanaka, M. Nikl, S. Baccaro, A. Cecilia, M. Diemoz, and I. Dafinei, Nucl. Instruments Methods Phys. Res. Sect. A Accel. Spectrometers, Detect. Assoc. Equip. **404**, 149 (1998).
[27] M. Kobayashi, Y. Usuki, M. Ishii, N. Senguttuvan, K. Tanji, M. Chiba, K. Hara, H. Takano, M. Nikl, P. Bohacek, S. Baccaro, A. Cecilia, and M. Diemoz, Nucl. Instruments Methods Phys. Res. Sect. A Accel. Spectrometers, Detect. Assoc. Equip. **434**, 412 (1999).
[28] M. Nikl, P. Boháček, E. Mihóková, M. Martini, F. Meinardi, A. Vedda, P. Fabeni, G. P. Pazzi, M. Kobayashi, M. Ishii, and Y. Usuki, J. Appl. Phys. **87**, 4243 (2000).
[29] S. Baccaro, P. Bohacek, A. Cecilia, A. Cemmi, S. Croci, I. Definei, M. Diemoz, P. Fabeni, M. Ishii, M. Kobayashi, M. Martini, E. Mihokova, M. Montecchi, M. Nikl, G. Organtini, G. P. Pazzi, Y. Usuki, and A. Vedda, Phys. Status Solidi **179**, 445 (2000).
[30] P. Bohacek, N. Solovieva, and M. Nikl, IEEE Trans. Nucl. Sci. **55**, 1289 (2008).
[31] R. W. Novotny, W. M. Döring, F. Hjelm, D. Melnychuk, K. Makonyi, A. Reiter, C. Salz, M. Steinacher, M. Thiel, and B. Zwieglinski, IEEE Nucl. Sci. Symp. Conf. Rec. **1**, 244 (2005).
[32] G. M. Sessler and M. G. Broadhurst, editors , *Electrets* (Springer-Verlag, Berlin; New York, 1980).
[33] M. J. Weber, Solid State Commun. **12**, 741 (1973).
[34] G. Blasse and A. Bril, Appl. Phys. Lett. **11**, 53 (1967).
[35] M. Moszyński, T. Ludziejewski, D. Wolski, W. Klamra, and L. O. Norlin, Nucl. Inst. Methods Phys. Res. A **345**, 461 (1994).
[36] T. Kanai, M. Satoh, and I. Miura, J. Am. Ceram. Soc. **91**, 456 (2008).
[37] K. Kamada, T. Yanagida, J. Pejchal, M. Nikl, T. Endo, K. Tsutumi, Y. Fujimoto, A. Fukabori, and A. Yoshikawa, J. Phys. D. Appl. Phys. **44**, 505104 (2011).
[38] K. Kamada, T. Endo, K. Tsutumi, T. Yanagida, Y. Fujimoto, A. Fukabori, A. Yoshikawa, J. Pejchal, and M. Nikl, Cryst. Growth Des. **10**, 4484 (2011).
[39] M. Tyagi, F. Meng, M. Koschan, S. B. Donnald, H. Rothfuss, and C.

L. Melcher, J. Phys. D. Appl. Phys. **46**, (2013).

[40] J. M. Ogiegło, A. Katelnikovas, A. Zych, T. Ju, A. Meijerink, and C. R. Ronda, J. Phys. Chem. A **117**, 2479 (2013).

[41] W. Drozdowski, K. Brylew, M. E. Witkowski, A. J. Wojtowicz, P. Solarz, K. Kamada, and A. Yoshikawa, Opt. Mater. (Amst). **36**, 1665 (2014).

[42] P. Sibczynski, J. Iwanowska-Hanke, M. Moszyński, L. Swiderski, M. Szawłowski, M. Grodzicka, T. Szczęs□niak, K. Kamada, and A. Yoshikawa, Nucl. Instruments Methods Phys. Res. Sect. A Accel. Spectrometers, Detect. Assoc. Equip. **772**, 112 (2015).

[43] M. Nikl, A. Yoshikawa, K. Kamada, K. Nejezchleb, C. R. Stanek, J. A. Mares, and K. Blazek, Prog. Cryst. Growth Charact. Mater. **59**, 47 (2013).

[44] M. Nikl, E. Mihokova, J. Pejchal, A. Vedda, Y. Zorenko, and K. Nejezchleb, Phys. Status Solidi Basic Res. **242**, 119 (2005).

[45] S. K. Yadav, B. P. Uberuaga, M. Nikl, C. Jiang, and C. R. Stanek, Phys. Rev. Appl. **4**, 1 (2015).

[46] M. Nikl, J. Pejchal, E. Mihokova, J. A. Mares, H. Ogino, A. Yoshikawa, T. Fukuda, A. Vedda, and C. D'Ambrosio, Appl. Phys. Lett. **88**, 10 (2006).

[47] R. D. Shannon, Acta Crystallogr. Sect. A **32**, 751 (1976).

[48] M. Fasoli, A. Vedda, M. Nikl, C. Jiang, B. P. Uberuaga, D. A. Andersson, K. J. McClellan, and C. R. Stanek, Phys. Rev. B - Condens. Matter Mater. Phys. **84**, 1 (2011).

[49] C. R. Stanek, C. Jiang, S. K. Yadav, K. J. Mcclellan, B. P. Uberuaga, D. A. Andersson, and M. Nikl, Phys. Status Solidi Basic Res. **250**, 244 (2013).

[50] P. Wu and A. D. Pelton, J. Alloys Compd. **179**, 259 (1992).

[51] M. Raukas, S. A. Basun, W. Van Schaik, W. M. Yen, and U. Happek, Appl. Phys. Lett. **69**, 3300 (1996).

[52] T. Yanagida, K. Kamada, Y. Fujimoto, H. Yagi, and T. Yanagitani, Opt. Mater. (Amst). **35**, (2013).

[53] M. Nikl and A. Yoshikawa, Adv. Opt. Mater. **3**, 463 (2015).

[54] M. T. Lucchini, S. Gundacker, P. Lecoq, A. Benaglia, M. Nikl, K. Kamada, A. Yoshikawa, and E. Auffray, Nucl. Instruments Methods Phys. Res. Sect. A Accel. Spectrometers, Detect. Assoc. Equip. **852**, 1 (2017).

[55] K. Kamada, S. Kurosawa, P. Prusa, M. Nikl, V. V. Kochurikhin, T. Endo, K. Tsutumi, H. Sato, Y. Yokota, K. Sugiyama, and A. Yoshikawa, Opt. Mater. (Amst). **36**, 1942 (2014).

[56] A. Yoshikawa, Y. Fujimoto, A. Yamaji, S. Kurosawa, J. Pejchal, M. Sugiyama, S. Wakahara, Y. Futami, Y. Yokota, K. Kamada, K. Yubuta, T. Shishido, and M. Nikl, Opt. Mater. (Amst). **35**, 1882 (2013).

[57] S. Gundacker, R. M. Turtos, E. Auffray, and P. Lecoq, Nucl.

Instruments Methods Phys. Res. Sect. A Accel. Spectrometers, Detect. Assoc. Equip. **891**, 42 (2018).

[58] S. Gundacker, F. Acerbi, E. Auffray, A. Ferri, A. Gola, M. V. Nemallapudi, G. Paternoster, C. Piemonte, and P. Lecoq, J. Instrum. **11**, (2016).

[59] C. Piemonte, A. Ferri, A. Gola, T. Pro, N. Serra, A. Tarolli, and N. Zorzi, IEEE Trans. Electron Devices **60**, 2567 (2013).

[60] A. V Gektin, A. N. Belsky, and A. N. Vasil'ev, IEEE Trans. Nucl. Sci. **61**, 262 (2014).

[61] O. Sidletskiy, A. Gektin, and A. Belsky, Phys. Status Solidi **211**, 2384 (2014).

[62] M. Korjik and A. Gektin, editors , *Engineering of Scintillation Materials and Radiation Technologies* (Springer International Publishing, 2017).

[63] P. Solarz, M. Głowacki, M. Berkowski, and W. Ryba-Romanowski, J. Alloys Compd. **689**, 359 (2016).

[64] S. Feofilov, A. Kulinkin, K. Ovanesyan, A. Petrosyan, and C. Dujardin, Phys. Chem. Chem. Phys. **16**, 22583 (2014).

[65] N. M. Khaidukov, V. N. Makhov, Q. Zhang, R. Shi, and H. Liang, Dye. Pigment. **142**, 524 (2017).

[66] Y. Wu, G. Ren, D. Ding, F. Yang, and S. Pan, Appl. Phys. Lett. **100**, 021904 (2012).

[67] J. M. Ogieglo, Luminescence and Energy Transfer in Garnet Scintillators, Utrecht University, 2012.

[68] J. A. Mares, M. Nikl, E. Mihokova, A. Beitlerova, A. Vedda, and C. D'Ambrosio, IEEE Trans. Nucl. Sci. **55**, 1142 (2008).

[69] V. Laguta, Y. Zorenko, V. Gorbenko, A. Iskaliyeva, Y. Zagorodniy, O. Sidletskiy, P. Bilski, A. Twardak, and M. Nikl, J. Phys. Chem. C **120**, 24400 (2016).

[70] H. L. Kim, H. J. Kim, E. J. Jang, W. G. Lee, M. K. Ki, H. D. Kim, G. S. Jun, and V. Kochurikhin, J. Ceram. Process. Res. **16**, 124 (2015).

[71] N. J. Cherepy, S. A. Payne, S. J. Asztalos, G. Hull, J. D. Kuntz, T. Niedermayr, S. Pimputkar, J. J. Roberts, R. D. Sanner, T. M. Tillotson, E. Van Loef, C. M. Wilson, K. S. Shah, U. N. Roy, R. Hawrami, A. Burger, L. A. Boatner, W. S. Choong, and W. W. Moses, IEEE Trans. Nucl. Sci. **56**, 873 (2009).

[72] E. V.D. Van Loef, P. Dorenbos, C. W. E. Van Eijk, K. Krämer, and H. U. Güdel, Appl. Phys. Lett. **79**, 1573 (2001).

[73] Z. Yan, T. Shalapska, and E. D. Bourret, J. Cryst. Growth **435**, 42 (2016).

[74] K. Kamada, M. Nikl, S. Kurosawa, A. Beitlerova, A. Nagura, Y. Shoji, J. Pejchal, Y. Ohashi, Y. Yokota, and A. Yoshikawa, Opt. Mater. (Amst). **41**, 63 (2015).

[75] M. A. Spurrier, P. Szupryczynski, K. Yang, A. A. Carey, and C. L. Melcher, IEEE Trans. Nucl. Sci. **55**, 1178 (2008).

[76] S. Blahuta, A. Bessiere, B. Viana, P. Dorenbos, and V. Ouspenski, IEEE Trans. Nucl. Sci. **60**, 3134 (2013).

[77] M. T. Lucchini, V. Babin, P. Bohacek, S. Gundacker, K. Kamada, M. Nikl, A. Petrosyan, A. Yoshikawa, and E. Auffray, Nucl. Instruments Methods Phys. Res. Sect. A Accel. Spectrometers, Detect. Assoc. Equip. **816**, 176 (2016).

[78] C. L. Melcher and J. S. Schweitzer, IEEE Trans. Nucl. Sci. **39**, 502 (1992).

[79] C. L. Melcher, J. Nucl. Med. **41**, 1051 (2000).

[80] D. L. Bailey, D. W. Townsend, P. E. Valk, and M. N. Maisey, *Positron Emission Tomography* (Springer Science & Business Media, 2006).

[81] A. Di Francesco, R. Bugalho, L. Oliveira, L. Pacher, A. Rivetti, M. Rolo, J. C. Silva, R. Silva, and J. Varela, J. Instrum. **11**, (2016).

[82] R. Bugalho, A. Di Francesco, L. Ferramacho, C. Leong, T. Niknejad, L. Oliveira, L. Pacher, M. Rolo, A. Rivetti, M. Silveira, J. C. Silva, R. Silva, S. Tavernier, and J. Varela, Nucl. Instruments Methods Phys. Res. Sect. A Accel. Spectrometers, Detect. Assoc. Equip. **912**, 195 (2018).

[83] H. Suzuki, T. A. Tombrello, C. L. Melcher, and J. S. Schweitzer, Nucl. Inst. Methods Phys. Res. A **320**, 263 (1992).

[84] D. W. Cooke, K. J. McClellan, B. L. Bennett, J. M. Roper, M. T. Whittaker, R. E. Muenchausen, and R. C. Sze, J. Appl. Phys. **88**, 7360 (2000).

[85] I. A. Kamenskikh, V. V Mikhailin, I. H. Munro, D. A. Shaw, P. A. Studenikin, A. N. Vasil, and I. A. Zagumennyi, Radiat. Eff. Defects Solids **135**, 391 (1995).

[86] B. H. T. Chai and Y. Ji, US 6624420 B1 (2003).

[87] A. N. Belsky, E. Auffray, P. Lecoq, C. Dujardin, N. Garnier, H. Canibano, C. Pedrini, and A. G. Petrosyan, IEEE Trans. Nucl. Sci. **48**, 1095 (2001).

[88] B. H. T. Chai, US 7166845 (2007).

[89] K. Yang, C. L. Melcher, P. D. Rack, and L. A. Eriksson, IEEE Trans. Nucl. Sci. **56**, 2960 (2009).

[90] H. E. Rothfuss, C. L. Melcher, L. A. Eriksson, and M. A. Spurrier Koschan, IEEE Trans. Nucl. Sci. **56**, 958 (2009).

[91] M. A. Koschan, C. L. Melcher, L. A. Erikkson, H. E. Rothfuss, L. A. Eriksson, M. A. Koschan, C. L. Melcher, and H. E. Rothfuss, US 8617422 B2 (2013).

[92] M. Koschan, K. Yang, M. Zhuravleva, and C. L. Melcher, J. Cryst. Growth **352**, 133 (2012).

[93] N. C. George, K. A. Denault, and R. Seshadri, Annu. Rev. Mater. Res. **43**, 481 (2013).

[94] W. M. Yen, S. Shionoya, and H. Yamamoto, *Phosphor Handbook* (2007).

[95] S. Koh, W. Van Driel, and G. Q. Zhang, 2011 12th Int. Conf. Therm.

Mech. Multi-Physics Simul. Exp. Microelectron. Microsystems, EuroSimE 2011 3 (2011).

[96] Y. Muramoto, M. Kimura, and S. Nouda, Semicond. Sci. Technol. **29**, (2014).

[97] Y. Kim and S. Kang, Ceram. Int. **39**, S619 (2013).

[98] L. M. Chepyga, E. Hertle, A. Ali, L. Zigan, A. Osvet, C. J. Brabec, and M. Batentschuk, J. Lumin. **197**, 23 (2018).

[99] G. Ramakrishna, R. Naik, H. Nagabhushana, R. B. Basavaraj, S. C. Prashantha, S. C. Sharma, and K. S. Anantharaju, Optik (Stuttg). **127**, 2939 (2016).

[100] Y. Tratsiak, A. Fedorov, G. Dosovitsky, O. Akimova, E. Gordienko, M. Korjik, V. Mechinsky, and E. Trusova, J. Alloys Compd. **735**, 2219 (2018).

[101] M. Bessho and K. Shimizu, Electron. Commun. Japan **95**, 1 (2012).

[102] J. G. Li, X. Li, X. Sun, and T. Ishigaki, J. Phys. Chem. C **112**, 11707 (2008).

[103] J. C. Park, H. K. Moon, D. K. Kim, S. H. Byeon, B. C. Kim, and K. S. Suh, Appl. Phys. Lett. **77**, 2162 (2000).

[104] X. Liu, G. Chen, Y. Chen, and T. Yang, J. Non. Cryst. Solids **476**, 100 (2017).

[105] H. Karimi, Y. Zhang, S. Cui, R. Ma, G. Li, Q. Wang, J. Zhao, X. Qiao, J. Du, and X. Fan, J. Non. Cryst. Solids **406**, 119 (2014).

[106] P. Dorenbos, J. Lumin. **91**, 155 (2000).

[107] M. Y. A. Yagoub, H. C. Swart, R. E. Kroon, and E. Coetsee, Phys. B Condens. Matter **535**, 310 (2018).

[108] M. Borlaf, M. Frankowska, W. W. Kubiak, and T. Graule, Mater. Res. Bull. **100**, 413 (2018).

[109] V. Singh, K. N. Shinde, N. Singh, M. S. Pathak, P. K. Singh, and V. Dubey, Optik (Stuttg). **156**, 677 (2018).

[110] C. Gheorghe, S. Hau, L. Gheorghe, F. Voicu, M. Greculeasa, M. Enculescu, K. N. Belikov, E. Y. Bryleva, and O. V. Gaiduk, J. Alloys Compd. **739**, 806 (2018).

[111] K. Binnemans, Coord. Chem. Rev. **295**, 1 (2015).

[112] N. Narendran, Y. Gu, J. P. Freyssinier, H. Yu, and L. Deng, J. Cryst. Growth **268**, 449 (2004).

[113] R. Marin, G. Sponchia, P. Riello, R. Sulcis, and F. Enrichi, J. Nanoparticle Res. **14**, 1 (2012).

[114] Y. S. Lin, R. S. Liu, and B.-M. Cheng, J. Electrochem. Soc. **152**, J41 (2005).

[115] P. Y. Jia, J. Lin, X. M. Han, and M. Yu, Thin Solid Films **483**, 122 (2005).

[116] H. Yang and Y.-S. Kim, J. Lumin. **128**, 1570 (2008).

[117] N. J. Cherepy, J. D. Kuntz, T. M. Tillotson, D. T. Speaks, S. A. Payne, B. H. T. Chai, Y. Porter-Chapman, and S. E. Derenzo, Nucl. Instruments Methods Phys. Res. Sect. A Accel. Spectrometers, Detect.

Assoc. Equip. **579**, 38 (2007).

[118] K. Kamada, T. Endo, K. Tsutumi, T. Yanagida, Y. Fujimoto, A. Fukabori, A. Yoshikawa, J. Pejchal, and M. Nikl, Cryst. Growth Des. **11**, 4484 (2011).

[119] H. Yang, D.-K. Lee, and Y.-S. Kim, Mater. Chem. Phys. **114**, 665 (2009).

[120] Y. Pan, M. Wu, and Q. Su, J. Phys. Chem. Solids **65**, 845 (2004).

[121] S. Lee, D. S. Jung, J. M. Han, H. Young Koo, and Y. C. Kang, J. Alloys Compd. **477**, 776 (2009).

[122] H. S. Jang, W. B. Im, D. C. Lee, D. Y. Jeon, and S. S. Kim, J. Lumin. **126**, 371 (2007).

[123] Y. X. Pan, W. Wang, G. K. Liu, S. Skanthakumar, R. A. Rosenberg, X. Z. Guo, and K. K. Li, J. Alloys Compd. **488**, 638 (2009).

[124] M. K. Ashurov, Y. Voronko, V. V Osiko, A. A. Sobol, and M. I. Timoshechkin, Phys. Status Solidi **42**, 101 (1977).

[125] F. Euler and J. A. Bruce, Acta Crystallogr. **19**, 971 (1965).

[126] C. R. Stanek, K. J. McClellan, M. R. Levy, C. Milanese, and R. W. Grimes, Nucl. Instruments Methods Phys. Res. Sect. A Accel. Spectrometers, Detect. Assoc. Equip. **579**, 27 (2007).

[127] F. C. Hawthorne, J. Solid State Chem. **37**, 157 (1981).

[128] Y. Zhang, L. Li, X. Zhang, and Q. Xi, J. Rare Earths **26**, 446 (2008).

[129] X. Wang and Y. Wang, J. Phys. Chem. C **119**, 16208 (2015).

[130] M. Minsky, Scanning **10**, 128 (1988).

[131] M. Kavatsyuk, D. Bremer, V. Dormenev, P. Drexler, T. Eissner, W. Erni, E. Guliyev, T. Hennino, B. Krusche, B. Lewandowski, H. L??hner, M. Moritz, R. W. Novotny, K. Peters, J. Pouthas, P. Rosier, M. Steinacher, G. Tambave, and A. Wilms, Nucl. Instruments Methods Phys. Res. Sect. A **648**, 77 (2011).

[132] M. Nikl, P. Bohacek, E. Mihokova, M. Kobayashi, M. Ishii, Y. Usuki, V. Babin, A. Stolovich, S. Zazubovich, and M. Bacci, J. Lumin. **87**, 1136 (2000).

[133] E. Auffray, O. Buganov, a Fedorov, M. Korjik, P. Lecoq, G. Tamulaitis, S. Tikhomirov, and a Vasil’ev, J. Phys. Conf. Ser. **587**, 012056 (2015).

[134] J.-C. Diels and W. Rudolph, *Ultrashort Laser Pulse Phenomena* (Elsevier, 2006).

[135] S. Chernov, D. Millers, L. Grigorjeva, and V. Pankratov, Radiat. Meas. **33**, 659 (2001).

[136] E. Auffray, O. Buganov, A. Fedorov, M. Korjik, V. Mechinsky, A. Tikhomirov, A. Vasil’ev, and P. Lecoq, J. Instrum. **9**, P07017 (2014).

[137] Y. Zhang, N. a W. Holzwarth, and R. T. Williams, Phys. Rev. B Condens. Matter **57**, 12738 (1998).

[138] M. Lucchini, T. Medvedeva, K. Pauwels, C. Tully, A. Heering, C. Dujardin, K. Lebbou, P. Lecoq, and E. Auffray, J. Instrum. **8**, P10017 (2013).

[139] K. Pauwels, C. Dujardin, S. Gundacker, K. Lebbou, P. Lecoq, M. Lucchini, F. Moretti, a G. Petrosyan, X. Xu, and E. Auffray, J. Instrum. **8**, P09019 (2013).

[140] D. Ding, B. Liu, Y. Wu, J. Yang, G. Ren, and J. Chen, J. Lumin. **154**, 260 (2014).

[141] C. L. Melcher, S. Friedrich, S. P. Cramer, M. A. Spurrier, P. Szupryczynski, and R. Nutt, IEEE Trans. Nucl. Sci. **52**, 1809 (2005).

[142] L. Ning, L. Lin, L. Li, C. Wu, C. K. Duan, Y. Zhang, and L. Seijo, J. Mater. Chem. **22**, 13723 (2012).

[143] M. V. Nemallapudi, S. Gundacker, P. Lecoq, E. Auffray, A. Ferri, A. Gola, and C. Piemonte, Phys. Med. Biol. **60**, 4635 (2015).

[144] E. Pratiwi, K. Kamada, S. Yamamoto, M. N. Ullah, J.-Y. Yeom, A. Yoshikawa, and J. H. Park, Nucl. Instruments Methods Phys. Res. Sect. A Accel. Spectrometers, Detect. Assoc. Equip. **911**, 115 (2018).

[145] S. Gundacker, R. M. Turtos, E. Auffray, M. Paganoni, and P. Lecoq, Phys. Med. Biol. **64**, 055012 (2019).

[146] S. Blahuta, A. Bessière, B. Viana, V. Ouspenski, E. Mattmann, J. Lejay, and D. Gourier, Materials (Basel). **4**, 1224 (2011).

[147] E. Auffray, A. Barysevich, A. Fedorov, M. Korjik, M. Koschan, M. Lucchini, V. Mechinski, C. L. Melcher, and A. Voitovich, Nucl. Instruments Methods Phys. Res. Sect. A Accel. Spectrometers, Detect. Assoc. Equip. **721**, 76 (2013).

[148] Y. Wu, M. Tian, J. Peng, M. Koschan, I. Greeley, C. Foster, and C. L. Melcher, Phys. Status Solidi - Rapid Res. Lett. **13**, 1 (2019).

[149] M. V Korzhik and W. P. Trower, Appl. Phys. Lett. **66**, 2327 (1995).

[150] K. Kamada, T. Endo, K. Tsutumi, T. Yanagida, Y. Fujimoto, A. Fukabori, A. Yoshikawa, J. Pejchal, and M. Nikl, Cryst. Growth Des. **11**, 4484 (2011).

[151] K. Kamada, T. Yanagida, J. Pejchal, M. Nikl, T. Endo, K. Tsutsumi, Y. Fujimoto, A. Fukabori, and A. Yoshikawa, IEEE Trans. Nucl. Sci. **59**, 2112 (2012).

[152] J. Ueda, K. Aishima, and S. Tanabe, Opt. Mater. (Amst). **35**, 1952 (2013).

[153] B. Zhang, J. He, Z. Jia, Y. Li, S. Liu, Z. Wang, R. Wang, X. Liu, and X. Tao, Appl. Phys. Express **6**, 15 (2013).

[154] D. L. Dexter, J. Chem. Phys. **21**, 836 (1953).

[155] K. Brylew, W. Drozdowski, A. J. Wojtowicz, K. Kamada, and A. Yoshikawa, J. Lumin. **154**, 452 (2014).

[156] M. Kitaura, A. Sato, K. Kamada, A. Ohnishi, and M. Sasaki, J. Appl. Phys. **115**, 083517 (2014).

[157] E. Mihóková, K. Vávrů, K. Kamada, V. Babin, A. Yoshikawa, and M. Nikl, Radiat. Meas. **56**, 98 (2013).

[158] D. M. Kondratiev, M. V. Korzhik, A. A. Fyodorov, and V. B. Pavlenko, Phys. Status Solidi **197**, 251 (1996).

[159] V. V. Laguta, M. Nikl, and S. Zazubovich, Opt. Mater. (Amst). **36**,

1636 (2014).

[160] P. Dorenbos, J. Lumin. **134**, 310 (2013).

[161] N. J. Cherepy, Z. M. Seeley, S. A. Payne, P. R. Beck, O. B. Drury, S. P. O'Neal, K. M. Figueroa, S. Hunter, L. Ahle, P. A. Thelin, T. Stefanik, and J. Kindem, IEEE Trans. Nucl. Sci. **60**, 2330 (2012).

[162] I. Muliuoliene, S. Mathur, D. Jasaitis, H. Shen, V. Sivakov, R. Rapalaviciute, A. Beganskiene, and A. Kareiva, Opt. Mater. (Amst). **22**, 241 (2003).

[163] Y. Qiang, Y. Yu, G. Chen, and J. Fang, Ceram. Int. **42**, 767 (2016).

[164] J. Xu, S. Tanabe, A. D. Sontakke, and J. Ueda, Appl. Phys. Lett. **107**, 081903 (2015).

[165] J. Ueda, K. Kuroishi, and S. Tanabe, Appl. Phys. Express **7**, 062201 (2014).

[166] J. Ueda, K. Kuroishi, and S. Tanabe, Appl. Phys. Lett. **104**, 101904 (2014).

[167] P. Dorenbos, ECS J. Solid State Sci. Technol. **2**, R3001 (2013).

[168] Y. Wu, F. Meng, Q. Li, M. Koschan, and C. L. Melcher, Phys. Rev. Appl. **2**, 1 (2014).

[169] A. Ferri, A. Gola, N. Serra, A. Tarolli, N. Zorzi, and C. Piemonte, Phys. Med. Biol. **59**, 869 (2014).

[170] M. Nikl, V. Babin, J. Pejchal, V. V. Laguta, M. Buryi, J. A. Mares, K. Kamada, S. Kurosawa, A. Yoshikawa, D. Panek, T. Parkman, P. Bruza, K. Mann, M. Müller, and M. Muller, IEEE Trans. Nucl. Sci. **63**, 433 (2016).

[171] A. Nakatsuka, A. Yoshiasa, and T. Yamanaka, Acta Crystallogr. Sect. B Struct. Sci. **55**, 266 (1999).

[172] F. Meng, M. Koschan, Y. Wu, C. L. Melcher, and P. Cohen, Nucl. Instruments Methods Phys. Res. Sect. A Accel. Spectrometers, Detect. Assoc. Equip. **797**, 138 (2015).

[173] K. Mamoru, K. Kei, K. Shunsuke, A. Junpei, O. Akimasa, Y. Akihiro, and H. Kazuhiko, Appl. Phys. Express **9**, 072602 (2016).

[174] E. Mihóková, K. Vávrů, K. Kamada, V. Babin, A. Yoshikawa, M. Nikl, K. Vávr, K. Kamada, V. Babin, A. Yoshikawa, and M. Nikl, Radiat. Meas. **56**, 98 (2013).

[175] V. Alenkov, O. Buzanov, G. Dosovitskiy, V. Egorychev, A. Fedorov, A. Golutvin, Y. Guz, R. Jacobsson, M. Korjik, D. Kozlov, V. Mechinsky, A. Schopper, A. Semennikov, P. Shatalov, and E. Shmanin, Nucl. Instruments Methods Phys. Res. Sect. A Accel. Spectrometers, Detect. Assoc. Equip. **916**, 226 (2019).

[176] Y. Shao, Phys. Med. Biol. **52**, 1103 (2007).

[177] M. Korjik and E. Auffray, IEEE Trans. Nucl. Sci. **63**, 552 (2016).

[178] E. Auffray, A. Fedorov, V. Dormenev, J. Houžvička, M. Korjik, M. T. Lucchini, V. Mechinsky, and S. Ochesanu, Nucl. Instruments Methods Phys. Res. Sect. A Accel. Spectrometers, Detect. Assoc. Equip. **856**, 7 (2017).

[179] R. Autrata, P. Schauer, J. Kvapil, and J. Kvapil, 10 (1978).

[180] J. Kvapil, J. Kvapil, B. Manek, and B. Perner, J. Cryst. Growth **52**, 542 (1981).

[181] E. Auffray, A. Fedorov, M. Korjik, M. Lucchini, V. Mechinski, N. Naumenko, and A. Voitovich, IEEE Trans. Nucl. Sci. **61**, 495 (2014).

[182] N. E. Shchegoleva, P. D. Sarkisov, L. A. Orlova, and N. V. Popovich, Glas. Ceram. (English Transl. Steklo i Keramika) **69**, 117 (2012).

[183] M. Sitarz and M. Szumera, J. OfThermal Anal. Calorim. **91**, 255 (2008).

[184] H. M. H. Fadlalla and C. C. Tang, Mater. Chem. Phys. **114**, 99 (2009).

[185] C.-Y. Shen, K. Li, Q. Hou, H.-J. Feng, and X.-Y. Dong, IEEE Photonics Technol. Lett. **22**, 884 (2010).

[186] G. P. Shevchenko, E. V. Tret'yak, S. K. Rakhmanov, and G. E. Malashkevich, Russ. J. Phys. Chem. A **87**, 1397 (2013).

[187] Z. Yang, X. Li, Y. Yang, and X. Li, J. Lumin. **122–123**, 707 (2007).

[188] K. Zhang, W. Hu, Y. Wu, and H. Liu, Ceram. Int. **35**, 719 (2009).

[189] K. Zhang, H. Liu, Y. Wu, and W. Hu, J. Mater. Sci. **42**, 9200 (2007).

[190] N. Zhang, D. Wang, L. Li, Y. Meng, X. Zhang, and N. Ming, J. Rare Earths **24**, 294 (2006).

[191] S. A. Samoylenko, E. V. Tret'yak, G. P. Shevchenko, S. E. Kichanov, D. P. Kozlenko, G. E. Malashkevich, A. P. Stupak, and B. N. Savenko, J. Appl. Spectrosc. **81**, 1048 (2015).

AUGUSTAS VAITKEVIČIUS| CV

Birthdate	1991/01/27
Email	Augustas.vaitkevicius@ff.vu.lt; Augustas.vaitkevicius@gmail.com

EDUCATION

2015–2019	PhD studies in Physics Vilnius University, Institute of Photonics and Nanotechnology
2013–2015	Master‘s degree in Materials Technology Vilnius University, Department of Physics Studies: Optoelectronic Material and Technology Thesis: Optical Properties of Rare Earth Doped Oxide Scintillators and Phosphors. Supervised by Prof. habil. dr. Gintautas Tamulaitis
2009–2013	Bachelor’s degree in Physics Vilnius University, Department of Physics Studies: Applied Physics Thesis: Influence of Trench Defects on Photoluminescence in InGaN Quantum Wells. Supervised by Prof. habil. dr. Gintautas Tamulaitis.

RESEARCH / WORK EXPERIENCE

	Vilnius University, Department of Semiconductor Physics and Institute of Applied Research, Institute of Photonics and Nanotechnology
2016 – present	Junior research fellow
2015–2016	Engineer
2011–2014	Laboratory technician

Paper P1

Application of two-photon absorption in PWO scintillator for fast timing of interaction with ionizing radiation

E. Auffray, O. Buganov, M. Korjik, A. Fedorov, S. Nargelas, G. Tamulaitis, S. Tikhomirov, **A. Vaitkevičius**

Nucl. Instruments Methods Phys. Res. Sect. A Accel. Spectrometers, Detect. Assoc. Equip. 804 (2015) 194–200.

doi:10.1016/j.nima.2015.09.017.

Reprinted with permission from Elsevier Science & Technology Journals.

Nuclear Instruments and Methods in Physics Research A 804 (2015) 194–200

Contents lists available at ScienceDirect

Nuclear Instruments and Methods in Physics Research A

journal homepage: www.elsevier.com/locate/nima

Application of two-photon absorption in PWO scintillator for fast timing of interaction with ionizing radiation

E. Auffray [a], O. Buganov [b], M. Korjik [c], A. Fedorov [c], S. Nargelas [d], G. Tamulaitis [d], S. Tikhomirov [b], A. Vaitkevičius [d,*]

[a] CERN, Geneva, Switzerland
[b] Stepanov Institute of Physics, Minsk, Belarus
[c] Research Institute for Nuclear Problems, Belarus State University, 11 Bobruiskaya, 220030 Minsk, Belarus
[d] Semiconductor Physics Department and Institute of Applied Research, Vilnius University, Saulėtekio 9-III, LT-10222 Vilnius, Lithuania

ARTICLE INFO

Article history:
Received 2 April 2015
Received in revised form
20 August 2015
Accepted 8 September 2015
Available online 16 September 2015

Keywords:
Radiation detectors
Scintillators
Lead tungstate
Two-photon absorption

ABSTRACT

This work was aimed at searching for fast phenomena in scintillators in sub-10-ps range, a benchmark timing for the time response of radiation detectors in particle colliders. The pump-and-probe optical absorption technique with a tunable-wavelength parametric oscillator as the pump and a continuous-spectrum source as the probe beam was used to study lead tungstate $PbWO_4$ (PWO) single crystals. It is shown that the rise time of the probe pulse absorption induced by the pump pulse is shorter than the pump pulse width of 200 fs. The approximately linear dependence of the probe absorption on the pump pulse energy density evidences that the induced absorption is caused by two-photon absorption involving one probe and one pump photon. We demonstrate that the intensity of the induced absorption at certain wavelengths is influenced by gamma irradiation, provided that an appropriate light polarization is selected. The application of the irradiation-sensitive nonlinearity for fast timing in radiation detectors is discussed.

1. Introduction

Currently, the development of the experiments at future high energy particle colliders is the main stream in experimental high energy physics. Since the interaction length, where the particle bunches collide, is small (e.g., ~30 cm in the Large Hadron Collider at CERN [1]), timing becomes the key issue in the detection of rare events. A good timing measurement requires detectors with a high time resolution. Unfortunately, the time resolution of the detectors currently used in high energy physics experiments is limited to 50–70 ps that is definitely insufficient for applications in high luminosity accelerators. The time resolution of the majority of modern detectors is limited by the time response of the signal generated after the relaxation of carriers produced during the interaction. For example, in scintillation materials, the emission occurs after the relaxation of hot carriers lasting approximately 1 ps and the consecutive transfer of the carriers to emission centers, which takes 100 ps and more [2]. The Cherenkov radiation in inorganic medium occurs as a result of its polarization by a fast charged particle within 10^{-12} s; however, the small yield of this radiation and the large dispersion of the optical path lengths for the light collected in the volume of the detectors do not allow for a better time resolution than that in scintillation detectors.

The target 10 ps timing is beyond the capabilities of the conventional scintillator detecting systems based on the excitation relaxation and transfer to emitting centers. This publication presents the results of an attempt to search for qualitatively novel approaches to ensure the time marks in the detection. The final design of the detecting system will depend on the optimal methods and materials for this purpose. As the first step, we propose the two-photon absorption as a phenomenon prospective for fast timing and demonstrate that the nonlinear response in PWO is influenced by gamma irradiation.

The scintillator interaction with ionizing radiation generates an instantaneous elastic impact via local displacement of the lattice atoms. First of all, the medium might be elastically polarized by the ionization inducing the generation of holes in the inner atom shells and hot electrons [3]. The electrons and holes form dipoles localized in close vicinity to the particle track. Thus, the lattice polarization occurs along the entire track.

Another process of lattice distortion is the impact displacement of atoms from their regular sites in the lattice which happens under the intense flux of electrons or X-rays as described in [4]. The impact displacement of matrix ions occurs in the case when

---

* Corresponding author.
E-mail address: augustas.vaitkevicius@ff.vu.lt (A. Vaitkevičius).

http://dx.doi.org/10.1016/j.nima.2015.09.017
0168-9002/

the energy ($\leq$ 100 eV) passed to an ion is insufficient to knock it into an intersite position in the host matrix.

Finally, the generation of an ensemble of free carriers in the crystal is followed by transient phenomena related with the transformation of the ensemble of hot carriers into the system of thermalized carriers. It has been suggested using the transient phenomena (luminescence and absorption) in transparent dielectric materials to obtain a time tagging of the interaction of ionizing radiation with scintillator material [5]. The hot intraband luminescence resulting in emission of photons with energy below the band gap can be detected and used as the time mark. The major disadvantage of such time mark is a small yield of the hot intraband luminescence. In particular, experiments in CeF_3 excited by short UV laser pulses showed that the pulse energy of several microjoules is necessary to observe the absorption from the lowest excited state of Ce^{3+} ions [6]. This corresponds to an instantaneous energy release of 10–20 TeV per cm^3. Actually, this energy deposit could be expected in the detectors in the experiments at future colliders like FCC [7].

We suppose that the most promising process among the fast phenomena discussed above is the elastic polarization due to the charge redistribution when the electrons are displaced and holes generated. The formation of a hole in the shell of an atom in the crystal lattice naturally results in the transformation of the atom environment due to charge compensation. Since these atom displacements are produced via interaction with phonons, the lattice distortion occurs on the time scale comparable with the period of lattice vibrations, i.e., within 10^{-14}–10^{-12} s. This local distortion in the lattice results in the redistribution of the electron density in the conduction band in the close vicinity of the hole. The relaxation of the elastic polarization might proceed via different radiative and non-radiative channels. The key feature of the elastic polarization is its short time response, which makes it promising to use as an optically detectable time mark.

In this paper, we investigated the fast optical response in lead tungstate ($PbWO_4$, PWO) scintillator by using a pump and probe technique with sub-picosecond time resolution. The influences of wavelength, pump intensity and light polarization were under study.

The effect of elastic polarization should, probably, be observed in many crystals; however, the strongest effect might be expected in compounds with the bottom of the conduction band formed by nd orbitals of the lattice cations. According to the crystal field theory, these orbitals are most sensitive to distortions of the crystal field in the vicinity of emitting centers. To enhance the effect, self-activated crystals with lattice cations acting as emission centers need to be selected. From this point of view, good candidates could be crystals like molybdates and tungstates, where the lattice-forming atom groups MeO_4^{2-} (Me=W, Mo) act also as luminescence centers [2]. The undistorted group MeO_4^{2-} has the point symmetry T_d; therefore, any lattice distortions in the vicinity of MeO_4^{2-} will decrease its symmetry and, consequently, will impose an additional splitting of d states and a change in the electron density at the bottom of the conduction band. This should result in the transformation of the band-to-band absorption spectrum. The direct observation of the changes in the absorption spectrum is hindered by the strong band-to-band absorption. Thus, we used the pump and probe technique to detect it.

For our study, we selected lead tungstate crystal, because it is already well studied and extensively used in scintillation detectors [8,3]. The two-photon absorption of femtosecond laser pulses in PWO single crystal has recently been observed in our previous work [9]. The band gap of PWO at room temperature is 4.33 eV. Thus, a defect-free PWO crystal has no optical absorption in the visible region. However, two-photon absorption at the total energy of the two absorbed photons close to 6 eV and above results in the excitation to the electronic states near the bottom of the conduction band. The bottom of the conduction band in PWO is formed by d orbitals of tungsten ions, and the density of states has two bands peaking at 5 and 6.5 eV [10]. According to the crystal field theory, the lowest peak corresponds to the triplet states $^3T_1$ and $^3T_2$, while the upper one is formed with a strong contribution of singlet states $^1T_1$ and $^1T_2$ [11].

The density of electronic states in the conduction band was simulated in PWO crystal with various defects [10]. The generation of nonequilibrium electrons and holes by ionizing radiation might also be treated as instantaneous creation of electron- or hole-type defects with simultaneous formation of elastic polarization. Therefore, the wavelength dependence of the two-photon absorption due to the optical transitions from the ground state formed by the upper $^1A_1$ state in the valence band to the conduction band should be correlated with the change in the electron density of states in the conduction band, while the ionizing radiation should change the wavelength dependence of such absorption.

2. Experimental

The changes in the density of the electronic states in the conduction band were studied using the ultrafast optical pump and probe technique. Two-photon absorption involving one pump and one probe photon has been exploited. The pump and probe laser pulses were focused on the sample surface at a small angle (see more detailed description of the technique in Ref. [6]). The pump-induced changes in the probe absorption have been recorded. The change in the sample absorption in the units of the thousandths of optical density (mOD) was estimated as the decimal logarithm of the measured ratio between the intensities of the transmitted probe beam propagating with and without pump beam:

$$\text{Differential absorption [mOD]} = \log\left(\frac{I_{\text{with pump}}}{I_{\text{without pump}}}\right) \times 1000.$$

The time evolution of the changes is revealed by changing the delay between pump and probe beams. The nonlinear absorption takes place only in the sample volume where the pump and probe beams propagate through the crystal spatially overlap.

Two pump and probe setups were used in our study.

In the first setup, 140 fs long pulses of the second harmonic of $Al_2O_3{:}Ti^{3+}$ laser radiation were used as a pump with the wavelength fixed at 395 nm (3.15 eV). A white continuum in the range from 400 to 1100 nm was used for probe. The continuum was generated in a water cuvette by a split fraction of the fundamental laser radiation at 790 nm. The initial spectrum of the continuum had the shape of two exponentially decreasing wings on both sides of the laser line at 790 nm. The approximately white spectrum of the continuum was achieved using colored absorption filters. The setup is described in detail elsewhere [6,12].

The first setup was used to study the nonlinear absorption under ionizing radiation. Samples in a shape of $10 \times 10 \times 1$ mm^3 plates were cut from high structural quality PWO single crystals meeting the CMS specifications [2,8] intentionally doped by lanthanum and yttrium at the total concentration of 100 ppm. The face edges of the plate were oriented along the crystallographic axes *b* and *c*, while the pump and probe beams propagated at small angles to the axis *a* (i.e., nearly perpendicularly to the plate surface). The light in the pump beam was polarized along the axis *b*. The polarization of the probe either coincided or was at 75^o from the polarization of the pump beam. A shielded ^{57}Co source of ionizing radiation (122 keV, 2 mCi) was mounted at a distance of 1 cm from the plate surface. The plate size and the experiment configuration enabled absorption of 90% of the gamma radiation energy in the geometry close to $1/4\pi$. The measurements have been carried out at room temperature with the irradiation source on and off.

The second setup was used for pump and probe experiments at different pump photon energies: 394 nm (3.15 eV), 360 nm (3.44 eV), 346 nm (3.58 eV), and 654 nm (1.9 eV). The nonlinear absorption was studied along the crystallographic axis a in 1 cm thick samples. The light in the probe beam was polarized either along the axis b or c. The system was based on a femtosecond Yb: KGW laser producing 200 fs pulses at 1030 nm with a repetition rate of 30 kHz. A small part of the fundamental radiation was passed through an opto-mechanical delay line, frequency doubled (515 nm) and focused by a 10 cm focal length lens onto a 5 mm thick sapphire plate to generate a broad spectrum (supercontinuum) probe beam. The range between 350 and 530 nm was used for probing in our experiments. The major part of the fundamental laser beam was used to pump an optical parametric amplifier (OPA) continuously tunable in the range from 630 to 2600 nm. The OPA radiation was frequency doubled and used as a tunable-wavelength pump source. The intensity of the pump beam was attenuated by a neutral density filter wheel. The probe beam, tunably delayed in respect to the pump pulse, was dispersed by an imaging spectrograph and detected using a CCD camera. The spectral resolution of the system was 0.7 nm/pix. Since the continuum spectrum was not flat, the spectrum of the nonlinear absorption has been digitally normalized to obtain the response to a white spectrum probe.

3. Results and discussion

3.1. Fast nonlinear optical response due to two-photon absorption

The change in the optical density for the probe beam induced by the pump at the wavelength of 394 nm is presented in Fig. 1a. The shape of the response is basically similar to that reported in [9]. It has a short rise time, a decay with characteristic time constant of few picoseconds, and a faster decay afterwards. The fast decrease of the absorption at the rear part of the response could be explained by the separation in space of the pump and probe beams, which are impinging the sample surface at slightly different angles. The overlap volume in a thick sample depends on the wavelengths of the two beams due to the light velocity dispersion. Thus, the delay between the leading front and the rear part of the nonlinear absorption depends on the pump and probe wavelengths due to the light group velocity dispersion.

The leading edge of the differential transmittance is displayed in Fig. 1b for several wavelengths of the probe beam. The figure proves that the time response on the leading edge is limited by the laser pulse shape rather than by the material properties. Thus, the processes responsible for the nonlinear absorption happen on a femtosecond time scale.

Fig. 2 presents the differential optical absorption versus the energy density of the pump pulse at 394 nm for different wavelengths of the probe pulse delayed by 1 ps. The data for Fig. 2 were obtained in the experiment configuration with the electric field of the probing light parallel to the c axis ($E\|c$). Quite similar dependences have been observed in the $E\|b$ configuration (not shown in this paper). The observed dependences of the differential absorption of the probe signal with the pump pulse energy density are approximately linear. This is the experimental evidence that the absorption is caused by a two-photon absorption process involving one pump and one probe photon [13].

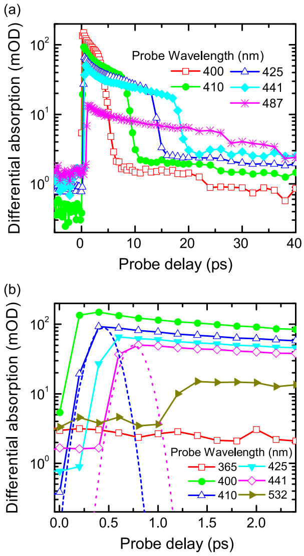

Fig. 1. Differential absorption (a) and the initial part of it (b) in PWO scintillation crystal at 394 nm pump and different probe wavelengths (indicated). The pump pulse shapes are depicted by dashed curves.

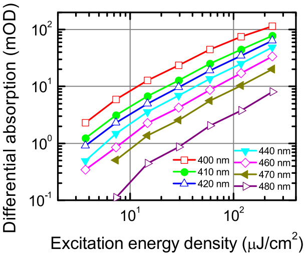

Fig. 2. Differential absorption versus energy density of pump pulse at 393 nm for different wavelengths (indicated) of the probe pulse delayed by 1 ps.

3.2. Influence of gamma irradiation on the nonlinear absorption

Fig. 3 presents the spectra of the differential absorption for different delays between pump and probe within the first 400 fs. Standard deviations of the data on the plots were estimated from spectra recorded at −1 ps probe pulse delay and found to be 1.9 mOD at 500 nm and 3 mOD at 700 nm wavelengths.

For the pump light polarization along the crystal axis b, the spectrum has a band peaking at ~3.13 eV (400 nm). Taking into account the pump photon energy of 3.15 eV (395 nm), the energy of the optical transition in this two-photon absorption is equal to 6.28 eV. This value is in agreement with our previous result observed in a crystallographically unoriented PWO crystal [6] and matches well with the energy of the second peak in the spectrum of the density of states calculated in [10]. When the pump light polarization is rotated

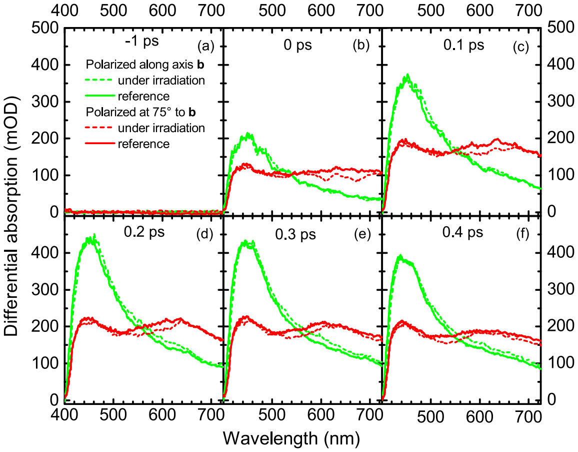

Fig. 3. Spectra of differential optical absorption induced by 500 mJ/cm^2 pump at 395 nm polarized along the crystal axis *b* and polarized at 75° to the crystal axis *b* (indicated) under (dashed lines) and without (solid lines) gamma irradiation. Delays of probe pulse are indicated.

away from the axis *b*, an additional band peaking at 2 eV (620 nm) appears simultaneously with the first band in the differential absorption spectrum. The peak position corresponds to the total transition energy of 5.15 eV and matches well with the low-energy band in the spectrum of the density of states [10].

The spectra in Fig. 3 were measured under and without gamma irradiation. No significant influence of the gamma irradiation was observed in the polarization configuration *Eb*, when only one band peaking around 450 nm in the differential absorption spectrum was observed. Meanwhile, certain damping of the low energy band peaking in the vicinity of 620 nm was observed under the influence of the irradiation in the second polarization configuration (see Fig. 3c and d). This change in the optical absorption could be used for the fast timing in radiation detectors.

We also observed a small change in the front shape of the response under irradiation; however, the change in the pulse shape is too weak to be exploited in a real detector.

Since the amplitudes of the electric field in the light wave of the probe and even pump (10^3 V/cm) are considerably lower than the typical crystal field (10^7–10^8 V/cm), the pump and probe experiments do not induce significant distortion to the crystal symmetry including the structural polyhedrons. However, the situation considerably changes under ionizing radiation. The electrons generated from the inner atom shells move to a distance of up to several tens of microns during their thermalization. Meanwhile, the holes relax within distances comparable to the interatomic distance. As a result, an excessive positive charge is created along the track of the gamma or the particle in ionizing radiation. The electric dipoles form a low-symmetry component of the electric field, which acts in addition to the usual crystal field. As discussed above, this results in a redistribution of the electronic density. For example, the electric field of the dipole created by the hole and electron near the first coordination sphere of hole is proportional to the distance r as r^{-3} and reaches 10^5–10^7 V/cm at the distance of ~5 nm. A more accurate estimation of the electric field in the tracks requires application of the Ewald mathematical apparatus [14] and is outside the scope of the current publication.

Since the bottom of the conduction band in PWO is formed by polyhedrons WO_4^{2-}, we can estimate the fraction of distorted polyhedrons in the crystal under irradiation used in our experiments. In our experimental conditions, not less than 3×10^{10} electron–hole pairs per second are generated by the gamma irradiation. The average track of the hot electron in PWO occupies a volume with approximately 0.2 μm in diameter and 40 μm in length, thus, $\sim 0.4\times10^{-12}$ cm^3 in volume. Accordingly, the total rate of the track volume formation is 1.2×10^{-2} cm^3 per second. Since the density of WO_4^{2-} polyhedrons in the PWO single crystal is $\sim 10^{22}$ cm^{-3}, the density of the polyhedrons within the volume of the irradiation-formed tracks equals approximately 10^{20} cm^{-3}. We should take into account that the lifetime of the elastic deformation is limited by the relaxation of free carriers. In PWO, the relaxation occurs via radiative recombination with a time constant of ~10 ns. Therefore, the non-equilibrium density of the polyhedrons distorted by irradiation is below 10^{12} cm^{-3}. This density seems to be too low for reliable detection. Thus, the crystal volume with polyhedrons distorted by elastic polarization supposedly extends outside the track volume. The dependence of the experimentally observed effect on the light polarization in respect to the crystallographic axes is an indication that the distortion of the low-symmetry structural polyhedrons is more effective along certain directions in the crystal matrix.

3.3. Nonlinear absorption as a function of pump photon energy

Depending on the combination of the wavelengths of the pump and the probe pulses, the absorption is caused by either two-photon or two-step absorption in the sample. In the latter case, the formation of a color center at the first absorption step might be expected. The major difference between these two absorption modes is that the two-photon absorption is an instantaneous process and takes place only if pump and probe pulses overlap in time inside the sample, while the time response in the two-step absorption depends on the population of real electronic states. The absorption from the state occupied after the absorption of the pump photon depends on the intra-state relaxation and the rate of

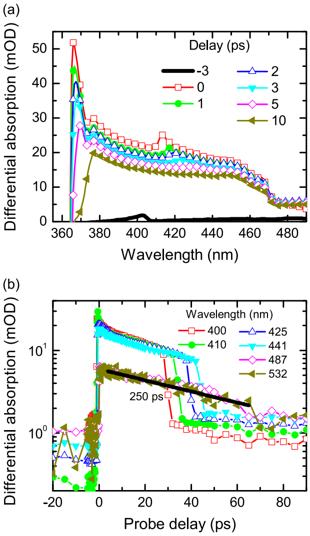

Fig. 4. Spectra (a) at different delays (indicated) and decay kinetics (b) at different wavelengths (indicated) of the differential absorption induced by pump at 360 nm (3.44 eV).

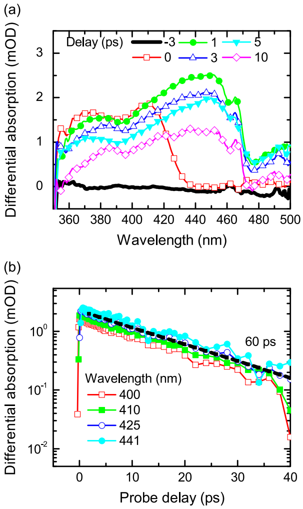

Fig. 5. Spectra (a) at different delays (indicated) and decay kinetics (b) at different wavelengths (indicated) of the differential absorption induced by pump at 346 nm (3.58 eV) in in $E\parallel c$ configuration.

the color center recombination. It is well known [8] that point defects, particularly the oxygen vacancies (V$_O$), form a variety of shallow electron centers in PbWO$_4$ crystal with the thermal activation energy E_{TA} in the range from 0.029 to 0.7 eV. Two centers, WO$_4^{3-}$ polaronic center (E_{TA}=0.05 eV) and WO$_4^{3-}$+RE (RE=Y, La), were detected using electron paramagnetic resonance (EPR) at the temperatures of liquid nitrogen or lower. Thus, they should relax very fast at room temperature. Some other centers were detected only by means of the thermo-stimulated luminescence (TSL). They have no paramagnetic states, so it was supposed that they are stable after capturing two electrons and forming centers F (V$_O$+2e$^-$). Consequently, the centers F$^+$(V$_O$+e$^-$) in the host matrix do not become stable after capturing an electron [8].

As discussed above, the differential absorption induced by pump at 394 nm (3.15 eV) is caused by two-photon absorption. Meanwhile, the excitation involving electron transition to a real state close to the band gap was observed when the pump wavelength was shifted to 346 nm.

Fig. 4 presents the spectra at different delays and the decay kinetics at different wavelengths of the differential absorption induced by pump at 360 nm (3.44 eV). The experiments were performed in $E\parallel c$ configuration for the light polarization. Fig. 4a depicts only the region of the high energy band, since the spectral range in the second setup used in these experiments was limited.

The decay kinetics of the induced absorption (Fig. 4b) is characterized by a fast increase, then a nearly exponential decay with the same rate for all probe wavelengths, a fast decrease due to separation of pump and probe in real space, and, finally, a slow decay with the time constant considerably exceeding the time scale in our experiments. The excitation of PWO at 360 nm delivers electrons to the deepest electron-type center in PWO, a Frenkel type defect (FTD), which is an oxygen vacancy V$_O$ with a neighboring oxygen ion in the interstitial position. Capturing only one electron at this center does not form a stable color center [2]. Thus, the observed fast kinetics with 250 ps time constant for the induced probe absorption decay (see Fig. 4) is probably determined by subsidence of FTDs charged with one electron.

Moreover, the induced absorption is still observed even after the long delays (exceeding tens of picoseconds), when the pump and probe beams do not overlap in space and the probe absorption is influenced just by the carriers excited by probe photons. This behavior is in agreement with the transient absorption observed in PWO under excitation with nanosecond laser pulses [15].

As shown in Fig. 5a, the differential absorption is considerably weaker and its spectrum changes substantially when the pump wavelength is shifted to 346 nm (3.58 eV). In contrast to the spectra induced by the photons of smaller energy, no band corresponding to two-photon absorption is observed. Instead, two broad, strongly overlapping bands peaking at 380 and 410 nm appear at zero delay. At delays above 1 ps, a short wavelength wing of a new broad band (with the peak obviously beyond the spectral range of our experiment) is observed. The new band probably evidences that, in addition to FTD, V$_O$-based centers are populated with electrons generated by pump. Similarly as for FTDs, capturing of one electron does not ensure the stability of these centers. As a result, the induced absorption decreases with time delay. The kinetics presented in Fig. 5b show that the decay is exponential with a time constant of 60 ps. The decay is caused by the electron relaxation to the bottom of the state or by trapping of the electrons to deeper defect-related states.

It is worth noting that the light polarization in respect to the crystallographic axes is practically unimportant when color centers are involved in the process. Fig. 6 presents the spectra and kinetics of the differential absorption induced by pump in $E\parallel b$ configuration. Comparison with the corresponding results obtained in $E\parallel c$ configuration (see Fig. 5) shows that the spectra are quite similar and the decay kinetic is characterized by time constants of the same order of magnitude (60 and 25 ps) in both configurations.

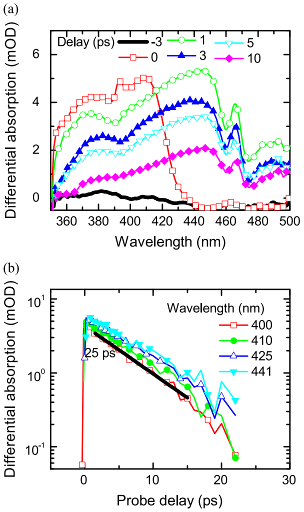

Fig. 6. Spectra (a) at different delays (indicated) and decay kinetics (b) at different wavelengths (indicated) of the differential absorption induced by pump at 346 nm (3.58 eV) in *E*ll*b* configuration.

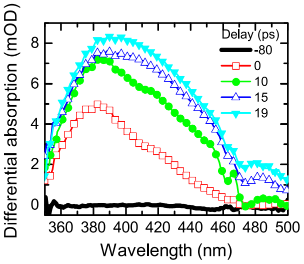

Fig. 7. Spectra at different delays (indicated) of the differential absorption induced by pump at 654 nm (1.9 eV).

The spectrum of the differential absorption at pump photon energy of 1.9 eV (654 nm) is presented in Fig. 7. The spectrum has two overlapping bands peaking at 380 and 410 nm and is similar to that obtained for UV pump at 3.58 eV (346 nm). Probably, the same centers are populated by absorption of a single 3.58 eV photon and by two-photon absorption of 1.9 eV photons.

The dependence of the spectral and time properties of the differential absorption on pump wavelength discussed above demonstrates that the selection of the proper wavelength to observe the nonlinear response from PWO crystals without population of defect-related states is of importance for implementation of this material in fast radiation detection systems.

3.4. Applications in detection of ionizing radiation

The effects observed in our study might be exploited for detection of ionizing radiation in parallel with the detection of scintillation signal in the same material. The two-photon absorption can be used as a time tag to detect the initial moment of the interaction of ionizing radiation with the detector material, while the scintillation signal provides information on the absorbed energy. In the case of PWO, the wavelength of 500 nm corresponding to the total energy of two photons of 5 eV would be optimal.

The light propagating along the scintillation crystal and reflecting from the front face of the crystal could be used to observe the two-photon absorption. This configuration would also reduce the problems of the spatial overlap of the beams. Particularly, we consider this approach to be suitable for application in inorganic scintillation fibers in the detecting modules of SPOCAL or dual readout types [16,17]. The detection could be technically achieved by using a set of sub-picosecond pulses, e.g. 100 pulses with the total set duration of 0.1–1 ns. The set is injected into the crystal or fiber slightly before the time when the interaction products of the collision are expected to reach the detector modules. The laser pulses should be injected not in all fibers of the detecting modules but just to the specialized fibers in the module which are used for timing. The initial moment of the interaction between the collision products and the detector module is detected by comparing the set of pulses reflected back out of the crystal and a reference set. Thus, introducing the set of laser pulses with short spacing in the detecting module establishes a short-period time scale. The time resolution would be equal to the time span between the pulses in the set.

The radiation-induced changes either in spectral or time properties of the optical response could be exploited in the detectors. Further study is necessary to make the right choice ensuring a higher detection accuracy. The results obtained in our work are in favor of the exploitation of the change in the amplitude of the response at certain wavelengths.

The influence of ionizing radiation on the parameters of the two-photon absorption, which we observe in PWO crystal, should be observed also in other crystals and, probably, amorphous materials. The figures of merit for selection of the prospective materials should be a high point symmetry of the polyhedrons of metal ions forming the bottom of the conduction band, a high optical transparency at the wavelength used in the detection, and a high density of d-type electronic states in the lower part of the conduction band. The materials suitable for fabrication in a fiber shape have some additional advantages. Moreover, the experience accumulated on the propagation of ultrashort laser pulses in waveguides could be exploited in the development of such ultrafast detectors.

Acknowledgment

This work was carried out in the frame of the Crystal Clear Collaboration and the COST Action FAST (TD1401). Authors appreciate the fruitful discussions of the results and valuable remarks of Prof. A. N. Vasiliev. The study at Vilnius University was funded from the European Community's Social Foundation under Grant Agreement VP1-3.1-ŠMM-08-K-01-004/KS-120000-1756.

References

[1] L. Evans, P. Bryant (Eds.), The CERN Large Hadron Collider: Accelerator and Experiments, Vol. 1–2, CERN, Geneva, 2009.
[2] P. Lecoq, A. Annenkov, A. Gektin, M. Korzhik, C. Pedrini, Inorganic Scintillators for Detector Systems, Springer, Berlin, 2006.
[3] G.M. Sessler (Ed.), Electrets, Springer-Verlag, Berlin, 1980.
[4] V.I. Baryshnikov, T.A. Kolesnikova, Physics Solid State 47 (2005) 1776, http://dx.doi.org/10.1134/1.2087734.

[5] P. Lecoq, M. Korzhik, A. Vasiliev, IEEE Transactions on Nuclear Science NS61 (2014) 229, http://dx.doi.org/10.1109/TNS.2013.2282232.

[6] E. Auffray, O. Buganov, A. Fedorov, M. Korjik, V. Mechinsky, A. Tikhomirov, A. Vasil'ev, P. Lecoq, Journal of Instrumentation 9 (2014) P07017, http://dx.doi.org/10.1088/1748-0221/9/07/P07017.

[7] W. Barletta, M. Battaglia, M. Klute, M. Mangano, S. Prestemon, L. Rossi, P. Skands, Nuclear Instruments and Methods in Physics Research A 764 (2014) 352, http://dx.doi.org/10.1016/j.nima.2014.07.010.

[8] A.A. Annenkov, M. Korzhik, P. Lecoq, Nuclear Instruments and Methods in Physics Research A 490 (2002) 30, http://dx.doi.org/10.1016/S0168-9002(02)00916-6.

[9] E. Auffray, O. Buganov, A. Fedorov, M. Korjik, P. Lecoq, G. Tamulaitis, S. Tikhomirov, A. Vasil'ev, Journal of Physics: Conference Series 587 (2015) 012056, http://dx.doi.org/10.1088/1742-6596/587/1/012056.

[10] Y. Zhang, N.A.W. Holzwarth, R.T. Williams, Physical Review B 57 (1998) 12738, http://dx.doi.org/10.1103/PhysRevB.57.12738.

[11] R. Kebabcioglu, A. Müller, Chemical Physics Letters 8 (1970) 59 0.1016/0009-2614(71)80575-4.

[12] V.I. Stsiapura, A.A. Maskevich, S.A. Tikhomirov, O.V. Buganov, The Journal of Physical Chemistry A 114 (2010) 8345, http://dx.doi.org/10.1021/jp105186z.

[13] J.-C. Diels, W. Rudolph, Ultrashort Laser Pulse Phenomena, Elsevier, USA, 2006.

[14] (a) S.W. de Leeuw, J.W. Perram, E.R. Smith, Proceedings of the Royal Society of London A 373 (1980) 27;
(b) S.W. de Leeuw, J.W. Perram, E.R. Smith, Proceedings of the Royal Society of London A 373 (1980) 57.

[15] D. Millers, S. Chernov, L. Grigorieva et al., Luminescence and transient absorption of doped PWO scintillator crystals, in: V.V. Mikhailin (Ed.), Proceedings of the Fifth International Conference on Inorganic Scintillators and their Applications, SCINT99, Moscow University, Moscow, 2000, pp. 613–618.

[16] N. Luccini, T. Medvedeva, K. Pauwels, C. Tully, A. Heering, C. Dujardin, K. Lebbou, P. Lecoq, E. Auffray, Journal of Instrumentation 8 (2013) 10017, http://dx.doi.org/10.1088/1748-0221/8/10/P10017.

[17] K. Pauwels, C. Dujardin, S. Gundacker, L. Lebbou, P. Lecoq, M. Lucchini, F. Moretti, A.G. Petrosian, X. Xu, A. Auffray, Journal of Instrumentation 9 (2013) 09019, http://dx.doi.org/10.1088/1748-0221/8/109/P09019.

Paper P2

Distribution of luminescent centers in Ce^{3+}-ion doped amorphous stoichiometric glass $BaO–2SiO_2$ and dedicated glass ceramics

M.V. Korjik, **A. Vaitkevičius**, D. Dobrovolskas, E.V. Tret'yak, E. Trusova, G. Tamulaitis

Opt. Mater. (Amst). 47 (2015) 129–134.

doi:10.1016/j.optmat.2015.07.014.

Reprinted with permission from Elsevier Science & Technology Journals.

Optical Materials 47 (2015) 129–134

Contents lists available at ScienceDirect

Optical Materials

journal homepage: www.elsevier.com/locate/optmat

Distribution of luminescent centers in Ce^{3+}-ion doped amorphous stoichiometric glass $BaO–2SiO_2$ and dedicated glass ceramics

M.V. Korjik [a,*], A. Vaitkevicius [b], D. Dobrovolskas [b], E.V. Tret'yak [c], E. Trusova [d], G. Tamulaitis [b]

[a] Research Institute for Nuclear Problems of the BSU, 220030 Minsk, Belarus
[b] Semiconductor Physics Department and Institute of Applied Research, Vilnius University, Sauletekio 9-III, LT-10222 Vilnius, Lithuania
[c] Research Institute for Physical Chemical Problems of the BSU, 220080 Minsk, Belarus
[d] Belarusian State Technological University, 13a Sverdlova Str., 220006 Minsk, Belarus

ARTICLE INFO

Article history:
Received 25 May 2015
Received in revised form 6 July 2015
Accepted 7 July 2015
Available online 12 July 2015

Keywords:
Glasses
Glass–ceramics
Luminescence

ABSTRACT

We investigated the influence of crystallization conditions on the luminescent properties of Ce^{3+}-ions doped stoichiometric glass $BaO–2SiO_2$ at the different stages of its transformation from amorphous phase to glass ceramics. The samples were investigated by confocal luminescence spectroscopy. It was found that the luminescent properties of the cerium-doped glass and the glassceramics composite consisting of $BaSi_2O_5$ crystallites and residual glass are quite similar, though the luminescence band in the composites are slightly redshifted and narrower.

1. Introduction

There is a strong demand for development of new inorganic luminescent materials which nowadays shows tremendous progress through nano-engineering of the materials. Particularly, the last decade evidenced an impressive progress in the lighting technology based on the light emitting diodes (LED). The construction of the white LEDs is rather simple: the blue LED is encapsulated in a transparent material containing phosphor material YAG:Ce emitting yellow Photo Luminescence (PL). The combination of the two spectral components results in the spectrum accepted as a white light. However, to improve the color rendering of the white LED emission, more phosphors are necessary to be used however, not many phosphors are suitable to operate at blue light excitation. The shift of the excitation to the near UV (360–390 nm) increases the amount of the compounds and activating ions suitable for creation new phosphors for the LED based lighting.

Among variety of inorganic materials silicates are seems to be prospective to construct new phosphors. They find numerous application as luminescent materials in a crystalline phase. The rare earth (RE) containing single-crystalline oxy-ortho RE_2SiO_5 and pirochlor $RE_2Si_2O_7$ silicates doped with Ce are good scintillation materials [1]. Most of the silicate crystalline materials while doped with Ce, possess blue luminescence band at near UV excitation, what is a bottleneck that hinders their application for lighting.

In a glass form, silicates also possess several limitations, especially lower thermal conductivity and difficulty to stabilize activating ions in a needed valent state. For instance, pure SiO_2 does not allow an incorporation of RE-ions with reasonable concentration due to crystal-chemical reasons. Modification of the glass net with different additives, especially La, allows doping however, stabilization of needed valent state still remains the problem. Nevertheless, similar to single crystalline materials, some complicated silicate glasses show bright near UV or blue luminescence. For instance, lithium silicate glass is widely used for making of neutron sensitive scintillation sensors [2].

Glass ceramic materials possess several advantages combining the properties of crystals and glass, especially the high thermal conductivity. Their production is an industrial domain which promotes future development of the materials since sixties [3]. However, at the development of luminescent glass ceramics materials several matters still have to be answered. One of them is a transformation of the luminescent properties at the material crystallization. Disordering is replaced by ordering in a crystallized part of the material, so crystalline field, distribution of the local charge compensation in the vicinity of activator as well, are changed. For instance, recent study of europium doped barium disilicate glass system showed that luminescent properties of the material are strongly affected by crystallization [4,5]. Eu^{2+}-ions luminescence, which was not detected in a mother glass, became

---

* Corresponding author.
E-mail address: Mikhail.Korjik@cern.ch (M.V. Korjik).

http://dx.doi.org/10.1016/j.optmat.2015.07.014
0925-3467/

dominating when glass material was crystallized by thermal treatment. It was suggested that Eu^{3+}-ions delivering the red luminescence are preferably localized in the amorphous glass, while the Eu^{2+}-ions emitting in the blue–green region become dominating after partial crystallization of the glass. The results published in [6] showed that the significant amount of Eu^{3+}-ions is always present in fluorozirconate based glass ceramics reducing the performance of these materials as both scintillators and storage phosphors. Besides Eu luminescence, strong UV luminescent band was observed in barium disilicate phosphore at the doping with Pb ions [7]. However, Ce^{3+}-ions luminescence is not studied well in this material.

In our study we considered an effect of crystallization on luminescent properties of Ce^{3+}-ions in barium disilicate glass system. The disilicate of barium is unique by its capability to be manufactured in several states: amorphous at the stoichiometric mixture $BaO–2SiO_2$ produced by the ordinary glass production technique, as glass–ceramics [8], and in a crystalline form. The $BaO–2SiO_2$ system exhibits homogeneous nucleation [9], and the size of the crystallites can be controlled by the glass annealing temperature.

Similar to europium, cerium is also heterovalent ion and stabilized in inorganic compounds in three- to four-valent states [1]. Ce^{3+}-ions possesses bright interconfiguration *d–f* luminescence in many wide forbidden zone compounds. Ce^{4+}-ions does not show intrinsic luminescence properties however, it provides a wide unstructured absorption in UV range due to ligand–metal charge transfer transitions [10]. Large concentration of Ce^{4+}-ions in the material also provides a brownish color of the samples. To study the sensitivity of the resulting luminescence spectrum to the ratio between the crystallized and residual amorphous parts of the glass, we investigated the luminescence properties of cerium doped glass $BaO–2SiO_2$ and glass ceramics obtained from this glass at different temperature and duration of thermal treatment.

2. Materials and methods

2.1. Materials

Powders of $BaCO_3$ and SiO_2 with 99.99% purity were used. Powder of $Ce_2Si_2O_7$ were used as a source of Ce^{3+} ions. All the chemicals were produced by NeoChem (Russia).

2.2. $BaO–2SiO_2$ glass obtaining

Glass $BaO–2SiO_2$ was obtained by melting of mixture of 7.22 g. $BaCO_3$, 4.40 g. SiO_2 and 0.10 g. $Ce_2Si_2O_7$ (1 wt.% over the glass stoichiometry) in a aluminum oxide ceramic crucible in gas furnance (FALORNI) at 1450 °C for 2 h. To avoid crystallization during cooling and reducing the mechanical stresses in the samples, the glass was casted on a non-preheated steel block and subsequently treated in a muffle furnace preheated to 700 °C for 2 h. The obtained glass block was transparent and colorless, indicate about preservation of cerium ions oxidation level. The glass was cutted into plates with thickness of 1 mm, that then were annealed on air at 850 °C for 30 min and 900 °C for 15 min (crystallization of $BaSi_2O_5$ monoclinic symmetry occurs at ~880 °C [8]). The heating rate of the furnace was 50 °C/min. Transparent and colorless glass at first after thermal treatment at 850 °C became opaque and after heat treatment at 900 °C – lactescence. After heat treatment, all samples remained colorless.

2.3. Characterization

To observe an effect of crystallization on luminescent properties of the samples we investigated parameters of luminescent band at macro- and micro-level of the material. It allowed to observe a possible influence of samples structure ordering on the PL band. The PL mapping was performed using the microscope *WITec Alpha* 300 S in the confocal mode. An objective with the numerical aperture NA = 0.6 was used ensuring the lateral spatial resolution of ~250 nm and axial resolution of ~1.6 μm. The microscope was coupled via optical fiber with a spectrometer followed by a thermoelectrically cooled CCD camera. A violet laser diode (ALPHALAS) emitting at 405 nm was used in spatially-resolved photoluminescence spectroscopy experiments.

Mother glass and annealed samples were milled before infrared absorption (IR) spectra measurements. The IR spectra of the powdered samples were collected in 400–4000 cm^{-1} wave number ranges using the Thermo Nicolet Avatar FTIR-330 spectrometer at room temperature by diffuse reflectance method.

3. Results

The glass $BaO–2SiO_2$ doped with Ce^{3+} ions demonstrates bright interconfiguration *d–f* luminescence in a blue–green spectral range at room temperature. The excitation spectra include a strong band with maximum in the vicinity of 360–370 nm. Excitation band long wavelength shoulder is expanded up to 410 nm. At excitation near 360 nm luminescence maximum is near 460 nm and the quantum yield of approximately 0.3 at excitation by 360 nm. At the excitation near 400 nm (Fig. 1) luminescence maximum is shifted toward 490 nm. It indicates that Ce^{3+} ions occupies in the glass a variety of positions with slightly different surrounding.

The spectrally-integrated luminescence spectra of the samples under study are presented in Fig. 2. In spatially resolved experiments, we mapped areas of two sizes, 40 × 40 μm^2 and 90 × 90 μm^2, both with resolution of 200 × 200 points. The shape of the luminescence band and the center of the mass of the luminescence band to detect the possible formation of new bands or the transformations of the luminescence band were studied. The band width is a good indicator to observe the variations in emission properties due to the changes in the surrounding of the emitting ion that can be expected at the transition from amorphous to crystalline phase. We paid an especial attention to the changes near the macroscopic defects like bubbles or granules. The agglomeration of crystallites in the vicinity of the defects could be expected. This effect could cause the most substantial differences between luminescent properties in amorphous and crystalline phases. The luminescence parameters are summarized in Table 1.

The PL intensity in the sample annealed for 15 min at 900 °C is approximately 40% weaker than that of the reference sample. In

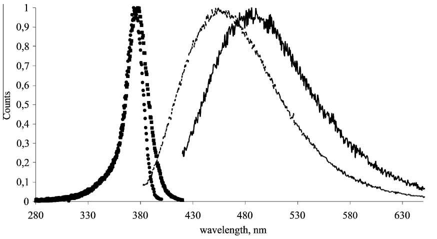

Fig. 1. Spectra of luminescence at excitation 370 nm (dashed line) and 400 nm (full line) and luminescence excitation at registration 450 nm (squares) and 500 nm (circles) of mother glass sample measured at room temperature.

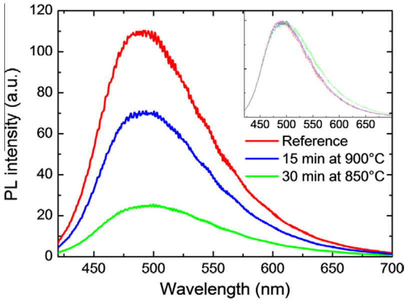

Fig. 2. Photoluminescence (excitation at 405 nm) spectra of untreated reference Ce^{3+}-doped glass (red curve) and annealed glasses (conditions indicated) at room temperature. Inset shows normalized spectra. (For interpretation of the references to color in this figure legend, the reader is referred to the web version of this article.)

comparison, PL intensity of the sample annealed for 30 min at 850 °C is approximately by a factor of 5 weaker than that of the reference sample. Probably, the different decrease in PL intensity is caused by decreased optical transmittance of samples due to partial crystallization of the samples. The PL band in the sample annealed for 30 min at 850 °C is redshifted by ~10 nm in respect to its position in the reference sample.

The spatial distribution of PL parameters is in general quite homogeneous. However, the glass contains at least two kinds of specific regions with distinctly different PL properties. The images presented in Fig. 3 encompass one of the typical features in the quite homogeneous background – an oval-shaped area with different PL properties. The area is 8–10 μm in diameter. In the PL intensity distribution (Fig. 3A) it is noticeable as a non-uniform loop of lower PL intensity. In the PL peak position (Fig. 3B) and spectral center of mass (Fig. 3B) mapping, a redshift of the PL band in this area is evident. The distinct area with lower PL intensity also exhibits a narrower band width (see the full width at half maximum in Fig. 3D).

Mappings of the PL parameters distributions perpendicularly to the sample surface, across the oval shaped area, are presented in Fig. 4. These measurements reveal a column-like structure extending ~30 μm into the sample.

Mappings of the PL parameters in the vicinity of the second typical distinct area are presented in Fig. 5. The area has the shape of a spherical bubble, roughly 27 μm in diameter.The region consists of a core, 15 μm in diameter, and a 6 μm thick shell. The PL intensity (Fig. 5A) in the core is smaller than that in the background by a factor of 5.7. The PL intensity in the shell changes gradually. The PL band peak position (Fig. 5B) is redshifted, and the redshift is stronger in the shell. The red shift is more pronounced in the spectral center of mass mapping image (Fig. 5C). The spatial distribution of FWHM is presented in Fig. 5D). A considerable narrowing of the PL band is evidenced, especially in the core region.

Table 1
Average values and standard deviations of PL parameters of the samples under study in the bulk of the glass 150 μm below the surface.

	Untreated mother glass	Annealed at 900 °C for 15 min	Annealed at 850 °C for 30 min
Peak position, nm	490(6)	496(9)	500(9)
Spectral center of mass, nm	517(1)	522(2)	524(2)
FWHM, nm	111(3)	92(9)	95(7)

After annealing, the sample remains predominantly homogeneous. The only influence of annealing on the spatial distribution of PL parameters was formation of regions of irregular shape where the PL intensity was lower than in the bulk of the sample by a factor of 1.1. This modification was observed for the samples subjected to annealing both at 850 °C and 900 °C.

The irregularly shaped regions are visible in the distributions of all parameters of the sample annealed at 850 °C (see Fig. 6). The inhomogeneity was checked by calculating Pearsons correlation coefficients (R) for the pairs of PL parameters obtained by spatially-resolved PL spectroscopy. The PL intensity and the blue shift of the PL spectral center of mass (see Fig. 6A and C) is significant ($R = 0.4$). No significant correlation ($R < 0.3$) has been observed for other pairs of PL parameters in this sample.

Images of mapping the PL parameters in the sample annealed at 900 °C are presented in Fig. 7. Strong correlation ($R = 0.6$) between PL intensity (Fig. 7A) and FWHM of the PL band (Fig. 7D) is evident. No significant correlation ($R < 0.3$) has been observed for other pairs of PL parameters.

4. Discussions

To justify an origin of minor Ce^{3+} luminescence band changes due to annealing we measured infrared (IR) transmittance spectra of mother glass and annealed samples. Fig. 8 shows IR spectra measured in the range 2000–400 cm^{-1}. Several characteristic bands dedicated to silicate systems were measured [11,12]. It is seen that crystallization of the mother glass does not affect characteristic peaks in the vicinity of 430 and 900 cm^{-1}. However, absorption band peaked at 755 cm^{-1} shows decreasing of intensity whereas band intensity near 634 cm^{-1} increases. It is in a good agreement with the fact that an amount of ring structures is decreased in partially crystallized glass. The band at 635 cm^{-1} shows growth due to the increased role of interaction through bridging oxygen with creation of junctions of type Si–O–Si between groups of the type ≡Si–O and $-SiO_3$. Thus, we supposed that crystallization in glass obtained from stoichiometric composition does not change dramatically vibration modes. Due to this reason no sufficient change of the configuration potential of the Ce^{3+} emitting level is expected.

The parameters of observed luminescence bands measured in the mother glass and treated samples are summarized in Table 1. To avoid any influence off the sample surface, the parameters were calculated using the PL spectra measured in the glass bulk 150 μm below the surface. They show that annealing of the glass imposes a red shift of the PL band. For both peak position and center of mass the red shift is larger in the sample annealed at 850 °C for 30 min. than that in the sample annealed at a higher temperature (900 °C) but for a shorter period (15 min). The standard deviation of both parameters increases after annealing from 6 nm to 9 nm for PL peak position and from 1 nm to 2 nm for spectral center of mass. The average PL band width decreases after annealing, and the standard deviation increases.

The increase of the standard deviation for all PL parameters is an indication of decreased homogeneity in the annealed samples, possibly, due to their partial crystallization.The decrease by 20% of the luminescence band width due to annealing can be interpreted by ordering of the crystalline field around the activator ions in the crystallites. Meanwhile, the relatively small spectral shift of the luminescence band peak position and spectral center of mass

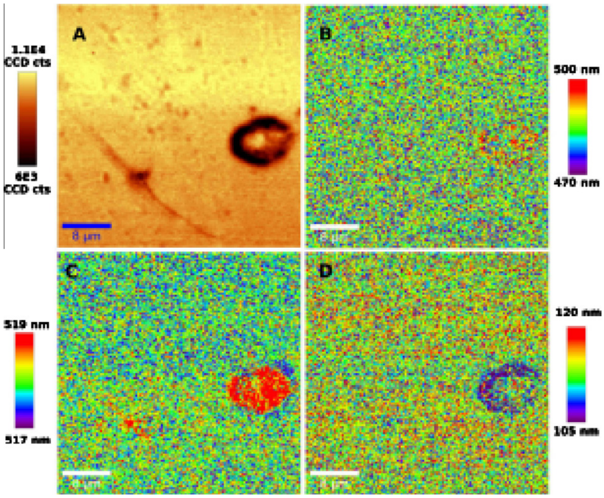

Fig. 3. Spatial distribution of spectrally integrated photoluminescence intensity (upper left, A), band peak position (upper right, B), spectral center of mass (lower left, C), and band FWHM (lower right, D) on the surface of untreated mother glass. A small scratch and pothole are visible.

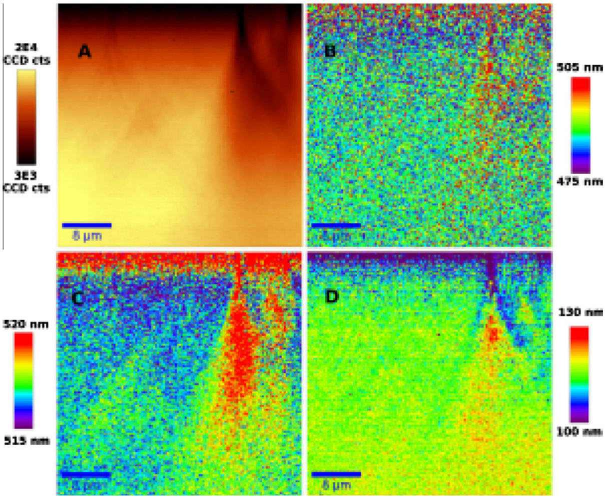

Fig. 4. Mappings of spectrally integrated PL intensity (upper left, A), peak position (upper left, B), spectral center of mass (lower left, C), and FWHM of the PL band (lower right, D) in the untreated mother glass with gnarls.

evidence that the glass transformation to crystalline phase proceeds without changing the Ce^{3+} ion positions in the matrix. Thus, the ordering of the structure during crystallization of $BaO–2SiO_2$ system occurs due to the change of the anion–cation distances without strong rearrangement of the net. We consider this effect to be an evident advantage of stoichiometric

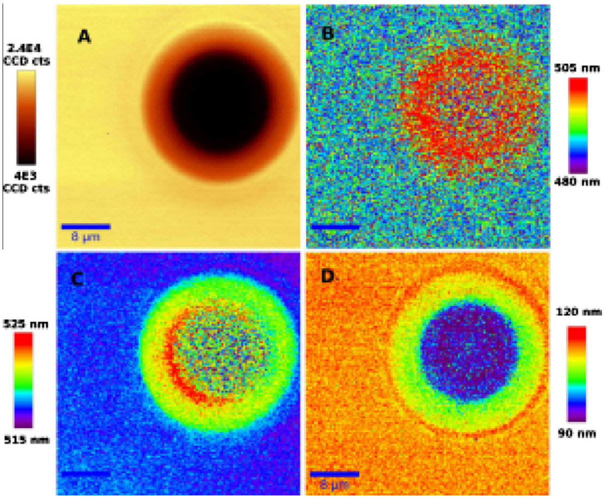

Fig. 5. Mapping images of spectrally integrated PL intensity (upper, left), peak position (upper, left), spectral center of mass (lower, left) and FWHM (lower, right) of the PL band in the untreated mother glass with a bubble. The planar scan crosses the bubble.

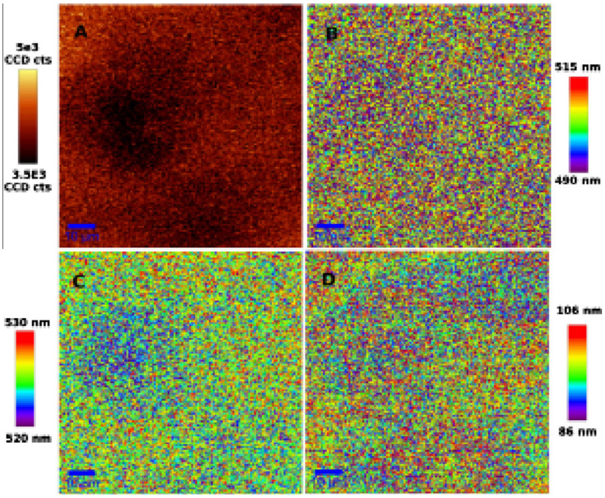

Fig. 6. Mapping image of spectrally integrated photoluminescence intensity (upper left, A), band peak position (upper left, B), spectral center of mass (lower left, C), and FWHM (lower right, D) in the sample annealed at 850 °C.

compositions. The spectral features of not annealed glass presented in Figs. 2–4 show that some nucleation of around defects occurs already in the mother glass. The luminescence band in the vicinity of the defects is redshifted and the FWHM is smaller. However, these changes are relatively small and do not make any significant influence on the average values.

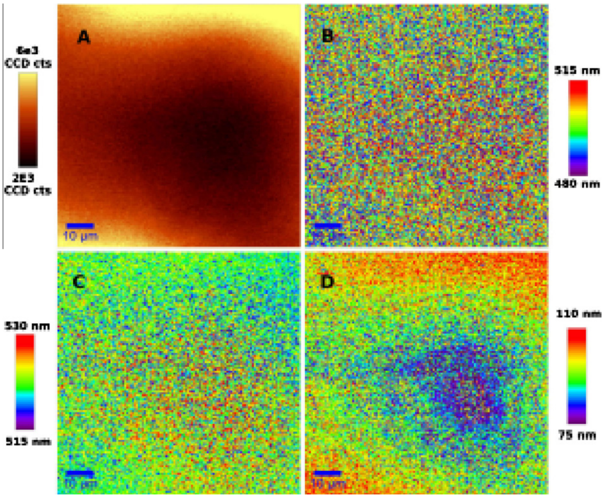

Fig. 7. Mapping image of spectrally integrated photoluminescence intensity (upper left, A), band peak position (upper left, B), spectral center of mass (lower left, C), and FWHM (lower right, D) in the sample annealed at 900 °C.

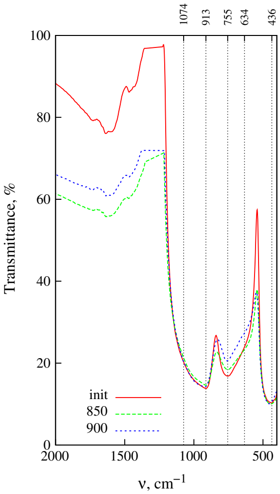

Fig. 8. IR spectra of mother glass (init) and glasses annealed at 850 °C (850) and 900 °C (900) for 30 and 15 min respectively.

5. Conclusion

In conclusion, crystallization of BaO–2SiO$_2$ system doped with Ce^{3+} ions results only in small changes of the luminescence parameters. Observed feature is favorable for application of this glass system as phosphor material with low sensitivity of spectral parameters to fabrication conditions resulting in various glass/to ceramics ratios in the final product. That the cerium-doped BaO–2SiO$_2$ glasses might be suitable to produce high luminosity phosphors under excitation in UV to violet spectral region.

References

[1] P. Lecoq, A. Annenkov, A. Gektin, M. Korzhik, C. Pedrini, Inorganic Scintillators for Detector Systems: Physical Principles and Crystal Engineering, Particle Acceleration and Detection, Springer, Berlin Heidelberg, 2006.

[2] A. Spowart, Neutron scintillating glasses: Part 1: Activation by external charged particles and thermal neutrons, Nucl. Instrum. Methods 135 (3) (1976) 441–453, http://dx.doi.org/10.1016/0029-554X(76)90057-4.

[3] P.W. McMillan, Glass–Ceramics, Academic Press, London; New York, 1964.

[4] J.H. Park, J.S. Kim, J.T. Kim, Luminescent properties of BaSi$_2$ O $_5$:Eu $^{2+}$ phosphor film fabricated by spin-coating of Ba–Eu precursor on SiO$_2$ glass, J. Opt. Soc. Korea 18 (1) (2014) 45–49, http://dx.doi.org/10.3807/JOSK.2014.18.1.045.

[5] A. Herrmann, A. Simon, C. Rssel, Preparation and luminescence properties of Eu^{2+}-doped BaSi$_2$O$_5$ glass–ceramics, J. Lumin. 132 (1) (2012) 215–219, http://dx.doi.org/10.1016/j.jlumin.2011.08.024.

[6] B. Henke, C. Palick, P. Keil, J.A. Johnson, S. Schweizer, Eu oxidation state in fluorozirconate-based glass ceramics, J. Appl. Phys. 106 (11) (2009) 113501–113506, http://dx.doi.org/10.1063/1.3259390.

[7] D.S. Thakare, S.K. Omanwar, P.L. Muthal, S.M. Dhopte, V.K. Kondawar, S.V. Moharil, UV-emitting phosphors: synthesis, photoluminescence and applications, Phys. Status Solidi (a) 201 (3) (2004) 574–581, http://dx.doi.org/10.1002/pssa.200306720.

[8] W. Holand, G. Beall, Glass Ceramic Technology, Wiley, 2012.

[9] Y. Takahashi, H. Masai, T. Fujiwara, Nucleation tendency and crystallizing phase in silicate glasses: a structural aspect, Appl. Phys. Lett. 95 (7) (2009), http://dx.doi.org/10.1063/1.3206931. 071904-3.

[10] D. Pauwels, N. Le Masson, B. Viana, A. Kahn-Harari, E. van Loef, P. Dorenbos, C. van Eijk, A novel inorganic scintillator: Lu$_2$Si$_2$O$_7$:Ce^{3+} (LPS), IEEE Trans. Nucl. Sci. 47 (6) (2000) 1787–1790, http://dx.doi.org/10.1109/23.914446.

[11] K. Rao, Structural Chemistry of Glasses, Elsevier Science Ltd, Oxford, 2002. <http://www.sciencedirect.com/science/book/9780080439587>.

[12] P. McMillan, Structural studies of silicate glasses and melts applications and limitations of raman spectroscopy, Am. Mineral. 69 (7–8) (1984) 622–644.

Paper P3

Free carrier absorption in self-activated $PbWO_4$ and Ce-doped $Y_3(Al_{0.25}Ga_{0.75})_3O_{12}$ and $Gd_3Al_2Ga_3O_{12}$ garnet scintillators

E. Auffray, M. Korjik, M.T. Lucchini, S. Nargelas, O. Sidletskiy, G. Tamulaitis, Y. Tratsiak, **A. Vaitkevičius**

Opt. Mater. (Amst). 58 (2016) 461–465.

doi:10.1016/j.optmat.2016.06.040.

Optical Materials 58 (2016) 461–465

Contents lists available at ScienceDirect

Optical Materials

journal homepage: www.elsevier.com/locate/optmat

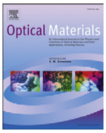

Free carrier absorption in self-activated $PbWO_4$ and Ce-doped $Y_3(Al_{0.25}Ga_{0.75})_3O_{12}$ and $Gd_3Al_2Ga_3O_{12}$ garnet scintillators

E. Auffray [a], M. Korjik [b], M.T. Lucchini [a], S. Nargelas [c], O. Sidletskiy [d], G. Tamulaitis [c], Y. Tratsiak [e, *], A. Vaitkevičius [c]

[a] CERN, Geneva, Switzerland
[b] Research Institute for Nuclear Problems, Belarusian State University, Bobruiskaya Str. 11, Minsk, Belarus
[c] Semiconductor Physics Department and Institute of Applied Research, Vilnius University, Universiteto Str. 3, Vilnius, Lithuania
[d] Institute for Scintillation Materials, Lenin Av. 60, Kharkov, Ukraine
[e] Research Institute for Chemical Problems, Belarusian State University, Leningradskaya Str. 14, Minsk, Belarus

A R T I C L E   I N F O

Article history:
Received 15 May 2016
Received in revised form
20 June 2016
Accepted 21 June 2016
Available online 28 June 2016

Keywords:
Scintillators
Free carrier absorption
Lead tungstate
Ceriumdoped
Garnets

A B S T R A C T

Nonequilibrium carrier dynamics in the scintillators prospective for fast timing in high energy physics and medical imaging applications was studied. The time-resolved free carrier absorption investigation was carried out to study the dynamics of nonequilibrium carriers in wide-band-gap scintillation materials: self-activated led tungstate ($PbWO_4$, PWO) ant two garnet crystals, GAGG:Ce and YAGG:Ce. It was shown that free electrons appear in the conduction band of PWO and YAGG:Ce crystals within a sub-picosecond time scale, while the free holes in GAGG:Ce appear due to delocalization from Gd^{3+} ground states to the valence band within a few picoseconds after short-pulse excitation. The influence of Gd ions on the nonequilibrium carrier dynamics is discussed on the base of comparison the results of the free carrier absorption in GAGG:Ce containing gadolinium and in YAGG without Gd in the host lattice.

1. Introduction

The high-energy physics experiments in sight and advanced medical imaging devices based on positron emission tomography (PET), positron annihilation lifetime spectroscopy (PALS) and other techniques require fast scintillation detectors. Currently the best time resolution of scintillation detectors is at the limit of 100 ps: ~200 ps is reported for detectors based on LYSO:Ce [1] and PWO [2], a sub-100-ps coincidence time resolution is reported for PET with LSO:Ce, Ca scintillation detectors, while a sub-100-ps time resolution was measured with PWO-based detectors in the CMS ECAL experiments [3]. A 10-ps-resolution is the next target in development of scintillation detectors [4,5]. The current demand for faster timing of scintillation detectors used both in high luminosity high energy physics experiments and in medical applications inspire deeper studies of the dynamics of nonequilibrium carriers generated in scintillator material.

Recently, we investigated the carrier dynamics in $PbWO_4$ (PWO) and $Gd_3Al_2Ga_3O_{12}$:Ce (GAGG:Ce) using time-resolved photoluminescence technique [6]. In the current paper, a time-resolved free carrier absorption technique was exploited. Three scintillation materials have been under study: self-activated led tungstate ($PbWO_4$, PWO) and two cerium-doped garnets, GAGG and $Y_3Al_2Ga_3O_{12}$ (YAGG).

PWO exhibits short emission decay time and has good radiation hardness to γ quanta. In spite of a comparatively low light yield, 200 ph/MeV, PWO-based scintillators are used in the radiation detectors, which are currently being exploited in several high-energy physics experiments, including such large experiments as CMS and ALICE at LHC(CERN) [7] and future PANDA detector at FAIR (GSI, Germany) [8]. The predominant luminescence mechanism in PWO is emission via quenched polaronic states, due to recombination of excitations on the host oxy-anionic complexes WO_4^{2-} [9,10].

Ce-doped yttrium and gadolinium aluminum gallium garnets, YAGG and GAGG, respectively, are an excellent example for engineering of the material luminescent properties [11].

The rise time of the luminescence response to short pulse excitation in GAGG:Ce was found to be in the range of several

---

* Corresponding author.
E-mail address: slon.zhenya@gmail.com (Y. Tratsiak).

http://dx.doi.org/10.1016/j.optmat.2016.06.040
0925-3467/

nanoseconds even at the direct resonant excitation of Ce^{3+} ions [6]. This feature was explained by taking into account possible carrier trapping at the sublattice of the host-building Gd^{3+} ions, which is in line with the excitation transfer from Gd^{3+} to Ce^{3+} studied in Gd_2SiO_5:Ce crystal [12]. A more detailed study of the role of Gd^{3+} subsystem in the energy transfer processes in garnet crystals plays important role in future optimization of these crystals for exploiting as scintillation material. In particular, scintillation crystals and phosphors based on mixed garnets doped with cerium attract considerable interest due to ability of manipulation with their luminescent and scintillation properties by changing the Al/Ga ratio in the compound [13]. This ability is enabled by the change in the strength of the crystal field acting on the activator ions and, consequently, by shifting the energy levels of Ce^{3+} relative to the bottom of the conduction band. Moreover, optimization of garnet composition serves also for the enhancement of the light yield of these scintillators [14]. The most impressive results have recently been achieved in GAGG:Ce, where the scintillation yield of up to 58,000 ph/MeV was demonstrated both in single crystals and transparent ceramics [13,15].

After demonstration of the formation $Y_3Al_2Ga_3O_{12}$ (YAGG) via sol-gel synthesis [16] and the micro-pulling down method [17], this mixed garnet attracts considerable interest as host material for Ce-based phosphors and scintillators. YAGG:Ce might be used as green phosphor in light-emitting diodes with high color rendering [18]. Strong persistent green [19] and yellow [20] luminescence was also observed in $Y_3Al_2Ga_3O_{12}$:Ce ceramics co-activated with chromium ions [19,20]. In both garnets, GAGG and YAGG, the second and third Stark components of $4f^05d^1$ configuration of Ce^{3+} ion are located in the conduction band [20]. However, the host matrix of YAGG does not contain Gd^{3+} sublattice. Therefore, the comparison of Ce-doped GAGG and YAGG offers an informative insight into the influence of gadolinium on the dynamics of nonequilibrium carriers.

2. Samples

The PWO crystal under study was grown by Czochralski technique as described in more detail in Ref. [9]. The $2 \times 2 \times 0.1$ cm^3 sample was prepared from the ingot of PWO-II quality [2].

$Y_3(Al_{0.25}Ga_{0.75})_3O_{12}$ and $Gd_3Al_2Ga_3O_{12}$ crystals doped with Ce were grown by Czochralski method from the melt containing 1 at.% of Ce in a slightly oxidized neutral atmosphere. The samples under study with dimensions $0.7 \times 0.7 \times 0.5$ cm^3 were cut from the seed part of the ingots exhibiting higher optical quality. The light yield of YAGG:Ce was found to be by a factor of 7 smaller than that of GAGG:Ce.

3. Experimental

The measurements of free carrier absorption have been performed by using a femtosecond Yb:KGW laser PHAROS (Light Conversion Ltd.) emitting at 1030 nm. The laser produced 200 fs pulses at 30 kHz repetition rate. A part of the fundamental laser harmonic was frequency-quadrupled using β-barium borate crystals and the light at 254 nm (4.9 eV) was used as a pump beam for pulsed excitation of free carriers. The excitation beam was focused on the sample surface into a spot of ~350 μm in diameter. The remaining part of laser radiation at 1030 nm was delayed by an opto-mechanical delay line and used as a probe to follow the time evolution of the induced absorption, which is proportional to free carrier density. All measurements were performed at room temperature.

4. Results and discussion

4.1. Free carrier absorption in $PbWO_4$

The excitation at 254 nm corresponds to interband transitions in lead tungstate crystal. Fig. 1 shows the decay of the excitation-induced free carrier absorption (FCA) in PWO crystal at different pulse energy densities of the excitation. The initial part of this decay is presented in Fig. 2. The increase in excitation intensity results in increased contribution of the fast decay component. The dependence of the peak induced absorption on excitation intensity is presented in Fig. 3 as the dependence of the induced absorption at the probe wavelength (1030 nm) on pump pulse energy density. The optical density of the induced absorption in PWO and in other two samples under study (not shown) was found to be proportional to the energy density in a wide dynamic range, as expected for free carrier absorption. This evidence confirms the assumption that the probe absorption originates exclusively from the carriers created via pumping.

The subpicosecond rise time of FCA at interband excitation in the self-activated luminescent lead tungstate is a clear indication that the nonequilibrium free electrons appear in the conduction band within subpicosecond time scale. This is in consistence with interpretation that the luminescent matrix-forming oxy-anionic complexes WO_4^{2-} provide conditions for formation of self-localized excitons. Furthermore, the FCA exhibits a respond kinetics, which correlates with the photoluminescence kinetics observed by us before [6].

The excitation at 254 nm generates free carriers in the PWO crystal in the subpicosecond domain. As the excitation density is increased, the probability of the non-germinal carrier recombination shows an increase resulting in acceleration of the initial part of the FCA decay. This effect was supported by our experimental results obtained with PWO sample.

4.2. Free carrier absorption in YAGG:Ce

The measured absorption spectrum of Ce^{3+} in YAGG:Ce crystal is similar to that reported before [21]: it contains three bands peaked at 448, 350, and 250 nm. Thus, pumping at 254 nm coincides pretty good with the upper, third, absorption band due to inerconfiguration electronic transition $4f^15d^0 \rightarrow 4f^05d^1$ of Ce^{3+} ions. Fig. 4 shows FCA kinetics in YAGG:Ce crystal for different excitation

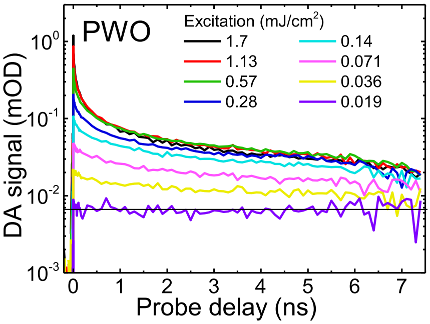

Fig. 1. Kinetics of optical density induced by short pulse excitation of PWO crystal at 254 nm, probed at 1030 nm, for different excitation pulse energy densities (indicated).

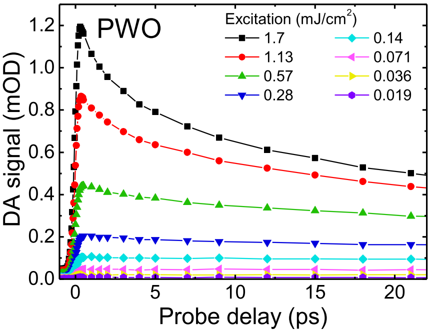

Fig. 2. Initial part of the kinetics presented in Fig. 1.

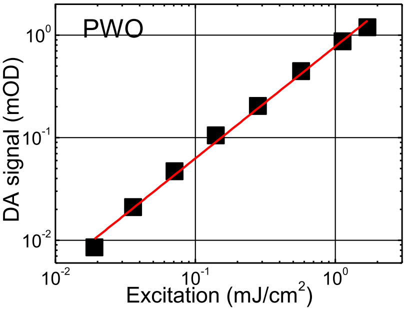

Fig. 3. Induced optical density at 1030 nm probe wavelength at 0.3 ps delay after short pump pulse at 254 nm versus pump pulse energy density.

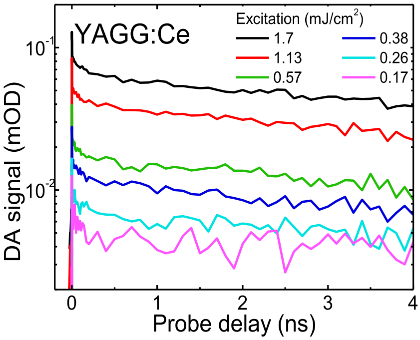

Fig. 4. Kinetics of optical density induced by short-pulse excitation of YAGG:Ce crystal at 254 nm for different excitation pulse energy densities (indicated).

energy densities at 254 nm. The initial part of the decay kinetics is depicted in Fig. 5. The kinetics consists of three components. The fast and intermediate components have characteristic decay times of 2 ps and ~100 ps with no significant dependence on excitation intensity. The decay time of the slow decay component is in nanosecond domain and decreases down to a few nanoseconds as the excitation intensity increases.

Since the excitation YAGG:Ce crystal with 4.9 eV (254 nm) photons corresponds to transition to the third Stark component of 4f^{0}5 d^1 configuration in Ce^{3+} ions, and the edge of the conduction band in Al/Ga mixed garnets has energy near 6.2 eV (200 nm) [22], the wavelength of 254 nm corresponds to the predominant excitation of Ce^{3+} ions. However, a fast delocalization of the electrons from Ce^{3+} is highly probable, since the excited state is within the conduction band. Thus, the initial FCA decay is, most probably, caused by fast delocalization within ~2 ps, the further kinetics of FCA with the decay time in the 100 ps range proceeds after the equilibrium among the processes of depopulation and repopulation of Ce^{3+} and recombination is established. The decay in the nanosecond time is influenced by capturing of electrons from the conduction band by traps due to shallow defect states, which are present in abundance in mixed garnets.

4.3. *Influence of gadolinium on carrier dynamics in GAGG:Ce*

Fig. 6 shows the absorbance spectrum of GAGG:Ce crystal at room temperature. The spectrum consists of absorption bands due to 4f^{1}5 d^0 → 4f^{0}5 d^1 interconfiguration transitions of Ce^{3+} ions and ^{8}S → ^{6}P, ^{6}I, ^{6}D intraconfiguration transitions of matrix-building gadolinium ions forming narrow subbands due to P, I, and D states. The absorption band corresponding to the transition to the third Stark component of 4f^{0}5 d^1 configuration is shifted to short wavelength range in GAGG in comparison with that in YAGG. Therefore, the photons of 254 nm wavelength excite Ce^{3+} ion only into the long-wavelength shoulder of the absorption band due to the third inerconfiguration electronic transition 4f^{1}5 d^0 → 4f^{0}5 d^1 and Gd^{3+} subsystem directly via ^{8}S → ^{6}D transitions.

Figs. 7 and 8 show FCA kinetics in GAGG:Ce crystal at different excitation pulse energy densities at the wavelength of 254 nm in the range of nanoseconds and within the first 20 ps after short-pulse excitation, respectively.

The FCA decay at low excitation intensities is monoexponential with the characteristic decay time substantially exceeding the time range under study (8 ns). The decay becomes increasingly

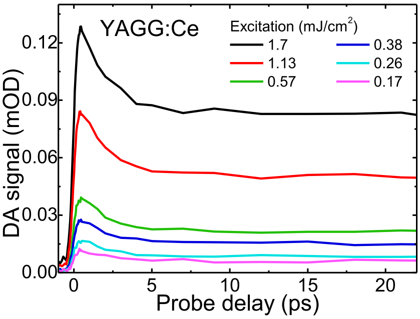

Fig. 5. Initial part of the kinetics presented in Fig. 4.

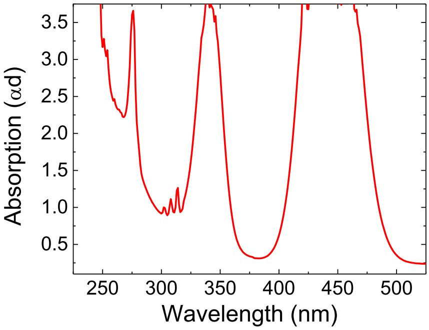

Fig. 6. Room temperature absorbance spectrum of GAGG:Ce.

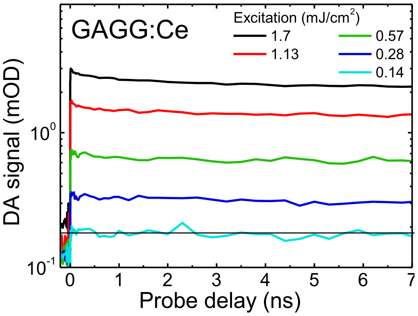

Fig. 7. Kinetics of optical density induced by short pulse excitation of GAGG:Ce crystal at 254 nm for different excitation pulse energy densities (indicated).

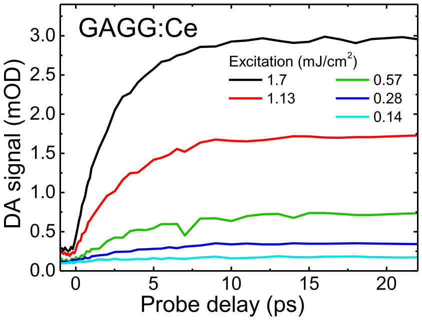

Fig. 8. Initial part of the kinetics presented in Fig. 7.

nonexponential at elevated excitation intensities. The most interesting feature in the FCA response to a short pulse excitation is the rising part of the response. In contrast to PWO and YAGG:Ce, where the rise time is below the time resolution in our experiments (200 fs), the rise of the FCA response in GAGG:Ce is considerably slower. The rise time is approximately 10 ps at low excitation of 0.14 mJ/cm^2 and decreases to 5 ps as the excitation is increased by an order of magnitude.

For GAGG:Ce scintillating crystals, the excitation with 4.9 eV (254 nm) photons corresponds to $^8S \rightarrow {}^6D_{7/2,9/2}$ transition of Gd $^{3+}$ ions and a weak excitation into the long wavelength wing of the band corresponding to transition to the third Stark component of $4f^05\ d^1$ Ce^{3+} electronic configuration. Similarly to YAGG crystal, the band gap due to p → d interband transitions has energy near 6.2 eV (200 nm) [22], thus, the wavelength of 254 nm corresponds to the predominant excitation of Gd^{3+} ions. Consequently, electrons do not appear in the conduction band due to this transition. Thus, the FCA signal we observed here is due to absorption by free holes, which are released from Gd^{3+} ^8S ground state into the valence band. This assumption is in good agreement with the analysis performed by P. Dorenbos [23], showing that the ground state of Gd^{3+} in $4f^7$ shell is localized in the valence band. The rise of FCA, which takes a few picoseconds, is caused by delocalization of holes from Gd^{3+} to valence band. When the hole is localized at the Gd^{3+} f-level, its direct transfer by absorption of photons to p orbitals, forming the top of valence band is forbidden. However, the transition might occur via mixed p-d orbitals in the valence band. This relaxation takes 5–10 ps, depending on the density of nonequilibrium holes, which is observed as the rise time in FCA experiments. The decay of FCA kinetics proceeds rather slow in comparison with that in PWO and YAGG:Ce, with the characteristic decay time of 1 ns even at the first decay stages and even more slowly afterwards. This time is required for the hole to be captured from the valence band by Ce^{3+} ion. This interpretation is consistent with the published observation that the luminescence rise time in GAGG:Ce equals several nanoseconds [6].

5. Conclusions

The time resolved study of free carrier absorption in three scintillation materials, self-activated PWO and cerium-doped GAGG and YAGG showed that the free electrons are instantaneously generated into the conduction band under band-to-band excitation of PWO and at the excitation to the third Stark component of $4f^05\ d^1$ Ce^{3+} configuration forming a state in the conduction band. Meanwhile in GAGG:Ce, a substantially slower relaxation of free carrier absorption was observed and attributed to the absorption by free holes. Moreover, the rise of FCA in GAGG:Ce, takes a few picoseconds, what is caused by delocalization of holes from Gd^{3+} to valence band. This observation is consistent with the conclusion reported in Ref. [23] that the ground state of the $^8S \rightarrow {}^6D_{7/2,9/2}$ intracenter transition of Gd^{3+} ions is located within the valence band. The results show that the hole trapping at Gd sublattice is an important factor deteriorating response rise in scintillators based on mixed garnets containing gadolinium.

Acknowledgement

This work has been carried out in line with the targets of Crystal Clear Collaboration and supported by H2020-INFRAIA-2014-2015 project no. 654168 (AIDA-2020). Authors are grateful to COST Action TD1401 “Fast Advanced Scintillator Timing (FAST)” for support of collaboration.

References

[1] D.N. ter Weele, D.R. Schaart, P. Dorenbos, Intrinsic scintillation pulse shape measurements by means of picosecond x-ray excitation for fast timing applications, Nucl. Instrum. Methods Phys. Res. Sect. A Accel. Spectrom. Detect. Assoc. Equip. 767 (2014) 206–211, http://dx.doi.org/10.1016/j.nima.2014.08.019.

[2] M. Kavatsyuk, D. Bremer, V. Dormenev, P. Drexler, T. Eissner, W. Erni, et al., Performance of the prototype of the electromagnetic calorimeter for PANDA, Nucl. Instrum. Methods Phys. Res. Sect. A 648 (2011) 77–91, http://dx.doi.org/10.1016/j.nima.2011.06.044.

[3] CMS Collaboration, Time reconstruction and performance of the CMS electromagnetic calorimeter, J. Instrum. 5 (2010) T03011, http://dx.doi.org/10.1088/1748-0221/5/03/T03011.

[4] P. Lecoq, M. Korzhik, A. Vasiliev, Can transient phenomena help improving time resolution in scintillators, IEEE Trans. Nucl. Sci. 61 (2014) 229–234, http://dx.doi.org/10.1109/TNS.2013.2282232.

[5] E. Auffray, O. Buganov, a Fedorov, M. Korjik, P. Lecoq, G. Tamulaitis, et al., New detecting techniques for a future calorimetry, J. Phys. Conf. Ser. 587 (2015) 012056, http://dx.doi.org/10.1088/1742-6596/587/1/012056.

[6] E. Auffray, R. Augulis, A. Borisevich, V. Gulbinas, A. Fedorov, M. Korjik, et al., Luminescence rise time in self-activated $PbWO_4$ and Ce-doped $Gd_3Al_2Ga_3O_{12}$ scintillation crystals, J. Lumin. 178 (2016) 54–60, http://dx.doi.org/10.1016/j.jlumin.2016.05.015.

[7] A. Breskin, R. Voss (Eds.), The CERN Large Hadron Collider: Accelerator and Experiments, CERN, Geneva, 2009.

[8] H.H. Gutbrod, I. Augustin, H. Eickhoff, K.-D. Groß, W.F. Henning, D. Krämer, et al. (Eds.), FAIR - Baseline Technical Report, vol. 1, Gesellschaft für Schwerionenforschung mbH, Darmstadt, 2006.

[9] A.A. Annenkov, M.V. Korzhik, P. Lecoq, Lead tungstate scintillation material, Nucl. Instrum. Methods Phys. Res. Sect. A Accel. Spectrom. Detect. Assoc. Equip. 490 (2002) 30–50, http://dx.doi.org/10.1016/S0168-9002(02)00916-6.

[10] M. Nikl, P. Bohacek, E. Mihokova, M. Kobayashi, M. Ishii, Y. Usuki, et al., Excitonic emission of scheelite tungstates AWO_4 (A = Pb, Ca, Ba, Sr), J. Lumin. 87 (2000) 1136–1139, http://dx.doi.org/10.1016/S0022-2313(99)00569-4.

[11] K. Kamada, T. Endo, K. Tsutumi, T. Yanagida, Y. Fujimoto, A. Fukabori, et al., Composition engineering in cerium-doped $(Lu,Gd)_3(Ga,Al)_5O_{12}$ single-crystal scintillators, Cryst. Growth Des. 3 (2011) 4484–4490, http://dx.doi.org/10.1021/cg200694a.

[12] D.M. Kondratiev, M.V. Korzhik, A.A. Fyodorov, V.B. Pavlenko, Scintillation in cerium-activated gadolinium-based crystals, Phys. Status Solidi. 197 (1996) 251–258, http://dx.doi.org/10.1002/pssb.2221970132.

[13] K. Kamada, S. Kurosawa, P. Prusa, M. Nikl, V.V. Kochurikhin, T. Endo, et al., Cz grown 2-in. size Ce:$Gd_3(Al,Ga)_5O_{12}$ single crystal; relationship between Al, Ga site occupancy and scintillation properties, Opt. Mater. Amst. 36 (2014) 1942–1945, http://dx.doi.org/10.1016/j.optmat.2014.04.001.

[14] O. Sidletskiy, A. Gektin, A. Belsky, Light-yield improvement trends in mixed scintillation crystals, Phys. Status Solidi. 211 (2014) 2384–2387, http://dx.doi.org/10.1002/pssa.201431137.

[15] N.J. Cherepy, Z.M. Seeley, S.A. Payne, P.R. Beck, O.B. Drury, S.P. O'Neal, et al., Development of transparent ceramic Ce-doped gadolinium garnet gamma spectrometers, IEEE Trans. Nucl. Sci. 60 (2012) 2330–2335, http://dx.doi.org/10.1109/NSSMIC.2012.6551400.

[16] I. Muliuoliene, S. Mathur, D. Jasaitis, H. Shen, V. Sivakov, R. Rapalaviciute, et al., Evidence of the formation of mixed-metal garnets via sol-gel synthesis, Opt. Mater. Amst. 22 (2003) 241–250, http://dx.doi.org/10.1016/S0925-3467(02)00271-9.

[17] K. Kamada, T. Yanagida, J. Pejchal, M. Nikl, T. Endo, K. Tsutumi, et al., Scintillator-oriented combinatorial search in Ce-doped $(Y,Gd)_3(Ga,Al)_5O_{12}$ multicomponent garnet compounds, J. Phys. D. Appl. Phys. 44 (2011) 505104, http://dx.doi.org/10.1088/0022-3727/44/50/505104.

[18] Y. Qiang, Y. Yu, G. Chen, J. Fang, Synthesis and luminescence properties of $Y_{2.94}Al_{5-m}Ga_mO_{12}$:$0.06Ce^{3+}$ ($1 \leq m \leq 2.5$) green phosphors for white LEDs, Ceram. Int. 42 (2016) 767–773, http://dx.doi.org/10.1016/j.ceramint.2015.09.001.

[19] J. Xu, S. Tanabe, A.D. Sontakke, J. Ueda, Near-infrared multi-wavelengths long persistent luminescence of Nd^{3+} ion through persistent energy transfer in Ce^{3+}, Cr^{3+} co-doped $Y_3Al_2Ga_3O_{12}$ for the first and second bio-imaging windows, Appl. Phys. Lett. 107 (2015) 081903, http://dx.doi.org/10.1063/1.4929495.

[20] J. Ueda, K. Kuroishi, S. Tanabe, Yellow persistent luminescence in Ce^{3+}-Cr^{3+}-codoped gadolinium aluminum gallium garnet transparent ceramics after blue-light excitation, Appl. Phys. Express 7 (2014) 062201, http://dx.doi.org/10.7567/APEX.7.062201.

[21] J. Ueda, K. Kuroishi, S. Tanabe, Bright persistent ceramic phosphors of Ce^{3+}-Cr^{3+}-codoped garnet able to store by blue light, Appl. Phys. Lett. 104 (2014) 101904, http://dx.doi.org/10.1063/1.4868138.

[22] J.M. Ogieglo, Luminescence and Energy Transfer in Garnet Scintillators, Utrecht University, 2012. http://dspace.library.uu.nl/handle/1874/257552.

[23] P. Dorenbos, A review on how lanthanide impurity levels change with chemistry and structure of inorganic compounds, ECS J. Solid State Sci. Technol. 2 (2013) R3001–R3011, http://dx.doi.org/10.1149/2.001302jss.

Paper P4

Luminescence rise time in self-activated $PbWO_4$ and Ce-doped $Gd_3Al_2Ga_3O_{12}$ scintillation crystals

E. Auffray, R. Augulis, A. Borisevich, V. Gulbinas, A. Fedorov, M. Korjik, M.T. Lucchini, V. Mechinsky, S. Nargelas, E. Songaila, G. Tamulaitis, **A. Vaitkevičius**, S. Zazubovich

J. Lumin. 178 (2016) 54–60.

doi:10.1016/j.jlumin.2016.05.015.

Luminescence rise time in self-activated PbWO4 and Ce-doped Gd3Al2Ga3O12 scintillation crystals

E. Auffray (CERN) *et al*

14 August 2016

The AIDA-2020 Advanced European Infrastructures for Detectors at Accelerators project has received funding from the European Union's Horizon 2020 Research and Innovation programme under Grant Agreement no. 654168.

Luminescence rise time in self-activated $PbWO_4$ and Ce-doped $Gd_3Al_2Ga_3O_{12}$ scintillation crystals

E. Auffray[a], R. Augulis[b], A. Borisevich[c], V. Gulbinas[b], A. Fedorov[c], M. Korjik[c], M.T. Lucchini[a], V. Mechinsky[c], S. Nargelas[d], E. Songaila[b], G. Tamulaitis[d], A. Vaitkevičius[d*], S. Zazubovich[e]

[a] CERN, Geneva, Switzerland
[b] Center for Physical Sciences and Technology, Savanorių av. 231, Vilnius, Lithuania
[c] Research Institute for Nuclear Problems, Bobruiskaya str. 11, Minsk, Belarus
[d] Vilnius University, Universiteto str. 3, Vilnius , Lithuania
[e] Institute of Physics, University of Tartu, W. Ostwaldi Str. 1, Tartu, Estonia
[*]-Corresponding author: E-mail: augustas.vaitkevicius@ff.vu.lt, Phone: +370 52366070

Highlights:

- Photoluminescence rise time is studied in two scintillators: PWO and GAGG:Ce
- Sub-picosecond photoluminescence rise time in PWO is observed for the first time
- A multicomponent luminescence rise edge is observed in GAGG:Ce
- The mechanisms behind luminescence kinetics in the crystals are under discussion

Keywords: Scintillator, luminescence, luminescence kinetics, radiation detector, lead tungstate, garnet

The time resolution of scintillation detectors of ionizing radiation is one of the key parameters sought for in the current and future high-energy physics experiments. This study is encouraged by the necessity to find novel detection methods enabling a sub-10-ps time resolution in scintillation detectors and is focused on the exploitation of fast luminescence rise front. Time-resolved photoluminescence (PL) spectroscopy and thermally stimulated luminescence techniques have been used to study two promising scintillators: self-activated lead tungstate (PWO, $PbWO_4$) and Ce-doped gadolinium aluminum gallium garnet (GAGG, $Gd_3Al_2Ga_3O_{12}$). A sub-picosecond PL rise time is observed in PWO, while longer processes in the PL response in GAGG:Ce are detected and studied. The mechanisms responsible for the PL rise time in self-activated and doped scintillators are under discussion.

1. Introduction

Scintillation detectors are the key instrument in many fields of high-energy physics, medical diagnostic devices, tools for inspection. Currently, operation speed steps forward as the most problematic property of the scintillation detectors in many applications. Faster detector response is seeked for in high-energy physics to prevent pile-up effect in high-luminosity experiments [1-2]. Faster readout improves the signal to noise ratio and, therefore, allows a decrease of the injected dose to the patient to accumulate sufficient information in positron emission tomography (PET) [3], positron annihilation lifetime spectroscopy (PALS) [4], and other scintillator-based medical devices. Time resolution of ~200 ps is reported for detectors based on LYSO:Ce [5] and PWO with readout using avalanche photodiodes [6]. Sub-100-ps coincidence time resolution for PET with LSO:Ce codoped with Ca is reported [7]. The recent progress in development of photo-detectors, especially of silicon photomultipliers (SiPM) [8], pushes the readout rate to the frontiers limited by the kinetic parameters of the scintillation. Therefore, it is an important question whether the rise time of scintillation will be the factor hindering the targeted time resolution by a factor of ten better than currently achieved.

The scintillation is basically the luminescence in transparent media initiated by ionizing radiation [9]. Thus, the rise time of the emission is governed mainly by the excitation relaxation and the transfer of the nonequilibrium carriers to the centers of development might be exploited for substantial shifting the time resolution to picosecond and sub-picosecond domain [10], as seeked for in many future applications. One of the novel approaches to substantially improve the time resolution is splitting the detection into the readout of the moment of irradiation interaction with the scintillator to ensure high time resolution and the readout of the amplitude of the scintillator response carrying information on the deposited energy of ionizing radiation (see [11] and references therein).

In this paper, we present the results of our study of the rise time in two scintillating materials: self-activated led tungstate ($PbWO_4$, PWO) and Ce-doped gadolinium aluminum gallium garnet ($Gd_3Al_2Ga_3O_{12}$:Ce, GAGG:Ce).

Lead tungstate is a self-activated scintillator with predominant emission of quenched polaronic states, which can be considered as excitations on the host oxy-anionic complexes WO_4^{2-} [12,13]. In spite of a comparatively low light yield (e.g. by two orders of magnitude lower than that in LYSO:Ce) PWO has a good radiation hardness to γ-quanta and exhibits a short emission decay time, which is of especial importance to avoid the signal pile up in high luminosity experiments [14]. PWO-based radiation detectors are currently being exploited in several high-energy physics experiments, including such large experiments as CMS and ALICE at LHC [1]. The self-activated emission mechanism is expected to be favourable for fast relaxation of the nonequilibrium carriers into the emitting state.

The second crystal under study is a cerium-doped scintillator GAGG:Ce. The crystal exhibits a high light yield of up to 50000 phot/MeV, has a short luminescence decay time (less than 100 ns) [15,16], and its emission band is peaked at ~540 nm perfectly matching the sensitivity spectrum of conventional SiPMs. Thus, this crystal might compete with LYSO:Ce and LSO:Ce in TOF-PETs and other applications. However, due to the considerably different ionic radii of Ga^{3+} and Al^{3+} in both octahedral and tetrahedral oxygen coordination, the compound of gadolinium garnets of gallium and aluminum should contain a higher density of structural defects with respect to that of single-component garnets. Introduction of a gallium ion in close proximity of an aluminum ion or vice versa results in considerable lattice strain and, as a consequence, leads to distortion of the polyhedra, which serve as trapping centers for nonequilibrium carriers. This feature has been confirmed by observation of the broadening of XRD lines in mixed gallium-gadolinium garnets [17]. Moreover, the distribution of gallium and aluminum in these garnets is random, leading to structure inhomogeneities, which significantly affect the processes of energy transfer and relaxation of electronic excitations. Therefore, the GAGG crystal has several different lattice positions for the trivalent dopant ions and exhibits significant inhomogeneous broadening in the absorption and emission spectra. These inhomogenities are being exploited for the generation of ultra-short laser pulses enabled by inhomogeneous broadening of spectral lines 4f and 3d of the activator ion, which is peculiar of the mixed garnets and is absent in single component garnets [18]. Therefore, substantial influence of structural defects on the spectra and other properties of luminescence in $Gd_3Al_2Ga_3O_{12}$:Ce is expected.

Time-resolved luminescence spectroscopy was exploited in the current study of the rise time of luminescence after short-pulse photoexcitation. To get a better understanding of the dynamics of nonequilibrium carriers generated by irradiation, the luminescence decay in these materials was also investigated, while the thermally stimulated luminescence characteristics were studied to get information on defect centers in GAGG:Ce.

2. Experimental

The PWO crystal under study was grown by Czochralski technique as described in more detail in [12]. The 2x2x0.1 cm^3 sample was prepared from the ingot of PWO-II [6] quality. The polished 2x2 cm^2 planes were perpendicular to the crystallographic axis **a.**

GAGG:Ce crystal was grown by Czochralski method in a slightly oxidized neutral atmosphere with 1 at.% Ce content in the melt. The sample under study with dimensions 0.7x0.7x0.5 cm^3 was cut from the seed part of the ingot exhibiting higher optical quality.

The time-resolved photoluminescence (TRPL) study has been performed by using a femtosecond Yb:KGW oscillator (Light Conversion Ltd.) emitting at 1030 nm. The oscillator produced 80 fs pulses at 76 MHz repetition rate. A harmonics generator (HIRO, Light Conversion Ltd.) was used to produce the third 343 nm (3.64 eV) and fourth 254 nm (4.9 eV) harmonics of the oscillator emission. The excitation beam was focused on the sample surface into a spot of ~100 μm in diameter, resulting in excitation pulse energy density of about 15 mJ/cm^2. The PL signal was detected using a Hamamatsu streak camera. Synchoscan detection mode with the 2.95 ps full-width at half maximum (FWHM) of instrumental response function was used for the measurements in subnanosecond time domain. The deconvolution of the instrumental response function and the PL signal enabled a subpicosecond resolution. Meanwhile, in the study of samples with significant long decay components, the camera could be operated only in single sweep mode with considerably poorer time resolution.

Photoluminescence measurements were performed at room temperature, which is a typical operation temperature of ionizing radiation detectors in laboratory conditions.

The steady-state emission and excitation spectra and the characteristics of the thermally stimulated luminescence (TSL) were measured using a setup consisting of the LOT-ORIEL xenon lamp (150 W) and two monochromators (SF-4 and SPM-1). The luminescence was detected by a photomultiplier tube FEU-79 connected with an amplifier and recorder. The TSL glow curves $I_{\mathrm{TSL}}(T)$ were measured at a heating rate of 0.2 K/s after selective irradiation of the crystal at different irradiation temperatures T_{irr} in the range from 94 to 300 K with different irradiation photon energies E_{irr} (2.2 - 4.8 eV). The crystals located in the nitrogen cryostat were irradiated with the xenon lamp through a monochromator. The spectral width of the monochromated light did not exceed 5 nm. The emission wavelength to be detected ($E_{\mathrm{em}} = 2.25$ eV) was selected by the second monochromator. The TSL glow curves were not corrected for the temperature dependence of the emission intensity.

3. Experimental Results

3.1 Kinetics of photoluminescence in PWO

Figure 1 shows a typical image of the photoluminescence intensity dependence on time and wavelength, which was obtained with the streak camera for the PWO sample under study.

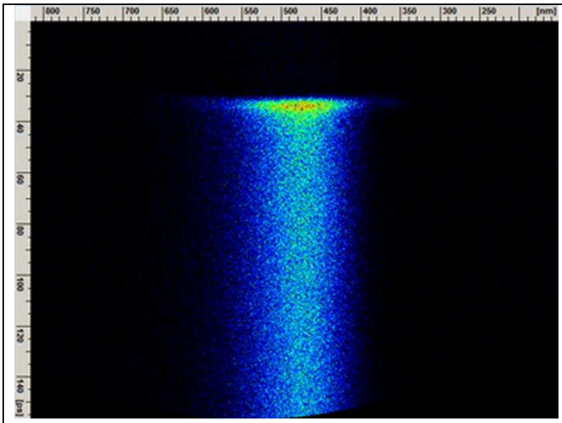

Fig. 1. Streak camera image of PL intensity versus wavelength (horizontal) and time (vertical) in $PbWO_4$. Color version available online.

Figure 2 shows the time-integrated PWO fluorescence spectra, measured at different excitation wavelengths. At the excitation into conduction band at 254 nm, the typical PWO blue luminescence is observed. For the excitation wavelength shifted to 343 nm, the green luminescence band due to recombination at oxygen deficient oxy-anionic complexes WO_3 [12] is also observed.

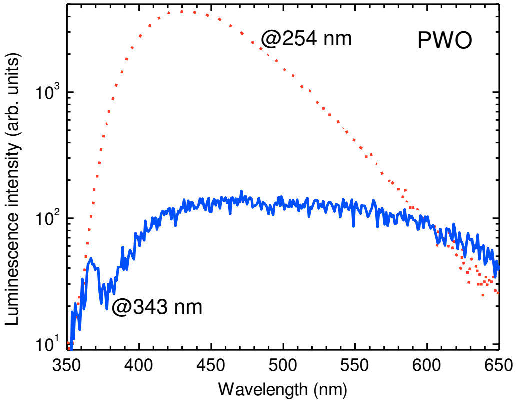

Fig. 2. Time-integrated $PbWO_4$ luminescence spectra after excitation at 254 nm (red dotted line) and 343 nm (blue solid line). Color version available online.

The PL intensity decay proceeds approximately at the same rate for all wavelengths within the PL band. The initial part in the kinetics of the PL intensity spectrally integrated within the entire band (400-600 nm) is presented in Fig. 3 together with the instrumental response function and the fit with the bi-exponential decay function. The full width at half maximum (FWHM) of the instrumental function was 2.95 ps. The measured PL rise is completely defined by the rise of the instrumental response function. This evidences that the PL rise time in PWO scintillation crystals is in subpicosecond domain.

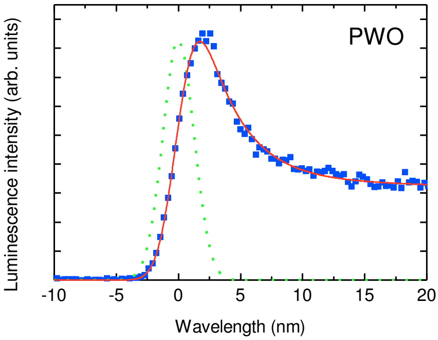

Fig. 3. Initial stage of spectrally integrated photoluminescence kinetics in $PbWO_4$ at 253 nm excitation (dots), the instrumental response function (green dotted line), and the best fit obtained using a bi-exponential decay function (red solid line). Color version available online.

It is interesting to note that both regular WO_4^{2-} and defect-related WO_3 luminescence centers show the same leading edge of the luminescence transient. This is an indication that no intermediate recapturing processes are involved in the energy transfer processes. Figure 4 shows the initial stage of PL decay. The decay has two decay components. Fitting the experimental PL transients with a bi-exponential decay function renders two effective decay times of $\tau_1 = 3.8$ ps and $\tau_2 = 683$ ps at 343 nm excitation and $\tau_1 = 5.9$ and $\tau_2 = 824$ ps, at 254 nm excitation. At the tail part of the measured kinetics curve, certain contribution of the slower component with the time constant of 8-10 ns, which is observed in routine start–stop measurements of PWO luminescence kinetics, might be traced. The intermediate component with decay times of approximately 700-800 ps is consistent with that reported in [19], while the fast component has not been observed before. The comparison of the PL transients measured at different excitation intensities (see Fig. 4) shows that the ratio between the two components does not depend on the density of the nonequilibrium carriers. The kinetics at 343 nm excitation was also measured in two spectral ranges: 400-500 and 500-600 nm. We did not find a significant difference in the response shape when intensities of blue and green luminescence bands became roughly the same. This is an indication that the fastest decay component is due to green luminescence emitting centers.

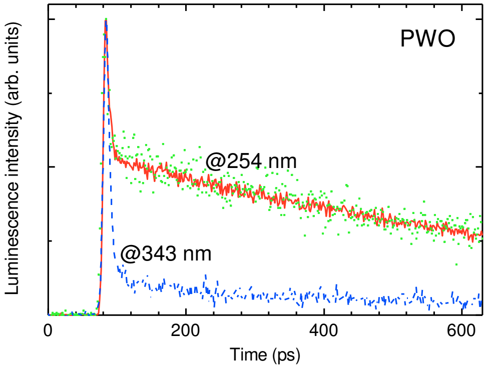

Fig. 4. Initial part of $PbWO_4$ photoluminescence kinetics at 343 nm excitation (blue dashed line) and 254 nm excitation with pulse energy of 15 mJ/cm^2 (red solid line) and 1.5 mJ/cm^2 (green dotted line). Color version available online.

3.2 Kinetics of photoluminescence in Ce-doped GAGG

Figure 5 shows the transmission and absorption spectra of GAGG:Ce crystal at room temperature. In UV-visible range, they are formed by $4f^15d^0 \rightarrow 4f^05d^1$ interconfiguration transitions of Ce^{3+} ions and $^8S \rightarrow ^6P$, ^6I, ^6D intraconfiguration transition of Gd^{3+} ions. Gd^{3+} is the matrix creating ion, so P, I and D states form narrow subzones. The photons of 254 nm wavelength excite both Ce^{3+} and Gd^{3+} subsystems in the crystal, whereas 343 nm photons excite predominantly Ce^{3+} ions.

The photoluminescence spectra of GAGG:Ce are presented in Fig. 6. The shape of the spectra is similar for both excitation wavelengths. In consistency with the published data [16], the spectra consist of two strongly overlapping bands caused by spin-orbit splitting of ground **f** level. Meanwhile, the emission intensity under matrix excitation (at 254 nm) is by two orders of magnitude lower than that under direct excitation of Ce ions (at 343 nm). Since the absorption coefficient is similar for the two wavelengths (see Fig. 5), it seems that the difference in PL intensity is caused by the losses of the nonequilibrium carriers due to nonradiative recombination in the process of carrier transfer from the matrix to the Ce ions.

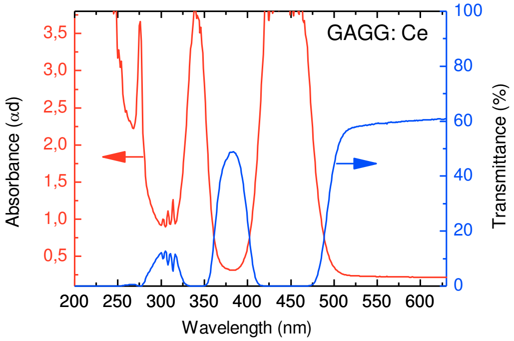

Fig. 5. Room temperature transmittance (blue) and absorption (red) spectra of GAGG:Ce sample. Color version available online.

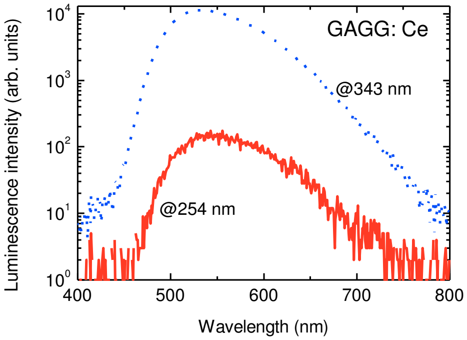

Fig. 6. Photoluminescence spectra of GAGG:Ce after short-pulse excitation at 254 nm (red solid line) and 343 nm (blue dotted line). Color version available online.

The photo-luminescence response after a short pulse excitation at 254 nm and 343 nm is presented in Fig. 7. Due to the presence of long PL decay components, the initial part of the response is measured at the instrumental function with the FWHM of 100 ps, which is, however, considerably shorter than any components in the rise of PL response in GAGG:Ce. The response was deconvoluted by taking into account the instrumental response function, an exponential rise with time constant τ_r and an exponential decay with time constant τ_d. The major part of the luminescence follows the leading edge of the instrumental function. However, at the excitation of Ce^{3+} luminescence through the matrix (at 254 nm), a slow rise with time constant τ_r = 8 ns is observed. For the 343 nm excitation corresponding to the absorption band of Ce^{3+}

ions, the slow rise component has a shorter time constant $\tau_r = 2.5$ ns, but still considerably longer than the instrumental response function. This is in consistence with the 2 ns rise time observed in GAGG:Ce under gamma irradiation [20].

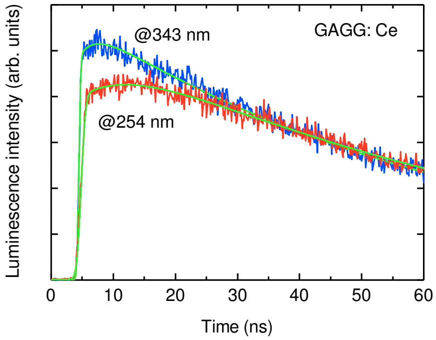

Fig. 7. The initial part of PL response to a short excitation pulse after excitation directly to Ce^{3+} ions at 343 nm and via the matrix of GAGG single crystal at 254 nm (indicated). Smooth lines represent the fitting functions. Color version available online.

Figure 8 presents the PL kinetics in a longer scale obtained at the two excitation wavelengths. The decay is mono-exponential with the decay times of 70 and 60 ns at 254 nm and 343 nm excitation wavelengths, respectively. The slightly longer decay time at excitation through the matrix might be explained by the process of Ce^{3+} luminescence sensitization [21].

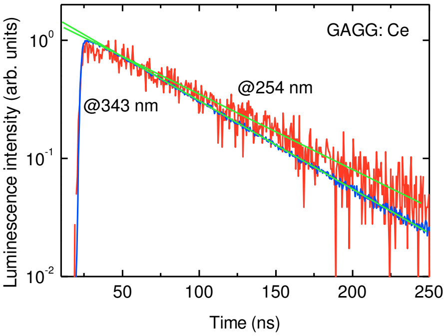

Fig. 8. Luminescence kinetics of Ce^{3+} at excitation directly to cerium ion at 343 nm and via the matrix of GAGG at 254 nm (indicated). Straight lines represent single

exponential fits. Color version available online.

3.3 Thermally stimulated luminesce in GAGG:Ce

Excitation of the GAGG:Ce crystal in the Ce^{3+}-related absorption bands results not only in the fast (ns) photoluminescence of Ce^{3+} but also in strong phosphorescence due to effective formation of stable electron and hole centers. These centers can be detected by TSL. As seen from Fig. 9, the TSL glow curves measured after irradiation of the GAGG:Ce crystal with different energies E_{irr} are similar.

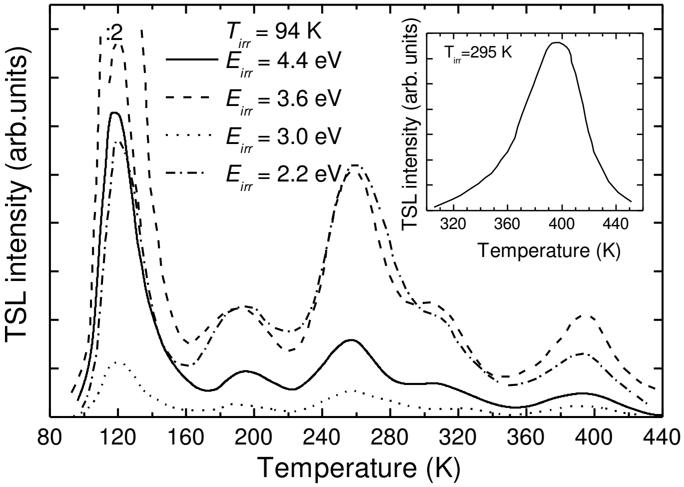

Fig. 9. Glow curves of thermally stimulated luminescence measured after irradiation of GAGG:Ce crystal at 94 K with photons of different energies E_{irr} indicated. In the inset, the TSL glow curve measured after irradiation with E_{irr} = 3.6 eV at 295 K. Color version available online.

After irradiation at 94 K, the TSL glow curve peaks located at 110, 190, 260, 310, and 395 K are observed. Most of the low temperature bands were described in detail elswhere [22-24]. After irradiation at 295 K, we observe a peak at 395 K (see the inset in Fig. 9). The resolved TSL peak above room temperature is detected for the first time. All the TSL peaks are observed for the Ce^{3+}-related emission peaked at 2.25 eV. This is an indication that all the TSL glow peaks are caused by thermally stimulated release of electrons from different electron traps and their subsequent recombination with the hole Ce^{4+} centers.

The dependences of the maximum TSL intensity at 395 K on the irradiation energy E_{irr} measured at $T_{irr} = 94$ K and $T_{irr} = 295$ K are presented in Figs. 10a and 10b, respectively (points). For comparison, excitation spectra of the Ce^{3+} emission, measured at exactly the same conditions, are also shown (solid lines). We observed that the excitation band consist of two overlapping bands. Only one of them, corresponding to 460 nm (2.7 eV) concides with the absorption band related to Ce^{3+}, as seen in Fig. 5.

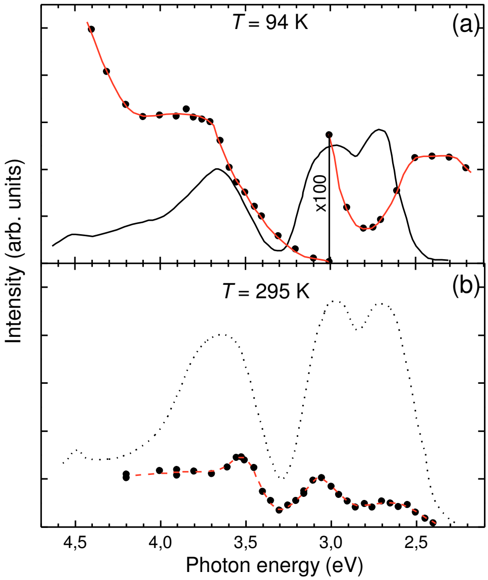

Fig. 10. Dependences of the maximum TSL intensity at 395 K on irradiation energy (points) and PL excitation spectra of the Ce^{3+} luminescence (lines) measured at irradiation temperatures of 94 K (a) and 295 K (b). Color version available online.

4. Discussion

4.1 On PWO results

The subpicosecond rise time of luminescence in lead tungstate is a clear indication that the relaxation of nonequilibrium carriers to recombination centers is an intrinsic process and is not significantly affected by any defects in a standard PWO II crystal. The short rise time at the excitation with photon energy of 4.9 eV (254 nm), which is larger than E_g by 0.6 eV [12], is consistent with the model of relaxation of germinal carrier pairs to the radiating states at oxy-complexes WO_4^{2-}. However, the fast rise time is observed also at excitation with energy 3.64 eV (343 nm), which is 0.6 eV smaller than E_g. This indicates that the process of release of electrons into conduction band from shallow traps is a weak process in this crystal. This is consistent with the assumption that the color centers with a captured electron (F+ type centers) are completely unstable in $PbWO_4$ structure at room temperature [12]. The F+ centers are based on WO_3 defect oxy-complexes and most probably have ground state inside conduction band, so they appear simultaneously with excited regular oxy-anionic groups.

The fast PL decay component with the decay time $\tau = 4\text{-}6$ ps is more pronounced at the excitation bellow E_g. Therefore, we assume that the fastest component in the luminescence kinetics is caused by radiative decay of F^+ centers. The second, intermediate decay component with the decay time $\tau = 600\text{-}800$ ps, which was explicitly revealed in our experiments using high time resolution streak camera, might be interpreted by WO_4^{2-} luminescence originating from quenched luminescence of complexes $WO_4^{2-}+RE^{3+}$ (RE = La^{3+} and Y^{3+}) [12]. Therefore, the intermediate decay component (600-800 ps) and the component with the decay time of 8-10 ns, originating from regular WO_4^{2-} complexes [19], provide simultaneous contributions to luminescence, which is strongly quenched at room temperature. The PWO crystals fabricated on a large scale for high energy physics applications are doped with trivalent La and Y ions at the total level of 100 ppm [12]. As a result, radiative recombination centers $WO_4^{2-}+La^{3+}$ and $WO_4^{2-}+Y^{3+}$ are formed with the ground states approximately 0.1 eV below the bottom of the conduction band. Therefore, in addition to the thermal quenching, they have additional nonradiative losses due to the thermal ionization to the conduction band, so their kinetics becomes shorter.

Our results are obtained under photoexcitation near the bottom of the conduction band. Under ionizing radiation, the geminal pairs might be disconnected during the thermalization process. Nevertheless, a dramatic increase in the rise time of the scintillation pulse is not expected, since the thermalization of the nonequilibrium carriers via the emission of phonons occurs on the time scale of picoseconds or even shorter. Moreover, the energy deposit in the high energy physics experiments, when PWO crystals interact with high-energy particles with energies of hundreds of GeV, like in LHC experiments, exceeds several GeV within a time of less than 1 ns. So the density of free carriers becomes high enough to provide prompt coupling of opposite carriers for recombination. Due to this reason we do not expect substantial increase of the scintillation rise time compared to photoluminescence rise time and estimate it at the level of less than 10 ps. Thus, the rise time of the intrinsic scintillation of PWO crystals might probably be used for fast timing with PWO crystals in high energy particles detectors with optical readout.

4.2 On GAGG:Ce results

For GAGG:Ce scintillating crystals, the excitation with 4.9eV (254 nm) photons corresponds to $^8S \rightarrow {}^6D_{7/2,9/2}$ transition of Gd^{3+} ions. The edge of the conduction band has energy near 6.2 eV (200 nm) [25], so the wavelength of 254 nm corresponds to the predominant excitation of Gd^{3+} ions. The excitation with 3.64 eV (343 nm) photons corresponds to a direct excitation of cerium ions in the second Stark component of $5d^1f^0$ configuration of Ce^{3+} ions. It is worth noting that the kinetics at both excitations shows the rise component on a nanosecond scale. The rise time at the sub-band-gap excitation (4.9eV) is only by a factor of three longer than that at the direct Ce^{3+} excitation. This is an indication of a considerable exchange of electrons between the radiative Ce^{3+} centers, sub-bands created by Gd^{3+} ions, traps, and the conduction band, where they might become trapped and reach the Ce^{3+} radiative centers with certain delay. This exchange results in slowing of the PL rise time even at the excitation wavelength corresponding to intracenter excitation.

To clarify the excitation transfer process in the crystal, we analyzed the dependences of the maximum TSL intensity at 395 K on irradiation energy. We observed that the creation spectrum of recombining electron and hole centers occurs under irradiation of the crystal in the Ce^{3+}-related absorption bands located at $E_{irr} >$ 3.3 eV and originating from the second Stark component of $5d^1f^0$ configuration (the band at 3.65 eV) and the upper electron transitions of Ce^{3+}. The population efficiency of these centers in the region of the lowest-energy absorption band of Ce^{3+} (around 2.8 eV) is substantially smaller (at least by two orders of magnitude). At 295 K, the radiative electron and hole centers are optically populated under irradiation in all the absorption bands of Ce^{3+} (Fig. 10b). These data indicate that the second Stark component of $5d^1f^0$ configuration of Ce^{3+} is located inside the conduction band, so that the excitation into of Ce^{3+} results in the ionization of Ce^{3+} even at 94 K. As a result, the hole centers Ce^{4+} and the electrons trapped at different electron traps are optically created. Their thermally stimulated recombination results in the the TSL glow curve peaks shown in Fig. 9.

The fast rise time in the Ce^{3+} luminescence kinetics at both 4.9 eV and 3.64 eV excitations indicates that Gd^{3+} ions play a significant role in the excitation transport even at Ce^{3+} intercenter excitation. After Ce^{3+} excitation into the second Stark component and subsequent ionization into conduction band, a considerable part of the electrons are captured by matrix-building Gd^{3+} ions. An important role of Gd^{3+} ions was revealed in the study of Gd_2SiO_5:Ce crystals [26]. The migration of the electrons along Gd^{3+} subsystem in the crystal slows down the rate of the electron transfer back to the Ce^{3+} ions, where they recombine radiatively.

Moreover, another, less effective process is also possible. This effect takes place at low temperatures under irradiation of the GAGG:Ce crystal in the energy range $E_{\mathrm{irr}} < 3.0$ eV. Indeed, TSL peaks at the same positions but of considerably lower intensity appear even after irradiation with $E_{\mathrm{irr}} = 2.2$ eV at 94 K (see Fig. 9), however the TSL intensity under this irradiation is even larger than under irradiation in the absorption band ($E_{\mathrm{irr}} = 2.8$ eV) (Fig. 10a). Probably, optically initiated population of defects in this case can be explained by charge-transfer processes, analogous to those considered in [27] for Ce^{3+}-doped oxyorthosilicates, e.g., by the optically stimulated electron transfer from the valence band to various electron traps existing in the crystal.

The TSL peak corresponding to the activation temperature near 395 K is also of interest. At room temperature, this color center undergoes slow spontaneous thermal ionization and can be a source of carriers for the subsequent capture by ions Ce^{3+}. Our results lead to certain considerations on the position of the energy level of this color center in the conduction band. Since the center is partially populated at room temperature, the position should not be above ^6P level of Gd^{3+}. The activation energy for the 395 K TSL peak under irradiation in the lowest absorption band (determined from the lnI_{TSL} dependence on 1/T_{irr}) is about 0.33 eV. The activation energy for quencing the Ce^{3+} luminescence is reported to be equal to 0.25 eV in a sintered sample [24] and 0.36 eV in a crystal [28]. Thus, we concluded that the ground states of both the Ce^{3+} radiating level and the color center are ~0.3 eV below the bottom of the conduction band. The nature of the color center is the subject of a separate publication. In this paper, we just point out that the spontaneous electron release from this color center at room temperature does not substantially affect the luminescence kinetics. As it can be seen in Fig.8, the decay is slightly slower at the excitation through Gd^{3+} ions but the difference in the decay times is less than 20%.

While scintillation occurs in GAGG:Ce crystal under ionizing radiation, the most of the carriers will be captuded by matrix-building Gd^{3+} ions. Thus, the rise time of the scintillation is expected in the range of few ns. The relatively long rise time of the scintillation might be the limiting factor to achieve acceptably fast timing by using detectors based on GAGG:Ce, especially in PET scanners, where the energy deposit is considerably lower than that in high energy applications.

5. Conclusions

A sub-picosecond rise time of luminescence in intrinsic PWO scintillation crystal is demonstrated for both emission components: the predominant component peaked at 430 nm, which is related with the regular crystal-building oxy-anionic complexes WO_4^{2-}, and the green component (peaked near 500 nm) due to oxygen deficient oxy-complexes WO_3. Two luminescence decay components with characteristic decay times of 4-6 ps and 600-800 ps, i.e., substantially faster than the decay component with the decay time of ~10 ns, which is usually observed in PWO scintillators, are explicitly revealed for the first time.

Meanwhile, the rise of the luminescence response to short pulse in GAGG:Ce takes several nanoseconds even at the direct resonant excitation of Ce^{3+} ions. This feature is explained by the position of the excited Ce^{3+} levels in the conduction band. This conclusion is supported by the study of thermally stimulated luminescence. The importance of the capture of nonequilibrium carriers by matrix-building Gd^{3+} ions for the luminescence response time is also concluded.

The results show that the fast rise of luminescence in PWO scintillators is short enough to be exploited for the sub-10-picosecond readout, which is targeted for the future scintillator detectors, while the rise time in cerium-doped GAGG crystal might be a limiting factor for fast timing in radiation detectors based on this scintillator. However, as recently demonstrated in [20] and references therein, the rise time of GAGG:Ce might be substantially decreased by co-doping by magnesium.

Acknowledgement

This work has been carried out in line with the targets of Crystal Clear Collaboration and supported by H2020-INFRAIA-2014-2015 project no. 654168 (AIDA-2020). Authors are grateful to COST Action TD1401 "Fast Advanced Scintillator Timing (FAST)" for support of collaboration. V.M. also acknowledges the support of the Belarus Fundamental Research Foundation. The work of S.Z. has been supported by the Institutional Research Funding IUT02-26 of the Estonian Ministry of Education and Research.

References

[1] A. Breskin, R. Voss (Eds.), The CERN large hadron collider: accelerator and experiments, CERN, Geneva, 2009.

[2] International Linear Collider Technical Design Report, Tokyo, Geneva, Chicago – 12 June 2013.

[3] W.W. Moses, Time of Flight in PET Revisited, IEEE Trans. Nucle.Sci. 50 (2003) 1325-1330.

[4] C. Fong, A.W. Dong, A.J. Hill, B.J. Boyd, C.J. Drummond, Positron annihilation lifetime spectroscopy (PALS): a probe for molecular organization in self-assembled biomimetic systems, Phys. Chem. Chem. Phys., 17 (2015) 17527-17540.

[5] D.N. ter Weele, D.R. Schaart, P. Dorenbos, Intrinsic scintillation pulse shape measurements by means of picosecond x-ray excitation for fast timing applications, Nucl. Instrum. Methods Phys. Res. A 767 (2014) 206-211.

[6] M. Kavatsyuk, D. Bremer, V. Dormenev, P. Drexler, T. Eissner, W. Erni, E. Guliyev, T. Hennino, B. Krusche, B. Lewandowski, H. Löhner, M. Moritz, R.W. Novotny, K. Peters, J. Pouthas, P. Rosier, M. Steinacher, G. Tambave, A. Wilms, On behalf of the PANDA Collaboration, Performance of the prototype of the electromagnetic calorimeter for PANDA, Nucl. Instrum. Methods Phys. Res. A 648 (2011) 77-91.

[7] M.V. Nemallapudi, S. Gundacker, P. Lecoq, E. Auffray, A. Ferri, A. Gola, C. Piemonte, Sub-100 ps coincidence time resolution for positron emission tomography with LSO:Ce codoped with Ca, Phys. Med. Biol. 60 (2015) 4635-4649.

[8] D.R. Schaart, E. Charbon, T. Frach, V. Schulz, Advances in digital SiPMs and their application in biomedical imaging, Nucl. Instrum. Methods Phys. Res. A, 809 (2016) 31-52.

[9] M. Korzhik, A. Khruchinski, P. Lecoq, The phenomenon of scintillation in solids, Nucl. Instrum. Methods Phys. Res. A, 486 (2002) 381-384.

[10] S. Gundacker, E. Auffray, K. Pauwels, P. Lecoq, Measurement of intrinsic rise times for various L(Y)SO and LuAG scintillators with a general study of prompt 460 photons to achieve 10 ps in TOF-PET, Phys. Med. Biol., 61 (2016) 2802-2837.

[11] E. Auffray, O. Buganov, M. Korjik, A. Fedorov, S. Nargelas, G. Tamulaitis, S. Tikhomirov, A. Vaitkevičius, Application of two-photon absorption in PWO scintillator for fast timing of interaction with ionizing radiation, Nucl. Instrum. Methods Phys. Res. A 804 (2015) 194-200.

[12] A. Annenkov, M. Korzhik, P. Lecoq, Lead tungstate scintillation material, Nucl. Instrum. Methods Phys. Res. A 490 (2002) 30-50.

[13] M. Nikl, Wide Band Gap Scintillation materials:Progress in the Technology and Material Undestanding, Phys. Stat.Sol.A 178 (2000) 595-620.

[14] W. Scandale, T. Talor, F. Zimmermann (eds.), Towards a Roadmap for the Upgrade of the CERN&GSI Accelerator Complexes, CERN, Geneva, 2007.

[15] K. Kamada, T. Endo, K. Tsutumi, T. Yanagida, Y. Fujimoto, A. Fukabori, A. Yoshikava, J. Pejchal, M. Nikl, Composition Engineering in Cerium Doped $(Lu,Gd)_3(Ga,Al)_5O_{12}$ Single-Crystal Scintillators, Cryst. Growth Des. 11 (2011) 4484-4490.

[16] K. Kamada, T. Yanagida, J. Pejchal, M. Nikl, T. Endo, K. Tsukumi, Y. Fujimoto, A. Fukabori, A. Yoshikava, Crystal Growth and Scintillation properties of Ce doped $Gd_3(Ga,Al)_5O_{12}$ Single Crystals, IEEE Trans. Nucl. Sci. 59 (2012) 2112-2115.

[17] J. Ueda, K. Aishima, S. Tanabe, Temperature and compositional dependence of optical and optoelectronic properties in Ce^{3+}-doped $Y_3Sc_2(Al_{1-x}$-$Ga_x)O_{12}$ (x=1,2,3), Opt. Mater. 35 (2013) 182-1857.

[18] B.-T. Zhang, J.-L. He, Z.-T. Jia, Y.-B. Li, S.-D. Liu, Z.-W. Wang, R.-H. Wang, X.-M. Liu, X.-T. Tao, Spectroscopy and Laser Properties of Yb-Doped $Gd_3 Al_x Ga_{5-x} O_{12}$ Crystal, Appl. Phys. Express 6 (2013) 082702.

[19] M. Nikl , P. Bohasek, E. Mihokova, M. Kobayashi, M. Ishii, Y. Usuki, V. Babin, S. Stolovich, S. Zazubovich, M. Bacci, Excitonic Emission of sheelite tungstates AWO_4 (A=Pb, Ca, Ba, Sr), J. Lumin. 87 (2000) 1136-1139.

[20] M.T. Lucchini, V. Babin, P. Bohacek, S. Gundacker, K. Kamada, M. Nikl, A. Petrosyan, A. Yoshikawa, E. Auffray, Effect of Mg^{2+} ions co-doping on timing performance and radiation tolerance of Cerium doped $Gd_3Al_2Ga_3O_{12}$ crystals, Nucl. Instrum. Methods Phys. Res. A 816 (2016) 176-183.

[21] D.L. Dexter, A Theory of Sensitized Luminescence in Solids, J. Chem. Phys. 21 (1951) 836–850.

[22] K. Brylew, W. Drozdowski, A.J. Wojtowicz, K. Kamada, A. Yoshikawa, Studies of low temperature thermoluminescence of GAGG:Ce and LuAG:Pr scintillator crystals using the T_{max}–T_{stop} method, J. Lumin. 154 (2014) 452–457.

[23] M. Kitaura, A. Sato, K. Kamada, A. Ohnishi, M. Sasaki, Phosphorescence of Ce-doped $Gd_3Al_2Ga_3O_{12}$ crystals studied using luminescence spectroscopy, J. Appl. Spectrosc. 115 (2014) 08351.

[24] E. Mihóková, K. Vávru, K. Kamada, V. Babin, A. Yoshikawa, M. Nikl, Deep trapping states in cerium doped $(Lu,Y,Gd)_3(Ga,Al)_5O_{12}$ single crystal scintillators, Radiat. Meas. 56 (2013) 98-101.

[25] J.M. Ogieglo, Luminescence and Energy Transfer in Garnet Scintillators, Utrecht University, Utrecht, 2012.

[26] D.M. Kondratiev, M.V. Korzhik, A.A. Fedorov, A.V. Pavlenko, Scintillation in cerium-activated gadolinium based crystals, Phys. Stat. Solidi (b) 197 (1996) 251-256.

[27] V. Laguta, M. Nikl, S. Zazubovich, Photothermally stimulated creation of electron and hole centers in Ce^{3+}-doped Y_2SiO_5 single crystals, Opt. Mater. 36 (2014) 1636-1641.

[28] P. Dorenbos, Electronic structure and optical properties of the lanthanide activated $RE_3(Al_{1-x}Ga_x)_5O_{12}$ (RE = Gd, Y, Lu) garnet compounds, J. Lumin. 134 (2013) 310-318.

Figure captions

Fig. 1. Streak camera image of PL intensity versus wavelength (horizontal) and time (vertical) in $PbWO_4$. Color version available online.

Fig. 2. Time-integrated $PbWO_4$ luminescence spectra after excitation at 254 nm (red dotted line) and 343 nm (blue solid line). Color version available online.

Fig. 3. Initial stage of spectrally integrated photoluminescence kinetics in $PbWO_4$ at 254 nm excitation (dots), the instrumental response function (green dotted line), and the best fit obtained using a bi-exponential decay function (red solid line). Color version available online.

Fig. 4. Initial part of $PbWO_4$ photoluminescence kinetics at 343 nm excitation (blue dashed line) and 254 nm excitation with pulse energy of 15 mJ/cm^2 (red solid line) and 1.5 mJ/cm^2 (green dotted line). Color version available online.

Fig. 5. Room temperature transmittance (blue) and absorption (red) spectra of GAGG:Ce sample. Color version available online.

Fig. 6. Photoluminescence spectra of GAGG:Ce after short-pulse excitation at 254 nm (red solid line) and 343 nm (blue dotted line). Color version available online.

Fig. 7. The initial part of PL response to a short excitation pulse after excitation directly to Ce^{3+} ions at 343 nm and via the matrix of GAGG single crystal at 254 nm (indicated). Smooth lines represent the fitting functions. Color version available online.

Fig. 8. Luminescence kinetics of Ce^{3+} at excitation directly to cerium ion at 343 nm and via the matrix of GAGG at 254 nm (indicated). Straight lines represent single exponential fits. Color version available online.

Fig. 9. Glow curves of thermally stimulated luminescence measured after irradiation of GAGG:Ce crystal at 94 K with photons of different energies E_{irr} indicated. In the inset, the TSL glow curve measured after irradiation with E_{irr}=3.6 eV at 295 K.

Fig. 10. Dependences of the maximum TSL intensity at 395 K on irradiation energy (points) and PL excitation spectra of the Ce^{3+} luminescence (lines) measured at irradiation temperatures of 94 K (a) and 295 K (b). Color version available online.

Paper P5

$Y_2CaAlGe(AlO_4)_3$:Ce and $Y_2MgAlGe(AlO_4)_3$:Ce garnet phosphors for white LEDs

Y. Tratsiak, Y. Bokshits, A. Borisevich, M. Korjik, **A. Vaitkevičius**, G. Tamulaitis

Opt. Mater. (Amst). 67 (2017) 108-112.

doi: 10.1016/j.optmat.2017.03.047.

Reprinted with permission from Elsevier Science & Technology Journals.

Optical Materials 67 (2017) 108–112

Contents lists available at ScienceDirect

Optical Materials

journal homepage: www.elsevier.com/locate/optmat

$Y_2CaAlGe(AlO_4)_3$:Ce and $Y_2MgAlGe(AlO_4)_3$:Ce garnet phosphors for white LEDs

Y. Tratsiak [a], [*], Y. Bokshits [a], A. Borisevich [b], M. Korjik [b], A. Vaitkevičius [c], G. Tamulaitis [c]

[a] Research Institute for Physical Chemical Problems of Belarusian State University, Leningradskaya str. 14, Minsk, Belarus
[b] Research Institute for Nuclear Problems, Belarusian State University, Bobruiskaya str. 11, Minsk, Belarus
[c] Semiconductor Physics Department and Institute of Applied Research, Vilnius University, Saulėtekio av. 3, Vilnius, Lithuania

ARTICLE INFO

Article history:
Received 13 February 2017
Received in revised form
24 March 2017
Accepted 26 March 2017
Available online 1 April 2017

Keywords:
Garnet
Substitution
Luminescence

ABSTRACT

New phosphors with the compositions $Y_2CaAlGe(AlO_4)_3$:Ce and $Y_2MgAlGe(AlO_4)_3$:Ce were obtained by co-precipitation technique. Their structural, morphological and luminescence properties were investigated. The 2Θ shift observed in XRD patterns was attributed to the substitution of Y^{3+} and Al^{3+} ions by Ca^{2+} (Mg^{2+}) and Ge^{4+} ions, respectively. It was shown that the composition of the new polycrystalline compounds is uniform. Both new phosphors exhibit a broad luminescence band, as usual for the Ce^{3+} ion emission in garnets. A shift of the band was observed and attributed to the different crystal field experienced by the Ce^{3+} ions in inequivalent sites in the complex garnets.

1. Introduction

White light-emitting diodes (LEDs) gain an increasing importance in general lighting and some other specific white-light applications due to their high efficiency, long lifetime, and other attractive properties [1–3]. In principle, two routes can be exploited for white light generation with LEDs: multichip blue-green-red color mixing, which is not currently exploited due to the different technological platforms necessary to fabricate the red, green, and blue light emitters, and phosphor-conversion LEDs consisting of InGaN-based blue LEDs and the phosphors emitting in green-yellow range.

The combination of InGaN LEDs with yttrium aluminum garnet activated by Ce^{3+} ions ($Y_3Al_5O_{12}$:Ce, YAG:Ce) dominates the market of the LED-based white light sources. The YAG:Ce phosphor efficiently absorbs 450 nm emission of InGaN LED and emits a broad luminescence band peaking at ~550 nm due to d-f interconfigurational transitions [4–10].

The white LEDs based on an InGaN chip and a single phosphor YAG:Ce are already more efficient than the current fluorescent lamps, however, they lack the emission in the red part of the spectrum to ensure a better color rendering, which is important for many white light applications [6]. The color rendering is being attempted to improve by the enhancement of the red component in the emission of phosphor-conversion LEDs [5,11–13]. Currently, two approaches are used: i) introduction of other rare earth (RE) ions (Eu^{3+}, Pr^{3+}, Sm^{3+}) [14–16] into the phosphor host matrix, along with the Ce^{3+} ions, or ii) partial isovalent replacement of Y^{3+} and Al^{3+} ions with other suitable cations to redshift the Ce^{3+} emission band [17–21].

The partial isovalent replacement of the host cations allows one to control the properties of the Ce^{3+} d-f interconfiguration luminescence by changing the crystal field in the position of the emitting Ce^{3+} ion. Therefore, the crystal structure engineering via the cation combinations in respect to the basic crystal composition ($Y_3Al_5O_{12}$), while the garnet crystal structure is maintained, might be attractive from the point of view of prospective applications. Partial substitution of trivalent Y cations, particularly, by the rare earth ions, and partial substitution of Al^{3+} by Ga^{3+}, results in a substantial improvement of the light yield by a factor of two, as compared to that in YAG:Ce single crystals and ceramics [22,23]. In addition to the change of the local crystal field, the variation of garnet composition also results in the band gap engineering. As a result, a blue shift of the resulting Ce^{3+} luminescence band is achieved by the introduction of In^{3+} or Ga^{3+} ions [17–19], while a red shift is achieved by the introduction of Gd^{3+}, Tb^{3+}, or La^{3+} ions [17–21] into the YAG:Ce structure.

Exploiting the isomorphism in garnets is another approach to obtain new compounds of this class. The compounds with garnet

---

[*] Corresponding author.
E-mail address: slon.zhenya@gmail.com (Y. Tratsiak).

http://dx.doi.org/10.1016/j.optmat.2017.03.047
0925-3467/© 2017 Elsevier B.V. All rights reserved.

structure belong to the Ia3d space group, and their general formula can be presented in the form $C_3[B]_2(A)_3O_{12}$, where, [], and () correspond to the cations in different crystalline positions: distorted dodecahedral, octahedral, and tetrahedral, respectively [24–27]. RE ions are located in dodecahedral positions. High tolerance of garnet crystalline lattice facilitates cation substitution. As a result, the corresponding metal-oxygen bond length changes, and the luminescence properties of RE ions are affected via the distortion of their crystalline environment. It should be noted that a heterovalent substitution of Y^{3+} and Al^{3+} ions in garnets is also possible but restricted by charge compensation [28,29].

This work was aimed at the study of potential of the co-precipitation technique for producing complex compounds with the garnet structure containing bi- and tetravalent cations. New phosphors with the garnet structure and the compositions $Y_2CaAlGe(AlO_4)_3$:Ce and $Y_2MgAlGe(AlO_4)_3$:Ce prospective for white light sources based on InGaN LEDs were fabricated and characterized. The ions in each of the pairs Ca^{2+} - Ge^{4+} and Mg^{2+} - Ge^{4+} were introduced in equal amounts to maintain the charge balance. Structural, morphological and luminescence properties of the new garnets are reported.

2. Experimental

2.1. Materials

Y_2O_3 (TU 48-4-191-72), $Al(NO_3)_3$ (Sigma-Aldrich, purum p.a.), $Ce(NO_3)_3\cdot 6H_2O$ (Fisher Chemical, laboratory reagent grade), NH_4HCO_3 (Sigma-Aldrich, puriss), $Mg(NO_3)_2$ (GOST 1108-75), $Ca(NO_3)_2$ (TU 6-09-1013-76), GeO_2 (TU 1774-001-95961127-2010), HNO_3 (GOST 4461-77) were used as reagents. 1 M water solution of $Y(NO_3)_3$ was prepared by dissolving Y_2O_3 in boiling HNO_3, while GeO_2 water solution was prepared by dissolving 0.4 g of GeO_2 per 100 ml of water. Aluminum nitrate was added in a form of 1 M aqueous solution. Aqueous solution of ammonium bicarbonate (15 g/100 g H_2 O) was used as a precipitant.

2.2. Synthesis procedures

Aqueous solution of metal containing precursors with stoichiometric proportions for Y_2 $CaAlGe(AlO_4)_3$:Ce (or Y_2 $MgAlGe(AlO_4)_3$:Ce) garnet were prepared by dissolving powdered $Ce(NO_3)_3\cdot 6H_2$ O and $Ca(NO_3)_2$ (or $Mg(NO_3)_2$) in the mixture of $Y(NO_3)_3$, $Al(NO_3)_3$ and GeO_2 solutions under intense stirring. Precursors were mixed in proportions that are necessary to substitute up to 50% of Al^{3+} ions in octahedral positions by Ge^{4+} ions and up to 33.3% of Y^{3+} ions in dodecahedral positions by Ca^{2+} or Mg^{2+} ions. Bi- and tetravalent cations were introduced in pairs Ca^{2+}-Ge^{4+} or Mg^{2+}-Ge^{4+} in order to maintain the charge balance.

Stirring was continued for 30 min to complete the dissolution of all components. Resulting transparent solution was then dropwise added to the precipitant solution under vigorous stirring. Obtained precipitate was separated via centrifugation and subsequently dried in air at 80 °C. After that dried precipitate was thermally treated in air in two steps: for 2 h at 600 °C, and for 2 h at 1500 °C.

2.3. Experimental techniques

X-ray diffraction (XRD) measurements were performed using diffractometer DRON 3 with CoKα radiation source. Lattice constants (a) were calculated with DICVOL06 software from FULLPROF package. The size of coherent scattering regions (CSR) and microstress values were calculated using Williamson-Hall analysis. Surface morphology of prepared samples was studied with scanning electron microscope LEO 1420. Photoluminescence (PL) measurements were performed using luminescence spectrometer SDL-2 and microscope system WITec Alpha 300S in confocal mode. For confocal measurements objective with the numerical aperture NA = 0.6 was used for excitation and collection of the PL signal ensuring spatial in-plane resolution of ~250 nm and axial resolution of ~1.6 μm. A CW laser diode (ALPHALAS) emitting at 405 nm was utilized for excitation. The microscope system was connected by an optical fiber to a spectrometer equipped with a thermo-electrically cooled CCD camera.

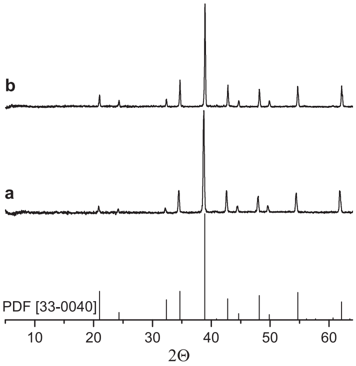

Fig. 1. XRD patterns of $Y_2CaAlGe(AlO_4)_3$:Ce (a) and $Y_2MgAlGe(AlO_4)_3$:Ce (b) garnets produced by co-precipitation. PDF[33-0040] is added for reference.

3. Results and discussion

X-Ray diffractograms of prepared $Y_2CaAlGe(AlO_4)_3$:Ce and $Y_2MgAlGe(AlO_4)_3$:Ce garnets are presented on Fig. 1.

Both samples exhibit intense reflections corresponding to the garnet phase (space group Ia3d). It should be noted that reflection lines of $Y_2CaAlGe(AlO_4)_3$:Ce are shifted to lower 2Θ angles with respect to those of $Y_2MgAlGe(AlO_4)_3$:Ce that, in turn, agree well with the Powder Diffraction File (PDF) reference [33-0040]. Such shift indicates that $Y_2CaAlGe(AlO_4)_3$:Ce has larger lattice constant than $Y_2MgAlGe(AlO_4)_3$:Ce.

After the comparison of ionic radii of corresponding cations with different oxygen coordinations (Table 1) one can see that aforementioned changes of the lattice constant are consistent with the substitution of Y^{3+} and Al^{3+} ions by larger ions Ca^{2+} and Ge^{4+}, respectively, in $Y_2CaAlGe(AlO_4)_3$:Ce. At the same time, since the radius of Mg^{2+} ion is smaller than Y^{3+} ion, the introduction of Mg^{2+} ions counterbalances the substitution of Al^{3+} ions by larger Ge^{4+} ions. As a result, no substantial changes of the lattice constant of $Y_2MgAlGe(AlO_4)_3$:Ce is observed.

The degree of powder crystallinity was estimated on the basis of the size of coherent scattering regions (CSR) and microstress values, which were determined from FWHM of the XRD lines

Table 1
Ionic radii of Y^{3+}, Al^{3+}, Mg^{2+}, Ca^{2+}, and Ge^{4+} in the garnet lattice sites with coordination numbers indicated in brackets.

Cation (c.n.)	Ca^{2+}(8)	Y^{3+}(8)	Mg^{2+}(8)	Al^{3+}(6)	Ge^{4+}(6)	Al^{3+}(4)	Ge^{4+}(4)
Ionic radii, Å	1.12	1.02	0.89	0.53	0.54	0.39	0.40

Table 2
Lattice constant, CSR size, and microstress value for $Y_2CaAlGe(AlO_4)_3$:Ce and $Y_2MgAlGe(AlO_4)_3$:Ce garnets.

Sample	a, Å	CSR, nm	ε, 10^{-5}
$Y_2CaAlGe(AlO_4)_3$:Ce	12.0531(2)	16.7	11
$Y_2MgAlGe(AlO_4)_3$:Ce	12.0014(5)	28.1	3.3

approximated by Voigt functions. The usual corrections for the CoKα2 radiation were taken into account. Estimated values are presented in Table 2.

Estimated CSR and microstress values of $Y_2MgAlGe(AlO_4)_3$:Ce are by factors of 1.7 larger and 3.3 smaller than those of $Y_2CaAlGe(AlO_4)_3$:Ce. Such discrepancies can be explained by the fact that identical processes occur in different temperature ranges during the heat treatment of the garnet precursors, due to the different chemical nature of the calcium and magnesium containing compounds. For example, magnesium and calcium carbonates decompose at 650 °C and 1000 °C, respectively, while garnets are formed only in the range of 900–1000 °C. Consequently, during the formation of $Y_2CaAlGe(AlO_4)_3$:Ce at least two concurrent processes take place at the same time, while the formation of $Y_2MgAlGe(AlO_4)_3$:Ce proceeds in the sequential manner upon temperature increase. As a result $Y_2CaAlGe(AlO_4)_3$:Ce has a larger defect density and smaller CSR.

Surface morphology of the obtained garnet samples was analyzed using SEM-images presented on Fig. 2. One can see that $Y_2CaAlGe(AlO_4)_3$:Ce and $Y_2MgAlGe(AlO_4)_3$:Ce powder grains have similar submicrometer scale structure. Particles are highly porous with aggregate size ranging from 0.5 to 100 μm. The aggregates of $Y_2CaAlGe(AlO_4)_3$:Ce and $Y_2MgAlGe(AlO_4)_3$:Ce are formed by crystallites with the diameter of ~200 nm and ~130 nm, respectively. Porosity of the aggregates could be caused by the gases released during the heat treatment of precursors or by heat-facilitated sintering of small particles resulting in the formation of intergranular voids on the aggregate surface.

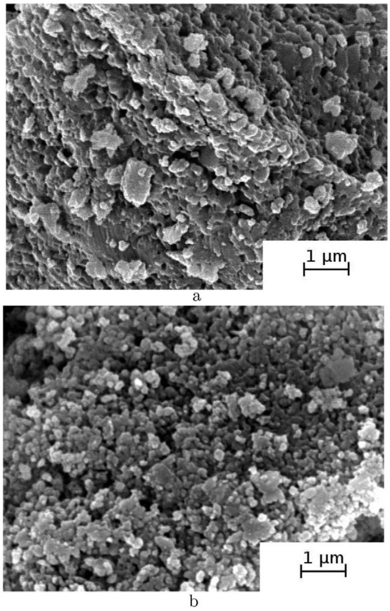

Fig. 2. SEM images of $Y_2CaAlGe(AlO_4)_3$:Ce (a) and $Y_2MgAlGe(AlO_4)_3$:Ce (b) samples.

The photoluminescence and photoluminescence excitation spectra of prepared samples (Fig. 3) have bands that are characteristic to interconfigurational transition between excited $4f^0\,5d^1$ and ground $4f^1$ electronic configurations of Ce^{3+} ion emission in garnet lattice [7,9,12,28,30–35].

Due to spin-orbit interaction, ground ^2F term is split into $^2F_{5/2}$ and $^2F_{7/2}$ multiplets separated by 2250 cm^{-1}. These two bands corresponding to the transitions from the lowest emissive level of $4f^0\,5d^1$ configuration to the $^2F_{5/2}$ and $^2F_{7/2}$ states strongly overlap and are unresolvable at room temperature. Typical luminescence excitation bands peaking at ~350 and ~440 nm arise from optical transitions from the $^2F_{5/2}$ ground state to the Stark components of $4f^0\,5d^1$ configuration. The most important difference of the PL excitation spectra of both garnets under study consists in a blue shift of the first PL excitation band for 20 nm with respect to bands in conventional YAG:Ce. Such shift enables more efficient excitation of luminescence in $Y_2CaAlGe(AlO_4)_3$:Ce and $Y_2MgAlGe(AlO_4)_3$:Ce by InGaN-based laser diodes with the emission peaking at 405 nm.

In addition to Ce^{3+} ions obtained garnets can be co-doped with RE ions to increase the emission in red spectral region (see, e.g., the spectrum with amplification factor of 1.66 in Fig. 3b). Under excitation at 405 nm, we observed several narrow luminescence bands in the spectral range between 550 and 720 nm. They correspond to luminescent transitions of the following ions: Pr^{3+} (bands at 546-552, 606-612, 614-630, 634-639, 688-709, and 713–763 nm) [36], Er^{3+} (two bands peaking at 542-561 and 644–682 nm) [36], and Eu^{3+} (bands peaking at 590-598, 610-630, 621-636, and 696–715 nm) [36]. This is a direct evidence that the trivalent ions of RE elements can be stabilized, along with Ce^{3+} ions in the lattice of garnets under study. The optimization of the controlled fabrication of co-doped garnets is the subject of further investigation. Results presented in Fig. 3b (see, e.g., the spectrum with amplification factor of 1.66) demonstrate that the emission spectra of the new Ce-doped garnets might be finetuned by controlled introduction of Eu^{3+}, Er^{3+}, or Pr^{3+} ions.

Emission spectra of $Y_2MgAlGe(AlO_4)_3$:Ce exhibit high aggregate-to-aggregate reproducibility. Meanwhile, significant aggregate-to-aggregate variations of luminescence intensity were observed in both compounds. These variations might be interpreted by different aggregate density influencing both the excitation depth and light extraction. Photoluminescence band parameters for $Y_2CaAlGe(AlO_4)_3$:Ce and $Y_2MgAlGe(AlO_4)_3$:Ce are listed in Table 3.

PL intensity of $Y_2MgAlGe(AlO_4)_3$:Ce is higher than that of $Y_2CaAlGe(AlO_4)_3$:Ce by a factor of 1.25. This feature can be explained by a better crystallinity, as evidenced by the higher average CSR and lower microstress values obtained on the basis of XRD measurements.

Since PL band consists of two strongly overlapping bands, we use the spectral center of mass (SCM) instead of the band peak position to characterize the PL band. We observe that in comparison to $Y_2MgAlGe(AlO_4)_3$:Ce and $Y_2CaAlGe(AlO_4)_3$:Ce garnets exhibits a blue shift of SCM. This shift might be attributed to larger lattice stresses due to a partial substitution of Y^{3+} and Al^{3+} cations in the garnet structure. When Al^{3+} ion is substituted by a Ge^{4+} ion and Y^{3+} is substituted by Ca^{2+}, the length of M – O (where M = Ge^{4+}, Ca^{2+}) bonds becomes larger than the length of bonds in

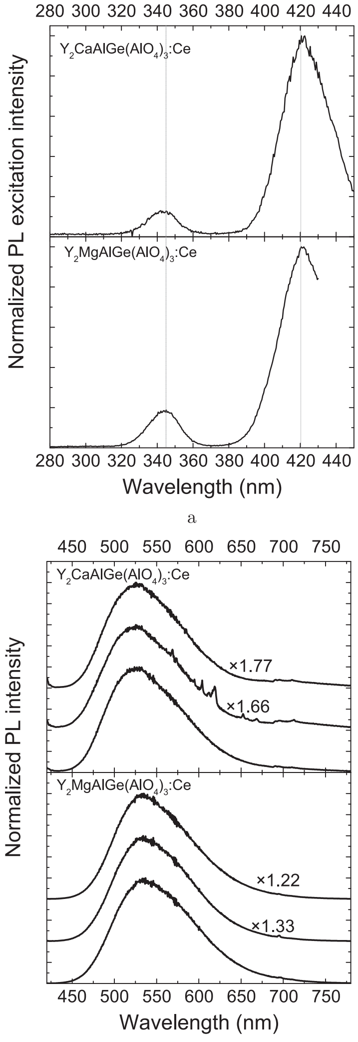

a

b

Fig. 3. Spatially-integrated normalized photoluminescence excitation spectra for luminescence at 550 nm (a) and luminescence spectra of three different grains of $Y_2CaAlGe(AlO_4)_3$:Ce [upper panel in (b)] and $Y_2MgAlGe(AlO_4)_3$:Ce [lower panel in (b)] under 405 nm excitation. The intensity normalization factors are indicated.

Table 3
Photoluminescence band characteristics of $Y_2CaAlGe(AlO_4)_3$:Ce and $Y_2MgAlGe(AlO_4)_3$:Ce garnets.

Sample	PL intensity, a.u	PL center of mass, nm	FWHM, nm
$Y_2CaAlGe(AlO_4)_3$:Ce	0.05	549°±°0.7	104°±°1
$Y_2MgAlGe(AlO_4)_3$:Ce	1	556°±°1.4	105°±°3

the original garnet prior to the substitution, thus expanding the crystal lattice (see Table 1). Hence, the bond length between Ce^{3+} and O^{2-} also increases and as a result the influence of the crystal field becomes weaker, and a blue shift of the emission wavelength occurs. The substitution of Y^{3+} by Mg^{2+} in the garnet structure results, on the contrary, in the decrease of Ce–O bond length in dodecahedral position and consequent strengthening of the crystal field and thus the emission band experiences red shift.

4. Conclusion

In this paper we described preparation of $Y_2CaAlGe(AlO_4)_3$:Ce and $Y_2MgAlGe(AlO_4)_3$:Ce garnets using co-precipitation technique. XRD reflections of $Y_2CaAlGe(AlO_4)_3$:Ce are shifted to lower 2Θ angles, as one can expect due to substituting Y^{3+} and Al^{3+} ions by Ca^{2+} and Ge^{4+} ions, respectively. $Y_2MgAlGe(AlO_4)_3$:Ce exhibit higher CSR and lower microstress values. SEM analysis of $Y_2CaAlGe(AlO_4)_3$:Ce and $Y_2MgAlGe(AlO_4)_3$:Ce obtained by co-precipitation shows that these garnets consist of up 100 μm aggregates of particles up to ~200 and ~130 nm in size for $Y_2CaAlGe(AlO_4)_3$:Ce and $Y_2MgAlGe(AlO_4)_3$:Ce, respectively.

Photoluminescence spectra of both garnets are dominated by a characteristic broad band of Ce^{3+} ions. Emission spectral center of mass of $Y_2MgAlGe(AlO_4)_3$:Ce is redshifted by 7 nm with respect to that of $Y_2CaAlGe(AlO_4)_3$:Ce. This effect is caused by the substitution of Mg^{2+} and Ge^{4+} for Y^{3+} and Al^{3+} ions in the garnet structure, respectively, what, in turn, results in an increased crystal field around Ce^{3+} ions. The study of photoluminescence with the spatial resolution high enough to resolve individual aggregates showed no spectral difference in different aggregates. This is an additional evidence of the high quality of the crystal structure of the particles forming the aggregates. Observed aggregate-to-aggregate variation of the luminescence intensity (on the order of 25%) might be attributed to different excitation and light extraction conditions for each aggregate.

Acknowledgements

The collaboration support by the COST Action TD1401 "Fast Advanced Scintillator Timing (FAST)" is gratefully acknowledged.

References

[1] E.F. Schubert, J.K. Kim, Solid-state light sources getting smart, Science 308 (5726) (2005) 1274–1278.

[2] S. Tanabe, S. Fujita, A. Sakamoto, S. Yamamoto, Glass ceramics for solid state lighting, Adv. Glass Opt. Mater. 173 (2012) 19–25, http://dx.doi.org/10.1002/9781118407974.ch3. http://doi.wiley.com/10.1002/9781118407974.ch3.

[3] S. Fujita, S. Yoshihara, A. Sakamoto, S. Yamamoto, S. Tanabe, YAG glass-ceramic phosphor for white LED (I): background and development, in: I.T. Ferguson, J.C. Carrano, T. Taguchi, I.E. Ashdown (Eds.), Fifth International Conference on Solid State Lighting, International Society for Optics and Photonics, 2005, p. 594111, http://dx.doi.org/10.1117/12.614668, in: http://proceedings.spiedigitallibrary.org/proceeding.aspx?doi=10.1117/12.614668.

[4] H.S. Jang, Y.-H. Won, D.Y. Jeon, Improvement of electroluminescent property of blue LED coated with highly luminescent yellow-emitting phosphors, Appl. Phys. B 95 (4) (2009) 715–720.

[5] R. Marin, G. Sponchia, P. Riello, R. Sulcis, F. Enrichi, Photoluminescence properties of YAG: Ce^{3+},Pr^{3+} phosphors synthesized via the Pechini method for white LEDs, J. Nanoparticle Res. 14 (6) (2012) 1–13.

[6] N. Narendran, Y. Gu, J.P. Freyssinier, H. Yu, L. Deng, Solid-state lighting: failure

analysis of white LEDs, J. Cryst. Growth 268 (34) (2004) 449–456.

[7] C.-Y. Shen, K. Li, Q.-l. Hou, H.-J. Feng, X.-Y. Dong, White LED based on YAG: Ce,Gd phosphor and CdSe-ZnS core/shell quantum dots, IEEE Photonics Technol. Lett. 22 (12) (2010) 884–886.

[8] T. Tamura, T. Setomoto, T. Taguchi, Illumination characteristics of lighting array using 10 candela-class white LEDs under AC 100 V operation, J. Lumin. 8789 (2000) 1180–1182.

[9] N. Zhang, D. Wang, L. Li, Y. Meng, X. Zhang, N. Ming, YAG: Ce phosphors for WLED via nano-pesudoboehmite sol-gel route, J. Rare Earths 24 (3) (2006) 294–297.

[10] S. Zhang, W. Zhuang, T. He, Y. Liu, R. Liu, W. Gao, Y. Hu, Z. Long, Study on co-precipitation synthesized $Y_3Al_5O_{12}$:Ce yellow phosphor for white LED, J. Rare Earths 28 (5) (2010) 713–716.

[11] Y.S. Lin, R.S. Liu, B.-M. Cheng, Investigation of the luminescent properties of Tb^{3+}-Substituted YAG: Ce, Gd phosphors, J. Electrochem. Soc. 152 (6) (2005) J41–J45.

[12] P.Y. Jia, J. Lin, X.M. Han, M. Yu, Pechini solgel deposition and luminescence properties of $Y_3Al_{5-x}GaxO_{12}$:Ln^{3+} (Ln^{3+}=Eu^{3+}, Ce^{3+}, Tb^{3+}; 0¡x¡5) thin films, Thin Solid Films 483 (12) (2005) 122–129.

[13] H. Yang, Y.-S. Kim, Energy transfer-based spectral properties of Tb-, Pr-, or Sm-codoped YAG: Ce nanocrystalline phosphors, J. Lumin. 128 (10) (2008) 1570–1576.

[14] Y. Zhou, J. Lin, M. Yu, S. Wang, H. Zhang, Synthesis-dependent luminescence properties of $Y_3Al_5O_{12}$:Re^{3+} (Re=Ce, Sm, Tb) phosphors, Mater. Lett. 56 (5) (2002) 628–636, http://dx.doi.org/10.1016/S0167-577X(02)00567-0.

[15] H.S. Jang, W.B. Im, D.C. Lee, D.Y. Jeon, S.S. Kim, Enhancement of red spectral emission intensity of $Y_3Al_5O_{12}$:Ce^{3+} phosphor via Pr co-doping and Tb substitution for the application to white LEDs, J. Lumin. 126 (2) (2007) 371–377, http://dx.doi.org/10.1016/j.jlumin.2006.08.093.

[16] S. Mukherjee, V. Sudarsan, R. Vatsa, A. Tyagi, Luminescence studies on lanthanide ions (Eu^{3+}, Dy^{3+} and Tb^{3+}) doped YAG: Ce nano-phosphors, J. Lumin. 129 (1) (2009) 69–72, http://dx.doi.org/10.1016/j.jlumin.2008.08.003.

[17] H. Yang, D.-K. Lee, Y.-S. Kim, Spectral variations of nano-sized $Y_3Al_5O_{12}$:Ce phosphors via codoping substitution and their white LED characteristics, Mater. Chem. Phys. 114 (23) (2009) 665–669.

[18] Y. Pan, M. Wu, Q. Su, Tailored photoluminescence of YAG: Ce phosphor through various methods, J. Phys. Chem. Solids 65 (5) (2004) 845–850.

[19] S. Lee, D.S. Jung, J.M. Han, H. Young Koo, Y.C. Kang, Fine-sized $Y_3Al_5O_{12}$:Ce phosphor powders prepared by spray pyrolysis from the spray solution with barium fluoride flux, J. Alloys Compd. 477 (12) (2009) 776–779.

[20] H.S. Jang, W.B. Im, D.C. Lee, D.Y. Jeon, S.S. Kim, Enhancement of red spectral emission intensity of $Y_3Al_5O_{12}$:Ce^{3+} phosphor via Pr co-doping and Tb substitution for the application to white LEDs, J. Lumin. 126 (2) (2007) 371–377.

[21] Y.X. Pan, W. Wang, G.K. Liu, S. Skanthakumar, R.A. Rosenberg, X.Z. Guo, K.K. Li, Correlation between structure variation and luminescence red shift in YAG: Ce, J. Alloys Compd. 488 (2) (2009) 638–642.

[22] N.J. Cherepy, J.D. Kuntz, T.M. Tillotson, D.T. Speaks, S.A. Payne, B. Chai, Y. Porter-Chapman, S.E. Derenzo, Cerium-doped single crystal and transparent ceramic lutetium aluminum garnet scintillators, Nucl. Instrum. Methods Phys. Res. Sect. A Accel. Spectrom. Detect. Assoc. Equip. 579 (1) (2007) 38–41, http://dx.doi.org/10.1016/j.nima.2007.04.009.

[23] K. Kamada, T. Endo, K. Tsutumi, T. Yanagida, Y. Fujimoto, A. Fukabori, A. Yoshikawa, J. Pejchal, M. Nikl, Composition engineering in cerium-doped $(Lu,Gd)_3(Ga,Al)_5O_{12}$ single-crystal scintillators, Cryst. Growth Des. 11 (10) (2011) 4484–4490, http://dx.doi.org/10.1021/cg200694a. http://pubs.acs.org/doi/abs/10.1021/cg200694a.

[24] M.K. Ashurov, Y. Voronko, V.V. Osiko, A.A. Sobol, M.I. Timoshechkin, Spectroscopic study of stoichiometry deviation in crystals with garnet structure, Phys. Status Solidi (A) 42 (1) (1977) 101–110.

[25] F. Euler, J.A. Bruce, Oxygen coordinates of compounds with garnet structure, Acta Crystallogr. 19 (6) (1965) 971–978.

[26] C.R. Stanek, K.J. McClellan, M.R. Levy, C. Milanese, R.W. Grimes, The effect of intrinsic defects on garnet scintillator performance, Nucl. Instrum. Methods Phys. Res. Sect. A Accel. Spectrom. Detect. Assoc. Equip. 579 (1) (2007) 27–30.

[27] F.C. Hawthorne, Some systematics of the garnet structure, J. Solid State Chem. 37 (2) (1981) 157–164.

[28] Y. Zhang, L. Li, X. Zhang, Q. Xi, Temperature effects on photoluminescence of YAG: Ce^{3+} phosphor and performance in white light-emitting diodes, J. Rare Earths 26 (3) (2008) 446–449.

[29] X. Wang, Y. Wang, Synthesis, structure, and photoluminescence properties of Ce^{3+} -doped Ca_2 YZr_2 Al_3 O_{12}:A novel garnet phosphor for white LEDs, J. Phys. Chem. C 119 (28) (2015) 16208–16214, http://dx.doi.org/10.1021/acs.jpcc.5b01552. http://pubs.acs.org/doi/abs/10.1021/acs.jpcc.5b01552.

[30] H.M.H. Fadlalla, C.C. Tang, YAG: Ce^{3+} nano-sized particles prepared by precipitation technique, Mater. Chem. Phys. 114 (1) (2009) 99–102.

[31] G.P. Shevchenko, E.V. Tret'yak, S.K. Rakhmanov, G.E. Malashkevich, Effect of polyvinylpyrrolidone on the morphology and spectral luminescence of $Y_3Al_5O_{12}$:Ce^{3+}, Russ. J. Phys. Chem. A 87 (8) (2013) 1397–1403, http://dx.doi.org/10.1134/S0036024413080219. http://link.springer.com/10.1134/S0036024413080219.

[32] Z. Yang, X. Li, Y. Yang, X. Li, The influence of different conditions on the luminescent properties of yag:ce phosphor formed by combustion, J. Lumin. 122123 (2007) 707–709, http://dx.doi.org/10.1016/j.jlumin.2006.01.266 luminescence and Optical Spectroscopy of Condensed MatterProceedings of the 2005 International Conference on Luminescence and Optical Spectroscopy of Condensed Matter2005 International Conference on Luminescence and Optical Spectroscopy of Condensed Matter, http://www.sciencedirect.com/science/article/pii/S0022231306002705.

[33] K. Zhang, W. Hu, Y. Wu, H. Liu, Influence of processing techniques on the properties of YAG: Ce nanophosphor, Ceram. Int. 35 (2) (2009) 719–723.

[34] K. Zhang, H. Liu, Y. Wu, W. Hu, Synthesis of $(Y,Gd)_3Al_5O_{12}$:Ce nanophosphor by co-precipitation method and its luminescence behavior, J. Mater. Sci. 42 (22) (2007) 9200–9204.

[35] S.A. Samoylenko, E.V. Tret'yak, G.P. Shevchenko, S.E. Kichanov, D.P. Kozlenko, G.E. Malashkevich, A.P. Stupak, B.N. Savenko, Crystal structure and optical properties of $Lu_3Al_5O_{12}$:Ce_3 obtained by a colloidal chemical synthesis method, J. Appl. Spectrosc. 81 (6) (2015) 1048–1055, http://dx.doi.org/10.1007/s10812-015-0049-4. http://link.springer.com/10.1007/s10812-015-0049-4.

[36] M. Sekita, H. Haneda, S. Shirasaki, T. Yanagitani, Optical spectra of undoped and rare-earth-(=Pr, Nd, Eu, and Er) doped transparent ceramic $Y_3Al_5O_{12}$, J. Appl. Phys. 69 (6) (1991) 3709–3718, http://dx.doi.org/10.1063/1.348959.

Paper P6

Non-Linear Optical Phenomena in Detecting Materials as a Possibility for Fast Timing in Detectors of Ionizing Radiation

M. V Korjik, E. Auffray, O. Buganov, A.A. Fedorov, I. Emelianchik, E. Griesmayer, V. Mechinsky, S. Nargelas, O. Sidletskiy, G. Tamulaitis, S.N. Tikhomirov, **A. Vaitkevičius**

IEEE Trans. Nucl. Sci. 63 (2016) 2979–2984.

doi:10.1109/TNS.2016.2617461.

Non-Linear Optical Phenomena in Detecting Materials as a Possibility for Fast Timing in Detectors of Ionizing Radiation

M. V. Korjik, E. Auffray, *Member, IEEE*, O. Buganov, A. A. Fedorov, I. Emelianchik, E. Griesmayer, V. Mechinsky, S. Nargelas, O. Sidletskiy, G. Tamulaitis, S. N. Tikhomirov, and A. Vaitkevičius

***Abstract*— The time resolution of the detectors currently in use is limited by 50–70 ps due to the spontaneous processes involved in the development of the response signal, which forms after the relaxation of carriers generated during the interaction. In this study, we investigate the feasibility of exploiting sub-picosecond phenomena occurring after the interaction of scintillator material with ionizing radiation by probing the material with ultra-short laser pulses. One of the phenomena is the elastic polarization due to the local lattice distortion caused by the displacement of electrons and holes generated by ionization. The key feature of the elastic polarization is its short response time, which makes it prospective for using as an optically detectable time mark. The nonlinear optical absorption of femtosecond light pulses of appropriate wavelength is demonstrated to be a prospective tool to form the mark. This study was aimed at searching for inorganic crystalline media combining scintillation properties and non-linear absorption of ultra-short laser pulses. The nonlinear pump-and-probe optical absorption technique with 200 fs laser pulses was used to study the effects in lead tungstate, garnet-type, and diamond scintillator crystals.**

***Index Terms*— Fast timing, inorganic scintillation material, particle colliders, two–photon absorption.**

I. INTRODUCTION

THE upcoming experiments in high-energy physics require the time resolution of scintillation detectors better than 10-20 ps. This is not feasible using the conventional scintillation detectors with the time response limited by the time of carrier relaxation and transfer to the radiative recombination centers in the scintillator material.

In this study, we investigate the feasibility of using the phenomena occurring in parallel with the carrier relaxation within the very first picoseconds after the ionization starts. One of the phenomena is the elastic polarization due to the local lattice distortion caused by the displacements of electrons and holes generated by the ionization. This local distortion in the lattice results in redistribution of the density of states (DOS) of electron in the conduction band in close vicinity of the hole. The key feature of the elastic polarization is its short response time, which makes it prospective for using as an optically detectable time mark. Nonlinear optical absorption of femtosecond light pulses at appropriate wavelength is considered to be a tool to form the mark.

The effect of elastic polarization should be observed in many crystalline compounds. According to our estimations, the strongest effect should be observed in compounds with the bottom of the conduction band formed by $n\mathbf{d}$ orbitals of the lattice cations. According to the crystal field theory, these orbitals are most sensitive to distortions of the crystal field in the vicinity of emitting centers. Thus, the crystals with lattice cations having strong contribution of **d** orbitals in conduction band (tungstates, molybdates, rare-earth and yttrium garnets, perovskites, oxy-orthosilicates, etc.) might be good candidates for using them as timing tools.

Our study was aimed at searching for inorganic crystalline media exhibiting good scintillation properties as well as strong non-linear absorption of ultra-short laser pulses. Accordingly, we selected three scintillation crystals: self-activated lead tungstate $PbWO_4$ and mixed $Gd_3(Ga_{0.5}\text{-}Al_{0.5})_5O_{12}$:Ce and yttrium $Y_3Al_5O_{12}$:Ce garnets. Lead tungstate is currently the most extensively used scintillation material in high energy physics experiments [1], while the recently developed mixed garnet crystals showed fast response and highlight yield up to 56000 ph/MeV [2]. YAG:Ce is also fast and bright scintillation material exhibiting one of the highest radiation hardness among the scintillators currently in use under both gamma and high energy proton irradiation [3]. Recently, we confirmed the influence of ionization at 122 keV on the two photon absorption of femtosecond laser pulses in $PbWO_4$ crystals [4]. The observed effect encouraged our further study in this direction to develop a novel detecting technique exploiting the interaction of short laser pulses with crystalline media excited

---

Manuscript received January 22, 2016; revised September 11, 2016 and September 20, 2016, and October 6, 2016; accepted October 10, 2016. Date of publication October 13, 2016; date of current version December 14, 2016. The joint research was supported by EC project AIDA 2020. The work was accomplished in the framework of activities of the network Crystal Clear Collaboration at CERN and supported by the AIDA-II Horizon 2020 Project and COST Action TD1401.

M. V. Korjik, A. A. Fedorov, I. Emelianchik, and V. Mechinsky are with the Research Institute for Nuclear Problems, 220030 Minsk, Belarus (e-mail: Mikhail.Korjik@cern.ch; Andrei.Fedorov@cern.ch; emelianchik@hep.by; Vitaly.Mechinsky@cern.ch).

E. Auffray is with CERN, 1211 Geneva, Switzerland (e-mail: Etiennette.Auffray@cern.ch).

O. Buganov and S. N. Tikhomirov are with Stepanov Physics Institute, 220072 Minsk, Belarus (e-mail: oleg.buganov@tut.by; tikhomirov@imaph.bas-net.by).

E. Griesmayer is with the Vienna University of Technology, 1040 Vienna, Austria (e-mail: erich.griesmayer@tuwien.ac.at).

S. Nargelas, G. Tamulaitis, and A. Vaitkevičius are with the Semiconductor Physics Department and Institute of Applied Research, Vilnius University, 10222 Vilnius, Lithuania (e-mail: saulius.nargelas@ff.vu.lt; gintautas.tamulaitis@ff.vu.lt; augustas.vaitkevicius@ff.vu.lt).

O. Sidletskiy is with ISMA, 61001 Kharkov, Ukraine (e-mail: osidletskiy@yahoo.com).

Digital Object Identifier 10.1109/TNS.2016.2617461

by ionizing radiation. The results of this study are presented in the current paper. In addition to pure scintillation materials synthetic diamond was probed with two-photon absorption.

II. One and Two-Photon Absorption in Scintillation Materials

One-photon absorption is extensively used to monitor different effects in ionizing radiation detectors. For instance, nanosecond laser pulses are used to monitor radiation damage effects in PWO crystals [5]. In fact, this technique enables monitoring slow change in the detector material properties, particularly accumulation of the color centers under ionizing radiation.

One-photon absorption is not convenient to explore changes in the DOS due to strong absorption of single photons via electronic transitions between valence and conduction bands. This is due to the origin of the bands of the majority of inorganic wide band gap compounds: p electronic states form the top of valence band, whereas d and f states of metal ions dominate in forming the bottom of the conduction band. Dipole-allowed p-d transitions result in the absorption coefficient for the interband transitions at the order of 10^5 cm^{-1}.

The selection rules for two-photon absorption are different [6]: p-d transitions become forbidden and their rate falls by orders of magnitude. Consequently, the photons absorbed via two-photon absorption propagate relatively long distances in the crystal.

Two-photon absorption can involve photons of the same frequency generated by the same laser or simultaneously available photons of different frequencies [7]. The two-photon absorption involving one pump and one probe photon is a convenient tool for studying both time and spectral parameters of the interband absorption. Recently, the pump-probe technique was exploited to study $PbWO_4$ crystals [8]. The pump-induced changes in material properties resulting in modified probe absorption in the sample volume where the pump and probe beams spatially overlap have been recorded.

III. Experimental

Two pump and probe setups were exploited in our study as described in [8]. In the first setup, the 140 fs long pulses of the second harmonic of $Al_2O_3:Ti^{3+}$ laser radiation was used to generate both the pump beam with a fixed wavelength of 395 nm and a white continuum ranging 400 to 1100 nm, which was generated in water by a fraction of the fundamental laser radiation at 790 nm and used as a probe.

The second setup was used for pump and probe measurements at different pump beam wavelengths from 346 to 650 nm. The experiments were performed at different pump pulse energies. The system was based on a femtosecond Yb:KGW laser producing 200 fs pulses at 1030 nm with repetition rate of 30 kHz.

The samples of $PbWO_4$ crystals under study were fabricated at the Bogoroditsk Technical Chemical Plant (Russia) for PANDA experiment at FAIR (Darmstadt, Germany). The garnet samples were produced by ISMA (Kharkov, Ukraine). All the samples under study had a thickness of 1cm.

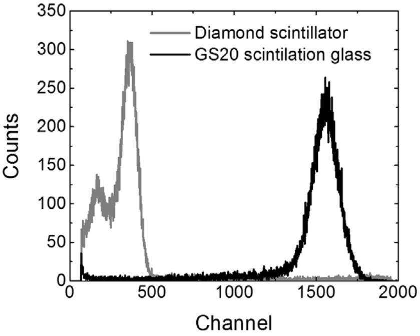

Fig. 1. ^{239}Pu alpha-particle amplitude spectra measured with diamond scintillator #11 (dots) and light GS20 scintillation glass (crosses).

The diamond samples were produced by (ADAMAS-BSU), Minsk, Belarus, using the High Pressure High Temperature (HPHT) technique. The samples had yellow coloration due to the presence of nitrogen. The cutoff of the transmission spectrum of both samples was found to be near 420 nm. They had dimensions of 4x4x0.3 mm. Both the samples under study had the charge collecting distance of $\sim$ 0.1 mm and were tested to detect the ionizing radiation via electrical signal readout with the electrodes evaporated on their larger surfaces. Both the crystals exhibited a luminescence band peaked in the vicinity of 530 nm and having a broad excitation band peaked at ~340 nm. One of the samples (4.8) was not scintillating, however another one (11) had a clear scintillation effect under excitation by alpha-particles. The scintillating crystal had a photo-excited luminescence intensity by one order of magnitude larger. In addition to HPHT diamonds a clear diamond produced by Chemical Vapor Deposition (CVD) method with dimensions 4x2x0.15 mm also was studied. Figure 1 shows the room temperature amplitude spectra of ^{238}Pu alpha-particles measured with 0.3 mm thick diamond crystal and a reference spectrum obtained with light scintillation glass GS20. CWD diamond also showed scintillations at the detection of alpha-particles, however its light output was found to be three times smaller than of HPHT diamond.

Luminescence of synthetic diamonds is well described [9], [10] and is related to the defects, which appear in the crystals due to peculiarities of technology. The green luminescence is caused by complex defects containing nickel and nitrogen.

All the measurements were performed at room temperature.

IV. Two-Photon Absorption in $PbWO_4$ Single Crystal

The change in optical density for the probe beam induced by the pump at the wavelength of 394 nm is presented as a function of the delay between pump and probe in Figure 2. The spectral dependence of the two-photon absorption is described elsewhere [4], [8]. The nonlinear response has a

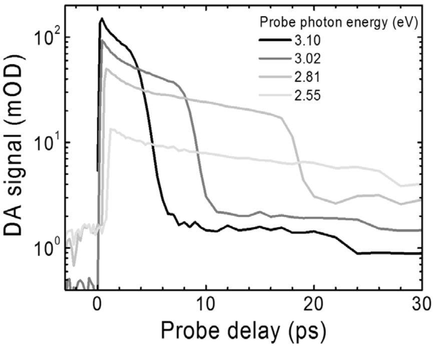

Fig. 2. Kinetics of differential absorption in PWO scintillation crystal for 394 nm pump at different probe wavelengths (indicated).

short rise time, decays with characteristic time constant of few picoseconds, and a slower decay afterwards. The fast decrease of the induced absorption at the rear edge of the response is explained by the separation of the pump and probe beams in space, since the beams are focused on the same spot of the sample surface at slightly different angles. The duration of the nonlinear absorption depends also on the pump and probe wavelengths due to the dispersion of the light velocity.

The most important feature of the response is that the leading edge of the differential absorption is limited by laser pulse shape rather than by material properties. Thus, the processes responsible for the nonlinear absorption occur on femtosecond domain.

V. TWO-PHOTON ABSORPTION IN $Gd_3(Al_{0.5}$-$Ga_{0.5})_5O_{12}$:Ce SINGLE CRYSTAL

Figure 3 shows the change in optical density at several wavelength induced by the pump at the wavelength of 360 nm (3.44 eV) in $Gd_3(Ga_{0.5}$-$Al_{0.5})_5O_{12}$:Ce (GAGG:Ce) crystal. GAGG:Ce has more complicated band structure than $PbWO_4$. The crystal contains a narrow sub-band formed by Gd^{3+}ions bellow the conduction band in the band gap, which equals 6.4 eV in this material. Moreover, the crystal is doped with Ce^{3+} ions causing two absorption bands peaked in the vicinity of 340 and 440 nm. Therefore, pumping of the sample was carried out by pulses at the wavelength between the two absorption bands of activator.

Note that the two-photon absorption in GAGG:Ce is an order of magnitude weaker than that in $PbWO_4$. Figure 4 shows the spectral dependence of the two-photon absorption at different delays after the pump pulse at 360 nm.

The two–photon absorption peak is observed when the total energy of pump and probe exceeds the band gap. As evident in Fig. 4, the effect appears, when the energy of the probe photon exceeds 3 eV.

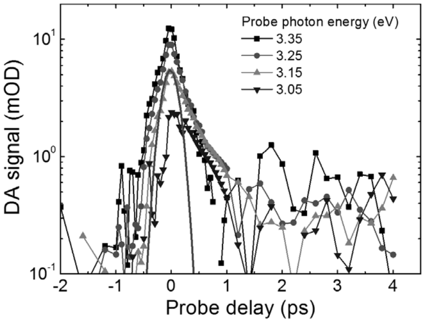

Fig. 3. Kinetics of differential absorption in $Gd_3(Ga_{0.5}$-$Al_{0.5})_5O_{12}$:Ce scintillation crystal for 360 nm (3.44 eV) pump at different probe energies (indicated).

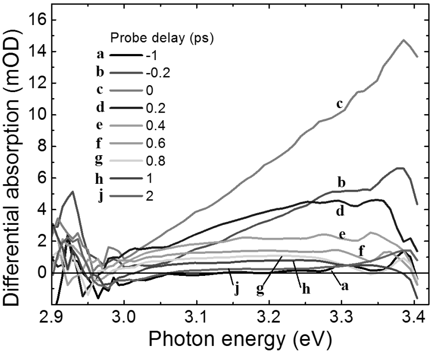

Fig. 4. Spectrum of differential absorption of $Gd_3(Ga_{0.5}$-$Al_{0.5})_5O_{12}$:Ce scintillation crystal for 360 nm (3.44 eV) pump at different delays between pump and probe (indicated).

VI. TWO PHOTON ABSORPTION IN Y_3 Al_5 O_{12}:Ce SINGLE CRYSTAL

The band gap of yttrium aluminum garnet is close to that of GAGG band gap, however, in contrast to PWO and GAGG, the DOS of conduction band in YAG is formed predominantly by 4d orbitals. Nevertheless, we did not observe two-photon absorption in YAG:Ce for the pump plus probe photon energies in the range 6.2-6.8 eV (see Figure 5). The drop in the spectrum in the vicinity of 6.9 eV is caused by contribution of scattered pump beam when the energies of pump and probe coincide.

When pump energy corresponds to the excitation to a higher level of d configuration of Ce^{3+} ions, the intracenter relaxation is observed in the kinetics of the differential absorption. Figure 6 shows this behavior at pump at 264nm (4.73 eV) and two different probe wavelength of 430 nm (2.9eV) and 700 nm (1.75 eV).

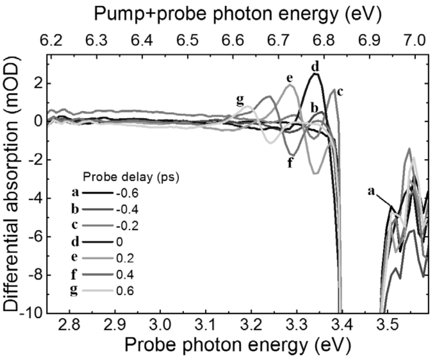

Fig. 5. Spectrum of differential absorption of $Y_3Al_5O_{12}$:Ce for 360 nm (3.44 eV) pump at different delays between pump and probe (indicated).

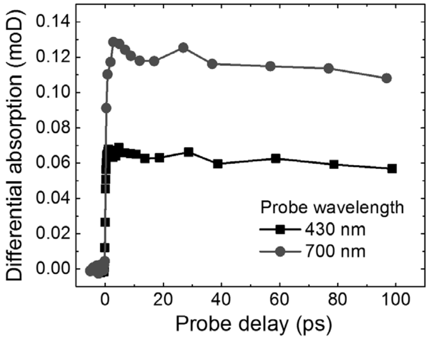

Fig. 6. Kinetics of differential absorption in $Y_3Al_5O_{12}$:Ce for 264 nm (4.73 eV) pump and two different probe wavelength.

Photons with energy 4.73 eV excite Ce^{3+} centers, the excitation promptly relax to the emitting state, while the probe photons throws the electrons up to conduction band. The observed decrease of induced absorption in time is caused by radiative recombination from the Ce^{3+} emitting level.

VII. Two-Photon Absorption in Synthetic Diamond Crystal

In contrary to the complex oxide crystals based on oxy-anionic complexes, diamond is a wide band gap indirect semiconductor having a relatively simple electronic band structure due to its monatomic network. Two-photon absorption in nitrogen-free diamond is studied in detail [11]. The lowest two-photon absorption band was observed to peak at the total energy of the two photons of 5.5 eV. This energy corresponds to the indirect transition to conduction band. The direct two-photon absorption was found to occur at 6.5 eV.

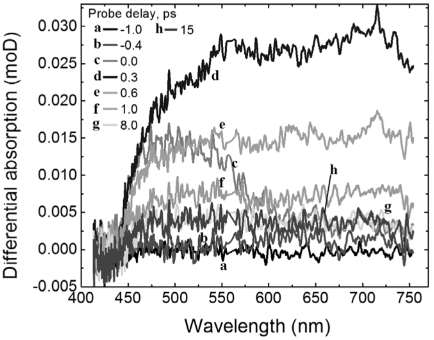

Fig. 7. Spectrum of differential absorption of diamond sample 4.8 at 395 nm (3.16 eV) pump at different delays between pump and probe (indicated).

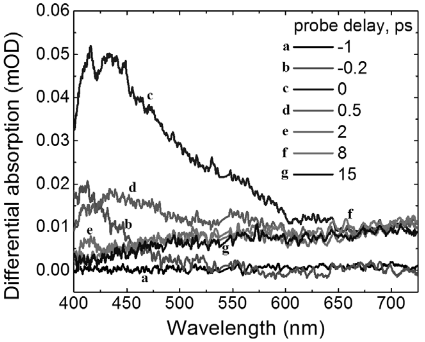

Fig. 8. Spectrum of differential absorption of CVD diamond sample at 264 nm (4.73 eV) pump at different delays between pump and probe (indicated).

We observed two-photon absorption in diamond samples under study. Figure 7 shows spectrum of differential absorption of diamond sample 4.8 at 395 nm (3.16 eV) pump at different delays between pump and probe.

The band peaked at~ 465 nm (2.6 eV) correlates fairly well with the energy of the indirect transition to conduction band. Another bands observed in the samples were peaked at ~550 and 700 nm.

On the contrary, CVD diamond did not show similar spectra of differential absorption at 395nm pump. Strong differential absorption was found only at pump 264 nm as seen from Fig. 8. Contrary to sample 4.8 we observed strong band in blue range peaked at 430 nm and also two weak bands roughly peaked at ~550 and 700 nm. So one can state that two last bands connected with defects which concentration is considerably larger in HPHT diamonds.

All bands of differential absorption in HPHT sample decay fast within the first picosecond and a slow decay component is

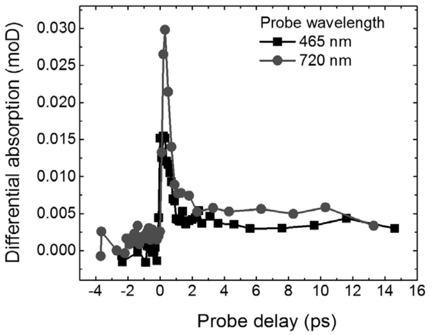

Fig. 9. Kinetics of differential absorption of HPHT diamond sample 4.8 at 395 nm (3.16 eV) pump and two probe wavelengths: 465 nm (2.7 eV) and 720 nm (1.74 eV).

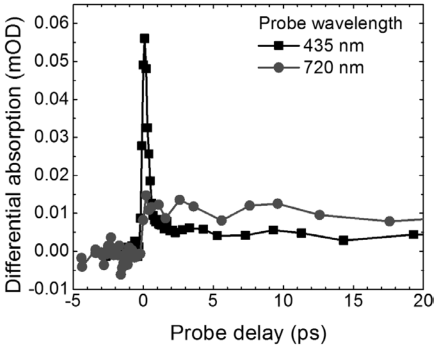

Fig. 10. Kinetics of differential absorption of CVD diamond sample at 264 nm (4.73 eV) pump and two probe wavelengths: 435 nm (2.9 eV) and 720 nm (1.74 eV).

practically absent (see Figure 9). The total energy of pump and probe photons for the 700 nm band was considerably smaller than band gap of diamond, so we concluded that defect centers are responsible for the two-photon absorption in this spectral region.

The different fast process of decay is observed in CVD diamond at UV pump and probing at 435 and 720 nm as seen from Figure 10. Due to small concentration of defects the signal is weak when probed with 720 nm. Also, contrary to colored HPHT diamonds, CVD diamond showed strong fast absorption at total energy 7.6 eV which correlates with data of [11]. The observed two-photon absorption effects in diamond demonstrate good perspectives of exploiting two photon and defect-related absorption for timing in radiation detectors.

When scintillating HPHT diamond sample is probed at 700 nm, the kinetics of differential absorption completely changes form as seen from Figure 11. There are two rise process: fast, less than one ps, which is dedicated to direct excitation of defect and slow, a few ps, which to our mind is due to a population of the defect by capturing of the carriers from conduction zone.

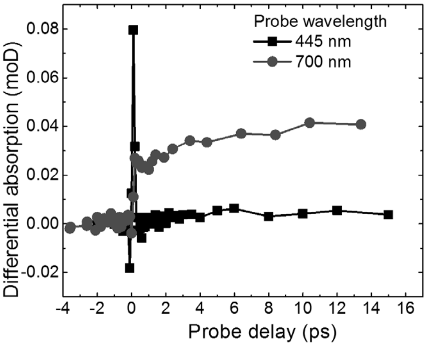

Fig. 11. Kinetics of differential absorption of scintillating diamond sample 11 at 395 nm (3.16 eV) pump and two probe wavelengths: 465 nm (2.7 eV) and 700 nm (1.7 eV).

The last process may be interesting to detect start of ionization in diamond at its interaction with ionizing radiation. In this case only probing of the diamond with near IR short laser pulses will follows to ionization pulse.

VIII. OUTLINE OF DETECTION TECHNIQUE

The effects observed in our study might be exploited for timing of the interaction with ionizing radiation in parallel with the detection of scintillation signal in the same material. The change in two-photon absorption can be used to form a time mark to detect the initial moment of the interaction of the ionizing radiation with the detector material, while the scintillation signal provides the information on absorbed energy. The feasibility of this approach is not clear for Ce^{3+} materials, where the two-photon interband absorption is relatively weak. Meanwhile, in PWO the effect is quite strong and sensitive to the presence of ionizing radiation. Thus, the two photon absorption in this scintillator can be exploited to form the time mark. It is worth noting that in real applications based on the two-photon absorption there will be no need to use the sophisticated setups we use to optimize the detection system. The laser sources based on Nd^{3+}-doped crystals are commercially available at relatively low cost. The second harmonic of their radiation can be used to produce the light in the wavelength range of 500-530 nm, which is optimal for timing.

The light propagating along the scintillation crystal and reflected from the front face of the crystal could be used to observe the two-photon absorption. This configuration would also diminish the problems of spatial overlap of the pump and probe beams. The detection could be accomplished by using a set of sub-picosecond pulses, e.g., 100 pulses with the total set duration of 0.1-1 ns. The set is injected into the crystal approximately at the time when the products of interaction in collider are expected to reach the detector. The initial moment of the interaction between the collision products and the detector material is detected by comparing the set of pulses reflected back out of the crystal and a reference set. In this scheme, the time resolution would be equal to the half of the time span between the pulses in the set. Other schemes are also feasible and should be worked out after a proper choice of the nonlinear optical response to be used.

Effects observed in diamond also suggest that start of ionization process in the material can be defined either by two-photon absorption or probing of population of the intrinsic defects.

REFERENCES

[1] A. Annenkov, M. Korzhik, and P. Lecoq, “Lead tungstate scintillation material,” *Nucl. Instrum. Methods Phys. Res. A, Accel. Spectrom. Detect. Assoc. Equip.*, vol. 490, nos. 1–2, pp. 30–50, Sep. 2002.

[2] K. Kamada, T. Yanagida T. Endo K. Tsutumi Y. Usuki, and M. Nikl, “2 inch diameter single crystal growth and scintillation properties of Ce:$Gd_3Al_2Ga_3O_{12}$,” *J. Cryst. Growth*, vol. 352, no. 1, pp. 88–90, 2012.

[3] K.-T. Brinkman *et al.*, “Radiation damage and recovery of medium heavy and light inorganic crystalline, glass and glass ceramic materials after irradiation with 150 MeV protons and 1.2 MeV gamma-rays,” in *Proc. IEEE Nucl. Sci. Symp. Med. Imag. Conf. (NSS/MIC)*, Nov. 2014, pp. 1–5, doi: 10.1109/NSSMIC.2014.7431066.

[4] E. Auffray *et al.*, “Application of two-photon absorption in PWO scintillator for fast timing of interaction with ionizing radiation,” *Nucl. Instrum. Methods Phys. Res. A, Accel. Spectrom. Detect. Assoc. Equip.*, vol. 804, pp. 194–200, Dec. 2015.

[5] L. Zhang, “A diode-pumped solid state blue laser for monitoring the CMS lead tungstate crystal calorimeter at the LHC,” *J. Phys.*, vol. 404, no. 1, p. 012042, 2012.

[6] N. B. Delone, *Interaction of Laser Radiation With Body: Lectures*, (in Russian). Moscow, Russia: Nauka, 1981, p. 280.

[7] J.-C. Diels and W. Rudolph, *Ultrashort Laser Pulse Phenomena*. New York, NY, USA: Elsevier, 2006.

[8] E. Auffray *et al.*, “New detecting techniques for a future calorimetry,” *J. Phys.*, vol. 587, no. 1, p. 012056, 2015.

[9] J. Lindblom, J. Holsa, Y. Papunen, and Y. Hakkanen, “Luminescence study of defects in synthetic as-grown and HPHT diamonds compared to natural diamonds,” *Amer. Mineralogist*, vol. 90, nos. 2–3, pp. 428–440, 2005.

[10] A. T. Collins, “The characterisation of point defects in diamond by luminescence spectroscopy,” *Diamond Rel. Mater.*, vol. 1, nos. 5–6, pp. 457–469, 1992.

[11] T. Roth and R. Raenen, “Absorption of free carriers in diamond determined from the visible to the mid-infrared by femtosecond two-photon absorption spectroscopy,” *Opt. Commun.*, vol. 189, nos. 4–6, pp. 289–296, 2001.

Paper P7

Subpicosecond luminescence rise time in magnesium codoped GAGG:Ce scintillator

G. Tamulaitis, **A. Vaitkevičius**, S. Nargelas, R. Augulis, V. Gulbinas, P. Bohacek, M. Nikl, A. Borisevich, A. Fedorov, M. Korjik, E. Auffray

Nucl. Instruments Methods Phys. Res. Sect. A Accel. Spectrometers, Detect. Assoc. Equip. 870 (2017) 25–29.

doi:10.1016/j.nima.2017.07.015.

Nuclear Inst. and Methods in Physics Research, A 870 (2017) 25–29

Contents lists available at ScienceDirect

Nuclear Inst. and Methods in Physics Research, A

journal homepage: www.elsevier.com/locate/nima

Subpicosecond luminescence rise time in magnesium codoped GAGG:Ce scintillator

G. Tamulaitis [a,*], A. Vaitkevičius [a], S. Nargelas [a], R. Augulis [b], V. Gulbinas [b], P. Bohacek [c], M. Nikl [c], A. Borisevich [d], A. Fedorov [d], M. Korjik [d], E. Auffray [e]

[a] Institute of Applied Research and Semiconductor Physics Department, Vilnius University, Saulėtekio al. 3, LT-10257, Vilnius, Lithuania
[b] Center for Physical Sciences and Technology, Saulėtekio al. 3, LT-10257, Vilnius, Lithuania
[c] Institute of Physics CAS, Cukrovarnicka 10, Prague, Czech Republic
[d] Research Institute for Nuclear Problems, Bobruiskaya str. 11, Minsk, Belarus
[e] CERN, Geneva, Switzerland

ARTICLE INFO

Keywords:
Scintillator
GAGG garnet crystal
Luminescence kinetics
Radiation detector

ABSTRACT

The influence of co-doping of $Gd_3Al_2GA_3O_{12}$:Ce (GAGG:Ce) scintillator with magnesium on the rise time of luminescence response was studied in two GAGG:Ce crystals grown in nominally identical conditions except of Mg co-doping in one of them. Time-resolved photoluminescence spectroscopy and free carrier absorption techniques were exploited. It is evidenced that the Mg co-doping decreases the rise time down to sub-picosecond domain. Meanwhile, the light yield decreases by ~20%. Thus, the feasibility of exploitation of the fast rise edge in luminescence response for ultrafast timing in scintillation detectors is demonstrated. The role of Mg impurities in facilitating the excitation transfer to radiative recombination centers is discussed.

1. Introduction

The improvement of time resolution down to ~10 ps is currently one of the hottest topics in the development of radiation detectors based on scintillation crystals [1]. The fast detector response is necessary to prevent the pile-up effect in high-luminosity high-energy physics experiments [2] as well as to enable the decrease of the dose injected to a patient in medical imaging, in particular, in time-of-flight positron emission tomography (TOF-PET) [3] and positron annihilation lifetime spectroscopy (PALS) [4]. Recent advances in photodetectors, especially in silicon multipliers (SiPMs) [5] resulted in a substantial shift of the frontiers in the development of fast photon counting devices towards the 10 ps target. Thus, the response time of bulk scintillation crystals currently becomes the bottleneck in the time resolution of the radiation detectors based on the scintillators. The currently fastest scintillation detectors are based on BaF_2, $LaBr_3$:Ce, $CeBr_3$, Pr-doped oxides [6], Ca-codoped LSO:Ce [7] and LYSO:Ce [8], and also trivalent-ion doped PWO [9]. To study the capability of scintillators to serve in fast radiation detectors, not only the emission decay time but also the rise time of their luminescence response is being currently reinvestigated. It is demonstrated that the scintillation rise time in many LSO-type scintillators is 70 ps, while LSO:Ce co-doped with Ca is expected to exhibit the rise time of 20 ps [10]. A sub-picosecond photoluminescence (PL) rise time is revealed in conventional PWO II scintillation crystals, while the PL response to short-pulse excitation takes a few nanoseconds in a solely Ce-doped gadolinium aluminum gallium garnet ($Gd_3Al_2Ga_3O_{12}$:Ce, GAGG:Ce) [11].

Due to a high light yield of up to 50000 ph/MeV, a short luminescence decay time ($<$ 100 ns) [12], and good matching of the emission band with the sensitivity spectrum of conventional SiPMs, GAGG:Ce is a promising scintillation material for certain particle physics experiments and might compete with Ce-doped LYSO and LSO crystals in TOF-PETs. Therefore, the luminescence rise time of this scintillator is of special importance. On the other hand, co-doping of GAGG:Ce by Mg results in a significant improvement of timing characteristics [13] and especially of the coincidence time resolution down to 233 ps due to faster rise and decay times of the scintillation response [14] and paves an efficient way for reaching a better time resolution in detectors based on this material. Moreover, the capability of reaching the time resolution below 50 ps, was demonstrated in GAGG:Ce,Mg thin crystals at the excitation with a high energy charged pion beam [15]. Meanwhile, the origin of the luminescence rise time shortening in Mg-codoped GAGG:Ce is still not unambiguously understood. A lack of information on scintillation kinetics in a

---

[*] Corresponding author.
E-mail address: gintautas.tamulaitis@ff.vu.lt (G. Tamulaitis).

http://dx.doi.org/10.1016/j.nima.2017.07.015
Received 6 April 2017; Received in revised form 19 June 2017; Accepted 9 July 2017

picosecond domain is one of the key problems. Better understanding of the mechanism of the scintillation build-up acceleration in magnesium codoped garnet crystal might be useful for the future improvement of the technology for growing mixed garnet scintillation crystals.

The study of the details of the luminescence kinetics in a ps-sub-ps domain is hardly feasible by using X-ray or particle beam sources and conventional coincidence technique. To investigate the excitation transfer in this time domain, we used excitation by femtosecond UV laser pulses. The luminescence response to the excitation by 80-fs-long pulses was studied using streak camera. To compare the PL response kinetics with the time evolution of the density of nonequilibrium carriers, free carrier absorption (FCA) has been also investigated in these two samples by using pump and probe configuration ensuring sub-picosecond time resolution.

2. Experimental

The samples under study were grown at the Institute of Physics, Czech Academy of Sciences, by the Czochralski method from iridium crucibles. Both samples were intentionally grown in nominally identical conditions except that the sample GAGG:Ce was doped only by 0.5 at% of cerium, while the sample GAGG:Ce, Mg was additionally co-doped with magnesium by adding 0.1 at.% of Mg into the melt. The samples were cut from single crystal boules in a shape of a block with dimensions of $3\times3\times5$ mm^3 and polished. The light yield of the samples was measured by using a photomultiplier tube (PMT) with bialkali photocathode and 1×1 inch CsI(Tl) reference crystal and found to be 35,000 ph/MeV and 27,000 ph/MeV for GAGG:Ce and GAGG:Ce,Mg, respectively.

The time-resolved photoluminescence (TRPL) study has been performed by using a Hamamatsu streak camera. A femtosecond Yb:KGW oscillator (Light Conversion Ltd.) emitting 65 fs pulses at 76 MHz repetition rate was used for excitation. The oscillator emission at 1030 nm was converted to the third 343 nm (3.64 eV) and fourth 254 nm (4.9 eV) harmonics by a harmonics generator (HIRO, Light Conversion Ltd.). The time resolution in these experiments was determined by the instrumental response function of the streak camera. In synchroscan operation mode, the best time resolution was limited by the instrumental response function with full width at half maximum (FWHM) of 3.38 ps.

The decay of nonequilibrium carriers was also investigated by studying free carrier absorption (FCA). Pump and probe configuration was used in these experiments. The free carriers were generated by 200-fs-long pump pulses with photon energy of 4.9 eV (254 nm). The fourth harmonic of the Yb:KGW laser radiation was generated for the pump from a fraction of the fundamental harmonic using β-barium borate crystals. The optical absorption of the samples was probed in the infrared region. The probe pulses were generated in a parametric generator at fixed wavelengths in the range from 1040 to 1712 nm (1.2 eV–0.73 eV). The variable delay of the probe beam enabled time-resolved measurements of free carrier absorption. The differential absorption (DA), i.e., the difference in the optical absorption observed with and without the pump was measured as a function of the delay between the pump and probe pulses. The DA in infrared region is caused predominantly by the free carrier absorption. Thus, the absolute value of DA is proportional to free carrier density.

All the measurements were performed at room temperature.

3. Results and discussion

The absorbance spectra of the samples GAGG:Ce and GAGG:Ce,Mg in the spectral range under study are presented in Fig. 1. They are dominated by the absorption bands due to optical transitions in Ce^{3+} ions: 4f-5d^1 at 2.79 eV and 4f-5d^2 at 3.64 eV. Co-doping by Mg results in unstructured enhancement of the absorption in the high-energy part of the spectrum. The absorption in this spectral region might be attributed to the broad band due to the charge transfer transition of Ce^{4+} stabilized by aliovalent doping of divalent magnesium [15,16], though the close values of the absorption coefficients in the band due to 4f-5d^1 transition in both samples shows that only a small part of Ce^{3+} is converted into Ce^{4+} state in the co-doped crystal. The sharp lines around 4 eV and 4.5 eV are due to the electronic transitions from ^{8}S ground state to higher ^{6}P and ^{6}I 4f states in Gd^{3+} ions. The co-doping does not affect the positions of the absorption bands caused by cerium, thus, the crystal field in the vicinity of Ce^{3+} ions is not affected by the introduction of magnesium. In addition, a wide absorption band in the range from 1.8 eV to 2.5 eV is strongly suppressed by the Mg codoping. The broad absorption band was observed in garnet type crystals at low doping level [17] and most probably is caused by structural imperfection of the host matrix.

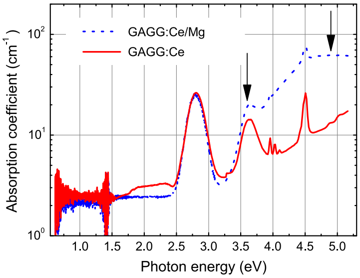

Fig. 1. (Color online) Room temperature absorption spectra of samples GAGG:Ce (red solid line) and GAGG:Ce.Mg (blue dotted line).

The activator luminescence spectra of both samples under study are identical within the limits of experimental error and are described elsewhere [11–13]. The spectrum has the shape of two strongly overlapping broad bands caused by transitions from 5d^1 excited state to ^{2}F$_{5/2}$ and ^{2}F$_{7/2}$ ground state doublet of Ce^{3+} ion [12]. The excitation at 254 nm produces also a weak and narrow Gd^{3+} emission band with the peak position at 318 nm and the intensity of two orders of magnitude weaker than that of activator luminescence. The similarity of the activator spectra in GAGG:Ce without and with codoping evidences negligible influence of Mg co-doping on the emission mechanism. Therefore, the influence of the Mg co-doping on the dynamics of nonequilibrium charge carriers and, consequently, on the emission kinetics might be expected via the impact on the transport of the nonequilibrium carriers to radiative recombination centers, i.e., Ce^{3+} ions.

The luminescence kinetics was studied by using time-resolved photoluminescence spectroscopy. To selectively excite predominantly Ce^{3+} and Gd^{3+} ions, two photon energies were selected for the photoluminescence excitation. They are indicated by arrows in Fig. 1. The photons of the third harmonic at 3.6 eV (343 nm) excite Ce^{3+} ion into the second Stark component of 5d excited energy level. The photon energy of the fourth harmonic at 4.9 eV (254 nm) corresponds to the energy of $^8\mathrm{S}\rightarrow{}^6\mathrm{D}_{7/2,9/2}$ transitions in Gd^{3+} ions and to the long wavelength wing of the absorption band due to optical transition to the third Stark component of 4f^{0}5d^1 Ce^{3+} electronic configuration overlapping with a broad band, which is probably caused by charge transfer absorption of Ce^{4+} in the crystal co-doped with magnesium. It is worth noting that the second Stark component of 5d level of Ce^{3+} in GAGG host is situated already in its conduction band [18–20], which enables electron escape from this level to the host conduction band and activates trapping–retrapping processes giving rise to a delayed radiative recombination at Ce^{3+} ions.

The initial part of the photoluminescence response to the same short pulse excitation (65 fs) is presented in Fig. 2 for both samples under study. The instrumental response functions are also presented in the

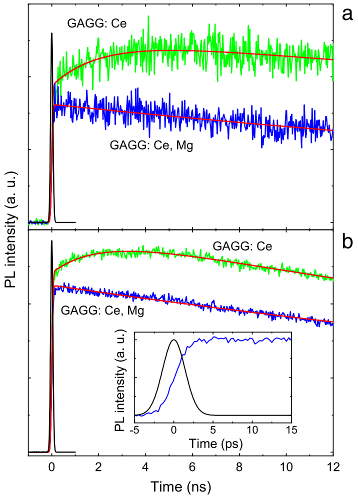

Fig. 2. (Color online) The initial part of photoluminescence response to a short excitation pulse 254 nm (a) and 343 nm (b) of GAGG:Ce and GAGG:Ce,Mg (indicated). Instrumental response function is also presented (black). Inset shows the rising part of the luminescence response in GAGG:Ce,Mg.

figure. The deconvolution of the instrumental response function and the luminescence response in the kinetics of GAGG:Ce luminescence after excitation at 3.64 eV (343 nm) shows that the response has two rise components. The first component is faster than the instrumental response function, while the second component has the time constant of 2 ns. The luminescence decays with the time constant of 47 ns (see Fig. 2(a)). The kinetics after 4.9 eV (254 nm) excitation is similar. The presence of the relatively long luminescence rise component seems to be caused by involvement of Gd subsystem: a part of the nonequilibrium electrons are trapped by shallow traps and are captured afterwards by deeper Gd^{3+} levels, which have poor resonance with Ce^{3+} excited state. The rising part of the GAGG:Ce,Mg was irresolvable within the time resolution in our experiment, while the decay was fitted with a single exponential decay with 48.3 ns time constant. In both cases, the experimental data was considered to be a convolution of the photoluminescence response and a Gaussian function with 110 ps FWHM, which closely matches the instrumental response function in our experiments. To resolve the luminescence rise of GAGG:Ce,Mg, the very initial part of the luminescence response was measured (see inset in Fig. 2) with considerably better time resolution ensured by the instrumental response function with FWHM of 3.4 ps. Even at this accuracy, the rising part of the luminescence response could not be quantified, i.e., the rising part of the response is in a sub-picosecond domain. The absence of the slow component in the build-up of photoluminescence response of the Mg-codoped sample is caused by the increased rate of repopulation of Ce^{3+} radiative recombination centers by electrons released from Ce^{3+} 5d level, which is in conduction band. The process might be facilitated by the presence of stable Ce^{4+} centers which effectively attract electrons and enable their immediate nongeminate radiative recombination giving rise to prompt Ce^{3+} luminescence or by introduction of Mg-based defect states in the band gap attracting electrons from shallow traps and supplying them to the radiative Ce^{3+} centers via Gd $^{3+}$ subsystem.

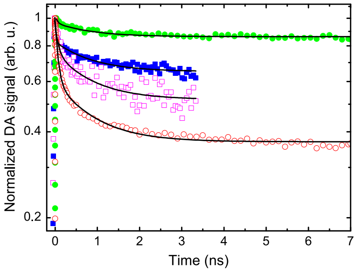

Fig. 3. (Color online) Kinetics of normalized differential absorption for pumping at 4.9 eV in GAGG:Ce (filled circles) and GAGG:Ce,Mg (open circles) and at 5.8 eV in GAGG:Ce (filled squares) and GAGG:Ce,Mg (open squares). All the transients were probed at 1.2 eV. The lines present bi-exponential fits of experimental kinetics.

To get a deeper insight into the dynamics of nonequilibrium carriers, the kinetics of differential absorption were studied in GAGG:Ce and GAGG:Ce,Mg for two pump photon energies, 4.9 eV and 5.8 eV (see Fig. 3). The pump photons of 4.9 eV are in resonance with the optical transition to the third excited state of Ce^{3+}, while they are also able to excite the matrix-building Gd^{3+} ions. The pump photon energy of 5.8 eV is still below the band gap of GAGG matrix but is sufficient to excite the electrons from the valence band to the trap states closely below the bottom of the conduction band. The 5.8 eV photons might also excite the activator ion Ce^{3+} to unlocalized states high in the conduction band. The FCA transients in Fig. 3 are presented in a normalized form to better compare their time evolution in the crystals with and without codoping and at different excitation conditions. All the transients have qualitatively the same shape: a short initial decay transforming into a considerably slower decay at longer delays. The decay times of the components are quite similar, but the relative contribution of the components is sensitive to codoping and depends on excitation wavelength. The smallest contribution (and the longest decay time of 268 ps that was determined with a large error due to small weight of this component) is observed in GAGG:Ce excited at 4.9 eV. Mg-codoping results in substantial enhancement of the fast component (68 ps). For excitation at 5.8 eV, the fast component in GAGG:Ce (58 ps) is stronger than that at 4.9 eV, while Mg-codoping increases the contribution of the fast component (79 ps), though not so strong as at 4.9 eV.

In Fig. 4, the PL kinetics (depicted in Fig. 2) are compared with the time evolution of FCA transients at 4.9 eV pump (depicted in Fig. 3) in the same two samples. The FCA curves represent the difference in absorbance of the probe beam (the photon energy of 1.20 eV) with and without the pump beam. The differential absorption in this spectral region is proportional to the density of free carriers. The results presented above are consistent with the assumption that the absorption of nonequilibrium holes is dominating over the absorption of nonequilibrium electrons in FCA of GAGG:Ce [21]. First of all, this assumption is confirmed by the results obtained at 4.9 eV excitation. The pump photons of 4.9 eV might be absorbed by Ce^{3+} to the third excited state as well as by Gd^{3+} ions in the crystal lattice. The second absorption channel should be stronger due to a high density of the matrix-building Gd^{3+} ions. Moreover, the excited states of the radiative Ce^{3+} ions are in the conduction band. Therefore, the population of electrons at excited Ce^{3+}, which determines the luminescence, and their population in conduction band, which is reflected in the FCA signal due to free electrons, should be in equilibrium. Instead, we observe an initial rise in luminescence intensity but a decrease in FCA (see Fig. 4) for approximately 1 ns after short-pulse excitation that is by far longer than the time necessary to establish the equilibrium. Thus, the FCA signal

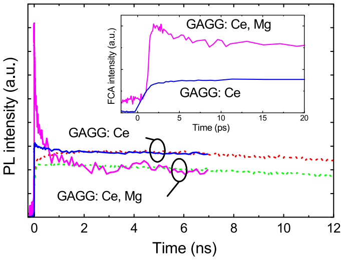

Fig. 4. (Color online) Kinetics of photoluminescence intensity (dotted curves), as in Fig. 2, and free carrier absorption (solid curves), as in Fig. 3, in GAGG:Ce and GAGG:Ce,Mg, as indicated. FCA curves are arbitrary shifted to match the PL curves at the late decay stage. The inset expands the initial part of the free carrier absorption kinetics.

in GAGG:Ce reflects the time evolution of free holes rather than that of free electrons. This conclusion is also supported by the qualitatively different behavior of FCA, which has previously been observed in Ce-doped YAGG, a garnet without gadolinium [21].

The strong enhancement of the fast decay component in FCA by Mg-codoping at predominant excitation of Gd^{3+} shows that the Mg doping introduces nonradiative recombination centers with rather strong coupling of the centers with Gd^{3+}. Thus, the Mg-codoping facilitates the excitation transfer from gadolinium sublattice to the radiative Ce^{3+} centers but simultaneously enhances nonradiative recombination and, consequently, decreases the light yield. The influence of the nonradiative recombination centers introduced by Mg-doping is weaker at 5.8 eV excitation (the fast component in Fig. 3 is less affected by Mg-codoping). It is worth noting that the decrease in the light yield of GAGG:Ce by ∼20%, which we observed in the Mg-codoped sample under study, is still acceptable for many applications of GAGG:Ce,Mg as a fast scintillator.

In nanosecond domain, the decay of PL and free hole absorption in the time range under study proceeds at the same rate (see Fig. 3). This rate is determined by thermal excitation of trapped electrons. The electrons detrapped into the conduction band either reach Ce^{3+} and recombine radiatively resulting in PL or are captured by nonradiative recombination centers and nonradiatively recombine with the holes in the valence band (their density is probed in FCA experiment). Thus, the rates of both processes depend on the population of free electrons in the same sink –the conduction band. As might be traced in Fig. 3 (see the lines depicting the bi-exponential fits of the experimental FCA transients presented by points), the codoping with magnesium slightly influences the decay rate: the decay time equals 3 ns in GAGG:Ce and 850 ps in GAGG:Ce,Mg and in the limits of experimental error does not depend on excitation wavelength.

The initial part of the time evolution of the density of free holes is presented in the inset of Fig. 4. As reported before, the PL intensity reaches the peak value within a few picoseconds after the short-pulse excitation. Note that the rise time of FCA signal in GAGG:Ce is by approximately three orders of magnitude shorter than that of the PL signal. Meanwhile, the FCA rise time in GAGG:Ce,Mg is in picosecond domain, shorter than the time resolution, which was limited in our pump and probe experiment by the pulse lengths of the beams (200 fs).

The discrepancy between the kinetics of free hole density and the time evolution of PL response evidences importance of excitation migration. Since the holes appear in the valence band (are observable in FCA) within several picoseconds even in GAGG:Ce without co-doping, that is the electronic part of the excitation that determines the recombination dynamics in this material. Trapping of electrons in host traps is highly probable in GAGG due to a considerable structural disorder and atomistic-scale composition fluctuations expected in this mixed garnet crystal. Thus, the rise time of luminescence in GAGG:Ce is probably determined by the time, which is necessary to establish equilibrium in the electron exchange between the traps and Ce^{3+} ions acting as radiative recombination centers. Co-doping by Mg partially facilitates the transfer of the electrons to Ce^{3+} radiation centers, however, in parallel, it provides an effective channel for nonradiative recombination. As a result, the rise time of PL response in GAGG:Ce,Mg becomes considerably shorter than that in the crystal without codoping (has no slow component, which is present in the crystal without codoping), while the light yield only slightly decreases. The enhancement of the transfer rate might also be caused by the stabilization of Ce^{4+}, which favors the immediate trapping of free electrons from conduction band by the stable Ce^{4+} ions followed by Ce^{3+} emission [22,23]. Anyway, the enhancement enables the immediate build-up of photoluminescence and scintillation responses with negligible rise time.

4. Conclusions

Co-doping of GAGG:Ce by magnesium decreases the rise time of luminescence after short-pulse excitation down to sub-picosecond domain. This short response time is beneficial for the exploitation of the luminescence rise edge for fast timing in scintillation detectors. The fast rising edge of luminescence response enables determination of the time, when the luminescence intensity reaches a certain level, with sub-picosecond accuracy irrespectively of the total height of the luminescence response pulse. The Mg co-doping decreases the light yield of GAGG:Ce by ∼20%, however, the light yield of GAGG:Ce,Mg is still high enough (27,000 ph/MeV in the sample under this study) to be competitive in many applications. The holes become active in free carrier absorption within sub-picosecond time in GAGG:Ce,Mg and within few picoseconds in GAGG:Ce. Meanwhile, the final rise in GAGG:Ce luminescence intensity takes a few nanoseconds even at the resonant excitation of Ce^{3+} ions into $5d^2$ level situated in the host conduction band. This feature is caused by efficient transfer of electrons from $5d^2$ level to host trapping centers. The introduction of magnesium facilitates the transfer of electrons to Ce^{3+} and results in the decrease of the luminescence rise time down to sub-picosecond domain. The magnesium-related substantial decrease in the luminescence rise time at a modest decrease in the light yield evidences that GAGG:Ce,Mg is a promising scintillating material for many applications, where the time resolution by an order of magnitude shorter than that in the currently conventional scintillator-based detectors is required.

Acknowledgments

This work has been carried out in line with the targets of Crystal Clear Collaboration and supported by H2020-INFRAIA-2014–2015 project no. 654168 (AIDA-2020). Authors are grateful to COST Action TD1401 “Fast Advanced Scintillator Timing (FAST)” for support of collaboration. Partial support of Czech Science Foundation project no. 16-15569S is also gratefully acknowledged.

References

[1] P. Lecoq, M. Korzhik, A. Vasiliev, Can transient phenomena help improving time resolution in scintillators, IEEE Trans. Nucl. Sci. 61 (2014) 229–234. http://dx.doi.org/10.1109/TNS.2013.2282232.

[2] M. Harrison, International Linear Collider Technical Design Report, Vols. 1 through 4, 2013. http://inis.iaea.org/Search/search.aspx?orig_q=RN:45110508 (accessed October 20, 2016).

[3] W.W. Moses, Time of flight in PET revisited, IEEE Trans. Nucl. Sci. 50 (2003) 1325–1330. http://dx.doi.org/10.1109/TNS.2003.817319.

[4] C. Fong, A.W. Dong, A.J. Hill, B.J. Boyd, C.J. Drummond, Positron annihilation lifetime spectroscopy (PALS): a probe for molecular organisation in self-assembled biomimetic systems, Phys. Chem. Chem. Phys. 17 (2015) 17527–17540. http://dx.doi.org/10.1039/C5CP01921D.

[5] D.R. Schaart, E. Charbon, T. Frach, V. Schulz, Advances in digital SiPMs and their application in biomedical imaging, Nucl. Instrum. Methods Phys. Res. A 809 (2016) 31–52. http://dx.doi.org/10.1016/j.nima.2015.10.078.

[6] P. Lecoq, A. Annenkov, A. Gektin, M. Korzhik, C. Pedrini, Inorganic Scintillators for Detector Systems, Springer, 2006, p. 256.

[7] M.V. Nemallapudi, S. Gundacker, P. Lecoq, E. Auffray, A. Ferri, A. Gola, et al., Sub-100 ps coincidence time resolution for positron emission tomography with LSO:Ce codoped with Ca, Phys. Med. Biol. 60 (2015) 4635–4649. http://dx.doi.org/10.1088/0031-9155/60/12/4635.

[8] D.N. ter Weele, D.R. Schaart, P. Dorenbos, Intrinsic scintillation pulse shape measurements by means of picosecond X-ray excitation for fast timing applications, Nucl. Instrum. Methods Phys. Res. A 767 (2014) 206–211. http://dx.doi.org/10.1016/j.nima.2014.08.019.

[9] M. Kavatsyuk, D. Bremer, V. Dormenev, P. Drexler, T. Eissner, W. Erni, et al., Performance of the prototype of the Electromagnetic Calorimeter for PANDA, Nucl. Instrum. Methods Phys. Res. A 648 (2011) 77–91. http://dx.doi.org/10.1016/j.nima.2011.06.044.

[10] S. Gundacker, E. Auffray, K. Pauwels, P. Lecoq, Measurement of intrinsic rise times for various L(Y)SO and LuAG scintillators with a general study of prompt photons to achieve 10 ps in TOF-PET, Phys. Med. Biol. 61 (2016) 2802–2837. http://dx.doi.org/10.1088/0031-9155/61/7/2802.

[11] E. Auffray, R. Augulis, A. Borisevich, V. Gulbinas, A. Fedorov, M. Korjik, et al., Luminescence rise time in self-activated PbWO$_4$ and Ce-doped Gd$_3$Al$_2$Ga$_3$O$_{12}$ scintillation crystals, J. Lumin. 178 (2016) 54–60. http://dx.doi.org/10.1016/j.jlumin.2016.05.015.

[12] K. Kamada, T. Yanagida, J. Pejchal, M. Nikl, T. Endo, K. Tsutsumi, et al., Crystal growth and scintillation properties of Ce doped Gd$_3$(Ga,Al)$_5$O$_{12}$ single crystals, IEEE Trans. Nucl. Sci. 59 (2012) 2112–2115. http://dx.doi.org/10.1109/TNS.2012.2197024.

[13] K. Kamada, M. Nikl, S. Kurosawa, A. Beitlerova, A. Nagura, Y. Shoji, et al., Alkali earth co-doping effects on luminescence and scintillation properties of Ce doped Gd$_3$A$_{12}$Ga$_3$O$_{12}$ scintillator, Opt. Mater. 41 (2015) 63–66. http://dx.doi.org/10.1016/j.optmat.2014.10.008.

[14] M.T. Lucchini, V. Babin, P. Bohacek, S. Gundacker, K. Kamada, M. Nikl, et al., Effect of Mg^{2+} ions co-doping on timing performance and radiation tolerance of Cerium doped Gd$_3$A$_{12}$Ga$_3$O$_{12}$ crystals, Nucl. Instrum. Methods Phys. Res. A 816 (2016) 176–183. http://dx.doi.org/10.1016/j.nima.2016.02.004.

[15] M.T. Lucchini, S. Gundacker, P. Lecoq, A. Benaglia, M. Nikl, K. Kamada, A. Yoshikava, E. Auffray, Timing capabilities of garnet crystals for detecion of high energy charged particles, Nucl. Instrum. Methods Phys. Res. A 852 (2017) 1–9. http://dx.doi.org/10.1016/j.nima.2017.02.008.

[16] M. Nikl, K. Kamada, V. Babin, J. Pejchal, K. Pilarova, E. Mihokova, et al., Defect engineering in Ce-doped aluminum garnet single crystal scintillators, Cryst. Growth Des. 14 (2014) 4827–4833. http://dx.doi.org/10.1021/cg501005s.

[17] Ji. Kvapil, Jo. Kvapil, B. Manek, B. Perner, R. Autrata, P. Shauer, Czochralski growth of YAG:Ce in reducing protective atmosphere, J. Cryst. Growth 52 (1981) 542–545. http://dx.doi.org/10.1016/0022-0248(81)90336-5.

[18] J.M. Ogiegło, A. Katelnikovas, A. Zych, T. Ju, A. Meijerink, C.R. Ronda, Luminescence and luminescence quenching in Gd$_3$(Ga,Al)$_5$O$_{12}$ scintillators doped with Ce^{3+}, J. Phys. Chem. A 117 (2013) 2479–2484. http://dx.doi.org/10.1021/jp309572p.

[19] Y. Wu, F. Meng, Q. Li, M. Koschan, C.L. Melcher, Role of Ce^{4+} in the scintillation mechanism of codoped Gd3Ga3Al2 O12:Ce, Phys. Rev. Appl. 2 (2014) 1–13. http://dx.doi.org/10.1103/PhysRevApplied.2.044009.

[20] P. Dorenbos, Electronic structure and optical properties of the lanthanide activated RE3(Al1-xGax)5O12 (RE = Gd, Y, Lu) garnet compounds, J. Lumin. 134 (2013) 310–318. http://dx.doi.org/10.1016/j.jlumin.2012.08.028.

[21] E. Auffray, M. Korjik, M.T. Lucchini, S. Nargelas, O. Sidletskiy, G. Tamulaitis, et al., Free carrier absorption in self-activated PbWO$_4$ and Ce-doped Y$_3$(Al$_{0.25}$Ga$_{0.75}$)$_3$O$_{12}$ and Gd$_3$Al$_2$Ga$_3$O$_{12}$ garnet scintillators, Opt. Mater. 58 (2016) 461–465. http://dx.doi.org/10.1016/j.optmat.2016.06.040.

[22] S. Blahuta, A. Bessiere, B. Viana, P. Dorenbos, V. Ouspenski, Evidence and Consequences of Ce in LYSO: Ce, Ca and LYSO: Ce, Mg single crystals for medical imaging applications, IEEE Trans. Nucl. Sci. 60 (2013) 3134–3141. http://dx.doi.org/10.1109/TNS.2013.2269700.

[23] M. Nikl, V. Babin, J. Pejchal, V.V. Laguta, M. Buryi, J.A. Mares, et al., The stable Ce^{4+} center: A new tool to optimize Ce-doped Oxide scintillators, IEEE Trans. Nucl. Sci. 63 (2016) 433–438. http://dx.doi.org/10.1109/TNS.2015.2495119.

Paper P8

Significant improvement of GAGG:Ce based scintillation detector performance with temperature decrease

M. Korjik, V. Alenkov, A. Borisevich, O. Buzanov, V. Dormenev, G. Dosovitskiy, A. Dosovitskiy, A. Fedorov, D. Kozlov, V. Mechinsky, R.W. Novotny, G. Tamulaitis, V. Vasiliev, H.-G. Zaunick, **A. Vaitkevičius**

Nucl. Instruments Methods Phys. Res. Sect. A Accel. Spectrometers, Detect. Assoc. Equip. 871 (2017) 42–46.

doi:10.1016/j.nima.2017.07.045.

Nuclear Inst. and Methods in Physics Research, A 871 (2017) 42–46

Contents lists available at ScienceDirect

Nuclear Inst. and Methods in Physics Research, A

journal homepage: www.elsevier.com/locate/nima

Significant improvement of GAGG:Ce based scintillation detector performance with temperature decrease

M. Korjik[a,*], V. Alenkov[c], A. Borisevich[a], O. Buzanov[c], V. Dormenev[d], G. Dosovitskiy[e], A. Dosovitskiy[f], A. Fedorov[b], D. Kozlov[a], V. Mechinsky[a], R.W. Novotny[d], G. Tamulaitis[g], V. Vasiliev[c], H.-G. Zaunick[d], A.A. Vaitkevičius[g]

[a] Research Institute for Nuclear Problems, Minsk, Belarus
[b] Radiation Instruments and New Components, Minsk, Belarus
[c] Fomos Crystals, Moscow, Russia
[d] Justus Liebig University, Giessen, Germany
[e] Institute of Chemical Reagents and High Purity Chemical Substances, IREA, Russia
[f] NeoChem, Moscow, Russia
[g] Vilnius University, Vilnius, Lithuania

ARTICLE INFO

Keywords:
Inorganic scintillation material
GAGG scintillator
γ-quanta
Photo-sensor

ABSTRACT

This report presents results on the significant improvement of GAGG:Ce based scintillation detector performance with temperature decrease. When temperature of a PMT based detector is lowered to −45 °C, its amplitude response at registration of γ-quanta is improved by 30%; FHHM was found to be better up to factor of 0.85, whereas scintillation kinetics become even faster in crystals co-doped with magnesium and magnesium and titanium. All this opens an opportunity for a wide application of GAGG scintillation detectors, particularly in a combination with SiPM photo-sensors, which signal-to-noise ratio would also improve with temperature decrease.

1. Introduction

Due to a high light yield of up to 50 000 phot/MeV, a short luminescence decay time (<100 ns) [1], and good matching of the emission band with the sensitivity spectrum of conventional SiPMs, Ce doped $Gd_3Al_2Ga_3O_{12}$ crystal (GAGG) is promising scintillation material for medical imaging and might compete with Ce-doped Lu_2SiO_5 crystal for PET application. Moreover, GAGG:Ce, co-doped with Mg, shows spectacular time resolution at different excitation [2,3]. GAGG is dense high light yield scintillator, hence it can be applied for a high resolution γ-radiation spectrometry similar to recently developed halide scintillators [4]. However, wide application of the material in detectors is limited. The material exhibits strong phosphorescence, both under photo-excitation and excitation by ionizing radiation. It is demonstrated that the phosphorescence might be diminished by co-doping of GGAG:Ce crystals with Mg [5]. However, contrary to many other scintillators [6–8] the co-doping of the GAGG material with the second group di-valent ions from the set of Mg, Ca, Sr results in a lower scintillation light yield.

Recently, we showed that light yield deterioration of the crystal at codoping with Mg is accompanied with a strong acceleration rate of the free carriers non-radiating recombination [9]. This effect becomes competing to a radiating recombination of free carriers via Ce^{3+} ions and, thus, results in decrease of the scintillator light yield. Non-radiative recombination occurs when hole, due to a migration, appears in the vicinity of the Mg^{2+} created defect. Moreover, some energy barrier in the vicinity of the recombination center has to be overcome by hole for a recombination. Both, migration rate and an ability to overcome barrier are dependent on the temperature. Thus, possible solution to recuperate light yield loss is a slowing down of the holes mobility. Due to a strong temperature (T) dependence of the both effects ~ exp(−E/kT), where E is the constant, dedicated to migration rate or transmission through the barrier, which are defined by the nature of the compound, k-Boltzmann constant, this can be achieved by cooling of the crystal or the whole detecting unit.

Cooling of the scintillation material to gain light yield works pretty good in self-activated scintillation materials which structural units,

---

[*] Correspondence to: 220030, Minsk, Bobruiskaya str. 11, Belarus.
E-mail address: Mikhail.Korjik@cern.ch (M. Korjik).

http://dx.doi.org/10.1016/j.nima.2017.07.045
Received 21 May 2017; Accepted 21 July 2017

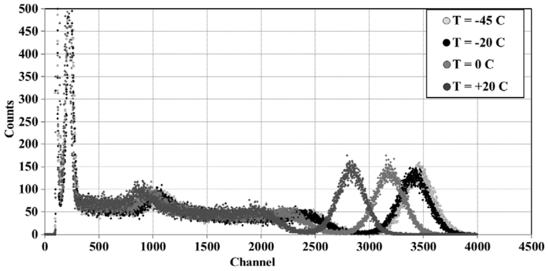

Fig. 1. Pulse height spectrum of ^{137}Cs gamma-source measured with S3 sample at four temperatures: +20 °C, 0 °C, −20 °C, −45 °C.

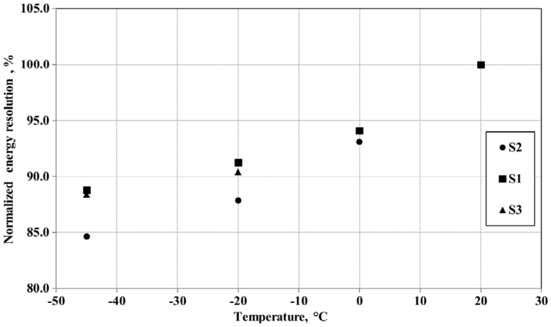

Fig. 2. Temperature change of energy resolution FWHM at 662 keV normalized to room temperature. Measurements have been performed with 1000 ns time gate.

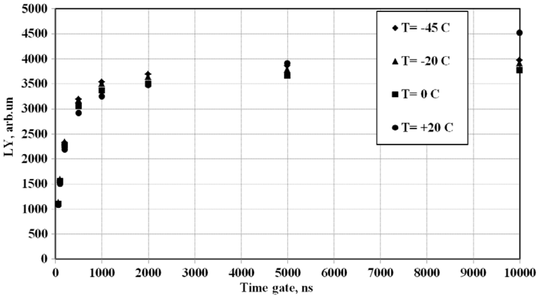

Fig. 3. Light yield of GAGG:Ce (S1) sample measured in different time gates in temperature range.

oxy-anionic complexes, possess highly temperature quenched luminescence. There are a reasonable amount of self-activated materials which includes widely used $PbWO_4$ and $Bi_4Ge_3O_{12}$ [4]. Note, last modification of $PbWO_4$, PWO-II, which is the crystal, doped with La, and Y at the total amount of less than 100 ppm. Doping ions create shallow electron capturing centers in the crystal matrix and prevents free carriers capture by deep traps, significantly improving tolerance of the PWO-II to ionizing radiation. Cooling of the crystal to the −25 °C allows to triplicate its light yield at simultaneous keeping the scintillation kinetics fast enough [10].

Contrary to self-activated material, the luminescence of Ce-doped scintillation material is caused by inter-configuration d-f luminescence, having a high quantum yield and low temperature quenching effect in the vicinity of room temperature. Thus, only a minor gain of the light yield of the Ce activated scintillation material is expected with decrease of the crystal temperature. Moreover, some of oxide scintillators doped

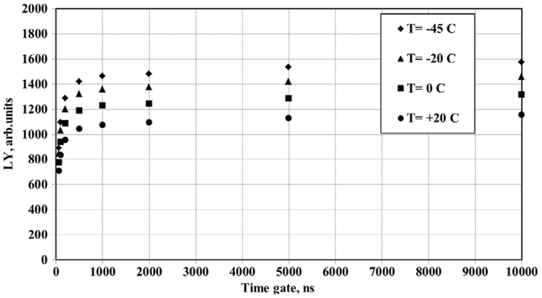

Fig. 4. Light yield of GAGG:Ce, Mg (S2) sample measured in different time gates in temperature range.

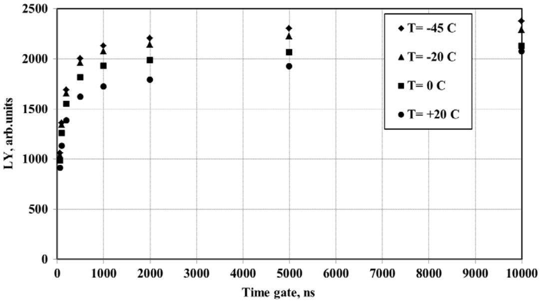

Fig. 5. Light yield of GAGG:Ce, Mg, Ti (S3) sample measured in different time gates in temperature range.

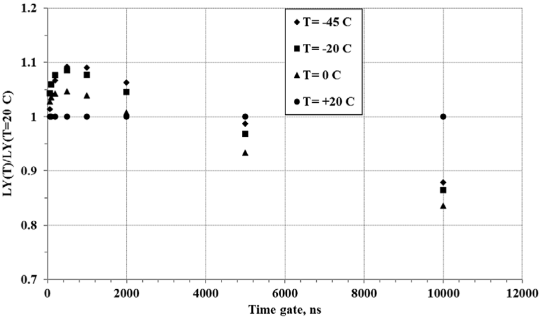

Fig. 6. Relative change of the light yield of GAGG:Ce (S1) sample normalized to 20 °C versus time gate at different temperatures.

with Ce, particularity perovskites of $YAlO_3$-$LuAlO_3$ family, demonstrate 10%–20% decrease of the light yield when temperature is lowered from room to −20 °C. Here we report an incredible improvement of GAGG:Ce, Mg and GAGG:Ce, Mg, Ti scintillation detectors performance with temperature decrease.

2. Samples

All the garnet samples under study were cut from single crystal boules, grown by the Czochralski method from iridium crucibles by Fomos Crystals from the melt close to $Gd_3Al_2Ga_3O_{12}$ stoichiometric

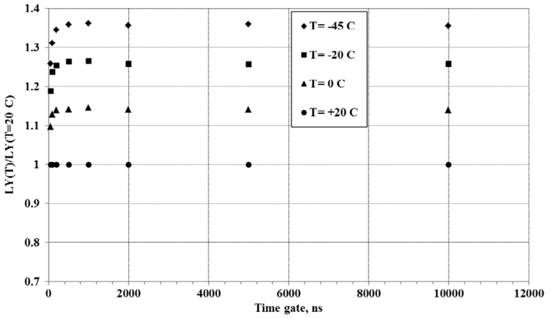

Fig. 7. Relative change of the light yield of GAGG:Ce (S2) sample normalized to 20 °C versus time gate at different temperatures.

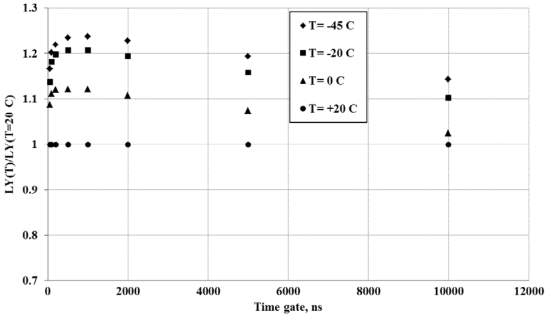

Fig. 8. Relative change of the light yield of GAGG:Ce (S3) sample normalized to 20 °C versus time gate at different temperatures.

composition. To compensate gallium leakage from the melt during the crystal growth, samples were grown with excessive Ga_2O_3 added into the melt in the crucible. The reference sample (S1) was doped with Ce (0.5 at.%) whereas two other studied crystals, S2 and S3, were co-doped by Mg (0.1 at.%) and Mg (0.05 at.%) and Ti (0.01at.%) correspondingly. Pulse height spectra of ^{137}Cs source with 662 keV energy of gamma-quanta have been measured with bialkali green-extended PMT Hamamatsu R329 in a thermostat within temperature range from +20 °C to −45 °C, with temperature stabilization accuracy 0.1 °C. Light was measured with bialkali PMT Hamamatsu R2059 in different time gates of charge sensitive gated ADC. Stability of PMT-photocathode sensitivity and PMT gain in the temperature range was controlled by a reference green LED light pulse source. Sample size was 15 × 18 × 7 mm. We used Basylon® optical grease and Teflon® light reflectors.

3. Experimental results and discussion

Change of the photo-peak position (i.e. light yield change), and change of energy resolution with temperature were measured in different time gates. Fig. 1 represents pulse height spectrum of ^{137}Cs gamma-source measured with S3 sample at four temperatures: +20 °C, 0 °C, −20 °C, −45 °C. Cooling of the detecting unit results in improvement both, peak position and energy resolution as well. Fig. 2 shows change of the normalized to room temperature and measured in 1000 ns gate FWHM of 662 keV photo-peak with temperature. The most prominent improvement has been achieved with the sample co-doped with Mg, whereas Ce doped and Ce doped and co-doped with Mg and Ti showed similar behavior.

Figs. 3–5 show light yield of the samples in various time gates, measured at different temperatures. It worth to note that largest improvement of the LY at cooling is observed in the crystals, co-doped with Mg and Mg, Ti. Figs. 6–8 show relative change of the light yield, normalized to 20 °C, versus time gate at different temperatures.

As it is seen, crystal doped only with Ce shows the lesser relative light yield increase at cooling. Moreover, behavior of the gated light yield shows that with temperature decrease a redistribution of the scintillation in the favor of slow components and phosphorescence occurs. Due to this reason, number of the detected photons in a long gate, for example 10 microseconds, is 20% less at −45 °C than at room temperature. Situation is drastically improved in co-doped crystals. More than 95% of the scintillation is collected in 300 ns, a weak dependence of the light yield on the gate is observed. This indicates that electron traps have a minor contribution to the farther stage of the scintillation kinetics and phosphorescence as well.

4. Conclusions

We observed a significant improvement of the detecting properties of GAGG/PMT based scintillation detectors at their cooling. Improvement that is even more spectacular is expected at the application of SiPM for the scintillation photon detection. SiPM noise is reduced by factor two for each 10 °C of temperature decrease, therefore combining of multidoped GAGG and SiPM readout opens an opportunity to create advantageous detectors, particularly for medical imaging applications.

References

[1] K. Kamada, T. Yanagida, J. Pejchal, M. Nikl, T. Endo, K. Tsukumi, Y. Fujimoto, A. Fukabori, A. Yoshikava, Crystal Growth, Scintillation properties of Ce doped Gd3(Ga,Al)5O12 single crystals, IEEE Trans. Nucl. Sci. 59 (2012) 2112–2115.

[2] M.T. Lucchini, V. Babin, P. Bohacek, S. Gundacker, K. Kamada, M. Nikl, A. Petrosyan, A. Yoshikawa, E. Auffray, Effect of Mg2+ ions co-doping on timing performance and radiation tolerance of cerium doped Gd3Al2Ga3O12 crystals, Nucl. Instrum. Methods Phys. Res. A 816 (2016) 176–183.

[3] M.T. Lucchini, S. Gundacker, P. Lecoq, A. Benaglia, M. Nikl, K. Kamada, A. Yoshikawa, E. Auffray, Timing capabilities of garnet crystals for detection of high energy charged particles, Nucl. Instrum. Methods Phys. Res. A 852 (2017) 1–9.

[4] P. Lecoq, A. Gektin, M. Korzhik, Inorganic Scintillators for Detector Systems, Springer, 2017, p. 408.

[5] K. Kamada, M. Nikl, S. Kurosawa, A. Beitlerova, A. Nagura, Y. Shoji, J. Pejchal, Y. Ohashi, Y. Yokota, A. Yoshikawa, Alkali earth co-doping effects on luminescence and scintillation properties of Ce doped $Gd_3Al_2Ga_3O_{12}$ scintillator, Opt. Mater. 41 (2015) 63–66.

[6] Use of codoping to modify the scintillation porperties of inorganic scintillators doped with trivalent activators, US Patent 8,617,422 B2, December 31, 2013.

[7] S. Blahuta, A. Bessiere, P. Dorenbos, V. Ouspensi, Evidence and conseqences of Ce^{4+} in LYSO:Ce, Ca and LYSO:Ce, Mg single crystal for medical imaging applications, IEEE Trans. Nucl. Sci. 60 (2013) 3134–3141.

[8] M. Koschan, K. Yang, M. Zhuravleva, C.L. Melcher, A comparison of the effect of Ca^{2+}codoping in cerium doped GSO with that of LSO and YSO, J. Cryst. Growth. 352 (2012) 133–136.

[9] E. Auffray, M. Korjik, M.T. Lucchini, S. Nargelas, O. Sidletskiy, G. Tamulaitis, Y. Tratsiak, A. Vaitkevičius, Free carrier absorption in self-activated $PbWO_4$ and Ce-doped Y_3 (Al $_{0.25}$ $Ga_{0.75})_3O_{12}$ and $Gd_3Al_2Ga_3O_{12}$ garnet scintillators, Opt. Mater. 58 (2016) 461–465.

[10] A. Borisevich, et al., Lead tungstate crystal with increased light yield for the PANDA electromagnetic calorimeter, Nucl. Instrum. Methods Phys. Res. A 537 (2005) 101–104.

Paper P9

Excitation Transfer Engineering in Ce-Doped Oxide Crystalline Scintillators by Codoping with Alkali-Earth Ions

E. Auffray, R. Augulis, A. Fedorov, G. Dosovitskiy, L. Grigorjeva, V. Gulbinas, M. Koschan, M. Lucchini, C. Melcher, S. Nargelas, G. Tamulaitis, **A. Vaitkevičius**, A. Zolotarjovs, M. Korzhik
Phys. Status Solidi Appl. Mater. Sci. 215 (2018) 1–10.

doi:10.1002/pssa.201700798.

Reprinted with permission from John Wiley and Sons

Excitation Transfer Engineering in Ce-Doped Oxide Crystalline Scintillators by Codoping with Alkali-Earth Ions

*Etiennette Auffray, Ramūnas Augulis, Andrei Fedorov, Georgy Dosovitskiy, Larisa Grigorjeva, Vidmantas Gulbinas, Merry Koschan, Marco Lucchini, Charles Melcher, Saulius Nargelas, Gintautas Tamulaitis, Augustas Vaitkevičius, Aleksejs Zolotarjovs, and Mikhail Korzhik**

Time-resolved spectroscopic study of the photoluminescence response to femtosecond pulse excitation and free carrier absorption at different wavelengths, thermally stimulated luminescence measurements and investigation of differential absorption are applied to amend the available data on excitation transfer in GAGG:Ce scintillators, and an electronic energy-level diagram in this single crystal is suggested to explain the influence of codoping with divalent Mg on luminescence kinetics and light yield. The conclusions are generalized by comparison of the influence of aliovalent doping in garnets (GAGG:Ce) and oxyorthosilicates (LSO:Ce and YSO:Ce). In both cases, the codoping facilitates the energy transfer to radiative Ce^{3+} centers, while the light yield is increased in the LYSO:Ce system but reduced in GAGG:Ce.

Dr. E. Auffray, Dr. M. Lucchini
CERN
1211 Geneva, Switzerland

Dr. R. Augulis, Dr. V. Gulbinas
Center for Physical Sciences and Technology
Savanorių av. 231, LT-02300 Vilnius, Lithuania

Dr. M. Koschan, Dr. C. Melcher
University of Tennessee
Knoxville, TN 37966, USA

Dr. G. Dosovitskiy
National Research Center "Kurchatov Institute"
Kurchatova 1, 123098 Moscow, Russia

Dr. L. Grigorjeva, Dr. A. Zolotarjovs
Institute of Solid State Physics
University of Latvia
LV-1063 Riga, Latvia

Dr. S. Nargelas, A. Vaitkevičius, Dr. G. Tamulaitis
Vilnius University
Universiteto str. 3, LT-1513 Vilnius, Lithuania

Dr. M. Korzhik, Dr. A. Fedorov
Research Institute for Nuclear Problems
Bobruiskaya str. 11, 220030 Minsk, Belarus
E-mail: mikhail.korjik@cern.ch

DOI: 10.1002/pssa.201700798

1. Introduction

Aliovalent codoping has been recently demonstrated to be a productive approach to improve the scintillation properties of bulk Ce-doped scintillators with different host structures. Codoping of Ce-doped gadolinium gallium aluminum garnet Gd$_3$Al$_2$Ga$_3$O$_{12}$ (GAGG) single crystals with the divalent cation Mg^{2+} is highly promising for applications of this scintillator in the new generation of PET (positron emission tomography) scanners.[1,2] This scintillator is a product of purposeful engineering of the band gap and the energy position of the activator levels in the gap.[3,4] The crystal exhibits a high light yield of up to ≈70 000 phot/MeV,[5] has luminescence decay time shorter than 100 ns, and its emission band peaks at ≈520 nm which perfectly matches the sensitivity spectrum of conventional Silicon Photomultipliers (SiPMs). Thus, the crystal might compete with Lu$_2$SiO$_5$:Ce (LSO:Ce) and (Lu$_{1-x}$-Y$_x$)$_2$SiO$_5$:Ce (LYSO:Ce) in Time-of-Flight Positron Emission Tomography (TOF-PET) applications. Moreover, GAGG:Ce might become the scintillator of choice in high-resolution γ-radiation spectrometry and compete with the halide scintillators recently developed for this purpose.[6–8] Finally, natural gadolinium is a mixture of six stable isotopes, ^{154}Gd (2.18%), ^{155}Gd (14.8%), ^{156}Gd (20.5%), ^{157}Gd (15.7%), ^{158}Gd (24.8%), and ^{160}Gd (21.9%), two of which, ^{155}Gd and ^{157}Gd, have the highest neutron capture cross section among all known stable isotopes, 61 000 and 254 000 barns, respectively. The capture of neutrons is accompanied by the emission of γ-quanta with a total energy of about 8 MeV: $n + {}^{155}\text{Gd} \rightarrow {}^{156}\text{Gd} + \gamma$ (8.5 MeV) and $n + {}^{157}\text{Gd} \rightarrow {}^{158}\text{Gd} + \gamma$ (7.9 MeV).

This energy release, as well as individual γ-quanta, can be detected by the same crystal in which the interaction takes place.

However, the outstanding characteristics of GAGG:Ce detectors are accompanied by certain shortcomings, hindering extensive application of the material in radiation detection. Particularly, the material exhibits strong phosphorescence, both under photoexcitation and excitation by ionizing radiation. It has been demonstrated that the phosphorescence might be diminished in the crystal and ceramics by codoping with Mg.[9,10]

Unfortunately, the codoping of GGAG:Ce by Mg results in a lower scintillation light yield (LY) at room temperature (RT), contrary to the codoping of LSO:Ce and LYSO:Ce by divalent Ca or Mg.[11,12] Recently, we demonstrated that the luminescence build up after short-pulse excitation becomes significantly faster, when GAGG:Ce crystal is codoped by Mg.[13] This observation of the shortening of the luminescence rise time is in line with the previous results on the coincidence time resolution, where substantial improvement of the response time in Mg-codoped GAGG:Ce crystals is observed at certain decrease of the light yield.[14] At a small energy release, using 511 keV gamma-rays from ^{22}Na source, the Coincidence Resolving Time (CTR) with full width at half maximum (FWHM) of 540 and 233 ps was measured in GAGG:Ce without and with Mg codoping, respectively. At high energy deposit, when high-energy charged particles have been used to excite the crystal, the Mg-codoped sample yielded a better single device time resolution of 30.5 ps sigma than that in Mg-free sample (36.2 ps sigma).[15] Finally, a significant improvement of GAGG:Ce,Mg light yield without changes in scintillation kinetics was observed, when the crystal temperature was progressively decreased down to −45 °C,[16] what was not detected in the crystals doped solely with Ce.[17] These features make GAGG:Ce,Mg the scintillator of choice to operate with SiPM readout at reduced temperatures.

In spite of the spectacular progress in the improvement of the performance parameters of oxide crystalline scintillators with aliovalent co-doping, the mechanism of the improvement is still not fully understood.

This aliovalent doping, in which a trivalent ion is substituted by a divalent second group cation in the host matrix, results in the formation of anionic vacancies that compensate for the resulting charge. The formation of a hole-type defect including Mg^{2+} and O^{-} in close proximity is also quite probable.[18,19] Moreover, the codoping of Ce-activated crystals by divalent ions (even at the level of less than 1 at.%) causes oxidation of part of the Ce^{3+} ions to Ce^{4+}. Both cerium ions are involved in the scintillation process.[12,20,21] Codoping by Ca^{2+} or Mg^{2+} of oxide material crystallized at high temperature seems to introduce similar defects in the matrix due to similarity of the cation properties in the same host, though different dependence of the light yield on their concentration was observed in GAGG:Ce.[9]

It has also been demonstrated that codoping of Y_2SiO_5:Ce, LYSO:Ce, $LaBr_3$:Ce, and $CeBr_3$ with divalent alkali-earth ions results in enhancement of scintillation light yield and improvement of the energy resolution of the detectors based on these materials.[12,22–25] Moreover, it was recently demonstrated that aliovalent co-doping by Sr^{2+} of the most widely used NaI(Tl) scintillation crystals also improves their energy resolution.[26] This is an indication that the defect associated with the alivovalent codoping (Mg^{2+}, Ca^{2+}, Sr^{2+}) is most likely a matrix host defect.

The cerium-doped lutetium oxyorthosilicate Lu_2SiO_5:Ce attracted our attention because of its extensive exploitation as scintillator in medical imaging devices. Codoping with divalent Ca results in substantial improvement of the scintillation properties of this crystal. Contrary to codoped GAGG:Ce, the light yield of aliovalently codoped LSO:Ce increases by 10–20%, the scintillation decay becomes faster, and the phosphorescence is significantly suppressed.[12,27] These improvements are primarily caused by suppression of free carrier trapping by deep intrinsic traps. Nevertheless, the negative influence of Ca-codoping on formation of nonradiative recombination centers in LSO scintillators is still under study.

The current paper is aimed at revealing the mechanisms through which codoping of Ce-doped scintillation single crystals by divalent alkali-earth ions influences the luminescence and scintillation properties of these materials. Our study was primarily focused on the investigation of GAGG:Ce, which is a complicated system in view of the excitation transfer processes. The generalization of the mechanisms is based on comparison of the results obtained for GAGG:Ce and LSO:Ce, two scintillators with substantially different crystal fields, which turned out to be of importance for the competition of excitation transfer in crystals codoped with divalent ions. We exploited steady-state, quasi-steady-state and time-resolved photoluminescence spectroscopy and pump-and-probe techniques to study the dynamics of nonequilibrium carriers. The thermally stimulated emission technique was used to characterize the energy levels of the traps in the band gap. This study enabled us to construct simple schematic energy-level diagrams, which allow explaining the main routes of excitation transfer and the influence of the aliovalent codoping.

2. Experimental Section

The GAGG:Ce samples used in this study were grown by the Czochralski technique from iridium crucibles. The samples, in the shape of a 3 × 3 × 5 mm^3 block, were cut from single crystal boules and subsequently polished. The key scintillation parameters of the samples are presented in **Table 1**.

Samples A1 and A2 were fabricated at the Institute of Physics, Czech Academy of Sciences. The crystals were grown in nominally identical conditions and with nominally the same cerium content of 0.5 at.%. In addition, A2 was codoped with magnesium at 0.1 at.%.

The set of GAGG:Ce samples labeled hereafter B1, B2, and B3 was prepared at the National Research Center “Kurchatov Institute” in Moscow, Russia, to investigate the influence of gallium evaporation on the crystal properties. These three samples, shaped as 10 × 10 × 7 mm^3 blocks, were produced using sintered raw materials. Sample B1 was grown from the melt with stoichiometric composition. To compensate for gallium volatilization from the melt during growth, sample B2 was grown with excess Ga_2O_3 added to the melt in the crucible. To further compensate for the volatilization of Ga and to inhibit the formation of oxygen vacancies more efficiently, codoping with tetravalent ions was exploited in sample B3 which was grown with 0.01 at.% of zirconium, in addition to the excess Ga_2O_3 added as was done during the growth of sample B2.

Two types of oxyorthosilicates, Lu_2SiO_5 and Y_2SiO_5, solely doped with Ce and codoped by Ca, both at 0.1 at.% in the melt, were labeled as L1 and L2 and measured to compare the change of the optical transmission spectra due to aliovalent codoping. The oxyorthosilicate boules, nominally 32 mm in diameter, were grown in inductively heated iridium crucibles by the Czochralski

Table 1. Scintillation parameters of GAGG samples under study.

Sample	Composition	Luminescence decay times ns (%) Fast	Intermediate	Slow	Phosphorescence level, arb. u.	Light yield, ph/MeV
A1	$Gd_3Ga_3Al_2O_{12}$:Ce	52(23)	130(68)	230(9)	80	35 000
A2	$Gd_3Ga_3Al_2O_{12}$:Ce, Mg	56(40)	100(60)	–	–	27 000
B1	$Gd_3Ga_3Al_2O_{12}$:Ce	52(22)	150(67)	700(10)	100	26 000
B2	$Gd_3Ga_3Al_2O_{12}$:Ce excess Ga	51(10)	150(39)	2125(51)	335	31 000
B3	$Gd_3Ga_3Al_2O_{12}$:Ce excess Ga + 0.001 at.% Zr	63(27)	150(73)	–	700	21 000

method (see Ref. [23] for more detail). Uncodoped LSO:Ce crystal was studied in detail to reveal the energy transfer processes. The sample (L3) had dimensions 10 × 10 × 2 mm.

The scintillation kinetics was measured by the start-stop method. The luminescence decay of the samples was characterized using a fit by three exponential components. The light yield was measured by photomultiplier tube XP2020 calibrated using 1 inch CsI(Tl) reference crystal produced by Institute of Scintillation Materials (ISMA), Kharkov, Ukraine. The light yield provided in Table 1 was measured in the samples unannealed after crystal growth. These samples were used in all our experiments. The phosphorescence level was estimated at the background plateau measured simultaneously with the scintillation kinetics by the start-stop method. The scintillation properties of the samples were evaluated at room temperature.

In thermally stimulated luminescence (TSL) experiments, the thermal activation energy of the traps E_{TA} has been determined by the fractional glow method.[28] The TSL peaks were measured in the luminescence spectral range from 300 to 800 nm at the heating rate of 6 K min^{-1}. The samples were activated for 30 min using an X-ray tube (30 kV, 15 mA) at 7 K.

The time-resolved photoluminescence (TRPL) study has been performed using a Hamamatsu streak camera. In synchroscan detection mode, the time resolution was limited by the instrumental response function with full-width at half maximum (FWHM) of 2.95 ps. To study the PL kinetics in the samples with long decay components, the camera could be operated only in a single sweep mode with considerably poorer time resolution. A femtosecond Yb:KGW oscillator (Light Conversion Ltd.) emitting at 1030 nm and producing 80 fs pulses at 76 MHz repetition rate was used as a primary excitation source. The third 3.64 eV (343 nm) and fourth 4.9 eV (254 nm) harmonics of the oscillator emission have been produced by a harmonics generator (HIRO, Light Conversion Ltd.) to ensure selective photoexcitation.

For GAGG:Ce crystals, the 3.6 eV (343 nm) emission resonantly excites Ce^{3+} ions into the lowest excited energy level. Meanwhile, the photon energy of 4.9 eV (254 nm) corresponds to $^8S \rightarrow {}^6D_{7/2,9/2}$ transition of Gd^{3+} ions and also is sufficient to cause transitions to the long-wavelength wing of the band due to excitation into the third component of Ce^{3+} electronic configuration $4f^05d^1$. For the LSO:Ce crystal, the 4.9 eV photons excite Ce^{3+} ions into the third component as well.

The dynamics of free nonequilibrium carriers was investigated using free carrier absorption (FCA), which was measured using a pump and probe technique. The free carriers were generated by short light pulses (200 fs) at 4.9 eV (254 nm). A part of the fundamental harmonic of the Yb:KGW laser described above was frequency-quadrupled using β-barium borate crystals and used for this purpose. The optical absorption of the samples was probed with a variable delay at different fixed wavelengths by using the output of a parametric generator in the infrared range 900–1700 nm (1.38–0.73 eV). The difference in the optical absorption with and without the pump (differential absorption, DA) was measured as a function of the delay between the pump and probe pulses. The DA in this spectral region is caused by the induced absorption, which is proportional to free carrier density.

3. Results

3.1. Photoluminescence and Free Carrier Absorption in GAGG:Ce and GAGG:Ce,Mg

The codoping of GAGG:Ce with magnesium introduces a broad absorption band that peaks at 4.7 eV (265 nm), which is not observed in the crystal without codoping. The spectrum of the difference in absorption coefficients measured in samples A1 (GAGG:Ce) and A2 (GAGG:Ce, Mg) is presented in **Figure 1**. Both samples are grown in nominally the same conditions and

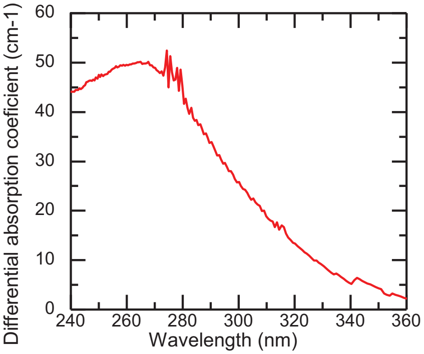

Figure 1. Spectrum of the difference in absorption coefficient of GAGG:Ce with and without magnesium codoping.

contain nominally the same concentration of Ce^{3+} ions. Thus, the change in absorption is caused by Mg codoping. However, no difference of the absorption intensity of the Ce^{3+} bands due to transfer to the first Stark component of Ce^{3+} electronic configuration $4f^05d^1$ was observed in the samples. It indicates that conversion of Ce^{3+} ions into the Ce^{4+} state at such a low Mg concentration does not affect Ce^{3+} concentration significantly. This absorption band is most probably caused by charge transfer (CT) transition from the valence band to the defect stabilized by Mg^{2+}, one of which may be a Ce^{4+} ion.

The photoluminescence response of GAGG:Ce after a short pulse excitation at 4.9 and 3.6 eV is shown in **Figure 2**. The decay at delays longer than ≈30 ns proceeds at approximately the same rate at both excitation photon energies, while the contribution of the fast decay component is considerably more pronounced at 3.6 eV excitation. The initial part of the PL response to short-pulse excitation for both GAGG:Ce and GAGG:Ce,Mg (samples A1 and A2) is presented in Figure 2. The instrumental response function is also depicted there. Due to the presence of long PL decay components, the FWHM of the instrumental function was 100 ps in these experiments. For clarity, only the fits to the experimental decay data are presented in Figure 2. The fit is illustrated in the inset of Figure 2. The major part of the GAGG:Ce luminescence grows instantaneously within the experimental response time, however, a slower rise component is also observed. Thus, the PL response was fitted as $f(t) = [A_1 + A_2 \exp(-t/\tau_r)]\exp(-t/\tau_d)$, where A_1 and A_2 are amplitudes of the fast and slow growth components, while τ_r and τ_d are the luminescence growth and decay times. This fluorescence profile was further convoluted with the experimentally obtained response function. At the excitation of Ce^{3+} luminescence through the matrix (at 4.9 eV), the time constant of the slow rise $\tau_r = 8$ ns. At 3.6 eV, corresponding to the resonant excitation to absorption band of Ce^{3+} ions, the time constant of the slow rise component $\tau_r = 2.5$ ns is shorter but still considerably longer than the instrumental response function. As reported before,[13] the slow rise component disappears in GAGG:Ce,Mg, and luminescence rise proceeds in subpicosecond time range.

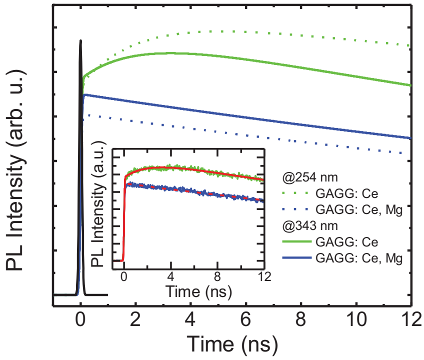

Figure 2. The initial part of PL response to a short excitation pulse at 343 nm of GAGG:Ce, sample A1 (green) and Mg codoped sample A2 (blue). Instrumental response function is also presented.

Mg-codoping also influences the luminescence kinetics. Scintillation kinetics with characteristic time constants of 60 and 54 ns are observed in GAGG:Ce at 254 and 343 nm excitation, respectively. The difference between the time constants disappears in the Mg-codoped crystal; for both excitation wavelengths was found to be 51 ns.

Free carrier absorption in GAGG:Ce with and without Mg-codoping was studied in pump and probe configuration. The difference between the absorption after excitation by a short pulse (pulse energy 0.48 mJ cm^{-2}) at 4.9 eV and the absorption without excitation was probed as a function of delay between pump and probe pulses at different probe wavelengths: 905 nm (1.38 eV), 1041 nm (1.2 eV), 1213 nm (1.03 eV), 1404 nm (0.89 eV), and 1712 nm (0.73 eV) both for GAGG:Ce (sample A1) and GAGG:Ce,Mg (A2). The decay of the normalized differential absorption signals of probing radiation at three typical probe wavelengths are presented in **Figure 3**.

For the probe photon energy down to ≈1 eV, the decay kinetics exhibit minor dependence on the probe photon energy. Both for GAGG:Ce and GAGG:Ce,Mg, the decay consists of a fast decay component and the decay proceeding at a slower rate, with the decay time of 40–50 ns for both crystals. The fast decay component is considerably more pronounced in GAGG:Ce,Mg. For probe photon energy of below 1 eV, the slow decay component becomes faster in GAGG:Ce, while the fast decay component becomes more pronounced in both crystals.

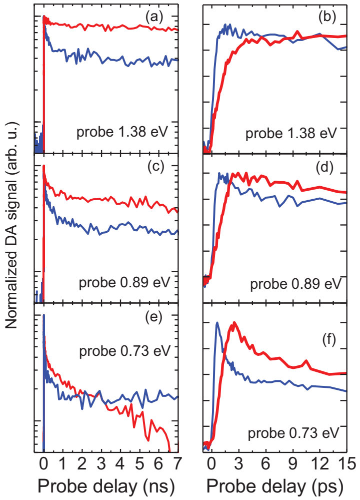

Figure 3. Normalized differential absorption signals at different probe photon energies (indicated) in nano- (left panel) and picosecond (right panel) domains of GAGG:Ce (red) and GAGG:Ce,Mg (blue).

As reported before,[13] the rise edge in the DA response of GAGG:Ce consists of two components: the first one is faster than the excitation pulse rise time (in subpicosecond domain), and the second is slower, on the order of a few picoseconds. In this paper, we show that decreasing the probe photon energy down to ≈1 eV does not have a substantial influence on the DA rise edge. Meanwhile, the slow rise component for the probe photon energy above ≈1 eV becomes more pronounced.

The dependence of the DA peak value on the probe photon energy is presented in **Figure 4**. The dependence does not follow the typical FCA spectrum but rather has distinct features, which are probably caused by absorption to specific energy levels.

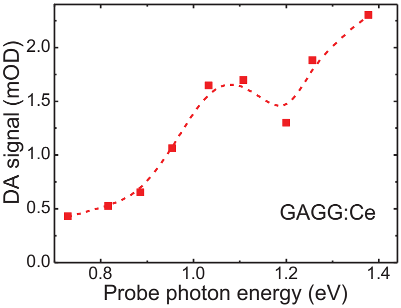

Figure 4. Peak differential absorption of GAGG:Ce as a function of probe photon energy.

3.2. Probing the Trapping Centers in GAGG:Ce Crystals by Thermally Stimulated Luminescence Technique

The trapping levels in GAGG with different structural defects were studied using the thermally stimulated luminescence (TSL) techniques in the set of three samples (B1–B3) grown with different deviations from crystal stoichiometry. This study was focused on revealing the crystal defects which come from the intrinsic properties of the material and are not influenced by technological conditions.

First of all, the defects caused by preferential evaporation of the most volatile component from the melt during crystal growth are expected. The formation of such defects has been clearly observed in the growth of single crystals in the binary systems PbO-WO_3 and Al_2O_3-Y_2O_3.[29] In the Gd_2O_3-Al_2O_3-Ga_2O_3 system, gallium oxide is the most volatile compound[30] and evaporates faster than other constituents in the melted raw material. The structure of the garnet-type crystals under study belongs to the cubic space group $Ia3d$ (#230) with the cations in spatial positions (on 16a, 24c, and 24d sites) and oxygen anions in the general positions (on 96h sites).[31] Three cations have tetrahedral coordination (24d sites) and two cations have octahedral (16a sites) coordination formed by oxygen ions. The eighth coordinate sites (dodecahedral, 24c sites) accommodate rare earth ion or yttrium. In a disordered GAGG crystal, 60% of Ga^{3+} ions occupy the tetrahedral sites, whereas 40% octahedral sites. The formation of cation vacancies due to the gallium evaporation inevitably leads to the formation of anionic vacancies in octahedrons and tetrahedrons and, as a consequence, of trapping centers based on such vacancies.

The use of the Al–Ga mixture to make crystal introduces two side effects: i) site occupancy disorder and ii) formation of additional defects that act as trapping centers for nonequilibrium carriers. The ratio of the ionic radii of Al and Ga is 0.83 and 0.85 in the oxygen tetrahedral and octahedral positions.[32] Therefore, even a random distribution of Al and Ga ions in the lattice results in considerable distortion of the lattice. Due to this reason the multicomponent gadolinium garnets containing gallium and aluminum should contain more structural defects than the binary garnet crystals do. Moreover, gallium and aluminum ions located in close proximity also result in considerable lattice strain, lead to distortion of the polyhedra, and, as a consequence, result in formation of numerous characteristic shallow trapping centers. The samples without codoping exhibit room temperature phosphorescence at photoexcitation in the absorption bands of both Ce^{3+} and Gd^{3+}. Worth to note, the spectra of the TSL glow creation, absorption spectra of Ce^{3+} ions and spectra of phosphorescence creation coincide.[33]

Figure 5 shows the TSL curves and the thermal activation energy E_{TA} of the traps corresponding to the glow peaks measured in the samples B1–B3. Similar to the data presented in Refs. [17,34,35], strong TSL peaks of complex structure have been detected in GAGG crystal in the temperature range 25–100 K. In TSL of all the samples, Ce^{3+} luminescence is observed and the TSL spectra also exhibit a glow peak above RT near 395 K, as reported in Ref. [33]. The shallow traps are better resolved in sample B1 (with stoichiometric melt composition) than in samples B2 and B3 (nonstoichiometric). We observed that the amount of the groups of the shallow traps having E_{TA} within the range 0.02–0.2 eV does not change drastically from sample to sample. However, the intensities of the corresponding TSL peaks are affected by the addition of excess Ga and Zr-codoping.

The comparison of TSL spectra in samples B1–B3 shows that the introduction of excess Ga increases the intensity of the TSL bands in the range 150–300 K. On the contrary, the codoping with Zr^{4+} reduces the intensity of the TSL bands in this temperature range but gives the rise to the band above 350 K. However, both additional Ga or Zr ions do not change significantly the group of TSL peaks bellow 150 K. Thus, we suggest that shallow traps with E_{TA} smaller than 0.1 eV most probably are caused by distortions of the polyhedra, as it was noted above, whereas the traps with larger E_{TA} correspond to structural point defects, most probably anion vacancies, the concentration of which is affected by applied codopings. It is worth noting that the activation energies of the deepest traps we observe by applying the TSL technique to the samples under study are smaller than ≈0.2 eV. This is consistent with the results presented in Ref. [36], where the deepest trapping levels are reported at ≈0.3 eV below the bottom of the conduction band.

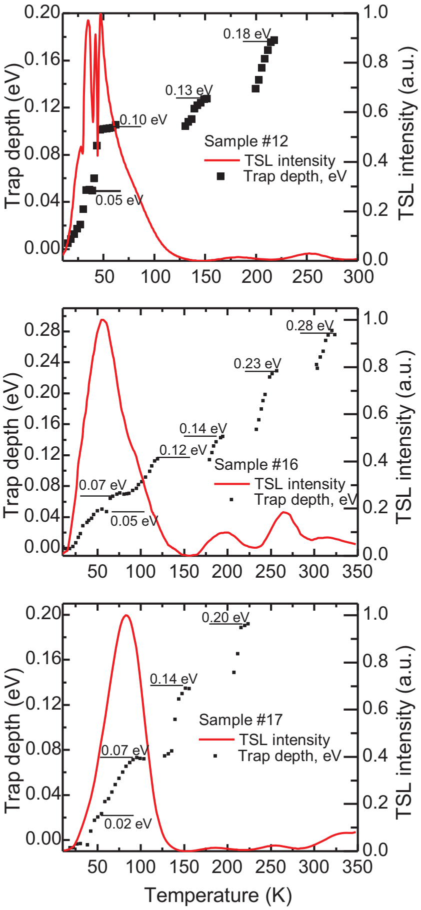

Figure 5. TSL curve (red) and E_{TA} of the traps (points) observed in samples B1, B2, and B3 (from top to bottom).

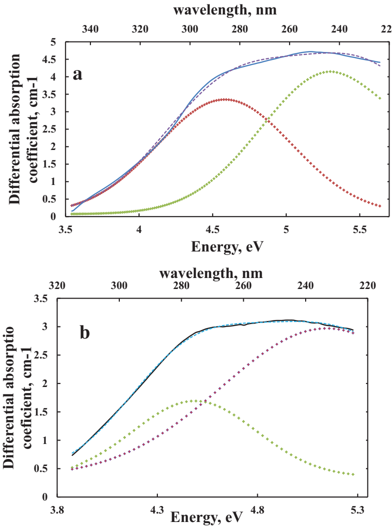

Figure 6. Spectra of difference in absorption coefficients with and without calcium codoping in LSO:Ce (a) and YSO:Ce (b). The dashed line represents the best fit by two Gaussian-shaped components (dotted lines).

3.3. Luminescence Build Up in LSO:Ce Crystals

The excitation transfer in GAGG is strongly influenced by Gd^{3+}. The transfer is expected to be simpler in oxyorthosilicate crystal Lu_2SiO_5 (LSO). Similarly to GAGG, aliovalent codoping introduces an additional absorption band in UV range. To reveal the general features of the codoping effect, we compared the differential absorption spectra of solely doped with Ce and codoped with Ca^{2+} crystals of Lu_2SiO_5 (L1) and isostructural Y_2SiO_5 (L2), see **Figure 6**. In oxyorthosilicate structure, calcium ions substitute lutetium ions, which have two inequivalent positions with six and seven oxygen neighbors. The introduction of divalent ions into the oxyorthosilicate single crystal results in a broad absorption band consisting of two strongly overlapping bands. The calcium-induced absorption spectrum can be well fitted by two Gaussian-shaped bands (dotted lines in Figure 6; Pearson's chi-square test value $\chi^2 = 4 \times 10^{-3}$ for LSO:Ce and 10^{-3} for LYSO:Ce). The two components have peaks at 270 and 235 nm in LSO:Ce and 275 and 240 in YSO:Ce. The two bands in the absorption spectrum of oxyorthosilicates are consistent with two possible Ca^{2+} ion positions of localization in the host matrix, 6(O) and 7(O), instead of a single position 8(O) in scintillators with a garnet structure. Obviously, a similar two-component absorption band should be formed in mixed crystal LYSO.

To get information on excitation transfer in LSO:Ce (a) and YSO:Ce, the nonlinear optical absorption induced by a short pulse of UV photons was studied. 200-fs-long pulses at 4.9 eV (254 nm) were used for excitation. The excitation photon energy is lower than the band gap of both LSO (6.4 eV) and YSO but is sufficient to excite cerium ions into the first and second excited state. The spectrum of the transient differential absorption (DA) of LSO:Ce (sample L3) contains one wide band overlapping the range 460–730 nm and peaked at 580 nm.

The initial part of the kinetics of the spectrally integrated DA signal is presented in **Figure 7**. The signal appears simultaneously with the leading edge of the pump pulse. The decay of the DA proceeds on a nanosecond time scale (see inset in

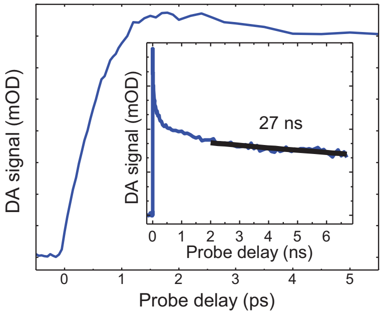

Figure 7. Kinetics of differential absorption in LSO:Ce, sample L3, in picosecond and nanosecond (inset) domains probed at 650 nm after 200-fs-pulse excitation at 254 nm.

Figure 7) and has two components. The fast component has the time constant of ≈200 ps and its time-integrated weight is small in comparison with that of the slow component decaying with the time constant of ≈27 ns. This time constant is close to the decay time of excitation at Ce^{3+} radiating level. This is an indication that the observed transient absorption is predominantly caused by electrons populating the Ce^{3+} radiating level. The fast decay component of the differential absorption can be reasonably explained by capturing of the photoexcited electrons from Ce^{3+} excited state by traps. The small relative weight of this component indicates low concentration of the trapping centers and, consequently, high structural perfection of the crystal.

4. Discussion

4.1. Excitation Transfer in GAGG:Ce and GAGG:Ce,Mg Crystals

The photon energy of 3.6 eV (343 nm) is well below the band gap of GAGG. Thus, such photons predominantly excite Ce^{3+} ions in GAGG crystal. Nevertheless, GAGG:Ce at such photoexcitation exhibits strong phosphorescence,[37] which could be explained by the transfer of photoexcited electrons from the first excited state of Ce^{3+} to the conduction band, their trapping at shallow defect-related levels, thermally induced detrapping and return back to Ce^{3+} ions to recombine radiatively and cause the phosphorescence. For the efficient transfer of photoexcited electrons from Ce^{3+} ions to the conduction band, the first Stark component of the $5d^1f^0$ configuration Ce^{3+} should be close to the bottom of the conduction band.

The photon energy of 4.9 eV (254 nm), which was also used for excitation in our experiments, is sufficient to excite not only Ce^{3+} ions, as at 3.6 eV excitation, but also Gd^{3+} ions via the $^8S \rightarrow {}^6D_{7/2,9/2}$ transitions. Thus, the photons with energy of 4.9 eV generate free electrons via absorption by Ce^{3+} and subsequent transfer of the electrons to the conduction band and free holes via excitation of gadolinium ions. The concentration of Ce^{3+} ions at the doping level of 0.5 at.% is substantially lower than the concentration of crystal-building Gd ions, therefore, the density of free electrons at this excitation is considerably smaller than that of free holes, in contrast to the excitation at 3.6 eV generating no free holes. As pointed out in our previous paper,[38] the PL kinetics is consistent with the assumption that the ground ^8S level of Gd^{3+} is in the valence band. The current results on the differential absorption (see Figure 4) enables us to define the position of the Gd^{3+} ground state in the valence band. The differential absorption caused by free holes in the valence band should have a smooth proportionality of the absorption coefficient on the wavelength squared. Instead, we observe a structured increase with the photon energy. This dependence should be explained by the influence of the resonant energy levels in the valence band. Thus, the hump in the DA spectrum peaked at 1.05 eV has to be attributed to the position of the Gd ground state, i.e., the state is ≈1 eV below the top of the valence band.

Furthermore, the excitations at 3.6 and 4.9 eV enables us to study the transfer of nonequilibrium electrons and holes, respectively, by comparing the PL kinetics of GAGG:Ce. The PL rise time in GAGG:Ce after direct excitation of Ce^{3+} at 3.64 eV is 2 ns. As suggested in Ref. [38], this substantial delay in reaching the peak PL intensity is caused by the time necessary for establishing the equilibrium between trapping and detrapping of the free electrons, which are released into the conduction band from the Ce^{3+} excited level. The PL rise time after the predominant Gd^{3+} excitation at 4.9 eV is by a factor of three longer than that after the direct excitation. Thus, the excitation transfer from the gadolinium sublattice to the radiative Ce^{3+} sites takes a few nanoseconds, what is caused by a relatively slow migration of excitations along the Gd sublattice.[39]

The presence of a distinct absorption band in the instantaneous DA spectrum correlates with the qualitative transformation of the DA kinetics (see Figure 3). The DA signal rises with characteristic time constant of 1.5 ps. The rise exhibits no significant dependence on the probe energy and, most probably, is predominantly determined by the relaxation of holes from the Gd^{3+} ground level toward the top of the valence band. The decay kinetics shows that the DA has two decay components. The response is dominated by a component with the characteristic decay time of 40–50 ns. In addition, a fast decaying component is observed at the initial part of the DA decay. The fast component might be attributed to absorption by free electrons. The time-integrated contribution of this component is approximately by three orders of magnitude smaller than that of the slow component caused by free hole absorption. Note that the fast component is more pronounced for the probe photon energy below ≈1 eV. At larger probe photon energies, when the free hole absorption is enhanced due to the optical transitions of free holes to the ground state of Gd ions, the relative contribution of the fast component becomes less pronounced.

The rising part in the DA response of the Mg-codoped crystal becomes considerably faster (see Figure 3) due to contribution of Mg^{2+}-based defect centers in the generation of free holes at the top of valence band by absorbing 4.9 eV pump light. The defect centers cause additional nonradiative recombination. As a result, the DA signal decay is faster in the codoped crystal.

Thus, the slow rise component with characteristic time of a few nanoseconds in the GAGG:Ce luminescence response after short-pulse excitation is caused by trapping and detrapping of nonequilibrium electrons. In Mg-codoped crystals, the trapped electrons predominantly relax to the energy levels introduced by Mg-doping and recombine nonradiatively or are transferred to Ce^{3+}. As a result, the luminescence response to a short-pulse excitation becomes shorter, but the light yield decreases.

To clarify the energy transfer processes in GAGG, we sketched a simple energy level diagram of all the main structural units involved in the excitation transfer process (see **Figure 8**a). This diagram does not include configuration potential curves for d-type states, which are usually considered for the transitions with a large Stokes shift. For simplicity, we considered just the positions of zero-phonon states of the Stark components of d-states. The energy diagrams in Gd-based crystals have been discussed in Refs. [40–42]. The energy-level diagram for Ce^{3+} in GAGG has been already described in Ref. [43], where the band gap of 6.8 eV was used. Different band gap values are also reported in Ref. [44]. The energy differences between Ce^{3+} levels used in this paper are based on the positions of the absorption and luminescence bands reported in Ref. [38]. Taking into account that the lowest zero-phonon radiating level of Ce^{3+} is located by 0.3 eV below the bottom of the conduction band,[33] we conclude that the center of gravity of the f^1-state is 2.6 eV below the radiating level. Thus, the f^1-level is ≈3.35 eV above the top of the valence band.

Our DA study described above shows that the position of the gadolinium ^8S level is by ≈1 eV lower than the top of the valence band. The position of the lowest terms corresponding to the excited states of f^7 Gd^{3+} was estimated using absorption spectra (see, e.g., Ref. [38]). The corresponding positions of narrow P, I, and D states without accounting for their splitting by spin-orbit interaction are indicated in the diagram. These energy positions favor the excitation transfer from the Gd^{3+} sublattice to Ce^{3+} ions. The efficiency of this transfer is evidenced by strong luminescence at Ce^{3+} ions even after the predominantly resonant excitation of gadolinium sublattice at excitation with 4.9 eV photons.

The band gap of GAGG contains defect-related states. As evidenced by the TSL study presented above, intrinsic structural defects impose the states, which are located below the band gap not deeper than ≈0.3 eV. These levels trap electrons from the conduction band, while the thermal reexcitation of the electrons back to the conduction band results in delayed luminescence.

Our results show that the defect related with Mg^{2+} in GAGG has a broad absorption band, most probably due to a charge transfer transition. Therefore, the corresponding energy level in the band gap of GAGG is well below the trapping states but higher than the P, I, and D states of Gd^{3+}. As seen in the diagram, Gd- and Ce-related transitions and traps have poor resonance conditions. Thus, the probability of tunneling from traps to Gd subsystem is low, a considerable fraction of the trapped electrons are detrapped and take part in phosphorescence. The defects introduced by codoping with Mg might capture the electrons trapped at shallow centers. This capture is evidenced by the substantial decrease in intensity of the TSL bands due to relatively shallow traps, as discussed above, and is consistent with the results presented in Refs. [34,36]. The electrons captured down to Mg-related defects might follow two possible roots: i) be transferred to Gd^{3+} states and further to Ce^{3+} or ii) recombine nonradiatively at the defect with the free hole from the valence band. The first root results in a faster rise of luminescence response after short-pulse excitation and diminishes the delayed luminescence. Meanwhile, the additional channel of nonradiative recombination, which is introduced by Mg-codoping, reduces the light yield of GAGG:Ce.

The results discussed above show that the nonequilibrium holes reach the radiative Ce^{3+} centers faster than the nonequilibrium electrons do. This is an indication that, at a relatively small concentration of Mg ions, as in the samples studied in the current paper, the scintillation mechanism due to the consecutive capturing of the carriers, holes and electrons, by Ce^{3+} ions is still dominating.

The competition of hole capturing by Ce^{3+} ion and its nonradiative recombination at Mg^{2+}-based defect explains the

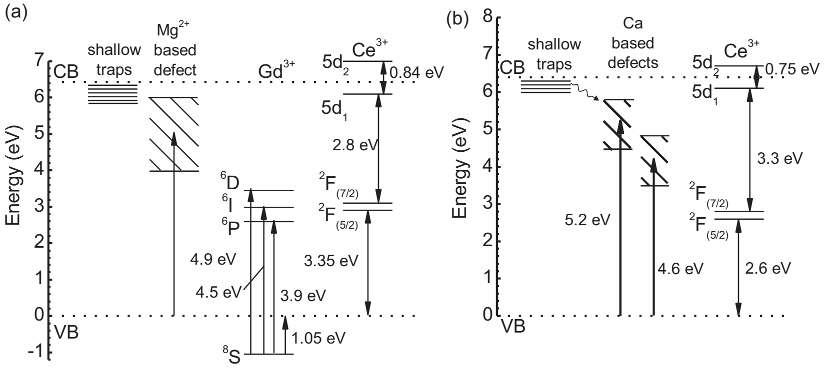

Figure 8. Energy-level diagram for GAGG crystal doped with Ce and codoped with Mg (a) and for LSO doped with Ce and codoped with Ca (b).

improvement of the light yield of codoped GAGG samples with temperature decrease, as described in Ref. [16], where it is shown by the gated light yield measurements that the scintillation kinetics is not changed in the temperature range from room temperature down to −45°C, while the light yield increases by 20%. An increase of the light yield with a minor temperature decrease bellow room temperature is not typical for Ce-doped scintillation crystals.[29] Most probably, the observed gain in the light yield at lower temperatures is the result of increased lifetime of holes. The carrier recombination, which is in our case a Shockey–Read–Hall process,[45–47] is temperature dependent. The carrier lifetime depends on the capture rate, which decreases as temperature is decreased. A possible mechanism of the decrease is longer time the holes remain at the ^{8}S level of Gd^{3+}, which is bellow the top of the valence band.

4.2. Excitation Transfer in Oxyorthosilicates

In crystals containing no matrix-building Gd^{3+} ions, the resonance conditions between Ce^{3+} and Ca (Mg) related defect play the crucial role. The crystal field at the Ce^{3+} ion positions is smaller in LSO, YSO, and LYSO than that is GAGG. Therefore, the energy difference between ^{2}F states and the first Stark component of 4f^{0}5d^1 configuration is larger. The energy level diagram for LSO, like that described above for GAGG:Ce, is presented in Figure 8b. Similar diagrams are also expected for YSO and LYSO crystals. The main deference between LSO and GAGG is a faster electron transfer due to a better overlapping between the broad subbands due to the defects associated with divalent ion and the interconfigration absorption bands of the radiative Ce centers.

In contrary to GAGG, where shallow defects dominate, LSO have trapping centers with large activation energy resulting in TSL peaks at 354, 410, 462, 524, and 569 K, which are related to oxygen vacancies.[48,49] Similar to GAGG:Ce, codoping with divalent ions facilitates the electron transfer from the traps to Ce^{3+}.

The codoping of oxyorthosilicates by divalent ions improves both the time characteristics of luminescence response and the light yield of the crystal. In contrary to GAGG, LSO has no peculiarities in the valence zone. Thus, hole dynamics in LSO and nonradiative recombination at the Ca-based centers are less sensitive to the temperature change. As a result, the luminescence build-up process is practically the same in LSO with and without codoping. This is also proven by gated light yield measurements showing that the light yield is insensitive to temperature down to −45 °C.[50]

The results discussed above allow making suggestions on the choice of the optimal oxide compound in view of both improvement of timing characteristics and a high light yield. First, the compound should have crystal field for Ce stabilization similar or larger than in orthosilicates in order to balance resonance transfer conditions from alkali-earth-based defect to activator. The choice of the crystal matrix with smaller crystal field at the Ce^{3+} position results in a decrease of the scintillation light yield, as in YAlO$_3$ codoped with Ce and Ca.[51] As already published, the defects practically do not affect the photoluminescence decay time, but strongly reduce the decay time of scintillation and the light yield. This is an evidence of weak quenching of Ce^{3+} luminescence by Ca-based defects and strong competition of the defects and Ce^{3+} ions in receiving excitation from matrix. Similar effect is observed when crystal is doped with Pr^{3+} and codoped with alkali-earth ions.[52] The inter-configuration $4f5d \rightarrow f^2$ luminescence of Pr^{3+} consists of two overlapped wide unstructured bands at room temperature, usually in the UV range. Large energy of the emitting state does not allow an effective transfer from alkali-earth-based defect.

5. Conclusion

Our time-resolved study of the photoluminescence response to short-pulse excitation at different wavelengths and free carrier absorption, supported by the results available in the literature, enabled us to explain the changes of the scintillation parameters of GAGG:Ce and LSO:Ce imposed by additional aliovalent codoping.

It is shown that the ground state of lattice-building gadolinium ions in GAGG crystal is in the valence band by ≈1 eV from its top. The gadolinium sublattice plays a significant role in the transfer of both nonequilibrium holes and electrons. As a result, the luminescence response to a short-pulse excitation becomes shorter, but the light yield decreases.

In Ce-doped oxyorthosilicates, the overlap between i) the electron trap levels; ii) a broad subband due to defects related with divalent ion; and iii) the excited level of radiative Ce^{3+} ions is better than that in GAGG:Ce,Mg, thus, codoping with divalent ions results in improvement of both time response and light yield.

Acknowledgments

This work has been supported by the European Social Fund Measure No. 09.3.3-LMT-K-712 activity Improvement of Researchers Qualification by Implementing the World-Class R&D Projects, and by grant #14. W03.31.0004 of the Russian Federation Government. Authors are grateful to CERN Crystal Clear Collaboration and COST Action TD1401 "Fast Advanced Scintillator Timing (FAST)" for support of collaboration.

Conflict of Interest

The authors declare no conflict of interest.

Keywords

excitation transfer, free carriers, multicomponent garnets, scintillators

Received: October 20, 2017
Revised: January 25, 2018

---

[1] K. Kamada, T. Endo, K. Tsutumi, T. Yanagida, Y. Fujimoto, A. Fukabori, A. Yoshikawa, J. Pejchal, M. Nikl, *Cryst. Growth Des.* **2011**, *3*, 4484.

[2] K. Kamada, T. Yanagida, J. Pejchal, M. Nikl, T. Endo, K. Tsutsumi, Y. Fujimoto, A. Fukabori, A. Yoshikawa, *IEEE Trans. Nucl. Sci*. **2012**, *59*, 2112.

[3] S. K. Yadav, B. P. Uberuaga, M. Nikl, C. Jiang, C. R. Stanek, *Phys. Rev. Appl*. **2015**, *4*, 1.

[4] M. Fasoli, A. Vedda, M. Nikl, C. Jiang, B. P. Uberuaga, D. A. Andersson, K. J. McClellan, C. R. Stanek, *Phys. Rev. B – Condens. Matter Mater. Phys*. **2011**, *84*, 1.

[5] H. L. Kim, H. J. Kim, E. J. Jang, W. G. Lee, M. K. Ki, H. D. Kim, G. S. Jun, V. Kochurikhin, *J. Ceram. Process. Res*. **2015**, *16*, 124.

[6] E. V. D. van Loef, P. Dorenbos, C. W. E. van Eijk, K. Krämer, H. U. Güdel, *Appl. Phys. Lett*. **2001**, *79*, 1573.

[7] N. J. Cherepy, S. A. Payne, S. J. Asztalos, G. Hull, J. D. Kuntz, T. Niedermayr, S. Pimputkar, J. J. Roberts, R. D. Sanner, T. M. Tillotson, E. Van Loef, C. M. Wilson, K. S. Shah, U. N. Roy, R. Hawrami, A. Burger, L. A. Boatner, W. S. Choong, W. W. Moses, *IEEE Trans. Nucl. Sci*. **2009**, *56*, 873.

[8] Z. Yan, T. Shalapska, E. D. Bourret, *J. Cryst. Growth* **2016**, *435*, 42.

[9] K. Kamada, M. Nikl, S. Kurosawa, A. Beitlerova, A. Nagura, Y. Shoji, J. Pejchal, Y. Ohashi, Y. Yokota, A. Yoshikawa, *Opt. Mater. (Amst)*. **2015**, *41*, 63.

[10] G. Dosovitskiy, A. Fedorov, V. Mechinsky, A. Borisevich, A. Dosovitskiy, E. Tret'jak, M. Korjik, *IOP Conf. Series: Mater. Sci. Eng*. **2017**, *169*, 012014.

[11] M. A. Spurrier, P. Szupryczynski, K. Yang, A. A. Carey, C. L. Melcher, *IEEE Trans. Nucl. Sci*. **2008**, *55*, 1178.

[12] S. Blahuta, A. Bessiere, B. Viana, P. Dorenbos, V. Ouspenski, *IEEE Trans. Nucl. Sci*. **2013**, *60*, 3134.

[13] G. Tamulaitis, A. Vaitkevičius, S. Nargelas, R. Augulis, V. Gulbinas, P. Bohacek, M. Nikl, A. Borisevich, A. Fedorov, M. Korjik, E. Auffray, *Nucl. Instruments Methods Phys. A* **2017**, *870*, 25.

[14] M. T. Lucchini, V. Babin, P. Bohacek, S. Gundacker, K. Kamada, M. Nikl, A. Petrosyan, A. Yoshikawa, E. Auffray, *Nucl. Instruments Methods Phys. A* **2016**, *816*, 176.

[15] M. T. Lucchini, S. Gundacker, P. Lecoq, A. Benaglia, M. Nikl, K. Kamada, A. Yoshikawa, E. Auffray, *Nucl. Instruments Methods Phys. A* **2017**, *852*, 1.

[16] M. Korjik, V. Alenkov, A. Borisevich, O. Buzanov, V. Dormenev, G. Dosovitskiy, A. Dosovitskiy, A. Fedorov, D. Kozlov, V. Mechinsky, R. W. Novotny, G. Tamulaitis, V. Vasiliev, H-G Zaunick, A. Vaitkevičius, *Nucl. Instruments Methods Phys. A* **2017**, *871*, 42.

[17] W. Drozdowski, K. Brylew, M. E. Witkowski, A. J. Wojtowicz, P. Solarz, K. Kamada, A. Yoshikawa, *Opt. Mater. (Amst)*. **2014**, *36*, 1665.

[18] M. Nikl, V. Babin, J. Pejchal, V. V. Laguta, M. Buryi, J. A. Mares, K. Kamada, S. Kurosawa, A. Yoshikawa, D. Panek, T. Parkman, P. Bruza, K. Mann, M. Müller, M. Muller, *IEEE Trans. Nucl. Sci*. **2016**, *63*, 433.

[19] C. Hu, S. Liu, M. Fasoli, A. Vedda, M. Nikl, X. Feng, Y. Pan, *Opt. Mater. (Amst)*. **2015**, *45*, 252.

[20] Y. Wu, F. Meng, Q. Li, M. Koschan, C. L. Melcher, *Phys. Rev. Appl*. **2014**, *2*, 1.

[21] M. Nikl, K. Kamada, V. Babin, J. Pejchal, K. Pilarova, E. Mihokova, A. Beitlerova, K. Bartosiewicz, S. Kurosawa, A. Yoshikawa, *Cryst. Growth Des*. **2014**, *14*, 4827.

[22] M. Spurrier, P. Szupryczanski, A. carey, K. Yang, C. Melcher, *IEEE Trans. Nucl. Sci*. **2008**, *55, 1178*.

[23] M. Koschan, K. Yang, M. Zhuravleva, C. L. Melcher, *J. Cryst. Growth* **2012**, *352*, 133.

[24] M. S. Alekhin, J. T. M. De Haas, I. V. Khodyuk, K. W. Krämer, P. R. Menge, V. Ouspenski, P. Dorenbos, *Appl. Phys. Lett*. **2013**, *102*, 1.

[25] F. G. A. Quarati, M. S. Alekhin, K. W. Krämer, P. Dorenbos, *Nucl. Instruments Methods Phys. Res. Sect. A Accel. Spectrometers, Detect. Assoc. Equip*. **2014**, *735*, 655.

[26] K. Yang, P. Menge, J. Frank, Scintillation crystal including a co-doped sodium halide, and a radiation detection apparatus including the scintillation crystal, International Patent Application PCT/US2016/017945.

[27] K. Yang, C. L. Melcher, P. D. Rack, L. A. Eriksson, *IEEE Trans. Nucl. Sci*. **2009**, *56*, 2960.

[28] R. Chen, V. Pagonis, *Thermally and Optically Stimulated Luminescence: A Simulation Approach*. John Wiley & Sons, USA **2011**, pp. 434.

[29] P. Lecoq, A. Gektin, M. Korzhik, Springer, Germany **2017**, p. 408.

[30] R. H. Lamoreaux, D. L. Hildenbrand, L. Brewer, *J. Phys. Chem. Ref. Data* **1987**, *16*, 419.

[31] A. Nakatsuka, A. Yoshiasa, T. Yamanaka, *Acta Crystallogr. Sect. B*. **1999**, *55*, 266.

[32] R. D. Shannon, *Acta Crystallogr. Sect. A* **1976**, *32*, 751.

[33] E. Auffray, R. Augulis, A. Borisevich, V. Gulbinas, A. Fedorov, M. Korjik, M. T. Lucchini, V. Mechinsky, S. Nargelas, E. Songaila, G. Tamulaitis, A. Vaitkevičius, S. Zazubovich, *J. Lumin*. **2016**, *178*, 54.

[34] E. Mihóková, K. Vávrů, K. Kamada, V. Babin, A. Yoshikawa, M. Nikl, K. Vávr, K. Kamada, V. Babin, A. Yoshikawa, M. Nikl, *Radiat. Meas*. **2013**, *56*, 98.

[35] K. Brylew, W. Drozdowski, A. J. Wojtowicz, K. Kamada, A. Yoshikawa, *J. Lumin*. **2014**, *154*, 452.

[36] K. Mamoru, K. Kei, K. Shunsuke, A. Junpei, O. Akimasa, Y. Akihiro, H. Kazuhiko, *Appl. Phys. Express* **2016**, *9*, 72602.

[37] G. Dosovitskiy, O. Buzanov, A. Dosovitskiy, A. Fedorov, L. Grigorjeva, M. Korjik, V. Mechinsky, S. Nargėlas, G. Tamulaitis, V. Vasiliev, S. Zazubovich, A. Zolotarjovs, $Gd_3Al_2Ga_3O_{12}$:Ce stoichiometry deviation influence on the crystal scintillation properties, 19th International Conference on Defects in Insulating Materials, Abstrct, ICDIM **2016**, 10–15 July 2015, Lyon, France.

[38] E. Auffray, M. Korjik, M. T. Lucchini, S. Nargelas, O. Sidletskiy, G. Tamulaitis, Y. Tratsiak, A. Vaitkevičius, *Opt. Mater. (Amst)*. **2016**, *58*, 461.

[39] N. V. Selina, E. N. Tumaev, *Optics and Spectroscopy* **2002**, *92*, 697.

[40] H. Suzuki, T. A. Tombrello, C. L. Melcher, C. A. Peterson, J. S. Schweitzer, *Nucl. Inst. Methods Phys. Res. A* **1994**, *346*, 510.

[41] H. Suzuki, T. A. Tombrello, C. L. Melcher, J. S. Schweitzer, *1993 IEEE Conf. Rec. Nucl. Sci. Symp. Med. Imaging Conf*. **1994**, *41*, 14.

[42] H. Suzuki, T. A. Tombrello, C. L. Melcher, J. S. Schweitzer, *J. Lumin*. **1994**, *60–61*, 960.

[43] F. Meng, M. Koschan, Y. Wu, C. L. Melcher, P. Cohen, *Nucl. Instruments Methods Phys. Res. Sect. A Accel. Spectrometers, Detect. Assoc. Equip*. **2015**, *797*, 138.

[44] J. M. Ogieglo, Luminescence and Energy Transfer in Garnet Scintillators, Doctoral Thesis, Utrecht University, **2012**.

[45] W. Shockey, W. T. Read, *Phys. Rev*. **1952**, *87*, 387.

[46] H. Queisser, *Solid-State Electron*. **1978**, *21*, 1495.

[47] J. Divkovic, *AUTOMATIKA* **2002**, *43*, 47.

[48] P. Dorenbos, C. W. E. van Eijk, A. J. J. Bos, C. L. Melcher, *J. Phys. Condens. Matter*. **1994**, *6*, 4167.

[49] S. Blahuta, A. Bessière, B. Viana, V. Ouspenski, E. Mattmann, J. Lejay, D. Gourier, *Materials (Basel)* **2011**, *4*, 1224.

[50] A. Vaitkevichus, Private communication, Vilnis 25 June **2017**.

[51] F. Moretti, K. Hovhannesyan, M. Derdzyan, G. A. Bizarri, E. D. Bourret, A. G. Petrosyan, C. Dujardin, *ChemPhysChem* **2017**, *18*, 493.

[52] J. Peichal, M. Buryi, V. Babin, A. Beitlerova, J. Barta, L. Havlak, K. Kamada, A. Yoshikawa, V. Laguta, M. Nikl, *J. Lumin*. **2017**, *181*, 277.

Paper P10

Barium and lithium silicate glass ceramics doped with rare earth ions for white LEDs

E. Trusova, **A. Vaitkevičius**, Y. Tratsiak, M. Korjik, P. Mengucci, D. Rinaldi, L. Montalto, V. Marciulionyte, G. Tamulaitis

Opt. Mater. (Amst). 84 (2018) 459–465.

doi:10.1016/j.optmat.2018.07.030.

Optical Materials 84 (2018) 459–465

Contents lists available at ScienceDirect

Optical Materials

journal homepage: www.elsevier.com/locate/optmat

Barium and lithium silicate glass ceramics doped with rare earth ions for white LEDs

E. Trusova[a], A. Vaitkevičius[b], Y. Tratsiak[c,*], M. Korjik[d], P. Mengucci[e], D. Rinaldi[e], L. Montalto[e], V. Marciulionyte[b], G. Tamulaitis[b]

[a] Belarusian State Technological University, Minsk, Belarus
[b] Institute of Photonics and Nanotechnology, Vilnius University, Lithuania
[c] Research Institute for Physical Chemical Problems of Belarusian State University, Minsk, Belarus
[d] Research Institute for Nuclear Problems, Minsk, Belarus
[e] Dipartimento di Scienze e Ingegneria della Materia, dell'Ambiente ed Urbanistica ("SIMAU") Università Politecnica delle Marche, Ancona, Italy

ARTICLE INFO

Keywords:
Photoluminescence
Glasses
Glass ceramics
Barium disilicate
Lithium disilicate

ABSTRACT

Novel glasses and glass ceramics with compositions corresponding to stoichiometric lithium and barium disilicates and doped with different combinations of Ce^{3+}, $Eu^{2+,3+}$, Tb^{3+}, and Dy^{3+} have been fabricated and studied as prospective light converters for white high-power light emitting diodes and laser diodes. Spatially resolved photoluminescence spectroscopy and structural analysis have been employed. The emission spectra and CIE color coordinates of these materials evidence their good prospective as phosphors for white light sources. Structural analysis proves a high level of crystallization of the ceramics fabricated by annealing the glasses, while spectroscopic study revealed the influence of crystallization on the emission properties of this system. The results show a high potential of these materials be exploited as temperature-resistant phosphors in high-power white light emitting diodes.

1. Introduction

Since the invention of the blue light emitting diode (LED), the solid state lighting technology achieved a tremendous progress. However, the adoption of LED lighting products for certain applications is hampered by the lack of high power white LEDs capable for long-lasting operation in harsh environment, especially, at elevated temperatures or strong ionizing radiation. Currently, the commercial white LEDs are composed of a blue InGaN LED covered by epoxy containing phosphor (usually YAG:Ce^{3+}) converting the blue emission to a broad band in yellow spectral region [1–5]. However, the epoxy materials in use suffer from poor stability when exposed to short-wavelength light and high temperatures [6]. This hampers the progress in the development of specific light sources powered by near UV LEDs, in production of LEDs operating in harsh environment, and in laser-diode-pumped high-luminosity light sources [7,8], which are currently on increasing demand.

Due to substantially higher operational performance, glass ceramics might be a relatively inexpensive alternative to the epoxy materials. The glass ceramics not only exhibit high stability at elevated temperatures and under exposition to UV radiation but also have high thermal conductivity [9]. These properties enable the development of high-power white LEDs and laser diodes with increased lifetime and higher light output. Moreover, the glass ceramic materials can be obtained via thermal annealing of glasses without affecting their external geometry [10]. It is well known that crystalline silicates doped with rare earth ions (REI), e.g., Gd_2SiO_5 (GSO), Y_2SiO_5 (YSO); SiO_2, are prospective emitting materials and are extensively used as phosphors or scintillation materials. Silicates in a glass form are well emitting materials too (e.g., GS20 from Scintacor or lithium or barium disilicate glasses) [11–14]. Two types of crystallization, avalanche and homogenous, might occur in glasses. The latter allows for controlling the formation of crystalline phase and, as a result, the transparency of the glass ceramics, what is important for their use in combination with LEDs. Previously, we demonstrated the possibility of homogenous crystallization and studied the influence of the crystallization on the structural and luminescence properties of barium disilicate doped with Ce^{3+} (DSB:Ce) [15].

When using UV LEDs as an excitation source to generate white light, the UV LED emission should be converted into blue, red and green light [16]. Several REI are considered to be promising activators for phosphors suitable to be exploited in combination with LEDs. The simultaneous LED excitation of three phosphors enables regulation of the color

---

[*] Corresponding author.
E-mail address: slon.zhenya@gmail.com (Y. Tratsiak).

https://doi.org/10.1016/j.optmat.2018.07.030
Received 14 May 2018; Received in revised form 21 June 2018; Accepted 12 July 2018

temperature of the white light by changing the contribution of blue, green, and red components and, on the other hand, to achieve good uniformity of the light field. Ions Ce^{3+}, Tb^{3+}, Dy^{3+}, Eu^{3+}, and Eu^{2+} are promising REI for generation of blue [15], green [14], and red [17,18] light. To use the emission efficiently, appropriate glass hosts have to be selected and fabricated. The glasses allowing simultaneous doping with these REI are of especial interest. Furthermore, glass ceramics might be fabricated to improve the thermal conductivity and stability of the phosphor, which, in combination with mechanical hardiness and good color rendering, improve the performance of LED-based lighting [19,20].

It is well known that the emission spectra of Ce^{3+} and Eu^{2+} due to d-f transitions strongly depend on the crystal field [21,22]. At excitation in UV region, weakening of the crystal field results in a blue shift of the Ce^{3+} emission band (e.g., from 550 nm in YAG:Ce [23] to 450 nm in DSB:Ce [15]). The emission of Eu^{2+} in glasses and crystalline materials are predominantly located in the blue spectral region. Thus, Eu^{2+} is a suitable dopant in glasses or glass ceramics for generating blue emission. Meanwhile, Tb^{3+}, Dy^{3+}, and Eu^{3+} emission due to f-f transitions are weakly affected by the crystal field. As a result, they are suitable to generate green (intense $^5D_4 - {}^7F_5$ transition of Tb^{3+} ions at 545 nm) [24], yellow ($^4F_{9/2} - {}^6H_{13/2}$ transition of Dy^{3+} ions at 575 nm) [25], and red ($^5D_0 - {}^7F_2$ transition of Eu^{3+} at 612 nm) [26] emission at UV LED excitation.

The prospects of using DSB:Ce glasses and glass-ceramics as phosphors has already been demonstrated [15]. In this paper, we report on the luminescence properties of DSB glasses and glass ceramics doped with several REI: Ce^{3+}, Tb^{3+}, Dy^{3+}, Eu^{3+}, and Eu^{2+}. We studied these materials in view of their exploitation as wavelength converters for white light sources pumped by UV LEDs. Rare-earth-doped lithium disilicate (DSL) glasses, having a lower glass forming temperature than that for DSB glasses, were also studied as an alternative to DSB glasses. Moreover, the investigation of the crystallization on the emission properties in REI-doped DSL glasses are of interest in view of their possible application as scintillators, since DSL:Ce^{3+} and DSL:Tb glasses are already known as prospective scintillators.

2. Experimental

The glass samples with composition of Li_2O (BaO) and SiO_2 at 33 to 67 in mol. % were synthesized for this study by the melt-quenching technique. The raw materials (99.99% purity) were weighted and homogenized in a 20 cm^3 aluminum oxide ceramic crucible. Oxides CeO_2, Tb_2O_3, Eu_2O_3, and Dy_2O_3 have been used as doping sources for Ce^{3+}, Tb^{3+}, Eu^{3+}/Eu^{2+}, and Dy^{3+}, respectively, and were added to the raw material in amount of 6 wt. % for CeO_2 and Tb_2O_3 and 3 wt.% for Dy_2O_3 and Eu_2O_3. The RE ions were introduced at the levels of 1–5 at. %, which are typical for their efficient performance in most luminescent materials The contents of the activators in at. % introduced into the glass matrix by the substitution of Li^+ (Ba^{2+}) ions are listed in Table 1.

The glass synthesis has been performed for 2 h at the temperature of 1420 °C for DSL glass and 1500 °C for DSB glass in the gas furnace with CO-rich atmosphere. The melt was casted on the steel surface, and the samples were afterwards annealed at 450–700 °C for 4 h in a muffle furnace. The glass samples were cooled down to the room temperature at the rate of ~50 °C per hour. The glass samples were transparent, did not contain any cracks and had no opalescence. The samples were cut and polished in the shape of plates with a thickness of 1–2 mm.

Table 1
Content of activators introduced into the glass matrix by substitution of Li^+ (Ba^{2+}) ions.

REI dopant	Substitution of Ba^{2+} by REI in DSB, at. %	Substitution of Li^+ by REI in DSL, at. %
Ce^{3+}	1.88	2.65
Tb^{3+}	1.77	2.50
Dy^{3+}	0.87	1.22
Eu^{3+}	0.92	1.30

Afterwards, the DSB:Ce glasses were thermally treated in Lenton Furnace Eurotherm 2416CC at 750 °C, 800 °C, 850 °C, or 900 °C for 1 h and then cooled down. The targeted temperature has been reached at a rate of 5°/minute. The XRD study of the annealed samples has been carried out using Bruker D8 Advance X-ray diffractometer equipped with a θ-θ goniometer and using Cu-Kα radiation. The measurements to obtain the information on the compound formed during the heat treatments were performed in Bragg-Brentano geometry within the 2θ angular range of 15°–70°.

The DSL:Ce glasses have been thermally treated in Nabertherm LHT-18/04 at 500 °C, 550 °C, 600 °C, or 650 °C for 1 h and then cooled down. The X-ray diffraction patterns of the synthesized glass ceramic samples were obtained using Empyrean X-ray diffractometer with CuKα radiation in the 2θ angular range of 4°–70°.

To study the emission properties of DSB and DSL glasses and glass ceramics doped with different REI, we investigated the photoluminescence (PL) spectra with spatial resolution on a submicrometer scale. This allowed us to observe the influence of the sample structure on the PL spectrum and intensity. The PL spectroscopy has been performed using the microscopic system *WITec Alpha 300S* operated in confocal mode. An objective with the numerical aperture NA = 0.6 was used for excitation and collection of the PL signal ensuring the in-plane spatial resolution of ~250 nm and the axial resolution of ~1.6 μm. A laser diode (*ALPHALAS*) emitting at 405 nm was exploited for excitation. The microscopic system was connected by an optical fiber to a spectrometer with a thermoelectrically cooled CCD camera. The chromatic properties of the emission from the glasses and glass ceramics were calculated using the CIE 1931 standard color matching functions, as described in Ref. [27].

3. Results and discussion

The photoluminescence spectra of DSB and DSL glasses doped with Ce^{3+}, Dy^{3+}, and Eu^{3+} are presented in Fig. 1. No emission from glasses doped solely with Tb^{3+} has been detected.

As seen in Fig. 1, the emission of Ce^{3+} is observed in both glass matrixes. As reported for many host matrices before, the Ce^{3+} emission consists of two bands due to transitions $^5d_1$-$^2F_{5/2}$ and $^5d_1$-$^2F_{7/2}$, which

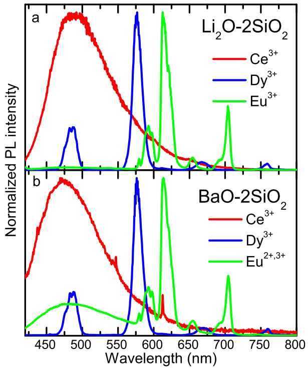

Fig. 1. Normalized photoluminescence spectra of DSB (a) and DSL (b) glasses doped with different rare earth ions (indicated).

are indistinguishably overlapped at room temperature [15]. The PL band in DSB:Ce^{3+} glass is redshifted in respect to its position in DSL:Ce^{3+} glass. The PL band peak positions are 488 nm and 473 nm in DSL:Ce^{3+} and DSB:Ce^{3+}, respectively. It is well known that the spectral positions of the absorption and emission bands due to the inter-configuration f-d transitions of Ce^{3+} strongly depend on the environment of the ion. The redshift indicates a larger crystal field splitting in the DSL glass due to a stronger internal electric field [14]. The full width at a half maximum (FWHM) of the PL emission band is ~10 nm smaller in DSB:Ce^{3+} glass than that in DSL:Ce^{3+}. This is an indication of a smaller variation in the environment of Ce^{3+} in DSB glass [15].

The emission from Dy^{3+} was observed in both DSB:Dy^{3+} (Fig. 1b) and DSL:Dy^{3+} (Fig. 1a) glasses. Four PL bands were detected: the band peaked at 485 nm was attributed to the $^4H_{15/2}-{}^6H_{15/2}$ transition, while the bands peaked at 575 nm, 667 nm, and 760 nm were attributed to the transitions from $^4F_{9/2}$ level to the $^6H_{13/2,}$ $^6H_{11/2}$, and $^6H_{9/2}/{}^6F_{11/2}$ multiplets, respectively [28–30]. Their spectral position, shape and intensity ratios do no exhibit considerable differences in the two matrixes.

The emission from glasses doped with Eu^{3+} has a complex structure and depends on the composition of the glass matrix [31–33]. The sets of multiple narrow PL bands are identical in DSB and DSL glasses and are caused by $^5D_0-{}^7F_J$ (J = 1, 2, 3,4) radiative transitions of Eu^{3+}. The wide PL band observed clearly in the DSB glass is assigned to inter-configurational radiative 5d-4f transitions in the Eu^{2+} and is sensitive to crystal field [34,35]. Meanwhile, the Eu^{2+} emission is negligible in DSL glass. The substantially stronger contribution of Eu^{2+} emission in DSB matrix might be a result of two factors: the influence of reducing atmosphere during the glass formation and the interaction of Eu^{3+} with defects in the glass matrix. The latter effect for DSB glasses can be presented by the following equations (designations by the Kroger-Vink):

$$3Ba_{Ba} + 2Eu^{3+} = 3Ba^{2+} + 2Eu_{Ba}^{\cdot} + V_{Ba}'' \quad (1)$$

$$V_{Ba}'' = V_{Ba}^{x} + 2e \quad (2)$$

$$2Eu_{Ba}^{\cdot} + 2e = 2Eu_{Ba}^{x} \quad (3)$$

Such transformation of europium valence state was previously observed in other material systems, e.g., in glass ceramics containing SrF$_2$ nanocrystals [36] and Eu^{2+} activated ZnO–B$_2$O$_3$–P$_2$O$_5$ glasses [37].

This process for DSL glasses can be presented as follows:

$$3Li_{Li} + Eu^{3+} = 3Li^{+} + Eu_{Li}^{\cdot\cdot} + 2V_{Li}' \quad (4)$$

$$2V_{Li}' = 2V_{Li}^{x} + 2e \quad (5)$$

$$Eu_{Li}^{\cdot\cdot} + e = Eu_{Li}^{\cdot} \quad (6)$$

The excess electrons generated in accordance with equation (5) can take part in the reduction of the valence state of Eu^{3+}. Furthermore, the presence of Eu ions in +2 oxidation state in DSB glasses may be explained similarity of ionic radii. The ionic radii of Eu^{3+}, Eu^{2+}, Ba^{2+} and Li^{+} ions with coordination number 6 are 0.947, 1.17, 1.35, and 0.76 A, respectively. Thus, Ba^{2+} and Eu^{2+} have close values of ionic radii and introduction of the Eu ions in +2 oxidation state into the Ba^{2+} network is more preferable to minimize the structural distortion in DSB, while Eu in the oxidation state +3 is more preferable in DSL, since Eu^{3+} and Li^{+} radii are similar.

The PL spectra of DSB glasses co-doped with the pairs of ions (Ce^{3+}and Tb^{3+}, Ce^{3+} and Eu^{3+}, Tb^{3+} and Eu^{3+}, Tb^{3+} and Dy^{3+}) and for DSL and DSB glasses co-doped with three ions (Ce^{3+}, Tb^{3+}, Eu^{3+}) are presented in Fig. 2 and Fig. 3, respectively. These samples have been selected from a variety of doping combinations in view of the best CIE color coordinates to generate white light (see Fig. 4 and discussion afterwards).

Codoping results in substantial changes in emission spectra in comparison with the spectra in single-doped glasses. For DSB:Ce,Tb, in addition to the emission of Ce^{3+} due to 4 d–5f transitions, narrow

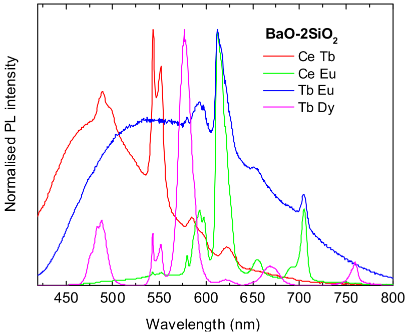

Fig. 2. Normalized PL spectra of DSB glasses doped with different combinations of rare earth ions (indicated).

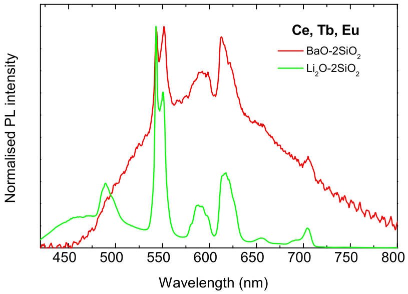

Fig. 3. Normalized PL spectra of DSB and DSL glasses doped with Ce^{3+}, Tb^{3+}, and Dy^{3+} ions.

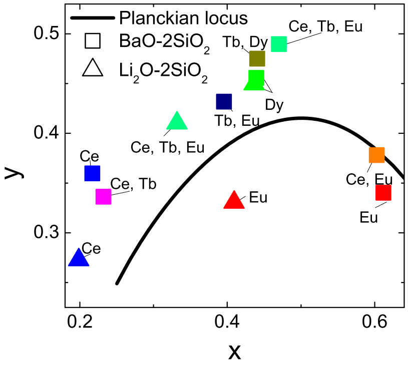

Fig. 4. CIE color coordinates of DSB (squares) and DSL (triangles) glasses doped with different combinations of rare earth ions (indicated). Excitation wavelength was 405 nm. (For interpretation of the references to color in this figure legend, the reader is referred to the Web version of this article.)

emission lines due to Tb^{3+} are clearly observable in the PL spectra and are attributed to $^5D_4 - {}^7F_J$ (J = 6, 5, 4, 3) transitions (see Fig. 2). Since no PL was observed in the glasses doped solely with Tb^{3+}, these emission lines might be attributed to the excitation transfer from Ce^{3+} to Tb^{3+}. The effect of sensitizing Tb^{3+} by Ce^{3+} has been previously observed in lithium disilicate and gadolinium borosilicate glasses [14,38].

The emission spectra of DSB:Eu, Tb glass are composed of bands associated with Eu^{2+} and Eu^{3+}, and no band to be attributed to emission at Tb^{3+} is observed. However, the relative intensity of Eu^{2+} emission is much higher in the codoped sample. This feature might be caused either by improved charge transfer from the glass matrix to Eu^{2+} due to Tb^{3+} acting as an intermediate step or by the transformation of europium valence state facilitated by Tb-doping, the latter effect being more likely [39]. On the other hand, the absence of the emission bands due to optical transitions at Tb^{3+} might be caused by quenching of Tb^{3+} by Eu-ions.

The emission spectra of DSB:Dy, Tb glass are similar to the emission of Dy^{3+} in single-doped DSB:Dy glass, with the addition of low-intensity PL lines associated with the $^5D_4 - {}^7F_5$ transition in Tb^{3+}, which probably occurs due to excitation transfer to Tb^{3+}.

In DSB:Ce, Eu glass, only the emission from the Eu^{3+} is observed. The absence of the emission from Eu^{2+} might be attributed to quenching by Ce^{3+}, while the Ce^{3+} emission is possibly quenched by Eu^{3+}.

The PL spectra of DSB and DSL glass codoped with the combination of Ce, Tb and Eu are different. In DSB:Ce,Tb,Eu, the resulting spectrum consists of PL lines associated with the transitions at Tb^{3+}, Eu^{3+} and Ce^{3+} and/or Eu^{2+} (see Fig. 3). In DSL:Ce,Tb,Eu, the PL spectrum is dominated by the bands due to Tb^{3+}, while Ce^{3+} and Eu^{3+} emit at substantially lower efficiency. It should be noted that the emission of divalent Eu^{2+}, which is quite strong in DSL:Eu, is completely quenched in DSL:Ce,Tb,Eu.

The CIE color points (see Fig. 4) of the samples under study are distributed in the vicinity of the Planckian locus. By combining the emission from DSL:REI glasses, it is possible to compile white light sources with color temperature above 3000 K. However, no combination of REIs in one matrix ensures the production of white light. The white light might be produced only by mixing REI-doped DSB and DSL glasses. Nonetheless, the color points and, as a result, the color temperature can be tuned by the variation of REI concentration in the glasses.

Though the selection of the matrix and the optimization of doping by REI is easier to perform in glasses, at least due to their inexpensive and flexible fabrication, glasses are not preferable materials for using in combination with LEDs, first of all, due to their low thermal conductivity negatively impacting the LED lifetime. From the point of view of thermal conductivity, glass ceramics are substantially more preferable than glasses. The high thermal conductivity of glass ceramics is a result of the composition of the ceramic material consisting of small particles of crystalline phase. The crystallites also scatter the emitted light. During the formation of crystallites, capturing of REIs into the crystallites occurs. Changing the crystalline environment also affects their luminescence properties. The influence of the annealing temperature on the crystalline structure were studied by XRD analysis. 2Θ scans of samples thermally treated at different temperatures are presented in Fig. 5. The luminescence spectra of Ce- and Eu-doped glasses and glass ceramics of DSB (annealed at 900 °C for 1 h) and DSL (at 750 °C for 1 h) are compared in Fig. 6.

The influence of annealing temperature on the crystalline structure was studied by XRD analysis. 2Θ scans of DSB:Ce samples thermally treated at different temperatures are presented in Fig. 4. The crystallization of DSB:Ce samples becomes more pronounced with the increase in annealing temperature. After the annealing at 900 °C, the system crystallizes as a mixture of $BaSi_2O_5$ and β-$BaSiO_3$. Crystals of $BaSi_2O_5$ are orthorhombic (sanbornite type) with a = 4.63 Å, b = 7.69 Å, and c = 13.53 Å, Space Group (S.G.) *Pcmn* [International Centre for Diffraction Data card n. 01-072-017]. The phase β-$BaSiO_3$, although also orthorhombic, has different lattice parameters: a = 5.61820 Å, b = 12.44500 Å, and c = 4.58160 Å, S.G. *Pmmm* [International Centre for Diffraction Data card n. 00-026-1402]. Narrowing of the reflections with the annealing temperature increasing from 750 to 900 °C is probably a result of the larger sizes of the coherent scattering regions and, consequently, indicates the increase in crystallinity. The XRD study shows that DSB:Dy and DSB:Tb glasses tend to crystallize with prevalence of the β phase and a lower degree of crystallization with respect to those of DSB:Ce. DSB:Tb exhibits the lowest degree of crystallization.

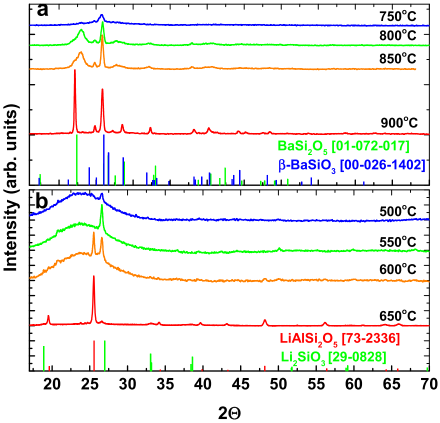

Fig. 5. XRD patterns of DSB:Ce (a) and DSL:Ce (b) glasses annealed at different temperatures (indicated). Standard reference data are provided, as labeled.

The crystallization of DSL:Ce glasses occurs at lower temperatures than that of DSB:Ce and starts at ~500 °C. In the XRD patterns of the glasses annealed at 500 °C and 550 °C, the reflections corresponding to Li_2SiO_3 phase are clearly observed. The phase is orthorhombic with a = 5.3975 Å, b = 9.3974 Å, and c = 4.6615 Å, S.G. *Cmc*2_1 [Powder Diffraction File n. 29-0828]. The XRD 2Θ scan of DSL:Ce annealed at 650 °C is dominated by strong reflections corresponding to $LiAl(SiO_3)_2$ phase, which is hexagonal with a = 5.2170 Å, c = 5.4640 Å, S.G. P6222 [Powder Diffraction File n.73-2336], while weak reflections due to Li_2SiO_3 phase are also observed. For the glass annealed at a lower temperature, 600 °C, the XRD reflections due to Li_2SiO_3 and $LiAl(SiO_3)_2$ are of equal intensity, while a broad band (peaked at 2Θ of ~25) due to amorphous phase dominates. The formation of $LiAl(SiO_3)_2$ might be attributed to the diffusion of Al^{3+} ions from the corundum crucible used to glass fabrication.

The luminescence spectra of Ce- and Eu-doped glasses and glass ceramics of DSB (annealed at 900 °C for 1 h) and DSL (at 750 °C for 1 h) are compared in Fig. 6.

The PL spectra of DSB:Ce^{3+} and DSB:$Eu^{2+,\,3+}$ glasses and ceramics are presented in Fig. 6a. Annealing of DSB:Ce results is a small red shift of the emission band without considerable change of the band shape. Meanwhile, the annealing of DSB:Eu glass causes substantial changes in the emission spectrum: the intensity ratio between the emission lines due to Eu^{3+} and the Eu^{2+}-related broad band peaked at 515 nm is drastically changed in favor of the emission caused by Eu^{2+}. The positions of the PL bands associated with the emission from Eu^{2+} and Eu^{3+} remain unchanged.

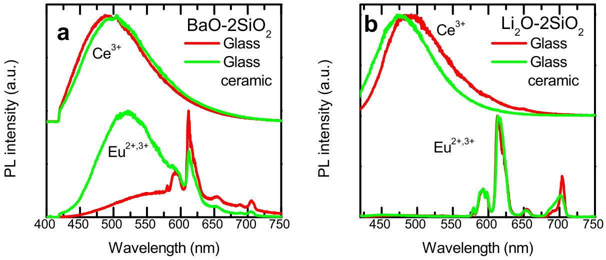

Fig. 6. Normalized PL spectra from DSB (a) and DSL (b) glass (red line) and glass ceramics (green line) doped with Ce^{3+} and $Eu^{2+,3+}$ ions at 405 nm excitation. (For interpretation of the references to color in this figure legend, the reader is referred to the Web version of this article.)

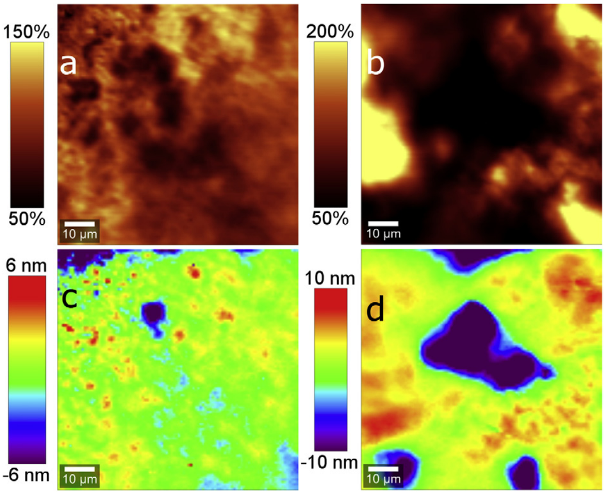

Fig. 7. Spatial distribution of spectrally-integrated PL intensity (a, b) and PL spectral center of mass (c, d) in Eu-doped DSL glasses (a, c) and glass ceramics (b, d).

The PL spectra of DSL glasses and ceramics are presented in Fig. 6b. Annealing of DSL:Ce results is a small blue shift of the emission band without considerable change of the band shape. Annealing of DSL:Eu glass has negligible influence on the emission spectrum, with the exception of the lowest energy band becoming less intense after annealing.

The small change in the spectral properties of PL of DSB:Ce^{3+} shows that the transformation from amorphous to crystalline phase proceeds without imposing change on the Ce^{3+} position in the matrix. The increasing fraction of the Eu^{2+}, which is reflected by the increasing intensity of the emission due to Eu^{2+}, is probably caused by the necessity to maintain the charge neutrality as the europium ions enter the crystallites, as described by equations (1)–(3). In addition, structural distortion is different in glass matrix and crystal. The glass matrix provides a continuum of crystalline surroundings with different values of structural distortion, while the structural distortion is the same for all Eu ions in the crystallite. This effect is studied in more detail in Ref. [14].

To compare the spatial distribution of the emission properties in REI-doped glasses and ceramics, we performed PL spectroscopy with spatial resolution by using confocal microscope. Mappings of PL parameters in the glasses and ceramics of DSL:Eu and DSB:Eu are presented in Figs. 7 and 8, respectively. The colors in parts (a) and (b) reflect the deviation of the PL intensity in every spot of the scan from the average intensity value in the entire mapping area. The colors in parts (c) and (d) reflect the corresponding deviation of the PL spectral center of mass.

The mappings of DSL:Eu glass show that the PL intensity is randomly distributed within the scanned area. The mappings of the glass ceramics evidence formation of crystallites of a typical size of the order of 10 µm. The PL intensity in the crystallites is substantially higher than that in the surrounding areas. The emission from the crystallites is also redshifted in respect to the surroundings and to the spectral position in the glass sample, in accordance with the observation of the red shift observed in the spatially-integrated spectra of glass ceramics (see Fig. 6).

The formation of crystallites in the process of crystallization from glass to ceramics is also observed in the PL mappings of DSB:Eu samples. The PL in the glass sample is quite homogeneous in view of both intensity and wavelength. The mappings presented in Fig. 8b,d are

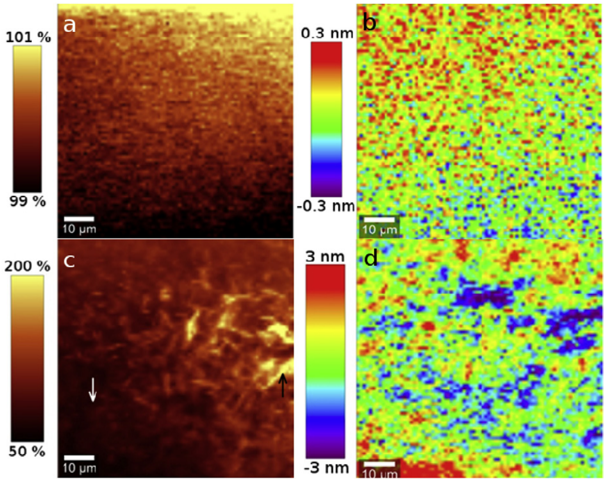

Fig. 8. Spatial distribution of spectrally-integrated PL intensity (a, b) and spectral center of mass (c, d) in Eu- doped DSB glasses (a, c) and glass ceramics (b, d).

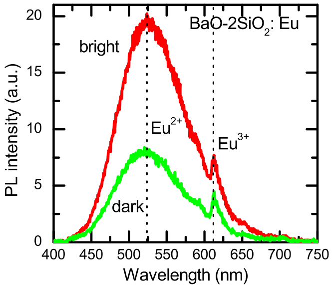

Fig. 9. PL spectra from bright and dark areas in Eu-doped DSB glass ceramics (in the areas indicated by arrows in Fig. 7b).

obtained in the sample annealed at 900 °C. XRD patterns (see Fig. 5) evidences high crystallinity of the sample. The crystallites are also observed in the PL mappings, especially in the PL intensity map. The typical size of the crystallites is of the order of several micrometers, considerably smaller than that in DSL ceramics. Though correlation between the PL intensity and the spectral center of mass is not strong, certain blue shift of the emission spectrum in the crystallites might be traced. The comparison of the spectra from crystallites and from the surrounding area (see Fig. 9) shows that the contribution of the emission related with Eu^{2+} is enhanced in the crystallites substantially more than that related with Eu^{3+}.

The comparison of spatial distributions of PL parameters in both DSB:Ce and DSB:Eu shows that the emission related to the ions of europium experience a considerably stronger influence during the transformation of glass matrix into glass ceramics than the influence experienced by cerium ions. This behavior might be interpreted by different values of ionic radii of Ce^{3+} and Eu^{2+} (for coordination number 6, 1.01 A and 1.17 A, respectively) and, consequently, by their ability to replace Ba^{2+} in the crystallites building the corresponding glass ceramics.

4. Conclusion

The study of the emission of stoichiometric DSL and DSB glasses doped with different combinations of Ce^{3+}, Eu$^{2+,3+}$, Tb^{3+}, and Dy^{3+} showed that several mixes of DSL and DSB glasses with appropriate dopants enable production of white light at 405 nm excitation of the phosphors, though no combination of the rare earth ions in a single glass matrix was found to ensure the white light generation. For example, mixing the light emitted from just two phosphors, DSB:Eu and DSL:Ce,Eu, ensures production of white light with color temperature of 3400 K. It is demonstrated that the high-crystallinity glass ceramics containing crystallites with typical size of 10 μm might be obtained by annealing DSL glass at the temperatures no lower than ~650 °C, while ~900 °C temperature is necessary for formation of glass ceramics from DSB glass. In the latter case, smaller crystallites of several micrometers in size are formed. The crystallization of the glass matrix into ceramics has no significant influence on the PL spectra of Ce^{3+}, Tb^{3+}, and Dy^{3+}, while the spectrum of emission related to europium drastically changes in the matrix transition from the glass to ceramics. The change is caused by the transformation of the valence from Eu^{3+} to Eu^{2+} of a considerable part of europium ions entering the crystallites in the Eu-doped glass ceramics. Results shows the high potential of the studied materials for their use in white leds.

Acknowledgements

This research was supported by the project FARAD (09.3.3-LMT-K-712-01-0013) funded by the European Social Fund and Belarusian State Program of Scientific Research “Photonics, Opto- and Microelectronics” (task no. 1.2.03). Authors are grateful to COST Action TD1401 “Fast Advanced Scintillator Timing (FAST)” for support of collaboration.

References

[1] J. Huang, H-Ch Kuo, Sh–Ch Shen, Nitride Semiconductor Light-emitting Diodes (LEDs), second ed., Elsevier, 2018, https://doi.org/10.1016/B978-0-08-101942-9.00005-8.

[2] N. Shuji, G. Fasol, The Blue Laser Diode: GaN Based Light Emitters and Lasers, Springer, Berlin, 1997.

[3] N.C. George, K.A. Denault, R. Seshadri, Phosphors for solid-state white lighting, Annu. Rev. Mater. Res. 43 (2013) 481–501, https://doi.org/10.1146/annurev-matsci-073012-125702.

[4] W.M. Yen, S. Shionoya, H. Yamamoto, Phosphor Handbook, (2007).

[5] L-Ch Chen, Z.-L. Tseng, W.-W. Chang, Y. Wen Lin, Warm white light-emitting diodes using organic–inorganic halide perovskite materials coated YAG: Ce3+ phosphors, Ceram. Int. 44 (2018) 3868–3872, https://doi.org/10.1016/j.ceramint.2017.11.176.

[6] S. Koh, Willem Van Driel, G.Q. Zhang, Degradation of epoxy lens materials in LED systems, 12th Intl. Conf. On Thermal, Mechanical & Multi-physics Simulation and Experiments in Microelectronics and Microsystems, 18–20, April 2011 PP. 1/5–5/5.

[7] A. Kitai (Ed.), Materials for Solid State Lighting and Displays, Wiley & Sons Ltd., 2017.

[8] Y. Muramoto, M. Kimura, S. Nouda, Development and future of ultraviolet light-emitting diodes: UV-LED will replace the UV lamp, Semicond. Sci. Technol. 29 (2014) 084004–084012, https://doi.org/10.1088/0268-1242/29/8/084004.

[9] Y. Kim, S. Kangn, The thermal properties of cordierite/diopside composites fabricated by glass–ceramics process for LED packages, Ceram. Int. 39 (2013) S619–S622, https://doi.org/10.1016/j.ceramint.2012.10.148.

[10] W. Höland, G.H. Beall, Glass-ceramic Technology, second ed., Wiley, 2012.

[11] P. Lecoq, A. Gektin, M. Korzhik, Inorganic Scintillators for Detecting Systems, Springer, 2017.

[12] L.M. Chepyga, E. Hertle, A. Alia, L. Ziganc, A. Osveta, Ch J. Brabec, M. Batentschuk, Synthesis and photoluminescent properties of the Dy^{3+} doped YSO as a high-temperature thermographic phosphor, J. Lumin. 197 (2018) 23–30, https://doi.org/10.1016/j.jlumin.2017.12.072.

[13] G. Ramakrishna, Ramachandra Naik, H. Nagabhushanac, R.B. Basavara, S.C. Prashantha, S.C. Sharma, K.S. Anantharaju, White light emission and energy transfer ($Dy^{3+} \rightarrow Eu^{3+}$) in combustion synthesized YSO: Dy3+, Eu3+ nanophosphors, Optik 127 (2016) 2939–2945.

[14] Y. Tratsiak, A. Fedorov, G. Dosovitsky, O. Akimova, E. Gordienko, M. Korjik, V. Mechinsky, E. Trusova, Scintillation efficiency of binary Li_2O-$2SiO_2$ glass doped with Ce^{3+} and Tb^{3+} ions, J. Alloy. Comp. (2018), https://doi.org/10.1016/j.jallcom.2017.11.386.

[15] M.V. Korjik, Vaitkevicius, D. Dobrovolskas, E.V. Tret'yak, E. Trusova, G. Tamulaitis, Distribution of luminescent centers in Ce^{3+}-ion doped amorphous stoichiometric glass BaO–$2SiO_2$ and dedicated glass ceramics, Opt. Mater. 47 (2015) 129–134, https://doi.org/10.1016/j.optmat.2015.07.014.

[16] M. Bessho, K. Shimizu, Latest trends in LED lighting, Electron. Commun. Jpn. 95 (1) (2012) 1–7, https://doi.org/10.1002/ecj.10394.

[17] Ji-Guang Li, X. Li, X. Sun, T. Ishigaki, Monodispersed colloidal spheres for uniform Y_2O_3:Eu^{3+} red-phosphor particles and greatly enhanced luminescence by simultaneous Gd^{3+} doping, J. Phys. Chem. C 112 (31) (2008) 11707–11716, https://doi.org/10.1021/jp802383a.

[18] Jung-Chul Park, Hye-Kyung Moon, Morphology and cathodoluminescence of Li-doped Gd_2O_3:Eu^{3+},Gd_2O_3:Eu^{3+}, a red phosphor perating at low voltages, Appl. Phys. Lett. 77 (2000) 2162, https://doi.org/10.1063/1.1315341.

[19] H. Karimi, Y. Zhang, Sh Cui, R. Ma, Gu Li, Q. Wang, J. Zhao, Xvs Qiao, J. Du, X. Fan, Spectroscopic properties of Eu-doped oxynitride glass–ceramics for white light LEDs, J. Non-Cryst. Solids 406 (2014) 119–126, https://doi.org/10.1016/j.jnoncrysol.2014.10.003.

[20] X. Liu, G. Chen, Yo Chen, T. Yang, Luminescent haracteristics of Tm^{3+}/Tb^{3}+/Eu^{3+} tri-doped phosphate transparent glass ceramics for white LEDs, J. Non-Cryst. Solids 476 (2017) 100–107, https://doi.org/10.1016/j.jnoncrysol.2017.09.032.

[21] P. Dorenbos, 5D level positions of the trivalent lanthanides in inorganic compounds, J. Lumin. 91 (2000) 155–176, https://doi.org/10.1016/S0022-2313(00)00229-5.

[22] M.Y.A. Yagoub, H.C. Swart, R.E. Kroon, Elizabeth Coetsee, Low temperature photoluminescence study of Ce^{3+} and Eu^{2+} ions doped SrF_2 nanocrystals, Physica B 535 (2018) 310–313, https://doi.org/10.1016/j.physb.2017.08.011.

[23] M. Borlaf, M. Frankowska, Wl W. Kubiak, Th Graulea, Strong photoluminescence emission at low dopant amount in YAG: Ce and YAG: Eu phosphors, Mater. Res. Bull. 100 (2018) 413–419, https://doi.org/10.1016/j.materresbull.2018.01.005.

[24] Vijay Singh, K.N. Shinde, N. Singh, M.S. Pathak, Pramod K. Singh, Vikas Dubey, Green emitting Tb doped $LiBaB_9O_{15}$ phosphors, Optik 156 (2018) 677–683, https://doi.org/10.1016/j.ijleo.2017.11.145.

[25] C. Gheorghe, S. Hau, L. Gheorghe, F. Voicu, M. Greculeasa, M. Enculescu, K.N. Belikov, E. Yu Bryleva, O.V. Gaiduk, Yellow laser potential of cubic $Ca_3(Nb,Ga)_5O12$:Dy^{3+} and $Ca_3(Li,Nb,Ga)_5O1_2$:Dy^{3+} single crystals, J. Alloy. Comp. 739 (2018), https://doi.org/10.1016/j.jallcom.2017.12.259 806e816..

[26] K. Binnemans, Interpretation of europium(III) spectra, Coord. Chem. Rev. 295 (2015) 1–45, https://doi.org/10.1016/j.ccr.2015.02.015.

[27] A. Žukauskas, M.S. Shur, R. Gaska, Introduction to Solid-state Lighting, Wiley, New York, 2002.

[28] F. Ahmadi, R. Hussin, S.K. Ghoshal, Optical transitions in Dy^{3+}-doped magnesium zinc sulfophosphate glass, J. Non-Cryst. Solids 452 (2016) 266–272, https://doi.org/10.1016/j.jnoncrysol.2016.09.005.

[29] V. Uma, K. Maheshvaran, K. Marimuthu, G. Muralidharan, Structural and optical investigations on Dy^{3+}doped lithium tellurofluoroborate glasses for white light applications, J. Lumin. 176 (2016) 15–24, https://doi.org/10.1016/j.jlumin.2016.03.016.

[30] E. Kaewnuam, N. Wantana, H.J. Kim, J. Kaewkha, Development of lithium yttrium borate glass doped with Dy^{3+} for laser medium, W-LEDs and scintillation materials applications, J. Non-Cryst. Solids 464 (2017) 96–103, https://doi.org/10.1016/j.jnoncrysol.2017.03.027.

[31] M. Dejneka, E. Snitzer, R.E. Riman, Blue, green and red fluorescence and energy transfer of Eu^{3+} in fluoride glasses, J. Lumin. 65 (1995) 227–245, https://doi.org/10.1016/0022-2313(95)00073-9.

[32] J. Anjaiah, C. Laxmikanth, N. Veeraiah, Spectroscopic properties and luminescence behaviour of europium doped lithium borate glasses, Physica B 454 (2014) 148–156, https://doi.org/10.1016/j.physb.2014.07.070.

[33] L. Xia, L. Wang, Q. Xiao, Z. Li, W. You, Q. Zhang, Preparation and luminescence properties of Eu^{3+}-doped calcium bismuth borate red-light-emitting glasses for WLEDs, J. Non-Cryst. Solids 476 (2017) 151–157, https://doi.org/10.1016/j.jnoncrysol.2017.09.049.

[34] H. Yanlin, E. Cho, K. Jang, Ho S. Lee, W. Xigang, Q. Dake, J. Chuanfang, A blue luminescence glass-ceramics of Eu^{2+} ions activated Li_2O-BaO-B_2O_3, J. Rare Earths 26 (2) (2008) 215–219, https://doi.org/10.1016/S1002-0721(08)60068-X.

[35] G. Gao, S. Krolikowski, M. Peng, L. Wondraczek, Tailoring super-broad photoluminescence from $Eu^{2+}$and dual-mode Eu^{2+}/Eu^{3+}-doped alkaline earth aluminoborate glasses through site-similarity and ligand acidity, J. Lumin. 180 (2016) 234–240, https://doi.org/10.1016/j.jlumin.2016.08.025.

[36] Q. Luo, X. Qiao, X. Fan, S. Liu, H. Yang, X. Zhang, Reduction and luminescence of europium ions in glass ceramics containing SrF_2 nanocrystals, J. Non-Cryst. Solids 354 (2008) 4691–4694, https://doi.org/10.1016/j.jnoncrysol.2008.07.019.

[37] Z. Lian, J. Wang, Y. Lv, S. Wang, Q. Su, The reduction of Eu^{3+} to Eu^{2+} in air and luminescence properties of Eu^{2+} activated ZnO-B_2O_3-P_2O_5 glasses, J. Alloy. Comp. 430 (2007) 257–261, https://doi.org/10.1016/j.jallcom.2006.05.002.

[38] Zh Fu, P. Xu, Y. Yang, Ch Li, H. Lin, Q. Chen, G. Yao, Y. Zhou, F. Zeng, Study on luminescent properties of Ce^{3}+ sensitized Tb^{3+} doped gadolinium borosilicate scintillating glass, J. Lumin. 196 (2018) 368–372, https://doi.org/10.1016/j.jlumin.2017.12.070.

[39] X. Liang, Zh Lin, Yu Yang, Zh Xing, G. Chen, Luminescence properties of Tb–Eu Co-Doped aluminosilicate and zinc silicate glasses, J. Am. Ceram. Soc. 95 (1) (2012) 275–279, https://doi.org/10.1111/j.1551-2916.2011.04772.x.

Paper P11

Improvement of response time in GAGG: Ce scintillation crystals by magnesium codoping

G. Tamulatis, G. Dosovitskiy, A. Gola, M. Korjik, A. Mazzi, S. Nargelas, P. Sokolov, **A. Vaitkevičius**

J. Appl. Phys. 124 (2018) 215907.

doi: 10.1063/1.5064434.

Journal of Applied Physics

Improvement of response time in GAGG:Ce scintillation crystals by magnesium codoping

Cite as: J. Appl. Phys. **124**, 215907 (2018); https://doi.org/10.1063/1.5064434
Submitted: 04 October 2018 . Accepted: 15 November 2018 . Published Online: 06 December 2018

G. Tamulatis, G. Dosovitskiy, A. Gola, M. Korjik, A. Mazzi, S. Nargelas, P. Sokolov, and A. Vaitkevičius

J. Appl. Phys. **124**, 215907 (2018); https://doi.org/10.1063/1.5064434 **124**, 215907

JOURNAL OF APPLIED PHYSICS **124**, 215907 (2018)

Improvement of response time in GAGG:Ce scintillation crystals by magnesium codoping

G. Tamulatis,[1] G. Dosovitskiy,[2,3] A. Gola,[4] M. Korjik,[5] A. Mazzi,[4] S. Nargelas,[1]
P. Sokolov,[2,3] and A. Vaitkevičius[1]
[1]*Institute of Photonics and Nanotechnology, Vilnius University, Vilnius, Lithuania*
[2]*National Research Center "Kurchatov Institute," Moscow, Russia*
[3]*NRC "Kurchatov Institute"—IREA, Moscow, Russia*
[4]*Fondazione Bruno Kessler, Trento, Italy*
[5]*Research Institute for Nuclear Problems, Minsk, Belarus*

(Received 4 October 2018; accepted 15 November 2018; published online 6 December 2018)

Dynamics of the population of the excited Ce states responsible for the luminescence response time in $Gd_3Al_2Ga_3O_{12}$:Ce scintillating crystals is studied by revealing the dynamics of nonequilibrium carriers in the picosecond domain. Optical pump and probe technique exploiting selective excitation of structural units of the crystal and probing the induced absorption as a function of time and spectral position is exploited. A fast response within a few picoseconds due to the absorption by holes at Gd ions and by electrons occupying the first excited state of Ce ions with the intracenter relaxation time of 500 fs are identified. Trapping of nonequilibrium electrons during their migration through the matrix to the emitting Ce ions are shown to be responsible for the slow component in the population of the excited Ce state. Elimination of the slow component is evidenced even at Mg codoping as low as 10 ppm. The elimination correlates with the acceleration of the response in coincidence time resolution experiments showing potential of GAGG:Ce, Mg in medical and high-energy physics applications. *Published by AIP Publishing.* https://doi.org/10.1063/1.5064434

INTRODUCTION

Several Ce-doped multicomponent garnet-type crystals exhibit an excellent combination of scintillation properties.[1,2] In comparison with binary garnets, the multicomponent garnets have an inherent feature: disordering of the matrix due to local variation in the content of isovalent ions. The random distribution of matrix-building ions causes spatial fluctuations of the bandgap, reduces the carrier diffusion lengths, facilitates recombination of geminate pairs,[3] and, as a consequence, leads to an increase of the light yield due to the improved conversion efficiency.[3–5] The disorder also results in inhomogeneous broadening of the 4f-related emission lines of activator ions, caused by various positions of the ions in the lattice distorted by the fluctuations of crystal composition,[6–8] which is absent in binary garnets. Moreover, the random distribution of cations in the multicomponent garnets leads to the shrinkage of the bandgap[9–11] observed in $(Lu_{1-x}Y_x)AlO_3$:Ce and many other multicomponent oxides.[12] The down-shifted conduction band might cover shallow traps located below the bottom of this band[13] and, as a consequence, diminish the scintillation efficiency losses due to carrier trapping.

Recently, Ce-doped gallium gadolinium garnets ($Gd_3Al_2Ga_3O_{12}$, GAGG) attracted considerable attention due to high stopping power to gamma-radiation and neutrons, a high light yield, luminescence decay time shorter than 80 ns, and excellent matching of the emission peak at ~520 nm with the sensitivity spectrum of the conventional silicon photo-multipliers (SiPMs).[14,15] However, the time resolution in coincidence time resolution (CTR) measurements using GAGG:Ce scintillators was measured to be ~480 ps,[14] i.e., definitely inferior to that obtained by using LSO:Ce and LYSO:Ce scintillators.[16–18] Recently, an improvement of the time response down to 233 ps was demonstrated in Mg-codoped GAGG:Ce,[19] in line with the improvement of time response of other Ce-doped scintillators by codoping with divalent dopants.[20,21] The time-resolved luminescence study of uncodoped and codoped crystal showed that Mg-codoping eliminates the slow component in the front of photoluminescence response and the rise time of GAGG:Ce, Mg is in the subpicosecond domain.[19] However, the introduction of Mg also results in a decrease of the light yield.[19] Though the influence of the Mg-codoping on GAGG:Ce, Mg properties is well studied, the optimization of the trade-off between the acceleration of the time response and the decrease in the light yield needs dedicated studies.

The current work is focused on the investigation of the origin of the slow component in the luminescence response of GAGG:Ce and the influence of magnesium co-doping on the response time at different Mg contents in the crystal by studying the kinetics of electron population at cerium ions. We exploited the optical pump and probe technique and used the capabilities of this technique: (i) high time resolution limited by the laser pulse duration (200 fs in our experiments), (ii) selective excitation of different structural units of the crystal, and (iii) simultaneous monitoring of time and spectral characteristics of the response enabling to spot specific features due to the contributions of different structural units and response mechanisms. A set of GAGG:Ce samples with different levels of codoping was prepared for the study; a sample cut from a crystal without any intentional doping was also added to the set for comparison. The response time of the samples under study in our optical pump and probe experiments was tested and compared under gamma-ray excitation using the coincidence time resolution technique, which is a conventional measurement configuration in medical imaging applications and in many high-energy physics experiments.

EXPERIMENTAL

The GAGG single crystals, nominally undoped, solely doped with Ce, and codoped by Mg and Ti have been produced by the Czochralski technique at the Institute of Scintillation Materials, Kharkov, Ukraine; Furukawa Scintitech Corporation, Japan; and Fomos Materials, Moscow, Russia. The crystals were pulled out from iridium crucibles.

A sample of nominally undoped GAGG was fabricated to be used for reference. The rest of the samples used in this study were doped by Ce at a similar level, which has been measured by means of the Glow Discharge Mass Spectroscopy for sample S2 or estimated by comparing the optical absorption at the peak of the first allowed f-d transition of Ce^{3+} ions in other samples. The codoping of the GAGG:Ce crystals by magnesium was applied at different levels and estimated by comparing the optical absorption due to Mg-related defects, as described in Ref. 22. One of the samples was codoped with Ce, Mg, and Ti. A small amount of titanium (at the level of 20 ppm in the charge) was introduced with an expectation to inhibit stabilization of Ce^{4+} ions. The crystal samples in the shape of blocks with the dimensions of $3 \times 3 \times 5\ mm^3$ for CTR measurements and $10 \times 10 \times 1$-$3\ mm^3$ for study by nonlinear optics technique have been prepared from single-crystal ingots having the diameter not less than 45 mm and the length exceeding 80 mm. All surfaces of the blocks have been polished. Four samples were prepared for the study: nominally undoped GAGG (labeled hereafter as S0), GAGG:Ce with 550 ppm of Ce (S1), GAGG:Ce, Mg with 530 ppm of Ce and 10 ppm of Mg (S2), and GAGG:Ce, Mg, Ti codoped with 800, 20, and 20 ppm of Ce, Mg, and Ti, respectively (S3).

The absorption spectra of GAGG with different doping are provided in Fig. 1. The nominally undoped GAGG exhibits narrow lines attributed to the f-f absorption bands of matrix-building gadolinium ions[21] and a broad absorption tail toward the bandgap energy. The spectra of Ce-containing samples have, as usual, two distinct absorption lines due to optical transition from the ground state to two components of d level split by crystal field. Magnesium introduces a broad absorption band in the near UV region, most probably caused by a charge transfer transition to a defect state, stabilized by Mg^{2+}, from the valence band.[23]

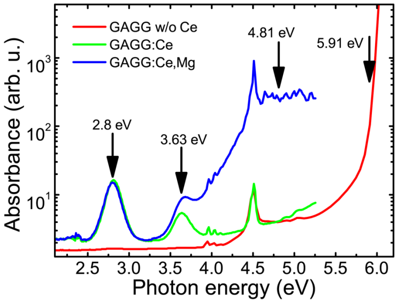

FIG. 1. Absorption spectra of nominally undoped GAGG, GAGG:Ce, and GAGG:Ce, Mg. Pump energies used in our transient absorption experiments are indicated by arrows.

The transient optical absorption was studied using the optical pump and probe technique. The samples were excited at the pump photon energies indicated by arrows in Fig. 1. The experimental setup was based on a KGW:Yb laser emitting 200 fs pulses at a wavelength of 1030 nm, a repetition rate of 30 kHz, and an average power of 6 W (*Pharos, Light Conversion*). The laser output was split into two beams. The first beam was used as a pump and was equipped with β-barium borate crystals for frequency doubling/quadrupling and a parametric amplifier (*Orpheus, Light Conversion*) to ensure gradual tunability of the pump photon energy. The samples were probed by the second beam converted into a white light continuum in the range from 1.3 to 2.7 eV using a 5 mm-thick sapphire plate. The variable optomechanical delay of the probe pulse in respect to the pump pulse enabled measurements of time evolution of the transient absorption with time resolution limited only by laser pulse duration. The difference in the optical absorption with and without the pump (differential absorption, DA) was measured as a function of the delay between pump and probe pulses. The DA is caused by the induced absorption, which is proportional to the density of nonequilibrium carriers: the electrons in the conduction band, the holes in the valence band, the carriers located at activator ions and trapped at defect-related levels. The contributions of the different populations were revealed by their spectral signatures under selective excitation of different structural units of the crystal.

To measure CTR, pixels were combined into detecting modules with SiPMs developed at Fondazione Bruno Kessler (FBK SiPMs). The detectors employed in this study were $4 \times 4\ mm^2$ RGB-HD SiPMs with $25\,\mu m$ cell pitch. RGB-HD technology is based on an n-on-p junction and features a peak photo-detection efficiency of more than 40% at 550 nm, considering $25\,\mu m$ cells.[15] The pixels were wrapped in Teflon and optically coupled to SiPMs by using Cargille Meltmount optical glue (refractive index $n = 1.539$). The time coincidence setup consisted of two identical detecting modules placed on the same axis, at the same distance from a ^{22}Na source providing 511 keV coincidence events. The SiPMs were loaded on two double-stage amplifiers with two outputs. The first stage was used to measure the energy of the detected gamma quanta in order to select only the events in the 511 keV photopeak. The second stage, based on the pole-zero filtering,[18] was used for high-resolution timing measurements. The energy discrimination was performed through charge integration within a time window of 500 ns. CTR was measured on couples of identical detecting modules as a function of voltage threshold and SiPM excess bias under controlled temperature (+20 °C).

RESULTS

Photons at the energy of 2.8 eV (443 nm) were used for resonant intracenter excitation of Ce^{3+} ions from the ground state into the first excited level 5d$_1$. In Fig. 2, the color-coded intensity of differential absorption, i.e., the difference in the absorption of the probe with and without a pump, is presented as a function of the probe photon energy and the delay between subpicosecond pump and probe pulses for samples S1 (a) and S2 (b). The spectrum of the nonlinear absorption is centered at ∼1.35 eV and extends to the high-energy side for a few hundreds of meV. No detectable influence of Mg-doping on the nonlinear absorption at this pump photon energy was observed either in the sample S2, as depicted in Fig. 2(b), or in the samples with higher Mg content. The nonlinear absorption in the nominally undoped GAGG was by orders of magnitude lower and indicated a low content of unintentionally introduced Ce. Therefore, this feature in the nonlinear absorption might be attributed to the electrons populating the first excited state of the Ce^{3+} ion. As expected, the population of the state instantaneously follows the excitation pulse (in the subpicosecond domain in our experiments) and decays in the nanosecond domain, consistent with many luminescence measurements in the nanosecond domain (see, e.g., Ref. 24).

The photon energy of 3.63 eV (342 nm) was selected to excite the Ce^{3+} ion into the second excited level 5d$_2$, which is above the bottom of the conduction band.[25,26] The spectrum of nonlinear absorption at this pump photon energy [see Figs. 3(a) and 3(b)] is also dominated by the component attributed (see above) to the absorption from the lowest Ce^{3+} excited state. All codoped samples exhibit actually the same spectral features and time evolution of their nonlinear absorption. Meanwhile, a slow component in the rising part of the nonlinear response is observed in the S1 sample without codoping. The kinetics of the differential absorption [i.e., the vertical cross sections of the data carpets like those in Figs. 3(a) and 3(b)] at the probe photon energy of 1.4 eV are provided in Fig. 3(c). Note that the magnesium-doping is sufficient to eliminate this slow rise component even at the Mg content as low as 10 ppm (sample S2).

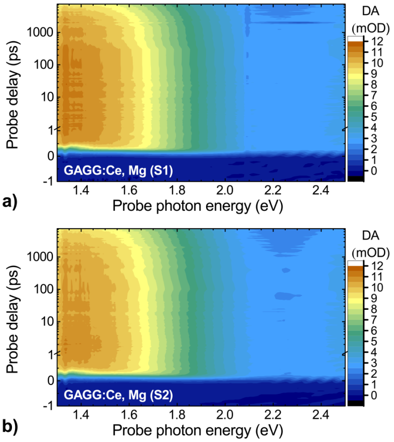

FIG. 2. Differential absorption of GAGG:Ce without, sample S1, (a) and with Mg codoping, S2, (b) as a function of probe photon energy and delay between pump and probe pulses at a pump photon energy of 2.8 eV. Note the scale change from linear to logarithmic at 1 ps.

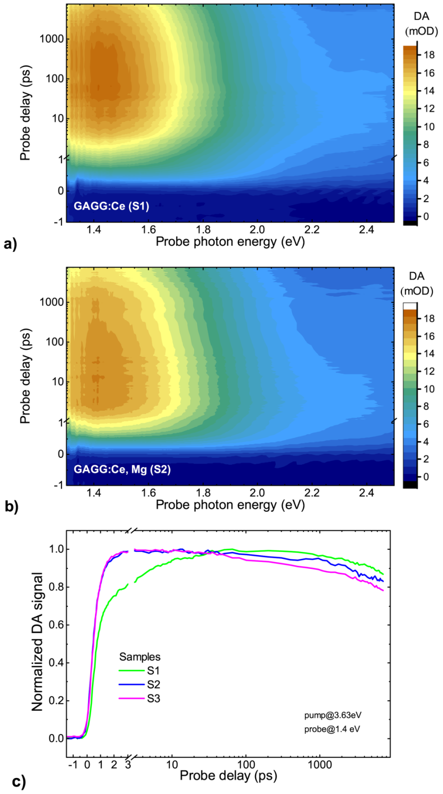

FIG. 3. Differential absorption of GAGG:Ce without, sample S1, (a) and with Mg codoping, S2, (b) as a function of probe photon energy and delay between pump and probe pulses at a pump photon energy of 3.63 eV and kinetics of differential absorption at 1.4 eV in the samples with different doping (c). Note the scale change from linear to logarithmic at 1 ps in (c).

The pump photons with an energy of 4.81 eV (258 nm) excite the Gd^{3+} ions via $^8S_{7/2}$-^6I_j electronic transition, while the photon energy is also sufficient for charge transfer optical transitions from Ce^{3+} ions to the conduction band. A typical differential absorption data carpet for this pump photon energy is presented in Fig. 4(a). A new feature appears both in the spectral and time domains: strong induced absorption with a broad spectrum ranging to ∼2.5 eV and decaying within a few picoseconds is observed. We attribute this component to nonlinear absorption due to the excitation of gadolinium ions. The kinetics of this component at its peak photon energy of 2.2 eV is presented in Fig. 4(b). Both components, the fast one due to Gd and the Ce-related component, though much weaker, have their contributions to the kinetics.

In Fig. 5, the data carpets displaying the dynamics of the differential absorption after excitation with the photon energy of 5.91 eV (210 nm) are presented for samples S0, S1, and S2. All the structural units discussed above as well as the trapping centers below the bandgap might be excited at this pump photon energy. Both components previously attributed to the absorption by electrons populating the lowest excited Ce^{3+} state and by absorption at the Gd^{3+} ion are observed at the 5.91 eV pump. As predicted theoretically[26] and evidenced experimentally,[21] the ground state of gadolinium is in the valence band. Thus, the excited electrons as well as the holes at the ground state of Gd or relaxed to the valence band might contribute to the differential absorption. However, the differential absorption extends to the probe photon energies well below 0.8 eV,[22] i.e., to the energies substantially smaller than the energy gap between the excited state of Gd^{3+} and the bottom of the conduction band. Consequently, the absorption is dominated by nonequilibrium holes. A short decay time of the corresponding component is an indication that the intracenter recombination of photoexcited electron and hole at the Gd ion occurs without relaxation of the holes to the valence band.

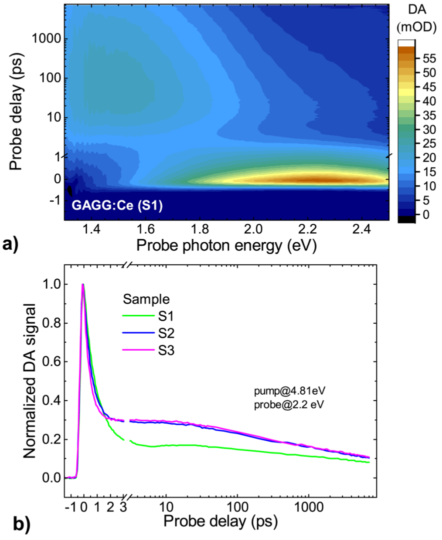

FIG. 4. Differential absorption of GAGG:Ce, sample S1, as a function of probe photon energy and delay between pump and probe pulses at a pump photon energy of 4.81 eV (a) and kinetics of differential absorption at 2.2 eV after short-pulse excitation of GAGG with different doping at 4.81 eV (b).

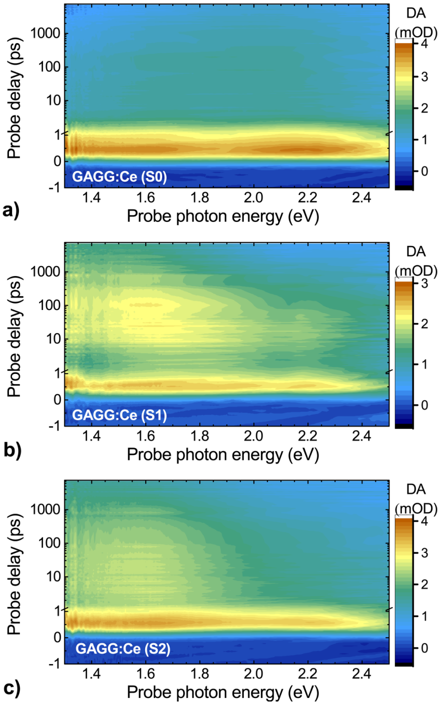

FIG. 5. Differential absorption of GAGG as a function of probe photon energy and delay between pump at a photon energy of 5.91 eV and probe pulses in samples S0 (a), S1 (b), and S2 (c). Note the scale change from linear to logarithmic at 1 ps.

The kinetics of differential absorption probed at 1.4 eV in all the samples studied after their excitation at 5.9 eV are compared in Fig. 6. The fast component due to the absorption by nonequilibrium holes at Gd ions and the component caused by electrons populating the first excited state of Ce^{3+} are evident in all the samples (as discussed above, the weak Ce-related component in sample S0 is caused by a trace amount of Ce). The population of Ce^{3+} has two components. The characteristic population rise time is below 1 ps for the fast component and of the order of a few picoseconds for the slow one. Codoping by magnesium results in the elimination of the slow component.

The correlation of the features in carrier dynamics observed by the optical pump and probe technique with the time response in detecting gamma quanta was tested by performing CTR measurements. The full width at half maximum of the timing histogram (CTR FWHM) is presented in Fig. 7 as a function of overvoltage. These data were obtained by using GAGG:Ce crystals without and with codoping. The measurements were performed at +20 °C, and the data reported in Fig. 7 are taken at the voltage

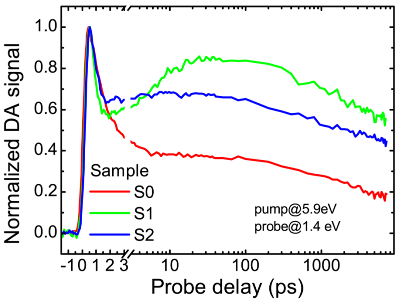

FIG. 6. Kinetics of differential absorption at 1.4 eV after short-pulse excitation of GAGG with different doping at 5.91 eV.

threshold optimal for each overvoltage. Sample S1 (GAGG:Ce) provided an optimal CTR of 193 ± 4 ps, which, to the best of our knowledge, is the best result currently available with GAGG:Ce.[14,27] The time resolution was further improved in the measurements with codoped crystals: samples S2 and S3 reached an optimal CTR of 169 ± 3 ps and 165 ± 3 ps, respectively. The data presented here show that the codoping by Mg even at the level as low as 10 ppm is sufficient to substantially improve the timing performance. These results confirm the previous indications that GAGG:Ce codoped with Mg is capable of better time resolution[14] but now at a significantly improved level.

DISCUSSION

The improvement of the time resolution by the introduction of Mg even at the level of 10 ppm observed in this study should be pointed out as one of the key results of this work and it is worth understanding the origin of this effect. The best value of FWHM demonstrated in the coincidence time resolution experiment was 165 ps. This is a remarkable result in view of prospective applications. The time resolution might be probably improved by dedicated matching of the scintillator and purposefully designed and fabricated SiPMs.

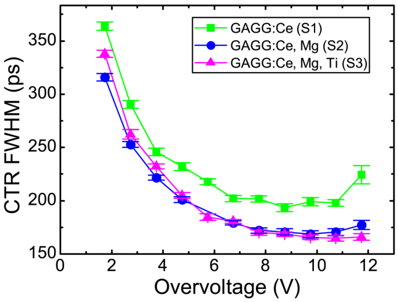

FIG. 7. CTR FWHM as a function of the overvoltage applied to RGB-HD SiPMs. The silicon detectors were coupled to 3 × 3 × 5 mm^3 GAGG:Ce (S1), GAGG:Ce, Mg (S2), and GAGG:Ce, Mg, Ti (S3).

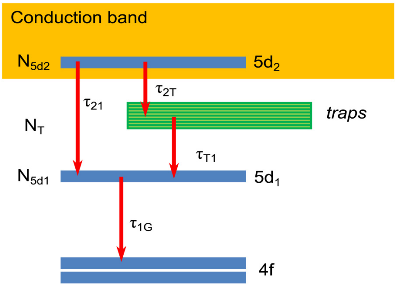

FIG. 8. Energy scheme of Ce^{3+} in GAGG (not to scale) with relaxation and recombination transitions described by Eqs. (1)–(3) indicated by arrows and labeled by the corresponding time constants for these transitions.

As presented above, the codoping by Mg eliminates the slow component of the population of Ce^{3+} excited state, when the nonequilibrium electrons are generated into the conduction band. The entire set of the results on the differential absorption finds an explanation by trapping of the nonequilibrium electrons moving through the crystal matrix. There are several processes influencing the population dynamics. To describe certain temporal characteristics of the processes, we used simple rate Eqs. (1)–(3) describing populations of the first (N_{5d1}) and second (N_{5d2}) excited states of Ce^{3+} and the population of electron traps N_T. Besides unintentional impurities and structural defects, the bandgap modulation due to composition fluctuations in a multicomponent garnet crystal GAGG might serve to form trapping centers for electrons in this crystal. All these traps are generalized in the model for rate equations by a single trapping level or band. The energy scheme is presented in Fig. 8, where the relaxation and recombination routes are marked by arrows with the corresponding time constants indicated. The time constants τ_{21}, τ_{2T}, τ_{T1}, and τ_{1G} are for relaxation transitions from state 5d$_2$ to 5d$_1$, state 5d$_2$ to trapping level, trapping level to state 5d$_1$, and 5d$_1$ to ground state, respectively. $G(t)$ denotes the Gaussian distribution function representing initial laser pulse,

$$\frac{dN_{5d2}}{dt} = G(t) - \frac{N_{5d2}}{\tau_{21}} - \frac{N_{5d2}}{\tau_{2T}}, \tag{1}$$

$$\frac{dN_T}{dt} = \frac{N_{5d2}}{\tau_{2T}} - \frac{N_T}{\tau_{T1}}, \tag{2}$$

$$\frac{dN_{5d1}}{dt} = \frac{N_{5d2}}{\tau_{21}} + \frac{N_T}{\tau_{T1}} - \frac{N_{5d1}}{\tau_{1G}}. \tag{3}$$

Fittings of the kinetics of differential absorption at 1.4 eV obtained experimentally in uncodoped and codoped GAGG:Ce after excitation at pump photon energy of 3.63 eV

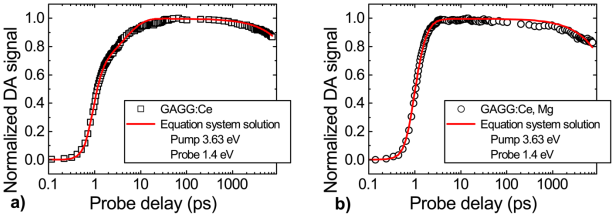

FIG. 9. Fittings of experimental (black points) and simulated (red lines) kinetics of differential absorption at 1.4 eV in uncodoped (a) and codoped (b) GAGG:Ce (samples S1 and S2, respectively).

are presented in Fig. 9. The characteristic time of relaxation from the second to the lowest excited state was maintained constant in all fittings. All the time constants for three samples with Ce and different Mg content are presented in Table I. The fitting enabled us to estimate the time of intracenter electron relaxation time to be ∼500 fs. The fitting results provide certain estimates of characteristic times for the main processes governing the nonequilibrium electron dynamics in uncodoped and codoped GAGG:Ce and evidence a clear feature that the constants experience a significant change in the Mg-codoped crystals.

The improvement of the time response by Mg-codoping at excitation of GAGG:Ce by gamma quanta is observed and interpreted by shifting of the valence state of Ce ions in favor of Ce^{4+} (see, e.g., Ref. 28). Our results on nonlinear optical absorption are not in line with this interpretation. First of all, we showed that the fast and slow rise components in population of the emitting level of the Ce ion occur even at direct excitation of cerium ions, when the availability of hole at the ground state in Ce^{4+} provides no advantage in view of response time over directly excited Ce^{3+} ion. The second important point is that we observe the improvement of time response even at Mg-codoping as low as 10 ppm. It might hardly be expected that the doping at such level could significantly change the ratio between the concentrations of Ce^{3+} and Ce^{4+}, which is close to 1:1 even in uncodoped GAGG:Ce. Provided that magnesium distribution in the crystal is homogeneous, Mg concentration at 10 ppm corresponds to one Mg^{2+} ion per 2700 nm^3 (∼1400 unit cells) of the GAGG matrix. At the Ce concentration of ∼500 ppm and homogeneous distribution, one Ce ion corresponds to the volume of ∼60 nm^3 (or less than 40 unit cells). Thus, the probability of Mg-Ce pairing to create a charge-balanced link Ce^{4+}-Mg^{2+} is low. To estimate the probability, the localization of Ce and Mg ions in specific sites of the garnet structure has to be taken into account. Let us assume that the pairing occurs when Ce and Mg ions appear at least in the second cation coordination sphere of each other. A garnet-type crystal structure belongs to the cubic space group *Ia3d* (*#230*) with cations at special positions (on *16a*, *24c*, and *24d* sites) and oxygen anions at general positions (on *96h* sites). Three cations have tetrahedral coordination (*24d* sites) and two cations have octahedral (*16a* sites) coordination formed by oxygen ions.[29] The 8th coordinate sites (dodecahedral, *24c* sites) accommodate Gd ions. There are eight formula units in a unit cell.

TABLE I. Time constants used in fitting the differential absorption kinetics obtained experimentally and simulated using Eqs. (1)–(3).

Sample	Mg content (ppm)	τ_{2T} (ps)	τ_{T1} (ps)	τ_{21} (ps)	τ_{1G} (ns)
S1	⋯	1.1	4.1	0.52	56
S2	10	11.8	1.4	0.52	32
S3	20	89	1	0.52	24

In the first coordination sphere of cation in position *24d*, there are four atoms in position *16a*, while in the first coordination sphere of cation in position *16a*, there are six atoms in position *24d*. In two cation coordination spheres, an Mg ion has in total 34 positions suitable for Ce stabilization. Thus, only nearly 1% of Ce^{3+} ions have a chance to appear in the first and second coordination spheres around the Mg ion. Consequently, the creation of Ce^{4+} due to pairing with Mg^{2+}, which is reported to be considerable at high codoping concentration in the crystals,[30] is not significant in codoping of GAGG:Ce with 10 ppm of Mg.

Taking into account the results obtained in the current study and the results on luminescence rise time,[21] carrier trapping should be considered as the key mechanism causing the luminescence response delay in GAGG:Ce. The observation that Mg-doping eliminates the slow component in the population of Ce^{3+} is in line with the published results evidencing that the doping inhibits formation of shallow traps.[31] The origin of these traps is still a subject for further studies. Considerable influence of certain dopants in low concentrations on trap formation is known in other scintillators. For example, there are experimental evidences of strong rearranging of traps in $PbWO_4$ crystal doped by La and Y at the level of 20-40 ppm.[32] It was demonstrated that such doping effectively inhibits the formation of di-vacancy centers, because the formation probability is proportional to the vacancy density squared. The suppression of di-vacancy related defects might be important also in GAGG. Certain results on thermo-stimulated luminescence in codoped GAGG crystals[22,31,33] are consistent with this assumption.

The results of the current study, which investigates predominantly geminate carrier pairs, can be extrapolated to the case of excitation by ionizing radiation. In this case, the population of shallow traps caused by disordering in the crystal and di-vacancy centers becomes a more efficient competitor for cerium ions to capture electrons. Therefore, the buildup of the population of Ce^{3+} radiating level would be longer than that observed in our study, since the average path of the migration of the nonequilibrium carriers through the matrix to the radiative

Ce center would be longer. Consequently, even a partial elimination of trapping would result in a significant enhancement for the population of the radiative Ce centers. This assumption is supported by the correlation of acceleration of the luminescence build up by Mg codoping with the improvement of response time in CTR measurements, shown in Fig. 7.

The introduction of Mg results not only in the improvement of luminescence response time but also in decreased light yield,[21] since the Mg-doping also facilitates the formation of nonradiative recombination centers. Our current observation of a significant improvement of the luminescence response time at low Mg content implies that such improvement might be achieved at a small loss in scintillation efficiency.

CONCLUSIONS

It is demonstrated that the substantial suppression of the slow component in the increase of the population of the lowest excited Ce^{3+} level, which acts as the emitting level and governs the luminescence kinetics, in GAGG:Ce single crystals is achieved by codoping of the crystal by divalent magnesium even at codoping levels as small as 10 ppm, which are insufficient to change the valence state of cerium ions from Ce^{3+} to Ce^{4+} significantly.

Optical probing of the decay of population of different structural units in GAGG:Ce evidenced that carrier trapping has the main influence on the rise time of the luminescence response of this scintillation crystal. It was also shown that codoping of GAGG:Ce by divalent ions of magnesium diminishes the influence of traps. The disappearance of the slow component in the luminescence rise time is correlated with the decrease in the FWHM in CTR measurements.

The best fits of the experimental data on the kinetics of the population of excited Ce^{3+} levels with the populations calculated by using the rate equations are obtained at the time of intracenter relaxation for 5d$_2$ to 5d$_1$ transition of ∼500 fs.

The time resolution in CTR measurements also depends on the type of SiPM used. Thus, the best FWHM value of 165 ps achieved in these measurements could be further improved by optimizing the matching of GAGG:Ce, Mg scintillator and the dedicated SiPM. This may be attractive for medical imaging devices and applications in high-energy physics experiments.

ACKNOWLEDGMENTS

This research was supported by the project FARAD (Grant No. 09.3.3-LMT-K-712-01-0013) funded by the European Social Fund via the Lithuanian Research Council. Support from the COST FAST action TD1401 is gratefully acknowledged. The authors are grateful to Furukawa Scintitech Corporation, Japan, and Fomos Materials, Moscow, Russia, for providing the samples for this investigation.

[1] P. Lecoq, A. Annenkov, A. Gektin, M. Korzhik, and C. Pedrini, *Inorganic Scintillators for Detector Systems* (Springer, 2006).

[2] M. Nikl and A. Yoshikawa, Adv. Opt. Mater. **3**, 463 (2015).

[3] A. V. Gektin, A. N. Belsky, and A. N. Vasil'ev, IEEE Trans. Nucl. Sci. **61**, 262 (2014).

[4] O. Sidletskiy, A. Gektin, and A. Belsky, Phys. Status Solidi **211**, 2384 (2014).

[5] *Engineering of Scintillation Materials and Radiation Technologies*, edited by M. Korjik and A. Gektin (Springer International Publishing, 2017).

[6] P. Solarz, M. Głowacki, M. Berkowski, and W. Ryba-Romanowski, J. Alloys Compd. **689**, 359 (2016).

[7] S. Feofilov, A. Kulinkin, K. Ovanesyan, A. Petrosyan, and C. Dujardin, Phys. Chem. Chem. Phys. **16**, 22583 (2014).

[8] N. M. Khaidukov, V. N. Makhov, Q. Zhang, R. Shi, and H. Liang, Dye. Pigment. **142**, 524 (2017).

[9] K. Kamada, T. Endo, K. Tsutumi, T. Yanagida, Y. Fujimoto, A. Fukabori, A. Yoshikawa, J. Pejchal, and M. Nikl, Cryst. Growth Des. **10**, 4484 (2011).

[10] Y. Wu, G. Ren, D. Ding, F. Yang, and S. Pan, Appl. Phys. Lett. **100**, 021904 (2012).

[11] J. M. Ogieglo, *Luminescence and Energy Transfer in Garnet Scintillators* (Utrecht University, 2012).

[12] J. A. Mares, M. Nikl, E. Mihokova, A. Beitlerova, A. Vedda, and C. D'Ambrosio, IEEE Trans. Nucl. Sci. **55**, 1142 (2008).

[13] V. Laguta, Y. Zorenko, V. Gorbenko, A. Iskaliyeva, Y. Zagorodniy, O. Sidletskiy, P. Bilski, A. Twardak, and M. Nikl, J. Phys. Chem. C **120**, 24400 (2016).

[14] S. Gundacker, F. Acerbi, E. Auffray, A. Ferri, A. Gola, M. V. Nemallapudi, G. Paternoster, C. Piemonte, and P. Lecoq, J. Instrum. **11**, P08008 (2016).

[15] C. Piemonte, A. Ferri, A. Gola, T. Pro, N. Serra, A. Tarolli, and N. Zorzi, IEEE Trans. Electron Devices **60**, 2567 (2013).

[16] M. A. Spurrier, P. Szupryczynski, K. Yang, A. A. Carey, and C. L. Melcher, IEEE Trans. Nucl. Sci. **55**, 1178 (2008).

[17] S. Blahuta, A. Bessiere, B. Viana, P. Dorenbos, and V. Ouspenski, IEEE Trans. Nucl. Sci. **60**, 3134 (2013).

[18] A. Gola, C. Piemonte, and A. Tarolli, IEEE Trans. Nucl. Sci. **60**, 1296 (2013).

[19] M. T. Lucchini, V. Babin, P. Bohacek, S. Gundacker, K. Kamada, M. Nikl, A. Petrosyan, A. Yoshikawa, and E. Auffray, Nucl. Instrum. Methods Phys. Res. A **816**, 176 (2016).

[20] K. Kamada, M. Nikl, S. Kurosawa, A. Beitlerova, A. Nagura, Y. Shoji, J. Pejchal, Y. Ohashi, Y. Yokota, and A. Yoshikawa, Opt. Mater. **41**, 63 (2015).

[21] G. Tamulaitis, A. Vaitkevičius, S. Nargelas, R. Augulis, V. Gulbinas, P. Bohacek, M. Nikl, A. Borisevich, A. Fedorov, M. Korjik, and E. Auffray, Nucl. Instrum. Methods Phys. Res. A **870**, 25 (2017).

[22] E. Auffray, R. Augulis, A. Fedorov, G. Dosovitskiy, L. Grigorjeva, V. Gulbinas, M. Koschan, M. Lucchini, C. Melcher, S. Nargelas, G. Tamulaitis, A. Vaitkevičius, A. Zolotarjovs, and M. Korzhik, Phys. Status Solidi Appl. Mater. Sci. **215**, 7 (2018).

[23] M. T. Lucchini, O. Buganov, E. Auffray, P. Bohacek, M. Korjik, D. Kozlov, S. Nargelas, M. Nikl, S. Tikhomirov, G. Tamulaitis, A. Vaitkevicius, K. Kamada, and A. Yoshikawa, J. Lumin. **194**, 1 (2018).

[24] E. Auffray, R. Augulis, A. Borisevich, V. Gulbinas, A. Fedorov, M. Korjik, M. T. Lucchini, V. Mechinsky, S. Nargelas, E. Songaila, G. Tamulaitis, A. Vaitkevičius, and S. Zazubovich, J. Lumin. **178**, 54–60 (2016).

[25] Y. Wu, F. Meng, Q. Li, M. Koschan, and C. L. Melcher, Phys. Rev. Appl. **2**, 044009 (2014).

[26] P. Dorenbos, J. Lumin. **134**, 310 (2013).

[27] A. Ferri, A. Gola, N. Serra, A. Tarolli, N. Zorzi, and C. Piemonte, Phys. Med. Biol. **59**, 869 (2014).

[28] M. Nikl, V. Babin, J. Pejchal, V. V. Laguta, M. Buryi, J. A. Mares, K. Kamada, S. Kurosawa, A. Yoshikawa, D. Panek, T. Parkman, P. Bruza, K. Mann, M. Müller, and M. Muller, IEEE Trans. Nucl. Sci. **63**, 433 (2016).

[29] A. Nakatsuka, A. Yoshiasa, and T. Yamanaka, Acta Crystallogr. Sect. B Struct. Sci. **55**, 266 (1999).

[30] F. Meng, M. Koschan, Y. Wu, C. L. Melcher, and P. Cohen, Nucl. Instrum. Methods Phys. Res. A **797**, 138 (2015).

[31] K. Mamoru, K. Kei, K. Shunsuke, A. Junpei, O. Akimasa, Y. Akihiro, and H. Kazuhiko, Appl. Phys. Express **9**, 072602 (2016).

[32] A. A. Annenkov, M. V. Korzhik, and P. Lecoq, Nucl. Instrum. Methods Phys. Res. A **490**, 30 (2002).

[33] E. Mihóková, K. Vávrů, K. Kamada, V. Babin, A. Yoshikawa, M. Nikl, K. Vávr, K. Kamada, V. Babin, A. Yoshikawa, and M. Nikl, Radiat. Meas. **56**, 98 (2013).

Paper P12

Measurement of non-equilibrium carriers dynamics in Ce-doped YAG, LuAG and GAGG crystals with and without Mg-codoping

M.T. Lucchini, O. Buganov, E. Auffray, P. Bohacek, M. Korjik, D. Kozlov, S. Nargelas, M. Nikl, S. Tikhomirov, G. Tamulaitis, A. **Vaitkevičius**, K. Kamada, A. Yoshikawa

CrystEngComm. 21 (2019) 687–693.

doi: 10.1016/j.jlumin.2017.10.005.

Journal of Luminescence 194 (2018) 1–7

Contents lists available at ScienceDirect

Journal of Luminescence

journal homepage: www.elsevier.com/locate/jlumin

Measurement of non-equilibrium carriers dynamics in Ce-doped YAG, LuAG and GAGG crystals with and without Mg-codoping

M.T. Lucchini[a,*], O. Buganov[b], E. Auffray[a], P. Bohacek[c], M. Korjik[d], D. Kozlov[d], S. Nargelas[e], M. Nikl[c], S. Tikhomirov[b], G. Tamulaitis[e], A. Vaitkevicius[e], K. Kamada[f], A. Yoshikawa[f]

[a] *CERN, CH-1211 Geneva 23, Switzerland*
[b] *Stepanov Institute of Physics, Minsk, Belarus*
[c] *Institute of Physics AS CR, Prague, Czech Republic*
[d] *Research Institute for Nuclear Problems, Minsk, Belarus*
[e] *Vilnius University, Vilnius, Lithuania*
[f] *C & A Corporation, T-Biz, Sendai, Japan*

ARTICLE INFO

Keywords:
Scintillators
Multi-component garnet crystals
Non-linear absorption spectroscopy
Excitation transfer

ABSTRACT

Non-linear absorption spectroscopy in pump and probe configuration has been used to test the population of non-equilibrium carriers in Ce-doped $Y_3Al_5O_{12}$ (YAG), $Lu_3Al_5O_{12}$ (LuAG), and $Gd_3Al_xGa_{(5\text{-}x)}O_{12}$ (GAGG) crystals with and without codoping by Mg^{2+} ions. A faster rise time of the induced optical density has been observed in all crystals codoped with Mg with respect to that in Mg-free samples. A significant difference in the time evolution of the differential optical density in GAGG with respect to YAG and LuAG crystals has also been measured. In both GAGG:Ce and GAGG:Ce,Mg an absorption band with maximum in the blue-green range and a decay time of 1.4 ps is present. This band is due to the absorption by free electrons before they are trapped or re-captured by Ce^{3+} ions. A broad absorption band in the yellow-red region with very short rise time and a decay time longer than 150 ps has been observed in all the Ce-doped garnets under study and can be attributed to the absorption from the Ce^{3+} excited states.

1. Introduction

The rise time of the scintillation signal plays a crucial role in defining the time resolution achievable with a given scintillator, which depends on the interplay between the light yield and the kinetics of the scintillation process [1]. A shorter and brighter scintillation pulse leads to a smaller jitter on the arrival time of the first photons at the photodetector. Therefore, these parameters are crucial in defining the potential application of inorganic scintillators for both time of flight positron emission tomography (TOF-PET) scans [2–4] and precision timing detectors in high energy physics experiments [5].

Recently, Ce-doped garnets with the chemical formula $M_3A_5O_{12}$, in which the metal M can be either a single yttrium/rare earth ion or their mixture; and the metal A can be Al, Ga or their mixture, have been extensively studied. Their main characteristics are high light yield, scintillation decay time shorter than 100 ns, and emission peaks around 540 nm, which can be exploited with the good sensitivity of silicon photo-multipliers (SiPM) at such wavelength.

The codoping of Ce-doped scintillation materials with alkali earth ions has been recently demonstrated to be a promising approach to improve the scintillation properties, especially in the scintillators with a garnet-type crystal matrix [6,7]. Such improvement is a combined result of the modification of electronic excitation transfer processes, achieved by band gap engineering, and the tailoring of the activator level energy within the gap, implemented via a variation of the garnet composition [8,9]. The codoping of the crystal using alkali earth ions results in the substitution of a trivalent ion in the host matrix with a divalent second-group cation and causes the formation of anionic vacancies that compensate the charge deficiency. The formation of a hole-type defect including Mg^{2+} and O^{-} in close proximity of the divalent cation is also favored [10,11]. Moreover, the codoping of Ce-activated crystals by divalent ions (even at the level of a few hundreds ppm) causes the oxidation of a fraction of the Ce^{3+} ions into Ce^{4+}. Both these types of cerium ions are then involved in the scintillation process but with different kinetics [12–14]. The result is a significant acceleration of the luminescence rise and decay times, as observed in $Gd_3Al_{2.3}Ga_{2.7}O_{12}$ (GAGG:Ce) crystals codoped with Mg [15]. This leads, as expected, to an improvement of the coincidence time resolution, as recently demonstrated for GAGG, $Y_3Al_5O_{12}$:Ce (YAG:Ce), and $Lu_3Al_5O_{12}$:Ce (LuAG:Ce) crystals [16,17].

---

[*] Corresponding author.
E-mail address: Marco.Toliman.Lucchini@cern.ch (M.T. Lucchini).

http://dx.doi.org/10.1016/j.jlumin.2017.10.005
Received 14 August 2017; Received in revised form 27 September 2017; Accepted 2 October 2017

With respect to YAG and LuAG crystals, GAGG shows a peculiar feature: it contains numerous levels of ^{7}f electronic states in the band gap, due to the presence of Gd^{3+} ions. As recently shown in [18], the ground state ^8S of Gd^{3+} ions in GAGG crystals is located about 1 eV below the top of the valence band. A substantial difference in the excitation transfer to the radiating level of Ce^{3+} in GAGG is thus expected with respect to Gd-free garnets. Since the luminescence build-up process is determined by the population of the Ce^{3+} radiating levels, studying the time evolution of the population is a powerful tool to investigate both the luminescence response and the dynamics of free carriers before they are captured by traps and radiative centers. To study these processes, the population of the lowest excited levels can be probed by exploiting the *optical pump-and-probe technique* in which a femtosecond pump pulse is used for photo-excitation and a probe pulse of similar duration but with variable delay (with respect to the excitation pulse) is used to probe the free carrier density and the population of the excited electronic energy levels. In the current paper, a comparison of the fast excitation transfer processes in Ce-doped GAGG, YAG, and LuAG crystals, with and without Mg-codoping, is provided.

2. Experimental methods

The six Ce-doped garnet samples used in this study were grown by Czochralski technique at a speed of about 1 mm/h using an iridium crucible under N_2 atmosphere, or, in case of GAGG, under atmosphere of N_2 with 2% of O_2. For the GAGG samples, the seed crystal of ⟨100⟩ orientation was purchased from C & A Corporation, Sendai, Japan. Mixtures of oxides of purity 5N with compositions of $Gd_{2.982}Ce_{0.015}Ga_{2.7}Al_{2.3}O_{12}$ and $Gd_{2.982}Ce_{0.015}Mg_{0.003}$ $Ga_{2.7}Al_{2.3}O_{12}$ were used as starting materials. For the YAG and LuAG samples a stoichiometric mixture of 4N $MgCO_3$, CeO_2, a-Al_2O_3, Y_2O_3 and Lu_2O_3 powders was used as starting material. Nominally, starting powders were prepared according to the formula of $(Mg_{0.005}Ce_{0.0005}Lu_{0.99})_3Al_5O_{12}$ and $(Mg_{0.005}Ce_{0.0005}Y_{0.99})_3Al_5O_{12}$ and seeds of ⟨111⟩ oriented YAG crystals were used. More details on the production method and the chemical compositions are described elsewhere [16,17]. All the samples were cut from single crystal ingots in the shape of a 2 × 2 × 10 mm^3 pixels and subsequently polished. The standard scintillation and optical properties of these samples were measured and discussed in [17].

The study of non-equilibrium carrier dynamics was performed using a pump-probe spectrometer based on an original femtosecond Ti:Al_2O_3 pulsed oscillator and a regenerative amplifier, both operating at 10 Hz repetition rate. A schematic diagram of the setup is shown in Fig. 1. The laser pulse duration and energy after amplification were 140 fs and up to 0.5 mJ, respectively, while the wavelength was tunable over the spectral range from 770 to 820 nm. The pulses of the fundamental frequency (the wavelength, λ, was set at 790 nm for the present study) were divided after the output of the amplifier into two parts at a ratio of 1:4. The beam of higher intensity was converted to the third harmonic ($\lambda \approx 263$ nm, pulse energy E up to 12 μJ) and used as the pump pulse. The pulse energy was selected low enough to prevent the sample surface from optical damage by the laser pulse. The second beam of smaller intensity was used as a probe.

After passing the delay line, the probe pulse was converted to a white super-continuum generated by focusing the beam into a 1 cm long water cell. By using a semi-transparent mirror, the super continuum radiation (360–800 nm) was subdivided into two pulses (reference and signal) of similar intensity. Both pulses were focused on the sample by mirror optics. The reference pulse was exploited to eliminate the impact of shot-to-shot instability of super-continuum. It passes the sample always before the pump pulse. The pump-induced change of the optical density was calculated as:

$$\Delta D(\lambda, \Delta t) = \log\left[\frac{E_{sg}(\lambda)}{E_{ref}(\lambda)}\cdot\frac{E_{ref}(\lambda, \Delta t)}{E_{sg}^{*}(\lambda, \Delta t)}\right] \tag{1}$$

where E_{sg}, E_{sg}^{*}, and E_{ref} are the energies of the signal pulses which passed the sample before and after the pump pulse, and the reference pulse, respectively. The beam spot diameter was 0.5 mm. The spectra of both pulses were recorded for each laser shot by a system including a polychromator equipped with a CCD camera and digitally processed. The absorption spectra of the white super continuum were measured in the spectral range from 400 to 700 nm. All measurements have been performed at room temperature. Additional details on the setup are provided in [19–22], where the same technique and instrumental apparatus have been used for studies of ultrafast phenomena in different materials.

3. Results

The absorption spectra of the crystals under study, measured through 2 mm thickness using a Perkin Elmer (Lambda 650 UV/VIS) spectrometer, are shown in Fig. 2. All the Mg-free crystals exhibit the 4f-5d absorption bands corresponding to inter-configuration transitions of Ce^{3+} ions. The samples codoped with Mg^{2+} ions additionally show a broad absorption band in the UV region (below 300 nm). This band, related to the charge transfer (CT) transition from the valence band to a defect stabilized by Mg^{2+} (e.g. Ce^{4+} ions) [10], is more pronounced in the LuAG:Ce crystals having the lowest concentration of Ce^{3+} ions. The absorption spectrum of the GAGG:Ce sample also shows a set of narrow absorption bands in the UV range corresponding to the transitions from ^8S ground state to the numerous components of P, I, and D terms split by spin-orbit interaction.

The transient induced absorption spectra of all samples for different delay times between the pump and the probe pulses are shown in Fig. 3.

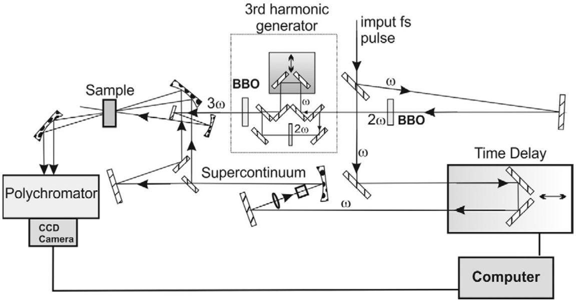

Fig. 1. Schematic diagram of the pump-probe spectrometer setup used to study non-equilibrium carrier dynamics.

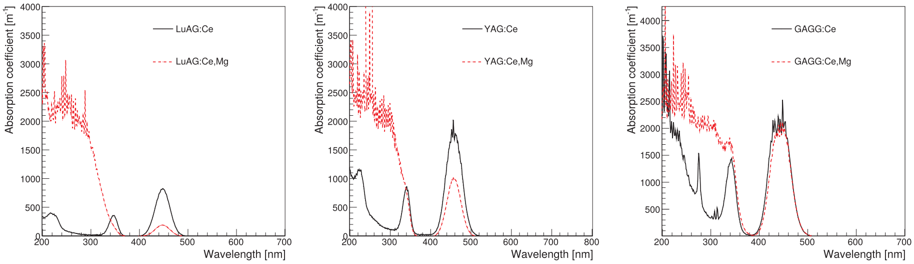

Fig. 2. Absorption spectra of LuAG:Ce, YAG:Ce and GAGG:Ce without (black solid) and with Mg codoping (red dotted). Fluctuations at low wavelengths are due to the lower light beam intensity of the spectrophotometer and larger light absorption by the crystals in the UV spectral range. These effects deteriorate the signal-to-noise ratio of the measurement.

The pump wavelength, λ_{ex} = 263 nm, was chosen to avoid direct excitation of Gd^{3+} states in GAGG crystals. For all the samples under study, such wavelength excites the Ce^{3+} ions in the tail of the third component of the inter-configuration transition $4f^1$-$5d^14f^0$ [23]. Since the corresponding excited level is located in the conduction band (CB), the de-localization of the non-equilibrium electrons and their capture might easily occur. In addition, the pump causes CT transitions in the defect centers due to the divalent ions introduced by the Mg-codoping. The differential optical density spectra of GAGG:Ce and YAG:Ce show a drop around 440–450 nm, in correspondence with the first $4f^1$-$5d^14f^0$ allowed transition of Ce^{3+} ions. This occurs due to a relatively larger concentration of Ce^{3+} in these samples with respect to the lower dopant concentration in LuAG.

The spectra of GAGG:Ce samples contain two overlapping and wide absorption bands (local maxima in the spectrum): a first band, B1, having its maximum in the blue-green range (around 480 nm) and a second band, B2, peaking around 680 nm. As shown in the differential absorption kinetics, in Fig. 4, these bands appear simultaneously with the leading edge of the excitation. The B1 band (probed at 480 nm) shows an extremely fast decay component with time constant of $\tau_{d,1} = 1.4 \pm 0.2$ ps followed by another component with slower decay constant (~150 ps). The time evolution of the B2 band intensity (probed at 680 nm) shows no fast component and decays with a comparably slow time constant as B1.

The B1 band is considerably less resolved in the absorption spectra of YAG:Ce and LuAG:Ce samples and no fast decay component in the kinetics is observed for the differential optical density probed at a spectral wavelength close to the B1 band (around 400 nm). The B2 band appears to have its maximum around 650 nm in YAG and LuAG samples and its slow decay time constant is also longer than in GAGG:Ce samples: it is about 400 ps for Mg-codoped LuAG and YAG and larger than 1000 ps for the respective Mg-free samples.

A comparison of the initial part of the differential optical density kinetics in LuAG:Ce, YAG:Ce and GAGG:Ce, with and without Mg-codoping, is better shown within a reduced time range in Fig. 5. The time evolution of the transient absorption in the Mg-codoped GAGG:Ce is similar to that in the sample without codoping, except for the fast component B1 which becomes faster and of smaller intensity. A faster rise time is also visible for LuAG:Ce and YAG:Ce Mg-codoped crystals with respect to the respective Mg-free samples and is further discussed in the following section.

4. Discussion

There is a significant difference between the defect formation process in YAG, LuAG and GAGG crystals. In garnet crystals containing two or more cations and isovalent doping ions, e.g. Ce^{3+} in our case, the defects are created by the preferential evaporation of the most volatile component from the melt during the crystal growth. In this case, randomly distributed vacancies will dominate. In GAGG crystals, where gallium is the most volatile component, the formation of cation vacancies due to the gallium evaporation inevitably leads to the formation of anionic vacancies and, consequently, to a higher concentration of trapping centers with respect to garnets grown from binary compositions. For example, oxygen vacancies create a set of electron trap levels with activation energy in the range up to 1 eV. Moreover, multi-component garnet crystals favor the formation of additional defects that act as trapping centers for non-equilibrium carriers. The ratio of the ionic radii of Al and Ga is 0.39 Å to 0.47 Å in the oxygen tetrahedral positions and 0.53 Å to 0.62 Å in octahedral positions [24]. Therefore, even a random distribution of Al and Ga ions in the lattice results in considerable distortion of the lattice. Closely located gallium and aluminum ions distort the polyhedral environment of each other and result in the formation of additional shallow trapping centers. For this reason, a higher concentration of shallow centers is expected in GAGG with respect to YAG and LuAG crystals. It is in fact reflected in low temperature TSL glow curve of these materials [25,26].

The existence of a fast decay component in the transient absorption of GAGG:Ce samples was previously observed in [27]. The results presented in this work confirm its presence in GAGG:Ce and show that such component is absent in YAG:Ce and LuAG:Ce crystals, independently from the presence of Mg^{2+} ions. This observation suggests that the transient absorption band peaking in the blue-green region, B1, cannot be associated with the excited radiating level of Ce^{3+}. Most probably, the B1 band is caused by free electron absorption, where the free electrons are generated via the absorption by Ce^{3+} and the subsequent transfer of the electrons to the conduction band. The spectral width of the B1 band might be attributed to structured density of states in the conduction band [28].

The fast decay of the free electron absorption can be explained by the localization of free electrons at the traps in GAGG. Conversely, a maximum of the transient absorption around 650–680 nm (broad B2 band) is observed in all samples under study and could be attributed to the absorption from the Ce^{3+} excited radiating levels.

This interpretation is also supported by the different kinetic behavior of the B1 and B2 absorption bands observed in the GAGG:Ce sample at the initial stage after the short-pulse excitation. The equilibrium between the free electrons and the electrons at the excited Ce^{3+} level is established within approximately 2 ps after the pump excitation, while the further decay of both free electron density (probed at 480 nm) and the population of the excited Ce^{3+} level (probed at 680 nm) proceeds at a similar rate, which is determined by radiative and non-radiative recombination processes. In the GAGG:Ce sample codoped with magnesium, the relative contribution of the fast component is smaller and its decay time faster ($\tau_d = 0.5 \pm 0.04$ ps) indicating that an additional recombination channel might have been introduced

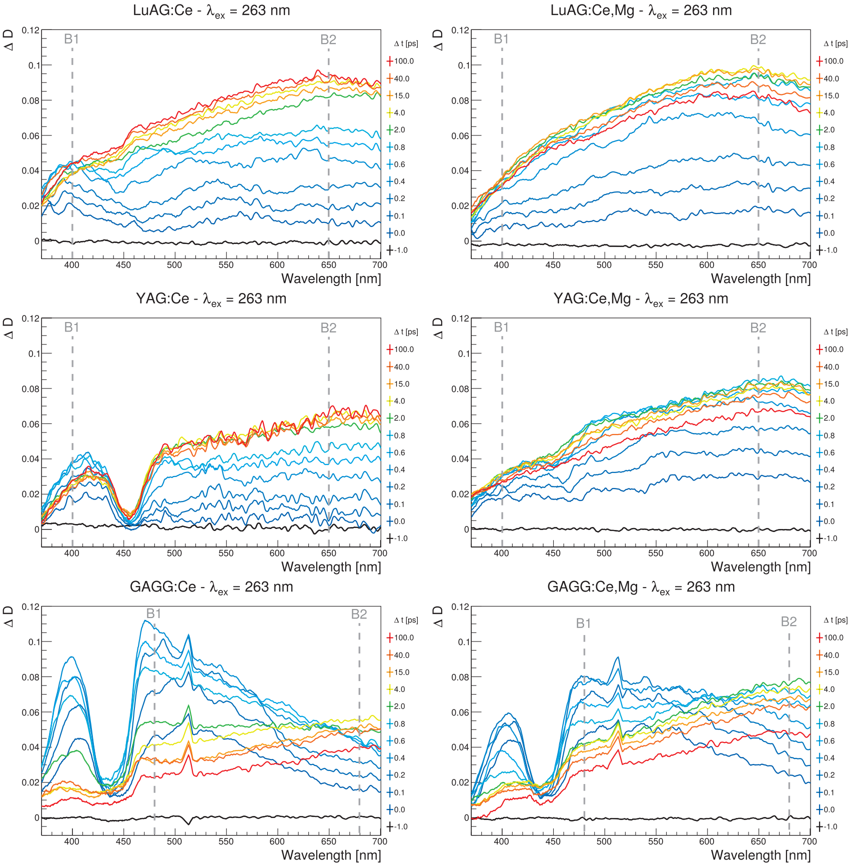

Fig. 3. Transient induced absorption spectra of LuAG:Ce, YAG:Ce and GAGG:Ce single crystals (from top to bottom) with (left) and without (right) Mg-codoping. The spectra are shown at different time delays between the pump and probe pulses (indicated) at pump pulse energy of 10 μJ.

by codoping.

A difference in the rising time of the transient B2 absorption band kinetics between Mg-codoped and Mg-free garnets has also been observed as shown in Fig. 5. This difference is minimal in GAGG crystal but, in YAG and LuAG samples, the rising edge of the transient absorption response of the Mg-codoped crystals is considerably shorter due to capturing of free electrons from shallow traps. The Mg^{2+}-based defect centers, having a CT transition peaked at 265 nm, create deep trap levels approximately 1.5 eV below the bottom of conduction band. This can cause the same electrons to be captured multiple times from shallow traps and prevents them from being re-captured by Ce^{3+} ions via the conduction band. Shallow traps capture electrons from the conduction band, while the thermal re-activation of the electrons back to the conduction band results in the population of Ce^{3+} radiating levels and is responsible for the delayed luminescence observed in such samples. In Mg-codoped crystals, this process is substantially suppressed by the re-capturing of trapped electrons by Mg-related centers and thus the re-population from the traps is less probable. As a result, the transient absorption decay is faster in the codoped crystals. Meanwhile, the additional channel of non-radiative recombination, which is introduced by Mg-codoping, reduces the scintillation efficiency of garnet crystals.

5. Conclusions

The transient differential absorption of a set of Ce-doped $Y_3Al_5O_{12}$, $Lu_3Al_5O_{12}$ and $Gd_3Al_2Ga_3O_{12}$ crystals with and without Mg-codoping has been measured by pump-probe method using femtosecond laser sources. The pump at the wavelength of 263 nm was used to create free carriers in all the samples under study, whereas white super-continuum

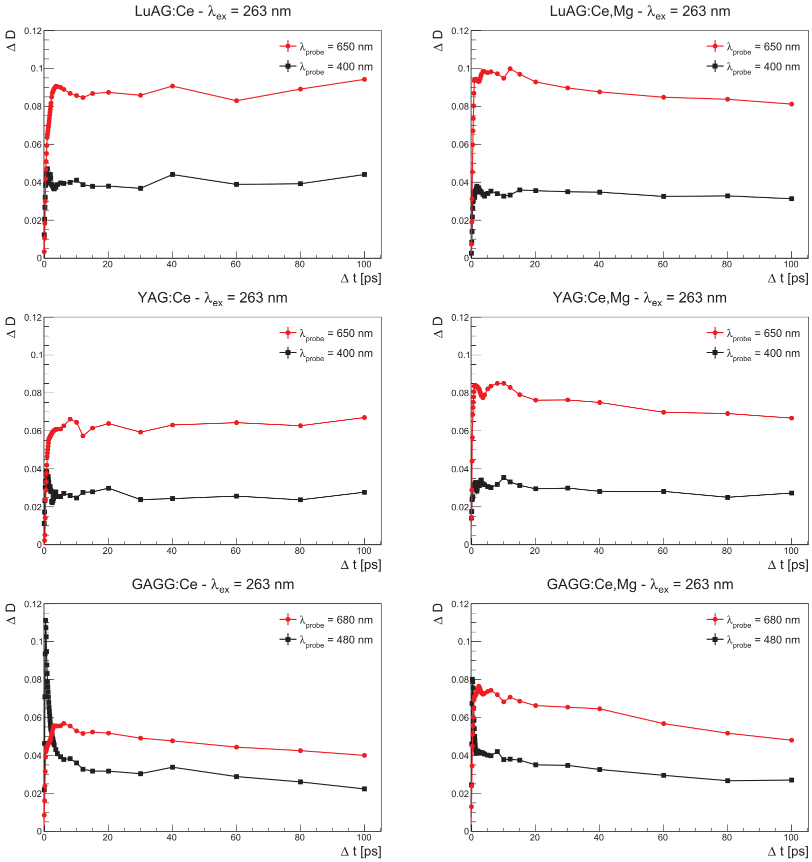

Fig. 4. Time evolution of the probe differential absorption, ΔD, at two different spectral regions of 400–480 and 650–680 nm for LuAG:Ce, YAG:Ce and GAGG:Ce single crystals (from top to bottom) with (left) and without (right) Mg-codoping.

was applied to measure transient absorption in the spectral range from 400 to 700 nm.

Substantial differences in the dynamics of population of the excited state of the activator ions in three garnet-type scintillators: YAG:Ce, LuAG:Ce, and GAGG:Ce were revealed. Two non-linear absorption bands were observed. The first band, present in all three garnets, is broad and extends from approximately 450 nm over the whole visible region and decays with a characteristic time constant ≳150 ps. This band is attributed to the absorption from the lowest excited state of Ce^{3+}. The second band is peaked at the blue-green region, emerges in the sub-picosecond domain and has a decay time of ~ 1.4 ps. The time evolution of this band implies that it is caused by the light absorption by free electrons released to the conduction band after photo-excitation of Ce^{3+} ions and rapidly captured by trapping states. This band is most pronounced in GAGG:Ce due to the influence of the second excited state of Ce^{3+}, which is in the conduction band close to its bottom, and is hardly traced in LuAG:Ce.

Pairs of samples of the crystals, nominally identical except of co-doping by magnesium, were prepared to reveal the influence of co-doping by divalent ions. We show that Mg-codoping introduces additional levels into the band gap, which facilitate transferring the trapped electrons back to the Ce ions.

Acknowledgments

This work was performed in the framework of the Crystal Clear Collaboration and received funding from the European Union's Horizon 2020 research and innovation program under the Marie Skodowska-Curie grant agreement no. 644260 (Intelum). Support has been received also from the AIDA2020 European project, the ASCIMAT project under grant agreement no. 690599 and from COST Action TD1401 (FAST). We also acknowledge the support from the Belarus Foundation for

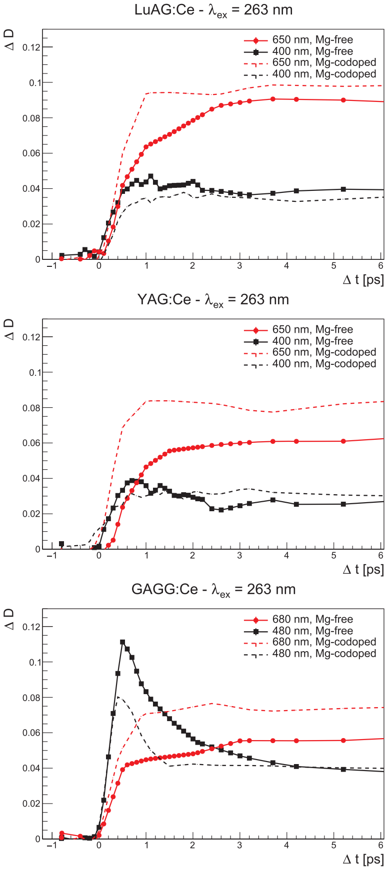

Fig. 5. Comparison of the early kinetics of the probe differential absorption, Δ*D*, at two different spectral regions of 400–480 and 650–680 nm between Mg-codoped (dotted line) and Mg-free (solid line) samples of LuAG:Ce, YAG:Ce and GAGG:Ce single crystals (from top to bottom).

Fundamental Research and by the Czech Science Foundation 16-15569S.

References

[1] S. Gundacker, et al., Measurement of intrinsic rise times for various L(Y)SO and LuAG scintillators with a general study of prompt photons to achieve 10 ps in TOF-PET, Phys. Med. Biol. 61 (7) (2016) 2802–2837, http://dx.doi.org/10.1088/0031-9155/61/7/2802.

[2] W.W. Moses, et al., Time of flight in PET revisited, IEEE Trans. Nucl. Sci. 50 (2003) 1325–1330, http://dx.doi.org/10.1109/TNS.2003.817319.

[3] M. Conti, et al., State of the art and challenges of time-of-flight PET, Phys. Med. 25 (2009) 1, http://dx.doi.org/10.1016/j.ejmp.2008.10.001.

[4] S. Gundacker, et al., State of the art timing in TOF-PET detectors with LuAG, GAGG and L(Y)SO scintillators of various sizes coupled to FBK-SiPMs, J. Instrum. 11 (08) (2016) P08008.

[5] CMS Collaboration, Technical proposal for the Phase-II upgrade of the Compact Muon Solenoid, CERN-LHCC-2015-010 (2015) LHCC-P–008.

[6] K. Kamada, T. Yanagida, J. Pejchal, M. Nikl, T. Endo, K. Tsutsumi, Y. Fujimoto, A. Fukabori, A. Yoshikawa, Scintillator-oriented combinatorial search in Ce-doped (Y,Gd)$_3$(Ga,Al)$_5$O$_{12}$ multicomponent garnet compounds, J. Phys. D: Appl. Phys. 44 (50) (2011) 505104.

[7] K. Kamada, T. Yanagida, J. Pejchal, M. Nikl, T. Endo, K. Tsutsumi, Y. Fujimoto, A. Fukabori, A. Yoshikawa, Crystal growth and scintillation properties of Ce-doped Gd$_3$(Ga,Al)$_5$O$_{12}$ single crystals, IEEE Trans. Nucl. Sci. 59 (5) (2012) 2112–2115, http://dx.doi.org/10.1109/TNS.2012.2197024.

[8] I.I. Vrubel, R.G. Polozkov, I.A. Shelykh, V.M. Khanin, P.A. Rodnyi, C.R. Ronda, Bandgap engineering in YttriumAluminum garnet with Ga-doping, Cryst. Growth Des. 17 (4) (2017) 1863–1869, http://dx.doi.org/10.1021/acs.cgd.6b01822.

[9] M. Fasoli, A. Vedda, M. Nikl, C. Jiang, B.P. Uberuaga, D.A. Andersson, K.J. McClellan, C.R. Stanek, Band-gap engineering for removing shallow traps in rare-earth Lu$_3$Al$_5$O$_{12}$ garnet scintillators using Ga^{3+} doping, Phys. Rev. B 84 (2011) 081102, http://dx.doi.org/10.1103/PhysRevB.84.081102.

[10] M. Nikl, V. Babin, J. Pejchal, V.V. Laguta, M. Buryi, J.A. Mares, K. Kamada, S. Kurosawa, A. Yoshikawa, D. Panek, T. Parkman, P. Bruza, K. Mann, M. Mller, The stable Ce^{4+} center: a new tool to optimize Ce-doped oxide scintillators, IEEE Trans. Nucl. Sci. 63 (2) (2016) 433–438, http://dx.doi.org/10.1109/TNS.2015.2495119.

[11] C. Hu, S.-P. Liu, M. Fasoli, A. Vedda, M. Nikl, X.-Q. Feng, Yu-Bai, ESR and TSL study of hole and electron traps in LuAG:Ce,Mg ceramic scintillator, Opt. Mater. 45 (2015) 252–257, http://dx.doi.org/10.1016/j.optmat.2015.03.049.

[12] S. Blahuta, et al., Evidence and consequences of Ce^{4+} in LYSO: Ce,Ca and LYSO: Ce,Mg single crystals for medical imaging applications, IEEE Trans. Nucl. Sci. 60 (2013) 3134–3141, http://dx.doi.org/10.1088/0031-9155/60/12/4635.

[13] Y. Wu, et al., Role of Ce^{4} in the scintillation mechanism of co-doped Gd$_3$Al$_2$Ga$_3$O$_{12}$:Ce, Phys. Rev. Appl. 2 (41) (2014) 044009, http://dx.doi.org/10.1103/PhysRevApplied.2.044009.

[14] M. Nikl, et al., Defect engineering in Ce-doped aluminum garnet single crystal scintillators, Cryst. Growth Des. 14 (2014) 4827–4833, http://dx.doi.org/10.1021/cg501005s.

[15] E. Auffray, R. Augulis, A. Borisevich, V. Gulbinas, A. Fedorov, M. Korjik, M. Lucchini, V. Mechinsky, S. Nargelas, E. Songaila, G. Tamulaitis, A. Vaitkeviius, S. Zazubovich, Luminescence rise time in self-activated PbWO$_4$ and Ce-doped Gd$_3$Al$_2$Ga$_3$O$_{12}$ scintillation crystals, J. Lumin. 178 (2016) 54–60, http://dx.doi.org/10.1016/j.jlumin.2016.05.015.

[16] M. Lucchini, V. Babin, P. Bohacek, S. Gundacker, K. Kamada, M. Nikl, A. Petrosyan, A. Yoshikawa, E. Auffray, Effect of Mg^{2+} ions co-doping on timing performance and radiation tolerance of cerium doped Gd$_3$Al$_2$Ga$_3$O$_{12}$ crystals, Nucl. Instrum. Methods Phys. Res. Sect. A: Accel., Spectrometers Detect. Assoc. Equip. A816 (2016) 176–183, http://dx.doi.org/10.1016/j.nima.2016.02.004.

[17] M. Lucchini, S. Gundacker, P. Lecoq, A. Benaglia, M. Nikl, K. Kamada, A. Yoshikawa, E. Auffray, Timing capabilities of garnet crystals for detection of high energy charged particles, Nucl. Instrum. Methods Phys. Res. Sect. A: Accel., Spectrometers Detect. Assoc. Equip. 852 (2017) 1–9, http://dx.doi.org/10.1016/j.nima.2017.02.008.

[18] E. Auffray, M. Korjik, M. Lucchini, S. Nargelas, O. Sidletskiy, G. Tamulaitis, Y. Tratsiak, A. Vaitkeviius, Free carrier absorption in self-activated PbWO$_4$ and Ce-doped Y$_3$(Al$_{0.25}$Ga$_{0.75}$)$_3$O$_{12}$ and Gd$_3$Al$_2$Ga$_3$O$_{12}$ garnet scintillators, Opt. Mater. 58 (2016) 461–465, http://dx.doi.org/10.1016/j.optmat.2016.06.040.

[19] A.J. Taylor, E.S. Davies, J.A. Weinstein, I.V. Sazanovich, O.V. Bouganov, S.A. Tikhomirov, M. Towrie, J. McMaster, C.D. Garner, Ultrafast intramolecular charge separation in a donoracceptor assembly comprising bis(5-cyclopentadienyl) molybdenum coordinated to an ene-1,2-dithiolate-naphthalenetetracarboxylicdiimide ligand, Inorg. Chem. 51 (24) (2012) 13181–13194, http://dx.doi.org/10.1021/ic301436t.

[20] V.I. Stsiapura, A.A. Maskevich, S.A. Tikhomirov, O.V. Buganov, Charge transfer process determines ultrafast excited state deactivation of thioflavin t in low-viscosity solvents, J. Phys. Chem. A 114 (32) (2010) 8345–8350, http://dx.doi.org/10.1021/jp105186z.

[21] O.V. Buganov, A.S. Grabtchikov, Y.I. Malakhov, Y.M. Popov, V.A. Orlovich, S.A. Tikhomirov, Features of raman amplification in kgw and barium nitrate crystals at excitation by femtosecond pulses, Laser Phys. Lett. 9 (11) (2012) 786 (http://stacks.iop.org/1612-202X/9/i = 11/a = 005 〉).

[22] M. Smirnov, O. Buganov, E. Shabunya-Klyachkovskaya, S. Tikhomirov, O. Ovchinnikov, A. Vitukhnovsky, A. Perepelitsa, A. Matsukovich, A. Katsaba, Dynamics of electronic excitations relaxation in hydrophilic colloidal CdS quantum dots in gelatin with involvement of localized states, Phys. E: Low.-Dimens. Syst. Nanostruct. 84 (Supplement C) (2016) 511–518, http://dx.doi.org/10.1016/j.physe.2016.07.004.

[23] P.A. Tanner, L. Fu, L. Ning, B.-M. Cheng, M.G. Brik, Soft synthesis and vacuum ultraviolet spectra of YAG:Ce 3+ nanocrystals: reassignment of Ce 3+ energy levels, J. Phys.: Condens. Matter 19 (21) (2007) 216213.

[24] R.D. Shannon, Revised effective ionic radii and systematic studies of interatomic distances in halides and chalcogenides, Acta Crystallogr. Sect. A 32 (5) (1976) 751–767, http://dx.doi.org/10.1107/S0567739476001551.

[25] K. Brylew, W. Drozdowski, A.J. Wojtowicz, K. Kamada, A. Yoshikawa, Studies of low temperature thermoluminescence of GAGG:Ce and LuAG:Pr scintillator crystals using the T$_{max}$-T$_{stop}$ method, J. Lumin. 154 (2014) 452–457, http://dx.doi.org/10.1016/j.jlumin.2014.05.035.

[26] W. Drozdowski, K. Brylew, M. Witkowski, A. Wojtowicz, P. Solarz, K. Kamada, A. Yoshikawa, Studies of light yield as a function of temperature and low temperature thermoluminescence of Gd$_3$Al$_2$Ga$_3$O$_{12}$:Ce scintillator crystals, Opt. Mater. 36 (10) (2014) 1665–1669, http://dx.doi.org/10.1016/j.optmat.2013.12.044 (sI:

IWASOM'13).

[27] G. Tamulaitis, A. Vaitkeviius, S. Nargelas, R. Augulis, V. Gulbinas, P. Bohacek, M. Nikl, A. Borisevich, A. Fedorov, M. Korjik, E. Auffray, Scintillator-oriented combinatorial search in Ce-doped $(Y,Gd)_3(Ga,Al)_5O_{12}$ multicomponent garnet compounds, Nucl. Instruments Methods Phys. Res. Sect. A Accel. Spectrometers, Detect. Assoc. Equip. (2017) (to be published).

[28] Y.-N. Xu, W.Y. Ching, Electronic structure of yttrium aluminum garnet $(Y_3Al_5O_{12})$, Phys. Rev. B 59 (1999) 10530–10535, http://dx.doi.org/10.1103/PhysRevB.59.10530.

Paper P13

Garnet-type crystallites, their isomorphism and luminescence properties in glass ceramics

Y. Tratsiak, E. Trusova, Y. Bokshits, M. Korjik, **A. Vaitkevičius**, G. Tamulaitis

CrystEngComm. 21 (2019) 687–693.

doi:10.1039/C8CE01547C.

CrystEngComm

PAPER

View Article Online
View Journal | View Issue

Cite this: *CrystEngComm*, 2019, **21**, 687

Garnet-type crystallites, their isomorphism and luminescence properties in glass ceramics

Yauhen Tratsiak, *[a] Ekaterina Trusova,[b] Yulia Bokshits,[a] Mikhail Korjik,[c] Augustas Vaitkevičius[d] and Gintautas Tamulaitis[d]

Received 11th September 2018, Accepted 7th December 2018

DOI: 10.1039/c8ce01547c

rsc.li/crystengcomm

Glass ceramics based on Ce-doped garnets were fabricated by the controlled crystallization of CaO(MgO)–Y_2O_3–Al_2O_3–GeO_2–SiO_2–CeO_2 glasses. The optimal conditions for transforming these glasses into ceramics by heat treatment were found by using differential scanning calorimetry: 1400 °C for MgO–Y_2O_3–Al_2O_3–GeO_2–SiO_2–CeO_2 and 1500 °C for CaO–Y_2O_3–Al_2O_3–GeO_2–SiO_2–CeO_2. The structure was characterized by X-ray diffraction (XRD) and energy-dispersive X-ray spectroscopy techniques, while the emission properties were studied by photoluminescence (PL) spectroscopy. The fine structure of XRD patterns evidences contributions from garnets of different compositions. Spatially-resolved PL spectroscopy using confocal microscopy shows that the garnet crystallites have a layered structure. The capability of tuning the PL peak position within the range from 530 to 580 nm by changing the excitation wavelength was demonstrated. This effect is caused by the localization of Ce^{3+} ions at the positions with different crystal fields, which varies due to a composition gradient in the crystallites. These glass ceramics have high potential for exploitation as phosphors in high-power white light sources.

Introduction

Light conversion by phosphors is the dominant approach in the fabrication of white light-emitting diodes (LEDs) based on high-brightness InGaN-based blue LEDs. Ce-doped yttrium aluminum garnet $Y_3Al_5O_{12}$ (YAG:Ce) is the most common phosphor for white LEDs.[1–5] This phosphor is usually dispersed in a transparent encapsulation (usually made of polymeric epoxides) covering an InGaN chip. In modern mass-produced white LEDs, the system works without significant aging throughout the entire chip lifetime of up to 100 000 hours. However, certain applications require white light sources of considerably higher brightness. The increase in brightness is accompanied by heating of LEDs to the temperatures that deteriorate the conventional encapsulation materials. This problem is of especial importance for the white light sources based on blue laser diodes. Exploitation of glass ceramics or single crystals as light converting media is a prospective approach to solve this problem.

Both single crystals and glass ceramics have high heat resistance and thermal conductivity and excellent optical and mechanical properties that allow them to be employed in a variety of applications. At the same time, glass ceramics have a number of advantages over single crystals: glass ceramics might be easily obtained by spontaneous or controllable crystallization of the initial glass[6–13] and inexpensively produced in different sizes and volumes, they can be doped with trivalent rare earth ions, such as cerium, europium, and terbium,[14–16] and a wide range of glass compositions to prepare YAG-based glass ceramics might be exploited.[17–24] The high propensity of the garnet structure to isomorphism (including both the homo- and heterovalent substitution abilities) prejudges the variety of compounds with this structure that in combination with the high sensitivity of Ce^{3+} ions to their crystalline environment is widely used in garnet engineering to develop new phosphors with an intentionally tunable position of the emission band. However, there are no reports on glass ceramics based on Ce-doped substituted garnets. The realization of such an approach would enable the development of thermally stable phosphors with additional spectral tunability for high-power white light emitters.

The current work is focused on the development of glass ceramics based on complex-substituted garnets with two expected compositions: $Y_2CaAlGe(AlO_4)_3$:Ce and $Y_2MgAlGe(AlO_4)_3$:Ce. The optimization of the thermal treatment for the conversion of glass into ceramics was based on the differential scanning calorimetry data and was tested by structural XRD analysis and photoluminescence (PL) spectroscopy. A spatially-resolved photoluminescence study enabled

---

[a] *Research Institute for Physical Chemical Problems, Belarusian State University, Leningradskaya str. 14, Minsk, Belarus. E-mail: slon.zhenya@gmail.com*
[b] *Belarusian State Technological University, Sverdlova str. 13a, Minsk, Belarus*
[c] *Research Institute for Nuclear Problems, Belarusian State University, Bobruiskaya str. 11, Minsk, Belarus*
[d] *Institute of Photonics and Nanotechnology, Vilnius University, Universiteto str. 3, Vilnius, Lithuania*

determination of the spatial distribution of the emission properties within the crystallites of the ceramic material.

Experimental

Synthesis procedure

Cerium-doped glasses were obtained by the conventional melt-quenching technique. The mixtures of MCO_3 (6.65 g of $CaCO_3$ or 5.6 g of $MgCO_3$), 12.75 g of SiO_2, 15.03 g of Y_2O_3, 13.87 g of Al_2O_3, 7.15 g of GeO_2, 0.86 g of CeO_2, and 1.11 g of Li_2CO_3 were used as the initial reactants. The amounts listed above correspond to the expected garnet compositions: $Y_2CaAlGe(AlO_4)_3$:Ce or $Y_2MgAlGe(AlO_4)_3$:Ce. Some initial reactants were taken in excess to form the glass medium. CeO_2 was taken in an amount corresponding to the substitution of 1 at% Y^{3+} and Ca^{2+} (Mg^{2+}) in dodecahedral positions by Ce^{3+}.

The raw materials (99.99% purity) were weighed and homogenized in a 50 cm^3 aluminum oxide ceramic crucible. The synthesis was performed in a CO-rich atmosphere at the maximum temperature of 1550 °C for 2 h in a gas furnace. Afterwards, the glasses were annealed at 500 °C for 4 h in a muffle furnace. The annealed glass blocks were transparent and colorless. Cubic 8 × 8 × 8 mm blocks were cut for studying and further annealing.

To transform the glasses into ceramic materials, the glass cubes were annealed in air at different temperatures: for 180 min at 1300 °C and 1400 °C and for 105 min at 1500 °C. The annealed blocks of glass ceramics were cut into 1 mm-thick plates and polished.

The glasses containing Ca^{2+} and Mg^{2+} are referred to as glass 1 and glass 2, respectively, while the corresponding glass ceramics obtained by annealing of glass 1 and glass 2 at 1500 °C are referred to as GC1 and GC2, respectively.

Thermal analysis

Differential scanning calorimetric (DSC) measurements were performed using Mettler Toledo Instruments TGA/DSC-1/1600 HF. The heating range was up to 1450 °C at a speed of 3 K min^{-1}.

X-ray analysis

The crystalline structure was investigated by X-ray diffraction (XRD) measurements using a diffractometer DRON 3 with a CoKα radiation source. The software DICVOL06 from the FULLPROF package was used to calculate the lattice constants.

Photoluminescence

Photoluminescence (PL) measurements were performed by using a microscope system WITec Alpha 300S operated in confocal mode. An objective with a numerical aperture NA = 0.6 was used for excitation and collection of the PL signal and ensured the spatial in-plane resolution of ∼250 nm and the axial resolution of ∼1.6 μm. A CW laser diode (ALPHALAS) emitting at 405 nm was exploited for PL excitation. The microscope system was connected by an optical fiber to the spectrometer equipped with a thermoelectrically cooled charge-coupled device (CCD) camera.

Scanning electron microscopy and energy-dispersive X-ray spectroscopy

Scanning electron microscopy (SEM) and energy-dispersive X-ray spectroscopy (EDS) measurements have been performed using a JED-2201 system coupled with a JSM-5610 LV (JEOL) scanning electron microscope.

Results and discussion

The glass ceramics have been prepared by thermal annealing of the glasses. DSC analysis was used to investigate the processes occurring during the heat treatment and to optimize the conditions for ceramic formation.[25] The DSC curves for both glasses studied are presented in Fig. 1. They are nearly identical for both glasses, indicating that the processes proceed during the heat treatment in a similar way. For both glasses, endothermic effects in a wide temperature range from 810 to 1050 °C, a strong exothermic effect between 1050 °C and 1150 °C, and a few endothermic effects within the temperature ranges of 1217–1230 °C and 1337–1361 °C are observed. The small discrepancy in the DSC curves might be caused by the different chemical natures (compositions) of the glasses and as a result, by the different temperatures required for the same processes to occur.

The endothermic effect within the wide temperature range from 810 to 1050 °C for both glasses might be caused by softening and liquation processes simultaneously occurring in close temperature ranges.[26–28] The glass liquation proceeds as nuclei formation and their subsequent growth. Several liquation processes might proceed in parallel at the same or close temperatures. As a result, nuclei of different compositions are formed and grow simultaneously. The feature in the range of 1030–1150 °C appearing due to the exothermic effect corresponds to the complete glass crystallization (indicated as T_c), while its broadness points to the formation of nuclei of different phases in the glass matrix. Endothermic effects at temperatures above 1200 °C (marked as T_{m1} and T_{m2}) are

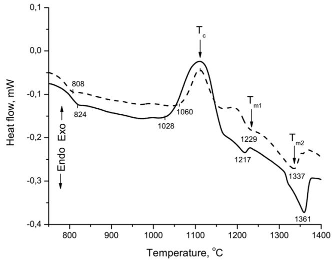

Fig. 1 DSC curves for glass 1 (solid line) and glass 2 (dashed line).

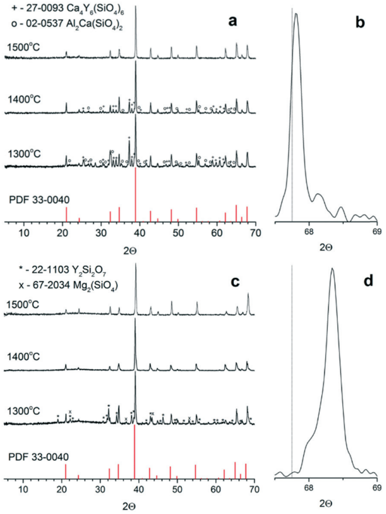

Fig. 2 XRD patterns of glass ceramics obtained by the heat treatment of glass 1 (a and b) and glass 2 (c and d) at different temperatures. Red vertical lines correspond to the reference pattern [33-0040] of YAG single crystals. Impurity phases are indicated as (+) for $Ca_4Y_6(SiO_4)_6$ (PDF 27-0093), (○) for $Al_2Ca(SiO_4)_2$ (PDF 02-0537), (*) for $Y_2Si_2O_7$ (PDF 22-1103), and (×) for Mg_2SiO_4 (PDF 67-2034). The thin structure of GC1 and GC2 reflections is presented in (b) and (d), respectively.

observed for both glasses and are attributed to the gradual melting of the crystalline phases. Their low intensities are due to the low content of such crystalline phases in the glass matrix. Thus, temperatures above 1300 °C were used for the heat treatment of the glasses.

The XRD patterns of the glass ceramics obtained by the heat treatment of glass 1 and glass 2 at 1300–1500 °C are presented in Fig. 2.

As seen in Fig. 2a and c, the increase in the heat treatment temperature results in the decrease of the content of impurity phases, which may be explained by their dissolution in the glass matrix. The glass ceramics containing a single garnet phase are formed at 1500 °C for glass 1 and at 1400 °C for glass 2. The thermal treatment of the glasses at temperatures above 1500 °C results in the formation of a transparent and yellowish material exhibiting weak luminescence. The transparency is an indication of the absence of the crystalline phase. The yellow colour is probably caused by the

Table 1 Cell parameters of the glass ceramics obtained by annealing of glass 1 and glass 2 at different temperatures

	Cell parameter *a*, Å		
Composition	1300 °C	1400 °C	1500 °C
Glass 1	11.9797(11)	11.9800(3)	11.9823(6)
Glass 2	11.9296(11)	11.9427(10)	11.9429(11)

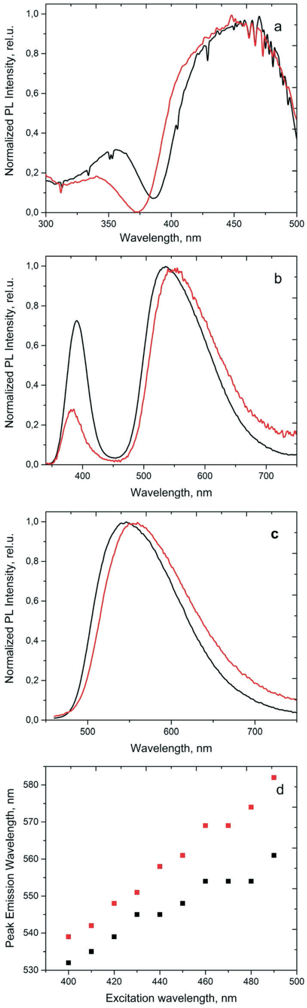

Fig. 3 Normalized photoluminescence excitation spectra at 550 nm (a), photoluminescence spectra under excitation at 365 nm (b) and 442 nm (c), and excitation wavelength dependence of the emission peak position (d) for GC1 (black points) and GC2 (red points).

absorption by Ce^{4+} ions. The initial glasses were obtained in a CO-rich (reducing) atmosphere, thus, most of the Ce ions were in a trivalent state, which was stabilized by the garnet matrix. Further annealing in air at 1500 °C, the Ce^{3+} ions transform into Ce^{4+}.

The fine structure of the XRD reflections for GC1 and GC2 is presented in Fig. 2b and d. The shift of the reflection with respect to its position in YAG indicates the formation of substituted garnets, while the reflection asymmetry shows that the substitution is spatially inhomogeneous. The formation of differently substituted garnets might be related to the glass composition variations in the vicinity of garnet nuclei during their formation. The incorporation of excess elements during the nucleus formation and crystallite growth might lead to gradual modification of the crystallite composition. In general, the proposed mechanism is similar to the epitaxial growth of films, where each subsequent layer inherits the structure of the previous one but has a slightly different composition. The garnet nucleus here plays the role of a substrate.

Since the composition of the garnets slightly varies within the crystallites, the cell parameters calculated using the XRD data reflect the average values. These values for both glass ceramics studied are listed in Table 1.

A common trend for both ceramics can be traced in the data presented in Table 1: the cell parameters become larger with increasing treatment temperature. The cell parameter of the glass ceramics fabricated by heating glass 1 is larger than that of the glass ceramics fabricated from glass 2. This is in line with the substitution of Y^{3+} (ionic radius 1.02 Å) by Ca^{2+} (1.12 Å) and Mg^{2+} (0.89 Å), respectively. For both glass ceramics with average crystallite compositions of $Y_2CaAlGe(AlO_4)_3$:Ce and $Y_2MgAlGe(AlO_4)_3$:Ce, the cell parameters are smaller than those for the powders of the corresponding composition.[29] Such a difference might be explained by the partial substitution of Al^{3+} by Si^{4+}, which is present in excess in the glass matrix. In contrast to Ge^{4+}, Si^{4+} has smaller ionic radii in both lattice positions: $r(Si^{4+})_{c.n.4}$ = 0.26 Å, $r(Ge^{4+})_{c.n.4}$ = 0.39 Å, and $r(Al^{3+})_{c.n.4}$ = 0.40 Å and $r(Si^{4+})_{c.n.6}$ = 0.4 Å, $r(Ge^{4+})_{c.n.6}$ = 0.53 Å, and $r(Al^{3+})_{c.n.6}$ = 0.53 Å.

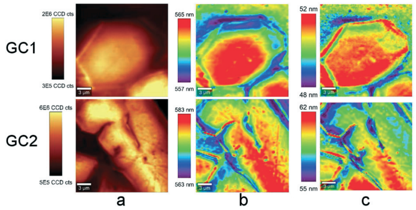

Fig. 4 Mapping images of PL intensity (column a), band peak position (column b) and FWHM (column c) under excitation at 442 nm recorded for typical areas of 20 × 20 µm in size for ceramics GC1 and GC2.

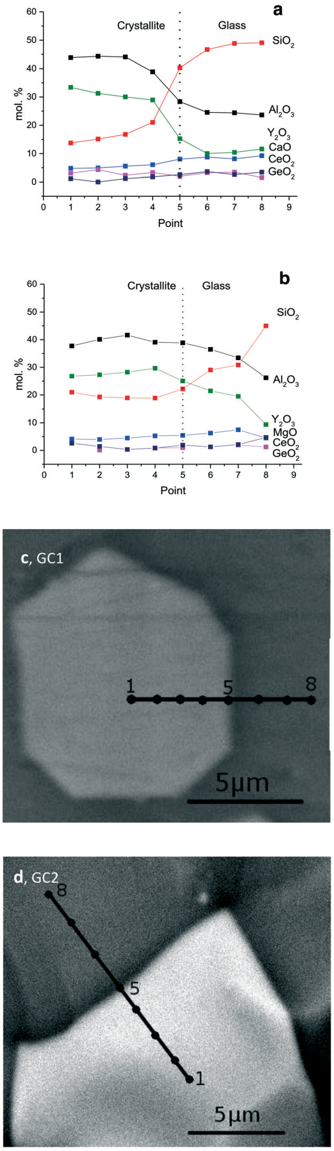

Fig. 5 The oxide compositions (in mol%) for GC1 (a) and GC2 (b) at the points of crystallites and surrounding glass indicated in the SEM images of (c) GC1 and (d) GC2.

The luminescence excitation spectra of GC1 and GC2 (see Fig. 3a) consist of two broad bands peaking at 350 nm and 450 nm corresponding to the 4f–5d optical transitions.[29] In comparison to typical absorption bands of Ce-doped garnets, the observed bands of both samples are broader and asymmetric. These features might be explained by the contribution of Ce^{3+} with slightly different environment and, consequently, crystal field as well as by additional absorption in the vicinity of 350 nm by Ce^{3+} ions in the glass matrix.[30]

For both glass ceramics, the PL spectra registered under excitation at 365 nm (Fig. 3b) consist of two bands. The spectra are dominated by the band in the range of 530–550 nm due to the emission of Ce^{3+} in the garnet structure.[29] The second, less intense band peaking at 390 nm is related to the emission of Ce^{3+} in the glass matrix.[30] Under excitation at 442 nm, the PL spectra have a single broad emission band peaking at 530–550 nm. The red shift of this band for GC2 with respect to its position in the GC1 spectrum is the effect of cation substitution and is similar to that reported for $Y_2CaAlGe(AlO_4)_3$:Ce and $Y_2MgAlGe(AlO_4)_3$:Ce garnets.[29]

The PL of the Ce-doped garnets is a result of the optical transitions of Ce^{3+} ions, and the PL spectra consist of two broad overlapping bands appearing due to the splitting of the ground state into two sublevels. The local field alters the sublevel energy and consequently, shifts the spectral position of the band. To obtain a better understanding of this shift, we studied the dependence of the luminescence peak position on the excitation wavelength in the range from 400 nm to 490 nm (see Fig. 3d), which corresponds to the main absorption band observed in the photoluminescence excitation spectra presented in Fig. 3a. In this excitation range, a considerable band shift by ~40 nm for GC2 and by ~30 nm for GC1 is observed. This shift might be explained by the different contributions of Ce^{3+} located in garnet crystallites with different compositions and consequently, different local fields.

The dependence of the photoluminescence properties on the composition of the garnet matrix surrounding the emitting Ce^{3+} ions was studied by confocal microscopy. Typical mapping images of the PL intensity, band peak position and its FWHM are presented for GC1 and GC2 in Fig. 4.

As demonstrated in Fig. 4, the morphologies of GC1 and GC2 are slightly different. In GC1, most crystallites have a hexagonal habit, which is typical for the garnet structure. The crystallites in GC2 are bigger and predominantly have an elongated shape. The difference in the shape and habit of GC2 crystallites might be caused by their growth specifics or partial dissolution. Also, the PL in GC2 is stronger than that in GC1.

A strong correlation between the photoluminescence characteristics and the location of the emitting spot inside and outside the grains is evident for both ceramics (see Fig. 4). A blue shift of the PL peak position in the direction from the center of a crystallite to its border is observed. This feature can be explained by the different crystal fields in the vicinity of the emitting Ce^{3+} as a result of variation in the composition of the garnet surrounding the ions. The variable composition is probably caused by the layer-by-layer growth of the crystallite, which is discussed above. The FWHM increases from the crystallite center to its edges. This is an indication that the variation in the crystallite composition in the vicinity of Ce^{3+} becomes more pronounced, as the crystallite grows from a nucleus to a size of a few micrometers and above.

To define the precise composition of the crystallites, EDS analysis was employed. The garnet compositions in specific crystalline regions are shown in Fig. 5.

An increase in Ca^{2+} content accompanied by a decrease in Y^{3+} content in points 1–5 is clearly observed for GC1 (see Fig. 5a and Table 2). The ionic radii of Ca^{2+} and Y^{3+} at the 8-fold coordination position are 1.12 Å and 1.02 Å, respectively. Therefore, the substitution of Y for Ca results in an increase of the Y(Ca)–O bond length. Accordingly, the Ce–O bond becomes longer, since Ce^{3+} occupies the position of Y(Ca). This, in turn, should lead to a decrease of the crystalline field strength causing the blue shift observed in the PL spectra, which is in good correspondence with the spatial distribution of PL parameters presented in Fig. 4b. Substitution of Al^{3+} by Si^{4+} might also result in the compensation of the contributions changing the dodecahedral volume.

The composition change in GC2 at the set of points 1–5 is less pronounced, most likely due to the ability of Mg^{2+} to localize at both Y^{3+} and Al^{3+} positions, while Ca^{2+} can replace only Y^{3+}. Close ratios of Y^{3+} and Mg^{2+} are observed at points 1–3. Meanwhile, only the increase in Al^{3+} content accompanied by the decrease in Si^{4+} content is observed at these points. Thus, a nearly constant length of the Ce–O bond is expected. At point 4, the contents of Y^{3+} and Mg^{2+} are smaller, while the content of Al^{3+} is larger, in comparison with the corresponding contents at points 1–3. Furthermore, the total Y^{3+} and Mg^{2+} content, which reflects the fraction of ions in dodecahedral positions at point 4, exceeds that corresponding to the empirical formula. Thus, we can conclude that some Mg^{2+} ions are localized in Al^{3+} positions. Therefore, the fraction of Y^{3+} in the dodecahedral position is increased. This should lead to the increase of the Ce–O bond length and as a result, to the blue shift of the emission band (see Fig. 4b).

Table 2 Garnet composition at points indicated in Fig. 5(c) and (d) for GC1 and GC2, respectively

Point	GC1	GC2
1	$Y_{2.9}Ca_{0.21}Ce_{0.05}Al_{3.88}Si_{0.62}Ge_{0.14}O_{12}$	$Y_{2.64}Mg_{0.2}Ce_{0.13}Al_{3.7}Si_1O_{12}$
2	$Y_{2.76}Ca_{0.22}Ce_{0.001}Al_{3.94}Si_{0.66}Ge_{0.19}O_{12}$	$Y_{2.65}Mg_{0.19}Ce_{0.07}Al_{3.91}Si_{0.93}O_{12}$
3	$Y_{2.67}Ca_{0.23}Ce_{0.05}Al_{3.93}Si_{0.77}Ge_{0.11}O_{12}$	$Y_{2.65}Mg_{0.21}Ce_{0.02}Al_{3.98}Si_{0.9}O_{12}$
4	$Y_{2.65}Ca_{0.27}Ce_{0.08}Al_{3.59}Si_{1.1}Ge_{0.15}O_{12}$	$Y_{2.8}Mg_{0.24}Ce_{0.04}Al_{3.68}Si_{0.89}Ge_{0.04}O_{12}$
5	$Y_{1.6}Ca_{0.43}Ce_{0.13}Al_{2.9}Si_{2.12}Ge_{0.1}O_{12}$	$Y_{2.44}Mg_{0.26}Ce_{0.09}Al_{3.78}Si_{1.1}Ge_{0.05}O_{12}$

The change in the composition at different points inside and outside the crystallites for glass ceramics GC1 and GC2 confirms the suggested mechanism of the layer-by-layer growth of garnet crystallites in the glass matrix.

Conclusions

In conclusion, glass ceramic materials based on multicomponent-substituted garnets are fabricated using controlled glass crystallization. The crystallites formed in the ceramics have a garnet-type crystal structure. The heat treatment conditions to convert the initial glasses into ceramics are 1500 °C for 105 min. At lower temperatures, impurity phases are formed, while crystallite dissolution becomes more pronounced at higher temperatures.

The average cell parameters obtained for these ceramics by XRD correlate well with those expected after the substitution of Y^{3+} by Ca^{2+} and Mg^{2+} and Al^{3+} by Si^{4+} and/or Ge^{4+} in the garnet structure. However, the crystallites exhibit a gradient in their emission properties: in the direction from the crystallite center to its edge the photoluminescence bands exhibit a blue shift and become broader. This effect is attributed to the change of the garnet composition, which occurs during the layer-by-layer growth of the crystallite in the environment with slightly changing ratios of the lattice-forming elements. This conclusion is supported by the results of EDS analysis. As a result of the composition gradient, the photoluminescence peak position can be tuned within the range from 530 to 580 nm by changing the excitation wavelength. The peak emission intensity is obtained by pumping the ceramics in the vicinity of 450 nm, *i.e.*, in the spectral region, where high-power light emitting diodes and laser diodes are commercially available. Thus, these ceramics can be considered as promising phosphors for white light sources with tunable emission.

Conflicts of interest

There are no conflicts to declare.

Acknowledgements

This research was supported by the project FARAD (09.3.3-LMT-K-712-01-0013) funded by the European Social Fund and the Belarusian State Program of Scientific Research "Photonics, Opto- and Microelectronics" (task no. 1.2.03). The authors acknowledge the collaboration support of COST Action TD1401FAST.

References

1 *Phosphors, up conversion nano particles, quantum dots and their applications*, ed. R.-S. Liu, Springer-Verlag, Berlin Heidelberg, 2017, vol. 1, p. 593.
2 E. F. Schubert and J. K. Kim, Solid-state light sources getting smart, *Science*, 2005, **308**, 1274–1278.
3 Z. Wu and Z. Xia, *Nitride Semiconductor Light-Emitting Diodes (LEDs) (Second Edition), Materials, Technologies, and Applications*, Woodhead Publishing Series in Electronic and Optical Materials, 2018, pp. 123–208.
4 D. Feezell and Sh. Nakamura, Invention, development, and status of the blue light-emitting diode, the enabler of solid-state lighting, *C. R. Phys.*, 2018, **19**, 113–133, DOI: 10.1016/j.crhy.2017.12.001.
5 M. R. Krames, O. B. Shchekin, R. Mueller-Mach, G. O. Mueller, Z. Ling, G. Harbers and M. G. Craford, Status and Future of High-Power Light-Emitting Diodes for Solid-State Lighting, *J. Disp. Technol.*, 2007, **3**, 160–175.
6 W. Höland and G. H. Beall, *Glass-ceramic technology*, Wiley, Canada, 2nd edn, 2012.
7 D. Chena, W. Xiang, X. Liang, J. Zhong, H. Yu, M. Ding, H. Lu and Zh. Ji, Advances in transparent glass–ceramic phosphors for white light-emitting diodes – A review, *J. Eur. Ceram. Soc.*, 2015, **35**, 859–869, DOI: 10.1016/j.jeurceramsoc.2014.10.002.
8 J. Huang, X. Liang, W. Xiang, M. Gong, G. Gu, J. Zhong and D. Chen, Synthesis and luminescence properties of Ce:$Y_3Al_5O_{12}$ glass ceramic by spontaneous crystallization, *Mater. Lett.*, 2015, **151**, 31–34, DOI: 10.1016/j.matlet.2015.03.023.
9 A. Keshavarzi, C. Bocker and C. Rüssel, Nano lamellae composed of yttrium aluminum garnet and yttrium silicate by surface crystallization of glass, *J. Mater. Sci.*, 2015, **50**, 848–854, DOI: 10.1007/s10853-014-8645-x.
10 A. Prnova, A. Plsko, J. Valuchova, P. Svancarek, R. Klement, M. Michalkova and D. Galusek, Crystallization kinetics of yttrium aluminate glasses, *J. Therm. Anal. Calorim.*, 2018, **133**, 227–236, DOI: 10.1007/s10973-017-6948-2.
11 A. Tarafder, A. R. Molla and B. Karmakar, Effects of nano-YAG ($Y_3Al_5O_{12}$) crystallization on the structure and photoluminescence properties of Nd^{3+}-doped K_2O-SiO_2-Y_2O_3-Al_2O_3 glasses, *Solid State Sci.*, 2010, **12**, 1756–1763.
12 J. Liu, M. Zhang and X. Yang, Preparation and characterization of yttrium iron garnet glass-ceramics, *Adv. Mat. Res.*, 2013, **785–786**, 767–770.
13 G. He, Y. Li, C. Bu, G. Liu, W. Jiang and J. Li, Preparation of Ce-doped $(Y,Gd)_3Al_5O_{12}$ nanoceramics by sintering and crystallization of glass microspheres, *Mater. Res. Bull.*, 2015, **66**, 45–50.
14 D. Chen and Y. Chen, Transparent Ce^{3+}:$Y_3Al_5O_{12}$ glass ceramic for organic-resin-free white-light-emitting diodes, *Ceram. Int.*, 2014, **40**, 15325–15329, DOI: 10.1016/j.ceramint.2014.06.073.
15 J. Yang, B. Chen, E. Y. B. Pun, B. Zhai and H. Lin, Excitation wavelength-sensitive multi-colour fluorescence in Eu/Tb ions doped yttrium aluminium garnet glass ceramics, *J. Lumin.*, 2013, **134**, 622–628, DOI: 10.1016/j.jlumin.2012.07.018.
16 A. Tarafder, A. R. Molla and B. Karmakar, Processing and Properties of Eu^{3+} Doped Transparent YAG ($Y_3Al_5O_{12}$) Nanoglass–Ceramics, *J. Am. Ceram. Soc.*, 2010, **93**, 3244–3251, DOI: 10.1111/j.1551-2916.2010.03898.x.
17 S. Alahraché, M. Deschamps, J. Lambert, M. R. Suchomel, D. D. S. Meneses, G. Matzen, D. Massiot, E. Véron and M. Allix, Crystallization of Y_2O_3–Al_2O_3 Rich Glasses: Synthesis of YAG Glass-Ceramics, *J. Phys. Chem. C*, 2011, **115**, 20499–20506, DOI: 10.1021/jp207516w.

18 H. Lin, T. Hu, Y. Cheng, M. Chen and Y. Wang, Glass Ceramic Phosphors: Towards Long-Lifetime High-Power White Light-Emitting-Diode Applications. A Review, *Laser Photonics Rev.*, 2018, **12**, 1700344, DOI: 10.1002/lpor.201700344.

19 C.-C. Tsai, Process dependent luminescence characteristics of low-temperature Ce^{3+}:YAG doped glass for phosphor-converted white-light-emitting diodes, *Optik*, 2015, **126**, 655–658, DOI: 10.1016/j.ijleo.2014.09.011.

20 A. Keshavarzi and C. Rüssel, The effect of TiO_2 and ZrO_2 addition on the crystallization of Ce^{3+} doped yttrium aluminum garnet from glasses in the system $Y_2O_3/Al_2O_3/SiO_2/AlF_3$, *Mater. Chem. Phys.*, 2012, **132**, 278–283.

21 L. Wang, L. Mei, G. He, G. Liu, J. Li and L. Xu, Crystallization and fluorescence properties of Ce:YAG glass-ceramics with low SiO_2 content, *J. Lumin.*, 2013, **136**, 378–382, DOI: 10.1016/j.jlumin.2012.12.019.

22 S. Fujita, A. Sakamoto and S. Tanabe, Luminescence characteristics of YAG glass–ceramic phosphor for white LED, *IEEE J. Sel. Top. Quantum Electron.*, 2008, **14**, 1387–1391.

23 G. He, Y. Li, C. Bu, G. Liu, W. Jiang and J. Li, Preparation of Ce-doped $(Y,Gd)_3Al_5O_{12}$ nanoceramics by sintering and crystallization of glass microspheres, *Mater. Res. Bull.*, 2015, **66**, 45–50.

24 J. Liu, M. Zhang and X. Yang, Preparation and characterization of yttrium iron garnet glass-ceramics, *Adv. Mater. Res.*, 2013, **785–786**, 767–770.

25 M. Affatigato, *Modern glass characterization*, Wiley, Canada, 2012.

26 A. I. Berejnoy, *Glass ceramics and fotoglassceramics [in Russian]*, Mashinostroenie, Moscow, 1981.

27 M. Sitarz and M. Szumera, Crystallization of silico-phosphate glasses, *J. Therm. Anal. Calorim.*, 2008, **91**, 255–260.

28 N. E. Shchegoleva, P. D. Sarkisov, L. A. Orlova and N. V. Popovich, Physical-chemical and structural processes occurring during heat-treatment of strontium-aluminosilicate glass, *Glass Ceram.*, 2012, **69**, 117–121.

29 Y. Tratsiak, Y. Bokshits, A. Borisevich, M. Korjik, A. Vaitkevicius and G. Tamulaitis, $Y_2CaAlGe(AlO_4)_3$:Ce and $Y_2MgAlGe(AlO_4)_3$:Ce garnet phosphors for white LEDs, *Opt. Mater.*, 2017, **67**, 108–112, DOI: 10.1016/j.optmat.2017.03.047.

30 Y. Tratsiak, E. Trusova, G. Dosovitsky, M. Fasoli, M. Korjik, F. Moretti and A. Vedda, Photo- and radio-luminescence properties of $3CaO\text{-}2SiO_2$ and $3CaF_2\text{-}2SiO_2$ glasses doped by Ce^{3+} ions, *J. Lumin.*, 2017, **188**, 289–294, DOI: 10.1016/J.JLUMIN.2017.04.051.

Paper P14

Timing properties of Ce-doped YAP and LuYAP scintillation crystals

M. Korzhik, A. Gola, J. Houžvička, A. Mazzi, S. Nargelas, S. Sýkorová, G. Tamulaitis, A. Vaitkevičius, S. Sykorová, G. Tamulaitis, **A. Vaitkevičius**

Nucl. Instruments Methods Phys. Res. Sect. A Accel. Spectrometers, Detect. Assoc. Equip. 927 (2019) 169–173.

doi:10.1016/j.nima.2019.02.036.

Nuclear Inst. and Methods in Physics Research, A 927 (2019) 169–173

Contents lists available at ScienceDirect

Nuclear Inst. and Methods in Physics Research, A

journal homepage: www.elsevier.com/locate/nima

Timing properties of Ce-doped YAP and LuYAP scintillation crystals

M. Korzhik [a], A. Gola [b], J. Houžvička [c], A. Mazzi [b], S. Nargelas [d], S. Sýkorová [c], G. Tamulaitis [d], A. Vaitkevičius [d,*]

[a] *Research Institute for Nuclear Problems, Bobruiskaya str. 11, Minsk, Belarus*
[b] *Fondazione Bruno Kessler, Via Sommarive, 18, Povo, Trento, Italy*
[c] *Crytur, Na Lukách 2283, Turnov, Czech Republic*
[d] *Vilnius University, Saulėtekio al. 3, LT-10257, Vilnius, Lithuania*

ARTICLE INFO

Keywords:
Scintillators
Coincidence time resolution
Perovskites
Pump and probe technique
Silicon photomultipliers

ABSTRACT

The timing performance of radiation detectors based on Ce-doped perovskites $YAlO_3$ (YAP) and $(Lu_{1-x}\text{-}Y_x)AlO_3$ (LuYAP) coupled with near-UV sensitive silicon photomultipliers (NUV-HD SiPMs) have been compared in coincidence time resolution (CTR) experiments. The single-detector time resolution full width at half maximum (FWHM) of YAP was found to be 169 ps, i.e., by a factor of two better than that observed earlier with photomultiplier readout. Introduction of lutetium into YAP structure deteriorates the time resolution to 286 ps and 309 ps for a Lu/Y atomic ratio of 1:1 and 0.7:0.3, respectively. The study of the dynamics of Ce^{3+}excited state population after selective optical excitation with short (200 fs) pulses by using the differential absorption technique in pump and probe configuration evidenced the importance of electron trapping, which is enhanced by antisite Lu_{Al} defects having favorable conditions to occur in LuAP.

1. Introduction

The family of perovskite-type Ce- and Pr-doped scintillators $YAlO_3$, $(Y_x\text{-}Lu_{1-x})AlO_3$, and $LuAlO_3$ is prospective for developing fast radiation detectors [1]. The best-studied representative of this family $YAlO_3$:Ce (YAP) exhibits a good linearity of the scintillation response for γ-quanta with energy down to a few keV and a high energy resolution, which is favorable for precision spectrometry in X-ray range. Due to relatively light ions building the YAP matrix, the dependence of the attenuation factor on energy is linear and enables very good energy resolution in the soft energy range of γ quanta. Although this scintillation material has been discovered in the seventies, large-scale applications started a few years later with the development of the production technology of YAP with a high light yield [2–4]. Praseodymium-doping of YAP was introduced later in the nineties [5]. YAP:Pr exhibits the best combination of light yield and scintillation decay time. In Table 1, the structural and scintillation parameters of YAP are compared with those of BaF_2, currently the fastest scintillator. Similarly to BaF_2, YAP:Pr has luminescence bands in UV, away from the sensitivity spectral range of currently common photo-detectors.

A distinctive feature of YAP scintillators is a weak temperature dependence of their light yield. The material has also excellent mechanical hardness and resistance to fast temperature changes [6]. These features enable application of YAP scintillators in detectors for oil well logging [7]. In spite of a low efficiency to detect γ-quanta in MeV range, YAP-based detectors show a good energy resolution of 4.38% full width at half maximum (FWHM) at 661.6 keV (^{137}Cs) [8]. Another important capability of YAP scintillation crystals is their suitability for detection of α-particles [9], which is an attractive feature for their applications in various devices, e.g., in 14 MeV pulsed neutron generators [10].

Table 1
Density, effective nucleus charge, light yield, emission band peak position, and decay time of scintillation response of Ce- and Pr-doped YAP:Ce single crystals and BaF_2 [1].

Material	Density (g/cm^3)	$Z_{eff.}$	LY (ph/MeV)	λ_{em} (nm)	τ_{sc} (ns)
$YAlO_3$:Ce	5.35	36	20 000	347	28
$YAlO_3$:Pr	5.35	36	7 000	260, 295	13.3
BaF_2	4.88	52.7	1 430	220	0.6 (fast)

Ce-doped $LuAlO_3$ (LuAP) is the heaviest aluminum perovskite [1]. In spite of technological difficulties in the production of high quality crystals, a few transparent LuAP:Ce crystals were fabricated, and the dominating luminescence decay component is demonstrated to have the decay time as short as 17 ns. LuYAP crystal, $(Lu_{1-x}\text{-}Y_x)AlO_3$, is shown to be applicable for engineering of its properties by composition variation [1], as in multicomponent garnets [11,12]. In spite of a relatively low light yield of about 11 400 ph/MeV, the crystal exhibits the same energy resolution as LSO:Ce, which has the light yield by a factor of 2 to 3 larger. The optimization of Y and Lu contents in the crystal was found to be a successful approach to overcome the technological

---

[*] Corresponding author.
E-mail address: augustas.vaitkevicius@ff.vu.lt (A. Vaitkevičius).

https://doi.org/10.1016/j.nima.2019.02.036
Received 10 December 2018; Received in revised form 23 January 2019; Accepted 13 February 2019

Table 2
Density, light output for specified geometry, emission band peak position, and decay times (with the weight coefficients of the corresponding decay components indicated in brackets) of scintillation response of samples studied.

Sample	Density (g/cm^3)	LO (ph/MeV)	λ_{em} (nm)	τ_{sc} (ns)
YAP	5.35	19 000	347	28
LuYAP1	6.5	14 000	375	21 (60%) 85 (20%) 400 (20%)
LuYAP2	7.3	12 000	375	17 (40%) 70 (35%) 400 (25%)

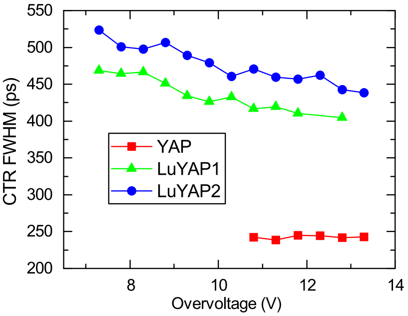

Fig. 1. CTR FWHM versus overvoltage measured by coupling FBK NUV-HD SiPMs with LuYAP:Ce samples with different lutetium content: YAP (squares), LuYAP1 (triangles), and LuYAP2 (circles).

difficulties encountered in the production of LuAP crystals [13,14]. Moreover, the principal result of the cation exchange in the matrix was an increase of the light yield at equal Lu and Y concentrations ($x = 0.5$) in $(Lu_{1-x}\text{-}Y_x)AlO_3$ [12]. The composition variations enable changing the material density from 5.35 to 8.34 g/cm^3. Tuning the Y content in the crystal allows one to modify also the optical, chemical, and physical parameters and to better meet the requirements for various applications, like soft γ-quanta detection, positron emission tomography (PET) instrumentation, and oil well logging.

The current study is focused on investigation of the timing properties of YAP-LuYAP scintillation crystals coupled to silicon photomultipliers (SiPMs) having a high photodetection efficiency (PDE) in near ultraviolet region (NUV-HD technology SiPMs, produced by FBK). The comparison of the results obtained in coincidence time resolution (CTR) measurements with the study of nonequilibrium carrier dynamics by using the differential optical absorption performed under selective excitation of the materials show the perspective of application of this scintillator for radiation detection in time-of-flight (TOF) mode.

2. Experimental

The YAP:Ce crystals studied were produced from molybdenum crucibles in vacuum by Crytur, Czech Republic. The YAP:Ce crystals currently produced at Crytur have a light yield (LY) not less than 24 300 ph/MeV (measured for standard sample 10 × 10 × 1 mm^3) and an energy resolution of 4.2% FWHM at 662 keV at room temperature. In this study, YAP:Ce samples were prepared as plates with dimensions of 10 × 10 × 1 mm^3 for spectroscopic measurements and as pixels with dimensions of 3 × 3 × 5 mm^3 for CTR measurements.

LuYAP crystals were produced from iridium crucibles in neutral gas atmosphere by Czochralski technique at Bogoroditsk Technical Chemical Plant (Bogoroditsk, Russia). Samples with a density of 6.5 g/cm^3 (LuYAP1) and 7.3 g/cm^3 (LuYAP2) were grown from the melt with Lu/Y atomic ratios of 1:1 and 0.7:0.3, respectively. The LuYAP samples were prepared as 10 × 10 × 1 mm^3 plates and 2 × 2 × 7 mm^3 pixels. The scintillation properties of the samples studied are listed in Table 2. The light output (LO) presented in the table was measured with PMT (type XQ2020) for the Teflon-wrapped samples prepared for CTR measurements.

To measure CTR, the diced samples were combined into detecting modules with NUV-HD SiPMs, 4 × 4 mm^2 active area with 35 μm cells, developed at Fondazione Bruno Kessler as p-on-n-type devices with PDE peaked at 400–420 nm [15]. The pixels were optically coupled to SiPMs by using Cargille Meltmount optical glue with refractive index $n = 1.539$ and wrapped in Teflon. The CTR setup consisted of two identical detecting modules placed at the same distance from a ^{22}Na point source, providing 511 keV coincidence events. The two scintillation detectors were placed on the same axis and mounted on two double-stage amplifiers with two signal outputs each. The first output of the amplifiers was used for measuring the energy of the detected gamma quanta, by charge integration. An integration window of 500 ns was used to select the events in the 511 keV photopeak. The second stage of the amplifiers was based on the pole-zero filtering and was used for discriminating the arrival time. The details of the pole-zero filtering method is described in [16]. CTR was measured as a function of SiPM excess bias under controlled temperature (+20 °C).

The dynamics of nonequilibrium carriers was studied using the optical pump and probe technique. The nonequilibrium carriers were generated by short light pulses (200 fs) delivered by a Yb:KGW laser equipped with harmonics generators and a parametric amplifier to tune the excitation at the photon energies corresponding to Ce^{3+} intracenter absorption to the first excited level (at 4.35 eV, 285 nm) and to the second excited level (at 5.91 eV, 210 nm), which is located near the bottom of the conduction band. The density of nonequilibrium carriers was probed by a tunably delayed laser pulse spectrally transformed into a white light continuum (see more details in [17]).

3. Results

Fig. 1 shows the CTR FWHM measured as a function of overvoltage at room temperature. The results show a clear trend: the time resolution deteriorates with increasing Lu content. The CTR FWHM is 239 ± 6 ps in sample YAP, 405 ± 6 ps in sample LuYAP1 with equal Y and Lu content, and 438 ± 6 ps in sample LuYAP2 with a dominant fraction of Lu in the crystal.

To compare with the results available in literature, the time resolution of single detector was calculated for YAP/SiPM and LuYAP/SiPM modules. The single-detector time resolution FWHM, which is defined as CTR/$\sqrt{2}$, equals 169, 286, and 309 ps in samples YAP, LuYAP1, and LuYAP2, respectively. These values are by a factor of two better than those observed with PMT readout [18]. Thus, the improvement of both crystal growth conditions and novel SiPMs enabled a substantial progress in time resolution towards that achieved by using other Ce-doped scintillators like LSO, LYSO, GAGG, and LaBr$_3$, which are currently exploited in radiation detectors for measuring with a high time resolution at a low energy deposit [19,20].

The results show that the introduction of Lu, though very attractive for increasing the crystal density, results in deterioration of CTR. Moreover, codoping of perovskites with aliovalent impurities like Ca^{2+} or Mg^{2+}, which improve the performance of garnet- and orthosilicate-type scintillators [21], was found to be not effective for perovskite scintillators [22]. These features restrict the application of high-Lu-content LuYAP:Ce scintillators in the detection techniques, where the TOF discrimination plays the key role.

The light yield also decreases with increasing Lu content (see Table 2), however, the deterioration of LuYAP:Ce timing properties is

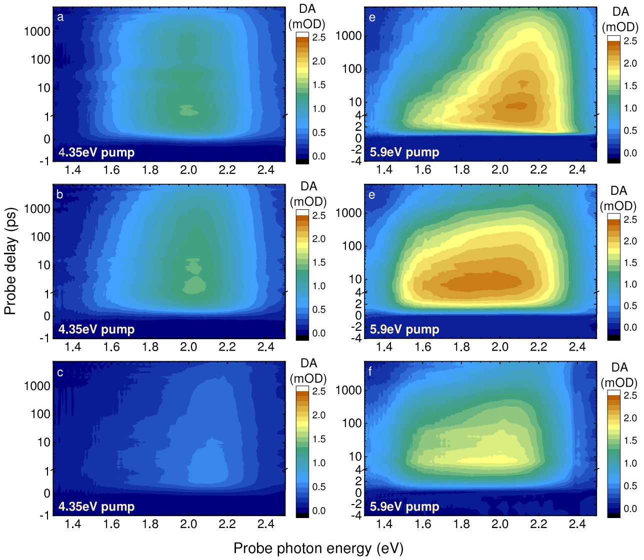

Fig. 2. Differential absorption (color scale) imposed by pump photons of energy 4.35 eV (left column) and 5.91 eV (right column) in samples YAP (a,d), LuYAP1 (b,e), and LuYAP2 (c,f) as a function of probe photon energy and delay between pump and probe pulses.

probably caused not only by a lower light yield. To clarify the origins of the deterioration of LuYAP timing properties, we studied the nonequilibrium carrier dynamics using the optical pump and probe technique and exploiting selective excitation. The band gap of YAP is 7.8 eV and does not change significantly with the introduction of lutetium [23]. The ground f state of Ce^{3+} ion is 1.8 eV above the top of the valence band [24]. Thus, a 4.35 eV photon resonantly excites Ce^{3+} ions to their first excited level 5d^1, which is well below the bottom of the conduction band. Consequently, no exchange of the nonequilibrium electrons between this lowest excited Ce^{3+} state and the conduction band should be expected for this photon energy. The photon energy of 5.91 eV corresponds to the optical transition to the second excited Ce^{3+} level 5d^2. At this photon energy, the electrons are delivered to the edge of the conduction band. Thus, their transfer to the conduction band and possible further trapping might be expected. At such excitation, the excited electron has two routes for the relaxation to the radiative level 5d^1: the dominating intracenter relaxation from 5d^2 to 5d^1 and a less probable relaxation via the extended states in the conduction band. The second route might involve also trapping and de-trapping of the nonequilibrium electrons and takes longer.

Fig. 2 shows the differential absorption, i.e. the difference in optical absorbance with and without pump pulse, as a function of the probe photon energy and the delay between pump and probe pulses for pump photon energies of 4.35 eV and 5.91 eV. At 4.35 eV photon excitation, only the absorption of probe photons from the first excited state of Ce^{3+} might be expected. The corresponding DA features are spectrally centered in the vicinity of 2.1 eV. The low energy edge of this feature corresponds to the energy difference between the first excited Ce^{3+} level and the bottom of the conduction band. The spectral position of this feature slightly shifts with increasing Lu content. This shift is probably caused by the changes in the density of states available for the nonequilibrium electrons absorbing the probe photon. After the short-pulse excitation at 5.9 eV, when electrons from Ce^{3+} ions are excited into the second excited state laying close to the bottom of the conduction band, the spectrum of differential absorption is broader, indicating the contribution of an additional component, which is probably related to the absorption by free or trapped electrons, which are expected due to the transition of the excited electrons from Ce^{3+} to the bottom of the conduction band.

Fig. 3 shows the DA kinetics measured at typical probe photon energies. The kinetics are qualitatively similar for all three samples. For the excitation to the first excited Ce^{3+} state, the front of the DA response is instantaneous on a picosecond scale, what is expected at the direct excitation of the emitting level. The DA signal decays on a subnanosecond scale with similar decay constants for YAP, LuYAP1, and LuYAP2.

At the excitation with 5.91 eV photons, the rise in the DA response is substantially slower than that at the resonant excitation to the first excited Ce^{3+} level. Moreover, the rise time increases with increasing Lu content.

4. Discussion

As expected, the DA response at the pump photon energy of 4.35 eV has a very short rise time in sub-picosecond domain. Meanwhile, the rise kinetics was found to be more complex after the excitation to the second excited Ce^{3+} level 5d^2. A slight delay on the response front is observed already in YAP:Ce. The delay substantially increases with increasing Lu content in the crystal.

At excitation to the second Ce^{3+} state, the DA response has also a second component, which has a broader spectrum and a faster decay. Two components in the DA response have been previously observed

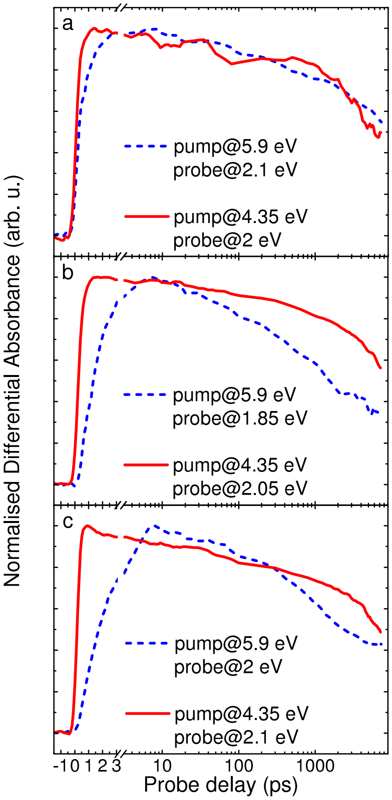

Fig. 3. Differential absorption kinetics in YAP (a), LuYAP1 (b), and LuYAP2 (c) samples excited at 4.35 eV (solid line) and 5.91 eV (dashed line) and probed at energies indicated.

at the resonant excitation of Ce^{3+} in GAGG:Ce and attributed to the absorption of the electrons populating the lowest excited state and free electrons in the conduction band, respectively [25,26]. These contributions might be expected also in perovskites. The two components can be explained by assuming that a part of the electrons excited in a close proximity of the conduction band might become free in the band. A considerable part of them return back to the geminate Ce^{3+}. This process is strongly influenced by electron trapping, which causes the delay in the population of the lowest excited state. Trapping centers are formed by certain impurities and structural defects. In multicomponent crystals, composition fluctuations (at least statistic ones) result in a band gap modulation. Consequently, the nonequilibrium electrons might be trapped in the minima of the corresponding potential fluctuations.

Moreover, in Lu-containing crystals, antisite defects Lu_{Al} [27] serve as a source of the disorder leading to additional carrier localization. Lutetium ions have the smallest ionic radius among all the rare earth elements. The radius varies from 0.86 in six-fold to 1.03 Å in nine-fold oxygen coordination. In the orthorhombic structure, three additional oxygen O^{2-} ions are located farther than the other nine. Thus, the Lu ionic radius in 12(O)-fold coordination will be close to that in 9(O)-fold coordination. During the crystal growth, a fraction of Lu ions is stabilized in oxygen octahedra and form additional trapping centers. In Lu-containing garnets, such traps have a localization energy of ∼0.2 eV [28]. In the garnet structure, these traps are deeper than those created by the cation content fluctuations in multicomponent crystals. A similar situation is observed in crystals with perovskite structure [14,29]. Thus, Lu_{Al} antisite defects are expected to slow down the population of Ce^{3+} radiative level. The effect should be stronger in perovskites than in oxyorthosilicates, e.g., in $(Lu_x\text{-}Y_{1-x})_2SiO_5$, with the host matrix formed by silicon tetrahedra, where Lu ions cannot be localized. As a result, the influence of Lu_{Al} antisite defects is diminished, and Lu-containing silicates exhibit a better time resolution [30].

5. Conclusions

The combination of optimally grown YAP:Ce crystals with the NUV-HD SiPMs developed at Fondazione Bruno Kessler with enhanced sensitivity in UV region improve the time resolution in detection of 511 keV gamma quanta to a single-detector resolution FWHM of 169 ± 6 ps. The incorporation of lutetium into the crystal improves the scintillator stopping power for ionizing irradiation. However, Lu in perovskite structure delays the excitation transfer to the lowest excited Ce^{3+} level and, consequently, deteriorates the timing properties of luminescence response. We show that electron trapping is important for the delay in population of the lowest excited Ce^{3+} level, which serves as a radiative level. In the multicomponent LuYAP:Ce, the trapping is possibly enhanced by the spatial potential fluctuations due to composition fluctuations, which become more pronounced as the Lu/Y ratio approaches 1:1, and the disorder imposed by the formation of antisite defects Lu_{Al}. The results show that a tradeoff between timing and other parameters important for LuYAP as scintillation material should be optimized for specific applications.

Acknowledgments

The research at Vilnius University was supported by the project FARAD (09.3.3-LMT-K-712-01-0013) funded by the European Social Fund via the Lithuanian Research Council. Facilitation of collaboration by the Crystal Clear Collaboration at CERN and the COST FAST action TD1401 is gratefully acknowledged.

References

[1] P. Lecoq, A. Gektin, M. Korzhik, Inorganic Scintillators for Detector Systems, Springer International Publishing, 2017, http://dx.doi.org/10.1007/978-3-319-45522-8.

[2] V.G. Baryshevsky, M.V. Korzhik, V.I. Moroz, V.B. Pavlenko, A.A. Fyodorov, S.A. Smirnova, O.A. Egorycheva, V.A. Kachanov, $YAlO_3$: Ce-fast-acting scintillators for detection of ionizing radiation, Nucl. Instrum. Methods Phys. Res. B. 58 (1991) 291–293, http://dx.doi.org/10.1016/0168-583X(91)95605-D.

[3] M.V. Korzhik, O.V. Misevich, A.A. Fyodorov, $YAlO_3$: Ce scintillators: application for X- and soft γ-ray detection, Nucl. Instrum. Methods Phys. Res. B. 72 (1992) 499–501, http://dx.doi.org/10.1016/0168-583X(92)95151-G.

[4] M. Kobayashi, T. Shinkawa, T. Sato, S. Sugimoto, M.V. Korzhik, A.A. Fyodorov, V.A. Kachanov, $YAlO_3$: Ce-Am light pulsers as a gain monitor for undoped CsI detectors in a magnetic field, Nucl. Instrum. Methods Phys. Res. A. 337 (1994) 355–361, http://dx.doi.org/10.1016/0168-9002(94)91103-7.

[5] V.G. Baryshevski, R.F. Zuevski, M.V. Korzhik, et al., Fast scintillator $YAlO_3$: Pr, JETP Lett. 17 (1991) 82–85.

[6] J.A. Mareš, M. Nikl, C. Pédrini, B. Moine, K. Blažek, A study of Ce^{3+} fluorescence emission of ions in $YAlO_3$ crystals by the influence of doping concentration and codoping with Nd^{3+} and Cr_{3+}, Mater. Chem. Phys. 32 (1992) 342–348, http://dx.doi.org/10.1016/0254-0584(92)90178-B.

[7] S. Petrovic, A. Kepic, M. Carson, Scintillators for PGNAA in mineral exploration, ASEG Ext. Abstr. 2018 (2018) 1–6, http://dx.doi.org/10.1071/ASEG2018abT4_4D.

[8] M. Moszyński, Inorganic scintillation detectors in γ-ray spectrometry, Nucl. Instrum. Methods Phys. Res. Sect. A 505 (2003) 101–110, http://dx.doi.org/10.1016/S0168-9002(03)01030-1.

[9] V.A. Kachanov, V.V. Rykalin, V.L. Solovyanov, V.Y. Hodyrev, M.V. Korzhik, V.I. Moroz, A.S. Lobko, A.A. Fyodorov, A.F. Novgorodov, B.A. Khachaturov, S.A. Smirnova, Light source for energy stabilization of calorimetric detectors based on photodetectors, Nucl. Instrum. Methods Phys. Res. A. 314 (1992) 215–218, http://dx.doi.org/10.1016/0168-9002(92)90518-9.

[10] S. Pesente, G. Nebbia, M. Lunardon, G. Viesti, D. Sudac, K. Nad, S. Blagus, V. Valković, Detection of hidden explosives by using tagged neutron beams with sub-nanosecond time resolution, Nucl. Instrum. Methods Phys. Res. Sect. A 531 (2004) 657–667, http://dx.doi.org/10.1016/j.nima.2004.05.114.

[11] M. Fasoli, A. Vedda, M. Nikl, C. Jiang, B.P. Uberuaga, D.A. Andersson, K.J. McClellan, C.R. Stanek, Band-gap engineering for removing shallow traps in rare-earth $Lu_3al_5O_{12}$ garnet scintillators using Ga^{3+} doping, Phys. Rev. B - Condens. Matter Mater. Phys. 84 (2011) 1–4, http://dx.doi.org/10.1103/PhysRevB.84.081102.

[12] M. Nikl, K. Kamada, V. Babin, J. Pejchal, K. Pilarova, E. Mihokova, A. Beitlerova, K. Bartosiewicz, S. Kurosawa, A. Yoshikawa, Defect engineering in Ce-doped aluminum garnet single crystal scintillators, Cryst. Growth Des. 14 (2014) 4827–4833, http://dx.doi.org/10.1021/cg501005s.

[13] A. Annenkov, A. Fedorov, M. Korzhik, V. Ligoun, O. Missevitch, A. Tkachev, P. Lecoq, Industrial growth of LuYAP scintillation crystals, Nucl. Instrum. Methods Phys. Res. Sect. A 537 (2005) 182–184, http://dx.doi.org/10.1016/j.nima.2004.08.003.

[14] A.N. Belsky, E. Auffray, P. Lecoq, C. Dujardin, N. Garnier, H. Canibano, C. Pedrini, A.G. Petrosyan, Progress in the development of $LuAlO_3$-based scintillators, IEEE Trans. Nucl. Sci. 48 (2001) 1095–1100, http://dx.doi.org/10.1109/23.958730.

[15] C. Piemonte, F. Acerbi, A. Ferri, A. Gola, G. Paternoster, V. Regazzoni, G. Zappala, N. Zorzi, Performance of NUV-HD silicon photomultiplier technology, IEEE Trans. Electron Devices 63 (2016) 1111–1116, http://dx.doi.org/10.1109/TED.2016.2516641.

[16] A. Gola, C. Piemonte, A. Tarolli, Analog circuit for timing measurements with large area sipms coupled to LYSO crystals, IEEE Trans. Nucl. Sci. 60 (2013) 1296–1302, http://dx.doi.org/10.1109/TNS.2013.2252196.

[17] G. Tamulaitis, A. Vaitkevičius, S. Nargelas, R. Augulis, V. Gulbinas, P. Bohacek, M. Nikl, A. Borisevich, A. Fedorov, M. Korjik, E. Auffray, Subpicosecond luminescence rise time in magnesium codoped GAGG: Ce scintillator, Nucl. Instrum. Methods Phys. Res. Sect. A 870 (2017) 25–29, http://dx.doi.org/10.1016/j.nima.2017.07.015.

[18] W. Chewpraditkul, A. Phunpueok, T. Szczesniak, M. Moszynski, V. Babin, M. Nikl, Influence of lutetium content on the scintillation properties in $(Lu_xY_{1-x})AlO_3$:Ce single crystals, Phys. Status Solidi Appl. Mater. Sci. 210 (2013) 1903–1908, http://dx.doi.org/10.1002/pssa.201329159.

[19] D.R. Schaart, S. Seifert, R. Vinke, H.T. Van Dam, P. Dendooven, H. Löhner, F.J. Beekman, $LaBr_3$:Ce and SiPMs for time-of-flight PET: achieving 100 ps coincidence resolving time, Phys. Med. Biol. 55 (2010) http://dx.doi.org/10.1088/0031-9155/55/7/N02.

[20] M.V. Nemallapudi, S. Gundacker, P. Lecoq, E. Auffray, A. Ferri, A. Gola, C. Piemonte, Sub-100 ps coincidence time resolution for positron emission tomography with LSO:Ce codoped with Ca, Phys. Med. Biol. 60 (2015) 4635–4639, http://dx.doi.org/10.1088/0031-9155/60/12/4635.

[21] M.T. Lucchini, V. Babin, P. Bohacek, S. Gundacker, K. Kamada, M. Nikl, A. Petrosyan, A. Yoshikawa, E. Auffray, Effect of Mg^{2+} ions co-doping on timing performance and radiation tolerance of cerium doped $Gd_3Al_2Ga_3O_{12}$ crystals, Nucl. Instrum. Methods Phys. Res. Sect. A 816 (2016) 176–183, http://dx.doi.org/10.1016/j.nima.2016.02.004.

[22] F. Moretti, K. Hovhannesyan, M. Derdzyan, G.A. Bizarri, E.D. Bourret, A.G. Petrosyan, C. Dujardin, Consequences of Ca codoping in $YAlO_3$:Ce single crystals, ChemPhysChem. 18 (2017) 493–499, http://dx.doi.org/10.1002/cphc.201601190.

[23] M. Korzhik, Physics of scintillation in oxide crystals, 2003.

[24] S.-W. Yu, M.H. Carpenter, F. Ponce, S. Friedrich, J.-S. Lee, P. Olalde-Velasco, W.L. Yang, D. Åberg, Energy levels of the Ce activator relative to the YAP(Ce) scintillator host, J. Phys. Condens. Matter. 27 (2015) 185501, http://dx.doi.org/10.1088/0953-8984/27/23/239601.

[25] E. Auffray, R. Augulis, A. Borisevich, V. Gulbinas, A. Fedorov, M. Korjik, M.T. Lucchini, V. Mechinsky, S. Nargelas, E. Songaila, G. Tamulaitis, A. Vaitkevičius, S. Zazubovich, S. Nargelas, G. Tamulaitis, A. Vaitkevičius, S. Zazubovich, Luminescence rise time in self-activated $PbWO_4$ and Ce-doped $Gd_3Al_2Ga_3O_{12}$ scintillation crystals, J. Lumin. 178 (2016) 54–60, http://dx.doi.org/10.1016/j.jlumin.2016.05.015.

[26] G. Tamulaitis, G. Dosovitskiy, A. Gola, M. Korzhik, A. Mazzi, S. Nargelas, P. Sokolov, A. Vaitkevičius, Improvement of response time in GAGG:Ce scintillation crystals by magnesium codoping, Approv. Publ. J. Appl. Phys..

[27] M. Nikl, E. Mihokova, J. Pejchal, A. Vedda, Y. Zorenko, K. Nejezchleb, The antisite Lu_{Al} defect-related trap in $Lu_3Al_5O_{12}$:Ce single crystal, Phys. Status Solidi Basic Res. 242 (2005) 119–121, http://dx.doi.org/10.1039/9781849730860-00143.

[28] M. Nikl, A. Vedda, M. Fasoli, I. Fontana, V.V. Laguta, E. Mihokova, J. Pejchal, J. Rosa, K. Nejezchleb, Shallow traps and radiative recombination processes in $Lu_3Al_5O_{12}$: Ce single crystal scintillator, Phys. Rev. B - Condens. Matter Mater. Phys. 76 (2007) 195121, http://dx.doi.org/10.1103/PhysRevB.76.195121.

[29] C.R. Stanek, K.J. McClellan, M.R. Levy, R.W. Grimes, Defect behavior in rare earth $REAlO_3$scintillators, J. Appl. Phys. 99 (2006) 113518, http://dx.doi.org/10.1063/1.2200759.

[30] S. Gundacker, F. Acerbi, E. Auffray, A. Ferri, A. Gola, M.V. Nemallapudi, G. Paternoster, C. Piemonte, P. Lecoq, State of the art timing in TOF-PET detectors with LuAG, GAGG and L(Y)SO scintillators of various sizes coupled to FBK-SiPMs, J. Instrum. 11 (2016) http://dx.doi.org/10.1088/1748-0221/11/08/P08008.

Paper P15

Improvement of the time resolution of radiation detectors based on $Gd_3Al_2Ga_3O_{12}$ scintillators with SiPM readout

E. Auffray, O. Buganov, M. Korjik, A. Fedorov, S. Nargelas, G. Tamulaitis, S. Tikhomirov, **A. Vaitkevičius**

IEEE Trans. Nucl. Sci. 66 (2019) 1879–1888.

doi:10.1109/TNS.2019.2919898.

Improvement of the Time Resolution of Radiation Detectors Based on $Gd_3Al_2Ga_3O_{12}$ Scintillators With SiPM Readout

G. Tamulaitis, A. Vasil'ev, M. Korzhik, A. Mazzi, A. Gola, S. Nargelas,
A. Vaitkevičius, A. Fedorov, and D. Kozlov

***Abstract*— Coincidence time resolution (CTR) of scintillation detectors based on Ce- and Mg-codoped $Gd_3Al_2Ga_3O_{12}$ (GAGG) scintillation crystals and high-density silicon photomultipliers (SiPMs) is shown to be 165 ps (full width at half maximum) for 511-keV γ-quanta, approaching that achieved by using LSO scintillators. To study the prospective for further improvement of the time resolution, the population of the emitting Ce centers was investigated by optical pump and probe technique using selective photoexcitation and probing by a white light continuum with subpicosecond time resolution. The importance of free electron trapping for excitation transfer to emitting Ce ions was revealed. The influence of transfer delay on the scintillation response time is described, and the dynamics of electron relaxation to the lowest excited level of Ce ion is studied experimentally and analyzed by taking into account intracenter relaxation and relaxation via conduction band. The influence of electron diffusivity on the rise time of the population of the emitting level is described. It is shown that codoping of GAGG:Ce by magnesium even at the level as low as 10 ppm efficiently decreases the scintillator response time by enhancing the electron diffusivity.**

***Index Terms*— Coincidence time resolution (CTR), free carrier absorption, garnets, radiation detectors, scintillators.**

I. INTRODUCTION

SILICON photomultiplier (SiPM) technology demonstrates a spectacular progress in the improvement of detecting properties [1]–[4]. Introduction of high density (HD) [5] and ultra HD (UHD) [6] devices substantially improved the photodetection efficiency (PDE) and decreased the dark count rate and jittering. A combination of novel scintillation materials with the HD and UHD SiPMs results in high energy and time resolutions and is prospective in radiation detectors for medical imaging [7] exploiting time-of-flight (TOF) technique [8].

The current progress in the time resolution of SiPMs and the demonstrations of sub-100-ps full width at half maximum (FWHM) in coincidence time resolution (CTR) measurements using $LaBr_3$:Ce [9], LSO:Ce,Ca [10], LGSO:Ce [11], and LSO crystals [12] puts forward the necessity to restudy the time response of scintillating materials, especially, the rise edge of their luminescence response, which had usually been considered to be substantially faster than other processes limiting the time resolution of scintillation detectors. This issue is of special importance for multicomponent garnet-type scintillators, in particular, GAGG:Ce single crystals exhibiting an attractive combination of scintillation properties: a high light yield of up to 50 000 phot/MeV, a short luminescence decay time of less than 100 ns [13], [14], and good matching of the emission spectrum peaked at 540 nm with the sensitivity spectra of SiPMs. The timing properties of GAGG:Ce scintillator might be substantially improved by codoping the crystal with magnesium [13], [15].

In this paper, we demonstrate that coupling of the RGB-HD SiPM developed at Fondazione Bruno Kessler with GAGG scintillator containing optimal Ce doping and Mg codoping enabled us to achieve a CTR FWHM as low as 165 ps at 511 keV. To study further prospective for improving the time resolution of the GAGG-based radiation detectors, we investigated the dynamics of the population of Ce ions. Selective optical excitation and measuring the differential absorption (DA) of a white light continuum with time resolution in the subpicosecond domain were exploited. Since the results indicated the importance of excitation transfer, we revised the description of the luminescence time response for three qualitatively different shapes of the response and compared the calculation and experimental results.

II. EXPERIMENT

Cerium-doped and codoped with Mg and Ti GAGG single crystals studied in this paper were produced by the Czochralski technique at Furukawa Electric Co., Ltd., Japan, and Fomos Crystals, Moscow, Russia. The crystals were pulled out from iridium crucibles in a slightly oxidizing atmosphere. Cerium was introduced in the initial charge for the crystal growth at a level of 1000 ppm for all samples, while the concentration of Mg was different in the range from 10 to 100 ppm in the initial charge. The samples were prepared from the ingots as $3 \times 3 \times 5$ mm^3 blocks and 10×10 mm^2 plates, 1–3 mm thick. The surfaces of the samples studied were mechanically

Manuscript received April 15, 2019; accepted May 19, 2019. Date of publication May 30, 2019; date of current version July 16, 2019. This work was supported in part by the European Social Fund via the Lithuanian Research Council through the project FARAD under Grant 09.3.3-LMT-K-712-01-0013 and in part by the Russian Federation Government under Grant 14.W03.31.0004.

G. Tamulaitis, S. Nargelas, and A. Vaitkevičius are with the Institute of Photonics and Nanotechnology, Vilnius University, 01513 Vilnius, Lithuania (e-mail: augustas.vaitkevicius@ff.vu.lt).

A. Vasil'ev is with the Institute of Nuclear Physics, Moscow State University, 119991 Moscow, Russia.

M. Korzhik and D. Kozlov are with the Research Institute for Nuclear Problems, 220030 Minsk, Belarus (e-mail: korzhik@bsu.inp.by).

A. Mazzi and A. Gola are with Fondazione Bruno Kessler, 38123 Trento, Italy.

A. Fedorov is with the Research Institute for Nuclear Problems, 220030 Minsk, Belarus, and also with the NRC "Kurchatov Institute," Moscow, Russia.

Color versions of one or more of the figures in this paper are available online at http://ieeexplore.ieee.org.

Digital Object Identifier 10.1109/TNS.2019.2919898

TABLE I

LIST OF GAGG SAMPLES STUDIED, THEIR SCINTILLATION PARAMETERS AND COINCIDENCE TIME, AND ENERGY RESOLUTION

Sample	Concentration of activators			Light yield at room temperature, ph/MeV	Luminescence decay time constants, ns, and their relative weights (%)	CTR FWHM, ps, at different temperatures			Energy resolution, %, at different temperatures		
	Ce, ppm	Mg, ppm	Ti, ppm			+20°C	0°C	-20°C	+20°C	0°C	-20°C
S1	550			46000	32 (36), 86 (53), 200 (8) + phosphorescence	193±4	198±4	203±4	7.8	7.1	6.8
S2	530	10		42000	27 (34), 73 (54), 180 (12)	169±3	165±3	168±3	7.2	6.9	6.7
S3	900	7		41000	28 (30), 68 (52), 168 (18)	182±3	188±2	182±3	7.3	7	6.7
S4	800	20	20	39000	33(30), 86 (56), 130 (14)	165±3	160±2	164±2	7.6	7.4	7.2
S5	950	46	50	36000	29 (25), 86 (60), 200 (15)	175±2	169±2	174±2	6.7	6.7	6.7

polished with diamond abrasives to the roughness $Ra_{0.01}$, as it is usually applied for the surface treatment of the samples of nonhygroscopic scintillation materials. The blocks were used in CTR measurements, while the plates were exploited for the investigation of nonequilibrium carrier dynamics in the optical pump and probe experiments. The list of the crystals studied is presented in Table I. The concentration of activator was measured by means of the Glow Discharge Mass Spectroscopy (GDMS) in sample $S2$ and estimated in other samples by comparing the absorption intensity at the bands due to the optical transitions in Ce^{3+} ions and the absorption centers related to Mg^{2+} [16]. Two of the samples studied ($S4$ and $S5$) were additionally codoped by titanium, as in [14], to further improve the timing properties by preventing stabilization of Ce^{4+} ions in the crystal, as suggested in [17]. The titanium content provided in Table I is the Ti concentration in the initial charge.

The scintillation parameters measured at room temperature are also presented in Table I. The light yield of the samples was measured by comparison with a reference sample of CsI(Tl); their scintillation decay kinetics were measured by start–stop method with ^{22}Na as an excitation source. The decay kinetics were fitted by a function with three exponential components. The decay time constants and weight coefficients of the components are presented in Table I. All the samples exhibit quite similar luminescence decay kinetics.

To measure CTR, pixels were combined into detecting modules with SiPMs developed at Fondazione Bruno Kessler (FBK SiPMs). In particular, the SiPMs used in these measurements were RGB-HD SiPMs with 4 mm × 4 mm active area and 25-μm cell pitch. RGB-HD SiPMs are n-on-p devices with PDE peaked at 550 nm [1], [2]. The pixels were optically coupled to SiPMs by using Cargille Meltmount optical glue with refractive index $n = 1.539$. The pixels were wrapped in Teflon.

A ^{22}Na point source provided 511-keV coincidence events. Two identical detecting modules were placed on the same axis, at the same distance from the radioactive source. The SiPM signal was read out by two double-stage amplifiers with two outputs each. The first output of the amplifiers was used to discriminate 511-keV events, through charge integration of the scintillation signals. The second output of the amplifiers featured a pole–zero (PZ) compensation circuit, an analog filtering method that allows for low-noise signal pickup at a low threshold. The analog circuits exploited are described in detail in [5]. The SiPMs were operated at an overvoltage of 10 V. The CTR setup was placed in a climatic chamber with temperature and humidity control.

The CTR values obtained using different experimental setups significantly depend on measurement conditions (sample geometry, coupling to SiPMs, etc.), which are differently presented in publications. Our current CTR measurements were carried out at nominally the same conditions for all the samples studied.

The energy resolution of the detecting modules was measured with the same experimental setup used for CTR measurements, just by operating a single detector. The energy spectra were obtained by charge integration of the scintillation signals with an integration window of 500 ns. The spectra were corrected for the SiPM nonlinearity by using the 1274-keV events of ^{22}Na.

The dynamics of nonequilibrium carriers were studied using the pump and probe technique (see the outline in Fig. 1).

The experimental setup for time-resolved DA is based on a commercial Yb:KGW (Yb:KGd(WO$_4$)$_2$) femtosecond laser (Pharos, Light Conversion). The output of the laser was split into two beams. The main part was used to pump the optical parametric amplifier (OPA, Orpheus, Light Conversion) producing tunable-wavelength light for excitation. The output of OPA was frequency doubled/quadrupled using β-BBO crystals to extend the pumping light wavelength to UV. The remaining part of the fundamental laser radiation was sent through a delay line (a moving retroreflector on a motorized translation stage) and then focused into a sapphire plate, where a white-light supercontinuum is generated. The generated probe light was focused by parabolic mirrors on the sample into a spot overlapping with the excitation beam spot. Typical diameters of pump and probe beams used in our experiments are 100 and 250–300 μm on the sample surface, respectively. The probe light transmitted through the sample was dispersed

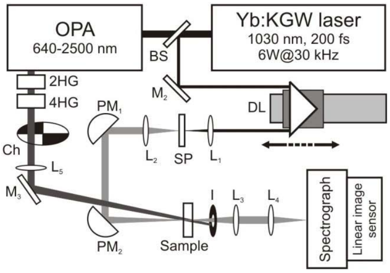

Fig. 1. Layout of time-resolved DA setup: OPA—optical parametric amplifier, BS—beam splitter, M—mirror, L—lens, DL—delay line, SW—sapphire plate, PM—parabolic mirror, I—iris, 2HG and 4HG—β-BBO crystals for frequency doubling and quadrupling, and Ch—chopper.

by a spectrograph and recorded using a linear image sensor. A chopper was used to periodically open and block the pump pulses to measure the transmitted probe light intensity when the sample is excited and unexcited. The time evolution of spectrally resolved DA signal, i.e., the difference of the optical absorption in the excited and unexcited samples, was measured by delaying the probe pulse with respect to the pump in the range from tens of femtoseconds to 8 ns. The measured DA signal is recorded as

$$\mathrm{DA}(\lambda) = \ln\left(\frac{\mathrm{I}(\lambda)_{\mathrm{unexc}}}{\mathrm{I}(\lambda)_{\mathrm{exc}}}\right) \qquad (1)$$

where $I(\lambda)_{\mathrm{unexc}}$ and $I(\lambda)_{\mathrm{exc}}$ are the probe light intensities when the sample is unexcited and excited.

The pump photon energies were tuned at several energies corresponding to Ce^{3+} intracenter absorption. A photon at 2.8 eV (443 nm) resonantly excites the Ce^{3+} ion to its first excited level $5\mathrm{d}^1$, which is below the bottom of the conduction band. Only fast relaxation via interaction with phonons within the $5\mathrm{d}^1$ Ce^{3+} level is expected after such excitation. The photon energy of 3.63 eV (342 nm) corresponds to the optical transition to the second excited Ce^{3+} level $5\mathrm{d}^2$, which is in the conduction band. Thus, the excited electron has two routes for the relaxation to the radiative level $5\mathrm{d}^1$: intracenter relaxation from $5\mathrm{d}^2$ to $5\mathrm{d}^1$ and relaxation via the extended states in the conduction band. The second route might involve also trapping and detrapping of the nonequilibrium electron and takes longer time.

The excitation-induced optical absorption was probed at a variable delay by using optomechanical delay line. White light continuum in the range from 1.3 to 2.7 eV (950–460 nm) generated in a sapphire plate was used for probing. The spectrum of DA, i.e., the difference in the optical absorption with and without the pump, was measured as a function of the delay between the pump and probe pulses. The time resolution in these experiments was limited by the laser pulse duration of 200 fs. The DA in these experiments is caused by the absorption by the free electrons and the electrons localized at Ce ions or trapping centers. The contribution of different DA mechanisms might be distinguished spectrally and in time.

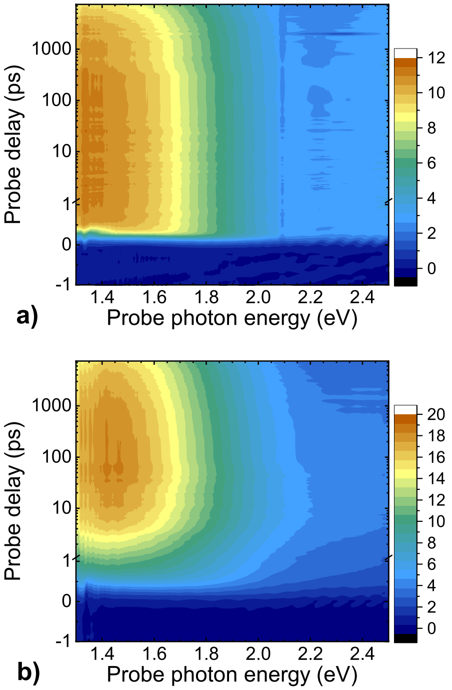

Fig. 2. DA in sample *S*1 as a function of probe photon energy and the delay between pump and probe pulses at pump photon energies of (a) 2.8 and (b) 3.63 eV.

III. Experimental Results

The main results of our CTR and energy resolution measurements with 511-keV gamma-quanta emitted by a 22Na source are summarized in Table I.

The data show that the time resolution is significantly improved down to 165 ps by Mg-codoping even at a quite low magnesium content. This CTR value is better than that achieved in demonstrator TOF-PET systems based on LYSO:Ce (200–250-ps FWHM) [18], [19], though still worse than the best resolution achieved with LSO:Ce,Ca [10] and L(Y)SO:Ce [20] in laboratory experiments.

To study the prospect for further improvement of the radiation detectors based on GAGG:Ce, we investigated the time evolution of the population of the Ce^{3+} radiating level in this material by using the optical pump and probe technique. The results on the typical DA measured in sample *S*1 are presented in Fig. 2 as a data carpet depicting the DA (see the color scale) as a function of the spectral position and the delay between pump and probe pulses.

The DA feature spectrally peaked at 1.4 eV, which we do observe in all GAGG:Ce studied and do not observe in GAGG without Ce doping, is attributed to the absorption by electrons

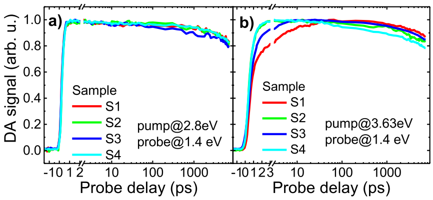

Fig. 3. DA kinetics at 1.4 eV of samples *S*1–*S*4 pumped at (a) 2.8 and (b) 3.63 eV.

occupying the lowest excited state of Ce^{3+}. The DA kinetics at this photon energy are depicted for samples *S*1–*S*4 in Fig. 3. The kinetics of *S*5 coincides with that of *S*4. The behavior of the samples containing Ti was similar to that in the samples codoped only with Mg. The DA kinetics presented in Fig. 3(a) reflects the time evolution of the population of the first excited Ce^{3+} level. At the excitation resonantly to this level, the rise time of the DA response is in the subpicosecond domain. The decay proceeds at a similar rate for all samples, and the decay constant is of the order of 60 ns, in correspondence to the luminescence decay time reported for GAGG:Ce in [21].

The DA kinetics at the resonant excitation to the second excited level of Ce^{3+} are presented in Fig. 3(b). Two components in the DA response front are observed for this pump photon energy: a fast component in the subpicosecond domain, as also observed for the excitation at 2.8 eV, and a slower component with a characteristic time of a few picoseconds. To extract the times characterizing the luminescence response front, a set of rate equations for the population of the two lowest excited states of Ce^{3+} and a trap level for nonequilibrium electrons was solved. The fast luminescence rise time was found to be ∼500 fs, while the slow rise time equals 4.1 ps in sample *S*1 without codoping and is smaller in the codoped samples: 1.4, 3.6, 1, and 1.2 ps for samples *S*2, *S*3, *S*4, and *S*5, respectively.

The slow rise component in the population of the lowest excited state of Ce^{3+} corresponds to the 2-ps luminescence rise time observed for uncodoped GAGG:Ce in time-resolved luminescence experiments [15], [22]. In both photoluminescence and optical pump and probe experiments with excitation of the second excited level, the lowest radiating level of Ce^{3+} has two population routes: the intracenter relaxation down from the second excited level and the excitation transfer via the crystal matrix. The second route might be influenced by electron trapping at shallow trap centers and, consequently, takes a longer time. The trapping centers might be caused by unintentional doping or structural defects. In GAGG, trapping centers due to content fluctuations might be expected: random distribution of Al and Ga ions in the multicomponent garnet leads to bandgap modulation, and the minima of these fluctuations serve for localization of free electrons. The codoping decreases the influence of trapping and facilitates a faster termination of the transfer of electrons back to Ce ions. Depletion of the trapping centers due to the relaxation of the trapped carriers to deeper states probably introduced by the introduction of codopants is one of the feasible mechanisms. The observation that the codoping also results in a decrease in the light yield, i.e., decreases the fraction of electrons recombining radiatively, supports this interpretation.

The results on the population of Ce^{3+} ion indicate a significant influence of electron trapping on the excitation transfer via the GAGG matrix even at selective photoexcitation Ce ions to higher excited levels. The effect of excitation transfer should be even more important after the excitation of the scintillator by high-energy quanta, e.g., by 511-keV gamma-quanta in our CTR experiments and future PET applications. To properly address the excitation transfer, we considered the scintillation response for three representative shapes of the emission kinetics.

IV. TIME RESOLUTION OF SCINTILLATION DETECTOR FOR DIFFERENT SHAPES OF LUMINESCENCE KINETICS

To clarify the role of the key processes in scintillation build-up, we studied the influence of different forms of scintillation kinetics on the time resolution of a scintillation detector: 1) instantaneous response with zero rise time; 2) response with a certain rise time, which is substantially faster than the decay time; and 3) build-up of the population of the luminescent centers via dipole–dipole interaction with excitons, denoting under the exciton all possible excitations populating the activator radiative level in the scintillator.

First, let us suppose that the energy deposit due to the interaction of ionizing radiation with a thin layer of scintillator media occurs instantaneously, and the effect of light collection can be neglected. The mean rate of photon emission after energy deposit is described by emission intensity $I(t)$. The number of photons emitted from the moment of energy deposit until the moment t is equal to $N(t) = \int_0^t I(t')dt'$. For simplicity, we assume that all the photons are emitted independently, and, therefore, the number of photons emitted during the time interval $(0, t)$ is distributed according to the Poisson distribution: $p_n(t) = (N^n(t)/n!)e^{-N(t)}$. Let us introduce the detection threshold Nth, meaning that registration of at least N_{th} photons is sufficient for the detection of an event. Therefore, the probability of event registration at timestamp t_{ts} is

$$p_{n\geq N_{\rm th}}(t_{\rm st}) = \sum_{n=N_{\rm th}}^{\infty} \frac{N^n(t_{\rm st})}{n!}e^{-N(t_{\rm st})} = 1-\sum_{n=0}^{N_{\rm th}-1} \frac{N^n(t_{\rm st})}{n!}e^{-N(t_{\rm st})} = 1-\frac{\Gamma(N_{\rm th}, N(t_{\rm st}))}{\Gamma(N_{\rm th})} \tag{2}$$

where $\Gamma(x)$ is the Euler gamma function and $\Gamma(x, z)$ is the incomplete Euler gamma function.

The density distribution function of the timestamps $t_{\rm st}$ is

$$G(t_{\rm st}) = \frac{dp_{n\geq N_{\rm th}}(t_{\rm st})}{dt_{\rm st}} = {\rm e}^{-N(t_{\rm st})}\frac{N^{N_{\rm th}-1}(t_{\rm st})}{(N_{\rm th}-1)!}I(t_{\rm st}). \tag{3}$$

The maximum of this function and its width are defined by the mean delay of the timestamp $\langle t_{\rm st}\rangle$ and the standard deviation of the timestamp $\sigma_{t\,\mathrm{st}}$

$$G(t_{\mathrm{s\,t}}) \sim e^{\frac{(t_{\mathrm{s\,t}}-\langle t_{\mathrm{s\,t}}\rangle)^2}{2\sigma_{t_{\mathrm{s\,t}}}^2}}. \tag{4}$$

The values of $\langle t_{\mathrm{st}}\rangle$ and $\sigma_{t_{\mathrm{st}}}$ can be evaluated for the three shapes of the scintillation kinetics described above.

For a negligible rise time, case i), the intensity of photon emission can be written as

$$I^{(1)}(t) = \frac{N_{\mathrm{em}}}{\tau_{\mathrm{em}}} e^{-\frac{t}{\tau_{\mathrm{em}}}} \tag{5}$$

where N_{em} is the number of photons emitted per one event and τ_{em} is the emission time. For small t, one can show that

$$I^{(1)}(t) \approx \frac{N_{\mathrm{em}}}{\tau_{\mathrm{em}}}. \tag{6}$$

In the case of short rise time, case ii), the signal exhibits a single-exponential rise; then

$$I^{(2)}(t) = \frac{N_{\mathrm{em}}}{\tau_{\mathrm{em}} + \tau_{\mathrm{rise}}}\left(e^{-\frac{t}{\tau_{\mathrm{em}}}} - e^{-\frac{t}{\tau_{\mathrm{rise}}}}\right) \tag{7}$$

with the peak value at $t_{\max} = (\tau_{\mathrm{em}}\tau_{\mathrm{rise}}/\tau_{\mathrm{em}} - \tau_{\mathrm{rise}})\ln(\tau_{\mathrm{em}}/\tau_{\mathrm{rise}})$.

For small t, one can show that

$$I^{(2)}(t) \approx \frac{N_{\mathrm{em}}t}{\tau_{\mathrm{em}}\tau_{\mathrm{rise}}}. \tag{8}$$

The analytical expression for the case of dipole–dipole transfer, case iii), is bulkier

$$\begin{aligned} I^{(3)}(t) = {} & \frac{N_{\mathrm{em}}q}{\sqrt{\tau_{\mathrm{em}}(\tau_{\mathrm{em}} - \tau_{\mathrm{ex}})}} \mathrm{e}^{-\frac{t}{\tau}+\frac{q^2\tau_{\mathrm{em}}}{\tau_{\mathrm{em}}-\tau_{\mathrm{ex}}}} \\ & \times \left(\mathrm{Erfc}\left(q\sqrt{\frac{\tau_{\mathrm{em}}}{\tau_{\mathrm{em}} - \tau_{\mathrm{ex}}}}\right)\right. \\ & \left. - \mathrm{Erfc}\left(\sqrt{\frac{t(\tau_{\mathrm{em}} - \tau_{\mathrm{ex}})}{\tau_{\mathrm{em}}\tau_{\mathrm{ex}}}} + q\sqrt{\frac{\tau_{\mathrm{em}}}{\tau_{\mathrm{em}} - \tau_{\mathrm{ex}}}}\right)\right) \end{aligned} \tag{9}$$

for $\tau_{\mathrm{em}} > \tau_{\mathrm{ex}}$ and

$$\begin{aligned} I^{(3)}(t) = {} & \frac{N_{\mathrm{em}}q}{\sqrt{\tau_{\mathrm{em}}(\tau_{\mathrm{ex}} - \tau_{\mathrm{em}})}} e^{-\frac{t}{\tau_{\mathrm{em}}}-\frac{q^2\tau_{\mathrm{em}}}{\tau_{\mathrm{ex}}-\tau_{\mathrm{em}}}} \\ & \times \left(\mathrm{Erfi}\left(q\sqrt{\frac{\tau_{\mathrm{em}}}{\tau_{\mathrm{em}} - \tau_{\mathrm{ex}}}}\right)\right. \\ & \left. + \mathrm{Erfi}\left(\sqrt{\frac{t(\tau_{\mathrm{em}} - \tau_{\mathrm{ex}})}{\tau_{\mathrm{em}}\tau_{\mathrm{ex}}}} - q\sqrt{\frac{\tau_{\mathrm{em}}}{\tau_{\mathrm{em}} - \tau_{\mathrm{ex}}}}\right)\right) \end{aligned} \tag{10}$$

for $\tau_{\mathrm{em}} > \tau_{\mathrm{ex}}$. Here, τ_{ex} is the exciton lifetime, $q = (2\pi^2/3)n_{\mathrm{A}}R_{d-d}^3$, R_{d-d} is the exciton-to-activator dipole–dipole transfer radius, and n_A is the activator concentration.

For small t, one can show that

$$I^{(3)}(t) \approx \frac{2N_{\mathrm{em}}q\sqrt{t}}{\tau_{\mathrm{em}}\sqrt{\tau}_{\mathrm{ex}}}. \tag{11}$$

The mean number of photons emitted during the period Δt from the energy deposit moment is equal to

$$N^{(1)}(\Delta t) = N_{\mathrm{em}}\left(1 - e^{-\frac{\Delta t}{\tau_{\mathrm{em}}}}\right) \approx N_{\mathrm{em}}\frac{\Delta t}{\tau_{\mathrm{em}}} \tag{12}$$

$$\begin{aligned} N^{(2)}(\Delta t) &= N_{\mathrm{em}}\frac{\left(1 - e^{-\frac{\Delta t}{\tau_{\mathrm{em}}}}\right)\tau_{\mathrm{em}} - \left(1 - e^{-\frac{\Delta t}{\tau_{\mathrm{rise}}}}\right)\tau_{\mathrm{rise}}}{\tau_{\mathrm{em}} - \tau_{\mathrm{rise}}} \\ &\approx N_{\mathrm{em}}\frac{(\Delta t)^2}{\tau_{\mathrm{em}}\tau_{\mathrm{rise}}} \end{aligned} \tag{13}$$

for cases i) and ii), respectively.

The corresponding expression for case iii) is rather bulky; however, its asymptotic value for small Δt is equal to

$$N^{(3)}(\Delta t) \approx N_{\mathrm{em}}\left(\frac{4q(\Delta t)^{3/2}}{3\tau_{\mathrm{em}}\sqrt{\tau}_{\mathrm{ex}}} - \frac{q^2(\Delta t)^2}{\tau_{\mathrm{em}}\tau_{\mathrm{ex}}}\right). \tag{14}$$

The estimations for the time resolution in the three cases are correspondingly

$$\langle t_{\mathrm{st}}\rangle \approx \tau_{\mathrm{em}}\frac{N_{\mathrm{th}}}{N_{\mathrm{em}}} \tag{15}$$

$$\langle t_{\mathrm{st}}\rangle \approx \sqrt{\tau_{\mathrm{em}}\tau_{\mathrm{rise}}\frac{N_{\mathrm{th}}}{N_{\mathrm{em}}}} \tag{16}$$

$$\langle t_{\mathrm{st}}\rangle \approx \left(\frac{3\tau_{\mathrm{em}}\sqrt{\tau_{\mathrm{ex}}}}{4\,q}\frac{N_{\mathrm{th}}}{N_{\mathrm{em}}}\right)^{2/3}. \tag{17}$$

The value of N_{th} has to be chosen, in accordance with signal-to-noise considerations, by taking into account the properties of the photodetector used to read out the signal.

Equation (15) shows that in the case of the instantaneous population of the luminescence centers, $\langle t_{\mathrm{st}}\rangle$ is proportional to τ_{em}. Thus, a fast luminescence decay is crucial for achieving good CTR, while a high light yield of scintillator material decreases the ratio $N_{\mathrm{th}}/N_{\mathrm{em}}$, where N_{th} depends on the detecting system and irradiation environment. The application of cross-luminescence scintillators corresponds to this situation [23]. The situation in detectors based on self-activated scintillators is close to the case ii). For example, lead tungstate ($PbWO_4$) single crystal has a short luminescence rise time in subpicosecond domain [23] and τ_{em} of less than 10 ns at room temperature [22], so the time resolution for measurements at high-energy deposit is proportional to $N_{\mathrm{em}}^{-1/2}$ and can be as low as 100 ps [24], [25].

The third case frequently occurs in activated scintillation materials, when the photons are emitted after the excitation is transferred to emitting centers, and the transfer process deteriorates the CTR.

The profiles of the initial parts of scintillation kinetics in the three cases are compared in Fig. 4. A set of the parameters typical for Ce doped scintillators was taken in the calculations: $N_{\mathrm{em}} = 10\,000$ ph, $\tau_{\mathrm{em}} = 30$ ns, $\tau_{\mathrm{rise}} = 20$ ps, $\tau_{\mathrm{ex}} = 100$ ns, and $q = 60$.

The most striking feature of the kinetics is the initial slope in the build-up of the response: even at $\tau_{\mathrm{ex}} \gg \tau_{\mathrm{rise}}$, the slope might be steeper in case iii) than that in case ii), though reaching the peak value takes longer time in case iii). The decay of the response proceeds at the same rate.

V. DISCUSSION

The estimates of the timestamps for different shapes of luminescence response show that the excitation transfer time influences the time resolution in a different way than that is

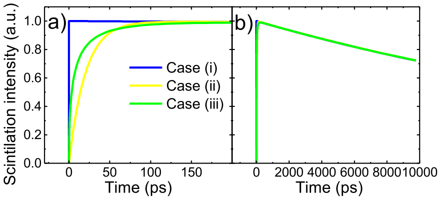

Fig. 4. (a) Initial part and (b) decay of scintillation kinetics for three cases of luminescence response discussed in the text: the case (i) blue line, (ii) yellow, and (iii) green.

usually considered in the description of the time resolution of the scintillation detectors. To test the relevance of the scintillation kinetics in GAGG:Ce without and with codoping with case iii), the correlation between the CTR and the rise time in a population of Ce^{3+} emitting level was analyzed.

The excitation of Ce^{3+} ion in GAGG:Ce by a 3.63-eV photon results in the transfer of an electron from level 4f to level $5d^2$, which overlaps in energy with the lower conduction band states (5d states of Gd ion). Therefore, this transfer can be considered as $h\nu + Ce^{3+} \rightarrow Ce^{4+}$ with the creation of a Ce^{4+} ion and an electron subjected to Coulomb attraction. The electron created in this transition might remain at Ce^{3+} ion forming an excited state $5d^2$ or can leave the Ce ion. After thermalization, the escaped electron might be recaptured by the geminate Ce^{4+} ion due to Coulomb interaction or escape from this ion to the infinity. This case was discussed in [26], where the electron thermalization length in ionic materials was estimated. The estimation is based on the following simplifications. An electron with the kinetic energy E_{kin} is thermalized in the conduction band, and the distance $l_e(E_{\text{kin}})$ of this thermalization depends on electron kinetic energy. The thermalization positions are spatially shifted from the electron birthplace by the distance r distributed according to the 3-D Gaussian distribution

$$f(r, l_e, (E_{\text{kin}})) = \frac{3\sqrt{6}\, r^2}{\sqrt{\pi}\, l_e^3(E_{\text{kin}})} \exp\left(-\frac{3r^2}{2l_e^2(E_{\text{kin}})}\right). \tag{18}$$

The return of the electron to Ce^{4+} ion is facilitated by the Coulomb interaction. The time-dependent equation of the electron diffusion in the Coulomb field has no analytical solution; however, this process can be approximately described by the model of the black sphere of recombination. All electrons within this black sphere are regarded as captured (to the lowest excited $5d^1$ Ce^{3+} state), while the electric field is neglected in the description of the electron diffusion outside the black sphere. The radius of the black sphere can be estimated as being equal to the Onsager radius $R_c = (e^2/4\pi\varepsilon\varepsilon_0 k_b T)$, where T is the crystal temperature, e is the electron charge, ε is the dielectric constant, ε_0 is the vacuum permittivity, and k_B is the Boltzmann constant.

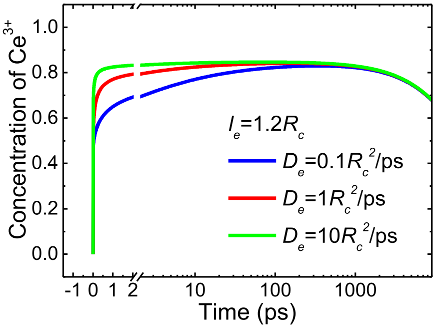

Fig. 5. Simulated kinetics of Ce^{3+} level population at different electron diffusion coefficients.

In this case, the electrostatic potential within the capture sphere is negative with the absolute value above $k_B T$ and can be regarded as strong (therefore, the electron cannot escape this sphere and recombines rapidly at Ce^{4+} ion). Meanwhile, outside this sphere, the absolute value of the attractive potential is less than $k_B T$, and the diffusion can be regarded as in free space. The fraction of electrons, which occur, after thermalization, within the capture sphere and, therefore, instantaneously form the excited Ce^{3+} state, equals

$$p(0) = \operatorname{erf}\left(\sqrt{\frac{3}{2}}\frac{R_c}{l_e}\right) - \sqrt{\frac{6}{\pi}}\frac{R_c}{l_e}\exp\left(-\frac{3R_c^2}{2l_e^2}\right) \tag{19}$$

and increases with time as

$$\begin{aligned} p(t) &= \operatorname{erf}\left(\sqrt{\frac{3}{2}}\frac{R_c}{l_e}\right) - \sqrt{\frac{6}{\pi}}\frac{R_c}{\sqrt{l_e^2 + 6D_e t}}\exp\left(-\frac{3R_c^2}{2(l_e^2 + 6D_e t)}\right) \\ &\quad \times \left(1 - \operatorname{erf}\left(\frac{3R_c}{l_e}\sqrt{\frac{D_e t}{l_e^2 + 6D_e t}}\right)\right). \end{aligned} \tag{20}$$

Here, D_e is the electron diffusion coefficient. For $t \gg l_e^2/D_e$, the probability for an electron to return to Ce^{4+} reaches the limit value $p(\infty) = \operatorname{erf}((3/2)(R_c/l_e))^{1/2}$. Thus, a fraction $1 - p(\infty)$ of nonequilibrium electrons leave the birthplace forever; their subsequent recombination is not geminate. After diffusion and trapping at different uncontrolled defects, the electrons recombine at Ce^{4+} centers created in other photon absorption events or via nonradiative recombination centers. This retarded process results in hyperbolic tails in the electron population decay [27], [28].

Fig. 5 presents the number of $5d^1$ Ce^{3+} excited states as a function of time for the parameters presented in the legend, and the decay time of the density of excited cerium ions equal to 40 ns. For $R_c = 10$ nm (a typical value for the Onsager radius at 300 K), the diffusion coefficient for the red curve equals $D_e = R_c^2/\text{ps} = 1\ \text{cm}^2/\text{s}$. This diffusion coefficient can be compared with the diffusion coefficient for electrons in CsI calculated using the value of electron mobility of 8 $\text{cm}^2/(\text{V s})$ estimated at room temperature in [29]. According to the Einstein formula, $\mu = qD/k_B T$, the corresponding diffusion coefficient in CsI is $D_e = 0.21\ \text{cm}^2/\text{s}$.

The simulated curves in Fig. 5 are similar to those obtained by measuring the kinetics of the DA [see Fig. 2(b)], which are

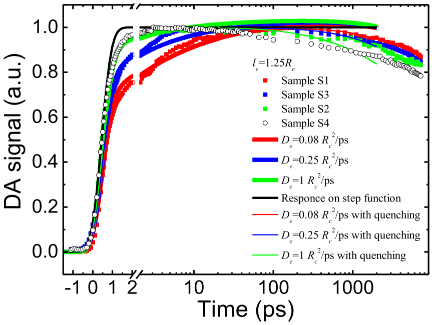

Fig. 6. DA kinetics at 1.4 eV measured in samples $S1$–$S4$ pumped at 3.63 eV (points), simulated kinetics at different diffusion coefficients (thick solid lines), the kinetics as a response to a step function (dashed line), and the kinetics simulated with quenching taken into account (thin solid lines).

proportional to the population of the 5d^1 level of Ce^{3+}. This means that the diffusion coefficient (affected predominantly by the concentration of shallow traps) is extremely sensitive to the concentration of the doping ions introduced at the crystal growth.

Though the measured and calculated kinetics of the population of Ce^{3+} level 5d^1 [see Fig. 3(b) a and Fig. 5, respectively] are similar, the rising part of the calculated kinetics is longer than that of the kinetics measured in DA experiments. This discrepancy might be caused by the contribution of the electrons escaped from their geminate Ce ions. Fig. 6 presents the results of a more detailed comparison of the experimental data (points) with the theoretical curves (thick solid lines). There, the experimental DA kinetics for three samples are compared with the convolution of the simulated response and the instrumental function with a Gaussian shape $(1/(2\pi\sigma^2)^{1/2})e^{((-t^2)/2\sigma^2)}$ at $\sigma = 400$ fs. The response on a step function is also presented in this figure for comparison as a dashed curve. The theoretical curves are calculated for $l_e = 1.25R_c$. The fit of the experimental data with the simulated curves is quite good, especially by taking into account the simplification due to the application of the model of a black sphere of recombination instead of any more complicated models with the Coulomb attractive potential taking into account. The diffusion coefficients used to simulate the red, blue, and green solid curves in Fig. 6 are 0.08, 0.25, and 1 cm^2/s, respectively.

Fig. 6 shows that in the subnanosecond range, the experimental curves show some decrease, whereas the theoretical curves still increase (see the plot part after the axis break). Moreover, the decrease of the experimental kinetics is sample dependent: for sample $S2$ (green squares), the decrease starts even after a few picoseconds after excitation, whereas in sample $S1$ (red points), the kinetics reaches the peak after ~100 ps. This decrease might be caused by an additional role of the electrons, which escape from the recombination sphere of the geminate cerium ions. These electrons can quench other excited cerium ions via the Auger-type reaction $\mathrm{Ce}^{3+*} + \mathrm{e} \rightarrow \mathrm{Ce}^{3+} + \mathrm{e}$. The quenching rate depends on the electron diffusion coefficient, the density of electrons (which is proportional to the concentration of ionized cerium ions Ce^{4+}), and the concentration of excited cerium ions Ce^{3+*}. The initial stages of the cerium de-excitation due to the radiative decay with a characteristic time τ_r of ~60 ns and the diffusion-controlled de-excitation due to the Auger process depends on time as $e^{(-(t/\tau_r)-a\sqrt{D_e t})}$, where a is a parameter depending on the electron density, the concentration of excited cerium ions, and the Auger interaction radius. According to this formula, the Auger de-excitation rate increases with increasing electron diffusion coefficient. The correction of the simulated curves by this quenching factor is also shown in Fig. 6 by thin lines. The correction improved the fitting of the experimental kinetics with the calculation results.

To match the experimental results obtained by studying the differential optical absorption and described by the model presented above with the results obtained under excitation of GAGG:Ce with large excess energy (ionizing particle or X-ray excitation), the carrier dynamics in these two cases should be compared. Under laser excitation, the absorbed photon creates a pair of Ce^{4+} ion and electron. The kinetic energy E_kin of the produced electron is equal to $h\nu - E_{4\mathrm{fCe}\rightarrow\mathrm{CB}}$, i.e., the difference of the photon energy $h\nu$ and the energy distance between Ce^{3+} electron level 4f and the bottom of the conduction band $E_{4\mathrm{fCe}\rightarrow\mathrm{CB}}$ (about 0.2–0.4 eV). Meanwhile, the energy transfer to Ce^{3+} ion under ionizing particle, X- or gamma-ray excitation has two more stages: 1) excitation relaxation and generation of electron–hole pairs and 2) transfer of the excitation to the Ce^{3+} ions.

In spite of the long period since the pioneering attempts in [29]–[31], the excitation transfer in Gd-based materials in general and GAGG, in particular, is not well understood. The transfer might proceed via different routes. One of the routes is the transfer via the Gd sublattice by Coulomb dipole–dipole interaction [31], [32]. However, the transfer time from Gd sublattice to Ce^{3+} 5d^1 was found to be in the microsecond and millisecond domains [32], [33]. Probably, the transfer by self-trapped excitons (STE) formed by the oxygen-based valence band and the conduction band, which was found to be quite efficient in Gd-free crystals [34], is a more important route for populating the Ce^{3+} state 5d^1. These excitons are optically inactive and are not observed in the absorption and emission of the material, but they might transfer the excitation energy to cerium ions. This is a diffusion-controlled dipole–dipole energy transfer. The transition time for each exciton equals approximately $(1/n_\mathrm{Ce}^{2/3} D_\mathrm{ex})$, since the mean distance, which an exciton should pass to reach a Ce^{3+} ion, is $n_\mathrm{Ce}^{-1/3}$. The final stage of the energy transfer is a bimolecular-type reaction between the excitons and cerium ions. Therefore, the rate of the excitation of Ce^{3+} ions by excitons is proportional to the exciton density. At this stage, the exciton transfers its energy to Ce^{3+} and creates a pair of Ce^{4+} and electron, like under excitation by a laser photon. The energy of the excitons is higher than the photon energy (3.63 eV in

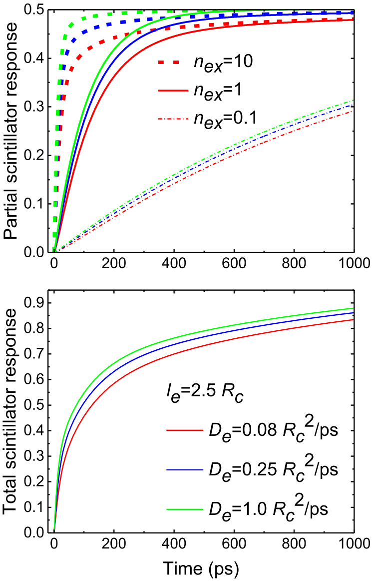

Fig. 7. Time evolution of the density of excited cerium centers at three relative exciton densities (indicated by line type), which was simulated using three values of electron diffusion coefficient, indicated by color (top).

our experiment), so the ionized states are created with higher electron kinetic energy E_{kin}. Consequently, the thermalization length for such electrons is higher than that at laser excitation, and the corresponding processes in the population of Ce ions should be considerably slower. Nevertheless, the dynamics of electrons is controlled, again, by the electron diffusion coefficient D_{e}.

Therefore, the rising time of the scintillator response depends on two diffusion coefficients, the electron diffusion coefficient D_{e} and the exciton diffusion coefficient D_{ex}, which is predominantly determined by the hole diffusion coefficient D_{h}. Thus, the increase of the electron diffusion coefficient (which is demonstrated by our DA experiments for the samples with codoping) plays an important role in the decrease in the rising time of the scintillator response.

There are no sufficient data on the processes forming the scintillator response, so the following considerations are schematic. The track of the ionizing particle consists of the regions with different excitation densities, and the excitations in the track region can be surrounded by another excitations at different concentrations from 10^{14} to 10^{21} cm^{-3} (see the estimates for CsI in [35]). The increase of the density of excited cerium centers for three relative exciton densities is presented in the top panel of Fig. 7 for the three diffusion coefficients, which have been estimated for different samples by fitting the experimental DA kinetics. The result of the

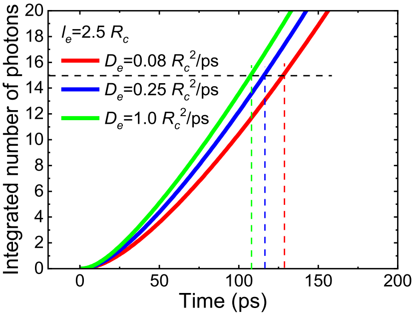

Fig. 8. Time evolution of the number of emitted photons calculated and for the three values of D_{e}, which were used to fit the experimental and simulated DA kinetics.

integration of these curves over the distribution of excitations is presented. We suppose that the average distance in the free electron distribution around Ce^{4+} after the excitonic energy transfer is larger than that after the laser excitation at 3.63 eV and assume that $l_{\mathrm{e}} = 2.5R_{\mathrm{c}}$. The curves in the bottom panel of Fig. 6 reflect an increase in the density of Ce^{3+*} excitations, since the lifetime of excited cerium in GAGG is substantially longer, about 60 ns. These curves and their rise profiles are qualitatively in consistent with the results of the measurements of the cerium emission leading edge in other garnet crystals [20].

The maximal photon count rate for GAGG:Ce with a light yield of about 40 000 ph/MeV after 511 keV excitation equals to 40 000 ph/MeV/60 ns × 0.511MeV = 340 ph/ns. Taking this value into account, the increase in the number of emitted photons with time was calculated and is presented in Fig. 8 for the three values of D_{e}, which were used to fit the experimental data for DA kinetics and for the calculation of the curves in Fig. 6. To detect a γ-quantum, the number of photoelectrons registered by a scintillator-coupled photodetector has to exceed a certain threshold number, say, 5. It is well known that the coupling imposes certain losses, while the quantum yield of the photodetector is well below 100%. Therefore, it is reasonable to assume that the number of photons sufficient for their detection is about 3 times higher than the number of photoelectrons, i.e., approximately 15. The time resolution for the detection of a 511-keV γ-quantum can be estimated as the time corresponding to the point, where the curves presented in Fig. 8 cross a horizontal line at the level of 15 photons. The scintillator time resolutions Δt obtained from Fig. 8 in this way are 108, 116, and 128 ps (see vertical lines). These Δt values correspond to the parameters used for fitting the DA results for samples $S4$, $S3$, and $S1$, respectively. The Δt values can also be calculated using the characteristic times Δt_{CTR} obtained in CTR experiments as $\Delta t = \Delta t_{\mathrm{CTR}}/\sqrt{2}$. For $S4$, $S3$, and $S1$ samples, these values are 117, 129, and 136 ps, respectively. The coincidence between the Δt values obtained from CTR experiments and those estimated from the detection threshold are fairly good. The key result is, however, not in a good correspondence (it is obtained under several quite rough assumptions) but rather in the fact that the differences observed for different GAGG:Ce crystals in the rise time of their DA kinetics of the order of 10 ps correlates well with the differences in time resolution of the order of 150 ps in the CTR experiments performed with these crystals. The correlation is based on the electron diffusion coefficient, which is important in both DA and CTR experiments. Thus, the measurement of DA, a contactless and fast experiment, is a convenient tool to study the timing properties of fast scintillating materials.

VI. CONCLUSION

GAGG:Ce scintillation material was found to be promising for designing scintillation detectors in combination with high-density SiPMs. Combining of the last achievements in the crystal growth and the SiPM production technologies enabled us to obtain the CTR for 511-keV quanta with 3 mm × 3 mm × 5 mm pixels at the level of 165 ps and the energy resolution better than 7%. The theoretical analysis of the time resolution of scintillation detectors on a sub-100-ps scale indicates the importance of the luminescence response time. Matching the experimental data on the time evolution of the differential optical absorption spectra, which, at a selective excitation of Ce^{3+} ions, reflects the population of the first excited Ce^{3+} state governing the luminescence intensity, and the results of the simulation of this process show that the GAGG:Ce response time is influenced by electron diffusion, which is strongly affected by crystal codoping. The estimates show that the differences observed for different GAGG:Ce crystals in the rise time of their DA kinetics of the order of 10 ps correlate well with the differences in the time resolution in CTR experiments of the order of 150 ps, since both of the parameters depend on the electron diffusion coefficient. Therefore, the time-resolved optical DA measurement, which is a contactless and fast experiment, was found to be an informative tool to study the timing properties of GAGG:Ce. The results obtained on the GAGG:Ce investigated in this paper show that codoping of this scintillation by Mg even at the level of 10 ppm efficiently decreases the scintillator response time by enhancement of the electron diffusivity.

ACKNOWLEDGMENT

This research has been carried out in line with the guidelines of Crystal Clear Collaboration at CERN. The authors would like to thank the COST action FAST (TD1401) for collaboration support. They would also like to thank Furukawa Electric Co., Ltd., Japan, and Fomos Crystals, Moscow, Russia, for providing the samples studied in this investigation.

REFERENCES

[1] C. Piemonte *et al.*, "Characterization of the first FBK high-density cell silicon photomultiplier technology," *IEEE Trans. Electron Devices*, vol. 60, no. 8, pp. 2567–2573, Aug. 2013.

[2] C. Piemonte *et al.*, "Performance of NUV-HD silicon photomultiplier technology," *IEEE Trans. Electron Devices*, vol. 63, no. 3, pp. 1111–1116, Mar. 2016.

[3] N. D'Ascenzo, W. Brockherde, S. Dreiner, A. Schwinger, A. Schmidt, and Q. Xie, "Design and characterization of a silicon photomultiplier in 0.35-μm CMOS," *IEEE J. Electron Devices Soc.*, vol. 6, pp. 74–80, 2018.

[4] A. Bornheim *et al.*, "LYSO-based precision timing detectors with SiPM readout," *Nucl. Instrum. Methods Phys. Res. A, Accel. Spectrom. Detect. Assoc. Equip.*, vol. 896, Aug. 2017, pp. 75–81, Jul. 2018.

[5] A. Gola, C. Piemonte, and A. Tarolli, "Analog circuit for timing measurements with large area SiPMs coupled to LYSO crystals," *IEEE Trans. Nucl. Sci.*, vol. 60, no. 2, pp. 1296–1302, Apr. 2013.

[6] F. Acerbi, G. Paternoster, A. Gola, V. Regazzoni, N. Zorzi, and C. Piemonte, "High-density silicon photomultipliers: Performance and linearity evaluation for high efficiency and dynamic-range applications," *IEEE J. Quantum Electron.*, vol. 54, no. 2, Apr. 2018, Art. no. 4700107.

[7] C. Dujardin *et al.*, "Needs, trends, and advances in inorganic scintillators," *IEEE Trans. Nucl. Sci.*, vol. 65, no. 8, pp. 1977–1997, Aug. 2018.

[8] S. E. Derenzo, W. W. Moses, R. H. Huesman, and T. F. Budinger, "Critical instrumen-tation issues for resolution smaller than 2 mm, high sensitivity brain PET," in *Quantification of Brain Function* (Tracer Kinetics and Image Analysis in Brain PET), K. Uemura, N. A. Lassen, T. Jones, and I. Kanno, Eds. Amsterdam, The Netherlands: Elsevier, 1993, pp. 25–37.

[9] D. R. Schaart *et al.*, "$LaBr_3$:Ce and SiPMs for time-of-flight PET: Achieving 100 ps coincidence resolving time," *Phys. Med. Biol.*, vol. 55, no. 7, p. N179, Mar. 2010.

[10] M. V. Nemallapudi *et al.*, "Sub-100 ps coincidence time resolution for positron emission tomography with LSO: Ce codoped with Ca," *Phys. Med. Biol.*, vol. 60, no. 12, pp. 4635–4649, May 2015.

[11] J. W. Cates and C. S. Levin, "Advances in coincidence time resolution for PET," *Phys. Med. Biol.*, vol. 61, no. 6, pp. 2255–2264, Feb. 2016.

[12] S. Gundacker *et al.*, "State of the art timing in TOF-PET detectors with LuAG, GAGG and L(Y)SO scintillators of various sizes coupled to FBK-SiPMs," *J. Instrum.*, vol. 11, no. 8, Aug. 2016, Art. no. P08008.

[13] K. Kamada *et al.*, "Alkali earth co-doping effects on luminescence and scintillation properties of Ce doped $Gd_3Al_2Ga_3O_{12}$ scintillator," *Opt. Mater.*, vol. 41, pp. 63–66, Mar. 2015.

[14] M. Korjik *et al.*, "Significant improvement of GAGG: Ce based scintillation detector performance with temperature decrease," *Nucl. Instrum. Methods Phys. Res. A, Accel. Spectrom. Detect. Assoc. Equip.*, vol. 871, pp. 42–46, Nov. 2017.

[15] M. T. Lucchini *et al.*, "Effect of Mg^{2+} ions co-doping on timing performance and radiation tolerance of Cerium doped $Gd_3Al_2Ga_3O_{12}$ crystals," *Nucl. Instrum. Methods Phys. Res. A, Accel. Spectrom. Detect. Assoc. Equip.*, vol. 816, pp. 176–183, Apr. 2016.

[16] E. Auffray *et al.*, "Excitation transfer engineering in Ce-doped oxide crystalline scintillators by codoping with alkali-earth ions," *Phys. Status Solidi Appl. Mater. Sci.*, vol. 215, no. 7, Apr. 2018, Art. no. 1700798.

[17] V. Alenkov, O. Buzanov, A. Dosovitsky, G. Dosovitskiy, M. Korzhik, A. Fedorov, and Fomos-Materials, Moscow, Russia, "Garnet-type single crystal for scintillation detectors and its production technology," U.S. Patent 2 646 407 RU, 2017.

[18] D. Schug *et al.*, "ToF performance evaluation of PET modules with digital silicon photomultiplier technology during MR operation," *IEEE Trans. Nucl. Sci.*, vol. 62, no. 3, pp. 658–663, Jun. 2015.

[19] G. Borghi, V. Tabacchini, R. Bakker, and D. Schaart, "TOF-PET imaging with sub-3 mm resolution and 215 ps coincidence resolving time using digital SiPM based monolithic scintillator detectors in a 70 cm diameter tomographic setup," *J. Nucl. Med.*, vol. 57, no. 2, p. 104, May 2016.

[20] S. Gundacker, E. Auffray, K. Pauwels, and P. Lecoq, "Measurement of intrinsic rise times for various L(Y)SO and LuAG scintillators with a general study of prompt photons to achieve 10 ps in TOF-PET," *Phys. Med. Biol.*, vol. 61, no. 7, pp. 2802–2837, Apr. 2016.

[21] E. Auffray *et al.*, "Luminescence rise time in self-activated $PbWO_4$ and Ce-doped $Gd_3Al_2Ga_3O_{12}$ scintillation crystals," *J. Lumin.*, vol. 178, pp. 54–60, Oct. 2016.

[22] G. Tamulaitis *et al.*, "Subpicosecond luminescence rise time in magnesium codoped GAGG: Ce scintillator," *Nucl. Instrum. Methods Phys. Res. A, Accel. Spectrom. Detect. Assoc. Equip.*, vol. 870, pp. 25–29, Oct. 2017.

[23] P. Lecoq, A. Gektin, and M. Korzhik, *Inorganic Scintillators for Detector Systems*. Berlin, Germany: Springer, 2017.

[24] M. Kavatsyuk *et al.*, "Performance of the prototype of the electromagnetic calorimeter for PANDA," *Nucl. Instrum. Methods Phys. Res. A, Accel. Spectrom. Detect. Assoc. Equip.*, vol. 648, no. 1, pp. 77–91, Aug. 2011.

[25] D. del Re, "Timing performance of the CMS ECAL and prospects for the future," *J. Phys., Conf. Ser.*, vol. 587, no. 1, 2015, Art. no. 012003.

[26] A. Belsky, K. Ivanovskikh, A. Vasil'ev, M. F. Joubert, and C. Dujardin, "Estimation of the electron thermalization length in ionic materials," *J. Phys. Chem. Lett.*, vol. 4, no. 20, pp. 3534–3538, Oct. 2013.

[27] G. Bizarri, W. W. Moses, J. Singh, A. N. Vasil'ev, and R. T. Williams, "The role of different linear and non-linear channels of relaxation in scintillator non-proportionality," *J. Lumin.*, vol. 129, no. 12, pp. 1790–1793, Dec. 2009.

[28] A. Vedda and M. Fasoli, "Tunneling recombinations in scintillators, phosphors, and dosimeters," *Radiat. Meas.*, vol. 118, pp. 86–97, Nov. 2018.

[29] H. Suzuki, T. A. Tombrello, C. L. Melcher, C. A. Peterson, and J. S. Schweitzer, "The role of gadolinium in the scintillation processes of cerium-doped gadolinium oxyorthosilicate," *Nucl. Instrum. Methods Phys. Res. A, Accel. Spectrom. Detect. Assoc. Equip.*, vol. 346, no. 3, pp. 510–521, Aug. 1994.

[30] H. Suzuki, T. A. Tombrello, C. L. Melcher, and J. S. Schweitzer, "Energy transfer from Gd to Ce in $Gd_2(SiO_4)O$: Ce," *J. Lumin.*, vols. 60–61, pp. 963–966, Apr. 1994.

[31] V. G. Baryshevsky, D. M. Kondratiev, M. V. Korzhik, V. B. Pavlenko, and A. A. Fedorov, "Mechanism of scintillations in cerium-doped gadolinium orthosilicate Gd_2SiO_5: Ce crystals," *J. Lumin.*, vols. 60–61, pp. 948–955, Apr. 1994.

[32] Z. Onderisinova, M. Kucera, M. Hanus, and M. Nikl, "Temperature-dependent nonradiative energy transfer from Gd^{3+} to Ce^{3+} ions in co-doped LuAG: Ce, Gd garnet scintillators," *J. Lumin.*, vol. 167, pp. 106–113, Nov. 2015.

[33] K. Bartosiewicz, V. Babin, K. Kamada, A. Yoshikawa, and M. Nikl, "Energy migration processes in undoped and Ce-doped multicomponent garnet single crystal scintillators," *J. Lumin.*, vol. 166, pp. 117–122, Oct. 2015.

[34] M. V. Korzhik and W. P. Trower, "Origin of scintillation in cerium-doped oxide crystals," *Appl. Phys. Lett.*, vol. 66, no. 18, pp. 2327–2328, May 1995.

[35] A. N. Vasil'ev, "Microtheory of scintillation in crystalline materials," in *Engineering of Scintillation Materials and Radiation Technologies*. Cham, Switzerland: Springer, 2017, pp. 3–34.

Paper P16

Irradiation Effects on $Gd_3Al_2Ga_3O_{12}$ Scintillators Prospective for Application in Harsh Irradiation Environments

E. Auffray, G. Dosovitskiy, A. Fedorov, I. Guz, M. Korjik, N. Kratochwill, M. Lucchini, S. Nargelas, D. Kozlov, V. Mechinsky, P. Orsich, O. Sidletskiy, G. Tamulaitis, **A. Vaitkevičius**

Radiat. Phys. Chem. 164 (2019) 108365.

doi: 10.1016/j.radphyschem.2019.108365.

Radiation Physics and Chemistry 164 (2019) 108365

Contents lists available at ScienceDirect

Radiation Physics and Chemistry

journal homepage: www.elsevier.com/locate/radphyschem

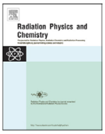

Irradiation effects on $Gd_3Al_2Ga_3O_{12}$ scintillators prospective for application in harsh irradiation environments

E. Auffray[a], G. Dosovitskiy[b], A. Fedorov[c,b], I. Guz[d], M. Korjik[c,*], N. Kratochwill[a], M. Lucchini[e], S. Nargelas[f], D. Kozlov[c], V. Mechinsky[c,b], P. Orsich[c], O. Sidletskiy[g], G. Tamulaitis[f], A. Vaitkevičius[f]

[a] CERN, Geneva, Switzerland
[b] National Research Center "Kurchatov Institute", Moscow, Russia
[c] Institute for Nuclear Problems BSU, Minsk, Belarus
[d] National Research Center "Kurchatov Institutute-IHEP", Moscow, Russia
[e] Princeton University, Princeton, NJ, USA
[f] Vilnius University, Vilnius, Lithuania
[g] Institute of Scintillation Materials of National Academy of Science of Ukraine, Kharkiv, Ukraine

ARTICLE INFO

Keywords:
Scintillators
Gadolinium aluminum gallium garnet
Radiation detectors
Radiation tolerance
Time resolution
Nonlinear optical absorption

ABSTRACT

We provide evidences that multicomponent garnet-type Ce-doped crystal GAGG ($Gd_3Al_2Ga_3O_{12}$) is a promising scintillator to be applied in harsh irradiation environments, particularly, in high-energy physics experiments and reactor research facilities, where long-term operation is mandatory. Applicability of this scintillator for the upgrade of the detectors at future accelerators with high luminosity like High luminosity LHC is considered and GAGG:Ce with different codopings is compared with Ce-doped oxyorthosilicate crystals, which are currently also strong candidates for such applications. It is shown that the irradiation with 24 GeV protons at a fluence of $5x10^{14}$ p/cm^2 has no significant effect on optical absorption in the spectral range of the scintillator emission. The contribution of radioisotopes formed in the material by irradiation with protons to the noise pedestal and the noise energy equivalent due to harmful radio-luminescence excited by the radionuclides remains negligible at short gates in collider experiments. Moreover, we show that the irradiation-generated color centers absorb outside the spectral range of Ce luminescence. These centers do not significantly affect the dynamics of nonequilibrium carriers, which is responsible for the timing properties of the scintillator. The density of free carriers decays with a characteristic time of 2 ps, while the decay constant for trapped carriers is ~50 ns both before and after irradiation.

1. Introduction

Heavy crystalline materials are extensively used in homogeneous electromagnetic calorimeters for high energy physics experiments. Bismuth germinate, $Bi_4Ge_3O_{12}$ (BGO), and lead tungstate, $PbWO_4$ (PWO), were successfully used to build and exploit the Electromagnetic Calorimeters of L3, CMS, and ALICE Collaborations at LEP and LHC accelerators at CERN (Breskin and Voss, 2009; Lecoq et al., 2017). Further physical programs at high-luminosity HL LHC or FCC will require a substantial increase in the accelerator luminosity. For example, the luminosity in HL LHC from 2026 on will be up to 300 fb^{-1} per year, and the integrated luminosity of 3000 fb^{-1} per decade will be accumulated. At such luminosities, the fluence of charged hadrons of up to 10^{15} p/cm^2 is expected in large pseudorapidity regions of the detectors. To avoid the volumetric factor of radiation damage in the detecting elements, "shaslik"-type or "spaghetti"-type detectors, consisting of detecting elements in a form of thin plates or fibers, respectively, in combination with heavy-metal-based absorber, are shown to be promising in experiments (Korjik and Auffray, 2016; Pauwels, 2017; Zhu, 2015).

Among inorganic scintillators, oxyorthosilicates (LSO or LYSO) and garnet-type crystals (YAG and most recently introduced GAGG) are potential candidates for future radiation detectors tolerant to high-dose-rate irradiation. The crystals have a high light yield, fast scintillation kinetics, and good response to minimum ionizing particles (MIPs) per 1 mm (see Table 1).

---

[*] Corresponding author. Bobruiskaya str. 11, Minsk, Belarus.
E-mail address: mikhail.korjik@cern.ch (M. Korjik).

https://doi.org/10.1016/j.radphyschem.2019.108365
Received 21 February 2019; Received in revised form 10 June 2019; Accepted 13 June 2019

Table 1
Density, light yield, luminescence decay time, MIP losses for ionization, and yield per MIP of several scintillation materials (Lecoq et al., 2017; Alenkov et al., 2019).

Material	Density, g/cm^3	LY, ph/MeV	Decay time, ns	dE/dx @ e$^-$ πMeV/mm	Yield, ph per 1 mm per MIP
$Y_3Al_5O_{12}$: Ce,Mg (YAG)	4.55	30000[a]	80[a]	0.59	17700
Lu_2SiO_5:Ce (LSO:Ce)	7.4	27000	40	0.87	23500
$(Lu_x\text{-}Y_{1\text{-}x})_2SiO_5$:Ce (LYSO:Ce)	7.2	29000	38	0.85	24600
$Gd_3Al_2Ga_3O_{12}$ (GAGG) multidoped	6.63	46000	60 (80%) 120 (20%)	0.81	37200

[a] S. Sykorova, Crytur, private communication 16.10.2018.

It has been shown that co-doping of these materials by divalent metal ions (Mg, Ca) results in a substantial improvement of scintillation response time, though at the expense of a slight decrease in the light yield (Kamada et al., 2015; Lucchini et al., 2016; Nemallapudi et al., 2015).

The composition of the multicomponent garnet-type scintillation materials can be purposefully selected for engineering the band gap and tuning the positions of activator energy levels in respect to the bottom of the conduction band to control the energy transfer processes (Fasoli et al., 2011; Yadav and Singh, 2015). As a result of the engineering of GAGG, a combination of a high light yield, fast scintillation kinetics, and a good energy resolution is achieved (Nikl et al., 2014). This scintillator has good prospects for applications in medical imaging instrumentation and γ-radiation spectrometry and is competitive to Ce-doped and Ce-based self-activated halide scintillators (see, e.g., Lecoq et al., 2017). The codoping of the Ce-doped single crystals affects trapping of nonequilibrium carriers and influences the excitation transfer to activator (Auffray et al., 2018). The engineered GAGG:Ce crystals might compete with the scintillators of Lu_2SiO_5 crystal family LSO:Ce and LYSO:Ce in applications requiring a good time resolution.

Until now, LSO, LYSO and YAG crystals were found to be the most tolerant to irradiation with different types of ionizing radiation (Auffray et al., 2017; Zhang et al., 2014). A high tolerance of optical absorption in GAGG:Ce codoped by Mg and Ti to irradiation with gamma quanta and protons has been demonstrated (Alenkov et al., 2019). Moreover, it was recently manifested that neutrons produce predominantly low-energy gamma-quanta in both GAGG and LYSO (Korzhik et al., 2019; Taggart et al., 2019). These gamma-quanta generate signals, which are usually bellow the detection threshold in high energy physics experiments. However, no estimation of the effect of the irradiation-induced damage on the deterioration of time resolution of the radiation detectors containing GAGG plates or fibers is provided.

The current work is focused on the study of GAGG scintillator capabilities to operate in harsh irradiation environment typical for collider experiments. The results obtained under irradiation with high-energy protons can be adopted to estimate the influence of neutrons and exploited for designing detectors for reactor research, industrial facilities, and spallators. Comparison of the properties of GAGG:Ce with LSO:Ce and LYSO:Ce is provided. Particular attention is paid to the damage in the materials imposed by irradiation by 24 GeV proton beam at CERN PS at different fluences of up to 3.1·10^{15} p/cm^2 and to the study of nonequilibrium carrier dynamics in the crystals after γ-irradiation.

2. Samples and experimental techniques

Two types GAGG crystals were studied. Undoped GAGG crystal was produced at ISMA (Kharkov, Ukraine). GAGG doped with Ce and co-doped with Mg and Ti were grown using high-purity raw materials prepared at the NRS Kurchatov Institute and supplied by FOMOS Crystals (Moscow, Russia).

Ce-doped GAGG crystals without codoping had the highest light yield (LY) of 46000 ph/MeV at room temperature, however, exhibited strong phosphorescence. The crystals codoped with Mg and Mg, Ti had LY at the level of 40000 ph/MeV and have no scintillation decay components longer than 200 ns (Korzhik et al., 2017). Their phosphorescence was substantially reduced to the level bellow 0.01% at ms. The crystals have good coincidence time resolution of 165 ps in the detection of 511 keV gamma-quanta, as shown in (Tamulaitis et al., 2019).

The irradiation of undoped samples with gamma quanta emitted by ^{60}Co to a dose of 2000 Gy has been performed at INP BSU (Minsk) irradiation facilities. The irradiation of multidoped GAGG:Ce,Mg,Ti was performed at CERN irradiation facilities at PS with 24 GeV protons to a fluence of 5·10^{14} p/cm^2. A cube-shaped sample with the side dimension of 1 cm was cut for the study from the same ingot as the sample irradiated to higher fluence in (Alenkov et al., 2019). The sample became available for characterization in two months after irradiation. The details of the measurement procedures are described elsewhere (Auffray et al., 2014, 2017; Auffray et al., 2018).

Differential optical absorption reflecting the dynamics of nonequilibrium carriers was studied before irradiation, 24 h after irradiation, and after saturation of spontaneous relaxation. A pump and probe configuration using a femtosecond laser (200 fs pulse duration) with its output split into a pump beam equipped with wavelength converters enabling selective photoexcitation and a tunably delayed probe beam converted to a white light continuum were exploited. The experimental details for these measurements are described elsewhere (Tamulatis et al., 2018).

3. Radiation damage effects

The induced optical absorption of GAGG:Ce,Mg,Ti in the range of Ce emission at the level of a few m^{-1} after irradiation with protons at a fluence of 3.1·10^{15} p/cm^2 is reported (Alenkov et al., 2019). The change in optical absorption coefficient of GAGG:Ce,Mg,Ti induced by proton irradiation at a fluence of 5x10^{14}p/cm^2 is presented in Fig. 1. No significant induced absorption in the vicinity of luminescence peak of this scintillator (520 nm) was observed. A negligible influence of proton-induced defects on the light yield of the scintillation element was observed, a shift of the photo-peak after irradiation was estimated to be less than 1% of the total light emitted by Ce^{3+}. However, the scintillator performance might be affected by the long- and short-living isotopes introduced in GAGG by proton irradiation.

The content and activity of the long-living proton-induced isotopes in codoped GAGG was simulated using FLUKA code and measured elsewhere (Alenkov et al., 2019). We used these results to verify the correctness of the simulation of isotope set in irradiated crystal and to estimate the influence of the short- and long-living isotopes to the emission noise background of the scintillator.

The proton-induced radioisotopes excite the scintillator and produce a harmful luminescence. This effect is stronger in high-light-yield scintillation materials. The harmful luminescence might be excited by all products of radioactive decay: γ-quanta, alpha and β$^{+,-}$ particles. Taking both short- and long-living isotopes into account in our simulation, we estimated the energy distribution of the number of γ-quanta and β$^{+,-}$ particles emitted by the radio-isotopes formed after irradiation (see Fig. 2). Alpha particles are also emitted by radio-nuclides, however, their quantity was estimated to be negligible. The similar simulations performed for LSO at the same fluence showed approximately

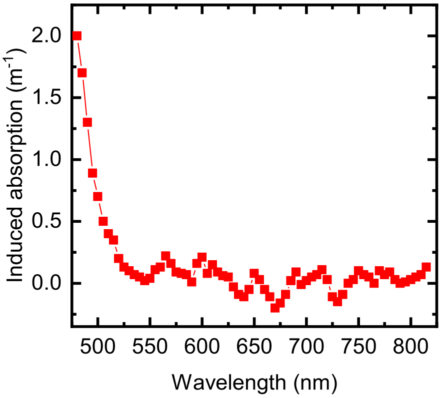

Fig. 1. Change in optical absorption coefficient of GAGG:Ce,Mg,Ti induced by proton irradiation at a fluence of 5x10^{14}p/cm^2.

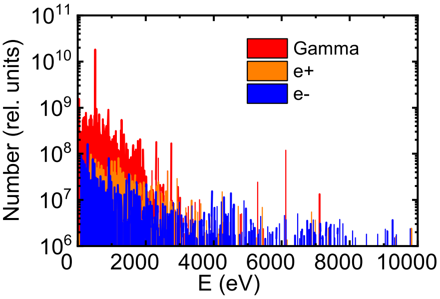

Fig. 2. Energy distribution of the number of gamma-quanta, electrons and positrons emitted by radio-isotopes after irradiation of GAGG at a fluence of 1.5·10^{15} p/cm^2.

similar distribution. This is an indication that the dose absorbed in small-volume GAGG and LSO scintillation crystals is practically the same.

Fig. 3 shows the simulated change of the dose rate due to γ and $\beta^{+,-}$ radio-isotopes in a GAGG plate with the dimensions of 2x2x0.2 cm^3 (typical dimensions of a scintillation element in the "shaslik"-type cell with tungsten absorber). The irradiation profile used in the simulations corresponded to 6 months of operation of HL LHC. The proton flux of 9.7·10^7 p/cm^2/s and the total fluence of 1.5·10^{15} p/cm^2 were used in the calculations. A similar dependence obtained for a LSO (LYSO) detecting elements with the same dimensions did not show a significant difference in the behavior of the residual nuclei dose rate.

The dose rate increases at the beam front and decreases after the beam termination with a time constant of ~10^4 s, which is a typical decay time of the most short-lived isotopes. At the beam termination, the dose rate decreases by a factor of ~100, what means that the dominant fraction of the dose rate is caused by the short-lived isotopes.

The radionuclides in the scintillator excite the harmful luminescence, which contributes, similarly to phosphorescence, to the optical noise. The intensity of the harmful luminescence I_{noise} in the entire sample can be estimated by using the following formula:

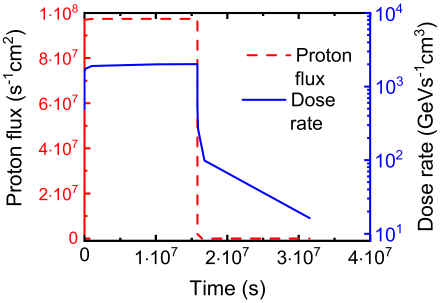

Fig. 3. Time evolution of proton flux (dashed red line) and residual nuclei dose rate (solid blue line) in a single GAGG detecting element with dimensions of 2x2x0.2 cm^3. (For interpretation of the references to colour in this figure legend, the reader is referred to the Web version of this article.)

$$I_{noise}[\text{ph/s}] = G\cdot V\cdot LY, \tag{1}$$

where G is the absorbed dose rate [in MeV/(s·cm^3)], V is the sample volume (cm^3), and LY is the light yield of the material (ph/MeV).

The scintillation signal is formed within a limited time interval determined by the scintillation kinetics. Meanwhile, the optical noise is emitted permanently. Consequently, for a correct comparison of the scintillation signal and the noise, it is necessary to reduce the value of the harmful luminescence intensity in accordance with the specific time window, the time interval of 25 ns between the collisions of the beams, in our case. The contribution of harmful luminescence photons in the noise pedestal can be estimated as in (Shao, 2007). The harmful luminescence also leads to broadening of the energy resolution by adding the noise energy equivalent ΔE_{noise}. For the time window Δt, the value of ΔE_{noise} can be estimated as:

$$\Delta E_{\text{noise}} = \frac{2.35\sqrt{G\cdot V\cdot \text{LY}\cdot \Delta t}}{\text{LY}\cdot\eta}. \tag{2}$$

Here, η is the fraction of the scintillation photons emitted during the time window Δt = 25 ns.

The results of the simulation of the harmful luminescence intensity within the time window of 25 ns, its contribution into the noise pedestal and the noise energy equivalent of GAGG and LSO samples with the same dimensions (2x2x0.2 cm^3) at the moment of termination of the irradiation with the dose rate profile shown in Fig. 3 are summarized in Table 2.

As evident in Table 2, the effect of activation by hadrons in LSO and GAGG is practically similar.

The high radiation tolerance of GAGG might be explained by the influence of the sublattice of lattice-building gadolinium. Gadolinium ions have numerous energy levels of electronic configuration f^7 located within a large energy range in the upper part of the band gap. A high concentration of Gd^{3+} ions in the crystal inhibits the long-term

Table 2
Contribution of harmful luminescence in optical noise, noise pedestal, and noise energy equivalent within 25 ns gate in GAGG and LSO crystals with dimensions of 2x2x0.2 cm^3.

Scintillator	GAGG	LSO
Additional noise intensity, ph	1600	1350
Additional pedestal, keV	156	108
Additional noise energy equivalent, keV	9.2	6.9

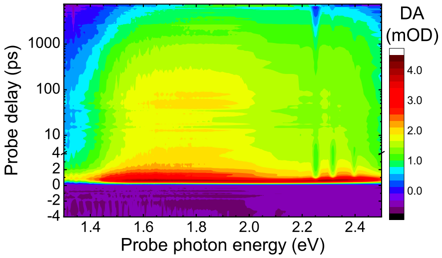

Fig. 4. Time evolution of the spectrum of differential absorption (see color scale) induced by a short pulse in undoped GAGG crystal at room temperature. (For interpretation of the references to colour in this figure legend, the reader is referred to the Web version of this article.)

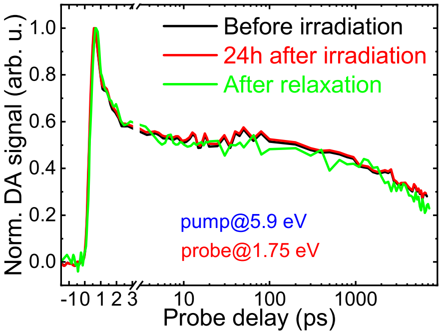

Fig. 5. Kinetics of differential optical absorption at 1.75 eV induced by a 200-fs pulse at 5.9 eV in undoped GAGG crystal before irradiation, 24 h after irradiation, and after spontaneous relaxation.

stabilization of electronic-type colour centers with the ground energy states more than 2 eV below the bottom of the conduction band. Therefore, no energy transfer from the colour centers to Gd^{3+} sublattice and further to Ce^{3+} ions occurs.

As discussed above, the irradiation-induced color centers do not have substantial influence on reabsorption in GAGG:Ce. The spectrum of irradiation-induced optical absorption can be easier revealed in undoped crystals, where it is not masked by a strong influence of activators (Korjik and Auffray, 2016; Auffray et al., 2017). As in other garnets (Autrata et al., 1978; Kvapil et al., 1981), the irradiation of undoped GAGG crystals does introduce certain amount of colour centers having absorption over visible spectral range, however, the induced absorption is not strong enough to cause significant reabsorption of the Ce^{3+} emission peaked at 520 nm. Moreover, Ce-doping substantially reduces the density of colour centers in oxide crystals (Auffray et al., 2014, 2017) and, consequently, increases the radiation hardness of GAGG:Ce.

4. Timing properties of codoped GAGG crystal

As reported before (Auffray et al., 2018; Tamulatis et al., 2018), the time resolution of GAGG:Ce is influenced by carrier trapping and can be controlled by appropriate co-doping. To study the influence of irradiation on trapping, we performed the measurements of dynamics of nonequilibrium carriers using optical pump and probe technique in undoped GAGG crystal, in which a large concentration of colour centers can be created even under gamma-irradiation. As mentioned above, the formation of colour centers is suppressed in Ce-doped crystals. Thus, the study of undoped crystals can provide information on the interaction of the Gd sub-lattice and defects in the crystal, since Gd^{3+} ions play a major role in excitation transfer to emitting Ce^{3+} ions. It is most important to understand the influence of colour centers and traps in the irradiated crystals on slowing the excitation transfer. This effect is hardly observable in proton-irradiated crystals, mainly because the samples are available for studying only in two months after irradiation (due to radiation safety reasons). Pump photon energy of 5.9 eV selected for generation of nonequilibrium carriers corresponded to the edge of band-to-band absorption of GAGG and excited electrons to shallow traps. To avoid the contribution to the differential absorption by the carriers populating the states of Ce^{3+}, the undoped GAGG was studied.

The differential absorption, i.e. the difference between the optical absorption with and without short-pulse (200 fs) excitation, as a function of probe photon energy and time after the excitation, is presented for GAGG crystal at room temperature in Fig. 4.

The differential absorption has two components. They strongly overlap spectrally but have substantially different decay time (see Fig. 5). The first component with a characteristic decay time of 2 ps reflects the density of free carriers, while the second, slow component decaying with the time constant of ~50 ns is caused by the absorption of trapped carriers.

No changes in the kinetics of both components have been observed after irradiation. This observation leads to the conclusion that the irradiation damage effects do not affect the carrier trapping and, consequently, the timing properties of GAGG scintillator.

5. Conclusions

The proton irradiation at a fluence of $5{\cdot}10^{14}$ p/cm^2 imposes no significant change in the optical transmittance of GAGG:Ce scintillators without and with Mg codoping. Thus, the proton-induced defects have no influence on the output of the light emitted by Ce^{3+} in the conditions typical of the future detectors at LHC operating at high luminosity. The contribution of harmful luminescence to optical noise, noise pedestal, and noise energy equivalent in GAGG is similar to that in LSO scintillators and is acceptable for application. The irradiation does not affect the kinetics of free carrier relaxation and the trapping rate; thus, the irradiation damage does not affect the carrier trapping and, consequently, the timing properties of GAGG scintillator. The obtained results show that the multicomponent garnet-type GAGG:Ce crystals could be prospective candidates for new detectors for reactor research facilities, spallators, and high-energy hadron colliders with harsh radiation environment.

Acknowledgement

This work has been carried out in the frame of Crystal Clear Collaboration with support of COST Action TD1401 (FAST), the Marie Skłodowska-Curie grant agreement No 644260 (Intelum); the research at Vilnius University was supported by the EU Social Fund grant 09.3.3-LMT-K-712-01-0013 under grant agreement with the Research Council of Lithuanian; the research at National Research Center Kurchatov Institute was supported by grant No. 14.W03.31.0004 of Russian Federation Government. Authors cordially thank Dr. A. Singovski for fruitful cooperation.

References

Alenkov, V., Buzanov, O., Dosovitskiy, G., Egorychev, V., Fedorov, A., Golutvin, A., Guz, Y., Jacobsson, R., Korjik, M., Kozlov, D., Mechinsky, V., Schopper, A., Semennikov, A., Shatalov, P., Shmanin, E., 2019. Irradiation studies of a multi-doped

$Gd_3Al_2Ga_3O_{12}$ scintillator. Nucl. Instruments Methods Phys. Res. Sect. A Accel. Spectrometers, Detect. Assoc. Equip. 916, 226–229. https://doi.org/10.1016/j.nima.2018.11.101.

Auffray, E., Augulis, R., Fedorov, A., Dosovitskiy, G., Grigorjeva, L., Gulbinas, V., Koschan, M., Lucchini, M., Melcher, C., Nargelas, S., Tamulaitis, G., Vaitkevičius, A., Zolotarjovs, A., Korzhik, M., 2018. Excitation transfer engineering in Ce-doped oxide crystalline scintillators by codoping with alkali-earth ions. Phys. Status Solidi Appl. Mater. Sci. 215, 1–10. https://doi.org/10.1002/pssa.201700798.

Auffray, E., Fedorov, A., Dormenev, V., Houžvička, J., Korjik, M., Lucchini, M.T., Mechinsky, V., Ochesanu, S., 2017. Optical transmission damage of undoped and Ce doped $Y_3Al_5O_{12}$ scintillation crystals under 24 GeV protons high fluence. Nucl. Instruments Methods Phys. Res. Sect. A Accel. Spectrometers, Detect. Assoc. Equip. 856, 7–10. https://doi.org/10.1016/j.nima.2016.09.037.

Auffray, E., Fedorov, A., Korjik, M., Lucchini, M., Mechinski, V., Naumenko, N., Voitovich, A., 2014. Radiation damage of oxy-orthosilicate scintillation crystals under gamma and high energy proton irradiation. IEEE Trans. Nucl. Sci. 61, 495–500. https://doi.org/10.1109/TNS.2013.2285249.

Autrata, R., Schauer, P., Kvapil, J., Kvapil, J., 1978. A Single Crystal of YAG-New Fast Scintillator in SEM Letters to the Editor A Single Crystal of 10–12.

Breskin, A., Voss, R. (Eds.), 2009. The CERN Large Hadron Collider: Accelerator and Experiments. CERN, Geneva.

Fasoli, M., Vedda, A., Nikl, M., Jiang, C., Uberuaga, B.P., Andersson, D.A., McClellan, K.J., Stanek, C.R., 2011. Band-gap engineering for removing shallow traps in rare-earth $Lu_3Al_5O_{12}$ garnet scintillators using Ga^{3+} doping. Phys. Rev. B Condens. Matter 84, 1–4. https://doi.org/10.1103/PhysRevB.84.081102.

Kamada, K., Nikl, M., Kurosawa, S., Beitlerova, A., Nagura, A., Shoji, Y., Pejchal, J., Ohashi, Y., Yokota, Y., Yoshikawa, A., 2015. Alkali earth co-doping effects on luminescence and scintillation properties of Ce doped $Gd_3Al_2Ga_3O_{12}$ scintillator. Opt. Mater. 41, 63–66. https://doi.org/10.1016/j.optmat.2014.10.008.

Korjik, M., Auffray, E., 2016. Limits of inorganic scintillating materials to operate in a high dose rate environment at future collider experiments. IEEE Trans. Nucl. Sci. 63, 552–563. https://doi.org/10.1109/TNS.2016.2527701.

Korzhik, M., Brinkmann, K.-T., Dosovitskiy, G., Dormenev, V., Fedorov, A., Komar, D., Kozemiakin, V., Kozlov, D., Mechinsky, V., Zaunick, H.-G., Yashin, I., Iyudin, A., Bogomolov, V., Svertilov, S., Maximov, I., 2019. Detection of neutrons in a wide energy range with crystalline $Gd_3Al_2Ga_3O_{12}$, Lu_2SiO_5 and $LaBr_3$ doped with Ce scintillators. Nucl. Instruments Methods Phys. Res. Sect. A Accel. Spectrometers, Detect. Assoc. Equip. 931, 88–91. https://doi.org/10.1016/j.nima.2019.04.034.

Korjik, M., Alenkov, V., Borisevich, A., Buzanov, O., Dormenev, V., Dosovitskiy, G., Dosovitskiy, A., Fedorov, A., Kozlov, D., Mechinsky, V., Novotny, R.W., Tamulaitis, G., Vasiliev, V., Zaunick, H.-G., Vaitkevičius, A.A., 2017. Significant improvement of GAGG:Ce based scintillation detector performance with temperature decrease. Nucl. Instruments Methods Phys. Res. Sect. A Accel. Spectrometers, Detect. Assoc. Equip. 871, 42–46.

Kvapil, J., Kvapil, J., Manek, B., Perner, B., 1981. Czochralski growth of YAG:Ce in a reducing protective atmosphere. J. Cryst. Growth 52, 542–545. https://doi.org/10.1016/0022-0248(81)90336-5.

Lecoq, P., Gektin, A., Korzhik, M., 2017. Inorganic Scintillators for Detector Systems. Springer International Publishing. https://doi.org/10.1007/978-3-319-45522-8.

Lucchini, M.T., Babin, V., Bohacek, P., Gundacker, S., Kamada, K., Nikl, M., Petrosyan, A., Yoshikawa, A., Auffray, E., 2016. Effect of Mg^{2+} ions co-doping on timing performance and radiation tolerance of Cerium doped $Gd_3Al_2Ga_3O_{12}$ crystals. Nucl. Instruments Methods Phys. Res. Sect. A Accel. Spectrometers, Detect. Assoc. Equip. 816, 176–183. https://doi.org/10.1016/j.nima.2016.02.004.

Nemallapudi, M.V., Gundacker, S., Lecoq, P., Auffray, E., Ferri, A., Gola, A., Piemonte, C., Gundacker, S., Nemallapudi, M.V., Piemonte, C., Auffray, E., 2015. Sub-100 ps coincidence time resolution for positron emission tomography with LSO:Ce codoped with Ca. Phys. Med. Biol. 60, 4635–4649. https://doi.org/10.1088/0031-9155/60/12/4635.

Nikl, M., Kamada, K., Babin, V., Pejchal, J., Pilarova, K., Mihokova, E., Beitlerova, A., Bartosiewicz, K., Kurosawa, S., Yoshikawa, A., 2014. Defect engineering in Ce-doped aluminum garnet single crystal scintillators. Cryst. Growth Des. 14, 4827–4833. https://doi.org/10.1021/cg501005s.

Pauwels, K., 2017. Calorimeter designs based on fibre-shaped scintillators. In: Korjik, M., Gektin, A. (Eds.), Engineering of Scintillation Materials and Radiation Technologies. Springer International Publishing, pp. 231–241. https://doi.org/10.1007/978-3-319-68465-9.

Shao, Y., 2007. A new timing model for calculating the intrinsic timing resolution of a scintillator detector. Phys. Med. Biol. 52, 1103–1117. https://doi.org/10.1088/0031-9155/52/4/016.

Taggart, M.P., Nakhostin, M., Sellin, P.J., 2019. Investigation into the potential of GAGG:Ce as a neutron detector. Nucl. Instruments Methods Phys. Res. Sect. A Accel. Spectrometers, Detect. Assoc. Equip. 931, 121–126. https://doi.org/10.1016/j.nima.2019.04.009.

Tamulatis, G., Dosovitskiy, G., Gola, A., Korjik, M., Mazzi, A., Nargelas, S., Sokolov, P., Vaitkevičius, A., Tamulaitis, G., Dosovitskiy, G., Gola, A., Korzhik, M., Mazzi, A., Nargelas, S., Sokolov, P., Vaitkevičius, A., 2018. Improvement of response time in GAGG:Ce scintillation crystals by magnesium codoping. J. Appl. Phys. 124, 215907. https://doi.org/10.1063/1.5064434.

Tamulaitis, G., Vasil'ev, A., Korzhik, M., Mazzi, A., Gola, A., Nargelas, S., Vaitkevičius, A., Fedorov, A., Kozlov, D., 2019. Improvement of the time resolution of radiation detectors based on $Gd_3Al_2Ga_3O_{12}$ scintillators with SiPM readout. IEEE Transactions on Nuclear Science. . https://doi.org/10.0.4.85/TNS.2019.2919898.

Yadav, A.K., Singh, P., 2015. A review of structure of oxide glasses by Raman spectroscopy. RCS Adv 5, 67583–67609. https://doi.org/10.1039/C5RA13043C.

Zhang, L., Mao, R., Yang, F., Zhu, R.Y., 2014. LSO/LYSO crystals for calorimeters in future HEP experiments. IEEE Trans. Nucl. Sci. 61, 483–488. https://doi.org/10.1109/TNS.2013.2279993.

Zhu, R.Y., 2015. The next generation of crystal detectors. J. Phys. Conf. Ser. 587. https://doi.org/10.1088/1742-6596/587/1/012055.

Paper P17

Improvement of the timing properties of Ce-doped oxyorthosilicate LYSO scintillating crystals

G. Tamulaitis, E. Auffray, A. Gola, M. Korzhik, A. Mazzi, V. Mechinski, S. Nargelas, Y. Talochka, **A. Vaitkevičius**

J. Phys. Chem. Solids. 139 (2020) 109356.

doi:10.1016/j.jpcs.2020.109356.

Journal of Physics and Chemistry of Solids 139 (2020) 109356

Contents lists available at ScienceDirect

Journal of Physics and Chemistry of Solids

journal homepage: http://www.elsevier.com/locate/jpcs

Improvement of the timing properties of Ce-doped oxyorthosilicate LYSO scintillating crystals

G. Tamulaitis [a,*], E. Auffray [b], A. Gola [c], M. Korzhik [d], A. Mazzi [c], V. Mechinski [d], S. Nargelas [a], Y. Talochka [d], A. Vaitkevičius [a], A. Vasil'ev [e]

[a] *Institute of Photonics and Nanotechnology, Vilnius University, Saulėtekio Al. 3, Vilnius, Lithuania*
[b] *CERN, Geneva, Switzerland*
[c] *Fondazione Bruno Kessler, Via Sommarive, 18, Povo, Trento, Italy*
[d] *Research Institute for Nuclear Problems, Bobruiskaya Str. 11, Minsk, Belarus*
[e] *Skobeltsyn Institute of Nuclear Physics of Moscow State University, Leninskie Gory, 1(2), Moscow, Russia*

ABSTRACT

The aim of this work has been to improve the time resolution of radiation detectors for future high-energy physics experiments and medical imaging applications. Ce-doped oxyorthosilicate Lu_2SiO_5:Ce (LSO) and mixed oxyorthosilicate $Lu_{1.6}Y_{0.4}SiO_5$:Ce (LYSO) have been investigated as prospective scintillators for such high-time-resolution applications. A differential optical absorption technique with sub-picosecond time resolution upon selective excitation of Ce^{3+} ions to different excited states has been adopted to study carrier dynamics in these scintillators, and coincidence time resolution measured using 511 keV γ-quanta has been exploited to test their timing properties. A delay in population of the emitting level of Ce^{3+} has been observed, and is interpreted in terms of electron trapping, which is more pronounced in mixed yttrium-containing LYSO crystals due to composition fluctuations. It is shown that the delay, which affects the luminescence response time, can be eliminated by co-doping of LYSO:Ce with calcium at concentrations as low as 5 ppm. The faster kinetics of electron transfer correlates with a better coincidence time resolution. Thermalization and spatial distribution of non-equilibrium carriers has been studied theoretically to link the results obtained by the time-resolved differential optical absorption technique with the behavior of the non-equilibrium carriers generated by irradiation.

1. Introduction

At present, time resolution is the property of scintillation detectors that requires substantial improvement for their applications in future high-luminosity high-energy physics experiments and in medical imaging equipment with a better spatial resolution and full-body scanning capability. As the requirements for time resolution move towards the ambitious target of 10 ps and the readout electronics continues to show spectacular progress, the timing properties of the scintillator material constitute a bottleneck in the development of fast radiation detectors. Scintillators of the family of lutetium oxyorthosilicate Lu_2SiO_5:Ce (LSO) are currently considered as having excellent prospects for fast timing applications. Originally, this scintillator was designed for well-logging applications [1] as a substitute for BGO. Though LSO is seven times faster and three times brighter than BGO [2], its application in oil field services was limited by performance deterioration at high temperatures. However, it could be effectively applied in the field of medical imaging, in particular positron emission tomography (PET) [3]. LSO scintillators are especially promising for developing PET devices operating in time-of-flight (TOF) mode, which enables an improved spatial resolution of PET images [4], introducing multi-modal systems, and moving progressively towards the ambitious target of designing a full-body PET scanner. The most recent generations of PET scanners have been equipped with silicon photomultipliers (SiPMs), enabling substantially improved read-out properties, and the speed of the electronics for data acquisition and signal processing has been effectively boosted [5,6]. As a result, the material properties of scintillators constitute the limiting factor in improving the timing properties of PET devices. A substantial improvement of the properties of LSO was achieved by the introduction of mixed oxyorthosilicate $(Lu_xY_{1\text{-}x})_2SiO_5$:Ce (LYSO), with the lutetium ions partially replaced by yttrium [7], in a similar way as in another Lu-based system, the perovskites [8]. This substitution reduced the scintillation afterglow and improved the light yield of the material. In addition, it was shown that annealing of oxyorthosilicates in an oxidizing atmosphere diminishes the amount of oxygen vacancies in the material and improves the time response of these scintillators [9].

Another approach for improving the properties of LYSO:Ce is co-doping of the crystals with aliovalent ions. The scintillation properties

---

[*] Corresponding author.
E-mail address: gintautas.tamulaitis@ff.vu.lt (G. Tamulaitis).

https://doi.org/10.1016/j.jpcs.2020.109356
Received 27 August 2019; Received in revised form 9 January 2020; Accepted 10 January 2020

of oxyorthosilicate crystals co-doped with Ce and divalent calcium are significantly improved: the light yield increases, the luminescence decay becomes faster, and the afterglow is diminished [10–13]. The positive effect of aliovalent co-doping has also been observed in other oxide and halide scintillation crystals, such as Y_2SiO_5:Ce, $LaBr_3$:Ce, and $CeBr_3$ [13–15].

The influence of aliovalent doping on scintillation properties is being intensively studied in Mg-doped $Gd_3Al_2Ga_3O_{12}$:Ce (GAGG:Ce), a highly promising scintillator for applications in various imaging devices and industry (see, e.g., Refs. [2,16] and references therein). It was demonstrated that the introduction of even a small amount of magnesium at a level of 10 ppm significantly improved the response times of radiation detectors based on GAGG:Ce,Mg coupled with SiPMs [17]. It has been shown that the carrier dynamics governing the luminescence response time is strongly affected by carrier trapping, which is enhanced by the traps formed as a result of composition fluctuations in mixed GAGG [18, 19]. Though the introduction of Ga into GAGG shifts the bottom of the conduction band downwards and many traps become buried in the conduction band [20,21], local deviations in the mixed garnet composition introduce trapping states of different kinds. Fluctuations in the distribution of different ions in a mixed crystal introduce an irregular modulation of the bottom of the conduction band, which results in the formation of randomly distributed shallow trapping centers. These centers slow down population of the radiating level of Ce^{3+} ions and lengthen the leading edge of the scintillation pulse. Aliovalent co-doping of GAGG results in the formation of centers capable of capturing the trapped carriers and facilitating their nonradiative recombination. As a result, the slow contribution of trapped carriers to the formation of the leading edge of luminescence response is reduced, though at the expense of the light yield, since a larger fraction of non-equilibrium carriers is channeled through nonradiative recombination due to the centers introduced by co-doping.

LYSO, similarly to GAGG, is a mixed crystal. Random modulation of the bottom of the conduction band occurs due to the irregular distribution of Lu and Y ions. In general, the substitution of Lu by Y leads to a minor change of the band structure; the most important change occurs only at the bottom of the conduction band. Due to a smaller effective nuclear charge of Y, the band gap in pure Lu_2SiO_5 is about 0.2 eV smaller than that in Y_2SiO_5. Thus, in locations in LYSO with excessive Lu ions, the conduction band has a dip, which might serve as a trapping center for electrons.

The differential optical absorption technique in pump-probe configuration has previously been demonstrated to be a useful tool for studying fast carrier dynamics in CsI:Tl, NaI:Tl, and SrI_2:Eu [22], $LaBr_3$:Ce [23], GAGG:Ce [17,18], YAG and LuAG [24], YAP-LuAP [25], and $CeBr_3$ [26]. In this work, the technique has been exploited to study the influence of trapping on carrier dynamics in LSO:Ce and LYSO:Ce. The pump photon energy was selected to resonantly excite specific centers in these scintillators. As discussed in Ref. [27], the resonant excitation of Ce^{3+} to higher excitation levels is useful to imitate the last stages of migration of non-equilibrium carriers after excitation with ionizing radiation. In this work, we have exploited this technique to study the migration of electrons to Ce^{3+} ions, the influence of their trapping, and the effect of co-doping of LYSO with calcium on the kinetics of Ce^{3+} population. The dependence of the electron thermalization length on the electron kinetic energy has been calculated. To link the peculiarities in carrier dynamics observed after femtosecond-pulse optical excitation with the timing properties of the material affected by ionizing radiation, coincidence time resolution experiments have been performed.

2. Experimental

Ce-doped lutetium yttrium oxyorthosilicates $Lu_{1.6}Y_{0.4}SiO5$ with different levels of co-doping by calcium used in this study were fabricated by CPI (USA), the Shanghai Project Crystal Co., Ltd. (China), and Saint Gobain (France). A typical sample of LSO:Ce was also used for comparison. Oxyorthosilicate ingots were grown by the Czochralski method in inductively heated iridium crucibles in an atmosphere containing nitrogen with a small fraction of oxygen (<1%). Block-shaped samples with dimensions of 3 × 3 × 5 mm^3 for coincidence time resolution (CTR) measurements and 10 × 10 × (1–3) mm^3 for measurements by the optical pump-and-probe technique were prepared from the same crystal ingots. All surfaces of the blocks were polished.

The pump-and-probe technique was used to study the density of non-equilibrium carriers. A short (200 fs) light pulse generated by a Yb:KGW laser was processed by harmonics generators and parametric amplifiers. Tuning of the pump photon energy enabled selective excitation of the Ce^{3+} activator in the crystals under study. The density of non-equilibrium carriers was monitored by spectrally converting the probe pulse in a sapphire plate to a white light continuum (1.3–2.7 eV; 950–460 nm). An optomechanical delay line was used to vary the delay of the probe. The differential absorption (DA), i.e., the difference between the optical absorption probed without pumping and with pumping at a certain delay after the pump pulse, was measured. The measurement technique and procedure are presented in more detail in Ref. [27]. The time resolution in such experiments is limited by the laser pulse duration, which was about 200 fs.

The pump pulse energy fluences (0.9 mJ/cm^2 at a photon energy of 3.47 eV, 2.3 mJ/cm^2 at 4.82 eV, and 0.23 mJ/cm^2 at 5.91 eV) used in our experiments corresponded to densities of pump photons per excited sample volume at least four orders of magnitude smaller than the density of Ce ions at a doping level of 100 ppm. Therefore, as expected and tested before performing the reported measurements, the variation of pump fluence around these values does not affect the kinetics of the transient absorption.

The DA intensity depends on the density of final states for the optical transitions, the absorption cross-section, and the density of carriers absorbing the probe light. For non-equilibrium electrons and holes generated by the pump beam, the DA signal is proportional to their densities, since the density of final states and the absorption cross-section are constant. Meanwhile, the latter two parameters influence the spectrum and the intensity of the DA response.

CTR was measured using SiPMs developed and manufactured at Fondazione Bruno Kessler (FBK). These SiPMs are based on NUV-HD technology employing a p-on-n junction [28]. The detectors employed in this study had an active area of 4 × 4 mm^2, a cell pitch of 35 μm, and have been demonstrated to show a photon detection efficiency (PDE) exceeding 55% at 420 nm [29]. For these experiments, the samples were coupled to SiPMs using Cargille Meltmount optical glue (refractive index $n = 1.539$) after being wrapped in Teflon tape. The experimental setup for the time coincidence measurements comprised a pair of identical detection modules equidistantly placed on opposite sides of a ^{22}Na source simultaneously emitting two 511 keV γ-ray photons. Each detection module was composed of an FBK SiPM and a double-stage amplifier with dual output. The first amplifier output was used for selection of 511 keV photopeak events by measuring the energy of the detected γ-photons. Charge integration over a 500 ns time window was used for energy discrimination. The second stage involved pole-zero filtering [30] and ensured a high time resolution. Varying the voltage threshold and the excess bias of the SiPM at different operating temperatures allowed us to establish the optimal operational conditions for each set of samples and to measure the optimal CTR.

3. Results

The optical absorption spectra of the studied LYSO and LSO samples are presented in Fig. 1. The absorption spectrum of LSO:Ce in the studied spectral range features three bands due to optical transitions from the 4f ground state to three lowest excited states of the Ce^{3+} activator ion $5d_{1,2,3}$ level split by a low-symmetry crystal field. The intensity of the absorption bands is slightly dependent on the light polarization with respect to the crystallographic orientation of the sample, since LSO has a

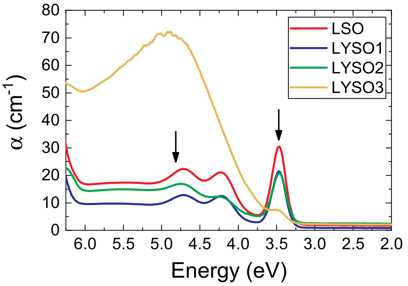

Fig. 1. Absorption spectra of LSO and LYSO crystals doped with Ce (LYSO1) and co-doped with increasing contents of Ca (5 ppm in LYSO2 and 30 ppm in LYSO3). Excitation photon energies used in pump and probe experiments are indicated by arrows.

monoclinic lattice and Ce ions occupy two sites in the lattice with different surroundings [1]. The spectral overlap of the two absorption bands due to the two different positions of Ce^{3+} in the LSO lattice, Ce(1) and Ce(2), is too strong to be resolved at room temperature. The ground state of Ce^{3+} is split into two sublevels, $^4F_{5/2}$ and $^4F_{7/2}$ [31]; however, only the lower spin-orbital sublevel causes absorption, since the upper sublevel is 0.24 eV higher in energy and is not populated at room temperature. Introduction of yttrium into the lattice of LSO does not significantly affect the spectral position of the Ce-ion-related absorption bands (compare the spectra of the LSO and LYSO1 samples in Fig. 1).

The Ce^{3+} concentrations in LSO and LYSO1-2 are very similar, whereas that in LYSO3 is lower by a factor of three. We estimate that LSO and LYSO1-2 contain approximately 1000 ppm of Ce. The intensities of the absorption bands mainly depend on the doping level, but may also be affected by the distribution of cerium valence states between Ce^{3+} and Ce^{4+}.

The introduction of calcium (5 ppm in sample LYSO2 and 30 ppm in LYSO3) gives rise to a broad absorption band (full-width at half-maximum, FWHM, of 1.66 eV) centered at 4.9 eV, as observed previously [11]. The formation of this band has been ascribed to an increased fraction of Ce ions in charge state Ce^{4+}, observed in Ca-co-doped LSO:Ce by X-ray absorption near-edge spectroscopy (XANES), and attributed to absorption through charge-transfer transitions from oxygen to Ce^{4+} ions [13]. The pump beam photon energies in our DA experiments (3.47 and 4.75 eV) were selected in accordance with the spectra presented in Fig. 1, and are indicated by arrows therein.

Upon excitation with 3.47 eV photons, transitions of Ce^{3+} to the first excited level are expected. CT transitions from oxygen orbitals forming the top of the valence band to the unoccupied electron state in the Ce^{4+} ion are also feasible. According to Ref. [32], a negligible fraction of Ce ions in LSO:Ce are in the state Ce^{4+}, but the fraction increases with Ca-co-doping. Similar behavior of Ce charge state is also expected for LYSO:Ce. Accordingly, two DA components are evident in the data carpets representing the DA intensity as a function of the time delay between pump and probe pulses and the probe photon energy (see Fig. 2) and in cross-sections of such carpets presented in Fig. 3 to show the kinetics of the DA signal at two typical probe photon energies. The spectrum of the first feature is approximately flat in the studied range (1.3–2.4 eV). The decay of this DA component is in the nanosecond domain and coincides with the luminescence decay reflecting the decay of the population of the first excited state of Ce^{3+}. Consequently, this component may be attributed to absorption from the first excited level of Ce^{3+}. The fast DA decay component is spectrally centered at around 2.3

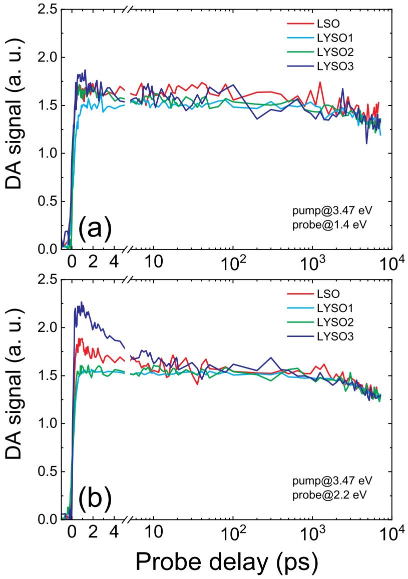

Fig. 3. Kinetics of differential absorption of LSO and three LYSO:Ce samples (indicated) at two probe energies, 1.4 eV (a) and 2.2 eV (b), after pumping with 3.47 eV photons. The arbitrary units are normalized for all of the samples by taking into account their thicknesses and absorption coefficients.

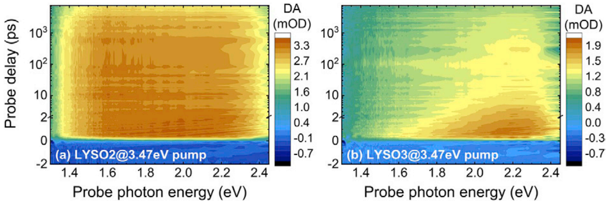

Fig. 2. Dependence of the intensity of differential absorption (color-coded as indicated in the sidebar) as a function of probe photon energy and delay between pump and probe beams in LYSO:Ce with (a) low (sample LYSO2) and (b) high (sample LYSO3) levels of Ca-co-doping.

eV and has a characteristic decay time of about 5 ps. This DA component might be attributed to absorption by free holes generated due to pump-induced CT transitions from the valence band to Ce^{4+}. This component is more pronounced for samples with a high Ca content (see the data carpet for LYSO3 in Fig. 2). The time-integrated contribution of this fast component is small compared with the contribution of the component decaying at the rate of luminescence decay.

As is evident from Fig. 3, the fast component is weak in non-co-doped LSO, absent for non-co-doped or slightly co-doped LYSO:Ce crystals (samples LYSO1 and LYSO2), but becomes pronounced with an elevated content of Ca (sample LYSO3 with a Ca content of 30 ppm). This enhancement can be explained by an increased density of Ce ions in state Ce^{4+} in the co-doped crystal, as would be expected in view of the results presented in Ref. [13]. The DA presented in Fig. 3 is normalized for each sample according to its thickness and absorption coefficient for the pump pulse to compare the DA responses of the same number of photogenerated carriers. Note that the slow DA component has the same absolute value and kinetics in all of the studied samples. This feature supports the assumption that the slow component is caused exclusively by absorption of the probe photons by electrons occupying the lowest excited state of the Ce^{3+} ion. Meanwhile, the fast component emerges on top of the slow one, as might be expected, provided that some proportion of Ce^{3+} is converted into Ce^{4+} due to Ca-co-doping. Note, however, that the time-integrated contribution of the fast component is rather small compared to that of the slow component.

The pump photon energy of 4.82 eV corresponds to an optical transition in the Ce^{3+} ion from the ground state to the third excited state, which is in the conduction band. The photoexcited electron can intracentrally relax to the lowest excited state of Ce^{3+} and recombine radiatively thereafter, as in resonant excitation to the lowest excited state, or leave the Ce^{3+} to become a free electron in the conduction band. The conditions of CT excitation from the oxygen orbitals in the valence band to the ground state of Ce^{4+} are similar to those upon excitation with 3.47 eV photons. In addition, the photon energy of 4.82 eV corresponds to the peak of the broad absorption band appearing in the absorption spectrum of the Ca-co-doped crystal (see Fig. 1). The assumption that this absorption band is at least partially caused by optical transitions from the valence band to defect centers induced by Ca-co-doping leads to the conclusion that additional holes must be generated through this mechanism upon 4.82 eV pumping. This conclusion is in line with the observation that free hole absorption peaked at 2.2 eV is enhanced by increasing the pump photon energy from 3.47 to 4.82 eV.

The DA kinetics at two typical probe photon energies are presented Fig. 4. A new fast component appears in the response, which is especially well pronounced in sample LYSO3 at the probe photon energy of 1.4 eV (see Fig. 4a). This component is probably related to the generation of free electrons, which were not generated at a pump photon energy of 3.84 eV. This contribution of electrons overlaps with the contribution of free holes in the vicinity of 2.2 eV, at which the free hole absorption is most pronounced. Consequently, the DA kinetics in this spectral region is less informative (see the DA kinetics at 2.2 eV in Fig. 4b).

The generation of free electrons also results in a slower front edge of the DA response observed for non-co-doped samples. Co-doping with Ca eliminates the slow rise of the DA response.

The fast decay component and delayed rise in DA kinetics are well pronounced in non-co-doped LYSO:Ce upon pumping with 5.91 eV photons. This photon energy is still below the band gap of LYSO, but sufficiently high for optical transitions from the valence band to defect-related states below the bottom of the conduction band. The excitation of Ce^{3+} to higher excited states or CT transitions to the Lu 5d state [33] forming the conduction band is still expected, as after Ce3+ excitation at lower pump photon energies, as discussed above.

Data carpets comparing the DA in LSO:Ce and LYSO:Ce are presented in Fig. 5.

Typical DA kinetics of LYSO:Ce are presented in Fig. 6b. Within the first 10 ps after pumping, the kinetics in the low-energy part of the probing spectrum is dominated by the fastest decay component. The slow rising component is better pronounced for probe photons of higher energy. The same features as in LYSO:Ce may also be qualitatively traced in the DA kinetics in LSO:Ce (see Fig. 6a), except that the rising component is substantially less pronounced.

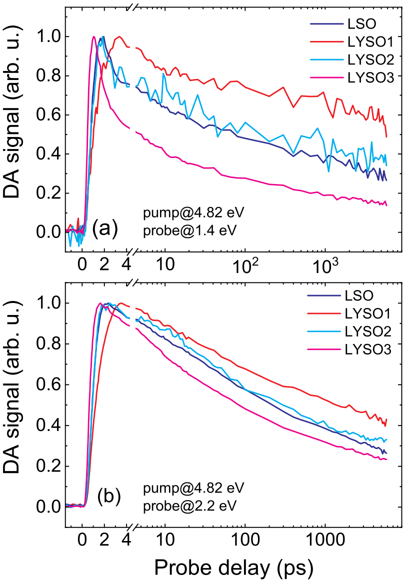

Fig. 4. Kinetics of differential absorption (normalized to peak value) in the LSO sample and three LYSO:Ce samples (indicated) with different contents of Ca at two different probe photon energies (indicated) after pumping with 4.82 eV photons.

To link the properties of the carrier dynamics observed by the DA technique with the response time after excitation with γ-quanta, we performed CTR measurements at 511 keV on the same crystals. The measurements were performed at three temperatures: 20 °C, 0 °C, and −20 °C. The results are presented in Table 1.

The CTR FWHM of LSO:Ce and LYSO:Ce crystals presented in Table 1 are similar to those reported in recent publications for samples of similar size: 85 ps [34], 77–117 ps [35], or 197 ps [36], and, recently, 58 ± 3 ps and 98 ± 3 ps for 2 × 2 × 3 mm^3 and 2 × 2 × 20 mm^3 samples, respectively [37]. The absolute values of the FWHM observed in CTR measurements strongly depend on sample shape and size, experimental geometry, coupling of the samples to SiPMs, the type of SiPM, and so on, and might even be influenced by the readout system used. Since there are no standards for performing CTR experiments and reporting the experimental conditions, comparisons of the absolute values obtained and reported by different research groups must be treated with caution. Meanwhile, all of the samples in our CTR experiments had the same size and were measured under nominally the same conditions. The largest CTR FWHM was observed in LSO:Ce (sample LSO). It was shorter in LYSO:Ce (sample LYSO1), and was further reduced by Ca-co-doping (samples LYSO2 and LYSO3). Note that even such a small amount of Ca as 5 ppm in LYSO2 was sufficient to substantially decrease the CTR FWHM, whereas the increase in Ca content up to 30 ppm did not further

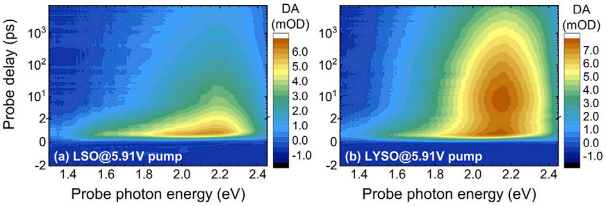

Fig. 5. Dependence of the intensity of differential absorption (color-coded as indicated in the sidebar) as a function of probe photon energy and delay between pump and probe beams in LSO:Ce and LYSO:Ce.

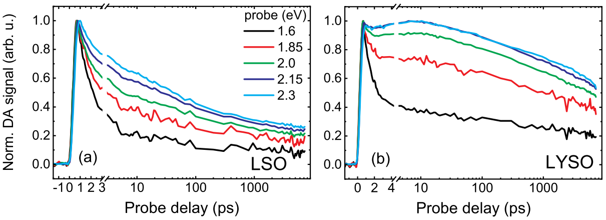

Fig. 6. Kinetics of normalized DA signal at different probe photon energies (indicated) in LSO:Ce (a) and LYSO:Ce (b) after pumping by 5.91 eV photons.

Table 1
FWHM (in ps) in coincidence time resolution (CTR) measurements at different temperatures.

Sample	LSO	LYSO1	LYSO2	LYSO3
20 °C	115 ± 1	105 ± 1	93 ± 1	93 ± 1
0 °C	117 ± 2	106 ± 1	95 ± 2	93 ± 1
−20 °C	121 ± 1	109 ± 1	104 ± 2	101 ± 2

improve the time response. Comparison of the studied samples shows that lowering the temperature results in degradation of the CTR for all samples. This temperature dependence is more pronounced in LYSO samples, especially in those co-doped with Ca (samples LYSO2 and LYSO3).

4. Theoretical study of thermalization and spatial distribution of non-equilibrium carriers in LYSO:Ce

LYSO is a mixed crystal. Therefore, even statistical fluctuations in the local density of Lu and Y atoms modulate the bottom of the conduction band, and the minima of the potentials experienced by electrons might serve for their trapping. The band gaps of Y_2SiO_5 and Lu_2SiO_5 have been determined with rather low accuracy; however, the results presented in Refs. [38–40] show that 6.4 eV and 6.2 eV might be taken as rough estimates for the band gaps of LSO and YSO, respectively. According to the composition and assuming a linear shift of the band gap with increasing Y content, the band gap of $Lu_{1.6}Y_{0.4}SiO_5$ may be estimated as 6.24 eV.

The magnitude of the band gap fluctuations can be estimated as proposed for binary solid solutions in Ref. [41]. In this approach, overlapping of the 5d states of Y and Lu with neighboring cations is

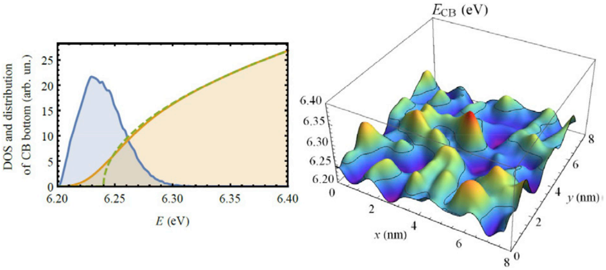

Fig. 7. Left panel: Energy dependence of the density of states (DOS) in the conduction band without localized states taken into account (green dashed curve), the distribution of the bottom of the conduction band due to spatial fluctuations of Lu and Y (blue solid line), and the total DOS (yellow solid line). Right panel: A typical profile of the spatial distribution of the bottom of the conduction band; the estimated percolation level is shown by the contour in this plot.

taken into account. Fig. 7 shows the energy dependence of the density of states (DOS) in the conduction band without localized states being taken into account, the distribution of the bottom of the conduction band due to spatial fluctuations of the components, and the total DOS. The spatial profile of the bottom of the conduction band is illustrated in the right-hand panel of Fig. 7. A random distribution of Lu^{3+} and Y^{3+} ions is assumed. Assuming that the percolation level for electrons (the energy sufficient for an electron to move through the crystal without tunneling through barriers) corresponds to the mean value of the bottom of the conduction band $<E_g>$, the typical depth of the traps due to random distribution of Y and Lu cations without any additional correlation is estimated to vary from 20 to 40 meV. Thus, the localized states might have a significant impact on carrier migration in LYSO at room temperature.

Band gap modulations should also be taken into account when describing the energy relaxation of electrons on the activator ion. To study the relaxation, we use the technique of configuration diagrams. Fig. 8 (a, b) shows the corresponding diagrams for Ce^{3+} and Ce^{4+} ions with excited and ionized states taken into account (following ref. [42]). The filled regions correspond to ionized states. The parabolas for ground and excited Ce^{3+} states are positioned to reproduce the experimentally observed absorption and emission spectra. The absorption spectrum calculated according to the configurational diagram is presented in Fig. 9 (cf. the experimental absorption spectra in Fig. 1). The local phonon energies are taken as 50 meV and 40 meV for the ground and excited Ce^{3+} states, respectively, as estimated for Ce in an LSO crystal [43], and 70 meV for the Ce^{4+} state. We assume the local phonon frequency for Ce^{4+} to be slightly larger than that for excited states based on the following considerations. The equilibrium position of the excited Ce^{3+} state (apex of the parabola) corresponds to a shift of a ligand ion off the cerium ion (since the radius of the excited cerium ion is larger than that of the ground Ce^{3+} state), whereas the parabola for Ce^{4+} is shifted in the opposite direction, since the radius of ionized cerium is smaller than that of the ground Ce^{3+} state, and coulomb interaction between cerium and the ligands is stronger for Ce^{4+} than for the Ce^{3+} state. The increase in local phonon frequencies in the sequence excited $Ce^{3+} \rightarrow$ ground $Ce^{3+} \rightarrow Ce^{4+}$ corresponds to the increase in the rigidity of the bonds between cerium and ligands with decreasing interior distances. Comparison of the corresponding spectra reveals that the optical transitions involving Ce^{4+} ions do not form new bands; rather, they smoothly enhance the absorption in the UV range.

The states involving electrons in the conduction band (e.g., $Ce^{4+} + e$ or $e + h + 4F_{5/2}$ Ce^{3+}) are represented by broad parabolas to illustrate 0.2 eV fluctuations of the conduction band bottom. These configuration diagrams are plotted only for Ce ions in the most populated Ce(1) position with seven-fold oxygen coordination. Diagrams for the Ce(2) position are characterized by a larger Stokes shift and a shift of the parabolas for excited states to larger Q values. As evidenced by their small contribution to the emission spectra, the occupation of these positions by cerium ions is small, and so for simplicity we do not consider them.

To calculate the energy distribution of ionized electrons, we exploited the Frank–Condon principle for optical transitions without changing the local phonon configuration coordinate Q and took into account the configuration distribution over Q. The corresponding Gaussian distributions are shown in Fig. 8 (a, b). The transitions initiated by the absorption of photons with certain energies are shown by red vertical arrows, and the possible final distributions are plotted as red arcs (the line width of the arcs reflects the initial Gaussian distribution over Q). Optical transitions cannot occur for any Q. For instance, absorption of a 3.47 eV photon can only occur for Q at the intersection of the corresponding arc with the $5d_1Ce^{3+}$ parabola and for Q corresponding to the part of the arc in the $Ce^{4+} + e$ region. Note that only the left wing of the arc for 3.47 eV overlaps with the $Ce^{4+} + e$ region. Thus, the fraction of ionized states for this energy is very small. The energy difference between the arc and the boundary of the corresponding

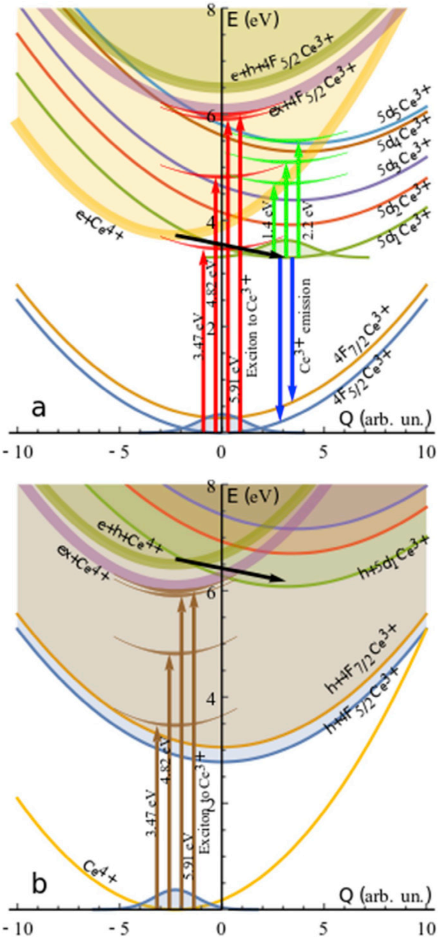

Fig. 8. Configuration diagrams for Ce^{3+} ion (a) and Ce^{4+} ion (b). The width of parabolas reflects the influence of fluctuations of the bottom of the conduction band. Gaussians show the thermal distribution functions. Red and brown arrows correspond to transitions initiated by pump photons with different energies (3.47 eV, 4.82 eV, and 5.91 eV) or by non-relaxed excitons; green arrows show transitions from the excited Ce^{3+} initiated by probe photons (1.4 eV, 1.8 eV, and 2.2 eV). Blue arrows correspond to emission lines. Arcs show possible positions of electrons after the transition (provided that the transition with certain Q can occur). Black arrows show the process of electron capture by relaxed Ce^{4+} with formation of an excited Ce^{3+} ion.

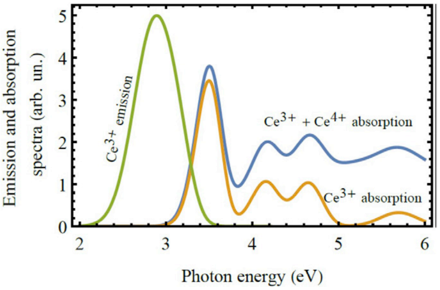

Fig. 9. Emission (green line) and absorption spectra for Ce^{3+} absorption (yellow) and for cumulative absorption of Ce^{3+} with the contribution of charge-transfer absorption of Ce^{4+} (blue) corresponding to arrows in Fig. 8 (a) and (b).

ionized state determines the kinetic energy of the excited electron.

The electron kinetic energies after the interaction of Ce^{3+} with pump photons are shown in Fig. 10 (a).The distributions of the kinetic energies of electrons excited by pump pulse at Ce^{3+} after they relax to the lowest excited state and thereafter absorb a probe photon are shown in Fig. 10 (b). Fig. 10 (a) also shows the kinetic energy distribution after dipole–dipole transfer from a non-relaxed exciton to Ce^{3+}.

Electrons lose their kinetic energy, E_{kin}, through the emission of bulk phonons, mainly longitudinal optical phonons in ionic crystals. The corresponding thermalization distance $l_{e,LO}(E_{kin})$ is described as follows (see, for example, ref. [44]):

$$l_{e,LO}(E_{kin}) = \frac{a_B}{2} \cdot \frac{\tilde{\varepsilon} m_0}{m_e} \sqrt{\frac{1}{6} \tanh\left(\frac{\hbar\Omega_{LO}}{2k_B T}\right) \mathrm{Ei}\left(3 \ln\left(\frac{4E_{kin}}{\hbar\Omega_{LO}}\right)\right)} \tag{1}$$

Here, a_B is the Bohr radius, m_0 is the free electron mass, m_e is the effective electron mass for the conduction band, $\tilde{\varepsilon} = (\varepsilon_\infty^{-1} - \varepsilon_{st}^{-1})^{-1}$ is the effective dielectric permittivity expressed in terms of high-frequency ε_∞ and static ε_{st} dielectric permittivities, $\hbar\Omega_{LO}$ is the bulk longitudinal optical phonon energy, and $\mathrm{Ei}(x)$ is the exponential integral function. The effective electron mass was estimated by applying the dispersion law to the bottom of the conduction band obtained for YSO (a structural analogue of LSO), which is available in the AFLOW database [45,46]. This estimation gives $m_e = 0.6m_0$. Taking the refractive index of YSO as $n = 1.78$–1.80 and the static dielectric permittivity as $\varepsilon_{st} = 9.6$–11.2 [47], we get $\tilde{\varepsilon} = (n^{-2} - \varepsilon_{st}^{-1})^{-1} = 4.56$–$4.73$. We take the bulk phonon energy for LYSO as being equal to the local phonon energy for the Ce^{3+} position estimated in Ref. [41] ($\hbar\Omega_{LO}$= 40 meV). The kinetic energy dependence of the thermalization length estimated according to Eq. (1) is shown by a blue line in Fig. 11 (a). This formula is valid for a parabolic dispersion law. However, the real dispersion law is far from parabolic, especially for energies >1 eV above the bottom of the conduction band. Therefore, we also use a modified model assuming the mean electron velocity and the electron-phonon scattering rate to be constant for electron kinetic energies above 1 eV. This approximation is similar to the approach used in Refs. [48,49]. Here, we assume that $l_{e,LO}^2(E_{kin} > 1\text{ eV}) = l_{e,LO}^2(1\text{ eV}) + A(E_{kin} - 1\ eV)$, where the constant $A = dl_{e,LO}^2(E_{kin})/dE_{kin}$ for $E_{kin} = 1$ eV. The corresponding dependence is shown in Fig. 11 (a) by a yellow line. We also use this model in the following estimations.

The thermalization positions are spatially shifted from the electron birthplace by the distance r distributed according to the 3D Gaussian (Maxwell-like) distribution:

$$f(r, l_e(E_{\mathrm{kin}})) = \frac{3\sqrt{6}r^2}{\sqrt{\pi}l_e^3(E_{\mathrm{kin}})} \exp\left(-\frac{3r^2}{2l_e^2(E_{\mathrm{kin}})}\right), \tag{2}$$

normalized as $\int_0^\infty f(r)dr = 1$.

To obtain the spatial distribution for electrons created by photon absorption, we have to convolute this Gaussian distribution with the distribution of electrons over their initial energies presented in Fig. 10 (a, b). The result of this convolution is shown in Fig. 12 (a, b).

After thermalization, the electrons can return to Ce^{4+} and form an excited $5d_1$ state of Ce^{3+}. This process is shown in Fig. 8 (a) by a black arrow. The corresponding process for initially stable Ce^{4+} ions is shown by a black arrow in Fig. 8 (b). Similar processes in GAGG:Ce are described in more detail in Ref. [27]. Only the electrons thermalized not too far from the Ce^{4+} ion (within a distance $r < R_{Ons} = \frac{e^2}{4\pi\varepsilon_0\varepsilon k_B T}$) can be captured without additional migration in the vicinity of the Ce^{4+} ion. R_{Ons} is the Onsager radius, i.e., the distance at which the absolute potential energy value for coulomb interaction between an electron and the Ce^{4+} ion is equal to the thermal energy. Only a fraction R_{Ons}/r of the electrons with $r > R_{Ons}$ return to the same center from which they were ionized. The rest of the electrons migrate to other Ce^{4+} centers or traps.

Thermalization plays an important role in the spatial distribution of electrons, not only after their interaction with pump or probe photons, but also after excitation with high-energy quanta initiating scintillation. After cascading down, the electrons show a smooth distribution of kinetic energies between 0 and the band-gap energy E_g (electrons with a higher kinetic energy lose their energy by scattering with the production of additional electron–hole pairs). This distribution shows a maximum at low energies and smoothly decreases to E_g. A similarly shaped distribution was obtained in Ref. [50]. The statistical distribution of

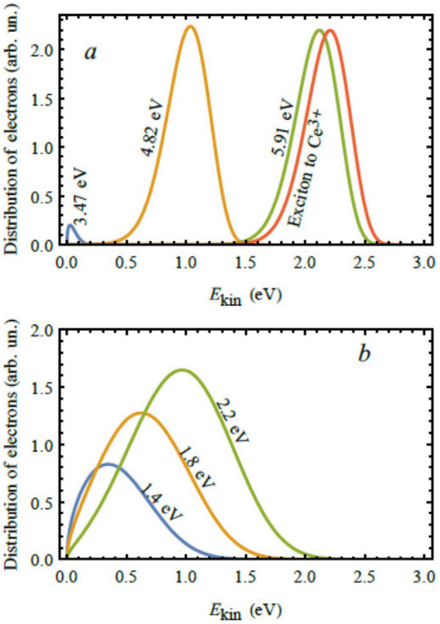

Fig. 10. Distributions of electron kinetic energies after absorption of pump (a) and probe (b) photons.

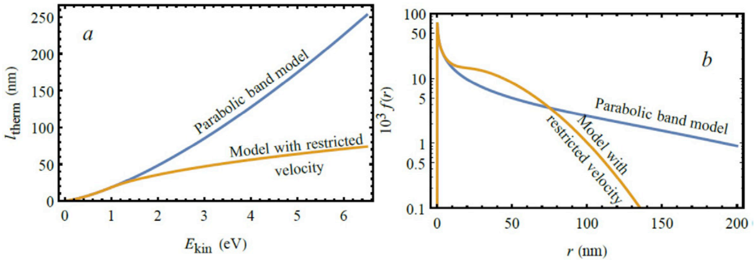

Fig. 11. Thermalization length l_{therm} as a function of kinetic energy (a) and spatial distribution of thermalized electrons $f(r)$ cascaded down after their generation by an ionizing particle (b) for the parabolic band model (blue line) and the model with a constant velocity for $E_{\text{kin}}>1$ eV (yellow line).

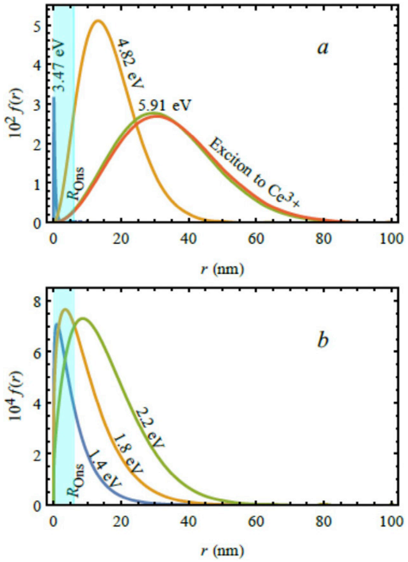

Fig. 12. Spatial distribution of thermalized electrons $f(r)$ after ionization of Ce^{3+} ion by 3.47 eV, 4.82 eV, and 5.91 eV pump photons (a) and by 1.4 eV, 1.8 eV, and 2.2 eV probe photons (b). The Onsager radius is shown by a vertical line.

electrons around their birthplace after interaction of the material with an ionizing particle is shown in Fig. 10 (b). This distribution controls the interaction of electrons with holes. The formation of excitons is, therefore, controlled by this distribution. After its migration, an exciton can transfer its energy to a Ce^{3+} ion. The exciton energy is well above the energy of the lowest *f-d* transition of Ce^{3+}, and thus ionization of the cation might occur. The energy distribution of ionized electrons after this transfer is shown in Fig. 10 (a), and the spatial distribution of such electrons is presented in Fig. 12 (a). These three stages of energy transfer from electron–hole pairs created by ionizing radiation ($e + h \rightarrow ex$, $ex + Ce^{3+} \rightarrow Ce^{4+} + e$, $Ce^{4+} + e \rightarrow Ce^{3+*}$) determine the timing properties of the leading part of the scintillation response and are responsible for CTR.

5. Discussion

The DA results show that free electrons disappear with a characteristic decay time of about 1.2 ps (the fastest decay component in the DA response to short-pulse excitation). Meanwhile, population of the lowest excited state of Ce^{3+} by electrons from the conduction band increases in non-co-doped LSO:Ce with a certain delay of the order of 5 ps, which is longer than the decay time of the free electron contribution. This delay might be attributed to the contribution of electrons trapped in shallow traps, as suggested to explain the electron dynamics in GAGG:Ce and GAGG:Ce,Mg [17]. The trapped electrons have certain probabilities to relax down to deeper defect centers acting as centers of nonradiative recombination or to be thermally detrapped and to reach the radiative Ce^{3+} centers, probably after multiple trapping and detrapping. Oxygen vacancies have been shown to be the main electronic defects in LYSO [51]. The density of oxygen vacancies is decreased by adding oxygen to the growth atmosphere [52] and annealing [8]. Recently, it has been claimed that the introduction of Li as a co-dopant reduces the density of oxygen vacancies [53]. As has been observed in many samples and demonstrated in Fig. 6, the delay in population of the Ce^{3+} 5d1 level by non-equilibrium electrons in LYSO:Ce is more pronounced than that in LSO:Ce. This feature might be explained in terms of additional trapping centers formed in the mixed LYSO crystal due to composition fluctuations, as discussed above.

Our experiments show that the slow component in the rise of population of the Ce^{3+} level 5d1 is the feature that most sensitively reflects carrier trapping. Note that co-doping of LYSO:Ce with Ca eliminates the slow rise component even at a co-doping level as low as 5 ppm. Such a small amount of calcium ions can hardly affect the ratio of the fractions of Ce ions in trivalent and tetravalent states. The change of valency is feasible for crystal growth under conditions favorable for coherent doping, that is, for the incorporation of Ca in the close vicinity of Ce. Thus, the stabilization of Ce^{4+} by Ca may only be expected at high co-doping levels. X-ray absorption (XANES) measurements have shown that the Ce^{4+} content in non-co-doped LSO:Ce is negligible [32], whereas 35% of the Ce ions are in the Ce^{4+} state in LYSO:Ce,Ca containing 30–40 ppm Ca [13]. Therefore, effects other than the influence of Ce^{4+}, which is currently being extensively cited in discussions of aliovalent co-doping (see, e.g., the review [16]), should be invoked to interpret the elimination of the delay in population of the lowest excited state of Ce^{3+}. The suppression of carrier trapping might be pointed out as such an effect. Trapping centers due to oxygen vacancies in the crystal are expected to be the dominant electron traps in LSO/LYSO. It is assumed that Ca^{2+} ions compensate for oxygen vacancies [10], though the compensation mechanism has yet to be clarified. Decreases in trap concentration with increasing contents of Ca were observed in thermoluminescence measurements on YSO:Ce [12] and LSO:Ce [11]. Such a decrease is the result of competition between two effects of aliovalent co-doping. In fact, co-dopants are introduced in the initial charge in excess of the stoichiometric composition. During crystal growth, the co-dopants decrease the concentrations of cation vacancies and, simultaneously, of anion vacancies [54]. On the other hand, aliovalent substitution of a trivalent ion by a divalent ion in the host matrix leads to an increase in the anion vacancy concentration. The results obtained lead to the conclusion that the slow component in the population of the lowest excited state of Ce^{3+} is caused by the electrons relaxing via the conduction band and then moving under the strong influence of trapping and detrapping processes. In aliovalently co-doped crystals, such electrons are captured by deeper levels due to defects introduced by the co-doping.

Furthermore, we have observed that vanishing of the slow component in population of the Ce^{3+} radiative level after optical excitation of Ce ions is linked to the faster response in CTR experiments, whereby the material is excited with 511 keV γ-quanta. Moreover, the CTR FWHM increases with decreasing temperature (see Table 1), with this temperature dependence becoming less pronounced in Ca-doped material. This behavior is consistent with the interpretation that transfer of an electron back to a Ce^{4+} ion created after ionization of Ce^{3+} by pump photons occurs by thermally activated hopping via localized states. Note that the increase in co-dopant content from 5 to 30 ppm did not have a substantial effect on the CTR FWHM. The correlation of the electron dynamics observed in optical pump and probe experiments with the response time of the material after excitation by ionizing particles should be considered in view of five qualitatively different processes occurring between the moment of generation of an electron–hole pair with high energy compared to the band gap and photon emission at the activator ion Ce^{3+}: i) relaxation of the electron and hole down to the edges of the band gap, ii) migration of electrons and holes to Ce ions, iii) transfer of the energy of electron–hole pair to excite the Ce ion, iv) relaxation of the electron at the excited Ce^{3+} ion to the lowest excited state 5d1, and v) optical transition of the electron between the 5d1 level and the ground state by emitting a photon. A part of the generated electron–hole pairs recombine nonradiatively and do not contribute to the scintillation signal.

Ionizing radiation generates an electron and a hole as a pair synchronously in time and at the same location in the crystal. However, the geminate electrons and holes become increasingly separated during their relaxation. Since the effective mass of holes is substantially larger than that of electrons and, consequently, the hole mobility is lower, the curves in Fig. 11 (b) reflect the distribution of the distances of electrons around the holes generated by electron–hole pair excitation. The results presented in Fig. 11 (b) show that the geminate electron–hole pairs are strongly separated during their relaxation, and migration of the electron and the hole starts after their separate relaxation. However, the electron and hole might form an exciton, i.e., a pair bound by coulomb attraction. Radiative exciton recombination is typical of oxide scintillation crystals [54] and has been observed in LSO and LSO:Ce [55,56]. Excitonic luminescence is quenched at temperatures above about 150 K, probably due to thermal dissociation of the excitons. Nevertheless, the electron remains predominantly in the vicinity of the hole, which migrates through the crystal substantially more slowly due to its larger effective mass and probably some self-trapping. Thus, excitation transfer to the activator ion might be viewed as exciton-like.

Energy transfer from the electron–hole pair to a Ce ion might occur subsequently, by capturing the hole and then the electron, or resonantly. However, no crucial evidence in favor of any of the transfer mechanisms has yet been obtained. The first mechanism is extensively cited in many publications without explaining the mechanism of releasing a large amount of energy necessary for the transition of a hole from the valence band to occupy the ground state of Ce^{3+}, which is around 2.6 eV above the valence band. This process might be facilitated by the simultaneous presence of an electron and a hole in the vicinity of a cerium ion. In this case, the excess energy can be transferred to the electron. Meanwhile, the resonant transfer of energy from an exciton-like electron–hole pair results only in excitation of the electron from the Ce^{3+} ground state to higher excited states of the ion or to states in the conduction band. Our calculations show (see Fig. 12 (a)) that the spatial distributions of the non-equilibrium electrons generated at Ce^{3+} upon excitation with 5.91 eV photons and by energy transfer from an exciton are very close. Thus, the optical pump-and-probe technique employed in this work tests the same electron dynamics as in the last stages after electron generation by an ionizing particle or a γ-quantum. Thus, the state of the Ce^{3+} ion after resonant energy transfer is identical to its state after photoexcitation in our experiments. The next stage towards radiative recombination is the relaxation of the electron at the excited Ce^{3+} ion to the lowest excited state 5d1. This relaxation can occur via two routes: intracenter relaxation, and relaxation via states in the conduction band. In the latter case, the relaxation in energy is accompanied by a distancing of the electron from the ion, as described by Eq. (1) and illustrated in Fig. 11 (a).

After auto-ionization, the electron either returns to the Ce^{3+} ion at which it was generated, or migrates away from the ion. As discussed above, the critical distance for this separation is the Onsager radius (5.4 nm for LYSO at room temperature). Thus, migration of these electrons back to the native Ce ion (within the Onsager radius) or to the neighboring Ce ions covers distances sufficiently long for electron trapping to be important.

Finally, the radiative recombination proceeds in a similar way after both radiation and optical excitation. It is usually assumed that all of the electrons from the Ce^{3+} state $5d_1$ recombine radiatively, and the luminescence decay time is determined by the rate of this radiative recombination. Variations in the luminescence decay time observed in different samples are caused by the competing contributions of emissions of Ce^{3+} ions located in two different positions in the crystal lattice. The luminescence decay times are 32 ns and 54 ns for Ce(1) and Ce(2) centers in the first and second positions, respectively [57]. The competition between Ce(1) and Ce(2) and, consequently, the resulting luminescence decay time, is influenced by the conditions of crystal growth and co-doping. Thus, the timing properties of LSO/LYSO-based radiation detectors depend not only on electron trapping, which is a property of the host crystal, influences the leading edge of the luminescence response, and might be studied in optical pump-and-probe experiments, but also on the competition between the contributions of cerium ions in the Ce(1) and Ce(2) positions.

6. Conclusions

The population kinetics of selectively excited Ce^{3+} ions in LSO:Ce and LYSO:Ce scintillators has been studied by means of the optical pump-and-probe technique in picosecond and subpicosecond domains. A delay in population of the $5d_1$ emitting level of Ce^{3+} has been observed. The delay increases with increasing excitation photon energy and is more pronounced in LYSO:Ce than in LSO:Ce. This delay is eliminated by aliovalent co-doping with calcium, even at concentrations as low as 5 ppm. The delay is interpreted in terms of electron trapping, which is enhanced in LYSO due to additional trapping states formed by composition fluctuations in this mixed crystal. Timing properties after γ-excitation have been studied by performing CTR measurements. It is shown that Ca-co-doping results in an improvement of the LYSO:Ce CTR FWHM to 93 ps. Calculations of the distributions of non-equilibrium electrons in energy and space and study of excitation transfer in this scintillator led us to the conclusion that the carrier dynamics after Ce^{3+} excitation to higher excited states by a subpicosecond optical pulse is actually similar to that governing the excitation transfer to Ce ions after γ-quantum excitation. Thus, the pump-and-probe technique is a convenient, fast, nondestructive, and contactless tool for studying the timing properties of LYSO:Ce and other scintillators.

Declaration of competing interest

The authors declare that they have no known competing financial interests or personal relationships that could have appeared to influence the work reported in this paper.

CRediT authorship contribution statement

G. Tamulaitis: Conceptualization, Supervision, Writing - review & editing. **E. Auffray:** Conceptualization, Validation. **A. Gola:** Methodology, Investigation. **M. Korzhik:** Conceptualization, Writing - original draft. **A. Mazzi:** Investigation, Writing - review & editing. **V. Mechinski:** Investigation. **S. Nargelas:** Methodology, Investigation. **Y. Talochka:** Investigation, Formal analysis. **A. Vaitkevičius:** Investigation, Visualization, Writing - original draft. **A. Vasil'ev:** Methodology, Formal analysis, Visualization, Writing - review & editing.

Acknowledgements

This research has been carried out in the frame of Crystal Clear Collaboration at CERN. The research has received funding from the European Social Fund under grant agreement with the Research Council of Lithuania (project No. 09.3.3-LMT-K-712-01-0013). Support for collaboration from the COST Action FAST (TD1401) is gratefully acknowledged.

References

[1] C.L. Melcher, J.S. Schweitzer, Cerium-doped lutetium oxyorthosilicate: a fast, efficient new scintillator, IEEE Trans. Nucl. Sci. 39 (1992) 502–505, https://doi.org/10.1109/23.159655.

[2] P. Lecoq, A. Gektin, M. Korzhik, Inorganic Scintillators for Detector Systems, Springer International Publishing, 2017, https://doi.org/10.1007/978-3-319-45522-8.

[3] C.L. Melcher, Scintillation crystals for PET, J. Nucl. Med. 41 (2000) 1051–1055, https://doi.org/10.1016/S0921-5093(99)00466-9.

[4] D.L. Bailey, D.W. Townsend, P.E. Valk, M.N. Maisey, Positron Emission Tomography, Springer Science & Business Media, 2006.

[5] A. Di Francesco, R. Bugalho, L. Oliveira, L. Pacher, A. Rivetti, M. Rolo, J.C. Silva, R. Silva, J. Varela, TOFPET2, A high-performance ASIC for time and amplitude measurements of SiPM signals in time-of-flight applications, J. Instrum. 11 (2016), https://doi.org/10.1088/1748-0221/11/03/C03042.

[6] R. Bugalho, A. Di Francesco, L. Ferramacho, C. Leong, T. Niknejad, L. Oliveira, L. Pacher, M. Rolo, A. Rivetti, M. Silveira, J.C. Silva, R. Silva, S. Tavernier, J. Varela, Experimental results with TOFPET2 ASIC for time-of-flight applications, Nucl. Instruments Methods Phys. Res. Sect. A Accel. Spectrometers, Detect. Assoc. Equip. 912 (2018) 195–198, https://doi.org/10.1016/j.nima.2017.11.034.

[7] B.H.T. Chai, Y. Ji, Lutetium orthosilicate single crystal scintillator detector, US 6624420 B1, http://stars.library.ucf.edu/patents/311, 2003.

[8] A.N. Belsky, E. Auffray, P. Lecoq, C. Dujardin, N. Garnier, H. Canibano, C. Pedrini, A.G. Petrosyan, Progress in the development of $LuAlO_3$-based scintillators, IEEE Trans. Nucl. Sci. 48 (2001) 1095–1100, https://doi.org/10.1109/23.958730.

[9] B.H.T. Chai, Method of Enhancing Performance of Cerium-Doped Lutetium Yttrium Orthosilicate Crystals and Crystals Produced Thereby, 2007. US 7166845.

[10] M.A. Spurrier, P. Szupryczynski, K. Yang, A.A. Carey, C.L. Melcher, Effects of Ca^{2+} co-doping on the scintillation properties of LSO:Ce, IEEE Trans. Nucl. Sci. 55 (2008) 1178–1182, https://doi.org/10.1109/TNS.2007.913486.

[11] K. Yang, C.L. Melcher, P.D. Rack, L.A. Eriksson, Effects of calcium codoping on charge traps in LSO:Ce crystals, IEEE Trans. Nucl. Sci. 56 (2009) 2960–2965, https://doi.org/10.1109/TNS.2009.2027018.

[12] H.E. Rothfuss, C.L. Melcher, L.A. Eriksson, M.A. Spurrier Koschan, The effect of Ca^{2+} codoping on shallow traps in YSO:Ce scintillators, IEEE Trans. Nucl. Sci. 56 (2009) 958–961, https://doi.org/10.1109/TNS.2008.2010621.

[13] S. Blahuta, A. Bessiere, B. Viana, P. Dorenbos, V. Ouspenski, Evidence and consequences of Ce^{4+} in LYSO:Ce, Ca and LYSO:Ce, Mg single crystals for medical imaging applications, IEEE Trans. Nucl. Sci. 60 (2013) 3134–3141, https://doi.org/10.1109/TNS.2013.2269700.

[14] M.A. Koschan, C.L. Melcher, L.A. Eriksson, H.E. Rothfuss, Use of Codoping to Modify the Scintillation Properties of Inorganic Scintillators Doped with Trivalent Activators, 2013. US 8617422 B2.

[15] M. Koschan, K. Yang, M. Zhuravleva, C.L. Melcher, A comparison of the effect of Ca^{2+} codoping in cerium-doped GSO with that of LSO and YSO, J. Cryst. Growth 352 (2012) 133–136, https://doi.org/10.1016/j.jcrysgro.2012.01.021.

[16] M. Nikl, A. Yoshikawa, Recent R&D trends in inorganic single-crystal scintillator materials for radiation detection, Adv. Opt. Mater. 3 (2015) 463–481, https://doi.org/10.1002/adom.201400571.

[17] G. Tamulaitis, G. Dosovitskiy, A. Gola, M. Korjik, A. Mazzi, S. Nargelas, P. Sokolov, A. Vaitkevičius, Improvement of response time in GAGG:Ce scintillation crystals by magnesium codoping, J. Appl. Phys. 124 (2018) 215907, https://doi.org/10.1063/1.5064434.

[18] G. Tamulaitis, A. Vaitkevičius, S. Nargelas, R. Augulis, V. Gulbinas, P. Bohacek, M. Nikl, A. Borisevich, A. Fedorov, M. Korjik, E. Auffray, Subpicosecond luminescence rise time in magnesium codoped GAGG:Ce scintillator, Nucl. Instruments Methods Phys. Res. Sect. A Accel. Spectrometers, Detect. Assoc. Equip. 870 (2017) 25–29, https://doi.org/10.1016/j.nima.2017.07.015.

[19] E. Auffray, R. Augulis, A. Fedorov, G. Dosovitskiy, L. Grigorjeva, V. Gulbinas, M. Koschan, M. Lucchini, C. Melcher, S. Nargelas, G. Tamulaitis, A. Vaitkevičius, A. Zolotarjovs, M. Korzhik, Excitation transfer engineering in Ce-doped oxide crystalline scintillators by codoping with alkali-earth ions, Phys. Status Solidi Appl. Mater. Sci. 215 (2018) 1–10, https://doi.org/10.1002/pssa.201700798.

[20] K. Kamada, T. Endo, K. Tsutumi, T. Yanagida, Y. Fujimoto, A. Fukabori, A. Yoshikawa, J. Pejchal, M. Nikl, Composition engineering in cerium-doped $(Lu,Gd)_3(Ga,Al)_5O_{12}$ single-crystal scintillators, Cryst. Growth Des. 11 (2011) 4484–4490, https://doi.org/10.1021/cg200694a.

[21] K. Kamada, T. Yanagida, J. Pejchal, M. Nikl, T. Endo, K. Tsutumi, Y. Fujimoto, A. Fukabori, A. Yoshikawa, Scintillator-oriented combinatorial search in Ce-doped $(Y,Gd)_3(Ga,Al)_5O_{12}$ multicomponent garnet compounds, J. Phys. D Appl. Phys. 44 (2011) 505104, https://doi.org/10.1088/0022-3727/44/50/505104.

[22] K.B. Ucer, G. Bizarri, A. Burger, A. Gektin, L. Trefilova, R.T. Williams, Electron thermalization and trapping rates in pure and doped alkali and alkaline-earth iodide crystals studied by picosecond optical absorption, Phys. Rev. B Condens. Matter Mater. Phys. 89 (2014) 1–15, https://doi.org/10.1103/PhysRevB.89.165112.

[23] P. Li, S. Gridin, K.B. Ucer, R.T. Williams, P.R. Menge, Picosecond absorption spectroscopy of self-trapped excitons and transient Ce states in $LaBr_3$ and $LaBr_3$:Ce, Phys. Rev. B. 97 (2018) 1–18, https://doi.org/10.1103/PhysRevB.97.144303.

[24] M.T. Lucchini, O. Buganov, E. Auffray, P. Bohacek, M. Korjik, D. Kozlov, S. Nargelas, M. Nikl, S. Tikhomirov, G. Tamulaitis, A. Vaitkevičius, K. Kamada, A. Yoshikawa, Measurement of non-equilibrium carriers dynamics in Ce-doped YAG, LuAG and GAGG crystals with and without Mg-codoping, J. Lumin. 194 (2018) 1–7, https://doi.org/10.1016/j.jlumin.2017.10.005.

[25] M. Korzhik, A. Gola, J. Houžvička, A. Mazzi, S. Nargelas, S. Sỳkorová, G. Tamulaitis, A. Vaitkevičius, Timing properties of Ce-doped YAP and LuYAP scintillation crystals, Nucl. Instruments Methods Phys. Res. Sect. A Accel. Spectrometers, Detect. Assoc. Equip. 927 (2019) 169–173.

[26] P. Li, S. Gridin, K.B. Ucer, R.T. Williams, P.R. Menge, Picosecond absorption spectroscopy of self-trapped excitons and Ce excited states in $CeBr_3$ and $La_{1-x}Ce_xBr_3$, Phys. Rev. B. 99 (2019) 1–9, https://doi.org/10.1103/PhysRevB.99.104301.

[27] G. Tamulaitis, A.N. Vasil'ev, M. Korjik, A. Mazzi, A. Gola, S. Nargelas, A. Vaitkevičius, A. Fedorov, D. Kozlov, Improvement of the time resolution of radiation detectors based on $Gd_3Al_2Ga_3O_{12}$ scintillators with SiPM readout, IEEE Trans. Nucl. Sci. 66 (2019) 1879–1888.

[28] C. Piemonte, F. Acerbi, A. Ferri, A. Gola, G. Paternoster, V. Regazzoni, G. Zappala, N. Zorzi, Performance of NUV-HD silicon photomultiplier technology, IEEE Trans. Electron Devices 63 (2016) 1111–1116, https://doi.org/10.1109/TED.2016.2516641.

[29] A. Gola, F. Acerbi, M. Capasso, M. Marcante, A. Mazzi, G. Paternoster, C. Piemonte, V. Regazzoni, N. Zorzi, NUV-sensitive silicon photomultiplier technologies developed at Fondazione Bruno Kessler, Sensors 19 (2019) 308, https://doi.org/10.3390/s19020308.

[30] A. Gola, C. Piemonte, A. Tarolli, Analog circuit for timing measurements with large area SiPMs coupled to LYSO crystals, IEEE Trans. Nucl. Sci. 60 (2013) 1296–1302, https://doi.org/10.1109/TNS.2013.2252196.

[31] D. Ding, B. Liu, Y. Wu, J. Yang, G. Ren, J. Chen, Effect of yttrium on electron-phonon coupling strength of 5d state of Ce^{3+} ion in LYSO:Ce crystals, J. Lumin. 154 (2014) 260–266, https://doi.org/10.1016/j.jlumin.2014.04.034.

[32] C.L. Melcher, S. Friedrich, S.P. Cramer, M.A. Spurrier, P. Szupryczynski, R. Nutt, Cerium oxidation state in LSO:Ce scintillators, IEEE Trans. Nucl. Sci. 52 (2005) 1809–1812, https://doi.org/10.1109/TNS.2005.856594.

[33] L. Ning, L. Lin, L. Li, C. Wu, C.K. Duan, Y. Zhang, L. Seijo, Electronic properties and 4f → 5d transitions in Ce-doped Lu_2SiO_5: a theoretical investigation, J. Mater. Chem. 22 (2012) 13723–13731, https://doi.org/10.1039/c2jm31631e.

[34] M.V. Nemallapudi, S. Gundacker, P. Lecoq, E. Auffray, A. Ferri, A. Gola, C. Piemonte, Sub-100 ps coincidence time resolution for positron emission tomography with LSO:Ce codoped with Ca, Phys. Med. Biol. 60 (2015) 4635–4649, https://doi.org/10.1088/0031-9155/60/12/4635.

[35] S. Gundacker, F. Acerbi, E. Auffray, A. Ferri, A. Gola, M.V. Nemallapudi, G. Paternoster, C. Piemonte, P. Lecoq, State of the art timing in TOF-PET detectors with LuAG, GAGG and L(Y)SO scintillators of various sizes coupled to FBK-SiPMs, J. Instrum. 11 (2016), https://doi.org/10.1088/1748-0221/11/08/P08008.

[36] E. Pratiwi, K. Kamada, S. Yamamoto, M.N. Ullah, J.-Y. Yeom, A. Yoshikawa, J. H. Park, Studies on sub-millimeter LYSO:Ce, Ce:GAGG, and a new Ce:GFAG block detector for PET using digital silicon photomultiplier, Nucl. Instruments Methods Phys. Res. Sect. A Accel. Spectrometers, Detect. Assoc. Equip. 911 (2018) 115–122, https://doi.org/10.1016/j.nima.2018.09.029.

[37] S. Gundacker, R.M. Turtos, E. Auffray, M. Paganoni, P. Lecoq, High-frequency SiPM readout advances measured coincidence time resolution limits in TOF-PET, Phys. Med. Biol. 64 (2019), 055012, https://doi.org/10.1088/1361-6560/aafd52.

[38] A. Lempicki, J. Glodo, Ce-doped scintillators: LSO and LuAP, Nucl. Inst. Methods Phys. Res. A. 416 (1998) 333–344, https://doi.org/10.1016/S0168-9002(98)00689-5.

[39] V.V. Laguta, M. Nikl, S. Zazubovich, Photothermally stimulated creation of electron and hole centers in Ce^{3+}-doped Y_2SiO_5 single crystals, Opt. Mater. 36 (2014) 1636–1641, https://doi.org/10.1016/j.optmat.2013.12.018.

[40] W. Drozdowski, A.J. Wojtowicz, D. Wiśniewski, P. Szupryczyński, S. Janus, J.-L. Lefaucheur, Z. Gou, VUV spectroscopy and low temperature thermoluminescence of LSO:Ce and YSO:Ce, J. Alloy. Comp. 380 (2004) 146–150, https://doi.org/10.1016/j.jallcom.2004.03.016.

[41] A. Belsky, A. Gektin, S. Gridin, A.N. Vasil'ev, Electronic and optical properties of scintillators based on mixed ionic crystals, in: M. Korzhik, A. Gektin (Eds.), Eng. Scintill. Mater. Radiat. Technol., Springer International Publishing, Cham, 2017, pp. 63–82.

[42] C. Pedrini, C. Dujardin, J.C. Gâcon, A.N. Belsky, A.N. Vasil'ev, A.G. Petrosyan, Cerium-doped fluorescent and scintillating ionic crystals, Radiat. Eff. Defects Solids 154 (2007) 277–286, https://doi.org/10.1080/10420150108214065.

[43] I.A. Kamenskikh, V.V. Mikhailin, I.H. Munro, D.A. Shaw, P.A. Studenikin, A. N. Vasil, I.A. Zagumennyi, LSO-Ce fluorescence spectra and kinetics for UV, VUV and X-ray excitation, Radiat. Eff. Defects Solids 135 (1995) 391–396, https://doi.org/10.1080/10420159508229873.

[44] R. Kirkin, V.V. Mikhailin, A.N. Vasil'ev, Recombination of correlated electron-hole pairs with account of hot capture with emission of optical phonons, IEEE Trans. Nucl. Sci. 59 (2012) 2057–2064, https://doi.org/10.1109/TNS.2012.2194306.

[45] S. Curtarolo, G.L.W. Hart, M.B. Nardelli, N. Mingo, S. Sanvito, O. Levy, The high-throughput highway to computational materials design, Nat. Mater. 12 (2013) 191, https://doi.org/10.1038/nmat3568.

[46] S. Curtarolo, W. Setyawan, S. Wang, J. Xue, K. Yang, R.H. Taylor, L.J. Nelson, G.L. W. Hart, S. Sanvito, M. Buongiorno-Nardelli, N. Mingo, O. Levy, AFLOWLIB.ORG: a distributed materials properties repository from high-throughput ab initio calculations, Comput. Mater. Sci. 58 (2012) 227–235, https://doi.org/10.1016/j.commatsci.2012.02.002.

[47] N.C. Carvalho, J.-M. Le Floch, J. Krupka, M.E. Tobar, Multi-mode technique for the determination of the biaxial Y_2SiO_5 permittivity tensor from 300 to 6 K, Appl. Phys. Lett. 106 (2015) 192904, https://doi.org/10.1063/1.4920987.

[48] H. Huang, Q. Li, X. Lu, Y. Qian, Y. Wu, R.T. Williams, Role of hot electron transport in scintillators: a theoretical study, Phys. Status Solidi Rapid Res. Lett. 10 (2016) 762–768, https://doi.org/10.1002/pssr.201600276.

[49] M.P. Prange, Y. Xie, L.W. Campbell, F. Gao, S. Kerisit, Monte Carlo simulation of electron thermalization in scintillator materials: implications for scintillator nonproportionality, J. Appl. Phys. 122 (2017) 234504, https://doi.org/10.1063/1.4998966.

[50] A.N. Vasil'ev, A. V Gektin, Multiscale approach to estimation of scintillation characteristics, IEEE Trans. Nucl. Sci. 61 (2014) 235–245, https://doi.org/10.1109/TNS.2013.2282117.

[51] S. Blahuta, A. Bessière, B. Viana, V. Ouspenski, E. Mattmann, J. Lejay, D. Gourier, Defects identification and effects of annealing on $Lu_{2(1-x)}Y_{2x}SiO_5$ (LYSO) single crystals for scintillation application, Materials 4 (2011) 1224–1237, https://doi.org/10.3390/ma4071224.

[52] E. Auffray, A. Barysevich, A. Fedorov, M. Korjik, M. Koschan, M. Lucchini, V. Mechinski, C.L. Melcher, A. Voitovich, Radiation damage of LSO crystals under γ- and 24 GeV protons irradiation, Nucl. Instruments Methods Phys. Res. Sect. A Accel. Spectrometers, Detect. Assoc. Equip. 721 (2013) 76–82, https://doi.org/10.1016/j.nima.2013.04.065.

[53] Y. Wu, M. Tian, J. Peng, M. Koschan, I. Greeley, C. Foster, C.L. Melcher, On the role of Li^+ codoping in simultaneous improvement of light yield, decay time, and afterglow of Lu_2SiO_5:Ce^{3+} scintillation detectors, Phys. Status Solidi Rapid Res. Lett. 13 (2019) 1–5, https://doi.org/10.1002/pssr.201800472.

[54] M. V Korzhik, W.P. Trower, Origin of scintillation in cerium-doped oxide crystals, Appl. Phys. Lett. 66 (1995) 2327–2328, https://doi.org/10.1063/1.113971.

[55] D.W. Cooke, B.L. Bennett, R.E. Muenchausen, J.K. Lee, M.A. Nastasi, Intrinsic ultraviolet luminescence from Lu_2O_3, Lu_2SiO_5 and Lu_2SiO_5:Ce^{3+}, J. Lumin. 106 (2004) 125–132, https://doi.org/10.1016/j.jlumin.2003.09.001.

[56] M. Kitaura, S. Tanaka, M. Itoh, Optical properties and electronic structure of Lu_2SiO_5 crystals doped with cerium ions: thermally-activated energy transfer from host to activator, J. Lumin. 158 (2015) 226–230, https://doi.org/10.1016/j.jlumin.2014.10.010.

[57] H. Suzuki, T.A. Tombrello, C.L. Melcher, J.S. Schweitzer, Emission mechanism of $Lu_2(SiO_4)O$:Ce, IEEE Trans. Nucl. Sci. 40 (1993) 380–383.

Paper P18

Engineering of a new single-crystal multi-ionic fast and high-light-yield scintillation material $(Gd_{0.5}$-$Y_{0.5})_3Al_2Ga_3O_{12}$:Ce,Mg

M. Korzhik, V. Alenkov, O. Buzanov, G. Dosovitskiy, A. Fedorov, D. Kozlov, V. Mechinsky, S. Nargelas, G. Tamulaitis, **A. Vaitkevičius**

CrystEngComm. 22 (2020) 2502–2506.

doi: 10.1039/D0CE00105H.

CrystEngComm

PAPER

Cite this: *CrystEngComm*, 2020, **22**, 2502

Engineering of a new single-crystal multi-ionic fast and high-light-yield scintillation material $(Gd_{0.5}–Y_{0.5})_3Al_2Ga_3O_{12}$:Ce,Mg

Mikhail Korzhik, *[a] Vladimir Alenkov,[b] Oleg Buzanov,[b] Georgy Dosovitskiy, [c] Andrei Fedorov,[ac] Dmitry Kozlov,[a] Vitaly Mechinsky,[ac] Saulius Nargelas,[d] Gintautas Tamulaitis[d] and Augustas Vaitkevičius[d]

Received 23rd January 2020, Accepted 6th March 2020

DOI: 10.1039/d0ce00105h

rsc.li/crystengcomm

A single crystal scintillation material $(Gd_{0.5}–Y_{0.5})_3Al_2Ga_3O_{12}$ (GYAGG) doped with Ce and codoped with Mg at a small concentration was grown by the Czochralski technique and studied for its scintillation properties for the first time. The Czochralski technique enabled this multi-ionic garnet to be produced from a melt in a single crystal form and allowed the problems of codoping peculiar to this material in a ceramic form to be solved. Due to codoping, the scintillation kinetics of a single crystal is shorter than that of GYAGG ceramics produced before. The scintillation properties of GYAGG were found to be superior to those of the solely Ce-doped or Mg-codoped $Gd_3Al_2Ga_3O_{12}$ crystal. The light yield of GYAGG:Ce,Mg was found to be 52 000 ph MeV^{-1}, the coefficient of the light yield temperature dependence in the temperature range 20–100 °C was equal to 0.37%/°C, and the scintillation decay time constant was 50 ns.

Introduction

Mixed garnet-type scintillators, in particular, Ce-doped $Gd_3Al_2Ga_30_{12}$ (GAGG) single crystals, show spectacular progress in the improvement of their capabilities to detect ionizing radiation of different kinds.[1] Their scintillation properties are superior to those of binary garnets due to a positive influence of the random distribution of Al and Ga ions in tetrahedral and octahedral oxygen coordinations in the crystal matrix. The corresponding fluctuation in the crystal composition introduces a modulation of the bottom of the conduction band. As a result of carrier trapping in these band bottom fluctuations, the carrier migration length becomes smaller, the density of nonequilibrium carriers becomes larger, and, consequently, the probability of the carriers to reach the emitting Ce center increases.[2,3] GAGG scintillators exhibit an attractive combination of a high light yield of up to 50 000 phot MeV^{-1}, a short scintillation decay time at the level of 80 ns,[4,5] and good matching of the emission spectrum peaking at 520 nm with the sensitivity spectra of silicon photomultipliers (SiPMs). The timing properties of a GAGG:Ce scintillator might be substantially improved by co-doping the crystal with magnesium.[6–8] Codoping, even at small concentrations of less than 10 ppm, improves the coincidence time resolution in positron annihilation with emission of γ-quanta down to 160 ps,[9] making the GAGG:Ce,Mg scintillator the material of choice in designing medical imaging scanners, particularly positron emission scanners utilizing the time-of-flight registration technique (TOF-PET).

The further improvement of certain scintillation properties was achieved by fabrication of GAGG and $(Gd_{0.5}–Y_{0.5})_3Al_2Ga_3O_{12}$ (GYAGG) garnets in a polycrystalline ceramic form.[10–12] Particularly, the possibility of introducing a larger concentration of activator Ce^{3+} facilitated an increase of the light yield. However, the scintillation kinetics in the ceramics became even slower than that in GAGG:Ce single crystals. Unfortunately, technological methods, which have efficiently been exploited to improve the timing properties of mixed crystals, are hardly applicable in ceramic materials. In particular, the ions of magnesium used as codopants are pushed to the boundaries of the grains in ceramic materials. As a result, it is difficult to achieve the necessary codopant concentration in the bulk of the grains. The effect of pulling out of the codopant to the grain boundaries is difficult to avoid because the process of ceramics production is based on hot pressing, which includes several stages until the ceramic material becomes transparent: initial charge preparation, green body production and calcination, and sintering by hot pressure (HIP) for densification.[13] The scintillation kinetics of

---

[a] *Institute for Nuclear Problems of Belarus State University, 11 Bobruiskaya, 220030, Minsk, Belarus. E-mail: mikhail.korjik@cern.ch*
[b] *Fomos Crystals, Moscow, Russia*
[c] *National Research Center Kurchatov Institute, Moscow, Russia*
[d] *Institute of Photonics and Nanotechnology, Vilnius University, Saulėtekio al.3, LT-10257, Vilnius, Lithuania*

GAGG:Ce and GYAGG:Ce transparent ceramics has slow components with their relative contribution affected by the conditions of annealing after the final HIP stage in the ceramics production.[14]

Moreover, a significant improvement of the scintillation properties of the single crystalline GAGG garnet one is expected to be achieved by the introduction of yttrium into the garnet structure. A partial substitution of Gd by Y ions in the GAGG matrix was produced by the micro-pulling down (mPD) crystal growth method[15–17] and vertical gradient freeze (VGT) technique.[18] The carrier trapping, due to an additional band gap modulation caused by fluctuations of Gd and Y content along the dodecahedral positions in the crystal matrices, even more, decreases the migration length of the nonequilibrium carriers. Nevertheless, the recently performed attempts to substitute a small fraction (∼20 at%) of Gd in the matrix by Y or Lu combined with Mg-codoping did not succeed in the improvement of scintillation properties.[19,20] The crystals had worse parameters in comparison with the conventional GAGG:Ce scintillator.

Crystal growth

GYAGG crystals were grown by the Czochralski technique from an iridium crucible in a neutral atmosphere containing a small (1–5 vol%) amount of oxygen. This technique is quite convenient to grow relatively large single crystals of binary garnets YAG[21] and ternary garnets containing three cations: GAGG[22,23] and YAGG.[24] Further increase of the number of cations in a quaternary crystal results in unprecedented difficulties in seeding the desired crystalline phase. The larger the number of cations in the melt, the stronger the competition between different crystalline phases, which can be seeded at a certain temperature by using a crystalline seed with lattice parameters close to those of the quaternary compound in many crystalline phases. The substitution of Gd by Y in the GAGG lattice inevitably makes seeding with GAGG or GGG useless. The utilization of YAG or YAGG seeds was also found to be of low success. To avoid the drawbacks pointed out above, we introduced a few key modifications of the technology, the combination of which made the growth of quaternary garnet crystals containing roughly equal atomic amounts of Gd and Y at an Al/Ga ratio of 2/3 from the melt possible by using the Czochralski technique. For the first modification, we used the initial charge of a quite homogeneous garnet structure, which has been obtained by numerous consequent solid synthesis processes. The same quality initial charge can be obtained by the procedure described in ref. 25. Such a garnet initial charge prevents strong evaporation of Ga from the not yet melted raw material while it is heated in the crucible and converted from the solid to liquid phase. The second modification of the conventional Czochralski technique was using the seed on a slightly concave surface in an iridium capillary. The modified growth technique enabled us to pull-out a 100 g phase-homogeneous crystal of good quality, which was sufficient to produce crystalline seeds for further growth. The crystals grown afterwards had nearly 800 ppm Ce and less than 15 ppm Mg. Fig. 1 shows the comparison of the GYAGG and GAGG ingots grown by the Czochralski method.

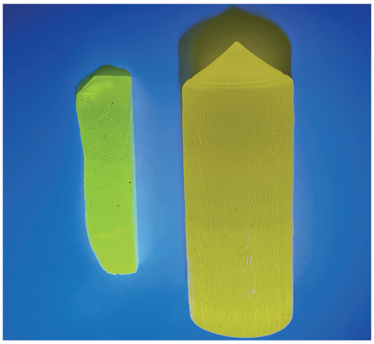

Fig. 1 GYAGG (left) and GAGG (right, diameter 50 mm) ingots obtained by the conventional Czochralski crystal growth method. The GYAGG ingot is shaped to produce a scintillation element for performance evaluation tests.

Fig. 2 shows a view of the crystal structure of disordered garnet generated with code.[26] It is worth noting that the cations are distributed randomly, and the anions occupy positions corresponding to the garnet structure. In fact, the anion net keeps the spatial symmetry of the compound with the ensuing consequences for the energy level structure and the phenomena of transfer of excitations.

The samples for performance evaluation tests were cut from single-crystal boules in the shape of blocks with dimensions of 3 × 3 × 5 mm^3 and 1 mm-thick plates and polished.

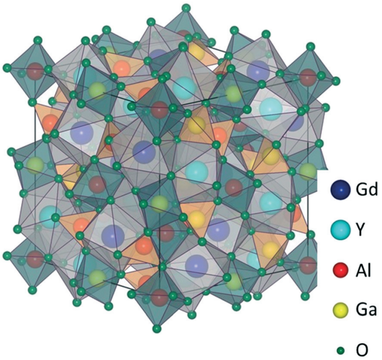

Fig. 2 Crystalline net of the disordered $(Gd_{0.5}-Y_{0.5})_3Al_2Ga_3O_{12}$ garnet.

Results and discussion

Samples were investigated for optical and scintillation properties with test benches described elsewhere.[5,20] Light yield was evaluated by comparison of the photo-peak maxima in the pulse height spectra of the 137-Cs (662 keV) source mounted at the top of the sample.

Scintillation kinetics was measured by a start-stop method with a 22-Na source and PMT XP2020 in both channels. The temperature of the samples was stabilised at the level 0.5 °C. The absorbance spectra of GAGG:Ce,Mg and GYAGG:Ce,Mg in the spectral range under study are presented in Fig. 3. It is worth noting that the absorption spectra measured with the samples extracted from the top and the bottom parts of the ingot are quite similar: the variation in the peak values of the absorption band corresponding to the first allowed interconfiguration transition was found to be less than 5%.

Typical absorption bands due to optical transitions in Ce^{3+} ions have been observed in GAGG:Ce,Mg: a band peaked at 442 nm due to 4f–5d_1 and a band peaked at 341 nm due to 4f–5d_2. Co-doping with Mg results in unstructured enhancement of the absorption in the high-energy part of the spectrum. The absorption in this spectral region might be attributed to the absorption involving defect centers stabilized by aliovalent doping of divalent magnesium.[7] The sharp lines below 350 nm are caused by the electronic transitions from the ^8S ground state to the higher ^6P and ^6I 4f states in Gd^{3+} ions. The absorption spectrum of GYAGG:Ce,Mg exhibits the same absorption bands as that of GAGG:Ce,Mg. However, the band due to the 4f–5d_1 transition of Ce^{3+} is blue-shifted[15] to the peak position at 436 nm, whereas the band due to the 4f–5d_2 transition is red-shifted and has the peak position at 345 nm. Therefore, the energy separation between the two excited states in Ce^{3+} in GYAGG:Ce,Mg is by 100 meV smaller than that in GAGG:Ce,Mg.

The photoluminescence (PL) and photoluminescence excitation (PLE) spectra of both samples under study are presented in Fig. 4. The shapes of the PL bands in the crystals are practically identical and caused by overlapped bands corresponding to the radiative transitions to two spin–orbital components of the ground f-level of the Ce^{3+} ion. Meanwhile, the PL band maximum of GYAGG:Ce,Mg is blue-shifted by 10 nm with respect to its position in the PL spectrum of GAGG:Ce,Mg.

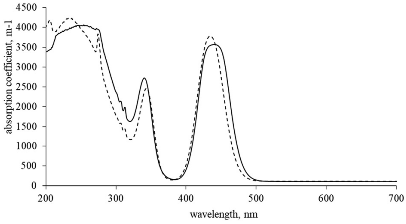

Fig. 3 Absorption spectra of GAGG:Ce,Mg (solid line) and GYAGG:Ce,Mg (dashed line) at room temperature.

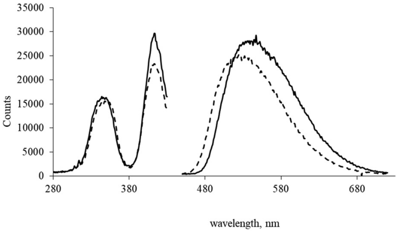

Fig. 4 Luminescence spectrum at 410 nm excitation (right part) and luminescence excitation spectrum measured at 550 nm (left part) of GAGG:Ce,Mg (solid line) and GYAGG:Ce,Mg (dashed line).

The luminescence kinetics of both GAGG:Ce,Mg and GYAGG:Ce,Mg after photoexcitation to the first excited level 5d_1 and the second excited level 5d_2 transitions shows a mono-exponential decay with the same decay time constant τ_d = 55 ns. The normalized decay kinetics for both excitation photon energies are presented in Fig. 5.

In addition to the difference in the luminescence band position, GAGG:Ce,Mg and GYAGG:Ce,Mg exhibit quite different scintillation properties. The comparison of the parameters of scintillation kinetics of a typical GAGG:Ce,Mg crystal and the two GYAGG:Ce,Mg crystals is presented in Table 1. The errors of the decay constants and the relative weights of the decay components in the kinetics are estimated to be ±1.5 and ±2%, respectively. The average decay constant has been evaluated as a sum of the products of the decay constants and the corresponding weight coefficients.

The second GYAGG crystal, which is quoted in the table, was grown after GYAGG:Ce,Mg from the same crucible and slightly codoped with titan Ti to avoid stabilization of some of the Ce ions in the Ce^{4+} valent state as described in ref. 5. Both GYAGG crystals exhibit a scintillation decay which is close to the single-exponential decay observed at photoexcitation. The averaged decay constant at γ-quanta excitation is similar to or even shorter than that at photoexcitation. This is an indication that the excitation

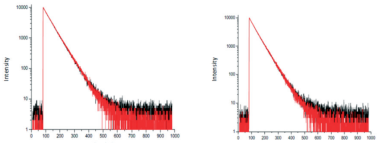

Fig. 5 Normalized photoluminescence kinetics of GAGG:Ce,Mg (left) and GYAGG:Ce,Mg (right) at 454 nm excitation (red) and 340 nm excitation (black) nm at room temperature.

Table 1 Scintillation decay parameters and light yield (LY) of GAGG:Ce,Mg and GYAGG:Ce,Mg crystals

Sample	Reference GAGG:Ce,Mg (ref. 9)	GYAGG:Ce,Mg after the first growth process	GYAGG:Ce,Mg,Ti after the second growth process
τ_{sc}, fraction, ns (%)	28 (30) 68 (52) 168 (18)	36 (80) 97 (20)	41 (89) 164 (11)
Average τ_{sc}, ns	72	48	53
LY, ph MeV^{-1}	41 000	52 000	52 300

transfer to the emitting Ce-ion is very effective. However, it might also indicate some additional quenching of the scintillation which makes its kinetics slightly faster than the kinetics of intracenter photo-luminescence.

As seen in Table 1, the light yield of GYAGG:Ce,Mg is substantially higher than that of GAGG:Ce,Mg. Moreover, the temperature dependence of the light yield was found to be substantially weaker. The relative variation of the light yield of GYAGG:Ce,Mg in the temperature range from 20 to 100 °C is shown in Fig. 6. The light yield temperature coefficient was measured to be 0.37/°C, which is by a factor of two smaller than that of GAGG:Ce,Mg. This property makes the GYAGG scintillator very promising for oil well logging exploration in the hydrocarbon industry.

The modification of growth technology introduced in this work enabled the growth of GYAGG crystals with substantially lower density of defects causing luminescence afterglow. Fig. 7 shows the scintillation kinetics of the crystals grown one after another from the same crucible. No increase of the level of random coincidence events, detected prior the scintillation kinetics curve, which is proportional to the afterglow in the scintillator, was observed from sample to sample.

Moreover, radiation induced absorption was found to be very small, which is consistent with the results of previous publications.[27,28] Fig. 8 shows the comparison of the induced absorption coefficient measured in GAGG and GYAGG crystals in the spectral range of scintillation after irradiation with a ^{60}Co source.

Two remarkable points of interest can be deduced from the results obtained. We confirmed that the Czochralski crystal growth technique is a very flexible method in view of the production of quaternary cation crystals with a garnet structure. The first results reported in this paper open opportunities for future work on perfection of scintillation materials of garnet structure by exploiting ion mixtures, which can be obtained experimentally or by combining experiments with modelling.

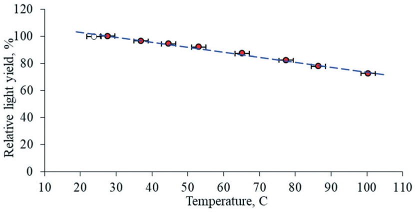

Fig. 6 Relative change of GYAGG:Ce,Mg light yield in the temperature range of 20–100 °C.

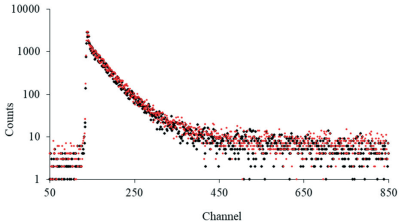

Fig. 7 Scintillation kinetics measured at room temperature of two GYAGG:Ce,Mg crystals grown at the first (black dots) and the second (red dots) process from the same crucible. One channel corresponds to 1.2 ns.

Then, the scintillation properties, light yield, and scintillation kinetics of GYAGG:Ce,Mg were found to be actually equal to those of novel halide scintillators like $LaBr_3$:Ce and $CeBr_3$.[1] Meanwhile, the oxide scintillators are superior to bromides in terms of stability, hygroscopicity, and capability for machining of the detecting elements into various shapes. So, we expect that quaternary garnets can substitute bromides in applications where combining excellent scintillation properties, mechanical stability and longevity in a harsh irradiation environment is demanded.

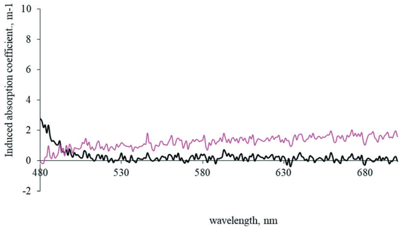

Fig. 8 Spectrum of induced optical absorption in the scintillation spectral range of GAGG:Ce,Mg (black) and GYAGG:Ce,Mg (magenta) after irradiation by a ^{60}Co source (at 2000 Gy).

Conclusions

A GYAGG:Ce,Mg single crystal scintillator was grown for the first time by the Czochralski technique from the melt containing equal atomic percentage of Gd and Y in the melt. The use of the highly homogenized garnet stoichiometric $(Gd_{0.5}–Y_{0.5})_3Al_2Ga_3O_{12}$ initial charge was found to be useful to ensure that a high quality single crystal was obtained. The scintillation properties of quaternary garnet composition were found to be superior to those achieved in Gd-based ternary garnets. We expect that combining this technological achievement in crystal growth with the outstanding progress in SiPM production technologies will enable new detectors of ionizing radiation to be obtained. The results obtained on GYAGG show that codoping of this scintillator with Mg even at the level of 10 ppm efficiently provides the scintillator with a fast response by facilitating faster excitation transfer from the matrix to Ce^{3+} ions. Therefore, our study confirms the productivity of the general approach of introducing a low concentration of an aliovalent codopant for improving the scintillation properties of mixed oxide single crystals.

Conflicts of interest

There are no conflicts to declare.

Acknowledgements

This research was partially supported by the AIDA2020 Project. The authors from the National Research Center Kurchatov Institute are grateful for support by grant No. 14. W03.31.0004 of the Government of the Russian Federation.

Notes and references

1 P. Lecoq, A. Gektin and M. Korzhik, *Inorganic Scintillators for Detecting Systems*, Springer, 2017.

2 A. Belsky, A. Gektin and A. Vail'ev, *Phys. Status Solidi B*, 2019, DOI: 10.1002/pssb.201900535.

3 M. Korzhik, G. Tamulaitis and A. Vasil'ev, *Physics of Fast Processes in Scintillators*, Springer, 2020, ISBN 978-3-030-21965-9.

4 K. Kamada, M. Nikl, S. Kurosawa, A. Beitlerova, A. Nagura, Y. Shoji, J. Pejchal, Y. Ohashi, Y. Yokota and A. Yoshikawa, *Opt. Mater.*, 2015, **41**, 63.

5 M. Korjik, V. Alenkov, A. Borisevich, O. Buzanov, V. Dormenev, G. Dosovitskiy, A. Dosovitskiy, A. Fedorov, D. Kozlov, V. Mechinsky, R. W. Novotny, G. Tamulaitis, V. Vasiliev, H.-G. Zaunick and A. A. Vaitkevičius, *Nucl. Instrum. Methods Phys. Res., Sect. A*, 2017, **871**, 42.

6 M. T. Lucchini, V. Babin, P. Bohacek, S. Gundacker, K. Kamada, M. Nikl, A. Petrosyan, A. Yoshikawa and E. Auffray, *Nucl. Instrum. Methods Phys. Res., Sect. A*, 2016, **816**, 176.

7 E. Auffray, R. Augulis, A. Fedorov, G. Dosovitskiy, L. Grigorjeva, V. Gulbinas, M. Koschan, M. Lucchini, C. Melcher, S. Nargelas, G. Tamulaitis, A. Vaitkevičius, A. Zolotarjovs and M. Korzhik, *Phys. Status Solidi A*, 2018, **215**, 1.

8 E. Auffray, R. Augulis, A. Borisevich, V. Gulbinas, A. Fedorov and M. Korjik, *et al.*, *J. Lumin.*, 2016, **178**, 54.

9 G. Tamulaitis, A. Vasil'ev, M. Korzhik, A. Mazzi, A. Gola, S. Nargelas, A. Vaitkevičius, A. Fedorov and D. Kozlov, *IEEE Trans. Nucl. Sci.*, 2019, **66**, 1879.

10 N. Cherepy, S. Payne, S. Asztalos, G. Hull and J. Kuntz, *et al.*, *IEEE Trans. Nucl. Sci.*, 2009, **56**, 873.

11 Z. Seeley, N. Cherepy and S. Payne, *J. Cryst. Growth*, 2013, **379**, 79.

12 A. Giaz, G. Hull, V. Fossati, N. Cherepy, F. Camera, N. Blasi, S. Brambilla, S. Coelli, B. Million and S. Riboldi, *Nucl. Instrum. Methods Phys. Res., Sect. A*, 2015, **804**, 212.

13 J. D. Kuntz, N. J. Cherepy, J. J. Roberts and S. A. Payne, Phase stable rare earth garnets, *US Pat.*, US8461535B2, 2013.

14 N. Cherepy, S. A. Payne, Z. Seeley, P. C. Cohen, M. S. Andreaco and M. J. Schmand, Transparent ceramic garnet scintillator detector for positron emission tomography, *US Pat.*, 10000698, 2018.

15 K. Kamada, T. Yanagida, J. Pejchal, M. Nikl, T. Endo, K. Tsutumi and A. Yoshikawa, *J. Phys. D: Appl. Phys.*, 2011, **44**(50), 505104.

16 C. Warut, D. Pánek, P. Brůža, W. Chewpraditkul, C. Wanarak, N. Pattanaboonmee, V. Babin, K. Bartosiewicz, K. Kamada, A. Yoshikawa and M. Nikl, *J. Appl. Phys.*, 2014, **116**, 083505.

17 C. Warut, D. Pánek, P. Brůža, W. Chewpraditkul, C. Wanarak, N. Pattanaboonmee, V. Babin, K. Bartosiewicz, K. Kamada, A. Yoshikawa and M. Nikl, *J. Lumin.*, 2016, **169**, 43.

18 D. Solodovnikov, M. H. Weber, D. T. Haven and K. G. Lynn, *J. Cryst. Growth*, 2012, **352**, 99.

19 W. Chewpraditkul, Luminescence and scintillation properties of Mg^{2+}-codoped $Lu_{0.6}Gd_{2.4}Al_2Ga_3O_{12}$:Ce single crystal, Presented at SCINT2019, 29 September – 4 October, 2019, Sendai, Japan.

20 C. Warut, Scintillation characteristics of Mg^{2+}-codoped $Y_{0.8}Gd_{2.2}Al_2Ga_3O_{12}$:Ce single crystal, Presented at SCINT2019, 29 September – 4 October, 2019, Sendai, Japan.

21 Crytur catalogue, https://www.crytur.cz (visited 1.12.2019).

22 Kei Kamada, Takayuki Yanagida, Takanori Endo, Kousuke Tsutumi and Akira Yoshikawa, *J. Cryst. Growth*, 2012, **352**, 88.

23 Fomos crystals web site, https://www.newpiezo.com.

24 O. Sidletskiy, I. Gerasymov, D. Kurtsev and V. Kononets, *et al.*, *CrystEngComm*, 2017, **19**(6), 1001.

25 M. Korzhik, V. Mechinsky, E. Tratsiak, G. Dosovitskiy, P. Sokolov, V. Alenkov, O. Buzanov, A. Fedorov, L. Grigorjeva, A. Zolotarjovs, V. Dormenev, A. Dosovitskiy, D. Agrawal, T. Anniyev, M. Vasilyev and V. Khabashesku, *Cryst. Res. Technol.*, 2019, **54**, 1800172.

26 K. Momma and F. Izumi, VESTA 3 for three-dimensional visualization of crystal, volumetric and morphology data, *J. Appl. Crystallogr.*, 2011, **44**, 1272.

27 M. Lucchini, V. Babin, P. Bohacek, S. Gundacker, K. Kamada, M. Nikl, A. Petrosyan, A. Yoshikawa and E. Auffray, *Nucl. Instrum. Methods Phys. Res., Sect. A*, 2016, **816**, 176.

28 V. Alenkov, O. Buzanov, G. Dosovitskiy, V. Egorychev, A. Fedorov, A. Golutvin, Y. Guz, R. Jacobsson, M. Korjik, D. Kozlov, V. Mechinsky, A. Schopper, A. Semennikov, P. Shatalov and E. Shmanin, *Nucl. Instrum. Methods Phys. Res., Sect. A*, 2019, **916**, 226.

Vilniaus universiteto leidykla
Saulėtekio al. 9, LT-10222 Vilnius
El. p. info@leidykla.vu.lt, www.leidykla.vu.lt
Tiražas 12 egz.